Tools for the study of dynamical spacetimes

Thesis by

Fan Zhang

In Partial Fulfillment of the Requirements

for the Degree of

Doctor of Philosophy

California Institute of Technology

Pasadena, California

2014

(Submitted June 20, 2013)

Acknowledgments

I would like to express my deepest gratitude towards my thesis adviser Mark Scheel, my formal adviser Yanbei Chen, my former formal adviser Kip Thorne, and my unofficial mentor Béla Szilágyi for their guidance, advice and help during my graduate studies. Needless to say, without the time and care they invested in me, my progress towards attaining the PhD degree would not be possible. I would like to also extend the same recognition to Alan Weinstein, who kindly agreed to serve on my thesis committee, and whose professional advice is greatly appreciated. I thank JoAnn Boyd and Shirley Hampton for taking care of numerous administrative issues, and Chris Mach for looking after my workstation.

Words can not do justice to how much I benefited from the wisdom shared by my collaborators in various projects, so I will not try, aside from offering a virtual hug to Emanuele Berti, Jeandrew Brink, Yanbei Chen, Jeffrey D. Kaplan, Lee Lindblom, Geoffrey Lovelace, Keith D. Matthews, David A. Nichols, Robert Owen, Mark A. Scheel, Béla Szilágyi, Tejaswi Venumadhav, Huan Yang, Zhongyang Zhang, Aaron Zimmerman, and Kip S. Thorne. I look forward to future adventures with these top class minds.

Illuminating discussions have also been had with Ernazar Abdikamalov, Luisa Buchman, Sarah Burke-Spolaor, Chad Galley, Roland Haas, Haixing Miao, Philipp Mösta, Samaya Nissanke, Christian Ott, Harald Pfeiffer, Richard Price, Christian Reisswig, Luke Roberts, Ulrich Sperhake, Nick Taylor, Saul Teukolsky, Lingqing Wen, Jeff Winicour, Anil Zenginoglu, and many visitors to Caltech as well as my fellow graduate students and undergraduate students, whom I am compelled to thank.

My research has been supported by NSF grants PHY-0653653, PHY-0601459, PHY-1068881, PHY-1005655, and PHY-0960291, as well as the Sherman Fairchild Foundation and the Brinson Foundation. As a graduate student, I thank these organizations for amongst other things, food and lodging. As a person, I thank them for their vision and contribution to science.

Abstract

This thesis covers a range of topics in numerical and analytical relativity, centered around introducing tools and methodologies for the study of dynamical spacetimes. The scope of the studies is limited to classical (as opposed to quantum) vacuum spacetimes described by Einstein's general theory of relativity. The numerical works presented here are carried out within the Spectral Einstein Code (`SpEC`) infrastructure, while analytical calculations extensively utilize Wolfram's Mathematica program. Each chapter in this thesis essentially comprises a published paper, and some content should be accredited to my collaborators whose names can be found in the highlighted notes at the beginning of each chapter, enumerating the relevant publications. Any mistakes that may arise during transcription is entirely my own. In Chapter 1, there is a short summary of my contributions to each project at the end of the sub-section describing that project.

We begin by examining highly dynamical spacetimes such as binary black hole mergers, which can be investigated using numerical simulations. However, there are difficulties in interpreting the output of such simulations. One difficulty stems from the lack of a canonical coordinate system (henceforth referred to as gauge freedom) and tetrad, against which quantities such as Newman-Penrose Ψ_4 (usually interpreted as the gravitational wave part of curvature) should be measured. We tackle this problem in Chapter 2 by introducing a set of geometrically motivated coordinates that are independent of the simulation gauge choice, as well as a quasi-Kinnersley tetrad, also invariant under gauge changes in addition to being optimally suited to the task of gravitational wave extraction.

Another difficulty arises from the need to condense the overwhelming amount of data generated by the numerical simulations. In order to extract physical information in a succinct and transparent manner, one may define a version of gravitational field lines and field strength using spatial projections of the Weyl curvature tensor. Introduction, investigation and utilization of these quantities will constitute the main content in Chapters 3 through 6.

For the last two chapters, we turn to the analytical study of a simpler dynamical spacetime, namely a perturbed Kerr black hole. We will introduce in Chapter 7 a new analytical approximation to the quasi-normal mode (QNM) frequencies, and relate various properties of these modes to wave packets traveling on unstable photon orbits around the black hole. In Chapter 8, we study a bifurcation in the QNM spectrum as the spin of the black hole approaches extremality.

Contents

List of Figures

List of Tables

Chapter 1

Introduction

Aside from the present introductory chapter, each subsequent chapter in this thesis was originally published as a paper in a peer-reviewed journal. These chapters can be grouped into three projects comprising of Chapter 2, Chapters 3 through 6, and Chapters 7 through 8, respectively. We briefly summarize each project in turn.

1.1 Removing tetrad uncertainty using a quasi-Kinnersley tetrad

In this project we investigate the suitability and properties of a quasi-Kinnersley tetrad and a geometrically motivated coordinate system as tools for quantifying both strong-field and wave-zone effects in numerical relativity (NR) simulations. We fix two of the coordinate degrees of freedom of the metric, namely the radial and latitudinal coordinates, using the Coulomb potential associated with the quasi-Kinnersley transverse frame. These coordinates are invariants of the spacetime and can be used to unambiguously fix the outstanding spin-boost freedom associated with the quasi-Kinnersley frame (and thus can be used to choose a preferred quasi-Kinnersley tetrad).

In the limit of small perturbations about a Kerr spacetime, these geometrically motivated coordinates and quasi-Kinnersley tetrad reduce to Boyer-Lindquist coordinates and the Kinnersley tetrad, irrespective of the simulation gauge choice.

We explore the properties of this construction both analytically and numerically, and we gain insights regarding the propagation of radiation described by a super-Poynting vector, further motivating the use of this construction in NR simulations. We also quantify in detail the peeling properties of the chosen tetrad and gauge. We argue that these choices are particularly well suited for a rapidly converging wave-extraction algorithm as the extraction location approaches infinity, and we explore numerically the extent to which this property remains applicable on the interior of a computational domain.

Using a number of additional tests, we verify numerically that the prescription behaves as required in the appropriate limits regardless of simulation gauge; these tests could also serve to benchmark other wave extraction methods. We explore the behavior of the geometrically motivated coordinate system in dynamical binary-black-hole NR mergers; while we obtain no unexpected results, we do find that these coordinates turn out to be useful for visualizing NR simulations (for example, for vividly illustrating effects such as the initial burst of spurious "junk" radiation passing through the computational domain). Finally, we carefully scrutinize the head-on collision of two black holes and, for example, the way in which the extracted waveform changes as it moves through the computational domain.

I initiated and led this project, as well as carrying out the majority of the analytical and numerical work. My collaborators contributed invaluable expertise in advisory roles in addition to writing certain sections such as the summary of the original peeling property derivation.

1.2 Frame-Drag Vortexes and Tidal Tendexes

Originally published as

Robert Owen, Jeandrew Brink, Yanbei Chen, Jeffrey D. Kaplan, Geoffrey Lovelace, Keith D. Matthews, David A. Nichols, Mark A. Scheel, Fan Zhang, Aaron Zimmerman, Kip S. Thorne

Phys. Rev. Lett, 106, 151101 (2011)

When one foliates spacetime with spacelike hypersurfaces, the Weyl curvature tensor $C_{\alpha\beta\gamma\delta}$ (same as Riemann in vacuum) splits into "electric" and "magnetic" parts $\mathcal{E}_{jk} = C_{\hat{0}j\hat{0}k}$ and $\mathcal{B}_{jk} = \frac{1}{2}\epsilon_{jpq}C^{pq}{}_{k\hat{0}}$ (see e.g. [1] and references therein); both $\mathcal{E}_{jk}$ and $\mathcal{B}_{jk}$ are spatial, symmetric, and trace-free. Here the indices are in the reference frame of "orthogonal observers" who move orthogonal to the space slices; $\hat{0}$ is their time component, ϵ_{jpq} is their spatial Levi-Civita tensor, and throughout we use units with $c = G = 1$.

Because two orthogonal observers separated by a tiny spatial vector $\boldsymbol{\xi}$ experience a relative tidal acceleration $\Delta a_j = -\mathcal{E}_{jk}\xi^k$, $\mathcal{E}_{jk}$ is called the *tidal field*. And because a gyroscope at the tip of $\boldsymbol{\xi}$ precesses due to frame dragging with an angular velocity $\Delta\Omega_j = \mathcal{B}_{jk}\xi^k$ relative to inertial frames at the tail of $\boldsymbol{\xi}$, we call $\mathcal{B}_{jk}$ the *frame-drag field*.

For a binary black hole, our space slices intersect the 3-dimensional (3D) event horizon in a 2D horizon with inward unit normal $\mathbf{N}$; so $\mathcal{B}_{NN}$ is the rate the frame-drag angular velocity around $\mathbf{N}$ increases as one moves inward through the horizon. Because of the connection between rotation and vorticity, we call $\mathcal{B}_{NN}$ the horizon's *frame-drag vorticity*, or simply its *vorticity*.

Because $\mathcal{B}_{NN}$ is boost-invariant along $\mathbf{N}$ [2], the horizon's vorticity is independent of how fast the orthogonal observers fall through the horizon, and is even unchanged if the observers hover immediately above the horizon (the FIDOs of the "black-hole membrane paradigm" [3]).

Figure 1.1 shows snapshots of the horizon for two identical black holes with transverse, oppositely directed spins $\mathbf{S}$, colliding head on. Before the collision, each horizon has a negative-vorticity region

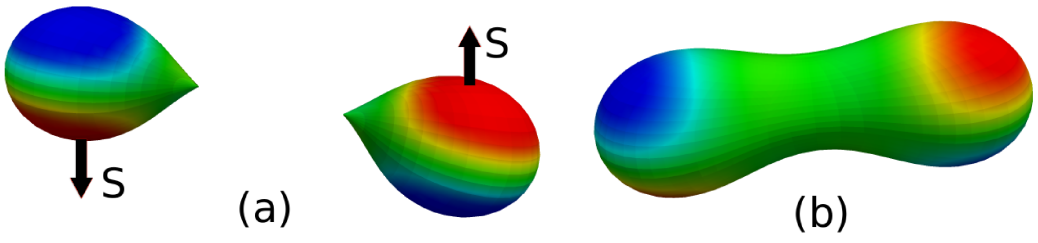

Figure 1.1: Vortexes (with positive vorticity blue, negative vorticity red) on the 2D event horizons of spinning, colliding black holes, just before and just after merger. (From the simulation reported in [4].)

(red) centered on **S**, and a positive-vorticity region (blue) on the other side. We call these regions of concentrated vorticity *horizon vortexes*. Our numerical simulation [4] shows the four vortexes being transferred to the merged horizon (Fig. 1.1b), then retaining their identities, but sloshing between positive and negative vorticity and gradually dying, as the hole settles into its final Schwarzschild state; see the movie in Ref. [5].

Because $\mathcal{E}_{NN}$ measures the strength of the tidal-stretching acceleration felt by orthogonal observers as they fall through (or hover above) the horizon, we call it the horizon's *tendicity* (a word coined by David Nichols from the Latin *tendere*, "to stretch"). On the two ends of the merged horizon in Fig. 1.1b there are regions of strongly enhanced tendicity, called *tendexes*; cf. Fig. 1.5 below.

An orthogonal observer falling through the horizon carries an orthonormal tetrad consisting of her 4-velocity **U**, the horizon's inward normal **N**, and transverse vectors $\mathbf{e_2}$ and $\mathbf{e_3}$. In the null tetrad $\mathbf{l} = (\mathbf{U} - \mathbf{N})/\sqrt{2}$ (tangent to horizon generators), $\mathbf{n} = (\mathbf{U} + \mathbf{N})/\sqrt{2}$, $\mathbf{m} = (\mathbf{e_2} + i\mathbf{e_3})/\sqrt{2}$, and $\mathbf{m}^*$, the Newman-Penrose Weyl scalar Ψ_2 [6] is $\Psi_2 = (\mathcal{E}_{NN} + i\mathcal{B}_{NN})/2$. Here we use sign conventions of [7], appropriate for our (- +++) signature.

Penrose and Rindler [8] define a complex scalar curvature $\mathcal{K} = \mathcal{R}/4 + i\mathcal{X}/4$ of the 2D horizon, with $\mathcal{R}$ its intrinsic (Ricci) scalar curvature (which characterizes the horizon's shape) and $\mathcal{X}$ proportional to the 2D curl of its Hájíček field [9] (the space-time part of the 3D horizon's extrinsic curvature). Penrose and Rindler show that $\mathcal{K} = -\Psi_2 + \mu\rho - \lambda\sigma$, where ρ, σ, μ, and λ are spin coefficients related to the expansion and shear of the null vectors **l** and **n**, respectively. In the limit of a shear- and expansion-free horizon (e.g. a quiescent black hole; Fig. 1.2a,b,c), $\mu\rho - \lambda\sigma$ vanishes, so $\mathcal{K} = -\Psi_2$, whence $\mathcal{R} = -2\mathcal{E}_{NN}$ and $\mathcal{X} = -2\mathcal{B}_{NN}$. As the dimensionless spin parameter a/M of a quiescent (Kerr) black hole is increased, the scalar curvature $\mathcal{R} = -2\mathcal{E}_{NN}$ at its poles decreases, becoming negative for $a/M > \sqrt{3}/2$; see the blue spots on the poles in Fig. 1.2b compared to solid red for the nonrotating hole in Fig. 1.2a. In our binary-black-hole simulations, the contributions of the spin coefficients to $\mathcal{K}$ on the apparent horizons are small [$L2$-norm $\lesssim 1\%$] so $\mathcal{R} \simeq -2\mathcal{E}_{NN}$ and $\mathcal{X} \simeq -2\mathcal{B}_{NN}$, except for a time interval $\sim 5M_{\rm tot}$ near merger. Here $M_{\rm tot}$ is the binary's total mass. On the event horizon, the duration of spin-coefficient contributions $> 1\%$ is somewhat longer, but we do not yet have a good measure of it.

Because $\mathcal{X}$ is the 2D curl of a 2D vector, its integral over the 2D horizon vanishes. Therefore, positive-vorticity regions must be balanced by negative-vorticity regions; it is impossible to have a horizon with just one vortex. By contrast, the Gauss-Bonnet theorem says the integral of $\mathcal{R}$ over the 2D horizon is 8π (assuming S_2 topology), which implies the horizon tendicity $\mathcal{E}_{NN}$ is predominantly negative (because $\mathcal{E}_{NN} \simeq -\mathcal{R}/2$ and $\mathcal{R}$ is predominantly positive). Many black holes have negative horizon tendicity everywhere (an exception is Fig. 1.2b), so their horizon tendexes must be distinguished by deviations of $\mathcal{E}_{NN}$ from a horizon-averaged value.

The frame-drag field $\mathcal{B}_{jk}$ is symmetric and trace free and therefore is fully characterized by its three orthonormal eigenvectors $\mathbf{e}_{\tilde{j}}$ and their eigenvalues $\mathcal{B}_{\tilde{1}\tilde{1}}$, $\mathcal{B}_{\tilde{2}\tilde{2}}$ and $\mathcal{B}_{\tilde{3}\tilde{3}}$. We call the integral curves along $\mathbf{e}_{\tilde{j}}$ *vortex lines*, and their eigenvalue $\mathcal{B}_{\tilde{j}\tilde{j}}$ those lines' *vorticity*, and we call a concentration of vortex lines with large vorticity a *vortex*. For the tidal field $\mathcal{E}_{jk}$ the analogous quantities are *tendex lines*, *tendicity* and *tendexes*. For a nonrotating (Schwarzschild) black hole, we show a few tendex lines in Fig. 1.2a; and for a rapidly-spinning black hole (Kerr metric with $a/M = 0.95$) we show tendex lines in Fig. 1.2b and vortex lines in Fig. 1.2c.

If a person's body (with length ℓ) is oriented along a positive-tendicity tendex line (blue in Fig. 1.2a), she feels a head-to-foot compressional acceleration $\Delta a = |\text{tendicity}|\ell$; for negative tendicity (red) it is a stretch. If her body is oriented along a positive-vorticity vortex line (blue in Fig. 1.2c), her head sees a gyroscope at her feet precess clockwise with angular speed $\Delta\Omega = |\text{vorticity}|\ell$, and her feet see a gyroscope at her head also precess clockwise at the same rate. For negative vorticity (red) the precessions are counterclockwise.

For a nonrotating black hole, the stretching tendex lines are radial, and the squeezing ones lie on spheres (Fig. 1.2a). When the hole is spun up to $a/M = 0.95$ (Fig. 1.2b), its toroidal tendex lines acquire a spiral, and its poloidal tendex lines, when emerging from one polar region, return to the other polar region. For any spinning Kerr hole (e.g. Fig. 1.2c), the vortex lines from each polar region reach around the hole and return to the same region. The red vortex lines from the red north polar region constitute a *counterclockwise vortex*: the blue ones from the south polar region constitute a *clockwise vortex*.

As a dynamical example, consider a Schwarzschild black hole's fundamental odd-parity $l = m = 2$ quasinormal mode of pulsation, which is governed by Regge-Wheeler perturbation theory [10] and has angular eigenfrequency $\omega = (0.74734 - 0.17792i)/2M$, with M the hole's mass. From the perturbation equations, we have deduced the mode's horizon vorticity: $\mathcal{B}_{NN} = \Re\{9\sin^2\theta/(2i\omega M^3)\exp[2i\phi - i\omega(\tilde{t} + 2M)]\}$. (Here $\tilde{t}$ is the ingoing Eddington-Finklestein time coordinate, and the mode's Regge-Wheeler radial eigenfunction $Q(r)$ is normalized to unity near the horizon.) At time $\tilde{t} = 0$, this $\mathcal{B}_{NN}$ exhibits four horizon vortexes [red and blue in Fig. 1.2d], centered on the equator at $(\theta, \phi) = (\pi/2, 1.159 + k\pi/2)$ $(k = 0, 1, 2, 3)$, and with central vorticities $\mathcal{B}_{NN} = -(-1)^k 39.22/(2M)^2$. From analytic formulae for $\mathcal{B}_{jk}$ and a numerical $Q(r)$, we have deduced the equatorial-plane red vortex lines and vorticities shown in Fig. 1.2d. As time $\tilde{t}$ passes, the vortexes rotate counterclockwise, so they resemble water splayed out from a turning sprinkler. The transition from near zone to wave zone is at $r \sim 4M$ (near the outermost part of the second contour line). As one moves into the wave zone, each of the red vortexes is smoothly transformed into a gravitational-wave trough and the 3D vortexes that emerge from the blue horizon vortexes (concentrated in the dark region of this figure) are transformed into gravitational-wave crests.

We have explored the evolution of frame-drag vortexes and tidal tendexes in numerical simula-

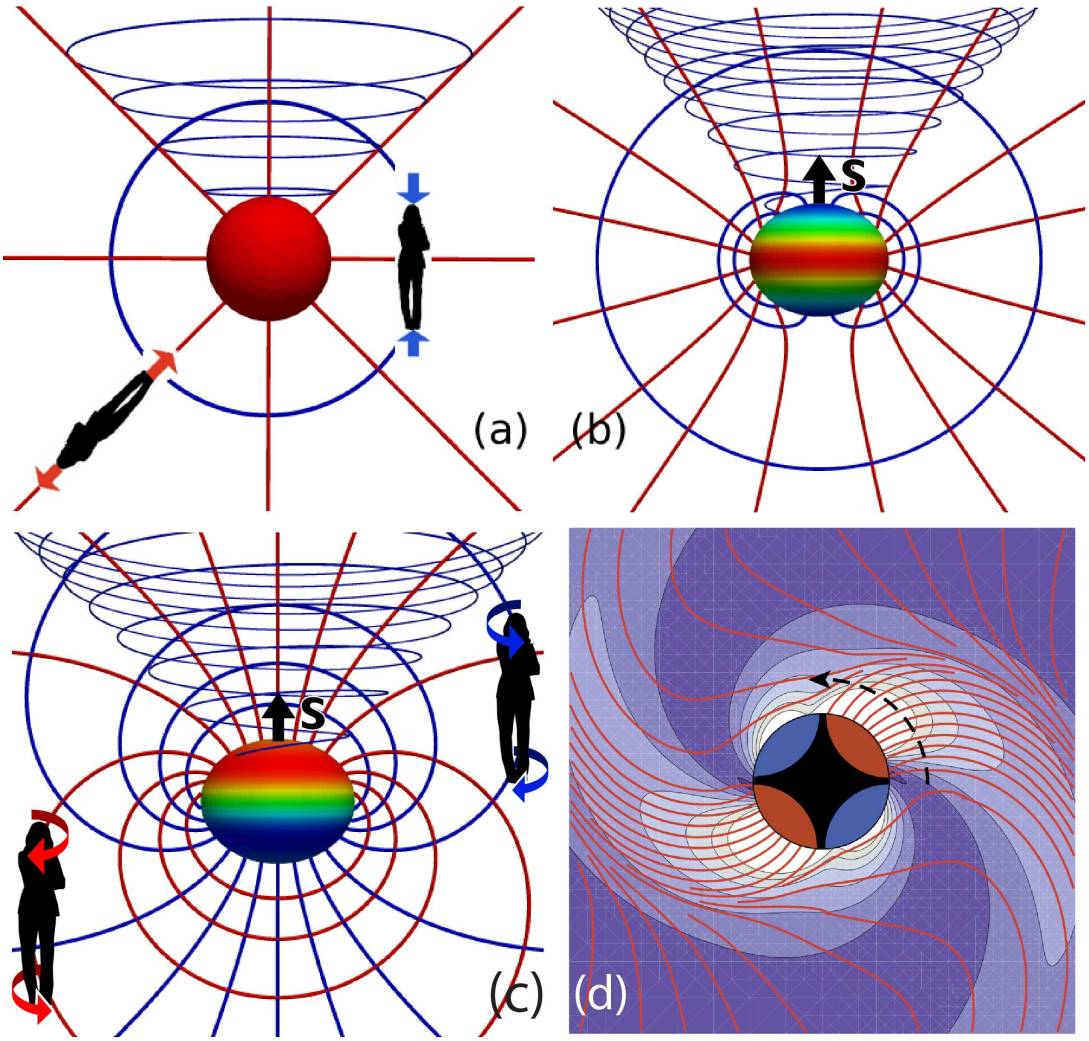

Figure 1.2: Four different black holes, with horizons colored by their tendicity (upper two panels) or vorticity (lower two panels), ranging from most negative (red) to most positive (blue); and with a Kerr-Schild horizon-penetrating foliation (Exercise 33.8 of Ref. [18]). (a) A nonrotating black hole and its tendex lines; negative-tendicity lines are red, and positive blue. (b) A rapidly rotating (Kerr) black hole, with spin $a/M = 0.95$, and its tendex lines. (c) The same Kerr black hole and its vortex lines. (d) Equatorial plane of a nonrotating black hole that is oscillating in an odd-parity $l = m = 2$ quasinormal mode, with negative-vorticity vortex lines emerging from red horizon vortexes. The lines' vorticities are indicated by contours and colors; the contour lines, in units $(2M)^{-2}$ and going outward from the hole, are -10, -8, -6, -4, -2.

tions of three BBHs that differ greatly from each other.

Our first simulation (documented in Ref. [4]; movies in Ref. [5]) is the head-on, transverse-spin merger depicted in Fig. 1.1 above, with spin magnitudes $a/M = 0.5$. As the holes approach each other then merge, their 3D vortex lines, which originally link a horizon vortex to itself on a single hole (Fig. 1.2c), reconnect so on the merged hole they link one horizon vortex to the other of the same polarity (Fig. 1.3a). After merger, the near-zone 3D vortexes slosh (their vorticity oscillates between positive and negative), generating vortex loops (Fig. 1.3b) that travel outward as gravitational waves.

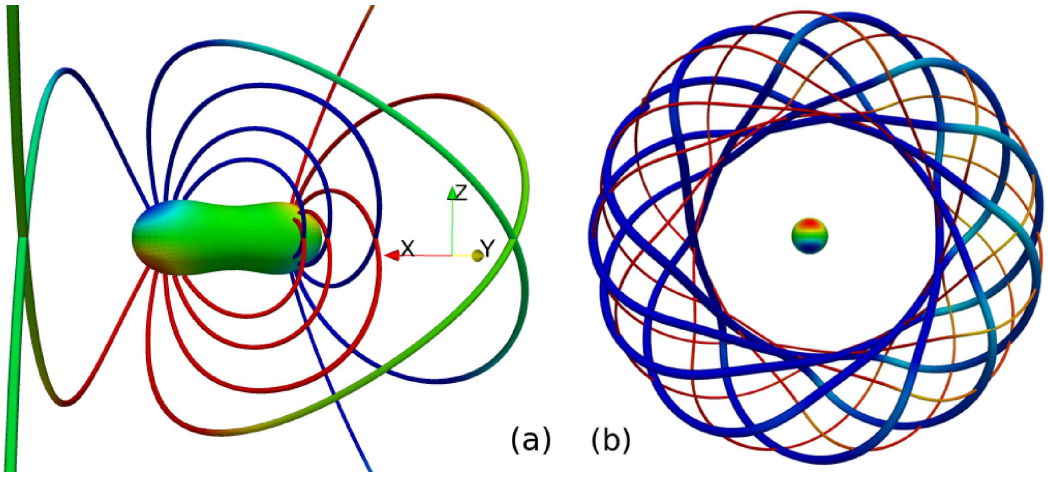

Figure 1.3: Head-on, transverse-spin simulation: (a) Shortly after merger, vortex lines link horizon vortexes of same polarity (red to red; blue to blue). Lines are color coded by vorticity (different scale from horizon). (b) Sloshing of near-zone vortexes generates vortex loops traveling outward as gravitational waves; thick and thin lines are orthogonal vortex lines.

Our second simulation (documented in Ref. [11]; movies in Ref. [12]) is the inspiral and merger of two identical, fast-spinning holes ($a/M = 0.95$) with spins antialigned to the orbital angular momentum. Figure 1.4 shows the evolution of the vorticity $\mathcal{B}_{NN}$ on the common apparent horizon beginning just after merger (at time $t/M_{\rm tot} = 3483$), as seen in a frame that co-rotates with the small horizon vortexes. In that frame, the small vortexes (which arise from the initial holes' spins) appear to diffuse into the two large central vortexes (which arise from the initial holes' orbital angular momentum), annihilating some of their vorticity. (This is similar to the diffusion and annihilation of magnetic field lines with opposite polarity threading a horizon [3].) Making this heuristic description quantitative, or disproving it, is an important challenge.

Our third simulation (see movies in Ref. [13]) is a variant of the "extreme-kick" merger studied by Campanelli et al. [14] and others [15, 16]: two identical holes, merging from an initially circular orbit, with oppositely directed spins $a/M = 0.5$ lying in the orbital (x, y) plane. In this case, the vortexes and tendexes in the merged hole's (x, y) plane rotate as shown in Fig. 1.2d. We have tuned the initial conditions to make the final hole's kick (nearly) maximal, in the $+z$ direction. The following considerations explain the origin of this maximized kick:

In a plane gravitational wave, all the vortex and tendex lines with nonzero eigenvalues lie in the wave fronts and make angles of 45 degrees to each other (bottom inset of Fig. 1.5.) For vectors $\boldsymbol{E}$ (parallel to solid, positive-tendicity tendex line) and $\boldsymbol{B}$ (parallel to dashed, positive-vorticity vortex line), $\boldsymbol{E} \times \boldsymbol{B}$ is in the wave's propagation direction.

Now, during and after merger, the black hole's near-zone rotating tendex lines (top left inset in Fig. 1.5) acquire accompanying vortex lines as they travel outward into the wave zone and become gravitational waves; and the rotating near-zone vortex lines acquire accompanying tendex lines.

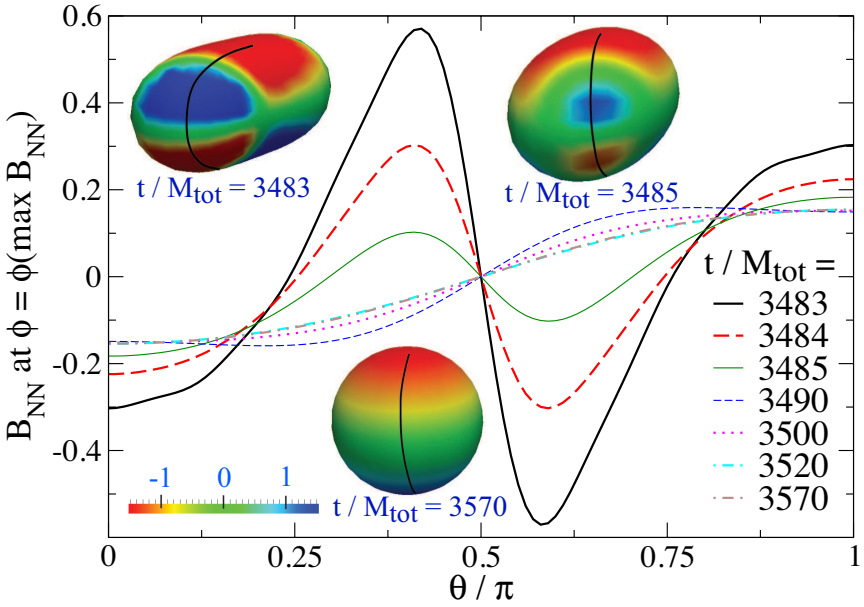

Figure 1.4: Insets: snapshots of the common apparent horizon for the $a/M = 0.95$ anti-aligned simulation, color coded with the horizon vorticity B_{NN}. Graphs: B_{NN} as a function of polar angle θ at the azimuthal angle ϕ that bisects the four vortexes (along the black curves in snapshots).

Because of the evolution-equation duality between $\mathcal{E}_{ij}$ and $\mathcal{B}_{ij}$, the details of this wave formation are essentially the same for the rotating tendex and vortex lines. Now, in the near zone, the vectors $\boldsymbol{E}$ and $\boldsymbol{B}$ along the tendex and vortex lines (Fig. 1.5) make the same angle with respect to each other as in a gravitational wave (45 degrees) and have $\boldsymbol{E} \times \boldsymbol{B}$ in the $-z$ direction. This means that the gravitational waves produced by the rotating near-zone tendex lines and those produced by the rotating near-zone vortex lines will superpose constructively in the $-z$ direction and destructively in the $+z$ direction, leading to a maximized gravitational-wave momentum flow in the $-z$ direction and maximized black-hole kick in the $+z$ direction. An extension of this reasoning shows that the black-hole kick velocity is sinusoidal in twice the angle between the merged hole's near-zone rotating vortexes and tendexes, in accord with simulations.

In our BBH simulations, the nonlinear dynamics of curved spacetime appears to be dominated by (i) the transfer of spin-induced frame-drag vortexes from the initial holes to the final merged hole, (ii) the creation of two large vortexes on the merged hole associated with the orbital angular momentum, (iii) the subsequent sloshing, diffusion, and/or rotational motion of the spin-induced vortexes, (iv) the formation of strong negative $\mathcal{E}_{NN}$ poloidal tendexes on the merged horizon at the locations of the original two holes, associated with the horizon's elongation, and a positive $\mathcal{E}_{NN}$ tendex at the neck where merger occurs, and (v) the oscillation, diffusion, and/or circulatory motion of these tendexes.

We *conjecture* that there is no other important dynamics in the merger and ringdown of BBHs. If

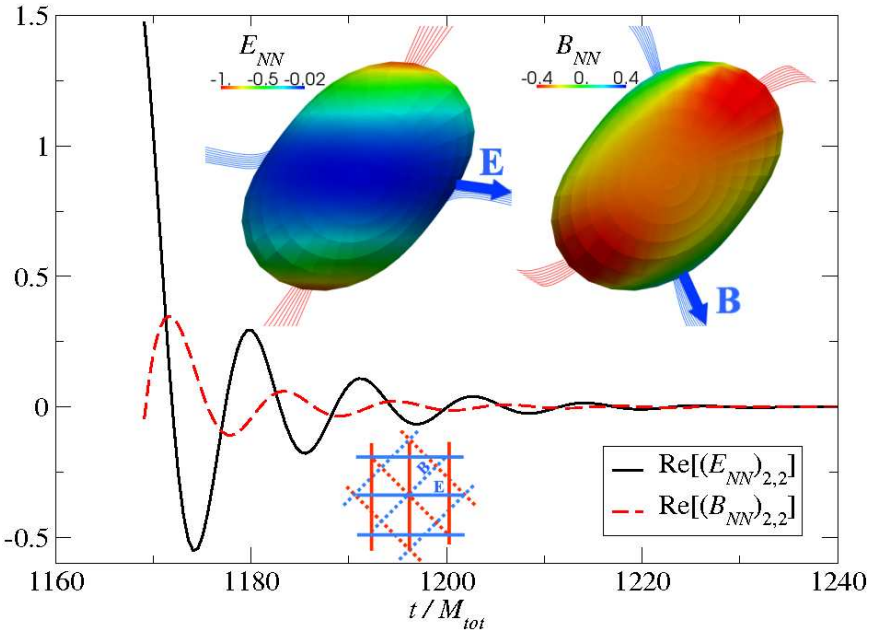

Figure 1.5: Bottom inset: tendex and vortex lines for a plane gravitational wave; $\boldsymbol{E} \times \boldsymbol{B}$ is in the propagation direction. Upper two insets: for the "extreme-kick simulation", as seen looking down the merged hole's rotation axis ($-z$ direction): the apparent horizon color coded with the horizon tendicity (left inset) and vorticity (right inset), and with 3D vortex lines and tendex lines emerging from the horizon. The tendexes with the most positive tendicity (blue; $\boldsymbol{E}$) lead the positive-vorticity vortexes (blue, $\boldsymbol{B}$) by about 45° as they rotate counterclockwise. This 45° lead is verified in the oscillating curves, which show the rotating $\mathcal{B}_{NN}$ and $\mathcal{E}_{NN}$ projected onto a nonrotating $\ell = 2$, $m = 2$ spherical harmonic.

so, there are important consequences: (i) This could account for the surprising simplicity of the BBH gravitational waveforms predicted by simulations. (ii) A systematic study of frame-drag vortexes and tidal tendexes in BBH simulations may produce improved understanding of BBHs, including their waveforms and kicks. The new waveform insights may lead to improved functional forms for waveforms that are tuned via simulations to serve as templates in LIGO/VIRGO data analysis. (iii) Approximation techniques that aim to smoothly cover the full spacetime of BBH mergers (e.g. the combined Post-Newtonian and black-hole-perturbation theory method [17]) might be made to capture accurately the structure and dynamics of frame-drag vortexes and tidal tendexes. If so, these approximations may become powerful and accurate tools for generating BBH waveforms.

Within this project, my role includes numerically investigating the tendex and vortex lines using a streamline integration code (credit goes to Keith Matthews, with limited maintainance work done by myself), generating the majority of the paraview (non-mathematica) figures in Chapters 3 through 6. Other numerical work include making the necessary improvements to the numerical infrastructure to enable description of high spin Kerr black holes in different slicings as well as different spatial coordinates, which constitutes a large part of Chapter 5. I am also an integral part of the team building up the physical pictures using the new tools introduced in this project, for

example I discovered the torus in Fig. 1.3 which is further investigated in Chapter 6 (mostly by my collaborators); constructed the matrix representation of the plane gravitational waves in Chapter 3 that forms the technological basis for Chapter 4, as well as establishing the tetrad independence of the conclusions of that Chapter; formulated the picture that the tendex and vortex lines track multipoles in the near zone but contain the same information in the wave zone, so the inductive mixing in the transition zone represents wave generation, whose details are under ongoing investigation. There are various other odd analytical contributions such as providing an initial proof of the conservation of $\mathcal{B}_{NN}$.

Bibliography

[1] R. Maartens and B. A. Bassett, Class. Quantum Grav. **15**, 705 (1998).

[2] R. H. Price and K. S. Thorne, Phys. Rev. D **33**, 330915 (1986).

[3] K. S. Thorne, R. H. Price, and D. A. MacDonald, *Black Holes: The Membrane Paradigm* (Yale University Press, New Haven and London, 1986).

[4] G. Lovelace, Y. Chen, M. Cohen, J. D. Kaplan, D. Keppel, K. D. Matthews, D. A. Nichols, M. A. Scheel, and U. Sperhake, Phys. Rev. D **82**, 064031 (2010).

[5] `http://www.black-holes.org/headon05aa.html`.

[6] E. Newman and R. Penrose, Journal of Mathematical Physics **3**, 566 (1962).

[7] V. P. Frolov and I. D. Novikov, *Black Hole Physics: Basic Concepts and New Developments* (Kluwer, 1998).

[8] R. Penrose and W. Rindler, *Spinors and Space-time, Volume 1* (Cambridge University Press, Cambridge, 1992).

[9] T. Damour, in *Proceedings of the Second Marcel Grossman Meeting on General Relativity*, edited by R. Ruffini (North-Holland Publishing Company, Amsterdam, 1982), pp. 587–606.

[10] S. Chandrasekhar and S. Detweiler, Proc. R. Soc. A **344**, 441 (1975).

[11] G. Lovelace, M. A. Scheel, and B. Szilagyi, Phys. Rev. D **83**, 024010 (2011), `arXiv:1010.2777`.

[12] `http://www.black-holes.org/inspiral95aa.html`.

[13] `http://www.black-holes.org/extreme-kick.html`.

[14] M. Campanelli, C. O. Lousto, Y. Zlochower, and D. Merritt, Phys. Rev. Lett. **98**, 231102 (2007), `gr-qc/0702133`.

[15] J. A. Gonzalez, M. D. Hannam, U. Sperhake, B. Brügmann, and S. Husa, Phys. Rev. Lett. **98**, 231101 (2007), `gr-qc/0702052`.

[16] C. O. Lousto and Y. Zlochower, Phys. Rev. D. **83**, 024003 (2011), arXiv:1011.0593.

[17] D. A. Nichols and Y. Chen, Phys. Rev. D **82**, 104020 (2010).

[18] C. W. Misner, K. S. Thorne, and J. A. Wheeler, *Gravitation* (Freeman, New York, New York, 1973).

[19] http://www.black-holes.org/SpEC.html.

1.3 Calculation and investigation of the quasinormal-modes of Kerr black holes

There is a well-known, intuitive geometric correspondence between high-frequency quasinormal modes of Schwarzschild black holes and null geodesics that reside on the light-ring (often called spherical photon orbits): the real part of the mode's frequency relates to the geodesic's orbital frequency, and the imaginary part of the frequency corresponds to the Lyapunov exponent of the orbit.

For slowly rotating black holes, the quasinormal-mode's real frequency is a linear combination of a the orbit's precessional and orbital frequencies, but the correspondence is otherwise unchanged.

In Chapter 7, we find a relationship between the quasinormal-mode frequencies of Kerr black holes of arbitrary (astrophysical) spins and general spherical photon orbits, which is analogous to the relationship for slowly rotating holes.

To derive this result, we first use the WKB approximation to compute accurate algebraic expressions for large-l quasinormal-mode frequencies. Comparing our WKB calculation to the leading-order, geometric-optics approximation to scalar-wave propagation in the Kerr spacetime, we then draw a correspondence between the real parts of the parameters of a quasinormal mode and the conserved quantities of spherical photon orbits. At next-to-leading order in this comparison, we relate the imaginary parts of the quasinormal-mode parameters to coefficients that modify the amplitude of the scalar wave.

With this correspondence, we find a geometric interpretation to two features of the quasinormal-mode spectrum of Kerr black holes: First, for Kerr holes rotating near the maximal rate, a large number of modes have nearly zero damping; we connect this characteristic to the fact that a large number of spherical photon orbits approach the horizon in this limit. Second, for black holes of any spins, the frequencies of specific sets of modes are degenerate; we find that this feature arises when the spherical photon orbits corresponding to these modes form closed (as opposed to ergodically winding) curves.

In Chapter 8, we show that nearly extremal Kerr black holes have two distinct sets of quasinormal modes, which we call zero-damping modes (ZDMs) and damped modes (DMs). The ZDMs exist for all harmonic indices l and $m \geq 0$, and their frequencies cluster onto the real axis in the extremal limit. The DMs have nonzero damping for all black hole spins; they exist for all counterrotating modes ($m < 0$) and for corotating modes with $0 \leq \mu \lesssim \mu_c = 0.74$ (in the eikonal limit), where $\mu \equiv m/(l + 1/2)$. When the two families coexist, ZDMs and DMs merge to form a single set of quasinormal modes as the black hole spin decreases. Using the effective potential for perturbations of the Kerr spacetime, we give intuitive explanations for the absence of DMs in certain areas of the spectrum and for the branching of the spectrum into ZDMs and DMs at large spins.

My contribution to this project concentrates in specific subsections of the two chapters. In Chapter 7, I wrote sections 7.3.2, 7.4.3 and part of 7.4.1, as well the somewhat extensive mathematica codes used to generate Fig. 7.15. For Chapter 8, I optimized the mathematica functions originally written by my collaborators and introduced additional approximations to reach the required computational speed for generating the main phase diagram Fig. 8.1 of the paper. I also disambiguated the confusion of whether null and timelike circular orbits are actually stuck on the event horizon, an important point for understanding the lack of decay for the zero damping modes.

Chapter 2

Removing tetrad uncertainty using a quasi-Kinnersley tetrad

Originally published as
Fan Zhang, Jeandrew Brink, Béla Szilágyi, and Geoffrey Lovelace,
Phys. Rev. D 86, 084020 (2012)

2.1 Introduction

Numerical relativity (NR) has made great strides in recent years and is now able to explore binary black hole, black hole - neutron star, and neutron star - neutron star mergers in a wide variety of configurations (see [1, 2] for recent reviews). Numerical simulations are crucial tools for calibrating and validating the large template bank of analytic, phenomenological waveforms that will be used to search for gravitational waves in data from detectors such as the Laser Interferometer Gravitational-Wave Observatory (LIGO) [3, 4], Virgo [5] and the Large-scale Cryogenic Gravitational-wave Telescope (LCGT) [6]. Numerical simulations also make it possible, for the first time, to explore fully dynamical spacetimes in the strong field region, such as the spacetime of a compact-binary merger.

An important attribute of any analysis performed on numerical simulations is the ability to extract information in a manner independent of the gauge in which one chooses to perform the simulation. In this paper, we suggest one such strategy: using a quasi-Kinnersley tetrad adapted to a choice of coordinates that are computed using the curvature invariants of the spacetime. Most calculations presented in this paper are local, allowing our tetrad and choice of geometrically motivated coordinates (and all quantities derived from them) to be computed in real time during a numerical simulation (i.e. without post-processing). The proposed scheme is also applicable throughout the spacetime, allowing us to study phenomena in both the strongly curved and asymptotic flat regions

with the same tools.

In order to extract the 6 physical degrees of freedom of a general Lorentzian metric in four dimensions expressed in terms of a tetrad formulation, 10 degrees of freedom have to be specified.Of these 10 degrees of freedom, 6 are associated with the tetrad at a particular point on the spacetime manifold and 4 originate from the freedom to label that point (the choice of gauge). A common choice of tetrad and the one adopted here is the Newman-Penrose (NP) null tetrad, which consists of two real null vectors denoted $\boldsymbol{l}$ and $\boldsymbol{n}$ as well as a complex conjugate pair of null vectors $\boldsymbol{m}$ and $\overline{\boldsymbol{m}}$. As we demonstrate explicitly in Sec. 2.2, where we consider the mathematical details in greater depth, the tetrad choice is not unique. The freedom to orient and scale the tetrad is expressed by 6 parameters associated with a general Lorentz transformation between two different null tetrads at a fixed point in the spacetime.

In order to extract physically meaningful quantities and to compare results from different simulations and numerical codes, an explicit prescription for the tetrad choice must be made. Two geometrically motivated prescriptions for orientating the tetrad immediately suggest themselves: choosing i) the principle null frame (PNF) or ii) the transverse frame (TF). (By "frame", we mean a set of tetrads related by a Type III transformation [Sec. 2.2.3].) The relationship between these two frames and their properties are discussed in greater detail in Secs. 2.2 and 2.3; either one of these two choices immediately removes 4 of the 6 possible tetrad degrees of freedom. The remaining 2 degrees of freedom in the tetrad choice are more subtle [see the discussion in Sec. 2.3.3].

The procedure we adopt in this paper is to choose a special transverse tetrad that becomes the Kinnersley tetrad [7] in Type-D spacetimes. The properties of these tetrads (known as quasi-Kinnersley tetrads, or QKTs) and their importance for NR have previously been explored in detail [8, 9, 10, 11, 12, 13]. Part of the motivation for choosing a QKT is implicit in Chandrasekhar's work on the gravitational perturbations of the Kerr black hole [14]: in this work, he showed that for a given perturbation of the Kerr metric (expressed in terms of the Weyl scalar $\delta\Psi_4$) it is always possible, working to linear order, to find a transverse tetrad and a gauge constructed from the Coulomb potential associated with this tetrad such that the Coulomb potential of the perturbed and background metrics are the same.

We revisit these ideas in Sec. 2.3, where we investigate the properties of the quasi-Kinnersley tetrad choice. We concentrate on the implications of the intrinsic geometrical properties of the tetrad, rather than (as previous works have done) focusing on the tetrad's properties in a perturbative limit. For example, we explore the directions of energy flow using the super-Poynting vector, showing that the choice of a QKT naturally aligns the tetrad with the wave-fronts of passing radiation. This observation suggests that, *even in the strong field regime*, the QKT is a natural, geometrically motivated tetrad choice for observing the flow of radiation and other spacetime dynamics.

After specializing to the transverse frame there exist two remaining degrees of tetrad freedom:

the freedom of the spin-boost transformations. We fix this remaining tetrad freedom by relying on a straightforward extension of Chandrasekhar's work [14] to the strong field regime. We present the mathematical details in Secs. 2.3.4 and 2.3.5: specifically, we use the Coulomb potential $\hat{\Psi}_2$ on the QKT to introduce a pair of geometrically motivated radial and latitudinal coordinates. Note that $\hat{\Psi}_2$ on the transverse frame is spin-boost independent, that the resulting coordinates can be constructed from the curvature invariants I and J only, and that these coordinates reduce to the Boyer-Lindquist radial and latitudinal coordinates for Kerr spacetimes. We then use these geometrically motivated coordinates to fix the spin-boost freedom by ensuring that the projection of the tetrad base vectors onto the gradients of the new coordinates obey the relations found for the Kinnersley tetrad in the Kerr limit.

One application of our chosen QKT and geometrically motivated coordinates is gravitational-wave extraction. For isolated, gravitating systems, gravitational radiation is only strictly defined at future null infinity; this is a consequence of the so-called "peeling property" that governs the behavior of the Weyl curvature scalars as measured on an affinely parametrized out-going geodesic. With the goal of using our tetrad and gauge prescription as a possible wave extraction method, we work out the implications that this peeling property has for the Weyl curvature scalar expressed on the QKT in Sec. 2.3.8. We highlight not only the falloff behavior of the QKT Newman-Penrose quantities but also the behavior of the geometrically constructed radial coordinate. We explore graphically some of the implications of the peeling property for the bunching of principle null directions and argue that the directions associated with QKT are the optimal out-going directions for ensuring rapid convergence of the computed radiation quantities to the correct asymptotic results.

We implement our geometrically motivated coordinates and QKT numerically within the context of a pseudospectral NR code in Sec. 2.4, and we present a number of numerical simulations demonstrating the behavior of our coordinates and QKT in Sec. 2.5. First, we carry out, for both non-radiative and radiative spacetimes, a few checks to verify that our scheme works correctly regardless of the choice of gauge in the simulation [Secs. 2.5.1 and 2.5.2, respectively]. We confirm that we obtain numerically the correct perturbation-theory results, and we suggest that these tests could be used to benchmark other wave-extraction algorithms.

Finally, we examine the application of the QKT scheme to NR simulations of binary-black-hole collisions in Sec. 2.6, considering both the wave zone and the strong field regions. We consider a 16 orbit, equal-mass binary-black-hole in-spiral and a head-on plunge, merger, and ringdown, explicitly illustrating many of the ideas in the theoretical discussions of the previous sections. We then briefly conclude with a discussion of our results and of prospects for the further development of our proposed scheme in Sec. 2.7.

2.2 Mathematical Preliminaries

In this section, we briefly summarize some important properties of Newman-Penrose and orthonormal tetrads [Sec. 2.2.1], the Weyl curvature tensor [Sec. 2.2.2], the Lorentz transformations of the Newman-Penrose tetrad [Sec. 2.2.3], and the Kinnersley tetrad in Kerr spacetime [Sec. 2.2.4]. Note that here and throughout this paper, letters from the front part of the Latin alphabet are used for four dimensional coordinate bases, those from the middle part of the Latin alphabet denotes quantities in three dimensional coordinate bases, while Greek indices are used for tetrad bases. Bold-face fonts denote vectors and tensors.

2.2.1 Newman-Penrose and orthonormal tetrads

Two types of tetrad basis are particularly useful for the exploration of generic spacetimes, such as the spacetimes of numerical-relativity simulations of compact-binary mergers: i) the Newman-Penrose (NP) tetrad basis $\{e_a^\alpha\} = \{l_a, n_a, m_a, \overline{m}_a\}$, and ii) an orthonormal tetrad $\{E_a^\alpha\} = \{T_a, E_a^2, E_a^3, N_a\}$, which is closely related to the NP tetrad as follows. The quantities $\boldsymbol{E^2}$ and $\boldsymbol{E^3}$ are generally associated with angular variables on a closed 2-surface and are related to the complex null vector $\boldsymbol{m}$ by $E_a^2 = \sqrt{2}\Re(m_a)$, $E_a^3 = \sqrt{2}\Im(m_a)$. Here $\Re(\boldsymbol{m})$ and $\Im(\boldsymbol{m})$ denote the real and imaginary parts of $\boldsymbol{m}$, respectively. The timelike vector $\boldsymbol{T}$ and spacelike vector $\boldsymbol{N}$ are related to the null vectors $\boldsymbol{l}$ and $\boldsymbol{n}$ by the transformations

$$l^a = \frac{1}{\sqrt{2}}(T^a + N^a), \qquad\qquad n^a = \frac{1}{\sqrt{2}}(T^a - N^a). \tag{2.1}$$

The metric expressed on the orthonormal basis is the Minkowski metric, $\gamma^{\alpha\beta} = \mathrm{diag}\{-1, 1, 1, 1\}$, while on the NP tetrad basis the metric is

$$\eta^{\alpha\beta} = \begin{pmatrix} 0 & -1 & 0 & 0 \\ -1 & 0 & 0 & 0 \\ 0 & 0 & 0 & 1 \\ 0 & 0 & 1 & 0 \end{pmatrix}. \tag{2.2}$$

On the coordinate basis, the components of the metric are given by

$$g^{ab} = \eta^{\alpha\beta} e_\alpha^a e_\beta^b = -2n^{(a}l^{b)} + 2m^{(a}\overline{m}^{b)}. \tag{2.3}$$

2.2.2 Representations of Weyl curvature tensor

One aim of this paper is to uniquely fix the NP tetrad basis to obtain a set of NP scalars from which an unambiguous measure of the Weyl curvature (equal to the Riemann curvature in vacuum) can

be read off.

On the NP tetrad, the curvature content of the Weyl tensor can be expressed in terms of five complex scalar functions

$$\Psi_0 = -C_{abcd} l^a m^b l^c m^d \tag{2.4}$$

$$\Psi_1 = -C_{abcd} l^a n^b l^c m^d \tag{2.5}$$

$$\Psi_2 = -C_{abcd} l^a m^b \overline{m}^c n^d \tag{2.6}$$

$$\Psi_3 = -C_{abcd} l^a n^b \overline{m}^c n^d \tag{2.7}$$

$$\Psi_4 = -C_{abcd} n^a \overline{m}^b n^c \overline{m}^d. \tag{2.8}$$

An equivalent description of the Weyl curvature can be found on the orthonormal frame with associated timelike vector $\boldsymbol{T}$. This is done by defining gravitoelectric $\boldsymbol{\mathcal{E}}$ and gravitomagnetic $\boldsymbol{\mathcal{B}}$ tensors by, respectively, twice contracting $\boldsymbol{T}$ with the Weyl tensor and with its Hodge dual:

$$\mathcal{E}_{ij} = h_i{}^a h_j^c C_{abcd} T^b T^d \,, \tag{2.9}$$

$$\mathcal{B}_{ij} = -\frac{1}{2} h_i{}^a h_j{}^c \epsilon_{abef} C^{ef}{}_{cd} T^b T^d \,. \tag{2.10}$$

Here $\boldsymbol{h}$ denotes the projection operator onto the local spatial hyper-surface orthogonal to $\boldsymbol{T}$. The normalization for the Levi-Civita tensors is such that $\epsilon_{0123} = 1$ and $\epsilon_{123} = 1$ in right-handed orthonormal tetrads and spatial triads respectively [see [15] for a discussion of different conventions in literature]. These two tensors can be combined to obtain a complex tensor

$$\mathcal{Q}_{ij} \equiv \mathcal{E}_{ij} + i\mathcal{B}_{ij}. \tag{2.11}$$

The curvature information contained in $\boldsymbol{\mathcal{Q}}$ is exactly the same as that contained in the five NP scalars. Recasting this information in terms of $\boldsymbol{\mathcal{Q}}$ allows us to make use of the fact that the $\boldsymbol{\mathcal{E}}$ and $\boldsymbol{\mathcal{B}}$ tensors describe the tidal acceleration and differential frame-dragging to visualize the curvature of spacetime [see, e.g., Refs. [16, 15, 17, 18, 19]].

To make the equivalence between $\Psi_0, \Psi_1, \Psi_2, \Psi_3, \Psi_4$ and $\boldsymbol{\mathcal{Q}}$ explicit, we note that the components of the complex gravitoelectromagnetic tensor expressed on the spatial triad $\{\boldsymbol{E^2}, \boldsymbol{E^3}, \boldsymbol{N}\}$ are

$$\boldsymbol{\mathcal{Q}} = \begin{bmatrix} \Psi_2 - \frac{\Psi_0+\Psi_4}{2} & i\frac{\Psi_0-\Psi_4}{2} & \Psi_1 - \Psi_3 \\ i\frac{\Psi_0-\Psi_4}{2} & \Psi_2 + \frac{\Psi_0+\Psi_4}{2} & -i(\Psi_1+\Psi_3) \\ \Psi_1 - \Psi_3 & -i(\Psi_1+\Psi_3) & -2\Psi_2 \end{bmatrix}. \tag{2.12}$$

Furthermore $\boldsymbol{\mathcal{Q}}$ is symmetric and trace free ($\mathcal{Q}^i{}_i = 0$). These results follow from direct substitution of the definition of the orthogonal basis vectors in terms of the NP basis vectors [Eq. (2.1)] and the

definition of the NP scalars [Eqs. (2.4)–(2.8)] into the definition of $\boldsymbol{\mathcal{Q}}$ [Eqs. (2.9), (2.10) and (2.11)].

Finally, note that for any spacetime in general relativity, there are a set of 16 scalar functions or Carminati-McLenaghan curvature invariants [20] that can be constructed from polynomial contractions of the Riemann tensor. In vacuum, four of these scalars are non-vanishing and comprise a complete set of invariants. These four scalars can be combined into two complex functions I and J and are independent of tetrad choice. In terms of the quantities already computed in this section, these curvature invariants can be expressed as

$$\begin{aligned} I =& \frac{1}{2}(\mathcal{E}^k{}_i\mathcal{E}^i{}_k - B^k{}_iB^i{}_k) + i(\mathcal{E}^k{}_iB^i{}_k) = \Psi_4\Psi_0 - 4\Psi_1\Psi_3 + 3\Psi_2^2 \\ J =& \frac{1}{6}(\mathcal{E}^k{}_i\mathcal{E}^i{}_l\mathcal{E}^l{}_k - 3\mathcal{E}^k{}_iB^i{}_lB^l{}_k) - \frac{i}{6}(B^k{}_iB^i{}_lB^l{}_k - 3\mathcal{E}^k{}_i\mathcal{E}^i{}_lB^l{}_k) = \begin{vmatrix} \Psi_4 & \Psi_3 & \Psi_2 \\ \Psi_3 & \Psi_2 & \Psi_1 \\ \Psi_2 & \Psi_1 & \Psi_0 \end{vmatrix} \end{aligned} \tag{2.13}$$

The invariants I and J play a key role in constructing our geometrically motivated coordinate system [Sec. 2.3].

2.2.3 Lorentz transformations

There are six transformations of the NP basis vectors e_a^α that retain the form of the metric given in Eq. (2.2). These are the six Lorentz transformations, which parametrize the six degrees of tetrad freedom [14]. The Lorentz transformations can be decomposed into three types depending on which null vector a particular transformation leaves unchanged:

- Type I: ($\boldsymbol{l}$ unchanged)

$$\boldsymbol{l} \to \boldsymbol{l}, \quad \boldsymbol{n} \to \boldsymbol{n} + \bar{a}\boldsymbol{m} + a\overline{\boldsymbol{m}} + a\bar{a}\boldsymbol{l}\boldsymbol{m} \to \boldsymbol{m} + a\boldsymbol{l}, \quad \overline{\boldsymbol{m}} \to \overline{\boldsymbol{m}} + \bar{a}\boldsymbol{l} \tag{2.14}$$

- Type II: ($\boldsymbol{n}$ unchanged)

$$\boldsymbol{l} \to \boldsymbol{l} + \bar{b}\boldsymbol{m} + b\overline{\boldsymbol{m}} + b\bar{b}\boldsymbol{n}, \quad \boldsymbol{n} \to \boldsymbol{n}\boldsymbol{m} \to \boldsymbol{m} + b\boldsymbol{n}, \quad \overline{\boldsymbol{m}} \to \overline{\boldsymbol{m}} + \bar{b}\boldsymbol{n} \tag{2.15}$$

- Type III: (both $\boldsymbol{l}$ and $\boldsymbol{n}$ unchanged)

$$\boldsymbol{l} \to A^{-1}\boldsymbol{l}, \qquad \boldsymbol{n} \to A\boldsymbol{n}, \qquad \boldsymbol{m} \to e^{i\Theta}\boldsymbol{m}, \qquad \overline{\boldsymbol{m}} \to e^{-i\Theta}\overline{\boldsymbol{m}} \tag{2.16}$$

Here the scalars a and b are complex, while A and Θ are real and can be combined into a single complex number $\mathcal{A} = A^{-1}\exp(i\Theta)$. The rescaling of $\boldsymbol{l}$ and $\boldsymbol{n}$ in Eq. (2.16) is called boost freedom,

and the phase change of $\boldsymbol{m}$ is called the spin freedom. We will follow the convention of Ref. [9] and call a set of tetrads related by Type III transformations a *frame*.

Under the different Lorentz transformations, the NP scalars transform as follows:

- Type I:

$$\begin{aligned}
\Psi_0 &\rightarrow \Psi_0 \\
\Psi_1 &\rightarrow \Psi_1 + \overline{a}\Psi_0 \\
\Psi_2 &\rightarrow \Psi_2 + 2\overline{a}\Psi_1 + \overline{a}^2\Psi_0 \\
\Psi_3 &\rightarrow \Psi_3 + 3\overline{a}\Psi_2 + 3\overline{a}^2\Psi_1 + \overline{a}^3\Psi_0 \\
\Psi_4 &\rightarrow \Psi_4 + 4\overline{a}\Psi_3 + 6\overline{a}^2\Psi_2 + 4\overline{a}^3\Psi_1 + \overline{a}^4\Psi_0
\end{aligned} \tag{2.17}$$

- Type II:

$$\begin{aligned}
\Psi_0 &\rightarrow \Psi_0 + 4b\Psi_1 + 6b^2\Psi_2 + 4b^3\Psi_3 + b^4\Psi_4 \\
\Psi_1 &\rightarrow \Psi_1 + 3b\Psi_2 + 3b^2\Psi_3 + b^3\Psi_4 \\
\Psi_2 &\rightarrow \Psi_2 + 2b\Psi_3 + b^2\Psi_4 \\
\Psi_3 &\rightarrow \Psi_3 + b\Psi_4 \\
\Psi_4 &\rightarrow \Psi_4
\end{aligned} \tag{2.18}$$

- Type III:

$$\Psi_0 \rightarrow A^{-2}e^{2i\Theta}\Psi_0, \quad \Psi_1 \rightarrow A^{-1}e^{i\Theta}\Psi_1, \quad \Psi_2 \rightarrow \Psi_2, \quad \Psi_3 \rightarrow Ae^{-i\Theta}\Psi_3, \quad \Psi_4 \rightarrow A^2e^{-2i\Theta}\Psi_4, \tag{2.19}$$

For any algebraically general spacetime, two special frame choices exist: the principle null frame (PNF) and the transverse frame (TF). The PNF is characterized by the property that $\Psi_4 = 0 = \Psi_0$; starting from a generic tetrad a PNF can be constructed by appropriate Type I and Type II Lorentz transformations. The TF is characterized by the property that $\Psi_3 = 0 = \Psi_1$; starting from a PNF, a TF can be constructed by additional Type I and Type II Lorentz transformations.

There are three TFs, but only one contains the Kinnersley tetrad in the Kerr limit [9]. In keeping with earlier literature [8, 9], we will call this frame the quasi-Kinnersley frame (QKF) and the particular tetrad we pick out of this frame the quasi-Kinnersley tetrad (QKT).

2.2.4 The Kerr metric and the Kinnersley tetrad

The no-hair theorems [21, 22] lead us to expect all binary-black-hole collisions to ring down to the Kerr spacetime after enough time has elapsed. The limiting Kerr metric in Boyer-Lindquist coordinates $(t,\ r,\ \theta,\ \phi)_{BL}$ can be expressed as:

$$ds^2 = -\left(1 - \frac{2Mr}{\Sigma}\right) dt^2 - \frac{4Mar\sin^2\theta}{\Sigma} dt d\phi + \frac{\Sigma}{\Delta} dr^2 + \Sigma d\theta^2 + \frac{\sin^2\theta}{\Sigma}\left[\left(r^2+a^2\right)^2 - a^2\Delta\sin^2\theta\right] d\phi^2, \tag{2.20}$$

where M and a are the mass and spin of the black hole, respectively, and the functions entering the metric are defined by

$$\Sigma = \rho\overline{\rho}, \qquad \rho = r - ia\cos\theta, \qquad \Delta = r^2 - 2Mr + a^2. \tag{2.21}$$

For the Kerr spacetime, one tetrad introduced by Kinnersley is particularly conducive for calculation. Among other things, on this tetrad the perturbation equations in the NP formalism decouple [23, 14]; this feature allows the perturbation problem to be reduced to the study of a single complex scalar ($\delta\Psi_4$) that governs the radiation content of the perturbed spacetime. The Kinnersley tetrad expressed on a Boyer-Lindquist coordinate basis is given by

$$l^a = \frac{1}{\Delta}\left[r^2 + a^2, \Delta, 0, a\right] \tag{2.22}$$

$$n^a = \frac{1}{2\Sigma}\left[r^2 + a^2, -\Delta, 0, a\right] \tag{2.23}$$

$$m^a = \frac{1}{\overline{\rho}\sqrt{2}}\left[i\ a\sin(\theta), 0, 1, i\ \csc(\theta)\right] \tag{2.24}$$

On the Kinnersley tetrad, the only non-vanishing NP curvature scalar is

$$\Psi_2 = \frac{M}{\rho^3}. \tag{2.25}$$

In the next section, we explore the behavior of the tetrad and curvature quantities defined in this section in cases where the physical metric is well understood. So doing, we build up some physical intuition that motivates our QKT choice, which we then apply to more complicated spacetimes, such as those found in numerical simulations.

2.3 Physical considerations for choosing a tetrad

In this section, we introduce several ideas that motivate the choice of tetrad and gauge; we will use these ideas to explore spacetimes produced by numerical-relativity simulations.

For our purposes, we wish to adopt a tetrad and gauge with the following properties (not in order of importance):

1. The tetrad (gauge) reduces to the Kinnersley tetrad (Boyer-Lindquist coordinates) when the spacetime is a weakly perturbed black hole.

2. The choice of tetrad and gauge should be independent of the coordinate system, including the slicing specified by the time coordinate, used in the NR simulation.

3. To facilitate their real-time computation during a NR simulation, all calculation should be local as far as possible.

4. The prescribed use for all computed quantities should be valid in strong field regions as well as in asymptotic regions of the spacetime.

5. The choice of tetrad directions should as far as possible be tailored to the physical content of the spacetime. For example, in asymptotic regions, one important direction is that of wave propagation; we seek a tetrad that asymptotically is oriented along this direction.

6. To facilitate gravitational-wave extrapolation (from the location on the NR simulation's computational domain where the waves are extracted to future null infinity $\mathscr{I}^+$), the falloff with radius of what we identify as the radiation field should match that of an isolated, radiating system; i.e., it should satisfy the expected "peeling properties".

We now consider in detail how we may achieve these criteria in the course of constructing our QKT.

This section roughly breaks into three parts:

1. We start [in Sec. 2.3.1] by motivating the use of QKF with a new insight regarding the relationship between its $\mathbf{l}$ basis vector and the super-Poynting vector, which allows it to satisfy criterion 5. We then review the construction of the QKF in Sec. 2.3.2.

2. Next, we concentrate on fixing the spin-boost freedom to select the QKT out of the QKF. First of all, in Sec. 2.3.3 we discuss several methods for fixing this freedom that have appeared in literature. Then we present our proposal to achieve a global and gauge independent fixing [in Sec. 2.3.5] using a pair of geometrically motivated coordinates defined in Sec. 2.3.4. We conclude this part with a brief discussion of issues related to the proposed scheme in Secs. 2.3.6 and 2.3.7.

3. Finally, we discuss [in Sec. 2.3.8] the conformity of the final QKT to criterion 6 and further motivate its use.

2.3.1 The TF and wave-propagation direction

The Kinnersley tetrad [Eqs. (2.22)–(2.24)] is both a PNF and a TF [24] [cf. Sec. 2.2.3]; this implies that the Kerr spacetime is Petrov Type D. Generic non-Type-D spacetimes do not have this property: for them no tetrad that is both a PNF and a TF exists, so one must decide which if either of these properties to preserve. Here, we do not want Ψ_4, which plays an important role in the perturbation problem, to vanish; therefore, we choose a tetrad that is a TF [8, 9, 10, 11, 12]. In fact, one particular advantage of selecting the TF is its ability to identify the direction of wave propagation in the asymptotic region [cf. criterion 5].

In electromagnetism, a local wave vector that points in the normal direction to the surfaces of constant phase (wavefronts) can be defined. If the medium through which the wave is travelling is isotropic, this direction corresponds to the direction of the waves' energy flow, or the "wave-propagation direction", which is determined by the direction of the Poynting vector,

$$\mathcal{P}_i = \epsilon_{ijk} E^j B^k \tag{2.26}$$

where the vectors E^j and B^k are the electric and magnetic field vectors. In this subsection, we summarize the relationship between the QKT and the gravitational waves' counterpart to Poynting vector.

One approach for constructing a geometrically motivated tetrad follows a suggestion by Szekeres [25], which is to create a gravitational compass out of a number of springs. Such a device is sensitive to the spacetime curvature and can be oriented so that the longitudinal gravitational wave components vanish; mathematically, this amounts to reorienting the observer's tetrad so that it is a TF, which can be done using Type I and Type II transformations to set $\Psi_1 = 0 = \Psi_3$. We note that Chandrasekhar [14] employed the use of a TF for his program of metric reconstruction from a small perturbation in curvature $\delta\Psi_4$ on a background Kerr metric.

Choosing a TF turns out to orient the tetrad along the direction of energy flow, i.e., along the super-Poynting vector [26, 27]

$$\mathcal{P}_i = \epsilon_{ijk} \mathcal{E}^j{}_l \mathcal{B}^{kl}, \tag{2.27}$$

which defines a spatial direction associated with the wave-propagation direction [28]. The super-Poynting vector's components in the orthonormal triad $\{E_i^2, E_i^3, N_i\}$, using the explicit form of gravitoelectromagnetic tensor in Eq. (2.12), are

$$\begin{aligned}
\mathcal{P}_{E^2} &= -P_0(0,1) - 3P_0(1,2) - 3P_0(2,3) - P_0(3,4) \\
\mathcal{P}_{E^3} &= P_1(0,1) + 3P_1(1,2) + 3P_1(2,3) + P_1(3,4) \\
\mathcal{P}_N &= \frac{1}{2}\left(-|\Psi_0|^2 - 2|\Psi_1|^2 + 2|\Psi_3|^2 + |\Psi_4|^2\right),
\end{aligned} \tag{2.28}$$

where the functions P_0 and P_1 are defined to be

$$\begin{aligned} P_0(p,q) &\equiv \Re(\Psi_p)\Re(\Psi_q) + \Im(\Psi_p)\Im(\Psi_q) \\ P_1(p,q) &\equiv \Re(\Psi_p)\Im(\Psi_q) - \Re(\Psi_q)\Im(\Psi_p). \end{aligned}$$

By transforming to a TF, where $\Psi_1 = 0 = \Psi_3$, Eq. (2.28) simplifies significantly, becoming

$$\boldsymbol{\mathcal{P}} = \frac{1}{2}\left(|\Psi_4|^2 - |\Psi_0|^2\right)\boldsymbol{N}, \tag{2.29}$$

where its direction corresponds to spatial normal direction $\boldsymbol{N}$ fixed by our choice of TF and Eq. (2.1), which relates $\boldsymbol{N}$ to the NP tetrad vectors $\boldsymbol{l}$ and $\boldsymbol{n}$. By selecting the TF, we have oriented the tetrad according to the flow of energy within the spacetime, achieving criterion 5. We believe this is one of the strongest motivating factors for making the TF choice.

2.3.2 Computing the quasi-Kinnersley frame on a given spacelike hypersurface

In this subsection, we review the procedure for constructing the TF that contains the Kinnersley tetrad in the Kerr limit. This, as stated before, is named the quasi-Kinnersley frame, or QKF. We follow mostly the derivation of Ref. [8].

2.3.2.1 A spatial eigenvector problem for the QKF

Numerical relativity simulations typically split the 4-dimensional spacetime to be computed into a set of 3-dimensional spatial slices. In the usual 3+1 split, the spacetime metric g_{ab} is split into a spatial metric h_{ij}, lapse α, and shift β^i according to

$$g_{ab}dx^a dx^b = -\alpha^2 dt^2 + h_{ij}(dx^i + \beta^i dt)(dx^j + \beta^j dt), \tag{2.30}$$

while the Einstein equations in vacuum split into evolution equations (for advancing from one slice to the next)

$$R_{ij} - \frac{1}{2}g_{ij}R = 0 \tag{2.31}$$

and constraint equations (satisfied on all slices)

$$R_{TT} - \frac{1}{2}g_{TT}R = 0, \tag{2.32}$$

$$R_{Tj} - \frac{1}{2}g_{Tj}R = 0, \tag{2.33}$$

where R_{ab} and R are the Ricci tensor and Ricci scalar of the spacetime, respectively, the component T is in the direction normal to the spatial slice, and the components i and j lie within the spatial slice.

As mentioned in Sec. 2.2, for a given spatial slice with future directed unit normal $\boldsymbol{T}$, the curvature can be expressed in terms of the gravitoelectric tensor $\boldsymbol{\mathcal{E}}$ and the gravitomagnetic tensor $\boldsymbol{\mathcal{B}}$ defined in Eqs. (2.9) and (2.10). In terms of the 3+1 quantities typically computed in NR codes, provided that the Einstein constraint equations are satisfied, the gravitoelectromagnetic tensors in vacuum can be expressed as

$$\begin{aligned} \mathcal{E}_{ij} &= {}^3R_{ij} + KK_{ij} - K_{ik}K^k_j \\ \mathcal{B}_{ij} &= -\epsilon_i{}^{kl} D_k K_{lj} \end{aligned} \tag{2.34}$$

where K is the trace of the extrinsic curvature K_{ij}, while ${}^3R_{ij}$ and D_k are the Ricci curvature and connection, respectively, associated with the spatial metric h_{ij}.

Given the gravitoelectric and gravitomagnetic tensors, a powerful tool [15, 16] for visualizing the curvature of spacetime is a plot of the "vortex" and "tendex" lines, which are the flow lines of the eigenvectors of the gravitoelectromagnetic tensors $\mathcal{E}_{ij}$ and $\mathcal{B}_{ij}$. The QKF is also related to an eigenvalue problem involving $\mathcal{E}_{ij}$ and $\mathcal{B}_{ij}$, albeit a complex one involving the complex tensor $\boldsymbol{\mathcal{Q}} \equiv \boldsymbol{\mathcal{E}} + i\boldsymbol{\mathcal{B}}$. Specifically, it was shown in Ref. [8] that the QKF can be constructed from the eigenvector $\tilde{\sigma}^i$ that satisfies the eigenvector equation

$$\mathcal{Q}^i_j \tilde{\sigma}^j = -2\hat{\Psi}_2 \tilde{\sigma}^i \tag{2.35}$$

where the eigenvalue $-2\hat{\Psi}_2$ has the value of $-2\Psi_2$ computed on the QKF. Here and throughout the rest of this paper, we adopt the convention of denoting quantities associated with a QKF (such as the NP tetrad vector $\tilde{\boldsymbol{l}}$) with an overscript tilde and quantities associated with the final tetrad, whose spin-boost degrees of freedom have been uniquely fixed (yielding a preferred QKT), with an overscript hat (e.g. $\hat{\boldsymbol{l}}$). As we will show in greater detail later in the section, the QKF's Coulomb potential $\hat{\Psi}_2$ can be constructed out of the curvature invariants I and J of the spacetime and is invariant under spin-boost transformations; therefore, we denote $\hat{\Psi}_2$ with a hat to indicate it has been fixed to its final value.

2.3.2.2 Selecting the correct eigenvalue

For any symmetric matrix $\mathcal{M}$, the eigenvalues associated with the eigenvector problem $\mathcal{M}^i_j \xi^j = \lambda \xi^i$ obey the characteristic equation $p(\lambda) = 0$ where $p(\lambda) = \det(\mathcal{M} - \lambda \mathcal{I})$ and $\mathcal{I}$ is the identity matrix.

For a 3×3 matrix, the characteristic equation becomes

$$p(\lambda) = -\lambda^3 + \lambda^2 \mathrm{tr}(\mathcal{M}) + \frac{1}{2}\lambda\left(\mathrm{tr}(\mathcal{M}^2) - \mathrm{tr}^2(\mathcal{M})\right) + \det(\mathcal{M}), \tag{2.36}$$

If $\mathcal{M}^i_j = \mathcal{Q}^i_j$, direct calculation using Eqs. (2.12) and (2.13) can verify that $\mathrm{tr}(\boldsymbol{\mathcal{Q}}) = 0$, $\det(\boldsymbol{\mathcal{Q}}) = 2J$ and $\mathrm{tr}(\boldsymbol{\mathcal{Q}}^2) = 2I$, which reduces the characteristic polynomial to

$$p_{\boldsymbol{\mathcal{Q}}}(\lambda) = -\lambda^3 + \lambda I + 2J. \tag{2.37}$$

The solution to this cubic equation can be expressed using the speciality index [29] $\mathcal{S} = 27J^2/I^3$ as

$$\lambda = \frac{3J}{I}\frac{W(\mathcal{S})^{1/3} + W(\mathcal{S})^{-1/3}}{\sqrt{\mathcal{S}}} \tag{2.38}$$

where $W(\mathcal{S}) \equiv \sqrt{\mathcal{S}} - \sqrt{\mathcal{S}-1}$. There are three solutions[1] corresponding to the three transverse frames, but only one (namely the QKF) contains the Kinnersley tetrad in the Kerr limit [9] (and thus satisfies criterion 1).

We must now select the correct eigenvalue to define the QKF. Only one of the three eigenvalues has an analytic expansion around $\mathcal{S} = 1$ (which holds for all Type-D spacetimes, including Kerr [29]). We select this eigenvalue (which we denote λ^0) to define the QKF, and so $-2\hat{\Psi}_2 = \lambda^0$. For reference, the series expansion of λ^0 and also the other two eigenvalues $\lambda^\pm$ around $\mathcal{S} = 1$ is

$$\begin{aligned} \lambda^0 = -2\hat{\Psi}_2 &\sim -\frac{2J}{I}\left[-3 + \frac{4}{3}(\mathcal{S}-1) + \cdots\right], \\ \lambda^\pm &\sim -\frac{2J}{I}\left[\frac{3}{2} \pm i\frac{\sqrt{3}}{2}\sqrt{\mathcal{S}-1} - \frac{2}{3}(\mathcal{S}-1) + \cdots\right]. \end{aligned} \tag{2.39}$$

In practice, this selection criterion is equivalent to choosing the eigenvalue with the largest magnitude [9].

2.3.2.3 Constructing the QKF tetrad vectors

We now summarize the necessary results that allow the reconstruction of the QKF from the eigenvector of the matrix $\boldsymbol{\mathcal{Q}}$; for a complete derivation, see Ref. [8]. The eigenvector corresponding to the eigenvalue $-2\hat{\Psi}_2$ can be expressed as

$$\tilde{\sigma}^j = \tilde{x}^j + i\tilde{y}^j \tag{2.40}$$

[1] The fraction on the right of Eq. (2.38) has a three-sheeted Riemann surface with branch points of order two at $\mathcal{S} = 0$ and $\mathcal{S} = 1$, as well as a branch point of order three at $\mathcal{S} = \infty$. The three different eigenvalues arise from the values on the three sheets respectively [8].

where the real vectors $\tilde{x}^j$ and $\tilde{y}^j$ are orthogonal with respect to the spatial metric h_{ij} and their normalization obeys the condition

$$\|\tilde{\boldsymbol{x}}\|^2 - \|\tilde{\boldsymbol{y}}\|^2 = 1.$$

Here and throughout this section, we will use $\|\boldsymbol{v}\|$ and $\boldsymbol{v}\cdot\boldsymbol{w}$ to represent norm and inner product of spatial vectors under h_{ij}. The vectors $\tilde{x}^j$ and $\tilde{y}^j$ can in turn be used to define the vectors

$$\tilde{\lambda}^i = \frac{\tilde{x}^i + \epsilon^{ijk}\tilde{x}_j\tilde{y}_k}{\|\boldsymbol{x}\|^2}, \quad \tilde{\nu}^i = \frac{-\tilde{x}^i + \epsilon^{ijk}\tilde{x}_j\tilde{y}_k}{\|\boldsymbol{x}\|^2}, \quad \tilde{\mu}^i = \frac{\tilde{\lambda}^i + \tilde{\nu}^i + i\epsilon^{ijk}\tilde{\lambda}_j\tilde{\nu}_k}{1 + \tilde{\boldsymbol{\lambda}}\cdot\tilde{\boldsymbol{\nu}}}, \tag{2.41}$$

where the normalization condition on $\tilde{\boldsymbol{\sigma}}$ [Eq. 2.41] ensures

$$\|\tilde{\boldsymbol{\lambda}}\| = \|\tilde{\boldsymbol{\nu}}\| = \|\Re(\tilde{\boldsymbol{\mu}})\|^2 - \|\Im(\tilde{\boldsymbol{\mu}})\|^2 = 1.$$

The resulting vectors $\tilde{\boldsymbol{\lambda}}$, $\tilde{\boldsymbol{\nu}}$ and $\tilde{\boldsymbol{\mu}}$ turn out to be proportional to the spatial projections of QKF basis vectors $\tilde{\boldsymbol{l}}$, $\tilde{\boldsymbol{n}}$ and $\tilde{\boldsymbol{m}}$ respectively. To see this, let the spatial vectors be expressed in terms of a spatial triad E^a_i which is part of an orthonormal tetrad E^a_α with $E^a_0 = T^a$; then, the full QKF tetrad can be constructed as follows:

$$\tilde{l}^a = \frac{|A|^{-1}}{\sqrt{1-\tilde{\boldsymbol{\lambda}}\cdot\tilde{\boldsymbol{\nu}}}}(T^a + \tilde{\lambda}^i E^a_i), \quad \tilde{n}^a = \frac{|A|}{\sqrt{1-\tilde{\boldsymbol{\lambda}}\cdot\tilde{\boldsymbol{\nu}}}}(T^a + \tilde{\nu}^i E^a_i), \quad \tilde{m}^a = \frac{e^{i\Theta}}{\sqrt{2}}\frac{\sqrt{1+\tilde{\boldsymbol{\lambda}}\cdot\tilde{\boldsymbol{\nu}}}}{\sqrt{1-\tilde{\boldsymbol{\lambda}}\cdot\tilde{\boldsymbol{\nu}}}}(T^a + \tilde{\mu}^i E^a_i). \tag{2.42}$$

Note that the residual spin-boost freedom [cf. Eq. (2.16)] has been made explicit in Eq. (2.42) by means of the parameters A and Θ (which have yet to be determined).

Also note that the equation for $\tilde{\boldsymbol{m}}$ above must be modified if the normal to the spatial slice $\boldsymbol{T}$ lies in the plane spanned by $\tilde{\boldsymbol{l}}$ and $\tilde{\boldsymbol{n}}$, since in this special case the vectors $\tilde{\boldsymbol{\lambda}}$ and $\tilde{\boldsymbol{\nu}}$ turn out not to be independent of each other (as is true generally) but are instead related by $\tilde{\lambda}^i = -\tilde{\nu}^i$. It is unclear whether such a slicing can be found for any spacetime, but once found, it is closely associated with a TF. In this case the vector $\tilde{\boldsymbol{\mu}}$ is undefined and $\tilde{\boldsymbol{m}}$ should be constructed from any real unit vector $\tilde{\boldsymbol{r}}$ in the spatial 2-plane orthogonal to $\tilde{\boldsymbol{\lambda}}$ and $\tilde{\boldsymbol{T}}$ according to

$$\tilde{m}^a = \frac{e^{i\Theta}}{\sqrt{2}}(\tilde{r}^i + i\epsilon^{ijk}\tilde{\lambda}_j\tilde{r}_k)E^a_i. \tag{2.43}$$

Because the spatial eigenvector problem (2.35) can be solved point-wise, the construction of the QKF is a local procedure and satisfies criterion 3. Furthermore, the procedure can be applied in the strong field region [cf. criterion 4], although the physical interpretation is only clear if the tetrad can be smoothly extended from there to infinity. By choosing our tetrad to be a QKF, we have used up

four of the six possible degrees of tetrad freedom and have uniquely fixed the directions associated with the real null vectors $\tilde{\boldsymbol{l}}$ and $\tilde{\boldsymbol{n}}$. We will address the remaining spin-boost freedom in the next three subsections.

2.3.3 The spin-boost tetrad freedom

After electing to work in the QKF, the residual tetrad freedom is restricted to a Type III spin-boost transformation [Eqs. (2.16) and (2.42)]. As seen in Eq. (2.19), the boost transformation affects the magnitude of $\tilde{\Psi}_4$, while the spin transformation modifies the phase of $\tilde{\Psi}_4$.

To gain some insight into what the spin-boost transformations do physically, consider a congruence of observers whose world lines are the integral curves of the $\boldsymbol{T}$ field in Eq. (2.1). For these observers, a spin transformation of the tetrad mixes up the two polarizations of gravitational wave by the induced phase rotation[2]; in practice, this rotation occurs because the observers are rotating the orientation of their coordinates and thus redefining what they consider to be the latitudinal and longitudinal directions. Similarly, the boost transformation in Eq. (2.16) alters the velocity with which these observers move along the direction of wave-propagation, causing the gravitational wave they observe to be redshifted or blueshifted.

In order to identify the gravitational wave and curvature content contained in Ψ_4 in an unambiguous manner, we need to provide a prescription for fixing A and Θ throughout the spacetime. Note that $\tilde{\lambda}$ and $\tilde{\nu}$ constructed in Eq. (2.41) are dependent on the choice of slicing; thus simply setting A and Θ in Eq. (2.42) to particular values does not select a tetrad in a slicing independent manner. Fixing these parameters but altering the slicing will lead to different tetrads in the same frame (the QKF), thus when we leave A and Θ undetermined, the frame as a whole that we obtain from Eq. (2.42) is slicing independent.

One example of fixing the spin-boost freedom in a gauge independent way often used in mathematical analysis is selecting the so-called canonical transverse tetrad (CTT) [24], which is defined by the condition that

$$\Psi_1 = 0 = \Psi_3 \quad \text{and} \quad \Psi_0 = \Psi_4. \tag{2.44}$$

The CTT has the property that the super-Poynting vector given in Eq (2.29) has vanishing magnitude; in this tetrad, the observers are co-moving with local wavefront in the asymptotic region and consequently measure $\|\boldsymbol{\mathcal{P}}\| = 0$. Since no physical observer can travel at the speed of light and co-move with the wavefront, we require a more physically motivated prescription for fixing the spin-boost freedom.

Several approaches for providing such a physically motivated prescription have been suggested. A common approach is to impose conditions on spin coefficients (such as $\epsilon = 0$ [7]). The Kinnersley

[2]Recall that for plane waves on Minkowski background, we have $\Psi_4 = -\ddot{h}_+ + i\ddot{h}_\times$, where h is the metric perturbation.

tetrad for the Kerr metric has spin coefficients[3] that obey $\kappa = \sigma = \lambda = \nu = \epsilon = 0$. The meaning of some of these coefficients can be gleaned from the equations governing how the tetrad evolves along the $\boldsymbol{l}$ direction, namely [14]

$$l^b l^a_{;b} = 2\Re(\epsilon) l^a - \kappa \overline{m}^a - \overline{\kappa} m^a, \tag{2.45}$$

$$l^b m^a_{;b} = 2i\Im(\epsilon) m^a + \overline{\pi} l^a - \kappa n^a. \tag{2.46}$$

If $\kappa = 0$ for example, the null vector $\boldsymbol{l}$ is tangent to a geodesic and further if $\Re(\epsilon) = 0$ this geodesic is affinely parameterized.

Note that choosing $\boldsymbol{l}$ to be geodesic or $\kappa = 0$ is not necessarily consistent with choosing to work in a TF, although these conditions are consistent in the Kerr limit. In a TF, the only freedom available to set the spin coefficients to zero is the spin-boost transformation. Since κ transforms as $\kappa \to A^{-2} e^{i\Theta} \kappa$ under Eq. (2.16), the spin coefficient κ cannot be set to zero. The spin coefficient ϵ, on the other hand, transforms as

$$\epsilon \to A^{-1}\epsilon - \frac{1}{2} A^{-2} l^a \nabla_a A + \frac{i}{2} A^{-1} l^a \nabla_a \Theta,$$

and can be made to vanish by suitably chosen A and Θ. Equations (2.45) and (2.46), indicate that the condition $\epsilon = 0$ can be used to fix the scaling of $\boldsymbol{l}$ as well as the phase of $\boldsymbol{m}$. Setting $\epsilon = 0$ can therefore be used as a means of fixing the spin-boost freedom, but this choice has the disadvantage that Eq. (2.47) must be solved in order to obtain A and Θ, which can be expensive numerically.

In the following subsections, we present an alternative method of fixing the spin-boost freedom by constructing a coordinate system based on the curvature invariants. Differentials of these new coordinates are then used to set the scale or fix the spin degree of freedom of the final QKT. This method avoids the need to solve differential equations by directly imposing local conditions of the the tetrad basis vectors.

2.3.4 A geometrically motivated coordinate system

In this paper, we fix the spin-boost freedom by exploiting the curvature invariant $\hat{\Psi}_2$ [identified in Eqs. (2.35) and (2.39) and computed using Eq. (2.38)] to define geometrically motivated and unambiguous radial and latitudinal coordinates. The quantity $\hat{\Psi}_2$ can be interpreted as the Coulomb potential experienced by an observer [25], and all observers in a QKF agree on its value. Our prescription for fixing the spin-boost freedom is to effectively tether our observers to a fixed position with respect to the coordinates associated with the instantaneous background Coulomb potential they experience. By doing this, we choose "stationary" observers that watch gravitational waves

[3] For how the spin coefficients [which are complex scalars] are defined in terms of the null tetrad, see e.g. Eq. (1.286) of Ref. [14].

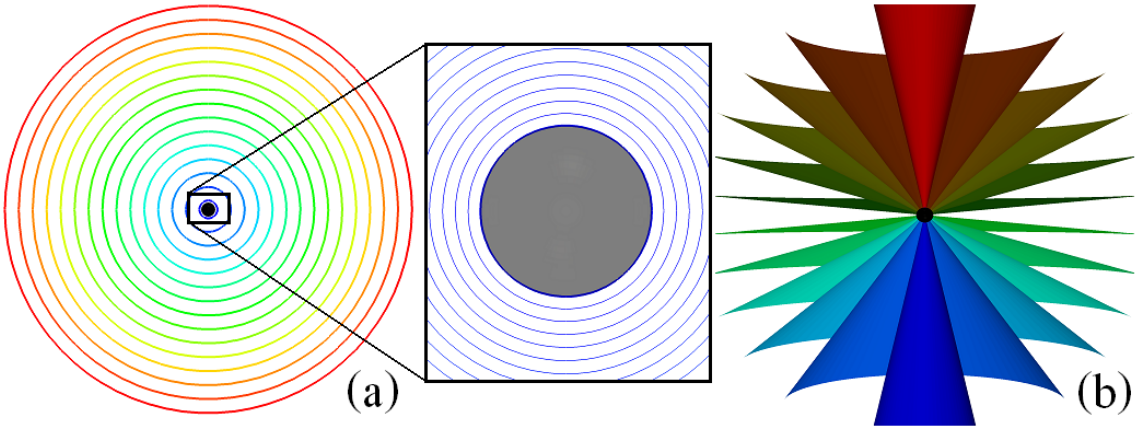

Figure 2.1: Properties of the $(\hat{r}, \hat{\theta})$ coordinates constructed from the Coulomb potential in the QKF. (a) The equatorial plane of a Kerr spacetime in a Kerr-Schild slicing with contours of constant Boyer-Lindquist radius $\hat{r}$ at equal increments. The inset zooms in around the event horizon (indicated by a transparent black disk). The $\hat{r}$ contour increments in the inset, while still uniform, are smaller than in the main figure, and the thick contour line coinciding with the event horizon matches the Boyer-Lindquist radius $\hat{r}_+$ in Eq. (2.49). (b) Surfaces of constant latitudinal coordinate $\hat{\theta}$ for the Kerr-Schild slicing.

pass, in contrast to the CTT observers (Sec. 2.3.3) that co-move with the waves. In Kerr limit, our choice amounts to selecting a set of stationary observers associated with the Boyer-Lindquist coordinate system.

To illustrate this idea more fully, note that when we work within the QKF, the complex gravitoelectromagnetic tensor from Eq. (2.12) reduces to

$$\tilde{\boldsymbol{\mathcal{Q}}} = \begin{bmatrix} \hat{\Psi}_2 - (\tilde{\Psi}_0 + \tilde{\Psi}_4)/2 & i(\tilde{\Psi}_0 - \tilde{\Psi}_4)/2 & 0 \\ i(\tilde{\Psi}_0 - \tilde{\Psi}_4)/2 & \hat{\Psi}_2 + (\tilde{\Psi}_0 + \tilde{\Psi}_4)/2 & 0 \\ 0 & 0 & -2\hat{\Psi}_2 \end{bmatrix}, \tag{2.47}$$

making $\tilde{\boldsymbol{N}}$ an eigenvector. Of particular interest is the component

$$\tilde{\mathcal{Q}}_{\tilde{N}\tilde{N}} = -2\hat{\Psi}_2 = \mathcal{E}_{\tilde{N}\tilde{N}} + i\mathcal{B}_{\tilde{N}\tilde{N}}.$$

As illustrated in detail in Section 1.2 (i.e. [16]) and particularly in Sec. IV A of Chapter 3 (i.e. Ref. [15]), within the context of vortexes and tendexes, $\mathcal{E}_{\tilde{N}\tilde{N}}$ measures tidal acceleration and $\mathcal{B}_{\tilde{N}\tilde{N}}$ the differential frame-dragging experienced by a person whose body is aligned along the radial $\tilde{\boldsymbol{N}}$ eigenvector. The frame dragging induced by the angular momentum of the source implies a latitudinal coordinate, and the radial tidal acceleration implies a radial coordinate. The Coulomb potential $\hat{\Psi}_2$ thus contains information about a pair of geometrically motivated coordinates $\hat{r}$ and $\hat{\theta}$.

To relate the Coulomb potential $\hat{\Psi}_2$ to the geometric coordinates $\hat{r}$ and $\hat{\theta}$ in a meaningful way

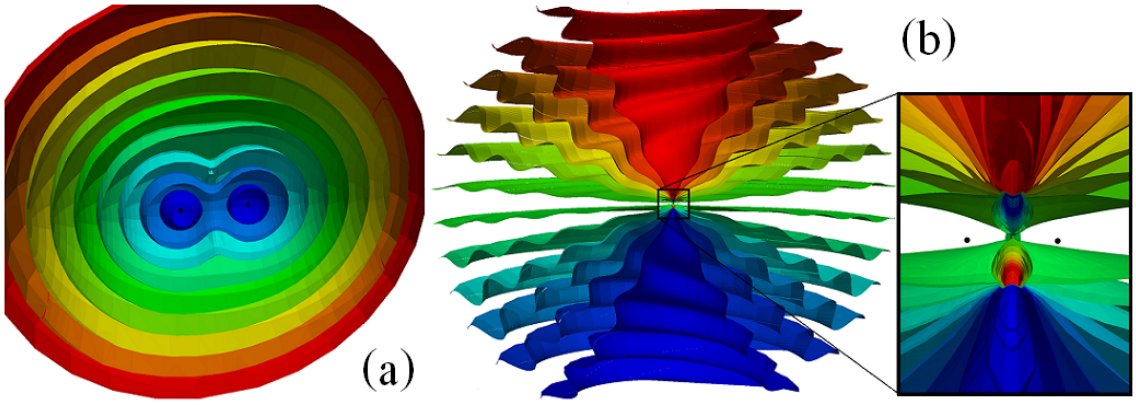

Figure 2.2: (a) Snapshot surfaces of constant $\hat{r}$ for an equal-mass nonspinning binary merger simulation taken during the inspiraling phase. Far away from the black holes, the contours represent those expected from a monopole moment. When moving closer to the black holes, higher order multipoles become important. (b) Constant $\hat{\theta}$ surfaces for the same simulation as in (a), shows a "spiral-staircase" pattern generated by rotating deformed cones as discussed in greater detail in Sec. 2.6.1.

that reduces to the Boyer-Lindquist coordinates in the Kerr limit (thus satisfying criterion 1), we make use of expressions for the Kerr spacetime [Eqs. (2.25) and (2.21)] to define the coordinates. In other words, we define $\hat{r}$ and $\hat{\theta}$ using the complex equation

$$\hat{\rho} = \hat{r} - i\hat{a}\cos(\hat{\theta}) = \left(\frac{\hat{M}}{\hat{\Psi}_2}\right)^{1/3} \tag{2.48}$$

where $\hat{M}$ and $\hat{a}$ are real constants that become just the mass and spin of the central black hole in the Kerr limit. A discussion regarding these parameters in dynamical simulations follows in Sec. 2.3.6. Recall that the Coulomb potential $\hat{\Psi}_2$ can be constructed directly from the curvature invariants I and J of the spacetime; the construction of the coordinates out of curvature invariants makes them slicing or gauge independent, thus satisfy criterion 2.

Figures 2.1 and 2.2 explore some properties of $\hat{r}$ and $\hat{\theta}$. The first property is the ability to recover the Boyer-Lindquist radial and latitudinal coordinates from a Kerr spacetime expressed in any slicing. A particular example using Kerr-Schild slicing is shown in Fig. 2.1, where we plot the contours of $\hat{r}$ and $\hat{\theta}$ under Kerr-Schild spatial coordinates (r, θ, ϕ). The resulting figures show that the coordinate transformations between $(\hat{r}, \hat{\theta})$ and (r, θ) (unlike those for Boyer-Lindquist t and ϕ) do not become singular at the event horizon [cf. criterion 4], which coincide with the contour of

$$\hat{r} = \hat{r}_+ \equiv \hat{M} + \sqrt{\hat{M}^2 - \hat{a}^2}$$

as expected. The $(\hat{r}, \hat{\theta})$ coordinate system for a dynamical simulation of two equal-mass, nonspinning black holes during their inspiral phase is shown in Fig. 2.2. The peanut shaped features in panel

(a) makes apparent the fact that the coordinate system is adjusting to the intrinsic geometry of the simulation. The cones of constant angular coordinate $\hat{\theta}$ display a wavy feature when compared to the simulation coordinate θ. This feature and its origin will be discussed in greater detail in Sec. 2.6.1, where we explore the binary simulation in more detail.

2.3.5 Fixing the spin-boost degrees of freedom

The previous subsection provides us with an unambiguous and geometrically motivated set of radial and latitudinal coordinates that are valid throughout the spacetime and that are independent of the choice of slicing. Our strategy for fixing the last two degrees of tetrad freedom is to require that the tetrad frames can be associated with observers that are in some sense "stationary" with respect to our geometrically motivated coordinates while also requiring that the selected tetrad reduces to the Kinnersley tetrad in the Type-D limit.

To achieve this construction (and thus to provide a global prescription for fixing the spin-boost freedom), note that $d\hat{r}$ provides a measuring rod in the radial direction, relative to the wavefront, against which the scale of the radial component of $\hat{\boldsymbol{l}}$ can be fixed. Similarly $d\hat{\theta}$ provides a transverse direction which can be used to fix the phase of $\hat{\boldsymbol{m}}$. Let us now begin with any tetrad in the QKF $\{\tilde{\boldsymbol{l}}, \tilde{\boldsymbol{n}}, \tilde{\boldsymbol{m}}, \overline{\tilde{\boldsymbol{m}}}\}$, constructed according to Eq. (2.42). The prescription we use to fix the parameters A and Θ associated with the spin-boost degrees of freedom to obtain the final QKT $\{\hat{\boldsymbol{l}}, \hat{\boldsymbol{n}}, \hat{\boldsymbol{m}}, \overline{\hat{\boldsymbol{m}}}\}$ is to require that the final tetrad obeys

$$\left(d\hat{r}\right)_a \hat{l}^a = 1; \tag{2.49}$$

$$\arg\left[\left(d\hat{\theta}\right)_a \hat{m}^a\right] = \arg\left[\hat{\rho}\right]. \tag{2.50}$$

Note that these conditions are exactly the conditions satisfied by the Kinnersley tetrad in Eq. (2.22) and (2.24) except that the Boyer-Lindquist coordinate has been replaced by its corresponding geometrically constructed counterpart introduced in Sec. 2.3.4. The reduction to the Kinnersley tetrad in the Type-D limit is thus trivial [cf. criterion 1]. Furthermore, conditions (2.49) and (2.50) contain only local differentiation and algebraic calculations and thus obey criterion 3. They also inherit gauge independence from the QKF and the geometric coordinates, thus satisfy criterion 2.

It turns out that the final QKT can be constructed by starting with a tetrad in the QKF with $A = 1$ and $\Theta = 0$ in Eq (2.42), computing the quantities

$$A = \left(d\hat{r}\right)_a \tilde{l}^a, \tag{2.51}$$

$$\Theta = -\arg\left[\left(d\hat{\theta}\right)_a \tilde{m}^a\right] + \arg\left[\hat{\rho}\right], \tag{2.52}$$

and then substituting these values back into Eq. (2.42) to obtain the final tetrad. Our fictitious

observers have now oriented and scaled their tetrads according to the Coulomb potential they experience by observing the local changes in tidal acceleration and differential frame dragging.

2.3.6 The effect of $\hat{a}$ and $\hat{M}$ on the tetrad choice

In the definition of the geometric coordinates $(\hat{r},\, \hat{\theta})$ in Eq. (2.48), two constants $\hat{M}$ and $\hat{a}$ corresponding to the mass and spin of a Kerr black hole in the Type-D limit entered our prescription. We now clarify their influence on the final computed quantities of $\hat{\Psi}_4$ and the constructed tetrad.

First, we observe that the spin $\hat{a}$ does not affect the spin parameter Θ in expression (2.52) and can be left undetermined, since only the direction of $d\hat{\theta}$ is required to determine the argument of its inner product with $\tilde{\boldsymbol{m}}$.

The final computed quantities are however dependent on the value of $\hat{M}$, which enters as a constant factor scaling the boost parameter A. The computed $\hat{\Psi}_4$ is simply rescaled by a constant scaling factor if the value of $\hat{M}$ is changed. This allows one to compute all quantities real time during the simulation with (say) $\hat{M} = 1$ and to a posteriori rescale the results once the final mass of the remnant black hole is known.

2.3.7 The remaining gauge freedom

Using the appropriate combination of the curvature invariants [Sec. 2.3.4] to prescribe radial and latitudinal coordinates $(\hat{r}, \hat{\theta})$ fixes two of the four degrees of gauge freedom, while the choice of a TF [Sec. 2.3.2] and the subsequent fixing of the spin-boost freedom [Sec. 2.3.5] removes all six degrees of tetrad freedom. What remains is to fix the final two degrees of gauge freedom: the slicing (or time coordinate $\hat{t}$) and the azimuthal coordinate $\hat{\phi}$.

For a given slicing, "far enough" from the strong field region, surfaces of constant $\hat{r}$ and $\hat{\theta}$ intersect in a circle. This can be seen graphically in Fig. 2.2 by superimposing plot (a) and (b) and taking "far enough" to mean the region where the mass monopole and current dipole are the dominant terms in the Coulomb background. The prescription of the azimuthal coordinate $\hat{\phi}$ is then as simple as requiring that given a specific (as yet undetermined) starting point, the proper distance increments $d\hat{\phi}$ along the circle remains constant.

Fixing the time slicing requires more finesse. One method of specifying the time slicing indirectly is by means of a congruence of outward propagating affinely parameterized null geodesics [see Sec. 2.3.8.2 below for a suggested congruence] starting from a fixed radius $\hat{r}$; the affine parameter τ is then used as a coordinate. This approach is particularly suited to the task of wave extraction where the quantities computed should exhibit the scaling laws predicted by the peeling property [30, 31].

The prescriptions given above contain residual freedom. Fixing them is beyond the scope of our

current work. In this paper, wherever needed, we simply use the coordinate time in the simulation and the simulation's azimuthal coordinate.

2.3.8 The peeling theorem

2.3.8.1 Peeling in Newman-Penrose scalars

In this section, we consider the peeling property, which describes the way in which, for an isolated gravitating system that is asymptotically flat, the components of the curvature tensor fall off as one moves farther away from the source of the emitted gravitational radiation. At sufficiently large distances, only Type N radiation is noticeable; the limiting Type N radiation can be identified as the gravitational-wave (GW) content of the spacetime (typically denoted as Ψ_4 on an affinely parameterized out-going geodesic null tetrad). [Note that gravitational radiation is only rigorously defined at future null infinity (denoted $\mathscr{I}^+$).] A caricature of this behavior is given in Fig. 2.3.

Here we review the usual derivation of the peeling property [30, 31, 32, 33, 24], commenting on some of the properties of the QKT within this context; an alternate derivation of the the peeling property using spinor notation can be found in [33]. The basic idea of the usual derivation is to introduce a new 'unphysical' metric $d\acute{s}$ that is conformally related to the physical metric ds by $d\acute{s} = \Omega\ ds$. The metric $d\acute{s}$ is finite and well defined where the physical metric blows up (points on $\mathscr{I}^+$ are infinitely distant from their neighbors [24]) and allows us to explore the properties of the spacetime at $\mathscr{I}^+$ or at conformal null infinity, where $\Omega \to 0$. All quantities associated with the conformal metric $d\acute{s}$ will be denoted with an acute (e.g. $\acute{ds}$).

The relationship between metric tensors can be expressed as

$$\acute{g}_{ab} = \Omega^2 g_{ab}, \qquad\qquad \acute{g}^{ab} = \Omega^{-2} g^{ab}, \tag{2.53}$$

and the topology at $\mathscr{I}^+$ is $S^2 \times \mathbb{R}$. Now let l^a be tangent to an affinely parameterized out-going null geodesic on the real spacetime, with an affine parameter τ such that $l^a \nabla_a \tau = 1$. Then let $\acute{l}^a$ be tangent to an affinely parameterized geodesic in the conformally related spacetime with affine parameter $\acute{\tau}$. Note that if we take $l^a = \Omega^2 \acute{l}^a$, then the geodesic equation in physical spacetime implies its counterpart in the conformal spacetime [24]; furthermore, if we choose $n^a = \acute{n}^a$ at $\mathscr{I}^+$, then we have that the direction of $(n^a = \acute{n}^a)|_{\mathscr{I}^+}$ does not depend on the geodesic and is tangent to $\mathscr{I}^+$ [24].

Substituting these choices into the expressions for the metric [Eq. (2.3)] and subsequently into Eq. (2.53) we have that at $\mathscr{I}^+$ the conformal tetrad relates to the physical tetrad by means of the

expressions

$$l^a = \Omega^2 \acute{l}^a, \quad m^a = \Omega \acute{m}^a, \quad n^a = \acute{n}^a. \tag{2.54}$$

Departing from $\mathscr{I}^+$ by moving into the manifold, differences in parallel transport in the physical and conformal manifolds lead to higher order terms in the $\boldsymbol{m}$ and $\boldsymbol{n}$ equations (see Eqs. (9.7.30) and (9.7.31) in Ref. [24]). By comparing the affine parameter on the two manifolds along a geodesic and imposing Einstein's vacuum field equations, we can show that in general $d\tau = \Omega^{-2} d\acute{\tau}$ and that for large affine parameter τ or small conformal affine parameter $\acute{\tau}$ we have [24]

$$\acute{\tau} = -A^{-2}\tau^{-1} + \sum_{n=2} D_n \tau^{-n}, \tag{2.55}$$

$$\tau = -A^{-2}\acute{\tau}^{-1} + \sum_{n=0} C_n \acute{\tau}^n, \tag{2.56}$$

$$\Omega = A^{-1}\tau^{-1} + \sum_{n=2} E_n \tau^{-n}, \tag{2.57}$$

$$\Omega = -A\acute{\tau} - \sum_{n=3} A_n \acute{\tau}^n, \tag{2.58}$$

where A_n, C_n, D_n, E_n are constants and $A = -\frac{d\Omega}{d\acute{\tau}}|_{\Omega\to 0}$ is a non-zero constant. Any quantity $\acute{\theta}_{\ldots}$ that is C^h continuous at $\mathscr{I}^+$ can be expressed in terms of a series expansion about $\mathscr{I}^+$ as follows

$$\acute{\theta}_{\ldots} = \sum_{n=0}^{h} \acute{\tau}^n \acute{\theta}^{(n)}_{\ldots} + o(\acute{\tau}^h) = \sum_{n=0}^{h} \tau^{-n} \theta^{(n)}_{\ldots} + o(\tau^{-h}). \tag{2.59}$$

Since the Weyl tensor is conformally invariant, $C^a{}_{bcd} = \acute{C}^a{}_{bcd}$, or

$$C_{abcd} = \Omega^{-2} \acute{C}_{abcd}, \tag{2.60}$$

all the relevant quantities can be computed on the conformal manifold where the metric is finite and well behaved, and then interpreted on the physical manifold where the metric quantities may have diverged. At $\mathscr{I}^+$ in an asymptotically flat spacetime, the Weyl tensor $\acute{C}_{abcd}$ vanishes and the dynamics of the gravitational field as one approaches $\mathscr{I}^+$ can be described using a tensor $\acute{K}_{abcd}$, where

$$\acute{C}_{abcd} = \Omega \acute{K}_{abcd} \tag{2.61}$$

and the components of $\acute{K}$ expressed on the tetrad basis $\{\acute{\boldsymbol{l}}, \acute{\boldsymbol{n}}, \acute{\boldsymbol{m}}, \acute{\overline{\boldsymbol{m}}}\}$ admit expansions in the form of Eq. (2.59).

The peeling-off property of the Weyl scalars naturally arises when one expresses the quantities

related to $\acute{\boldsymbol{K}}$ in terms of the physical metric and the tetrad basis $\{\boldsymbol{l},\ \boldsymbol{n},\ \boldsymbol{m},\ \overline{\boldsymbol{m}}\}$. Let us take a detailed look at Ψ_4: analogous to the definition of Ψ_4 in Eq (2.8), let

$$\acute{\Psi}_4 = -\acute{K}_{abcd}\acute{n}^a\acute{\overline{m}}^b\acute{n}^c\acute{\overline{m}}^d \tag{2.62}$$

The fact that $\acute{\boldsymbol{K}}$ is regular as we approach $\mathscr{I}^+$ implies that $\acute{\Psi}_4$ admits a series expansion of the form

$$\acute{\Psi}_4 = \sum_{n=0} \tau^{-n}\Psi_4^{(n)}, \tag{2.63}$$

where in particular $\Psi_4^{(0)} = \acute{\Psi}_4|_{\mathscr{I}^+}$. Similar expansions can be found for $\acute{\Psi}_i, i = 0, 1, 2, 3$. At $\mathscr{I}^+$, the physical Ψ_4 [defined by Eq. (2.8)] is related to $\acute{\Psi}_4$ by

$$\Psi_4 = -(\Omega^{-2}\acute{C}_{abcd})(\acute{n}^a)(\Omega\acute{\overline{m}}^b)(\acute{n}^c)(\Omega\acute{\overline{m}}^d) = \Omega\acute{\Psi}_4, \tag{2.64}$$

where we have used Eqs. (2.54), (2.60) and (2.61). By a similar argument as used for Ψ_4, the differing powers of Ω appearing in Eq. (2.54) result in a hierarchy being set up where

$$\Psi_i = \Omega^{5-i}\acute{\Psi}_i. \tag{2.65}$$

This expression is merely a product of the series in Eq. (2.57) and (2.59). Resumming the product of series implies that the physical Weyl scalars along an affinely parameterized out-going null geodesic can be expressed as

$$\Psi_i = \tau^{i-5}\sum_{n=0} \tau^{-n}\psi_i^{(n)} \tag{2.66}$$

where $\psi_i^{(n)}$ are constant along the geodesic.

2.3.8.2 Peeling in principal null directions

Note that the peeling property is not a function of which geodesic is chosen (provided that the geodesic strikes $\mathscr{I}^+$ and is affinely parameterized); on the contrary, it is a feature of the spacetime curvature and the distribution of principal null directions (PNDs) as one approaches $\mathscr{I}^+$. This feature is illustrated graphically in Fig. 2.3 (a): as one moves in toward the source from $\mathscr{I}^+$ along a null geodesic, the PNDs "peel off" away from the geodesic direction [33].

Let us now quantify this behavior more precisely. Starting from the $\boldsymbol{l}$ vector associated with the out-going null geodesic, perform a Type II Lorentz transformation, so from Eqs. (2.15) and (2.18)

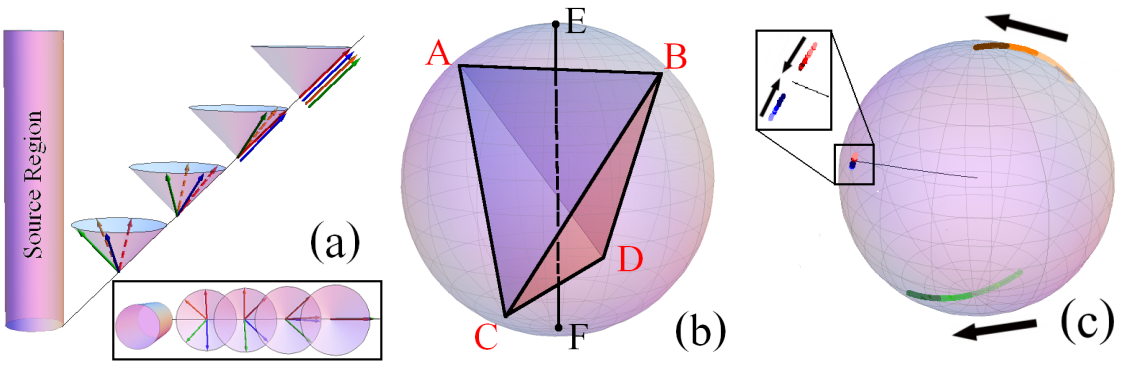

Figure 2.3: (a) A pictorial representation of the peeling property as bunching of principal null directions (PNDs) [24], with the inset showing a top-down view. (b) The relationship between the PNDs and the quasi-Kinnersley tetrad (QKT). Points A, B, C, D correspond to PNDs on the anti-celestial sphere, and are arranged as the vertexes of a tetrahedron. The anti-celestial sphere can be thought of as a spatial slice of the future null cone, where each point on the sphere represents a null direction. The line EF linking the mid-points of a pair of opposite edges strike the anti-celestial sphere at opposite poles which correspond to the null direction $\hat{\boldsymbol{l}}$ associated with the QKT at point (F) and to the null direction $\hat{\boldsymbol{n}}$ associated with the QKT at point (E) [cf. Fig. 8-5 in Ref. [24]]. (c) The four principal null directions recorded during a head-on numerical simulation [described in Sec. 2.6.2] are represented as points (in four different colors) on the anti-celestial sphere. We begin integrating a null geodesic in the $\hat{\boldsymbol{l}}$ direction and then compute the PNDs at discrete intervals along that geodesic. Darker colored points correspond to values farther along the geodesic (farther removed from source region). For cleaner visualization, the angular coordinates on the anti-celestial sphere in this figure are simply those of the simulation coordinates and not the abstract ones in Eq. (2.69). We nevertheless see that the PNDs are distributed in a pairwise symmetric manner relative to tangent $\boldsymbol{\ell}$ of the geodesic (denoted by the black radial line). Two of the PNDs stay close to $\boldsymbol{\ell}$, whose close-ups are shown in the framed inset. The other two demonstrate a clear motion toward $\boldsymbol{\ell}$, where arrows indicate progress along the null geodesic. The numerical findings are thus consistent with the bunching behavior depicted in panel (a).

we have that the four principle null direction (PNDs) can be expressed as:

$$\boldsymbol{k} = \boldsymbol{l} + \bar{b}\boldsymbol{m} + b\overline{\boldsymbol{m}} + b\bar{b}\boldsymbol{n}, \tag{2.67}$$

where b takes on the values of the four roots of the complex equation

$$\Psi_0 + 4b\Psi_1 + 6b^2\Psi_2 + 4b^3\Psi_3 + b^4\Psi_4 = 0. \tag{2.68}$$

From Eq (2.67) it becomes apparent that the magnitude of b determines the extent to which the PNDs depart from the null vector $\boldsymbol{l}$ since $k^a l_a = -b\bar{b}$. By making the identification proposed in [9] between a pair of spherical coordinates $(\theta,\ \phi)$ and the boost b,

$$b_{(i)} = \cot\left(\frac{\theta_i}{2}\right) e^{i\phi_i}, \qquad i \in \{1, 2, 3, 4\}, \tag{2.69}$$

we can graphically demonstrate the motion of the PNDs by plotting the four roots on the anti-

celestial sphere as shown in Fig. 2.3 (b). (The anti-celestial sphere can be thought of as the space of all possible directions associated with out-going null rays.) If $\theta_i = \pi$, then the magnitude of the boost $b_{(i)}$ vanishes and $\boldsymbol{k} = \boldsymbol{l}$ is a PND; on the other hand, if $\theta_i = 0$ then $\boldsymbol{k} \propto \boldsymbol{n}$.

Asymptotically, where the Weyl scalars admit power series expansions such as Eq. (2.66), we can obtain the dominant behavior of b by setting

$$b = \sum_{n=0} \tau^{-n} b^{(n)} \tag{2.70}$$

and substituting this expression into Eq. (2.68). We then have that $b^{(0)} = 0$ and $b^{(1)}$ can be found by finding the four roots of the equation

$$\psi_0^{(0)} + 4b^{(1)}\psi_1^{(0)} + 6\left(b^{(1)}\right)^2 \psi_2^{(0)} + 4\left(b^{(1)}\right)^3 \psi_3^{(0)} + \left(b^{(1)}\right)^4 \psi_4^{(0)} = 0. \tag{2.71}$$

Further higher order terms become more complicated and involve mixtures of higher order terms in the expansions of the Weyl tensor components.

The leading order coefficients $\psi_i^{(0)}$ in Eq. (2.66) are independent of the choice of geodesic path, while higher order terms $\psi_i^{(n)}$ with $n > 0$ are path or geodesic-dependent, which implies in turn that the $b^{(n+1)}$ are geodesic-dependent. This path dependence suggests the possible existence of an optimal null trajectory along which the series converges most rapidly and from which the GW content can be most effectively extracted. One approach to finding the optimal trajectory is to minimize the higher order terms, $\psi_i^{(n)}$ $(n > 0)$, achieving a rapidly converging series. Possibly the most rigorous method of ensuring rapid convergence would be to identify the Kinnersley tetrad and thus the wave propagation direction at $\mathscr{I}^+$ and then to integrate backward in time, but such a strategy cannot be executed real time during a numerical simulation. Instead, the method advocated here is to align the initial geodesic direction with the wave propagation direction in the computational domain and then to integrate forward in time. This direction can be identified in a slicing independent way by $\hat{\boldsymbol{l}}$ in the QKT as was shown in Sec. 2.3.1. In Sec. 2.6, we will demonstrate numerically the rapid convergence rate that results from this approach.

Choosing the QKT $\hat{\boldsymbol{l}}$ as the initial direction is further justified by considering the manner with which PNDs converge onto the outgoing geodesic's tangent direction. In the QKT $\hat{\Psi}_1 = 0 = \hat{\Psi}_3$, which greatly reduces the complexity of Eq. (2.68). The transformation from $\hat{\boldsymbol{l}}$ to PND takes the simplified form

$$\hat{b}^2 = \frac{1}{\hat{\Psi}_4}\left(-3\hat{\Psi}_2 \pm \sqrt{9\hat{\Psi}_2^2 - \hat{\Psi}_4\hat{\Psi}_0}\right). \tag{2.72}$$

The four roots now occur in pairs and can be parameterized using only two angles.

$$\begin{aligned} \hat{b}_{(1)} &= \cot\left(\frac{\hat{\theta}_1}{2}\right) e^{i\hat{\phi}_1}, \qquad \hat{b}_{(2)} = \cot\left(\frac{\hat{\theta}_1}{2}\right) e^{i\hat{\phi}_1 + i\pi} \\ \hat{b}_{(3)} &= \cot\left(\frac{\hat{\theta}_2}{2}\right) e^{i\hat{\phi}_2}, \qquad \hat{b}_{(4)} = \cot\left(\frac{\hat{\theta}_2}{2}\right) e^{i\hat{\phi}_2 + i\pi} \end{aligned} \tag{2.73}$$

The out-going null direction $\hat{\boldsymbol{l}}$ of the QKT thus finds itself in the center of the four PNDs due to the added symmetry imposed by the QKT. This situation is depicted graphically in Fig. 2.3 (b). By initially selecting a QKT direction in the interior of the computational domain from which to shoot the geodesics to infinity, we impose an additional symmetry on the manner in which the PNDs approach the geodesic's tangent initially, hoping that this additional symmetry is maintained as the geodesic approaches $\mathscr{I}^+$ to ensure the clean pairwise convergence of the PNDs to the geodesic's tangent.

Once the geodesic is shot off in the $\hat{\boldsymbol{l}}$ direction, there is nothing to ensure that it remains in the QK out-going null direction. In practice, however, the QK property appears to be maintained to a high degree of accuracy, as is indicated by the symmetric pairwise convergence of the PNDs onto the null geodesic shown in Fig. 2.3 (c). For this plot the angle between the QKT direction of $\hat{\boldsymbol{l}}$ and the tangent $\boldsymbol{\ell}$ to the geodesic remains less than $4.2 \times 10^{-4}\pi$.

2.3.8.3 Peeling of QKT quantities

We close this section on the peeling property by revisiting the geometrically motivated coordinate system (introduced in Sec. 2.3.4) in the asymptotic region. The curvature invariants I and J (and thus $\hat{\Psi}_2$) can be constructed using the series expressions Eq. (2.66). The dominant behavior of the curvature invariants are

$$I \sim \tau^{-6} I^{(0)}, \quad J \sim \tau^{-9} J^{(0)}, \quad \hat{\Psi}_2 \sim \tau^{-3} \hat{\psi}_2^{(0)}$$

[see Eq. (2.13)] where the quantities with a superscript $\cdot^{(0)}$ are constant along the geodesic. Assigning the radial coordinate using Eq (2.48) sets

$$\hat{r} \sim \tau \Re\left[\left(\hat{M}/\hat{\psi}_2^{(0)}\right)^{1/3}\right].$$

The peeling property states that the PNDs converge onto the out-going geodesic direction $\boldsymbol{\ell}$. Since each pair of PNDs are equidistant from the QKT $\hat{\boldsymbol{l}}$, this implies that $\hat{\boldsymbol{l}}$ approaches the $\boldsymbol{\ell}$ direction. The asymptotic relationship between $\hat{r}$ and τ given in Eq. (2.74), together with the condition Eq. (2.49) that we use to fix the boost freedom of the QKF, implies that $\hat{\boldsymbol{l}}$ not only asymptotes to the *direction*

of $\boldsymbol{\ell}$, it is also affinely parameterized in this limit. The geometrically constructed $\hat{r}$ asymptotically denotes the spherical wavefronts of light-rays approaching $\mathscr{I}^+$.

Lastly, we underscore the fact that using the QKT has the advantage of identifying a unique affine parameterization of the geodesic as it approaches $\mathscr{I}^+$. The prescription given in Eq. (2.49) for fixing the boost freedom of the QKT has used the geometry of the spacetime implicit in the Coulomb potential to fix the parameterization of $\hat{\boldsymbol{l}}$ in a global manner, removing the freedom to choose a different affine parameter through the transformation $\tau \to A\tau$. These ideas will be revisited in greater detail when we look at extrapolation in the context of the numerical simulations in Sec. 2.4.2.

2.4 Numerical implementation

In this section, we detail the numerical implementation of the analytic ideas mentioned in the previous sections using the Spectral Einstein Code (SpEC). A description of SpEC and the methods it uses are given in Ref. [34] and the references therein.

2.4.1 Constructing the QKT

We construct the QKT in a numerical simulation by first constructing an orthonormal tetrad adapted to the simulation's coordinate choice and then the orthonormal tetrad's null counterpart $\{\boldsymbol{l},\ \boldsymbol{n},\ \boldsymbol{m},\ \overline{\boldsymbol{m}}\}$ and the associated NP scalars Ψ_i. In order to find a QKF $\{\tilde{\boldsymbol{l}},\ \tilde{\boldsymbol{n}},\ \tilde{\boldsymbol{m}},\ \overline{\tilde{\boldsymbol{m}}}\}$, the construction described in Sec. 2.3.2 can be used; alternatively, the appropriate Type I and Type II transformations [Eqs. (2.14) and (2.15)] to the QKF can be found. Finally, we construct the geometrically motivated coordinate system $(\hat{r},\ \hat{\theta})$ described in Sec. 2.3.4, and we use these coordinates to fix the remaining Type III tetrad freedom to obtain the QKT.

2.4.1.1 Implementing a coordinate tetrad

Specifically, we begin our construction by noting that the SpEC code stores the spacetime metric g_{ab} on a Cartesian coordinate basis $\{x^a\} = \{t,\ x,\ y,\ z\}$. (Note that henceforth the index 0 refers to the time coordinate.) We can also define a set of related spherical coordinates $\{t,\ r,\ \theta,\ \phi\}$ by using the standard definitions

$$x = r\sin\theta\cos\phi, \quad y = r\sin\theta\sin\phi, \quad z = r\cos\theta. \tag{2.74}$$

We further define the time-like unit normal to the spatial slicing and radially outward-pointing vector as

$$T^a = \frac{\delta^a_0 - \beta^a}{\alpha}, \quad N^a = \frac{r^a}{\sqrt{r^b r_b}}, \tag{2.75}$$

respectively, where α is the lapse and β^a is the shift, and $\boldsymbol{r}$ is the spatial location vector. Inserting these orthonormal vectors into Eq. (2.1) yields $\mathbf{l}$ and $\mathbf{n}$, two legs of the null tetrad tied to the simulation's coordinates.

We next construct the remaining two tetrad legs $\{\mathbf{m},\ \overline{\mathbf{m}}\}$, ensuring that the normalization conditions of Eq. (2.2) are satisfied. In other words, we seek to construct the null vector $\boldsymbol{m} = 1/\sqrt{2}(\boldsymbol{E^2} + i\boldsymbol{E^3})$ where $\boldsymbol{E^2}$ and $\boldsymbol{E^3}$ are orthogonal to $\boldsymbol{T}$ and $\boldsymbol{N}$ and to each other and obey the normalization condition

$$\|\boldsymbol{E^2}\|^2 = \|\boldsymbol{E^3}\|^2 \quad = \quad 1.$$

Our construction begins by computing the vectors

$$\boldsymbol{K} = \frac{1}{r\sin\theta}\frac{\partial}{\partial\phi}, \quad \boldsymbol{F} = \frac{1}{r}\frac{\partial}{\partial\theta},$$

where θ, ϕ are spherical coordinates defined in Eq. (2.74). Then, we ensure orthogonality by means of the Grams-Schmidt-like construction

$$(\hat{F})^a \quad = \quad F^a + F^b l_b n^a + F^b n_b l^a, \tag{2.76}$$

rescaling appropriately to obtain the correct normalization as follows:

$$(E^2)^a = \frac{\hat{F}^a}{\sqrt{\hat{F}^a\hat{F}_a}}. \tag{2.77}$$

Similarly, for the final tetrad leg, we construct the orthogonal vector

$$(\hat{K})^a = K^a + K^b l_b n^a + K^b n_b l^a - K^b E^2_b (E^2)^a, \tag{2.78}$$

normalizing it as follows:

$$(E^3)^a = \frac{\hat{K}^a}{\sqrt{\hat{K}^a\hat{K}_a}} \tag{2.79}$$

2.4.1.2 Obtaining a tetrad in the QKF

Given the orthonormal coordinate tetrad $\{T^a,\ N^a,\ (E^2)^a,\ (E^3)^a\}$, we next construct a tetrad $\{\tilde{\boldsymbol{l}},\ \tilde{\boldsymbol{n}},\ \tilde{\boldsymbol{m}},\ \overline{\tilde{\boldsymbol{m}}}\}$ in the QKF by using the results of Sec. 2.3.2, in particular Eqs. (2.35), (2.40), (2.41) and (2.42). We can alternatively construct a QKF tetrad by explicitly rotating our initial coordinate tetrad into a transverse one via Type I and II transformations [Eqs. (2.14) and (2.15)]. We have implemented both constructions numerically and verified that they agree; in the remainder of this

subsubsection, we discuss details of each implementation in turn.

The hyper-surface approach of Sec. 2.3.2 requires us to solve the complex eigenvector problem in Eq. (2.35), with $\boldsymbol{Q}$ calculated either from Eq. (2.34) or from Eq. (2.12). Using Eq. (2.12), the eigenvector problem can be solved analytically. After computing the desired eigenvalue $\lambda = -2\hat{\Psi}_2$, which is the root of Eq (2.38) that admits the expansion (2.39) (in practice, it suffices to select the eigenvalue with the largest norm as suggested by Beetle et al. [8]), the corresponding un-normalized eigenvector $\tilde{\boldsymbol{\Sigma}}$ of matrix (2.12) is

$$\begin{aligned}
\tilde{\Sigma}_{E^2} =& 2\lambda^2 - \lambda\left(\Psi_0 + \Psi_4 - 2\Psi_2\right) + 2\left[\left(\Psi_1 + \Psi_3\right)^2 - \Psi_2\left(\Psi_0 + \Psi_4 + 2\Psi_2\right)\right], \\
\tilde{\Sigma}_{E^3} =& i\left[\lambda\left(\Psi_0 - \Psi_4\right) + 2\left(\Psi_3^2 - \Psi_1^2 + \Psi_2\left(\Psi_0 - \Psi_4\right)\right)\right], \\
\tilde{\Sigma}_{N} =& 2\left[\left(\Psi_0 + \Psi_2\right)\Psi_3 + \lambda\left(\Psi_1 - \Psi_3\right) - \Psi_1\left(\Psi_2 + \Psi_4\right)\right].
\end{aligned} \tag{2.80}$$

where the Ψ_i values are those extracted on the coordinate tetrad. (Note that this formula fails when $\Psi_1 = 0 = \Psi_3$, but in this case the coordinate tetrad is already in the QKF.) To normalize $\tilde{\boldsymbol{\Sigma}}$ into $\tilde{\boldsymbol{\sigma}}$ that satisfies Eq. (2.41), we multiply it with a suitable complex number, namely

$$\tilde{\boldsymbol{\sigma}} = \left[-\frac{1}{\sqrt{2}}\left(\frac{|\alpha|}{\alpha}\right)\frac{\sqrt{\beta+\gamma}}{\gamma} + \frac{\sqrt{2}|\alpha|}{\gamma\sqrt{\beta+\gamma}}i\right]\tilde{\boldsymbol{\Sigma}}$$

where

$$\begin{aligned}
\tilde{\Sigma}^a &= X^a + iY^a, \quad \alpha = X^a Y_a, \\
\beta &= ||\boldsymbol{X}||^2 - ||\boldsymbol{Y}||^2, \quad \gamma = \sqrt{\beta^2 + 4\alpha^2}.
\end{aligned}$$

Alternatively, we can construct the QKF using the Type I and II transformations applied to the coordinate frame as follows. Starting from a general Petrov Type I spacetime with five non-vanishing Weyl scalars, we perform a Type I rotation, introducing a parameter $\overline{a}$, followed by a Type II rotation that introduces a parameter b. These parameters can then be chosen to set $\Psi_1 = \Psi_3 = 0$ by solving the resulting system of two equations for the two parameters $\overline{a}$ and b. Reference [9] shows that the appropriate choice of parameters can be found by defining the intermediate quantities

$$H = \Psi_0\Psi_2 - \Psi_1^2, \quad G = \Psi_0^2\Psi_3 - 3\Psi_0\Psi_1\Psi_2 + 2\Psi_1^3 \tag{2.81}$$

and then setting

$$\Psi_1 + \Psi_0\overline{a} = \frac{G \pm \sqrt{G^2 + (\Psi_0\lambda - 2H)^2(H + \Psi_0\lambda)}}{\Psi_0\lambda - 2H} \tag{2.82}$$

$$b = -\frac{\Psi_3 + 3\overline{a}\Psi_2 + 3\overline{a}^2\Psi_1 + \overline{a}^3\Psi_0}{\Psi_4 + 4\overline{a}\Psi_3 + 6\overline{a}^2\Psi_2 + 4\overline{a}^3\Psi_1 + \overline{a}^4\Psi_0} \tag{2.83}$$

Note that this prescription becomes ill defined when Ψ_0 on the the initial tetrad approaches zero or when $\Psi_0\lambda - 2H = 0$, making it difficult to find $\overline{a}$ by solving Eq. (2.82); this problem is easily resolved by first applying a Type II transformation that takes the initial tetrad into one in which these pathologies do not arise. Furthermore, we have two possible solutions for $\overline{a}$ resulting from the freedom to interchange the $\tilde{\boldsymbol{l}}$ and $\tilde{\boldsymbol{n}}$ legs associated with the transverse frame; the convention we use is to choose the root that gives $(\tilde{l} - \tilde{n})_a l^a > 0$, i.e. we choose $\tilde{\boldsymbol{l}}$ to be outgoing in the simulation coordinates.

2.4.1.3 Obtaining the quasi-Kinnersley tetrad from the geometric coordinates

With a QKF in hand, we next seek to specialize to the particular QKT described in Sec. 2.3.5, where we use geometrically motivated coordinates $(\hat{r}, \hat{\theta})$ given by Eq. (2.48) to fix the final Type III degrees of freedom. In order to fix these freedom using Eqs. (2.49) and (2.50), we must calculate the one-forms $d\hat{r}$ and $d\hat{\theta}$. We compute the spatial derivatives spectrally, and we compute the time derivatives using the Bianchi identities in the $3+1$ form [35]

$$\begin{aligned}
\partial_t \mathcal{E}_{ij} =& \mathcal{L}_\beta \mathcal{E}_{ij} + \alpha \left[D_k \mathcal{B}_{l(i} \epsilon_{j)}{}^{kl} - 3\mathcal{E}^k_{(i} K_{j)k} + K^k_k \mathcal{E}_{ij} - \epsilon_i{}^{kl} \mathcal{E}_{km} K_{ln} \epsilon_j{}^{mn} + 2a_k \mathcal{B}_{l(i} \epsilon_{j)}{}^{kl} \right], \\
\partial_t \mathcal{B}_{ij} =& \mathcal{L}_\beta \mathcal{B}_{ij} + \alpha \left[-D_k \mathcal{E}_{l(i} \epsilon_{j)}{}^{kl} - 3\mathcal{B}^k_{(i} K_{j)k} + K^k_k \mathcal{B}_{ij} - \epsilon_i{}^{kl} \mathcal{B}_{km} K_{ln} \epsilon_j{}^{mn} - 2a_k \mathcal{E}_{l(i} \epsilon_{j)}{}^{kl} \right],
\end{aligned} \tag{2.84}$$

where $\mathcal{L}$ denotes Lie derivative, D is induced 3-D covariant derivative operator, α denotes the lapse, $\boldsymbol{\beta}$ the shift, $\boldsymbol{K}$ the extrinsic curvature, and $a_k = \partial_k \ln\alpha$. The time derivative of the metric $\partial_t g_{ij}$ is already known from the numerical evolution of the spacetime. Using the above equations and applying the chain rule, we compute the time derivatives of $\hat{r}$ and $\hat{\theta}$:

$$(\partial_t g_{ij}, \partial_t \mathcal{E}_{ij}, \partial_t \mathcal{B}_{ij}) \xrightarrow{\text{Eqns. (2.13),(2.38),(2.48)}} \left(\partial_t \hat{r}, \partial_t \hat{\theta} \right).$$

Equipped with all the components of $d\hat{r}$ and $d\hat{\theta}$, we can apply Eqs. (2.51) and (2.52) to fix spin-boost degree of freedom, finally obtaining the QKT on which we can then extract Newman-Penrose scalars $\hat{\Psi}_i$ via Eqs. (2.4-2.8).

We note that it may not always be possible to define the $\hat{r}$ and $\hat{\theta}$ coordinates using Eq. (2.48) for spacetimes with additional symmetries. For example, in axisymmetric spacetimes admitting a twist-free azimuthal Killing vector, $\hat{\Psi}_2$ is real, and as a result the $\hat{\theta}$ coordinate cannot be computed using Eq. (2.48). In fact, for Minkowski spacetimes, we cannot even define the $\hat{r}$ coordinate, because $\hat{\Psi}_2 = 0$. In such cases, the symmetries of the spacetime typically provide a set of preferred coordinates, which one would naturally adopt in a numerical simulation. In our QKT implementation, we presume that any such preferred coordinates are adopted, and we replace $(d\hat{r}, d\hat{\theta})$ by their simulation-coordinate counterparts when degeneracies occur.

2.4.2 Extrapolation

We now turn to extracting the asymptotic gravitational wave content at $\mathscr{I}^+$ by using the peeling property, i.e., to *extrapolation*, which necessarily involves information from several spatial slices in the spacetime. Our procedure is to shoot a null geodesic affinely parametrized by τ toward $\mathscr{I}^+$, monitoring $\hat{\Psi}_4$ along the geodesic. The best possible polynomial in $1/\tau$ is fitted to the result. The existence of this polynomial follows from the peeling property, which is made explicit in Eq. (2.66). We identify the coefficient of the $1/\tau$ term or $\psi_4^{(0)}$ with the radiation content at $\mathscr{I}^+$.

In contrast to the usual method (extrapolating Ψ_4 as computed using a tetrad parallel-transported along an outgoing null geodesic), note that here we choose to extrapolate $\hat{\Psi}_4$ (defined using the QKT), which we expect to also display the correct peeling behavior [see Sec. 2.3.8.3]. In addition, the initial direction of the outgoing null geodesic is along $\hat{\boldsymbol{l}}$, so at the geodesic's starting point $\Psi_4 = \hat{\Psi}_4$, and [Sec. 2.3.8], at $\mathscr{I}^+$ also the outgoing null geodesic is along $\hat{\boldsymbol{l}}$ so that $\Psi_4 = \hat{\Psi}_4$. In practice, as we integrate along these outgoing null geodesics, we monitor the difference between the null vector $\boldsymbol{\ell}$ tangent to the outgoing geodesic and $\hat{\boldsymbol{l}}$ from the QKT, and we find that this difference remains small (cf. Fig. 2.3 and the surrounding discussion). Therefore Ψ_4 and $\hat{\Psi}_4$ are not significantly different for the simulations we examined. When we extract the $\hat{\Psi}_4$ waveform, it converges rapidly to its asymptotic value with increasing extraction radius [Fig. 2.16].

Selecting the initial tangent of the geodesics to be $\hat{\boldsymbol{l}}$ determines the parameterization of these geodesics upto an additive constant B corresponding to the freedom to shift the zero point of the affine parameter, $\tau \to \tau + B$. The asymptotic waveform is insensitive to the choice of the field B. Nevertheless, to provide an exact prescription we fix B by recalling that in the Kerr limit, the affine parameter is just the Boyer-Lindquist $\hat{r}$ [14]. We thus choose B on the initial world tube (where we start shooting out null geodesics) to be such that $\tau = \hat{r}$.

2.4.3 Sensitivity of QKT method to numerical error

The numerical implementation of the QKT described in this section keeps the computation "as local as possible" in the following sense: the bulk of the calculation requires only local derivatives and knowledge of the metric and the extrinsic and intrinsic curvature of the spatial slice. However, this says nothing about the *accuracy* of our method, which depends on how susceptible our method is to numerical noise.

To begin addressing this issue, we first recall exactly how many numerical derivatives are to be taken. Equation (2.34), which is used to construct the gravitoelectromagnetic tensors $\boldsymbol{\mathcal{E}}$ and $\boldsymbol{\mathcal{B}}$, requires i) second spatial derivatives of the spatial metric in order to get the intrinsic Ricci curvature, in addition to ii) the first spatial derivatives of the extrinsic curvature of the slice. Once the gravitoelectromagnetic tensor is obtained and the resulting curvature invariants I and J are computed, another

derivative is required to compute the gradients of the coordinates $(\hat{r}, \hat{\theta})$ that then fix the Type III freedom of the tetrad. Note that the first step, i.e. the computation of the gravitoelectromagnetic tensors only requires spatial derivatives, which we can compute spectrally (i.e., inexpensively and accurately, since we expect to observe exponential convergence in spatial derivatives with increasing spatial resolution). However, taking the gradient of the coordinates constructed out of the curvature invariants requires both spatial derivatives and a time derivative. Fortunately, this time derivative can be computed using the Bianchi identities as described in Sec. 2.4.1.3, which again reduces the operation to spatial differentiation (although here the accuracy of the derivatives are also limited by the accuracy at which the constraint equations are satisfied).

What we find in practice is that the higher derivatives needed by our QKT method can at places have a significantly higher amount of numerical noise than the numerical derivatives directly used in the actual evolution system. This is a significant challenge to our method, since SpEC presently evolves the Einstein equations in first-order form, i.e., as a set of coupled partial differential equations containing only first derivatives in space and time. Therefore, the evolution equations themselves will only guarantee the existence of one derivative of the evolution variables (e.g., of the metric). Constraints show convergence which means, among other things, that the auxiliary variables (defined during the reduction of second order differential equations to first order) do converge to the appropriate metric derivative quantities. However, the evolution system, although quite capable at constraining the size of numerical error, does not necessarily force it to be smooth (differentiable to higher orders) at subdomain boundaries.

Consider the hypothetical example of adding white noise to a smooth analytical metric, such as the Kerr metric (2.20). No matter how small the magnitude of the noise, it would prevent us from taking derivatives analytically. Numerically, under-resolving the high-frequency noise would smooth out the data and allow differentiations to proceed without significantly amplifying the added noise; therefore, we expect that filtering (the spectral equivalent of finite-difference dissipation) would improve the smoothness of the numerical data and thus reduce difficulty in taking higher numerical derivatives. However, such filtering can effectively under resolve not only noise but also physical information. In other words, overly dissipative schemes tend to be *less* accurate; therefore, the current choice in SpEC is to dissipate as little as possible while still maintaining robust numerical stability. This criterion is different from the use of filtering to damp out on short time scales any high frequency modes that would be produced during an evolution.

A better approach for reducing non-smooth numerical error is to go directly to their source. The lack of smoothness in the constraints observed in a typical SpEC evolution is partly due to the penalty algorithm, which is known to produce convergent but non-smooth numerical errors at subdomain boundaries. [See Fig. 2.4(b) for an illustration of the penalty-algorithm induced non-smooth error.] Because this non-smoothness converges away with increased resolution, our method

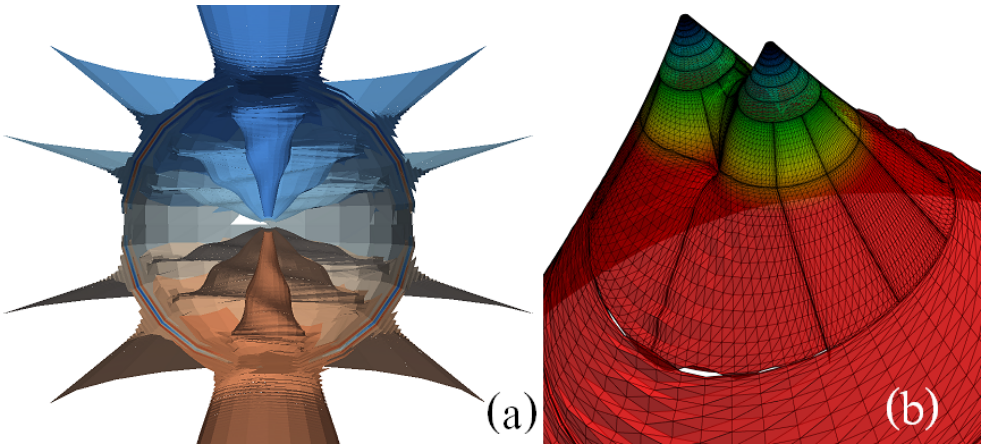

Figure 2.4: (a) $\hat{\theta}$ contours displaying a pulse of high frequency junk radiation propagating outward. Ahead of the pulse, the geometric coordinate contours are consistent with the Kerr-like initial data, but behind the pulse of junk radiation, the spacetime settles down to an actual binary inspiral with a signature "spiral-staircase" pattern also seen in Fig. 2.2(b). (b) The surface is a 2-D spatial slice containing the symmetry axis in a head-on simulation, warped and colored according to $\hat{r}$ value. The sub-domain boundaries are marked out with dense black lines, and appear to be a source of non-smooth noise. These noisy features are reduced by increasing resolution.

is observed to be viable given a sufficiently high numerical resolution; however, it remains to be seen whether "sufficiently high" means "significantly higher" than typical resolutions currently in use. Alternatively, improvement to non-smooth numerical error could come through the use of newer inter-patch boundary algorithms, such as Discontinuous Galerkin methods [36]. There also exists an ongoing effort to bring a (currently experimental) first-order-in-time, second-order-in-space version of SpEC [37] into a state suitable for accurate gravitational-wave production, with the hope of added efficiency and of achieving numerical error of higher differential order. Such possibilities as these, however, are future work, well outside the scope of this paper.

Lastly, we consider the non-smooth noise sensitivity of our QKT quantities from another point of view: it can be used as a diagnostic of high-frequency, non-smooth numerical error. For instance, one source of non-smooth constraint violation in numerical simulations is the high-frequency, spurious "junk" radiation present at the beginning of numerical simulations (because of how the initial data are constructed), which poses a particularly difficult numerical problem. The frequency of these modes is of $O(M)$, orders of magnitude higher than that of the orbital motion (and the associated gravitational waves). This makes resolving the junk radiation a difficult task. In the effort to reduce junk radiation, the geometric coordinates can be used as a visualization tool. Fig. 2.4(a) is an illustration of how the $\hat{\theta}$ contours, plotted as a function of code coordinates, react to the junk travelling through the grid, while adjusting themselves to reflect a more realistic spacetime. By comparing the difference ahead and behind the easily identifiable junk pulse in Fig. 2.4(a), one gets a glimpse of the missing pieces in the initial data.

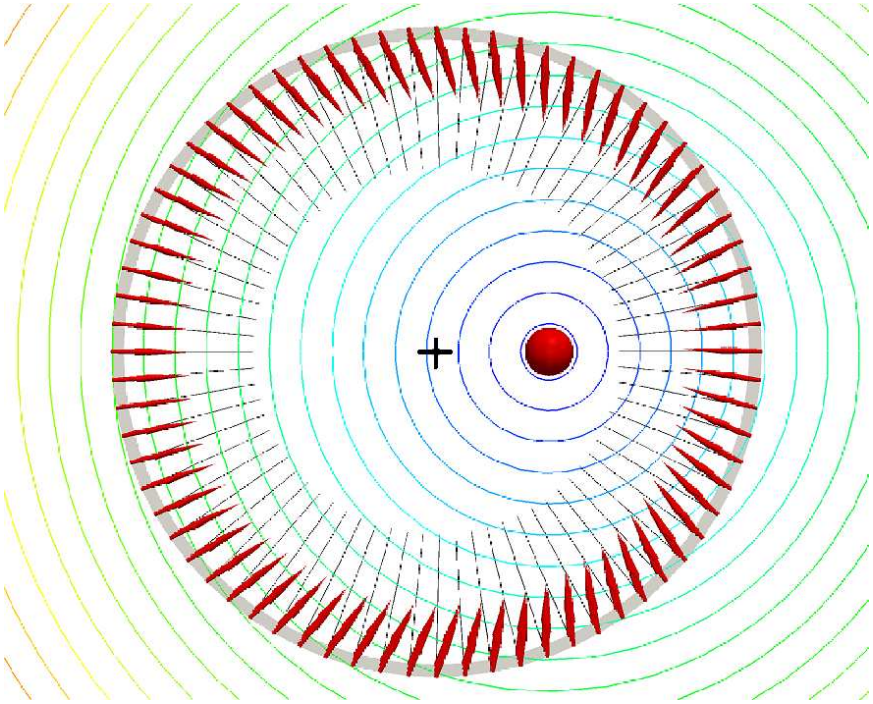

Figure 2.5: A Kerr-Schild black hole with $J/M^2 = 0.5$, with the coordinates translated a distance $9M$ along x axis. The red sphere indicates location of the black hole's horizon, and the black cross indicates the coordinate origin. The colored circles are constant geometric radius $\hat{r}$ contours; these demonstrate the ability of our geometric coordinates to select an origin based on the Coulomb potential of the QKF, i.e., an origin which reflects the gravitational curvature of the spacetime. Also shown are the spatial projections of the $\boldsymbol{n}$ direction of the coordinate and quasi-Kinnersley tetrads, at points on a narrow strip marked by a grey ring. The black lines indicate the $\boldsymbol{n}$ direction associated with the coordinate tetrad, which point toward the coordinate origin, and the red lines/arrows are QKT $\hat{\boldsymbol{n}}$ directions that identify the black hole as geometric origin, away from which the gravitational waves travel.

2.5 Numerical Tests of the QKT scheme

We now consider several numerical tests used to gauge the effectiveness of our proposed QKT scheme for waveform extraction. Most of these tests are motivated by analytic solutions and are used to verify that our choices of geometric coordinates and the QKT are yielding the expected results. These tests broadly fall into two classes: i) non-radiative spacetime tests and ii) radiative spacetime tests. Each will be considered in turn in the following subsections.

2.5.1 Non-radiative spacetimes

2.5.1.1 Kerr black hole in translated coordinates

The spacetime in this test is a Kerr black hole in Kerr-Schild coordinates, but the coordinate origin is translated away from the black hole along x or z axis. Here we work in units of the black hole mass, and the dimensionless spin is $J/M^2 = 0.5$ pointing in the z direction. Tetrads determined

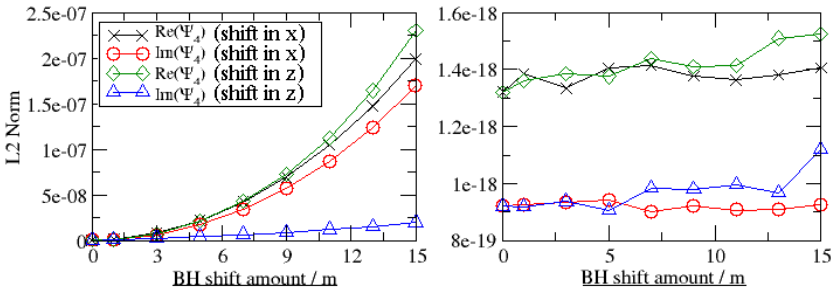

Figure 2.6: (a): The L_2 norm [Eq. (2.85)] of Newman-Penrose scalar Ψ_4 computed (between radii 50M and 140M) for the Kerr-Schild black hole in translated coordinates on the coordinate tetrad. (b): The Newman-Penrose scalar $\hat{\Psi}_4$ computed in the quasi-Kinnersley tetrad. Note the L_2 norm is eleven orders of magnitudes smaller for the QKT when compared to that of the coordinate tetrad, showing that the QKT correctly adapts to the underlying curvature of the spacetime.

only by our simulation coordinates [see Eqs. (2.75)-(2.79)] would not be aware of the translation, and the spatial projection of $\boldsymbol{n}$ would point toward the coordinate center instead of the black hole itself. In contrast, the QKT should adjust to the displaced origin, picking up the true geometrical origin of the gravitating system determined by the Coulomb potential of the QKF. Figure 2.5 shows the direction of spatial projection of $\boldsymbol{n}$ and $\hat{\boldsymbol{n}}$ associated with the two tetrads. The QKT identifies the black hole at the center of the circular shape, as do the geometrically motivated coordinate $\hat{r}$.

Figure 2.6 compares Ψ_4 extracted using the coordinate and quasi-Kinnersley tetrads, respectively, using the so-called "L_2 norm" as a measure. The L_2 norm of a quantity X is defined here as

$$L_2(X) = \sqrt{\sum_{i=1}^{N_{tot}} \frac{X(x_i)^2}{N_{tot}}}, \tag{2.85}$$

where x_i are the spectral collocation points of a pseudo-spectral grid and N_{tot} is the total number of points. The present study uses four spherical shells between radii 50M and 140M with $N_{tot} \approx 4 \times 45^3$ collocation points. The QKT correctly produces vanishing $\hat{\Psi}_4$ (up to numerical round-off error), while the coordinate tetrad fails to identify the correct out-going direction and as a result misinterprets $\hat{\Psi}_2$ as gravitational radiation content in Ψ_4. (We observe similar behavior for Ψ_0.) Using such a coordinate tetrad in a simulation with a displaced center will result in spurious effects being picked up in the extracted radiation, of a magnitude not necessarily smaller than the physical gravitational wave content of the spacetime.

In a simulation of a dynamical spacetime, a similar effect should be expected when the "center of mass" (e.g. in a Newtonian approximation) of the system does not coincide with coordinate center. For example, consider a binary merger of unequal mass holes with the coordinate origin placed at the midpoint between the black holes; Ψ_4 extracted at finite radii would pick up a slowly varying offset at an integer multiple of the orbital frequency, and this contribution would complicate the

extrapolated waveform.

2.5.1.2 A Schwarzschild black hole with translated coordinates and a gauge wave

We further explore the effects of coordinate choice or gauge by introducing a time dependent gauge wave into a Schwarzschild solution whose origin has been translated by a constant amount. The resulting metric components now have an explicit time dependence, and we expect the coordinate tetrad to produce a false gravitational wave signal, even though the Schwarzschild spacetime is static and emits no physical radiation.

The exact analytic solution we use for this test is constructed from the Schwarzschild solution in ingoing Eddington-Finkelstein coordinates. We then apply a time-dependent coordinate transformation that yields a metric of the form

$$\begin{aligned} ds^2 = &-(1+C)^2\left(1-\frac{2M}{r}\right)dt^2 + 2(1+C)\left[\frac{2M}{r} - \left(1-\frac{2M}{r}\right)C\right]dtdr \\ &+ (1+C)\left[1+\frac{2M}{r} - \left(1-\frac{2M}{r}\right)C\right]dr^2 + r^2 d\Omega^2 \end{aligned} \tag{2.86}$$

where $C(r,t)$ is the radial waveform of the introduced gauge wave. For our test we select generically chosen parameters

$$C = 0.7\sin(0.03(t+r)+3.1), \quad M = 1$$

Note that again we translate the black hole off the coordinate origin by a constant amount (here $r = 20$M) as described in the previous subsubsection.

Figure 2.7 shows spin-weighted spherical harmonic expansion coefficients $\Psi_4^{(l,m)}$ of Ψ_4, computed using the coordinate and quasi-Kinnersley tetrads. While only the three largest amplitudes are shown, we have computed all amplitudes up through $l = 35$. These scalars are computed on a sphere at a radius of 120M from the black hole, with the poles of harmonics aligned with the direction in which the black hole is shifted. As expected, the waveform extracted using the coordinate tetrad picks up a time dependence associated with the gauge wave, while the QKT returns vanishing values, correctly identifying the static spacetime solution.

In the generalized harmonic form of the Einstein field equations, the gauge may be set by the covariant wave equations

$$\Box x^a = H^a$$

where H is either a specified or evolved source function [38, 39, 40, 41]. It is thus probable that gauge modes similar to the one considered in this example may be present in fully dynamical sim-

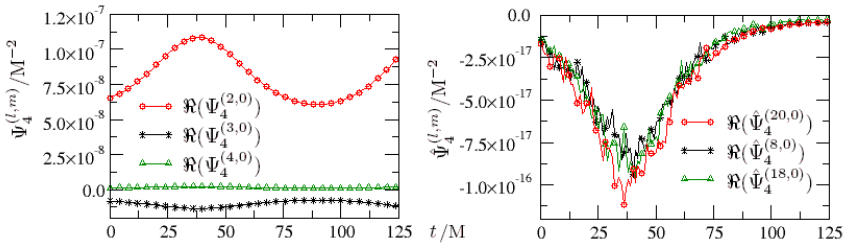

Figure 2.7: Spherical harmonic coefficients of Newman-Penrose Ψ_4 computed for the gauge wave solution, on a sphere of radius $r = 120$M centered on the black hole. (a): Ψ_4 extracted on the coordinate tetrad. (b): $\hat{\Psi}_4$ extracted on the QKT. Only the three largest (l, m) spin-weighted spherical harmonic modes (up through $l = 35$) are shown. Note the scaling on the two figures differ by nine orders of magnitude.

ulations. Consider a gauge wave that generates a deviation between the coordinate tetrad basis vectors $\{\boldsymbol{l},\ \boldsymbol{n},\ \boldsymbol{m},\ \overline{\boldsymbol{m}}\}$ and their counterparts in the QKT. Such differences can be represented by a sequence of type II, I and then III transformations parameterized by the time dependent transformation parameters $b(t)$, $a(t)$ and $\mathcal{A}(t)$ that appear in Eqs. (2.15), (2.14) and (2.16) respectively. If we restrict ourselves to asymptotic regions where $\hat{\Psi}_4$ dominates over other NP scalars, then according to Eqs. (2.18), (2.17) and (2.19), we have that to leading order in a and b the coordinate Ψ_4 is given by

$$\Psi_4 = (1 + 4\overline{a}(t)b(t))\,\mathcal{A}^{-2}(t)\hat{\Psi}_4.$$

If the gauge wave falls off when we move away from the source region, then we may have

$$(1 + 4\overline{a}(t)b(t))\,\mathcal{A}^{-2}(t) \to 1$$

and its effect can in principle be extrapolated away. However, for some cases, such as a plane gauge wave, the time dependent perturbation introduced into Ψ_4 could persist in the extrapolated waveform. Therefore, minimizing any such gauge-dependent content in Ψ_4 extracted at finite radii is preferable to relying on extrapolation to remove them; some pathological gauge modes might not fall off sufficiently quickly with radius.

2.5.2 Radiative spacetimes

Having observed that the QKT correctly reflects the curvature content of non-radiative spacetimes, including in the presence of a gauge wave, we next apply the QKT to spacetimes emitting gravitational radiation. In this subsection, we verify that the scheme is consistent with analytic perturbation theory results.

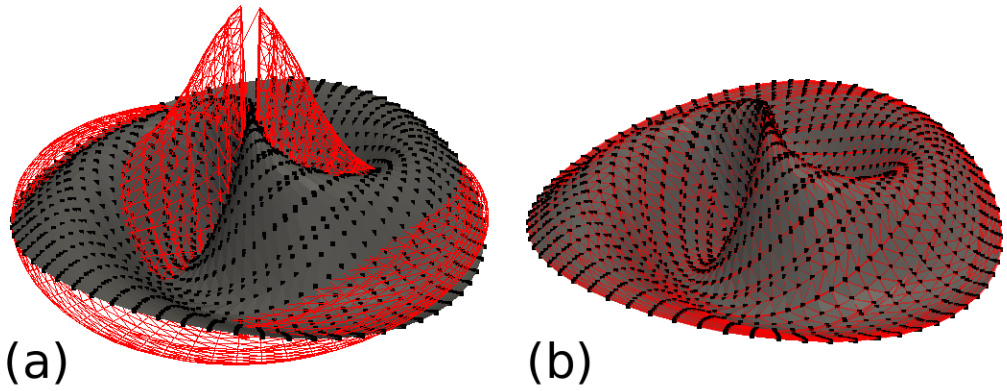

Figure 2.8: $\Re(\Psi_4)$ resulting from a traveling-wave perturbation on the equatorial plane of the computational domain. Panels (a) and (b) correspond to results obtained with and without the coordinate transformation (2.92). We use $\underline{\Psi_4}$, Ψ_4 and $\hat{\Psi}_4$ to respectively denote the analytical result and the values computed on the coordinate and quasi-Kinnersley tetrads. The height of the surface in the vertical direction indicates the value of $\Re(\Psi_4)$, the solid grey surface denotes $\Re(\underline{\Psi_4})$, the red wireframe $\Re(\Psi_4)$ and the black dots $\Re(\hat{\Psi}_4)$. The amplitude of the red wireframe has been suppressed by a factor of 10^3 in (a) so that it fits into the figure. The suppression factor has not been applied to Panel (b).

The QKT by construction reduces to the Kinnersley tetrad in the Kerr limit. Therefore, if we perturb a Kerr black hole by a small amount, the $\hat{\Psi}_4$ computed on the QKT should reproduce the analytic perturbation theory results computed on the Kinnersley tetrad associated with the unperturbed Kerr background. Verifying this correspondence provides us with the means to quantitatively test whether the QKT extracts the correct waveform and that we have all normalization conventions implemented correctly. The idea of ensuring the correspondence between the computed waveform and the perturbation theory results is what motivated the authors of Ref. [8] to adopt transverse tetrads in the first place; Chandrasekhar [14] also used the transverse tetrad in his metric reconstruction program, where he explicitly computed the perturbed tetrad and curvature perturbations on the tetrad, obtaining the expected correspondence. For simplicity, here we perturb a Schwarzschild black hole with an odd-parity Regge-Wheeler-Zerilli (RWZ) perturbation, as described in Ref. [42].

We start with a background Schwarzschild metric in Schwarzschild coordinates expressed in the standard form of [42]

$$ds^2 = (-\alpha^2 + \gamma^2\beta^2)dt^2 + 2\gamma^2\beta dt dx + \gamma^2 dx^2 + r^2(d\theta^2 + \sin^2\theta d\phi^2)$$

where

$$x = r, \quad \alpha(r) = \sqrt{1 - \frac{2M}{r}}, \quad \beta(r) = 0, \quad \gamma(r) = \frac{1}{\alpha(r)}. \tag{2.87}$$

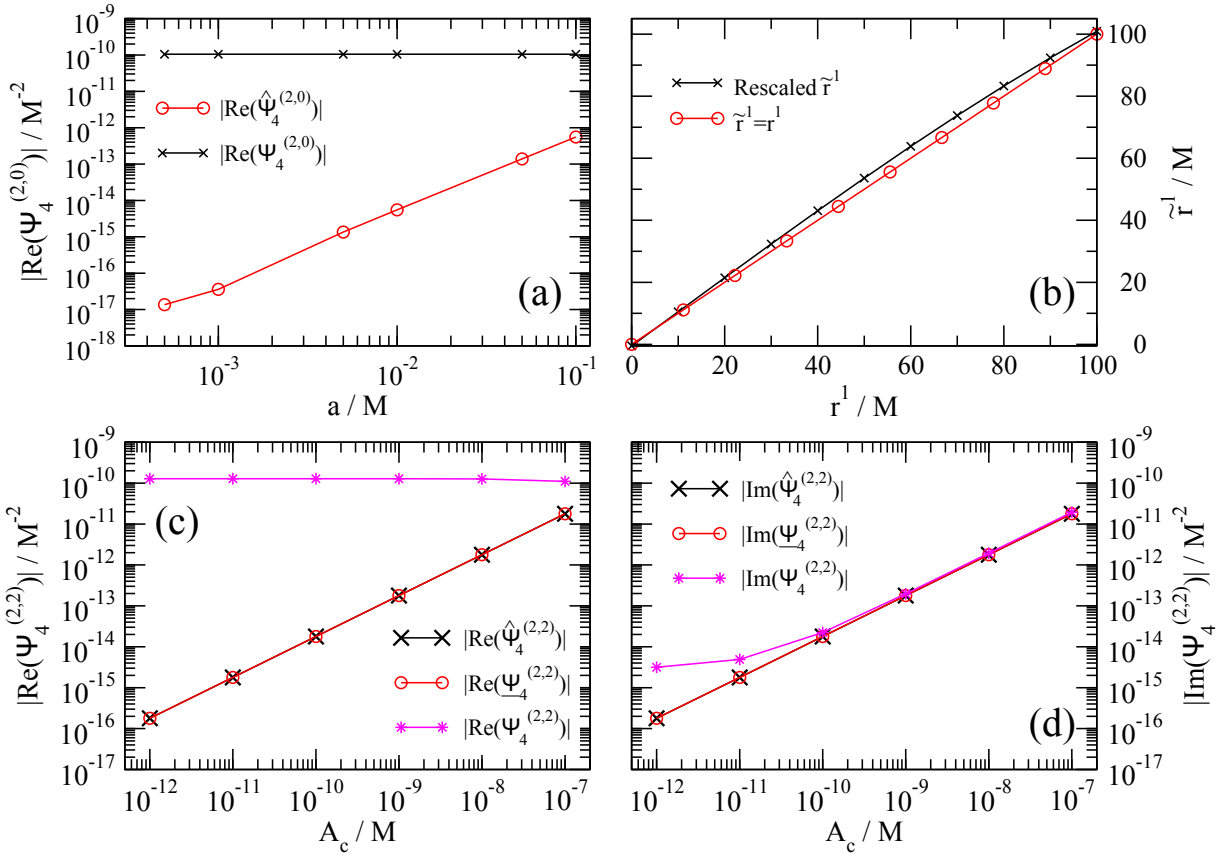

Figure 2.9: Testing the QKT's ability to recover perturbation theory results. An $l = 2, m = \pm 2$ perturbation, with magnitude A_c, is added as a function of retarded time in addition to an $l = 1$, $m = 0$ perturbation, and finally a cubic coordinate distortion is applied as described in Eq. (2.92). The spherical harmonic coefficients of the coordinate-tetrad Ψ_4 and QKT $\hat{\Psi}_4$ are then extracted at Boyer-Lindquist radius 95M and compared with the analytic results $\underline{\Psi}_4$. (a): The magnitude of the Ψ_4, $(l, m) = (2, 0)$ mode as a function of spin parameter a, with the radiative $(2, \pm 2)$ perturbation held fixed at $A_c = 10^{-9}$M. (b): Exploring the effect of cubic rescaling. The rescaled first component of $\tilde{\boldsymbol{r}}$ vector, $\tilde{r}^1$, is plotted against the original component r^1. The identity map ($\tilde{r}^1 = r^1$) is given for comparison. (c) and (d): The real and imaginary parts of the ${}_{-2}Y_{22}$ coefficient vs the amplitude A_c of the radiative perturbation. The $l = 1, m = 0$ mode amplitude is chosen so that the resulting angular momentum perturbation is held constant at $a = 0.001$M.

We then introduce $l = 2, m = \pm 2$ radiative perturbations. The full RWZ formalism giving the explicit calculation of the perturbed metric is expounded concisely in Appendix A of [42]; it turns out that the construction of the perturbed metric and the associated perturbed curvature quantities (such as Ψ_4) hinges on one function, the RWZ function Z, which obeys the RWZ equation

$$\frac{\partial^2 Z}{\partial t^2} = c_1 \frac{\partial^2 Z}{\partial t \partial r} + c_2 \frac{\partial^2 Z}{\partial r^2} + c_3 \frac{\partial Z}{\partial t} + c_4 \frac{\partial Z}{\partial r} - \alpha^2 V Z. \tag{2.88}$$

In the RWZ equation, the coefficients c_i are functions of α, β and γ, which for our chosen values

[Eq. (2.87)] become

$$\begin{aligned} c_1(r) &= 0 = c_3(r), \\ c_2(r) &= \left(1-\frac{2M}{r}\right)^2, \\ c_4(r) &= \frac{2M}{r^2}\left(1-\frac{2M}{r}\right), \\ \alpha^2 V &= \left(1-\frac{2M}{r}\right)\left(l(l+1)-\frac{6M}{r}\right)\frac{1}{r^2}. \end{aligned}$$

Given Z, the analytic solution $\underline{\Psi_4}$ for the gravitational wave content in the spacetime can be computed to first order using

$$\underline{\Psi}_4^{(1)} = -\sum_{lm}\left[\frac{i}{r}(\tilde{\Delta}+2\gamma+2\mu)\tilde{\Delta}Z_{lm}\right]C_l\left[{}_{-2}Y^{lm}\right], \tag{2.89}$$

where $C_l = \sqrt{(l-1)l(l+1)(l+2)/4}$, the operator $\tilde{\Delta}$ is $\underline{n}^a\nabla_a$ with $\underline{\boldsymbol{n}}$ being a null direction associated with the background Kinnersley tetrad, and γ and μ are spin coefficients associated with the same background tetrad, which for our case are [14]

$$\mu = -\frac{\Delta}{2\Sigma\rho}, \quad \gamma = \mu + \frac{r-M}{2\Sigma}$$

where Δ, Σ and ρ are defined in Eq. (2.21).

Note that in the discussion that follows, $\underline{\Psi_4}$ denotes the analytic result while Ψ_4 and $\hat{\Psi}_4$ are, respectively, the computed values on the coordinate and quasi-Kinnersley tetrads in the numerical implementation.

In order to solve the linear second order partial differential equation (2.88) for Z, an initial value and time derivative for Z must be specified. For our investigation, we make use of a traveling-wave perturbation of the form

$$Z(t_0,r) = A_c e^{i\omega(t_0-r_*)}, \quad \frac{\partial Z}{\partial t}(t_0,r) = i\omega A_c e^{i\omega(t_0-r_*)} \tag{2.90}$$

where r_* is the usual tortoise coordinate defined by $dr_*/dr = r/(r-2M)$, while $t_0 = 0$, $\omega = 0.1$ and A_c is a constant initial amplitude. For our test, we also set $M = 1$. This perturbation is graphically depicted in Fig. 2.8. The waveform constructed from the perturbation has the classical profile for Ψ_4, often observed during numerical binary black hole mergers; this is to be expected, since $l = 2$ is the dominant mode contributing to the gravitational radiation emitted by a binary.

Next, we numerically compare the coordinate-tetrad Ψ_4 and the QKT $\hat{\Psi}_4$ with the analytic perturbation-theory result $\underline{\Psi}_4$. In this test, we adopt the Boyer-Lindquist coordinates; therefore, the

corresponding coordinate orthonormal tetrad [see Eq. (2.75)] happens to coincide with a Kinnersley frame of the background spacetime [although it is boosted with respect to the Kinnersley tetrad in Eqs. (2.22)-(2.24)].

To illustrate this more clearly, observe that the standard coordinate tetrad we constructed in Sec. 2.4.1.1 results in orthonormal vectors T^a and N^a that are respectively

$$T^a = \left[\frac{1}{\alpha},\, 0,\, 0,\, 0\right], \quad N^a = [0,\, \alpha,\, 0,\, 0]$$

when expressed on the coordinate basis, where $\alpha = \sqrt{1-2M/r}$ is the lapse of the background metric. The resulting null vector l^a constructed according to Eq. (2.1) is

$$l^a = \frac{1}{\sqrt{2}}(T^a + N^a) = \frac{1}{\sqrt{2}}\left[\frac{1}{\alpha}, \alpha, 0, 0\right].$$

In the static limit, the Kinnersley tetrad [Eqs. (2.22) and (2.23)] reduces to

$$\hat{l}^a = \left[\frac{1}{\alpha^2},\, 1,\, 0,\, 0\right], \quad \hat{n}^a = \frac{1}{2}\left[1,\, -\alpha^2,\, 0,\, 0\right] \tag{2.91}$$

so $\hat{l}^a = \sqrt{2}l^a/\alpha$ and there exists a relative boost factor of $A = \alpha/\sqrt{2}$ between the coordinate and Kinnersley tetrads.

Therefore, to account for the difference, we will multiply the coordinate-tetrad Ψ_4 by $(1-2M/r)/2$ throughout this subsection to facilitate comparison with analytical and QKT values. With this adjustment, the extracted quantities Ψ_4 and $\hat{\Psi}_4$ both match the analytically calculated $\underline{\Psi}_4$ from perturbation theory. These results are graphically depicted in Fig. 2.8(b).

Next, we explore the gauge dependence of the QKT result. To this end, we introduce a coordinate transformation into some other gauge. As a result, the coordinate tetrad associated with the new "non-privileged gauge" differs from the QKT, resulting in a mismatch between the coordinate Ψ_4 and the analytic perturbation theory result $\underline{\Psi}_4$ [see Fig. 2.8(a)]. The QKT $\hat{\Psi}_4$ implemented in the code should then be able to recover the analytic result. As an illustrative example, for a gauge transformation we choose a cubic rescaling of the spatial coordinates, which takes the radial vector r^a expressed on a Cartesian coordinate basis defined in Sec. 2.4.1 to a vector with components $\tilde{r}^a$ using the equation

$$\tilde{r}^a = \left(\nu + \frac{\nu^0 - \nu}{R^2}|r - r_0|^2\right)(r^a - r_0^a) + r_0^a. \tag{2.92}$$

where we choose $r_0^a = (5M, 0, 0)$, $R = 100M$, $\nu_0 = 1$ and $\nu = 1.1$. Panel (b) of Fig. 2.9 compares the coordinates before and after rescaling.

We now calculate the perturbed metric in the new distorted coordinates and extract the gravita-

tional waves using both the coordinate tetrad and the QKT, comparing the results with the analytical $\underline{\Psi}_4$ calculated in the Boyer-Lindquist coordinates and visually portrayed in Fig. 2.8. When no coordinate distortions have been introduced [Fig. 2.8 (b)], the coordinate tetrad and the QKT both generate Ψ_4 that matches the analytical prediction. When we apply the cubic coordinate distortion described above however, the coordinate tetrad result deviates from $\underline{\Psi}_4$, but the QKT still recovers the analytical value [Fig. 2.8 (a)].

In addition to the coordinate transformation we also add a $l = 1$, $m = 0$ mode [explicit expressions for metric perturbation due to this mode can be found in Appendix A1a of Ref. [42]]. This mode should make no contribution to the detected radiation in $\hat{\Psi}_4$, but should introduce a small angular momentum perturbation affecting the spin of the spacetime, thus avoid degeneracy in $\hat{\theta}$. The amplitude of the perturbation is usually set so that the spin of the resulting spacetime is $a = J/M = 0.001$. After imposing the coordinate distortion and adding the $l = 1$ $m = 0$ mode, we extract ${}_{-2}Y_{lm}$ coefficients of Ψ_4 and $\hat{\Psi}_4$ on a sphere of Boyer-Lindquist radius 95M from the black hole. We begin by exploring the effect of the $l = 1$, $m = 0$ mode. Figure 2.9 (a) shows the effect of increasing the strength of the $l = 1$, $m = 0$ perturbation on the $l = 2$, $m = 0$ mode of extracted waveform; recall that we did not introduce an $l = 2$, $m = 0$ mode into the metric perturbation. The coordinate quantity $\Psi_4^{(2,0)}$ shows a constant value possibly originating from the cubic coordinate distortion. The quantity $\hat{\Psi}_4^{(2,0)}$, on the other hand, shows a strong dependence on the $l = 1$ perturbation amplitude; this could be due to the fact that the projection onto spherical harmonics, as opposed to spheroidal harmonics, is no longer correct when the perturbing spin is introduced. The effect is however small when compared to the magnitude of the $l = 2$, $m = 2$ modes.

The lower panels of Fig. 2.9 explore the effect of increasing the $l = 2$, $m = \pm 2$ perturbation amplitude A_c on the extracted $l = 2$, $m = \pm 2$ modes. In general the QKT shows very good agreement with analytical result over a range of perturbation magnitudes as desired, while the quantities computed on the coordinate tetrad disagree significantly with the analytic perturbative result.

2.6 Application of the QKT to numerical simulations of binary black holes

We now turn to exploring the properties and effectiveness of the QKT scheme when applied to more generic numerical simulations involving the collision of two black holes. We consider two examples: a circular inspiral of two equal-mass, nonspinning black holes [Sec. 2.6.1] and the head-on collision of two nonspinning, equal-mass black holes [Sec. 2.6.2].

2.6.1 Equal-mass, nonspinning binary-black-hole inspiral

In this subsection, we apply our QKT method to a fully dynamical simulation of two equal-mass, nonspinning black holes that inspiral through 16 orbits, merge, and ring down. We summarize some of the physical parameters of this simulation in Table 2.1 (which is a reproduction of Table II of Ref. [43]); further details of this simulation and the numerical method used are given in Ref. [43] and the references therein.

Initial orbital eccentricity:	$e \sim 5 \times 10^{-5}$
Initial spin of each hole:	$S_i/M^2 \leq 10^{-7}$
Duration of evolution:	$\Delta T/M = 4330$
Final black hole mass:	$M_f/M = 0.95162 \pm 0.00002$
Final spin:	$S_f/M_f^2 = 0.68646 \pm 0.00004$

Table 2.1: Physical properties of the equal-mass, nonspinning binary-black-hole inspiral reported in Ref. [43]. Here M is the sum of the Christodoulou masses of the initial holes, and M_f is the Christodoulou mass of the final hole.

We examine two aspects of the QKT that we have considered in previous sections: i) that the direction $\hat{\boldsymbol{l}}$ identified by the QKT corresponds to the wave-propagation direction (as discussed in Sec. 2.3.1) and the implications this has for the geometric coordinates $\hat{r}$ and $\hat{\theta}$, and ii) that the falloff rates of the Newman-Penrose scalars are consistent with the peeling property (as described in Sec. 2.3.8).

2.6.1.1 Wave-propagation direction

If (as claimed in Sec. 2.3.1) the vector $\hat{\boldsymbol{l}}$ associated with the QKT correctly identifies the out-going wave-propagation direction, one would expect that as one follows the wavefront out to infinity, the spacetime curvature along this trajectory and the associated derived quantities should become quite simple. To illustrate this, we consider an S^2 coordinate sphere in the original Cauchy slice and identify the correct null direction $\hat{\boldsymbol{l}}$ associated with the QKT at each point. We then integrate the null geodesic equations outward to produce a null hyper-surface and consider this null hyper-surface to be a new slicing and a preferred characteristic surface (PCS) of the spacetime. Identifying the geometrical coordinates $\hat{r}$ and $\hat{\theta}$ within this slicing, we plot their contours in the left-hand panels [plots (a) and (c) respectively] of Fig. 2.10. For comparison, we also show $\hat{r}$ and $\hat{\theta}$ computed within the original Cauchy slice. Note the simplicity of the computed geometric quantities within the PCS associated with the out-going wavefront as opposed to the corresponding quantities computed within the Cauchy surface.

The structure observed within the Cauchy surface can be understood as follows. The holes

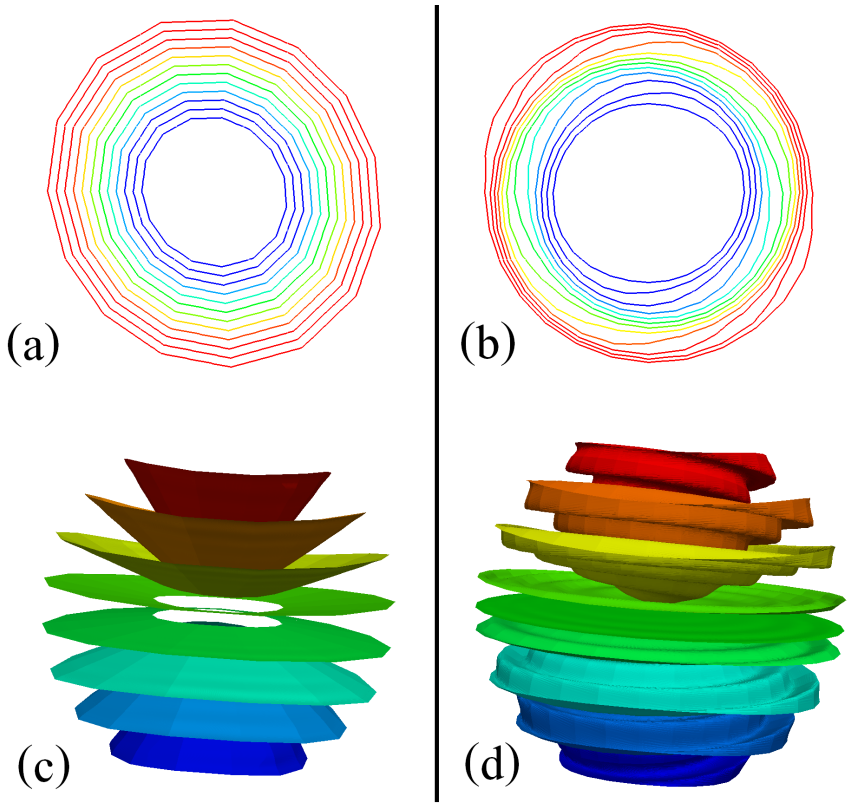

Figure 2.10: Geometrical coordinates obtained from the QKF $\hat{\Psi}_2$. (a) Contours of $\hat{r}$ on a slice of the null preferred characteristic surface (PCS) generated by the geodesic developments of $\hat{\boldsymbol{l}}$. (b) Contours of $\hat{r}$ on a constant-simulation-time Cauchy slice. (c) Contours of $\hat{\theta}$ on the same null surface as (a). (d) $\hat{\theta}$ contours in the same Cauchy slice as (b).

generate a rotating mass quadrupole approximately given by the Newtonian relation

$$\mathcal{I}_{ij}(t,r) \approx Mq^i(t-r)q^j(t-r) - \frac{MR^2}{12}\delta_{ij} = \frac{MR^2}{24}\begin{pmatrix} 3\cos\left[2\Omega t'\right]+1 & 3\sin\left[2\Omega t'\right] & 0 \\ 3\sin\left[2\Omega t'\right] & -3\cos\left[2\Omega t'\right]+1 & 0 \\ 0 & 0 & -2 \end{pmatrix}, \tag{2.93}$$

where M is total mass of the binary, R is the separation between the two black holes, $\boldsymbol{q}$ is the location of one of the black holes, and the choice of coordinates is such that the other black hole is located at $-\boldsymbol{q}$. In the matrix, $\Omega = \sqrt{M/R^3}$ is the orbital angular velocity and $t' = t - r$. This quadrupole moment deforms the $\hat{r}$ contour into an ellipsoid (or peanut shape when closer to the two holes [see Fig. 2.2 (a)]), while its time dependence causes the orientation of the ellipsoid to rotate at a frequency of 2Ω.

On the PCS, the structure is much simpler. The inner contour sets the basic shape for constant $\hat{r}$ surfaces, which are roughly ellipsoidal. These surfaces then expand, retaining their orientation as

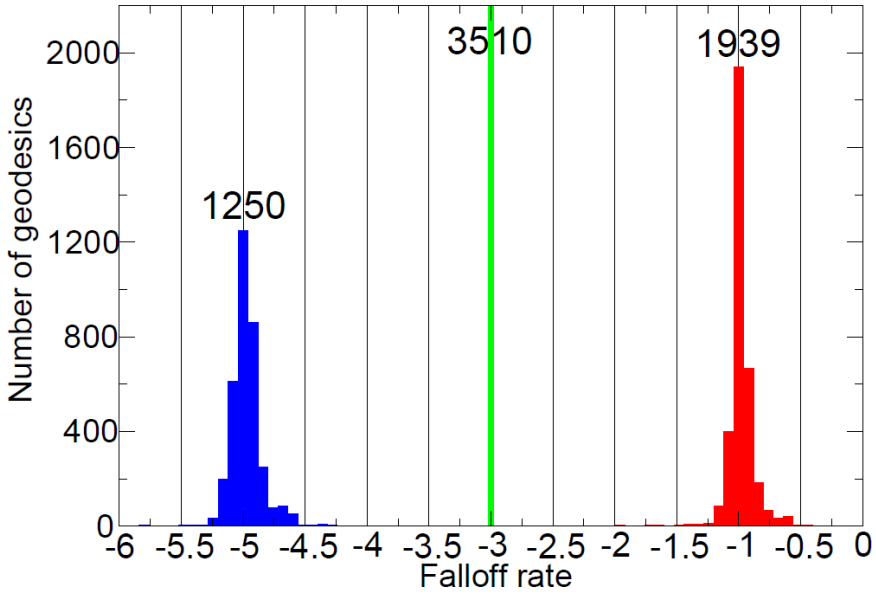

Figure 2.11: The distribution of power-law falloff rates of Newman-Penrose scalars $\hat{\Psi}_i$ against affine parameter τ. The three concentrations (colored blue, green and red) from left to right indicate falloff rates of $\hat{\Psi}_0$, $\hat{\Psi}_2$ and $\hat{\Psi}_4$, respectively. The vertical axis indicates the number of geodesics (totaling 3510) with falloff rate falling inside bins of width 0.08, and the number of geodesics for the center-most bins are shown.

the distortion is propagated outward at the speed of light along the wavefront. Figure 2.10 (a) shows a concentric pattern of $\hat{r}$ contours on the null hyper-surfaces, in contrast to the rotating contours on a spatial Cauchy hyper-surface that slices through many PCSs, as depicted in Figure 2.10 (b). The angular $\hat{\theta}$ coordinates similarly display a relative simplicity on the PCS, taking on the shape of a slightly deformed (squashed sideways) cone. Figures 2.10 (c) and (d) show the $\hat{\theta}$ surfaces on a PCS and in a spatial slicing respectively; the orientation of the deformed constant $\hat{\theta}$ cones is independent of the distance to black hole in the PCS, but rotates around when moving outwards on the spatial slice, forming a "spiral-staircase" pattern.

2.6.1.2 Peeling property

Next, we explore the falloff rate of the Newman-Penrose scalars computed on the QKT as one moves outward along the PCS generators (i.e., along the null geodesics tangent to the QKT $\hat{\boldsymbol{l}}$ where they originate). This rate allows us to quantify to what extent the QKT obeys the peeling property derived in Sec. 2.3.8 and to what extent the computed quantities are suitable for use in the extrapolation procedure prescribed in Sec. 2.4.2.

To this end, we start with 3510 null geodesics from the grid points of a mesh (of 351 points) covering a sphere of radius $\hat{r} \approx 150M$ surrounding the source region. Over a small time interval of $10M$, a new set of geodesics are shot off every $1M$. The affine parameter τ is initially set to $\hat{r}$ and

the geodesics are evolved for around $150M$. The Newman-Penrose $\hat{\Psi}_i$'s are recorded at intervals of $\Delta\tau = 1M$ along the geodesics. A histogram of the best fits for the power-law falloff (i.e., of the slopes of the $\ln(|\hat{\Psi}_i|)$ vs $\ln(\tau)$ graphs) for the 3510 geodesics are plotted in Fig. 2.11.

Recall that in fixing the spin-boost or Type III freedom of the QKF to obtain the QKT, the $\hat{\boldsymbol{l}}$ vector was scaled so that $\hat{\Psi}_2 \propto (\hat{r})^{-3}$. The very sharply defined peak at -3 in Fig. 2.11 provides direct numerical evidence that the relation $\tau \propto \hat{r}$ [cf. Secs. 2.3.8 and 2.4.2] remains valid at leading order for the considered range of the computational domain.

Figure 2.11 also indicates that $|\hat{\Psi}_0|$ and $|\hat{\Psi}_4|$ scale as τ^{-5} and τ^{-1}, respectively, as expected from Eq. (2.66). Here, the peaks are not as sharply defined, since we do not by construction enforce the power-law scalings of $\hat{\Psi}_0$ and $\hat{\Psi}_4$ (as we do for $\hat{\Psi}_2$).

2.6.2 Head-on nonspinning binary merger

To further examine the properties of the QKT and the geometrical coordinates we now take a detailed look at the numerical simulation of a head-on merger. The physical parameters of the simulation are given in Table 2.2.

Initial separation:	$d/M = 20$
Initial spin of each hole:	$S/M^2 \leq 2 \times 10^{-12}$
Duration of evolution:	$\Delta T/M = 600$
Final black hole mass:	$M_f/M = 0.987 \pm 2 \times 10^{-3}$
Final black hole spin:	$S_f/M_f^2 = 3. \times 10^{-7} \pm 2 \times 10^{-7}$

Table 2.2: Physical parameters of the head-on binary-black-hole merger considered in Sec. 2.6.2. Here M is the sum of the initial black hole Christodoulou masses, and all initial quantities are measured at the initial time $t = 0$ of the simulation.

The axisymmetric head-on collision of two nonspinning black holes has been studied extensively [44, 45, 46, 47, 48]; in many respects, these collisions serve as a simple, strongly nonlinear test of numerical relativity codes. The existence of a twist-free azimuthal Killing vector on this spacetime implies that the metric does not explicitly depend on the azimuthal coordinate ϕ defined about the symmetry axis and that the angular momentum of the spacetime is zero. We note that because of the symmetry of this configuration, the Coulomb potential associated with the transverse frame is real and thus that only one geometric coordinate, the radial coordinate $\hat{r}$, can be determined from it. Therefore, we fix the latitudinal coordinate to the simulation coordinate θ.

2.6.2.1 Geometric radial coordinate

We now explore some of the properties of radial coordinate $\hat{r}$, the emitted radiation profile, and the waveform. We show contour plots of the $\hat{r}$ coordinate at various times near merger in Fig. 2.12. The characteristic peanut shape expected from the merger event is clearly visible, and surfaces of constant $\hat{r}$ coordinate trace both the individual apparent horizon surfaces at early times and

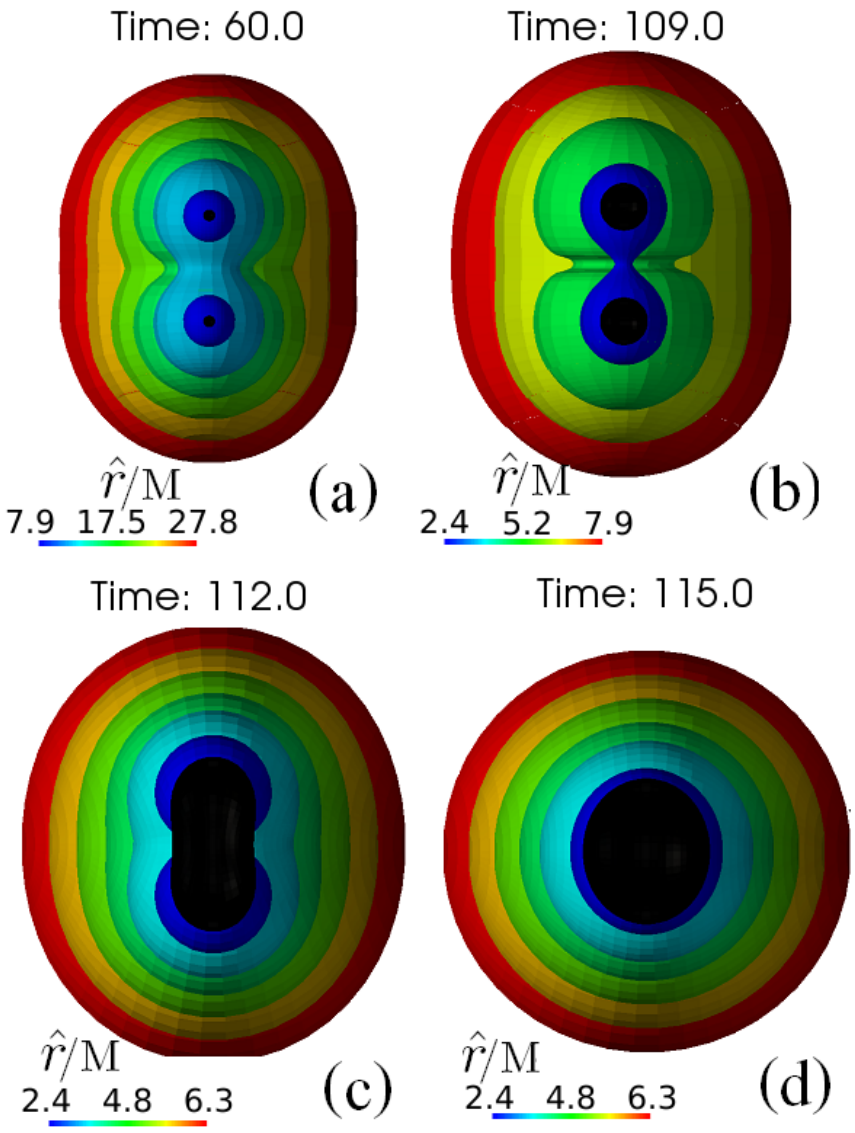

Figure 2.12: Here we show the evolution of $\hat{r}$ contours during the merger in the near zone; the black surfaces in these plots are the apparent horizons, and at $t = 112M$, the common apparent horizon forms.

the final apparent horizon surface at late times. Far from the source, constant $\hat{r}$ surfaces become roughly spherical, indicating that there the geometrical concept of radius and the gauge choice for the radial coordinate in the simulation coincide well. For the head-on collision, as well as in the more dynamical spacetimes depicted in Fig. 2.2, plotting surfaces of constant $\hat{r}$ turns out to be a useful tool for visualizing the spacetime geometry in a way that corresponds to an intuitive feel of the Coulomb potential's behavior.

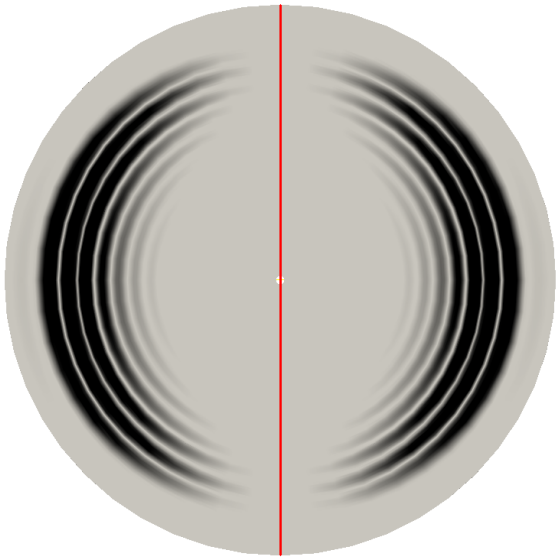

Figure 2.13: A snapshot (at $t = 242.25M$) of latitudinal distribution of radiation emitted by the head-on collision. The coloring is according to $|\Re(\hat{\Psi}_4)|$, with large values corresponding to darker color. The disk is a vertical slice of the computational domain with the thick red line denoting the symmetry axis.

2.6.2.2 Gravitational waveform

For twist-free axisymmetric spacetimes, one can show in general [44] that if the imaginary part of the tetrad null vector $\boldsymbol{m}$ or $\boldsymbol{E^3}$ (as defined in Sec. 2.2.1) has the same direction as the azimuthal Killing vector, then Ψ_4 expressed on this tetrad is real. Figure 2.13 depicts $\Re(\hat{\Psi}_4)$ for the head-on collision presently under consideration. Note the absence of radiation along the symmetric axis in Fig 2.13; this is a feature we will examine further later in this section in the context of PNDs.

We show two possible spherical harmonic decompositions of $\hat{\Psi}_4$ in Fig. 2.14. Panel (a) corresponds to the case where the azimuthal Killing vector determines the $\theta = 0$ direction; because the symmetry-axis corresponds to the $\theta = 0$ direction, axisymmetry implies that there are no $l = 2$, $m = \pm 2$ modes in the spherical harmonic decomposition, only $m = 0$ modes exist, and of those the $l = 2$, $m = 0$ mode makes the dominant contribution.

On the other hand, if one relabels the θ and ϕ coordinates on the extraction sphere, the spherical harmonic decomposition of the same waveform is very different. Panel (b) of Fig. 2.14 instead chooses the $\theta = 0$ line to be orthogonal to the axisymmetry axis rather than along it [as in panel (a)]; a significant $l = 2$, $m = 2$ mode appears. This is a simple example illustrating the well-known fact that unless a clear prescription for the preferred axis of a simulation is given, the $l = 2$, $m = 2$ mode is an ambiguous description of the radiation. Solutions to this problem for generic black hole binary simulations (which include precession) have been proposed in literature. For example, one may first choose a "radiation axis" [49, 50] to maximize the component of the angular

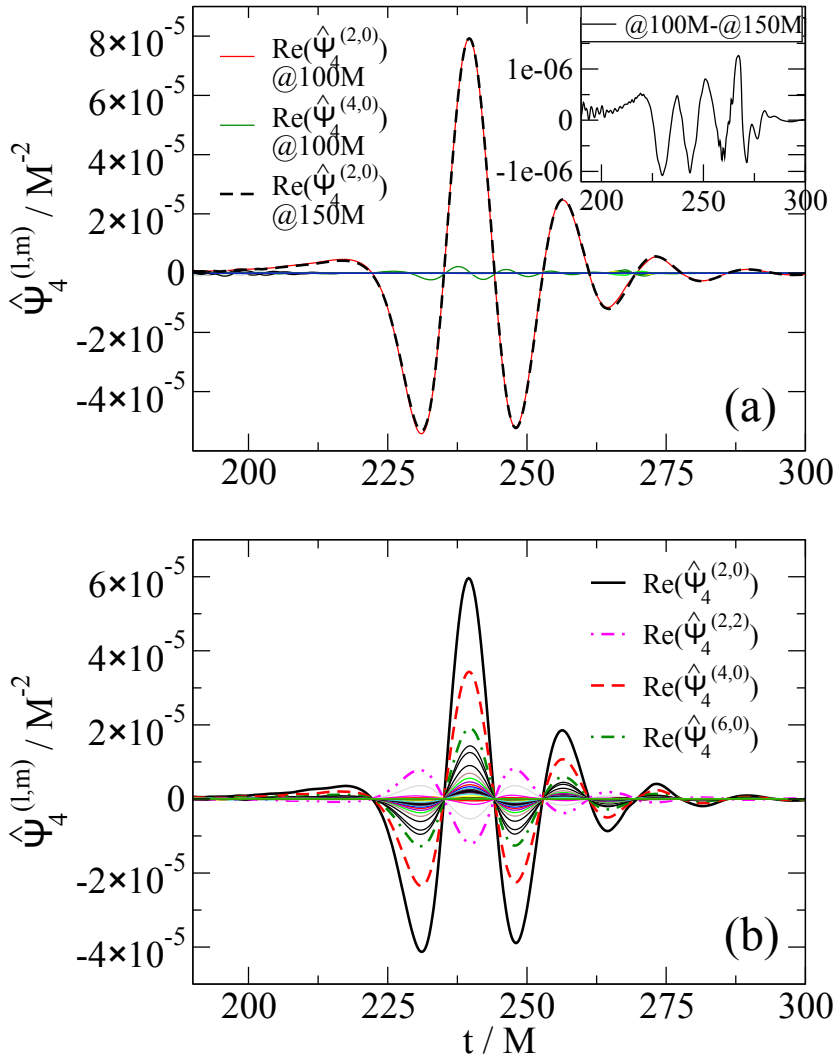

Figure 2.14: (a) The $\hat{\Psi}_4$ waveform for the head-on simulation extracted at coordinate radii of $r = 100M$ and $r = 150M$. For the waveform at $r = 100M$, all ${}_{-2}Y_{lm}$ modes up to $l = 35$ are shown. Only $\Re(\hat{\Psi}_4^{(2,0)})$ and $\Re(\hat{\Psi}_4^{(4,0)})$ are discernibly non-vanishing, with the former clearly dominating. For the $r = 150M$ waveform, only $\Re(\hat{\Psi}_4^{(2,0)})$ is shown, it is shifted temporally and rescaled by ≈ 1.5 so that its maximum peak location and magnitude match those of the $r = 100M$ waveform. The difference between the two waveforms is shown in the top-right inset. (b) The spherical harmonic decomposition for $\hat{\Psi}_4$ at $r = 100M$ obtained by choosing the poles of harmonics along a direction orthogonal to the symmetry axis. Multiple modes are visible, and a few with the largest magnitudes are labelled.

momentum along itself and secondly choose a preferred rotation about that axis [51]. Although not yet fully explored, our geometric coordinates suggest an alternative resolution. Namely we can use the extrema of the computed geometric $\hat{\theta}$ coordinates to identify the polar regions of a simulated

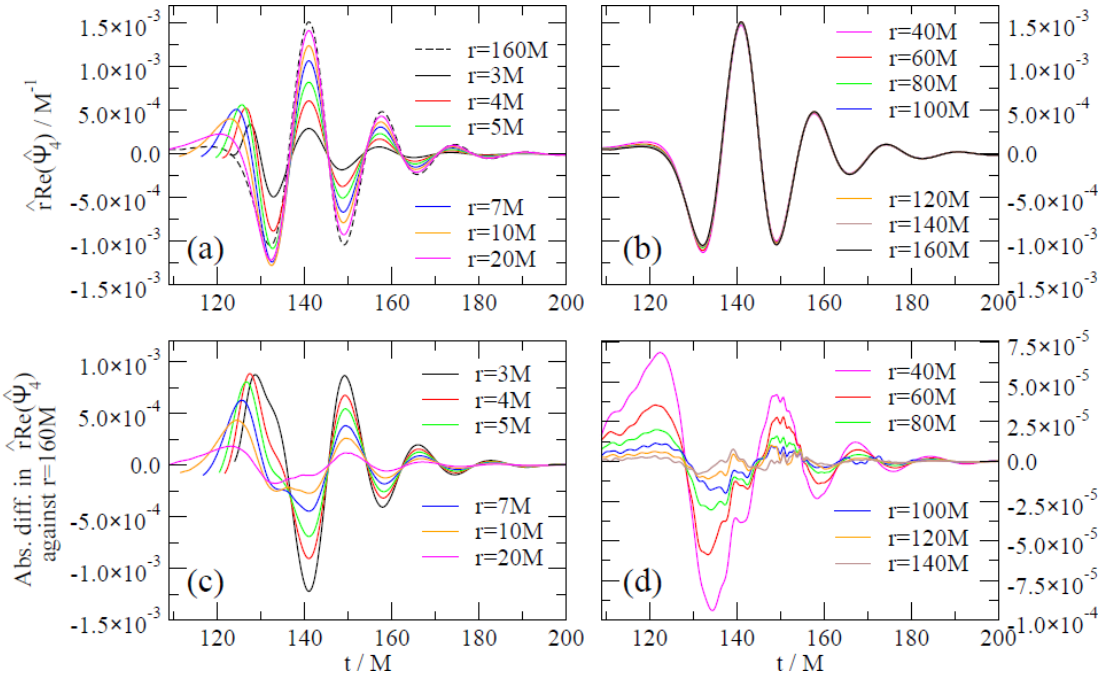

Figure 2.15: Panels (a) and (b): The gravitational-wave signal $\hat{r}\Re(\hat{\Psi}_4)$ curves extracted at several fixed spatial (simulation) coordinates. Panels (c) and (d): The absolute difference between these waveforms with a reference waveform computed at $r = 160M$.

spacetime.

Another question especially relevant to wave extraction is how rapidly the waveform computed from $\hat{\Psi}_4$ in the computational domain converges to "the" correct asymptotic waveform. In Sec. 2.3.8, we argue that asymptotically the QKT quantities on the correct out-going geodesics (as described in Sec. 2.4.2) should converge very rapidly to the desired result. We now explore this statement quantitatively for the emitted radiation on the equatorial plane in the head-on binary-black-hole merger we are considering. The goal is to determine at which radius a reliable approximation of the asymptotic waveform is attained.

To locate a good cut-off radius for wave extraction, consider a set of non-inertial observers hovering at different fixed spatial (simulation) radii in the equatorial plane. For each observer, in Fig. 2.15 we record the $\hat{r}\hat{\Psi}_4$ value as a function of time and plot the resulting curves, with the origin shifted so that the central maxima of all the curves coincide at around $t = 140M$. For clarity, we have divided the curves into two sets, those originating at $r < 30M$ and at $r > 30M$, which we display in panels (a) and (b), respectively. In both panels the curve traced out at $r = 160M$ is given for comparison, and we will refer to it as the reference waveform. Panels (c) and (d) show the absolute difference between the curves extracted at the various interior points and the reference waveform.

In Fig. 2.16, we plot the fractional difference between reference waveform and the interior wave-

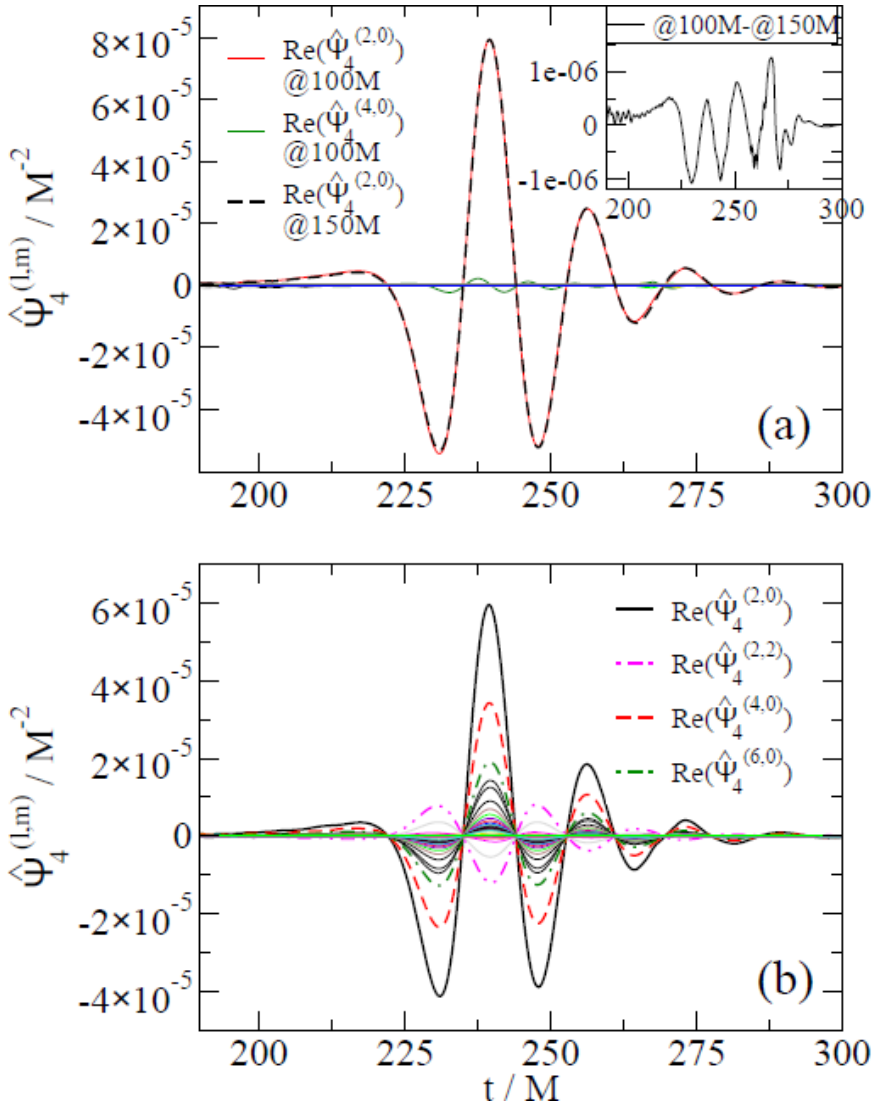

Figure 2.16: Exponential convergence of the QKT waveform extracted in the interior to the reference waveform measured at $r = 160M$. This plot shows the L_2 norm [defined in Eq. 2.94] of the absolute difference between the waveform at a particular extraction radius and the reference waveform at $r = 160M$ normalized by dividing by the L_2 norm of the reference waveform. Also shown is the red fitted exponential curve for radii $r > 40M$, which has a slope of -0.011.

form as a function of extraction radius. The quantity plotted is the L_2 norm of the absolute difference between the two waveforms divided by the L_2 norm of the reference waveform. The L_2 norm is defined here as

$$L_2[f] = \sqrt{\int_{t=125}^{200} f^2(t)dt}.$$

Comparing Fig. 2.16 and panel (b) in Fig. 2.15, we find that for radii greater than $r = 40M$ the extracted waveform corresponds closely, within $\sim 5\%$, to the reference waveform. Figure 2.16 quantifies this further: for $r < 40M$, the errors in the extracted $\hat{\Psi}_4$ waveform are large but the convergence to the reference waveform is super-exponential, while for $r > 40M$, the errors converge exponentially. This provides quantitative justification for the rapid-convergence claims we made in Secs. 2.3.8 with respect to the Newman-Penrose scalars calculated on the QKT. We conclude that the radius $\hat{r} = 40M$ appears to be a good minimal extraction radius for QKT quantities for head-on binary-black-hole collisions. It would be interesting to explore, using a similar analysis, whether the exponential convergence properties and the value for a good minimal extraction radius change considerably when applied to generic spacetimes (i.e., to spacetimes with less symmetry than the head-on collision we consider here).

2.6.2.3 Principal null directions

We conclude our investigation of the spacetime associated with the head-on collision of two black holes by exploring the behavior of the PNDs on and off the axis. As we have observed and shown graphically in Fig. 2.13, no radiation is emitted along the symmetry axis. This lack of radiation suggests that the PNDs do not all converge into a Type N pure radiation configuration as seen in Fig. 2.3 (c); instead, we would expect the PNDs to remain in a Type-D configuration, with two pairs of PNDs trapped at antipodal points of the anti-celestial sphere. On the axis, the only non-vanishing Newman-Penrose scalar on the QKT is $\hat{\Psi}_2$. The four solutions in Eq. (2.72) then divide into a pair whose value diverge and a pair that approach zero. The diverging solutions give us two PNDs pointing along the $\hat{\boldsymbol{n}}$ direction, while the vanishing solutions coincide with $\hat{\boldsymbol{l}}$. This situation is depicted in Fig. 2.17 (a): the two PNDs at the bottom of the sphere point away from $\hat{\boldsymbol{l}}$ (represented by the radial line) and do not converge onto the other two PNDs that coincide with $\hat{\boldsymbol{l}}$ at the top of the anti-celestial sphere. All the PNDs on the top of the sphere form angles smaller than $4 \times 10^{-7}\pi$ with the spatial projection of $\hat{\boldsymbol{l}}$, while the other two PNDs form angles with the spatial projection of $\hat{\boldsymbol{n}}$ that are smaller than $4 \times 10^{-6}\pi$. For comparison, in Fig. 2.17(b), we show the PND behavior on the celestial sphere as one moves along a geodesic that points away from the symmetry axis. The geodesic shown in this plot starts out at an orientation of 0.508π to the symmetry axis. (A similar plot is made in Fig. 2.3(c) where we showed a geodesic starting at 0.396π to the symmetry axis).

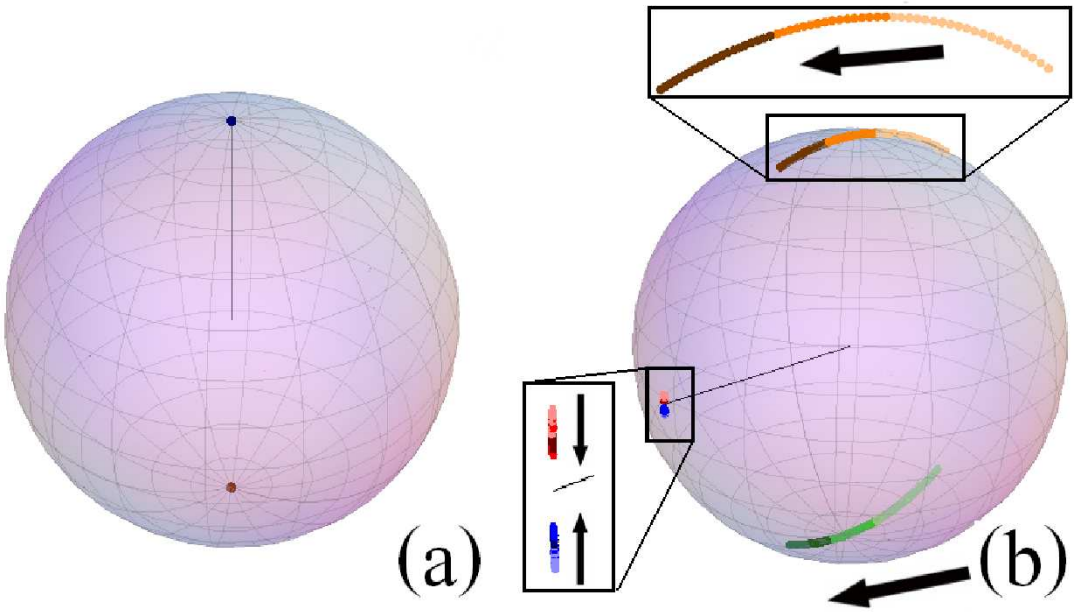

Figure 2.17: A graphical representation of the peeling-off behavior of the PNDs along out-going null geodesics for the head-on collision. The null geodesics start at $r = 30$M at time $t = 152$M. The tangent $\boldsymbol{\ell}$ to the geodesics coincide with $\hat{\boldsymbol{l}}$ along the geodesic and is denoted in the figures by black radial lines. The geodesic shown in panel (a) travels outward along the symmetry axis where no gravitational radiation is emitted. The geodesic shown in panel (b) starts off on the equatorial plane, and all PNDs converge toward the out-going $\hat{\boldsymbol{l}}$ direction pointing toward the front of the sphere. In this figure, the arrows indicate the movements of the PNDs as one travels further along the geodesic. Darker coloring indicates points calculated at larger affine parameter along the geodesic.

In these two cases, the presence of radiation causes the two PNDs pointing away from $\hat{\boldsymbol{l}}$ to converge onto the other two PNDs surrounding $\hat{\boldsymbol{l}}$ as one moves outward along the geodesic. The dominant rate of convergence is $1/\tau$ [cf. Eq. (2.71)].

The existence of "critical" directions as demonstrated here in the special case of axisymmetric spacetimes, is a generic feature of all dynamical spacetimes: it is a topological necessity [see Chapter 4 (i.e. [52]) and page 173 of [33]]. Specifically, in Ref. [52], the authors explain this feature as follows: In the asymptotic region, gravitational radiation is transverse and can be represented by tendex and vortex lines tangent to spheres of constant $\hat{r}$. Then, the Poincaré-Hopf theorem dictates that there must be locations on the sphere where the tendicity associated with the two transverse eigenbranches of the gravitoelectric tensor $\boldsymbol{\mathcal{E}}$ become degenerate. The trace-free property of $\boldsymbol{\mathcal{E}}$ then further constrains the tendicity to be zero—i.e., requires the gravitational radiation to vanish at the critical points.

Another useful characterization of dynamical numerical simulations is a measure of how rapidly the spacetime settles down to Petrov Type D at late times [see for example [53, 54]]. As a graphic depiction of this evolution of spacetime, one may generate PND diagrams similar to Fig. 2.17 along

timelike worldlines (instead of null geodesics). If one desires a quantitative estimate of the rate at which this "settling down" occurs, a metric on the anti-celestial sphere has to be defined in order to calculate distance between the PNDs. However a unique prescription of this metric requires a unique prescription of the tetrad, since Lorentz transformations on tetrad result in conformal transformations on the anti-celestial sphere. The QKT construction is useful in this context, because it uniquely prescribes all the tetrad degrees of freedom simultaneously across spacetime, including along timelike worldlines.

2.7 Conclusion

As the numerical relativity codes mature, it is becoming increasingly important to introduce a protocol that allows us to extract and compare physics from these codes in an unambiguous fashion. In particular, the quantities computed should be independent of the gauge or the formulation used. Ideally, such a protocol should be valid in the strong-field and wave zones and meet the physical criteria outlined in Sec. 2.3.

In this paper, we have suggested one such approach. Based on the Newman-Penrose formalism, our method fully specifies the tetrad degrees of freedom using purely geometric considerations, and two of the gauge degrees of freedom are also uniquely fixed using the curvature invariants I and J. In particular, our tetrad construction makes use of the quasi-Kinnersley frame (QKF) [8, 9, 10, 11, 12], which is a transverse frame (TF) that contains the Kinnersley tetrad in the Kerr limit.

By exploiting the relationship between QKF and eigenvectors of the matrix representation $\boldsymbol{\mathcal{Q}}$ [as in Eq. (2.12)] of the Weyl tensor, one can arrive at several insights regarding the physical properties of the QKF: i) its null vector $\tilde{\boldsymbol{l}}$ has a spatial projection pointing along the super-Poynting vector [Sec. 2.3.1] and thus along the direction of wave propagation, and ii) there is [Sec. 2.3.8] a close relationship [Fig. 2.3(b)] between the QKF null basis and principal null directions (PNDs) that makes the QKF naturally suited to measuring how quickly PNDs bunch together (as they converge onto $\tilde{\boldsymbol{l}}$). These features help Newman-Penrose scalars extracted using a QKT to fall off correctly in accordance with predictions by the peeling theorem.

In the QKF, the eigenvalue $\hat{\Psi}_2$ of the complex matrix $\boldsymbol{\mathcal{Q}}$ corresponding to the eigenvector that gave us QKF is a curvature invariant thus independent of the slicing in which the calculation was performed. The physical interpretation of $\hat{\Psi}_2$ is that it represents the Coulomb background portion of Weyl tensor; using this quantity, we define a pair of geometric coordinates $\hat{r}$ and $\hat{\theta}$ [Sec. 2.3.4]. These geometric coordinates vividly depict the multipolar structure in the Coulomb potential (as can be seen from Figs. 2.10 and 2.12). For example, they were used to demonstrate that far enough away from their source [see Sec. 2.6.2 for an empirical cutoff], the Coulomb background $\hat{\Psi}_2$ [Fig. 2.10] appears to propagate with an almost invariant form along preferred characteristic surfaces whose

generators are geodesics started off in the QKT $\hat{\boldsymbol{l}}$ direction. Besides fixing the gauge freedom, we have also used the differentials $d\hat{r}$ and $d\hat{\theta}$ [Sec. 2.3.5] to eliminate the spin-boost freedom remaining in QKF, yielding a final, gauge-invariant quasi-Kinnersley tetrad (QKT).

As our QKT is constructed from the gauge-invariant characteristic structure of Weyl tensor, it can be used to explore the physical features of numerical spacetimes in a gauge-invariant way. We have demonstrated this desirable property of our QKT with i) a stationary black hole spacetime where the hole is offset from the origin [Sec. 2.5.1.1] as well as ii) a gauge wave [Sec. 2.5.1.2] or iii) physical wave [Sec. 2.5.2] added to the spacetime of a Schwarzschild black hole. These examples serve as useful test beds for codes seeking to unambiguously extract the physically real effects as opposed to gauge induced false signals.

We have also used the QKT to analyze two equal-mass, nonspinning binary-black-hole merger simulations. In the first, the two black holes inspiral [Sec. 2.6.1] toward each other, while in the second they plunge head-on [Sec. 2.6.2]. We have confirmed that the Newman-Penrose scalars under the QKT do indeed fall off at the rates expected from peeling theorem in these simulations [Fig. 2.11 and Fig. 2.15], and we have explicitly examined the special peeling behavior along "critical" directions whose existence is ensured by topology [Fig. 2.17].

The gauge invariant feature of the proposed framework lends itself to several uses. One possible application is that they could help eliminate ambiguities such as the pole direction of harmonics used to express gravitational waves [see Sec. 2.6.2.2]. A further application is to use the QKT to reduce the ambiguity in measuring how quickly a spacetime settles down to a Type-D spacetime [see the end of Sec. 2.6.2]. The QKT also is promising as a wave extraction method that can be performed real time and ensures that waveform approaches its asymptotic value at infinity as rapidly as possible (this is illustrated in Fig. 2.15). For future work, we plan to make a comparison between QKT-based wave extraction and other wave extraction techniques (such as Cauchy Characteristic Extraction [55, 56, 57, 58, 59, 60]) using various numerical simulations with generic initial conditions.

The validity of geometric coordinates and the QKT throughout spacetime, including the strong field regions, suggests that they could be effectively utilized as a visualization and diagnostic tool capable of tracking the evolution of dynamical features of the spacetime. For example, in Fig. 2.4 (a), the geometric coordinates point out the missing rotating quadrupolar moment in the initial data. We expect this type of visualization to prove valuable in ongoing efforts to construct more realistic initial data and reduce spurious "junk" radiation. Other utilities for the geometric coordinates include, e.g., their potential for helping to improve boundary matching algorithms [see Fig. 2.4 (b)]. We would further like to examine in greater depth, with the help of QKT, the mechanics behind the changes in waveform, as one moves closer to the source region [see Fig. 2.15].

Finally, we note that there should exist a close relationship between the QKT and the tendex and vortex infrastructure introduced in [16, 15], which is based on the real eigenvectors and eigenvalues

of $\boldsymbol{\mathcal{E}}$ and $\boldsymbol{\mathcal{B}}$. Our geometric coordinates and QKT are, in contrast, based on the complex eigenvalues and eigenvectors of $\boldsymbol{\mathcal{Q}}$. We expect this connection to yield important insights such as the slicing dependence of the tendexes and vortexes.

Bibliography

[1] J. Centrella, J. G. Baker, B. J. Kelly, and J. R. van Meter, Rev. Mod. Phys. **82**, 3069 (2010).

[2] S. T. McWilliams, Class. Quantum Grav. **28**, 134001 (2011), 1012.2872.

[3] B. C. Barish and R. Weiss, Phys. Today **52**, 44 (1999), ISSN 00319228, URL http://dx.doi.org/10.1063/1.882861.

[4] D. Sigg and the LIGO Scientific Collaboration, Class. Quantum Grav. **25**, 114041 (2008), ISSN 0264-9381, 1361-6382, URL http://iopscience.iop.org/0264-9381/25/11/114041.

[5] F. Acernese et al., Class. Quantum Grav. **23**, S635 (2006).

[6] K. Kuroda and the LCGT Collaboration, Class. Quantum Grav. **27**, 084004 (2010), ISSN 0264-9381, URL http://iopscience.iop.org/0264-9381/27/8/084004.

[7] W. Kinnersley, J.Math.Phys. **10**, 1195 (1969).

[8] C. Beetle, M. Bruni, L. M. Burko, and A. Nerozzi, Phys. Rev. D **72**, 024013 (2005).

[9] A. Nerozzi, C. Beetle, M. Bruni, L. M. Burko, and D. Pollney, Phys. Rev. D **72**, 024014 (2005).

[10] L. M. Burko, T. W. Baumgarte, and C. Beetle, Phys. Rev. D **73**, 024002 (2006), URL http://link.aps.org/abstract/PRD/v73/e024002.

[11] A. Nerozzi, M. Bruni, V. Re, and L. M. Burko, Phys.Rev. **D73**, 044020 (2006), gr-qc/0507068.

[12] L. M. Burko, Phys.Rev. **D75**, 084039 (2007), gr-qc/0701101.

[13] M. Campanelli, B. Kelly, and C. O. Lousto, Phys. Rev. D **73**, 064005 (2006).

[14] S. Chandrasekhar, *The Mathematical Theory of Black Holes* (Oxford University Press, Oxford, 1983).

[15] D. A. Nichols, R. Owen, F. Zhang, A. Zimmerman, J. Brink, Y. Chen, J. Kaplan, G. Lovelace, K. D. Matthews, M. A. Scheel, et al. (2011), 1108.5486.

[16] R. Owen, J. Brink, Y. Chen, J. D. Kaplan, G. Lovelace, K. D. Matthews, D. A. Nichols, M. A. Scheel, F. Zhang, A. Zimmerman, et al., Phys. Rev. Lett. **106**, 151101 (2011).

[17] K. A. Dennison and T. W. Baumgarte (2012), `1207.2431`.

[18] F. B. Estabrook and H. D. Wahlquist, Journal of Mathematical Physics **5**, 1629 (1964).

[19] C. Schmid, Phys. Rev. D **79**, 064007 (2009).

[20] J. Carminati and R. McLenaghan, J. Math. Phys. **32**, 3135 (1991).

[21] P. T. Chrusciel, Contemp.Math. **170**, 23 (1994), `gr-qc/9402032`.

[22] M. Heusler, Living Rev.Rel. **1**, 6 (1998).

[23] S. Teukolsky, Phys. Rev. Lett. **29**, 1114 (1972).

[24] R. Penrose and W. Rindler, *Spinors and Space-time, Volume 2* (Cambridge University Press, Cambridge, 1986).

[25] P. Szekeres, Journal of Mathematical Physics **6**, 1387 (1965).

[26] R. Maartens and B. A. Bassett, Class. Quantum Grav. **15**, 705 (1998).

[27] V. Zakharov, *Gravitational Waves in Einstein's Theory* (Halsted Press, New York, 1973).

[28] P. Anninos, D. Hobill, E. Seidel, L. Smarr, and W.-M. Suen, Phys.Rev. **D52**, 2044 (1995), `gr-qc/9408041`.

[29] J. G. Baker and M. Campanelli, Phys.Rev. **D62**, 127501 (2000), `gr-qc/0003031`.

[30] R. Sachs, Proceedings of the Royal Society of London. Series A, Mathematical and Physical Sciences **264**, 309 (1961), ISSN 00804630.

[31] R. K. Sachs, Proc. R. Soc. Lond. A **270**, 103 (1962).

[32] R. Penrose, Phys. Rev. Lett. **10**, 66 (1963).

[33] R. Penrose, Proc. Roy. Soc. Lond. A **284**, 159 (1965).

[34] `http://www.black-holes.org/SpEC.html`.

[35] H. Friedrich, Class. Quantum Grav. **13**, 1451 (1996).

[36] J. Hesthaven and T. Warburton, *Nodal Discontinuous Galerkin Methods: Algorithms, Analysis, and Applications* (Springer-Verlag, New York, NY, 2008).

[37] N. W. Taylor, L. E. Kidder, and S. A. Teukolsky, Phys. Rev. **D82**, 024037 (2010), `1005.2922`.

[38] L. Lindblom, K. D. Matthews, O. Rinne, and M. A. Scheel, Phys. Rev. D **77**, 084001 (2008).

[39] F. Pretorius, Phys.Rev.Lett. **95**, 121101 (2005), gr-qc/0507014.

[40] F. Pretorius, Class. Quantum Grav. **23**, S529 (2006).

[41] L. Lindblom and B. Szilágyi, Phys. Rev. D **80**, 084019 (2009).

[42] O. Sarbach and M. Tiglio, Phys. Rev. D **64**, 084016 (2001).

[43] M. A. Scheel, M. Boyle, T. Chu, L. E. Kidder, K. D. Matthews and H. P. Pfeiffer, Phys. Rev. D **79**, 024003 (2009), arXiv:gr-qc/0810.1767.

[44] D. R. Fiske, J. G. Baker, J. R. van Meter, D.-I. Choi, and J. M. Centrella, Phys. Rev. D **71**, 104036 (2005).

[45] M. Alcubierre, B. Bruegmann, P. Diener, F. Herrmann, D. Pollney, et al. (2004), gr-qc/0411137.

[46] U. Sperhake, B. Kelly, P. Laguna, K. L. Smith, and E. Schnetter, Phys. Rev. D **71**, 124042 (2005).

[47] J. G. Baker, B. Bruegmann, M. Campanelli, and C. O. Lousto, Class.Quant.Grav. **17**, L149 (2000), gr-qc/0003027.

[48] J. G. Baker, M. Campanelli, C. O. Lousto, and R. Takahashi, Phys. Rev. **D65**, 124012 (2002), astro-ph/0202469.

[49] P. Schmidt, M. Hannam, S. Husa, and P. Ajith, Phys. Rev. D **84**, 024046 (2011), arxiv:1012.2879.

[50] OShaughnessy, R. and Vaishnav, B. and Healy, J. and Meeks, Z. and Shoemaker, D. (2011), arXiv:1109.5224.

[51] M. Boyle, R. Owen, and H. P. Pfeiffer, Phys. Rev. D **84**, 124011 (2011), arXiv:1110.2965.

[52] A. Zimmerman, D. A. Nichols, and F. Zhang, Phys. Rev. D **84**, 044037 (2011).

[53] M. Campanelli, C. O. Lousto, and Y. Zlochower, Phys. Rev. **D79**, 084012 (2009), 0811.3006.

[54] R. Owen, Phys. Rev. **D81**, 124042 (2010), 1004.3768.

[55] N. T. Bishop, R. Gómez, L. Lehner, and J. Winicour, Phys. Rev. D **54**, 6153 (1996), 0706.1319.

[56] N. T. Bishop, R. Gomez, L. Lehner, M. Maharaj, and J. Winicour, Phys. Rev. **D56**, 6298 (1997), gr-qc/9708065.

[57] N. T. Bishop, R. Gómez, R. A. Isaacson, L. Lehner, B. Szilágyi, and J. Winicour, in *Black Holes, Gravitational Radiation and the Universe*, edited by B. R. Iyer and B. Bhawal (Kluwer, Dordrecht, 1998), chap. 24.

[58] C. Reisswig, N. T. Bishop, D. Pollney, and B. Szilagyi, Class. Quant. Grav. **27**, 075014 (2010), 0912.1285.

[59] J. Winicour, Living Rev. Rel. **12** (2009), URL http://www.livingreviews.org/lrr-2009-3.

[60] M. C. Babiuc, B. Szilágyi, J. Winicour, and Y. Zlochower, Phys. Rev. D **84**, 044057 (2011), URL http://link.aps.org/doi/10.1103/PhysRevD.84.044057.

Chapter 3

Frame-Drag Vortexes and Tidal Tendexes I. General Theory and Weak-Gravity Applications

---

Originally published as

David A. Nichols, Robert Owen, Fan Zhang, Aaron Zimmerman, Jeandrew Brink, Yanbei Chen, Jeffrey D. Kaplan, Geoffrey Lovelace, Keith D. Matthews, Mark A. Scheel, Kip S. Thorne

Phys. Rev. D 84, 124014 (2011)

3.1 Motivation and Overview

In the 1950s John Archibald Wheeler coined the phrase *geometrodynamics* to epitomize his intuition that curved spacetime must have a rich range of nonlinear dynamical behaviors — behaviors that are important in our Universe and are worthy of probing deeply by both theoretical and observational means (see Ref. [2] and earlier papers by Wheeler reprinted therein and also Ref. [3]). It was obvious to Wheeler that analytical tools by themselves would not be sufficient to reveal the richness of geometrodynamics, so he encouraged his colleagues and students to begin developing numerical tools [4, 5, 6], and he encouraged Joseph Weber to develop technology for gravitational-wave observations [7].

Today, a half century later, numerical relativity has finally reached sufficient maturity (for a review, see Ref. [8] and the references therein) that, hand in hand with analytical relativity, it can be used to explore nonlinear geometrodynamics in generic situations; and gravitational-wave detectors are sufficiently mature [9, 10, 11, 12, 13] that they may soon observe nonlinear geometrodynamics

in black-hole collisions.

Unfortunately, there is a serious obstacle to extracting geometrodynamical insights from numerical-relativity simulations: a paucity of good tools for visualizing the dynamics of curved spacetime. We are reasonably sure that buried in the billions of numbers produced by numerical-relativity simulations there are major discoveries to be made, but extracting those discoveries is exceedingly difficult and perhaps impossible with the tools we have had thus far.

Until now, curved spacetime has been visualized primarily via (isometric) *embedding diagrams* (Sec. 23.8 of Ref. [14]): choosing spacelike two-dimensional surfaces in spacetime, and embedding them in flat 3-dimensional Euclidean space or 2+1-dimensional Minkowski spacetime in a manner that preserves the surfaces' intrinsic geometry. (For some examples of embedding diagrams applied to black-hole spacetimes, see, e.g., Refs. [15, 16, 17]). Unfortunately, such embedding diagrams are of very limited value. They capture only two dimensions of spacetime, and the 2-surfaces of greatest interest often cannot be embedded globally in flat Euclidean 3-space or flat Minkowski 2+1-dimensional spacetime [15, 18, 19, 20]. Mixed Euclidean/Minkowski embeddings are often required (e.g., Fig. 4 of Ref. [15]), and such embeddings have not proved to be easily comprehended. Moreover, although it is always possible to perform a local embedding in a flat 3-space (in the vicinity of any point on the two-surface), when one tries to extend the embedding to cover the entire two-surface, one often encounters discontinuities analogous to shocks in fluid mechanics [18, 20].

A systematic approach to understanding the connection between nonlinear near-field dynamics in general relativity and emitted gravitational waves is being developed by Rezzolla, Jaramillo, Macedo, and Moesta [21, 22, 23, 24]. This approach focuses on correlations between data on a surface at large radius (ideally null infinity) and data on world tubes in the source region (such as black-hole horizons). The purpose is to use such correlations to infer the dynamics of a black hole (e.g. the kick) directly from data on its horizon. While we find this approach exciting and attractive, in our own work we seek a more direct set of tools: tools that can probe the dynamics of spacetime curvature that cause such correlations in the first place, and that can be more readily and intuitively applied to a wider range of other geometrodynamic phenomena. It is our hope that eventually our tools and those of Rezzolla et. al. [21, 22, 23] will provide complementary pictures for understanding spacetime dynamics, and particularly black-hole kicks.

We have introduced our new set of tools in Chapter 1.2 (i.e. [1]). They are tools for visualizing spacetime curvature, called *tidal tendex lines, tendicities, and tendexes*; and *frame-drag vortex lines, vorticities and vortexes*. These tools capture the full details of the Weyl curvature tensor (vacuum Riemann tensor), which embodies spacetime curvature. They do so in three-dimensional, dynamically evolving pictures, of which snapshots can be printed in a paper such as this one, and movies can be made available online.[1] Specifically, as of this writing two movies can be seen at

[1]Just as there is no unique method to evolve field lines in electromagnetism, so too is there no unique way to

Refs. [26, 27]; one shows the vortex lines from a rotating current quadrupole, the other, vortex lines from two particles that collide head-on with transverse, antiparallel spins.

We have found these tools to be an extremely powerful way to visualize the output of numerical simulations. We have also used them to obtain deep new insights into old analytical spacetimes. We have applied them, thus far, to pedagogical linear-gravity problems (this paper and Chapter 4 or [28]), to stationary and perturbed black holes (Paper II in this series), and to simulations of the inspiral and mergers of spinning black holes (Chapter 1.2 (i.e. [1]) and Paper III). We plan to apply them in the future in a variety of other geometrodynamical venues, such as black holes ripping apart neutron stars and curved spacetime near various types of singularities.

This is the first of a series of papers in which we will (i) present these tools, (ii) show how to use them, (iii) build up physical intuition into them, and (iv) employ them to extract geometrodynamical insights from numerical-relativity simulations. Specifically:

In this paper (Paper I), we introduce these vortex and tendex tools, and we then apply them to weak-gravity situations (linearized general relativity) with special focus on the roles of vortexes and tendexes in gravitational-wave generation. In a closely related paper [28] (i.e. Chapter 4), three of us have applied these tools to visualize asymptotic gravitational radiation and explore the topology of its vortex and tendex lines, and also to explore a linearized-gravity model of an extreme-kick merger. In Paper II we shall apply our new tools to quiescent black holes and quasinormal modes of black holes, with special focus once again on the roles of vortexes and tendexes in generating gravitational waves. In Paper III and subsequent papers we shall apply our tools to numerical simulations of binary black holes, focusing on nonlinear geometrodynamics in the holes' near zone and how the near-zone vortexes and tendexes generate gravitational waves.

The remainder of this paper is organized as follows:

In Sec. 3.2.1 we review the well-known split of the Weyl curvature tensor into its "electric" and "magnetic" parts $\mathcal{E}_{ij}$ and $\mathcal{B}_{ij}$, and in Sec. 3.2.2 we review the Maxwell-like evolution equations for $\mathcal{E}_{ij}$ and $\mathcal{B}_{ij}$ and discuss the mathematical duality between these fields. Then in Sec. 3.3 we review the well-known physical interpretation of $\mathcal{E}_{ij}$ as the *tidal field* that drives geodesic deviation and the not so well-known interpretation of $\mathcal{B}_{ij}$ [29, 30] as the *frame-drag* field that drives differential frame dragging, and we derive the equation of differential frame dragging.

In Sec. 3.4 we introduce our new set of tools for visualizing spacetime curvature. Specifically: In Sec. 3.4.1 we introduce tendex lines and their tendicities, and we quantify them by their stretching or compressional force on a person; and we also introduce vortex lines and their vorticities and quantify them by their twisting (precessional) force on gyroscopes attached to the head and feet of

match tendex or vortex lines at one time with others at a later time. Nevertheless, animations of field lines are useful for pedagogical purposes and for building intuition [25]. While some of the authors and colleagues are investigating how to evolve tendex and vortex lines in generic situations, the animations of the lines posted online all have special symmetries that provide a natural way to connect lines at one time with lines at the next.

a person. Then in Sec. 3.4.2 we introduce *vortexes* and *tendexes* (bundles of vortex and tendex lines that have large vorticity and tendicity) and give examples.

In the remainder of this paper we illustrate these new concepts by applying them to some well-known, weak-gravity, analytic examples of spacetime curvature. In Sec. 3.5 we focus on the spacetime curvature of stationary systems, and in Sec. 3.6 we focus on dynamical systems and develop physical pictures of how they generate gravitational waves.

More specifically, in Sec. 3.5.1, we compute $\mathcal{E}_{ij}$ and $\mathcal{B}_{ij}$ for a static, gravitating, spinning point particle; we explain the relationship of $\mathcal{B}_{ij}$ to the particle's dipolar "gravitomagnetic field," we draw the particle's tendex lines and vortex lines, and we identify two vortexes that emerge from the particle, a counterclockwise vortex in its "north polar" region and a clockwise vortex in its "south polar" region. In Sec. 3.5.2, we draw the vortex lines for two spinning point particles that sit side-by-side with their spins in opposite directions, and we identify their four vortexes. Far from these particles, they look like a single point particle with a current-quadrupole moment. In Sec. 3.5.3, we draw the vortex lines for such a current-quadrupole particle and identify their vortexes. Then in Sec. 3.5.4, we show that the tendex lines of a mass-quadrupole particle have precisely the same form as the vortex lines of the current-quadrupole particle, and we identify the mass quadrupole's four tendexes.

Turning to dynamical situations, in Sec. 3.6.1 we compute $\mathcal{E}_{ij}$ and $\mathcal{B}_{ij}$ for a plane gravitational wave, we express them in terms of the Weyl scalar Ψ_4, and we draw their vortex and tendex lines. In Sec. 3.6.2 we explore the quadrupolar ($l = 2$, $m = 0$) angular pattern of gravitational waves from the head-on collision of two black holes, and we draw their vortex lines and tendex lines, intensity-coded by vorticity and tendicity, on a sphere in the wave zone. In Sec. 3.6.3 we compute $\mathcal{E}_{ij}$ and $\mathcal{B}_{ij}$ for a general, time-varying current-quadrupolar particle, and then in Secs. 3.6.4 and 3.6.5 we specialize to a rotating current quadrupole and an oscillating current quadrupole, and draw their vortex and tendex lines. Our drawings and the mathematics reveal that the particle's outgoing gravitational waves are generated by its near-zone vortexes. The rotating current quadrupole has four vortexes that spiral outward and backward like four water streams from a rotating sprinkler. As it bends backward, each vortex acquires an accompanying tendex, and the vortex and tendex together become a gravitational-wave crest or gravitational-wave trough. The oscillating current quadrupole, by contrast, ejects vortex loops that travel outward, acquiring accompanying tendex loops with strong tendicity on the transverse segment of each loop and weak on the radial segment—thereby becoming outgoing gravitational waves.

In Sec. 3.6.6 we show that a time-varying mass quadrupole produces the same phenomena as a time-varying current quadrupole, but with vortexes and tendexes interchanged.

In Sec. 3.6.7 we study the vortexes and tendexes of a slow-motion binary made of nonspinning point particles. In the near zone, the tendex lines transition, as one moves radially outward, from

those of two individual particles (radial and circular lines centered on each particle) toward those of a single spherical body (radial and circular lines centered on the binary and produced by the binary's mass monopole moment). In the transition zone and inner wave zone, the mass monopole continues to dominate. Then at radii $r \sim a^2/M$ (where a is the particles' separation and M is the binary's mass), the radiative quadrupole moment begins to take over and the tendex lines gradually transition into the outward-and-backward spiraling lines of a rotating quadrupole.

We make some concluding remarks in Sec. 3.7.

Throughout this paper we use geometrized units with $c = G = 1$, and we use the sign conventions of MTW [14] for the metric signature, the Weyl curvature, and the Levi-Civita tensor. We use Greek letters for spacetime indices (0–3) and Latin letters for spatial indices (1–3), and we use arrows over 4-vectors and bold-face font for spatial 3-vectors and for tensors. In orthonormal bases, we use hats over all kinds of indices.

3.2 The tidal field $\mathcal{E}_{ij}$ and frame-drag field $\mathcal{B}_{ij}$

3.2.1 3+1 split of Weyl curvature tensor into $\mathcal{E}_{ij}$ and $\mathcal{B}_{ij}$

For a given spacetime, the Weyl curvature tensor can be calculated from the Riemann tensor by subtracting Riemann's trace from itself; i.e., by subtracting from Riemann the following combinations of the Ricci curvature tensor $R^\mu{}_\nu$, and Ricci curvature scalar R (Eq. (13.50) of MTW [14]):

$$C^{\mu\nu}{}_{\rho\sigma} = R^{\mu\nu}{}_{\rho\sigma} - 2\delta^{[\mu}{}_{[\rho}R^{\nu]}{}_{\sigma]} + \frac{1}{3}\delta^{[\mu}{}_{[\rho}\delta^{\nu]}{}_{\sigma]}R\,. \tag{3.1}$$

Here $\delta^\mu{}_\rho$ is the Kronecker delta, and the square brackets represent antisymmetrization. Note that in vacuum, $C^{\mu\nu}{}_{\rho\sigma} = R^{\mu\nu}{}_{\rho\sigma}$, and thus in vacuum the Weyl tensor contains all information about the spacetime curvature.

Let us pick a foliation of spacetime into a family of spacelike hypersurfaces. We shall denote by u^μ the 4-velocity of observers who move orthogonal to the foliation's space slices, and by $\gamma_{\mu\nu} = g_{\mu\nu} + u_\mu u_\nu$ the induced spatial three metric on these slices, so that $\gamma_\alpha{}^\mu$ is the projection operator onto the slices. As is well-known, e.g. [31], using this projection operator, we can split the Weyl tensor covariantly into two irreducible parts, which are symmetric, trace-free (STF) tensors that lie in the foliation's hypersurfaces (i.e. that are orthogonal to u^μ). These pieces are

$$\mathcal{E}_{\alpha\beta} = \gamma_\alpha{}^\rho\gamma_\beta{}^\sigma C_{\rho\mu\sigma\nu}u^\mu u^\nu\ , \quad \text{i.e. } \mathcal{E}_{ij} = C_{i\hat{0}j\hat{0}}\ , \tag{3.2a}$$

an even-parity field called the "electric" part of $C^{\mu\nu}{}_{\rho\sigma}$, and

$$\mathcal{B}_{\alpha\beta} = -\gamma_\alpha{}^\rho \gamma_\beta{}^\sigma {}^*C_{\rho\mu\sigma\nu} u^\mu u^\nu \ , \quad \text{i.e. } \mathcal{B}_{ij} = \frac{1}{2}\epsilon_{ipq} C^{pq}{}_{j\hat{0}}, \tag{3.2b}$$

an odd-parity field known as the "magnetic" part of $C^{\mu\nu}{}_{\rho\sigma}$. Here the symbol * represents the (left) Hodge dual, ${}^*C_{\rho\mu\sigma\nu} = \frac{1}{2}\epsilon_{\rho\mu\eta\lambda} C^{\eta\lambda}{}_{\sigma\nu}$, and for each field the second expression is written in 3+1 notation: the Latin (spatial) indices are components in the foliation's hypersurface, and the $\hat{0}$ is a component on the foliation's unit time basis vector $\vec{e}_{\hat{0}} \equiv \vec{u}$. Our normalization for the Levi-Civita tensor is that of MTW: in a right-handed orthonormal frame, $\epsilon_{\hat{0}\hat{1}\hat{2}\hat{3}} = +1$, and the spatial Levi-Civita tensor is defined by $\epsilon_{ipq} = \epsilon_{\hat{0}ipq}$, with $\epsilon_{\hat{1}\hat{2}\hat{3}} = 1$ in a right-handed orthonormal basis. Note that Eqs. (3.2) are a direct and intentional analogy to the decomposition of the Maxwell tensor of electromagnetism $F_{\mu\nu}$ into the familiar electric and magnetic fields E_i and B_i [31]:

$$E_i = F_{i\hat{0}} \ , \quad B_i = -{}^*F_{i\hat{0}} = \frac{1}{2}\epsilon_{ipq} F^{pq}. \tag{3.3}$$

Note that our sign conventions differ from [31], where $\epsilon_{\hat{0}\hat{1}\hat{2}\hat{3}} = -1$, and so Eq. (3.2b) has an additional minus sign in order to maintain a strict analogy with the magnetic field B_i of electromagnetism. This results in a $\mathcal{B}_{ij}$ defined with a different sign convention than, for example, in [32, 33].

3.2.2 Evolution of $\mathcal{E}_{ij}$ and $\mathcal{B}_{ij}$

The propagation equations for the Weyl tensor and its gravito-electromagnetic representation are the Bianchi identities. We shall write them down and discuss them in three contexts: a general foliation and coordinate system, the local-Lorentz frame of a freely falling observer, and the weak-gravity, nearly Minkowski spacetimes of the current paper (Paper I in this series).

3.2.2.1 General foliation and coordinate system in the language of numerical relativity

Because this paper is a foundation for using $\mathcal{E}_{ij}$ and $\mathcal{B}_{ij}$ to interpret the results of numerical-relativity simulations, we shall write their evolution equations (the Bianchi identities) in a general coordinate system of the type used in numerical relativity, and we shall discuss these equations' mathematical structure in the language of numerical relativity.

We denote by t a time coordinate that is constant on the foliation's hypersurfaces, and by α and $\vec{\beta}$ the foliation's lapse and shift functions, so the orthogonal observers' 4-velocity is $\vec{u} = \alpha^{-1}(\vec{\partial}_t - \vec{\beta})$. The 3+1 split divides the Bianchi identities into evolution equations that govern the time evolution of the spatial fields, and constraint equations that are obeyed by the fields on each time slice. The

evolution equations are [34, 35]

$$\begin{aligned}\partial_t \mathcal{E}_{ij} =& \mathcal{L}_\beta \mathcal{E}_{ij} + \alpha[D_k \mathcal{B}_{l(i}\epsilon_{j)}{}^{kl} - 3\mathcal{E}^k{}_{(i}K_{j)k} + K^k{}_k \mathcal{E}_{ij} - \epsilon_i{}^{kl}\mathcal{E}_{km}K_{ln}\epsilon_j{}^{mn} + 2a_k \mathcal{B}_{l(i}\epsilon_{j)}{}^{kl}]\,, \\ \partial_t \mathcal{B}_{ij} =& \mathcal{L}_\beta \mathcal{B}_{ij} + \alpha[-D_k \mathcal{E}_{l(i}\epsilon_{j)}{}^{kl} - 3\mathcal{B}^k{}_{(i}K_{j)k} + K^k{}_k \mathcal{B}_{ij} - \epsilon_i{}^{kl}\mathcal{B}_{km}K_{ln}\epsilon_j{}^{mn} - 2a_k \mathcal{E}_{l(i}\epsilon_{j)}{}^{kl}]\,.\end{aligned} \tag{3.4}$$

Here the extrinsic curvature, Lie derivative on a second rank tensor, and acceleration of the slicing are respectively defined by

$$K_{ij} = -\frac{1}{2\alpha}(\partial_t \gamma_{ij} - D_i\beta_j - D_j\beta_i)\,, \tag{3.5}$$

$$\mathcal{L}_\beta \mathcal{E}_{ij} = \beta^k D_k \mathcal{E}_{ij} + \mathcal{E}_{ik}D_j\beta^k + \mathcal{E}_{kj}D_i\beta^k\,, \tag{3.6}$$

$$a_k = D_k \ln\alpha\,. \tag{3.7}$$

The derivative D_i is the covariant derivative associated with the induced metric γ_{ij} on the slices. The evolution system (3.4) is closed by an additional evolution equation for the 3-metric, which is Eq. (3.5), and evolution equations for the extrinsic curvature and the 3-dimensional connection Γ^k_{ij}, which are

$$\begin{aligned}\partial_t K_{ij} =& \mathcal{L}_\beta K_{ij} - \alpha[\partial_k \Gamma^k_{ij} - \Gamma^k_{lj}\Gamma^l_{ki} + \partial_i\partial_j q + \partial_i \ln\alpha\, \partial_j \ln\alpha - \Gamma^k_{ij}\partial_k q - 2\mathcal{E}_{ij} + K^k{}_k K_{ij}], \\ \partial_t \Gamma^k_{ij} =& \mathcal{L}_\beta \Gamma^k_{ij} - \alpha D^k K_{ij} + K_{ij}D^k\alpha - 2K^k{}_{(i}D_{j)}\alpha + 2\alpha\epsilon^{kl}{}_{(i}\mathcal{B}_{j)l},\end{aligned} \tag{3.8}$$

where we have defined

$$\begin{aligned} q &= \ln(\alpha\gamma^{-1/2}), \\ \mathcal{L}_\beta \Gamma^k_{ij} &= \beta^l\partial_l\Gamma^k_{ij} + 2\Gamma^k_{l(j}\partial_{i)}\beta^l - \Gamma^l_{ij}\partial_l\beta^k + \partial_i\partial_j\beta^k.\end{aligned} \tag{3.9}$$

The above equations are symmetric hyperbolic if q and β^i are specified functions of time and space.

The constraint equations on each slice are the definitions of $\mathcal{E}_{ij}$ and $\mathcal{B}_{ij}$,

$$\begin{aligned}\mathcal{E}_{ij} &= {}^{(3)}R_{ij} + K^k{}_k K_{ij} - K^k{}_i K_{jk}, \\ \mathcal{B}_{ij} &= \epsilon_j{}^{lk} D_k K_{li},\end{aligned} \tag{3.10}$$

from which the Einstein constraints follow from the condition that $\mathcal{E}_{ij}$ and $\mathcal{B}_{ij}$ are symmetric and trace-free, and the definition of Γ^k_{ij},

$$\Gamma^k_{ij} = \frac{1}{2}\gamma^{k\ell}\left(\partial_i\gamma_{j\ell} + \partial_j\gamma_{i\ell} - \partial_\ell\gamma_{ij}\right). \tag{3.11}$$

The Bianchi identities imply derivative constraints on $\mathcal{E}_{ij}$ and $\mathcal{B}_{ij}$:

$$\begin{aligned} D^i\mathcal{E}_{ij} &= \mathcal{B}_{ik}K^i{}_l\epsilon^{kl}{}_j \,, \\ D^i\mathcal{B}_{ij} &= -\mathcal{E}_{ik}K^i{}_l\epsilon^{kl}{}_j \,. \end{aligned} \tag{3.12}$$

These last equations are automatically satisfied if Eqs. (3.10) are satisfied. Equations. (3.12) are nonlinear, but otherwise they have the same structure as the constraints in simple electromagnetism.

Note also that the equations governing $\boldsymbol{\mathcal{E}}$ and $\boldsymbol{\mathcal{B}}$, Eqs (3.4) and (3.12) share another similarity with the field equations of electromagnetism. Namely, just as the Maxwell equations are invariant under the duality transformation

$$\boldsymbol{E} \to \boldsymbol{B} \,, \qquad \boldsymbol{B} \to -\boldsymbol{E} \,,$$

i.e. under a rotation in the complexified notation

$$\boldsymbol{E} - i\boldsymbol{B} \to e^{i\pi/2}(\boldsymbol{E} - i\boldsymbol{B}) \,,$$

so the exact Maxwell-like Bianchi identities (3.4) are also invariant under the same duality transformation

$$\boldsymbol{\mathcal{E}} \to \boldsymbol{\mathcal{B}} \,, \quad \boldsymbol{\mathcal{B}} \to -\boldsymbol{\mathcal{E}} \,. \tag{3.13}$$

This *duality* in the structure of Eqs. (3.4) and also (3.12) does not in general enable one to construct one metric solution of Einstein's equations from another, known solution. However, as we shall see, we can utilize this duality in weakly gravitating systems to find the $\boldsymbol{\mathcal{E}}$ and $\boldsymbol{\mathcal{B}}$ generated by one set of source moments, given the expressions for $\boldsymbol{\mathcal{E}}$ and $\boldsymbol{\mathcal{B}}$ for a dual set of moments.

3.2.2.2 Local-Lorentz frame of a freely falling observer

When one introduces the local-Lorentz frame of a freely falling observer in curved spacetime, one necessarily specializes one's foliation: (i) The local-Lorentz foliation's space slices are flat at first order in distance from the observer's world line, so its extrinsic curvature K_{ij} vanishes along the observer's world line. (ii) Because the observer is freely falling, her acceleration a_k vanishes, which means that successive hypersurfaces in the foliation are parallel to each other along the observer's world line.

These specializations, plus the vanishing shift $\beta_i = 0$ and unit lapse function $\alpha = 1$ of a local-Lorentz frame, bring the constraint and evolution equations (3.12) and (3.4) into the following

Maxwell-like form:

$$\begin{aligned} \boldsymbol{\nabla}\cdot\boldsymbol{\mathcal{E}} &= 0\,, \quad \boldsymbol{\nabla}\cdot\boldsymbol{\mathcal{B}} = 0\,, \\ \frac{\partial\boldsymbol{\mathcal{E}}}{\partial t} - (\boldsymbol{\nabla}\times\boldsymbol{\mathcal{B}})^S &= 0\,, \quad \frac{\partial\boldsymbol{\mathcal{B}}}{\partial t} + (\boldsymbol{\nabla}\times\boldsymbol{\mathcal{E}})^S = 0\,. \end{aligned} \tag{3.14}$$

Here the superscript S means "take the symmetric part" and the remaining notation is the same as in the flat-spacetime Maxwell equations (including changing from $\mathbf{D}$ to $\boldsymbol{\nabla}$ for the spatial gradient).

3.2.2.3 Weak-gravity, nearly Minkowski spacetimes

In this paper's applications (Secs. 3.5 and 3.6), we shall specialize to spacetimes and coordinate systems that are weakly perturbed from Minkowski, and we shall linearize in the perturbations. In this case, the Bianchi identities (3.4) take on precisely the same Maxwell-like form as in a local-Lorentz frame in strongly curved spacetime, Eqs. (3.14). To see that this is so, note that β_k, K_{jk}, a_k, $\mathcal{E}_{jk}$, and $\mathcal{B}_{jk}$ are all first-order perturbations and that α is one plus a first-order perturbation; and linearize Eqs. (3.4) in these first-order quantities.

When the weak-gravity spacetime is also characterized by slow motion, so its source regions are small compared to the wavelengths of its gravitational waves, the evolution equations control how the near-zone $\mathcal{E}_{jk}$ and $\mathcal{B}_{jk}$ get transformed into gravitational-wave fields. For insight into this, we specialize to harmonic gauge, in which the trace-reversed metric perturbation $\bar{h}_{\mu\nu}$ is divergence-free, $\partial^\mu\bar{h}_{\mu\nu} = 0$.

Then *in the near zone*, $\mathcal{E}_{jk}$ and $\mathcal{B}_{jk}$ [which are divergence-free and curl-free by Eqs. (3.14)] are expressible in terms of the metric perturbation itself as

$$\mathcal{E}_{ij} = -\frac{1}{2}\partial_i\partial_j h_{00}\,, \qquad \mathcal{B}_{ij} = \frac{1}{2}\epsilon_i{}^{pq}\partial_q\partial_j h_{p0}\,. \tag{3.15}$$

Because h_{00}, at leading order in $r/\lambda\!\!\!^{-}$ (ratio of radius to reduced wavelength), contains only mass multipole moments (Eq. (8.13a) of [36]), so also $\mathcal{E}_{jk}$ contains only mass multipole moments. And because h_{p0} at leading order in $r/\lambda\!\!\!^{-}$ contains only current multipole moments, so also $\mathcal{B}_{jk}$ contains only current multipole moments.

In the wave zone, by contrast, Eqs. (3.14) show that the locally plane waves are sustained by mutual induction between $\boldsymbol{\mathcal{E}}$ and $\boldsymbol{\mathcal{B}}$, just like for electromagnetic waves, which means that these two wave-zone fields must contain the same information. This is confirmed by the wave-zone expressions for $\mathcal{E}_{jk}$ and $\mathcal{B}_{jk}$ in terms of the metric perturbation,

$$\mathcal{E}_{ij} = -\frac{1}{2}\partial_0^2 h_{ij}\,, \qquad \mathcal{B}_{ij} = -\frac{1}{2}\epsilon_i{}^{pq}n_p\partial_0^2 h_{qj}\,. \tag{3.16}$$

Both fields are expressed in terms of the same quantity, h_{ij}. In addition, in the wave zone, $\boldsymbol{\mathcal{E}}$ and $\boldsymbol{\mathcal{B}}$

are related to each other through a $\pi/4$ rotation of their polarization tensors (see Sec. 3.6.1 below). Correspondingly, we will see in Sec. 3.6 that, if a time-varying mass moment produces + polarized radiation in the wave zone, then the current moment that is dual to it produces $\times$ polarized radiation of the same magnitude.

In the transition zone, the inductive coupling between $\boldsymbol{\mathcal{E}}$ and $\boldsymbol{\mathcal{B}}$, embodied in Eqs. (3.4), enables these equations to act like a blender, mixing up the multipolar information that in the near zone is stored separately in these two fields. After an infinite amount of inductive blending, we arrive at future null infinity, $\mathcal{I}^+$, where the mixing has been so thorough that $\boldsymbol{\mathcal{E}}$ and $\boldsymbol{\mathcal{B}}$ contain precisely the same information, though it is distributed differently among their tensor components [Eqs. (3.16)].

The details of this transition-zone mixing, as embodied in Eqs. (3.14), are in some sense the essence of gravitational-wave generation. We shall explore those details visually in Sec. 3.6 by tracking the tendex and vortex lines (introduced in Sec 3.4) that extend from the near zone, through the transition zone, and into the far zone.

Finally, note that the duality of $\boldsymbol{\mathcal{E}}$ and $\boldsymbol{\mathcal{B}}$ becomes especially convenient for slow-motion systems, where we can relate $\boldsymbol{\mathcal{E}}$ and $\boldsymbol{\mathcal{B}}$ to source multipole moments that appear in the weak-field near zone. In particular: to obtain the $\boldsymbol{\mathcal{E}}$ and $\boldsymbol{\mathcal{B}}$ generated by a specific current moment $\boldsymbol{\mathcal{S}}_\ell$, we can simply apply the duality transformation (3.13) to the $\boldsymbol{\mathcal{E}}$ and $\boldsymbol{\mathcal{B}}$ for its dual moment, which is the mass moment $\boldsymbol{\mathcal{I}}_\ell$, but with one caveat: The differing normalizations used for mass moments and current moments [36] enforce the duality relation

$$\boldsymbol{\mathcal{I}}_\ell \to \frac{2\ell}{\ell+1}\boldsymbol{\mathcal{S}}_\ell\ , \qquad \boldsymbol{\mathcal{S}}_\ell \to -\frac{\ell+1}{2\ell}\boldsymbol{\mathcal{I}}_\ell\ , \tag{3.17}$$

when making this duality transformation; note that both transformations, Eqs. (3.13) and (3.17), must be made at once to arrive at the correct expressions; see Sec. 3.6.

3.3 Physical Interpretations of $\mathcal{E}_{ij}$ and $\mathcal{B}_{ij}$

It is rather well-known that in vacuum[2] the electric part of the Weyl tensor, $\mathcal{E}_{ij}$, describes tidal gravitational accelerations: the relative acceleration of two freely falling particles with separation vector ξ^k is $\Delta a^i = -\mathcal{E}^i{}_j\xi^j$. For this reason $\mathcal{E}_{ij}$ is often called the *tidal field*, a name that we shall adopt.

Not so well-known is the role of the magnetic part of the Weyl tensor $\mathcal{B}_{jk}$ as governing differential frame dragging, i.e. the differential precession of inertial reference frames: in vacuum[2] a gyroscope

[2] In a non-vacuum region of spacetime, the local stress-energy tensor also contributes to tidal accelerations via its algebraic relation to the Ricci tensor which in turn contributes to the Riemann tensor. In this case, $\mathcal{E}_{ij}$ describes that portion of the tidal acceleration due to the "free gravitational field," i.e., the portion that is sourced away from the location where the tidal acceleration is measured; and similarly for $\mathcal{B}_{jk}$ and differential frame dragging. In this paper we shall ignore this subtle point and focus on tidal forces and differential frame dragging in vacuum.

at the tip of the separation vector ξ^k, as observed in the local-Lorentz frame of an observer at the tail of ξ^k, precesses with angular velocity $\Delta\Omega^j = \mathcal{B}^j{}_k\xi^k$. For this reason, we call $\mathcal{B}_{jk}$ the *frame-drag field*.

We deduced this frame-drag role of $\mathcal{B}_{jk}$ during our research and then searched in vain for any reference to it in the literature, while writing our Physical Review Letter on vortexes and tendexes [1] (i.e. Chapter 1.2 in this thesis). More recently we have learned that this role of $\mathcal{B}_{jk}$ was known to Frank Estabrook and Hugo Wahlquist [29] 46 years ago and was rediscovered two years ago by Christoph Schmidt [30] (who states it without proof).

For completeness, in this section we shall give a precise statement and proof of the frame-drag role of $\mathcal{B}_{jk}$, and a corresponding precise statement of the tidal-acceleration role of $\mathcal{E}_{jk}$.

3.3.1 Physical setup

Consider an event $\mathcal{P}$ in spacetime and an observer labeled A whose world line passes through $\mathcal{P}$ and has 4-velocity $\vec{u}$ there; see Fig. 3.1. Introduce an infinitesimally short 4-vector $\vec{\xi}$ at $\mathcal{P}$, that is orthogonal to $\vec{u}$ and thus is seen as spatial by observer A. Denote by $\mathcal{P}'$ the event at the tip of $\vec{\xi}$. Introduce a second observer B whose world line passes through $\mathcal{P}'$ and is parallel there to the world line of observer A, so if we denote B's 4-velocity by the same symbol $\vec{u}$ as that of A and imagine a vector field $\vec{u}$ that varies smoothly between the two world lines, then $\nabla_{\vec{\xi}}\vec{u} = 0$ at $\mathcal{P}$. Let $\vec{\xi}$ be transported by observer A in such a way that it continues to reach from world line A to world line B. Then the vectors $\vec{u}$ and $\vec{\xi}$ satisfy the following three relations at $\mathcal{P}$:

$$\vec{\xi}\cdot\vec{u} = 0\ , \quad [\vec{u},\vec{\xi}] = 0, \quad \nabla_{\vec{\xi}}\vec{u} = 0\ . \tag{3.18}$$

The first says that the separation vector is purely spatial at $\mathcal{P}$ in the reference frame of observer A; the second says that $\vec{\xi}$ continues to reach between world lines A and B, so the quadrilateral formed by $\vec{u}$ and $\vec{\xi}$ in Fig. 3.1 is closed; the third says that the two observers' world lines are parallel to each other at $\mathcal{P}$—i.e., these observers regard themselves as at rest with respect to each other.

3.3.2 Interpretation of $\mathcal{E}_{ij}$ as the tidal field

Let the two observers A and B fall freely, i.e. move on geodesics. Then for this physical setup, the equation of geodesic deviation states that [e.g. [14] Eq. (11.10)]

$$\nabla_{\vec{u}}\nabla_{\vec{u}}\vec{\xi} = -\mathsf{R}(\_\,,\vec{u},\vec{\xi},\vec{u})\ , \tag{3.19}$$

where R is the Riemann tensor. In physical language, the left side is the acceleration $\Delta\vec{a}$ of observer B at $\mathcal{P}'$, as measured in the local-Lorentz frame of observer A at $\mathcal{P}$. This relative acceleration

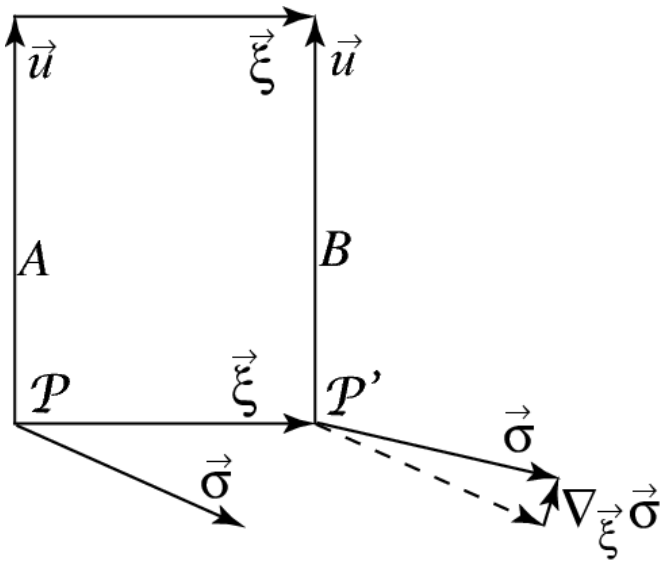

Figure 3.1: Spacetime geometry for computing the precession of a gyroscope at one location $\mathcal{P}'$, relative to gyroscopic standards at a nearby location $\mathcal{P}$.

is purely spatial as seen by observer A, and the right side of Eq. (3.19) tells us that in spatial, 3-dimensional vector and tensor notation (and in vacuum so $R_{\alpha\beta\gamma\delta} = C_{\alpha\beta\gamma\delta}$), it is given by

$$\Delta a^j = -R^j{}_{\hat{0}k\hat{0}}\xi^k = -\mathcal{E}^j{}_k\xi^k \; ; \quad \text{i.e. } \Delta \boldsymbol{a} = -\boldsymbol{\mathcal{E}}(\_\,, \boldsymbol{\xi}) \; . \tag{3.20}$$

Since (as is well-known) this relative acceleration produces the Earth's tides when $\mathcal{E}_{jk}$ is caused by the moon and sun, $\mathcal{E}_{jk}$ is called the *tidal field*, and Eq. (3.20) is known as *the tidal-acceleration equation*.

3.3.3 Interpretation of $\mathcal{B}_{ij}$ as the frame-drag field

Next let the two observers A and B in Fig. 3.1 be accelerated if they wish (with the same 4-acceleration $\vec{a}$ up to differences proportional to $\vec{\xi}$), and give each of them a spatial unit vector $\vec{\sigma}$ that is tied to an inertial-guidance gyroscope, so the following relations are satisfied:

$$\vec{\sigma} \cdot \vec{u} = 0 \; , \quad \vec{\sigma} \cdot \vec{\sigma} = 1 \; , \quad \nabla_{\vec{u}}\vec{\sigma} = (\vec{a} \cdot \vec{\sigma})\vec{u} \; , \quad \vec{a} \equiv \nabla_{\vec{u}}\vec{u} \; . \tag{3.21}$$

The first of these says that $\vec{\sigma}$ is purely spatial as seen in the observer's reference frame; the second says that $\vec{\sigma}$ has unit length; the third is the Fermi-Walker transport law for an inertial-guidance gyroscope.

The local-frame-dragging-induced rate of change of $\vec{\sigma}$ at $\mathcal{P}'$, as measured using inertial-direction

standards at $\mathcal{P}$, is $\nabla_{\vec{u}}\nabla_{\vec{\xi}}\vec{\sigma}$. We can write this as

$$\nabla_{\vec{u}}\nabla_{\vec{\xi}}\vec{\sigma} \quad = \quad \nabla_{\vec{\xi}}\nabla_{\vec{u}}\vec{\sigma} + [\nabla_{\vec{u}}, \nabla_{\vec{\xi}}]\vec{\sigma} = \nabla_{\vec{\xi}}\nabla_{\vec{u}}\vec{\sigma} + \mathsf{R}(\_, \vec{\sigma}, \vec{u}, \vec{\xi}) \ , \tag{3.22}$$

where R is the Riemann tensor and we have used the fact that $[\vec{u}, \vec{\xi}] = 0$; cf. Eqs. (11.8) and (11.9) of MTW [14].

Evaluating the first term $\nabla_{\vec{\xi}}\nabla_{\vec{u}}\vec{\sigma}$ using the Fermi-Walker transport law [the third of Eqs. (3.21)] and the fact that the observers are momentarily at rest with respect to each other [the third of Eqs. (3.18)], we bring Eq. (3.22) into the form

$$\nabla_{\vec{u}}\nabla_{\vec{\xi}}\vec{\sigma} = \mathsf{R}(\_, \vec{\sigma}, \vec{u}, \vec{\xi}) + \vec{u}\nabla_{\vec{\xi}}(\vec{a}\cdot\vec{\sigma}) \ . \tag{3.23}$$

We are only interested in the spatial part of this rate of change, so we can ignore the second term on the right side of the equation. We switch to the 3-dimensional viewpoint of the observer at $\mathcal{P}$ (where our calculation is being done) and we denote the spatial part of $\nabla_{\vec{u}}\nabla_{\vec{\xi}}\vec{\sigma}$ by $\dot{\boldsymbol{\sigma}}$:

$$\dot{\boldsymbol{\sigma}} \equiv \left[\nabla_{\vec{u}}\nabla_{\vec{\xi}}\vec{\sigma}\right]_{\text{project orthogonal to } \vec{u}} \ . \tag{3.24}$$

Equation (3.23) tells us that this rate of change is not only orthogonal to $\vec{u}$ (spatial) but also orthogonal to $\boldsymbol{\sigma}$; it therefore can be written as a rotation

$$\dot{\boldsymbol{\sigma}} = \Delta\boldsymbol{\Omega} \times \boldsymbol{\sigma} \tag{3.25}$$

Here $\Delta\boldsymbol{\Omega}$ *is the frame-dragging angular velocity at* $\mathcal{P}'$ *as measured using inertial standards at* $\mathcal{P}$. We can solve for this angular velocity $\Delta\boldsymbol{\Omega}$ by crossing $\boldsymbol{\sigma}$ into Eq. (3.25) and using $\boldsymbol{\sigma}\cdot\boldsymbol{\sigma} = 1$:

$$\Delta\boldsymbol{\Omega} = \boldsymbol{\sigma} \times \dot{\boldsymbol{\sigma}} \ . \tag{3.26}$$

Inserting expression (3.23) for $\dot{\boldsymbol{\sigma}}$ and switching to index notation, we obtain

$$\Delta\Omega_i = \epsilon_{ijk}\sigma^j R^k{}_{p\hat{0}q}\sigma^p\xi^q \ . \tag{3.27}$$

Rewriting the Riemann tensor component in terms of the gravitomagnetic part of the Weyl tensor (in vacuum), $R^k{}_{p\hat{0}q} = -\epsilon^k{}_{ps}\mathcal{B}^s{}_q$, performing some tensor manipulations, and noticing that because $\Delta\boldsymbol{\Omega}$ is crossed into $\boldsymbol{\sigma}$ when computing the precession any piece of $\Delta\boldsymbol{\Omega}$ along $\boldsymbol{\sigma}$ is irrelevant, we obtain

$$\Delta\Omega_i = \mathcal{B}_{ij}\xi^j \ , \quad \text{i.e. } \Delta\boldsymbol{\Omega} = \boldsymbol{\mathcal{B}}(\_, \boldsymbol{\xi}) \ . \tag{3.28}$$

Put in words: *in vacuum the frame-dragging angular velocity at $\mathcal{P}'$, as measured using inertial directions at the adjacent event $\mathcal{P}$, is obtained by inserting the vector $\boldsymbol{\xi}$ (which reaches from $\mathcal{P}$ to $\mathcal{P}'$) into one slot of the gravitomagnetic part of the Weyl tensor.*

Because of the role of $\mathcal{B}_{ij}$ in this *equation of differential frame dragging*, we call $\mathcal{B}_{ij}$ the *frame-drag field*.

3.4 Our New Tools: Tendex and Vortex Lines; Their Tendicities and Vorticities; Tendexes and Vortexes

3.4.1 Tendex lines and their tendicities; vortex lines and their vorticities

As symmetric, trace-free tensors, the tidal field $\boldsymbol{\mathcal{E}}$ and frame-drag field $\boldsymbol{\mathcal{B}}$ can each be characterized completely by its three principal axes (eigendirections) and its three associated eigenvalues.

If $\boldsymbol{p}$ is a (smoothly changing) unit eigenvector of the tidal field $\boldsymbol{\mathcal{E}}$ (or of the frame-drag field $\boldsymbol{\mathcal{B}}$), then the integral curves of $\boldsymbol{p}$ can be regarded as "field lines" associated with $\boldsymbol{\mathcal{E}}$ (or $\boldsymbol{\mathcal{B}}$). For $\boldsymbol{\mathcal{E}}$ we call these integral curves *tidal tendex lines*, or simply *tendex lines*[3], because $\boldsymbol{\mathcal{E}}$ tidally stretches objects it encounters, and the Latin word *tendere* means "to stretch." For $\boldsymbol{\mathcal{B}}$ we call the integral curves *frame-drag vortex lines*, or simply *vortex lines*, because $\boldsymbol{\mathcal{B}}$ rotates gyroscopes, and the Latin word *vertere* means "to rotate." At each point $\mathcal{P}$ in space there are three orthogonal eigendirections of $\boldsymbol{\mathcal{E}}$ (and three of $\boldsymbol{\mathcal{B}}$), so through each point there pass three orthogonal tendex lines and three orthogonal vortex lines.

Outside a spherically symmetric gravitating body with mass M, such as the Earth or a Schwarzschild black hole, the tidal field, in a spherical polar orthonormal basis, has components

$$\mathcal{E}_{\hat{r}\hat{r}} = -\frac{2M}{r^3} , \quad \mathcal{E}_{\hat{\theta}\hat{\theta}} = \mathcal{E}_{\hat{\phi}\hat{\phi}} = +\frac{M}{r^3} \tag{3.29}$$

(e.g. Sec. 1.6 and Eq. (31.4) of [14]). The tidal-acceleration equation $\Delta a^j = -\mathcal{E}^j{}_k \xi^k$ tells us that this tidal field stretches objects radially and squeezes them equally strongly in all tangential directions (see the people in Fig. 3.2). Correspondingly, one eigenvector of $\boldsymbol{\mathcal{E}}$ is radial, and the other two are tangential with degenerate eigenvalues. This means that one set of tendex lines is radial (the red tendex lines in Fig. 3.2), and any curve lying on a sphere around the body is a tendex line. If we break the tangential degeneracy by picking our tangential unit eigenvectors to be the basis vectors $\boldsymbol{e}_{\hat{\theta}}$ and $\boldsymbol{e}_{\hat{\phi}}$ of a spherical polar coordinate system, then the tangential tendex lines are those vectors' integral curves — the blue curves in Fig. 3.2.

When the spherical body is weakly gravitating and is set rotating slowly, then it acquires a

[3]The word tendex was coined by David Nichols.

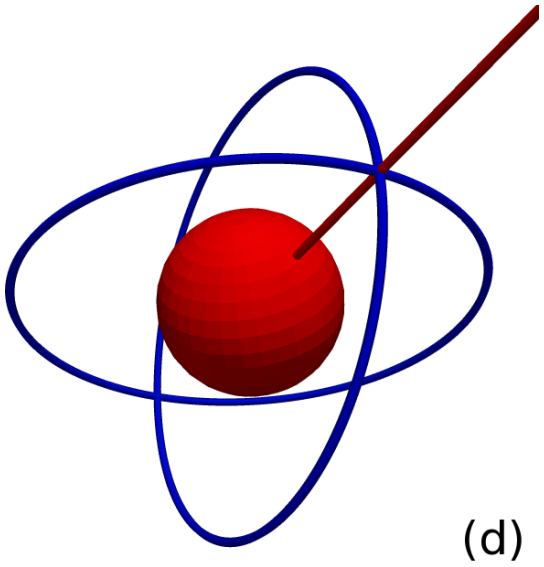

Figure 3.2: (color online). Tendex lines outside a spherically symmetric, gravitating body. The lines are colored by the sign of their tendicity: red lines have negative tendicity (they stretch a person oriented along them); blue lines have positive tendicity (they squeeze).

nonzero frame-drag field given by Eqs. (3.40) below. The corresponding vortex lines are shown in Fig. 3.3. (See Sec. 3.5.1 below for details.)

To any tendex (or vortex) line, with unit eigenvector $\boldsymbol{p}$, there is associated an eigenvalue $\mathcal{E}_{pp} = \mathcal{E}_{jk}p^j p^k$ which is called the line's *tendicity* (or $\mathcal{B}_{pp} = \mathcal{B}_{jk}p^j p^k$ which is called the line's *vorticity*). The physical meaning of this tendicity (or vorticity) can be read off the tidal-acceleration equation (3.20) [or the equation of differential frame dragging (3.28)]. Specifically, if a person's body (with length ℓ) is oriented along a tidal tendex line (Fig. 3.2), she feels a head-to-foot stretching acceleration $\Delta a = -\mathcal{E}_{pp}\ell$. If the line's tendicity $\mathcal{E}_{pp}$ is negative (red tendex line), her body gets stretched; if the tendicity is positive (blue tendex line), she gets compressed.

If her body is oriented along a vortex line (Fig. 3.3), then a gyroscope at her feet precesses around the vortex line with an angular speed, relative to inertial frames at her head, given by $\Delta\Omega = \mathcal{B}_{pp}\ell$. If the line's vorticity is negative (red vortex lines in Fig. 3.3), then the gyroscope at her feet precesses counterclockwise relative to inertial frames at her head, and (because $\mathcal{B}_{pp}$ is unchanged when one reverses the direction $\boldsymbol{p}$), a gyroscope at her head precesses counterclockwise relative to inertial frames at her feet. Correspondingly, we call the (red) vortex line a *counterclockwise vortex line*. If the line's vorticity is positive (blue vortex lines in Fig. 3.3), the precessions are clockwise and the vortex line is said to be clockwise.

For any spacetime, the tendex lines color coded by their tendicities (e.g. Fig. 3.2) and the vortex lines color coded by their vorticities (e.g. Fig. 3.3) depict visually all details of the Weyl curvature tensor.

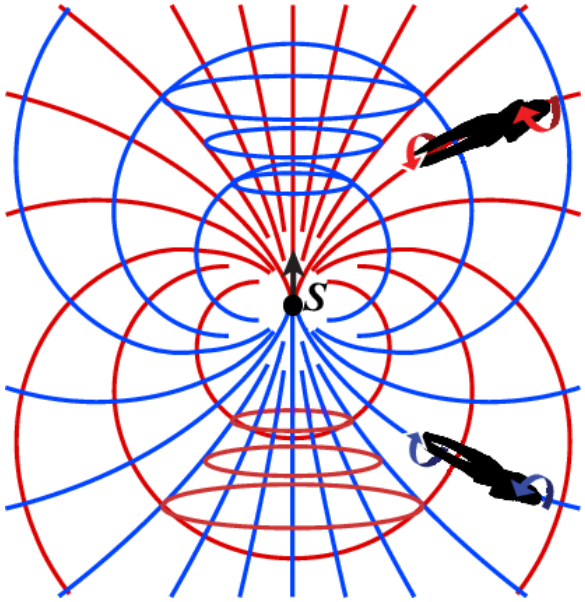

Figure 3.3: (color online). Vortex lines outside a slowly spinning, spherically symmetric, gravitating body with spin angular momentum $\boldsymbol{S}$. The lines are colored by the sign of their vorticity: red lines have negative vorticity (they produce a counterclockwise differential precession of gyroscopes); blue lines have positive vorticity (clockwise differential precession).

Since $\boldsymbol{\mathcal{E}}$ and $\boldsymbol{\mathcal{B}}$ are trace-free, at any point in space the sum of the three tendex lines' tendicities vanishes, and the sum of the three vorticities vanishes. Because $\boldsymbol{\mathcal{E}}$ and $\boldsymbol{\mathcal{B}}$ are also symmetric, each is characterized by five numbers at any point in space. The direction of one tendex line fixes two numbers and its tendicity fixes a third, leaving only two numbers to be specified. The direction of a second tendex line, in the plane orthogonal to the first, fixes a fourth number and the second line's tendicity fixes the fifth and final number — leaving the last line's direction and tendicity fully determined. Similarly, this is the case for vortex lines and their vorticities.

3.4.2 Vortexes and tendexes

We give the name *frame-drag vortex*, or simply *vortex*, to a bundle of vortex lines with large vorticity. In Fig. 3.3, the red vortex lines near the north polar axis, which are enclosed by blue circles, constitute a negative-vorticity (counterclockwise) vortex; the blue vortex lines near the south polar axis, which are enclosed by red circles, constitute a positive-vorticity (clockwise) vortex. These two vortexes emerge from the north and south poles of the spinning point particle.

Similarly, we give the name *tidal tendex*, or simply *tendex*, to a strong concentration of tendex lines. We shall meet our first example at the end of Sec. 3.5.4 below.

3.5 Weak-gravity, Stationary Systems

3.5.1 One stationary, weakly gravitating, spinning body

When gravity is weak and slowly changing (e.g., outside a slowly precessing, spinning, weakly gravitating body such as the Earth), one can write the spacetime metric in the form

$$ds^2 = -\alpha^2 dt^2 + \delta_{jk}(dx^j + \beta^j dt)(dx^k + \beta^k dt) \tag{3.30a}$$

(e.g. Sec. 23.9.3 of [37]; or Chap. 10 of MTW [14] with the spatial coordinates changed slightly). Here

$$\alpha^2 = \left(1 - \frac{2M}{r}\right) , \quad \boldsymbol{\beta} = -\frac{2\boldsymbol{S}}{r^2} \times \boldsymbol{n} , \tag{3.30b}$$

are the squared lapse function and the shift function, M is the body's mass, $\boldsymbol{S}$ is its spin angular momentum, and

$$r = \sqrt{x^2 + y^2 + z^2} , \quad \boldsymbol{n} = \boldsymbol{e}_{\hat{r}} \tag{3.30c}$$

are radius and the unit radial vector, with $\{x^1, x^2, x^3\} = \{x, y, z\}$. In spherical polar coordinates (associated with the Cartesian coordinates $\{x, y, z\}$ in the usual way), the metric (3.30a) becomes

$$\begin{aligned} ds^2 &= -\alpha^2 dt^2 + dr^2 + r^2 d\theta^2 + r^2 \sin^2\theta (d\phi - \omega dt)^2 , \\ \omega &= 2S/r^3 . \end{aligned} \tag{3.30d}$$

It is conventional to rewrite general relativity, in this weak-field, slow-motion situation, as a field theory in flat spacetime. In this language, the geodesic equation for a test particle takes the form

$$\frac{d^2\boldsymbol{x}}{dt^2} = \boldsymbol{g} + \boldsymbol{v} \times \boldsymbol{H} , \tag{3.31}$$

which resembles the Lorentz force law in electromagnetic theory; see, e.g., [38] and references therein, especially [39]. Here $\boldsymbol{v} = d\boldsymbol{x}/dt$ is the particle's velocity [Cartesian components $(dx/dt, dy/dt, dz/dt)$] and

$$\begin{aligned} \boldsymbol{g} &= -\frac{1}{2}\boldsymbol{\nabla}\alpha^2 = -\frac{M}{r^2}\boldsymbol{n} , \\ \boldsymbol{H} &= \boldsymbol{\nabla} \times \boldsymbol{\beta} = 2\left[\frac{\boldsymbol{S} - 3(\boldsymbol{S}\cdot\boldsymbol{n})\boldsymbol{n}}{r^3}\right] \end{aligned} \tag{3.32}$$

are the body's *gravitoelectric field* (same as Newtonian gravitational acceleration) and its *gravitomagnetic field*. Note that these fields have the same monopole and dipole structures as the electric and magnetic fields of a spinning, charged particle.

In this paper we shall adopt an alternative to this "gravito-electromagnetic" viewpoint. For the

gravitational influence of the mass M, we shall return to the Newtonian viewpoint of a gravitational acceleration $\boldsymbol{g}$ and its gradient, the tidal gravitational field (the electric part of the Weyl tensor)

$$\boldsymbol{\mathcal{E}} = -\boldsymbol{\nabla}\boldsymbol{g} \ , \quad \text{i.e., } \mathcal{E}_{ij} = -g_{i,j} = \Phi_{,ij} = \frac{1}{2}\alpha^2{}_{,ij} \ . \tag{3.33}$$

Here the comma denotes partial derivative (actually, the gradient in our Cartesian coordinate system) and Φ is the Newtonian gravitational potential, which is related to the lapse function by $\alpha^2 = 1+2\Phi$ in the Newtonian limit. The components of this tidal field in the spherical coordinates' orthonormal basis $\boldsymbol{e}_{\hat{r}} = \partial/\partial r$, $\boldsymbol{e}_{\hat{\theta}} = (1/r)\partial/\partial\theta$, $\boldsymbol{e}_{\hat{\phi}} = (1/r\sin\theta)\partial/\partial\phi$ are easily seen to be

$$\mathcal{E}_{\hat{r}\hat{r}} = -\frac{2M}{r^3} \ , \quad \mathcal{E}_{\hat{\theta}\hat{\theta}} = \mathcal{E}_{\hat{\phi}\hat{\phi}} = +\frac{M}{r^3} \ , \tag{3.34}$$

[Eqs. (3.29) above], which are symmetric and trace-free as expected. The field lines associated with this tidal field are easily seen to be those depicted in Fig. 3.2 above.

For the effects of the spin angular momentum, we shall think of the spinning body as "dragging space into motion" with a velocity and angular velocity (relative to our Cartesian coordinates) given by

$$\frac{d\boldsymbol{x}_{\rm space}}{dt} \equiv \boldsymbol{v}_{\rm space} = -\boldsymbol{\beta} = \frac{2\boldsymbol{S}}{r^2} \times \boldsymbol{n}; \ , \quad \frac{d\phi_{\rm space}}{dt} = \omega = \frac{2S}{r^3} \tag{3.35}$$

[cf. the $\delta_{jk}(dx^j + \beta^j dt)(dx^k + \beta^k dt)$ term in the metric (3.30a) and the $(d\phi - \omega dt)^2$ term in the metric (3.30d)]. Just as the vorticity $\boldsymbol{\nabla}\times\boldsymbol{v}$ of a nonrelativistic fluid with velocity field $\boldsymbol{v}(\boldsymbol{x})$ is twice the angular velocity $\boldsymbol{\Omega}$ of rotation of a fluid element relative to an inertial reference frame, so the vorticity associated with the "space motion," $\boldsymbol{\nabla}\times\boldsymbol{v}_{\rm space}$, turns out to be twice the vectorial angular velocity of an inertial-guidance gyroscope relative to inertial reference frames far from the body ("at infinity") — or equivalently, relative to our spatial Cartesian coordinates $\{x, y, z\}$, which are locked to inertial frames at infinity. In formulas: Let $\boldsymbol{\sigma}$ be a unit vector along the spin angular momentum vector of an inertial-guidance gyroscope. Viewed as a vector in our Cartesian basis, it precesses

$$\frac{d\boldsymbol{\sigma}}{dt} = \boldsymbol{\Omega}_{\rm fd} \times \boldsymbol{\sigma} \ , \tag{3.36}$$

with a *frame-dragging vectorial angular velocity* equal to half the vorticity of space viewed as a fluid:

$$\boldsymbol{\Omega}_{\rm fd} \quad = \quad \frac{1}{2}\boldsymbol{\nabla}\times\boldsymbol{v}_{\rm space} = -\frac{1}{2}\boldsymbol{\nabla}\times\boldsymbol{\beta} = -\frac{1}{2}\boldsymbol{H} = -\left[\frac{\boldsymbol{S} - 3(\boldsymbol{S}\cdot\boldsymbol{n})\boldsymbol{n}}{r^3}\right]; \tag{3.37}$$

see e.g. Eq. (25.14) of [37], or Eq. (40.37) of [14]. This dipolar frame-dragging angular velocity is shown in Fig. 3.4.

For dynamical black holes and other strong-gravity, dynamical situations, it is not possible to measure gyroscopic precession with respect to inertial frames at infinity, since there is no unambigu-

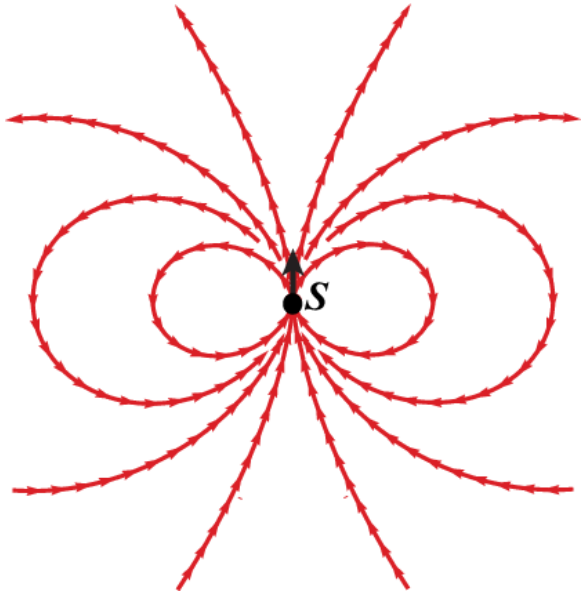

Figure 3.4: For a weakly gravitating, slowly rotating body with spin angular momentum $\boldsymbol{S}$, the dipolar frame-dragging angular velocity relative to inertial frames at infinity, $\boldsymbol{\Omega}_{\rm fd}$. The arrows are all drawn with the same length rather than proportional to the magnitude of $\boldsymbol{\Omega}_{\rm fd}$.

ous way to compare vectors at widely separated events.[4]

On the other hand, we *can*, in general, measure the precession of inertial-guidance gyroscopes at one event, with respect to inertial frames at a neighboring event — i.e., we can measure *differential frame dragging* as embodied in the frame-drag field (magnetic part of the Weyl tensor) $\mathcal{B}_{ij}$. In our weak-gravity, slow-motion situation, this frame-drag field is equal to the gradient of $\boldsymbol{\Omega}_{\rm fd}$ (Eq. (5.45b) of [42]):

$$\boldsymbol{\mathcal{B}} = \boldsymbol{\nabla}\boldsymbol{\Omega}_{\rm fd} \ , \quad \text{i.e. } \mathcal{B}_{jk} = \Omega_{{\rm fd}\,j,k} \ . \tag{3.38}$$

For our weakly gravitating, spinning body, $\boldsymbol{\Omega}_{\rm fd}$ has the dipolar form (3.37), so the frame-drag field is

$$\mathcal{B}_{jk} = \frac{3}{r^4}\left[2S_{(j}n_{k)} + (\boldsymbol{S}\cdot\boldsymbol{n})(\delta_{jk} - 5n_jn_k)\right] \ . \tag{3.39}$$

Here the parentheses on the subscripts indicate symmetrization. In spherical polar coordinates, the components of this frame-drag field are

$$\begin{aligned} \mathcal{B}_{\hat{r}\hat{r}} &= -2\mathcal{B}_{\hat{\theta}\hat{\theta}} = -2\mathcal{B}_{\hat{\phi}\hat{\phi}} = -\frac{6S\cos\theta}{r^4} \ , \\ \mathcal{B}_{\hat{r}\hat{\theta}} &= \mathcal{B}_{\hat{\theta}\hat{r}} = -\frac{3S\sin\theta}{r^4} \ . \end{aligned} \tag{3.40}$$

[4]There is an exception: One can introduce additional geometric structure, e.g, an auxiliary flat spacetime, that provides a way of carrying a reference frame inward from infinity to all other locations and thereby compare vectors at different events. Some of us have used this approach to localize linear momentum in the gravitational field around black holes [40, 41]. However, the auxiliary structure has great arbitrariness, and for the vortex and tendex concepts of this paper there is no need for such auxiliary structure, so we eschew it.

For this (and any other axially symmetric) frame-drag field, one of the three sets of vortex lines is along the ϕ direction (i.e. the $\boldsymbol{S}\times\boldsymbol{x}$ direction)—i.e., it is *axial*—and the other two are *poloidal*. By computing the eigenvectors of the tensor (3.39) and then drawing the curves to which they are tangent, one can show that the body's vortex lines have the forms shown in Fig. 3.3.

Notice that the poloidal, negative-vorticity vortex lines (the poloidal red curves in Fig. 3.3) all emerge from the north polar region of the spinning body, encircle the body, and return back to the north polar region.

Why do these have negative rather than positive vorticity? Choose the eigendirection $\boldsymbol{p}$ at the body's north pole to point away from the body. The body drags inertial frames in a right-handed manner (counterclockwise as seen looking down on the north pole), and the frame dragging is stronger at the tail of $\boldsymbol{p}$ (nearer the body) than at the tip, so the frame-dragging angular velocity decreases from tail to tip, which means it is more left-handed (clockwise) at the tip than the tail; it has negative vorticity.

The poloidal, positive-vorticity vortex lines (the poloidal blue curves in Fig. 3.3) all emerge from the body's south polar region, swing around the body, and return to the south polar region.

The azimuthal vortex lines have negative vorticity above the hole's equatorial plane (blue azimuthal circles) and positive vorticity below the hole's equatorial plane (red azimuthal circles).

3.5.2 Two stationary, weakly gravitating, spinning point particles with opposite spins

Consider, next, two weakly gravitating, spinning point particles with opposite spins, sitting side-by-side. Place the particles (named A and B) on the x axis, at locations $\{x_A, y_A, z_A\} = \{+a, 0, 0\}$, $\{x_B, y_B, z_B\} = \{-a, 0, 0\}$ and give them vectorial spins $\boldsymbol{S}_A = S\boldsymbol{e}_z$, $\boldsymbol{S}_B = -S\boldsymbol{e}_z$. Then the frame-drag angular velocity relative to inertial frames at infinity is

$$\boldsymbol{\Omega}_{\rm fd} \;=\; -\frac{\boldsymbol{S}_A - 3(\boldsymbol{S}_A\cdot\boldsymbol{n}_A)\boldsymbol{n}_A}{{r_A}^3} - \frac{\boldsymbol{S}_B - 3(\boldsymbol{S}_B\cdot\boldsymbol{n}_B)\boldsymbol{n}_A}{{r_B}^3}\,, \tag{3.41}$$

where $r_A = |\boldsymbol{x}-\boldsymbol{x}_A|$ and $r_B = |\boldsymbol{x}-\boldsymbol{x}_B|$ are the distances to the particles and $\boldsymbol{n}_A = (\boldsymbol{x}-\boldsymbol{x}_A)/r_A$ and $\boldsymbol{n}_B = (\boldsymbol{x}-\boldsymbol{x}_B)/r_B$ are unit vectors pointing from the particles' locations to the field point; cf. Eq. (3.37). This vector field is plotted in Fig. 3.5(a). It has just the form one might expect from the one-spin field of Fig. 3.4.

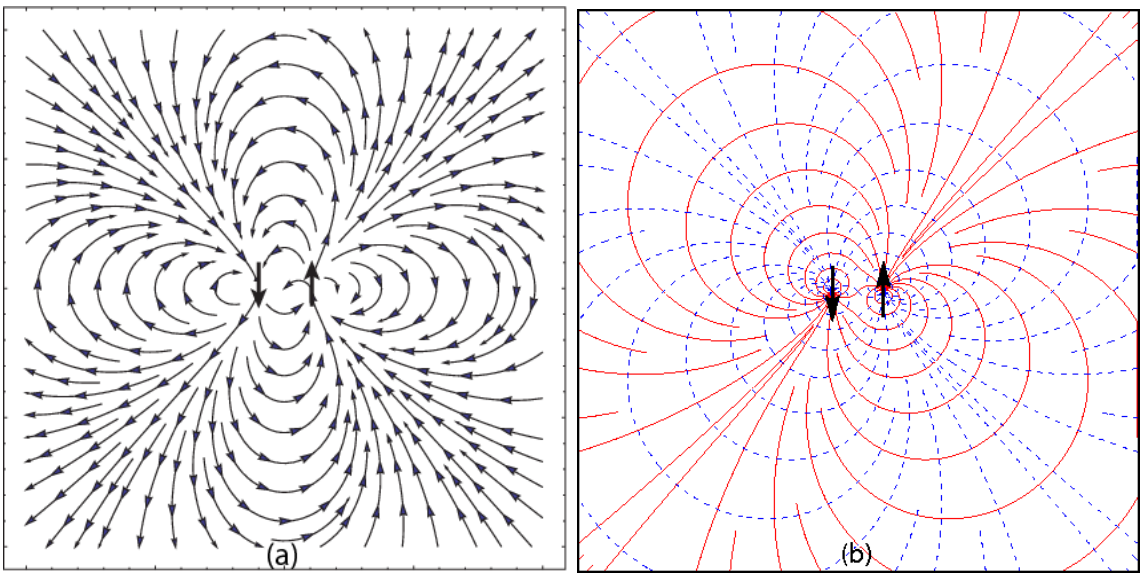

Figure 3.5: For two stationary point particles sitting side-by-side with their spins in opposite directions (thick black arrows), two types of streamlines in the plane of reflection symmetry formed by the particles' spins and their separation vector. (a) The frame-dragging angular velocity $\boldsymbol{\Omega}_{\rm fd}$ and its streamlines, with the arrows all drawn at the same length rather than proportional to the magnitude of $\boldsymbol{\Omega}_{\rm fd}$. (b): The two sets of vortex lines of the frame-drag field $\boldsymbol{\mathcal{B}}$. The negative-vorticity vortex lines are solid and colored red, and the positive-vorticity ones are dashed and blue. In this figure, as in preceding figures, the colors are not weighted by the lines' vorticities, but only by the signs of the vorticities.

For these two spinning particles, the frame-drag field (gradient of Eq. (3.41)] is

$$\begin{aligned}\mathcal{B}_{jk} &= \frac{3}{{r_A}^4}\left[2S_A^{(j}n_A^{k)} + (\boldsymbol{S}_A\cdot\boldsymbol{n}_A)(\delta^{jk}-5n_A^jn_A^k)\right]\\ &+ \frac{3}{{r_B}^4}\left[2S_B^{(j}n_B^{k)} + (\boldsymbol{S}_B\cdot\boldsymbol{n}_B)(\delta^{jk}-5n_B^jn_B^k)\right]\end{aligned} \tag{3.42}$$

[cf. Eq. (3.39)], where we have moved the vector and tensor indices up for simplicity of notation. (In our Cartesian basis, there is no difference between up and down indices.)

The best two-dimensional surface on which to visualize vortex lines of this $\boldsymbol{\mathcal{B}}$ is the x-z plane (the plane formed by the particles' spins and their separation vector). The system is reflection symmetric through this plane. On this plane, one of the principal directions of $\boldsymbol{\mathcal{B}}$ is orthogonal to it (in the y direction); the other two lie in the plane and are tangent to the in-plane vortex lines. By computing the eigendirections of $\boldsymbol{\mathcal{B}}$ [i.e., of the tensor (3.42)] and mapping out their tangent vortex lines, and checking the sign of $\mathcal{B}_{pp}$ along their tangent directions $\boldsymbol{p}$, we obtain Fig. 3.5.

Note that, as for a single spinning particle (Fig. 3.3) , so also here for two spins, the negative-vorticity vortex lines (solid red curves) emerge from the tips of the spins and the positive-vorticity vortex lines (dashed blue curves) emerge from their tails. For a single spin, the negative-vorticity

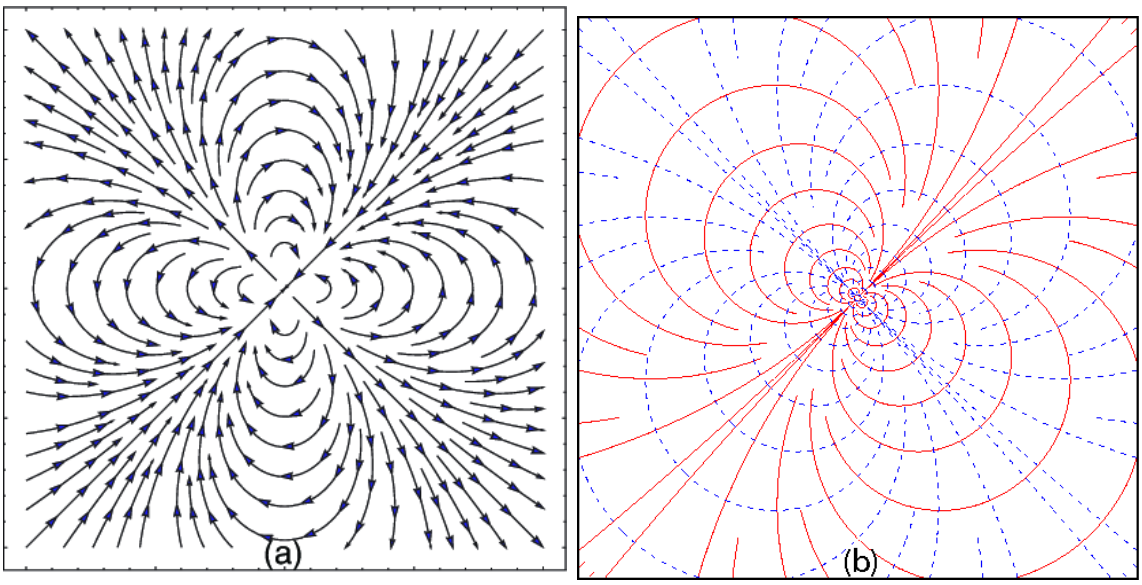

Figure 3.6: Current-quadrupolar streamlines associated with the two stationary spinning particles of Fig. 3.5, for which the current-quadrupole moment has nonzero components $\mathcal{S}_{xz} = \mathcal{S}_{zx} = Sa$. (a) The frame-dragging angular velocity $\mathbf{\Omega}_{\rm fd}$ and its streamlines, and (b) the two sets of vortex lines, in the x-z plane. Figure (b) also describes the tendex lines for a static mass-quadrupolar particle whose only nonzero quadrupole-moment components are $\mathcal{I}_{xz} = \mathcal{I}_{zx}$.

vortex lines emerge from the tip, travel around the body, and return to the same tip. Here, the lines close to each spinning body leave and enter the same body's tip, but the majority emerge from one body's tip, travel around that body and enter the other body's tip. Similarly the positive-vorticity vortex lines (dashed and blue) emerge from one body's tail, travel around that body, and enter the other body's tail (aside from the lines near each body that exit and return to the same body's tail).

The collection of solid red vortex lines near each arrow tip in Fig. 3.5(b) constitutes a negative-vorticity frame-drag vortex, and the collection of dashed blue vortex lines near each arrow tail is a positive-vorticity vortex.

3.5.3 The two spinning particles viewed from afar: Stationary, quadrupolar frame-drag field

When viewed from afar, the two spinning bodies produce a current-quadrupole gravitational field with quadrupole moment (e.g. Eq. (5.28b) of [36])

$$\begin{aligned} \mathcal{S}_{pq} &= \left(\int j_p x_q d^3x\right)^{\rm STF} = (S_p a_q + (-S_p)(-a_q))^{\rm STF} \\ &= S_p a_q + S_q a_p - \frac{2}{3}(\boldsymbol{S}\cdot\boldsymbol{a})\delta_{pq}\,. \end{aligned} \tag{3.43}$$

Here $j_p = S_p\delta(\boldsymbol{x}-\boldsymbol{a}) - S_p\delta(\boldsymbol{x}+\boldsymbol{a})$ is the angular momentum density. Since the only nonzero components of $\boldsymbol{S}$ and $\boldsymbol{a}$ are $S_z = S$ and $a_x = a$, the only nonzero components of the current-quadrupole moment are

$$\mathcal{S}_{xz} = \mathcal{S}_{zx} = Sa \ . \tag{3.44}$$

The frame-drag-induced velocity of space (negative of the shift function) for this current quadrupole, and the frame-drag angular velocity and frame-drag tensor field are

$$\begin{aligned} \boldsymbol{v}_{\rm space} &= -\boldsymbol{\beta} = \frac{4\boldsymbol{n}\times\boldsymbol{\mathcal{S}}\cdot\boldsymbol{n}}{r^3} \ , \\ \boldsymbol{\Omega}_{\rm fd} &= \frac{1}{2}\boldsymbol{\nabla}\times\boldsymbol{v}_{\rm space} \ , \quad \boldsymbol{\mathcal{B}} = \boldsymbol{\nabla}\boldsymbol{\Omega}_{\rm fd} \ . \end{aligned} \tag{3.45}$$

[e.g. Eq. (10.6b) of [36]; also Eqs. (3.37) and (3.38) above]. Inserting Eq. (3.44) for the quadrupole moment into Eqs. (3.45), and plotting $\boldsymbol{\Omega}_{\rm fd}$ and the vortex lines of $\boldsymbol{\mathcal{B}}$ in the x-z plane, we obtain the graphs shown in Fig. 3.6.

Notice that the current-quadrupolar frame-drag angular velocity in Fig. 3.6(a) is, indeed, the same as that for two oppositely directed spins [Fig. 3.5(a)] in the limit that the spins' separation goes to zero—i.e., as seen from afar—and the current-quadrupolar vortex lines of the frame-drag tensor field [Fig. 3.6(b)] is the vanishing-separation limit of that for the two oppositely directed spins (Fig. 3.5b).

Here, as for finitely separated spinning particles, there are two red frame-drag vortexes, one emerging from the origin in the upper right direction, the other in the lower-left direction; and similarly, there are two blue frame-drag vortexes, one emerging in the upper left direction and the other in the lower right direction.

3.5.4 Static, quadrupolar tidal field and its tendex lines and tendexes

For an idealized static particle with time-independent mass-quadrupole moment $\mathcal{I}_{pq}$ and all other moments (including the mass) vanishing, the squared lapse function is $\alpha^2 = 1+2\Phi = 1-(\mathcal{I}_{pq}/r)_{,pq}$ [36], where Φ is the Newtonian gravitational potential. Therefore, the particle's tidal field $\mathcal{E}_{jk} = \Phi_{,jk}$ [Eq. (3.37)] is

$$\mathcal{E}_{jk} = -\frac{1}{2}\left(\frac{\mathcal{I}_{pq}}{r}\right)_{,pqjk} \ . \tag{3.46}$$

For comparison, for a particle with time-independent current-quadrupole moment $\mathcal{S}_{pq}$, the shift function is $\beta_j = (-4/3)\epsilon_{jpq}(\mathcal{S}_{pk}/r)_{,kq}$, which implies that the frame-drag field is [Eqs. (3.45)]

$$\mathcal{B}_{jk} = -\frac{2}{3}\left(\frac{\mathcal{S}_{pq}}{r}\right)_{,pqjk} \ . \tag{3.47}$$

Notice that, once the differing normalization conventions (3.17) are accounted for, Eqs. (3.46)

and (3.47) are the same, as required by the duality relations (3.13) and (3.17). This means that, for a static current quadrupole whose only nonzero components are $\mathcal{I}_{xz} = \mathcal{I}_{zx}$, the tendex lines will have precisely the same forms as the vortex lines of the static current quadrupole (3.44); i.e., they will have the forms shown in Fig. 3.6b. In this case there are two negative-tendicity (solid red) tidal tendexes, one emerging from the origin in the upper right direction, and the other in the lower-left direction; and there are two positive-tendicity (dashed blue) tidal tendexes, one emerging in the upper left direction and the other in the lower right direction.

3.6 Gravitational Waves and their Generation

We turn now to dynamical situations, which we describe using linearized gravity. We first discuss the tendex and vortex structure of plane gravitational waves. We then examine wave generation by time-varying multipolar fields, and the accompanying tendex and vortex structures of these systems.

3.6.1 Plane gravitational wave

In this section, we will describe the features of $\boldsymbol{\mathcal{E}}$ and $\boldsymbol{\mathcal{B}}$ for plane gravitational waves, and connect our observations to the linearized-gravity and Newman-Penrose (NP) formalisms. In Appendix 3.8 we review the Newman-Penrose formalism and its connection to the spatial tensors $\boldsymbol{\mathcal{E}}$ and $\boldsymbol{\mathcal{B}}$.

Consider gravitational-wave propagation in an asymptotically flat spacetime, in transverse-traceless (TT) gauge. Near future null infinity, $\mathcal{I}^+$, we can linearize around a Minkowski background and obtain

$$\mathcal{E}_{ij} = -\frac{1}{2}\partial_0^2 h_{ij}\,, \qquad \mathcal{B}_{ij} = -\frac{1}{2}\epsilon_i{}^{pq} n_p \partial_0^2 h_{qj}\,. \tag{3.48}$$

It is convenient to expand these expressions in terms of the two gravitational-wave polarization tensors, e^+_{ij} and $e^\times_{ij}$,

$$\mathcal{E}_{ij} = -\frac{1}{2}(\ddot{h}_+ e^+_{ij} + \ddot{h}_\times e^\times_{ij}), \quad \mathcal{B}_{ij} = -\frac{1}{2}(\ddot{h}_+ e^\times_{ij} - \ddot{h}_\times e^+_{ij})\,, \tag{3.49}$$

where e^+_{ij} and $e^\times_{ij}$ are symmetric, trace-free, and orthogonal to the waves' propagation direction. Letting the unit-norm vector $\mathbf{e}_{\hat{1}}$ denote the direction of propagation of the gravitational wave, then one can expand the polarization tensors in terms of the remaining two vectors of an orthonormal triad, $\mathbf{e}_{\hat{2}}$ and $\mathbf{e}_{\hat{3}}$, as

$$\boldsymbol{e}_+ = \boldsymbol{e}_{\hat{2}} \otimes \boldsymbol{e}_{\hat{2}} - \boldsymbol{e}_{\hat{3}} \otimes \boldsymbol{e}_{\hat{3}}\,, \tag{3.50}$$

$$\boldsymbol{e}_\times = \boldsymbol{e}_{\hat{2}} \otimes \boldsymbol{e}_{\hat{3}} + \boldsymbol{e}_{\hat{3}} \otimes \boldsymbol{e}_{\hat{2}}\,. \tag{3.51}$$

Consider first a + polarized wave. We have that

$$\boldsymbol{\mathcal{E}} = -\frac{1}{2}\ddot{h}_+ \boldsymbol{e}^+ = \frac{1}{2}[(-\ddot{h}_+)\boldsymbol{e}_{\hat{2}} \otimes \boldsymbol{e}_{\hat{2}} + \ddot{h}_+ \boldsymbol{e}_{\hat{3}} \otimes \boldsymbol{e}_{\hat{3}}]\,, \tag{3.52}$$

so we see that $\mp\ddot{h}_+/2$ are the two eigenvalues of $\boldsymbol{\mathcal{E}}$ (the two tendicities), and $\boldsymbol{e}_{\hat{2}}$ and $\boldsymbol{e}_{\hat{3}}$ are the two corresponding eigenvectors. Now, define a second basis locally rotated at each point by $\pi/4 = 45^{\rm o}$,

$$\begin{pmatrix} \tilde{\boldsymbol{e}}_{\hat{2}} \\ \tilde{\boldsymbol{e}}_{\hat{3}} \end{pmatrix} = \begin{pmatrix} \cos\frac{\pi}{4} & \sin\frac{\pi}{4} \\ -\sin\frac{\pi}{4} & \cos\frac{\pi}{4} \end{pmatrix} \begin{pmatrix} \boldsymbol{e}_{\hat{2}} \\ \boldsymbol{e}_{\hat{3}} \end{pmatrix}\,. \tag{3.53}$$

Then, a simple calculation shows that

$$\boldsymbol{e}_\times = \tilde{\boldsymbol{e}}_{\hat{2}} \otimes \tilde{\boldsymbol{e}}_{\hat{2}} - \tilde{\boldsymbol{e}}_{\hat{3}} \otimes \tilde{\boldsymbol{e}}_{\hat{3}}\,, \tag{3.54}$$

and one can immediately see that $\boldsymbol{\mathcal{B}}$ is diagonal in this new basis

$$\boldsymbol{\mathcal{B}} = -\frac{1}{2}\ddot{h}_+ \boldsymbol{e}^\times = -\frac{1}{2}[\ddot{h}_+ \tilde{\boldsymbol{e}}_{\hat{2}} \otimes \tilde{\boldsymbol{e}}_{\hat{2}} - \ddot{h}_+ \tilde{\boldsymbol{e}}_{\hat{3}} \otimes \tilde{\boldsymbol{e}}_{\hat{2}}]\,. \tag{3.55}$$

The eigenvalues of $\boldsymbol{\mathcal{B}}$ (the vorticities), like those of $\boldsymbol{\mathcal{E}}$ (the tendicities), are $\mp\ddot{h}_+/2$, but $\boldsymbol{\mathcal{B}}$'s eigenvectors, $\tilde{\boldsymbol{e}}_{\hat{2}}$ and $\tilde{\boldsymbol{e}}_{\hat{3}}$, are locally rotated by $\pi/4$ compared to those of $\boldsymbol{\mathcal{E}}$. Correspondingly, the vortex lines of h_+ must be locally rotated by $\pi/4$ with respect to the tendex lines.

The local rotation of the tendex and vortex lines is most transparent for a plane gravitational wave. In Fig. 3.7, we show the tendex and vortex lines of a plane gravitational wave propagating out of the page (i.e. $\mathbf{e}_{\hat{1}} = \mathbf{e}_{\hat{z}}$ is the propagation direction). Because the eigenvectors of $\boldsymbol{\mathcal{E}}$ are $\mathbf{e}_{\hat{2}} = \mathbf{e}_{\hat{x}}$ and $\mathbf{e}_{\hat{3}} = \mathbf{e}_{\hat{y}}$, the tendex lines are the lines of constant x and y, illustrated by red (solid) lines and blue (dashed) lines, respectively, on the left of Fig. 3.7. Similarly, the vortex lines are lines of constant $x \pm y$, again drawn as blue (dashed) lines and red (solid) lines, respectively. The tendicity (vorticity) has constant magnitude along the lines, but the two sets of tendex (vortex) lines have opposite sign; consequently, the tidal (frame-drag) field produces a stretching (counterclockwise differential precession) along the solid red direction and a squeezing (clockwise differential precession) of the same magnitude along the dashed blue direction.

More generally, gravitational waves will contain both + and × polarizations, and to study their vortex and tendex lines, it will be useful to express the electric and magnetic tensors in the spatial

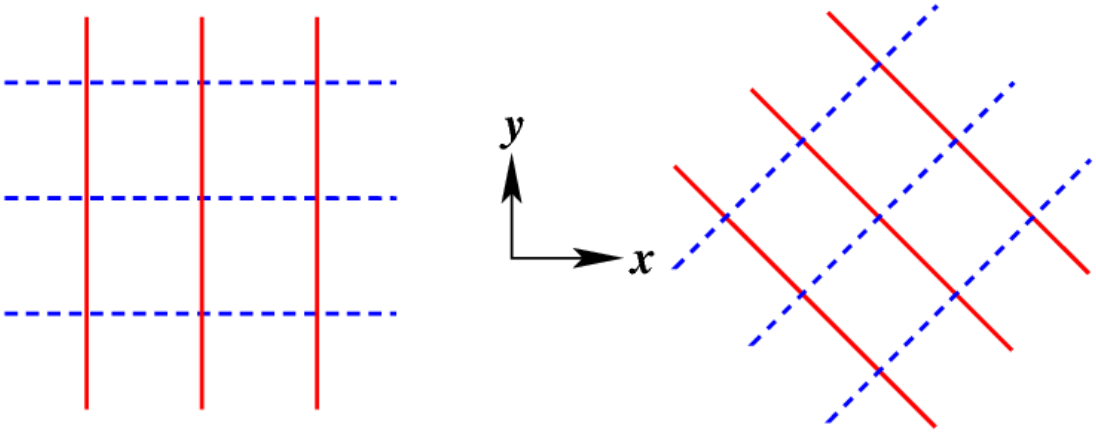

Figure 3.7: The tendex lines (left) and vortex lines (right) of a plane gravitational wave propagating in the z direction (out of the picture). The tendex lines are lines of constant x and y, and the vortex lines are rotated by $\pi/4$ (lines of constant $x \pm y$). The blue (dashed) curves correspond to positive tendicity and vorticity (squeezing and clockwise differential precessing, respectively) and the red (solid) curves denote negative tendicity and vorticity (stretching and counterclockwise precessing). The tendicity (vorticity) is constant along a tendex line (vortex line), and the tendicity (vorticity) of a red line is equal in magnitude but opposite in sign to that of a blue (dashed) line.

orthonormal basis $(\boldsymbol{e}_{\hat{1}}, \boldsymbol{e}_{\hat{2}}, \boldsymbol{e}_{\hat{3}})$. They can be written conveniently as matrices:

$$\mathcal{E}_{\hat{a}\hat{b}} = \frac{1}{2}\left(\begin{array}{c|cc} 0 & 0 & 0 \\ \hline 0 & -\ddot{h}_+ & -\ddot{h}_\times \\ 0 & -\ddot{h}_\times & \ddot{h}_+ \end{array}\right), \tag{3.56a}$$

$$\mathcal{B}_{\hat{a}\hat{b}} = \frac{1}{2}\left(\begin{array}{c|cc} 0 & 0 & 0 \\ \hline 0 & \ddot{h}_\times & -\ddot{h}_+ \\ 0 & -\ddot{h}_+ & -\ddot{h}_\times \end{array}\right). \tag{3.56b}$$

It is useful to introduce an associated Newman-Penrose null tetrad consisting of two real null vectors, $\vec{l}$ (along the waves' propagation direction) and $\vec{n}$, and a conjugate pair of complex null vectors $\vec{m}$ and $\vec{m}^*$ given by

$$\begin{aligned} \vec{l} &= \frac{1}{\sqrt{2}}(\vec{e}_{\hat{0}} + \vec{e}_{\hat{1}})\,, \qquad & \vec{n} &= \frac{1}{\sqrt{2}}(\vec{e}_{\hat{0}} - \vec{e}_{\hat{1}})\,, \\ \vec{m} &= \frac{1}{\sqrt{2}}(\vec{e}_{\hat{2}} + i\vec{e}_{\hat{3}})\,, \qquad & \vec{m}^* &= \frac{1}{\sqrt{2}}(\vec{e}_{\hat{2}} - i\vec{e}_{\hat{3}}) \end{aligned} \tag{3.57}$$

[Eqs. (3.71) of Appendix A]. For plane waves on a Minkowski background, the NP curvature scalar that characterizes the radiation is

$$\Psi_4 = C_{\mu\nu\rho\sigma} n^\mu m^{*\nu} n^\rho m^{*\sigma} = -\ddot{h}_+ + i\ddot{h}_\times\,, \tag{3.58}$$

so we can compactly rewrite Eqs. (3.56) as

$$\mathcal{E}_{\hat{a}\hat{b}} + i\mathcal{B}_{\hat{a}\hat{b}} = \frac{1}{2}\left(\begin{array}{c|cc} 0 & 0 & 0 \\ \hline 0 & \Psi_4 & i\Psi_4 \\ 0 & i\Psi_4 & -\Psi_4 \end{array}\right) . \tag{3.59}$$

This expression holds for any plane gravitational wave propagating in the $\vec{e}_{\hat{1}}$ direction.

For any outgoing gravitational wave in an asymptotically flat space, as one approaches asymptotic null infinity the general expression (3.73) for $\mathcal{E}_{\hat{a}\hat{b}} + i\mathcal{B}_{\hat{a}\hat{b}}$ reduces to expression (3.59), because all the curvature scalars except Ψ_4 vanish due to the peeling property of the Weyl scalars near null infinity. Further discussion of the tidal and frame-drag fields of radiation near null infinity and their tendex and vortex lines is given in Chapter 4 (i.e. [28]).

It is helpful to draw some simple analogies between gravitational and electromagnetic plane waves. For a generic mixture of + and × polarizations, the magnitudes of the nonvanishing eigenvalues of both $\boldsymbol{\mathcal{E}}$ and $\boldsymbol{\mathcal{B}}$ are simply

$$\frac{1}{2}\sqrt{\ddot{h}_+^2 + \ddot{h}_\times^2} = \frac{1}{2}|\Psi_4| . \tag{3.60}$$

This mirrors plane waves in electromagnetism, where $|\vec{E}| = |\vec{B}|$ is equal to the sum in quadrature of the magnitudes of the two polarizations. The absent longitudinal components in an electromagnetic plane wave correspond to the vanishing of the eigenvalues for the eigenvectors of $\boldsymbol{\mathcal{E}}$ and $\boldsymbol{\mathcal{B}}$ along the propagation direction. The orthogonality of the vectorial electromagnetic field strengths $\vec{E}\perp\vec{B}$ becomes the $\pi/4$ rotation between the meshes (Fig. 3.7) formed by the two transverse eigenvectors of the tensorial quantities $\boldsymbol{\mathcal{E}}$ and $\boldsymbol{\mathcal{B}}$.

3.6.2 Gravitational waves from a head-on collision of two black holes

As an example of the usefulness of this approach, we calculate the tendex and vortex lines at large radii for gravitational waves emitted by the head-on collision of two equal-mass nonspinning black holes. If the holes move along the z axis and we use as our spatial triad the unit vectors of spherical polar coordinates, $(\mathbf{e}_{\hat{1}}, \mathbf{e}_{\hat{2}}, \mathbf{e}_{\hat{3}}) = (\mathbf{e}_{\hat{r}}, \mathbf{e}_{\hat{\theta}}, \mathbf{e}_{\hat{\phi}}) = (\partial_r, r^{-1}\partial_\theta, (r\sin\theta)^{-1}\partial_\phi)$, and choose our null tetrad in the usual way (3.57), then we can apply the results described by Fiske et al. [43], namely, that $\Re[\Psi_4]$ is axisymmetric [and, when decomposed into spin-weighted spherical harmonics, is dominated by the $l = 2$, $m = 0$ harmonic, ${}_{-2}Y_{2,0}(\theta,\phi)$] and that $\Im[\Psi_4] = 0$. Then the electric and magnetic

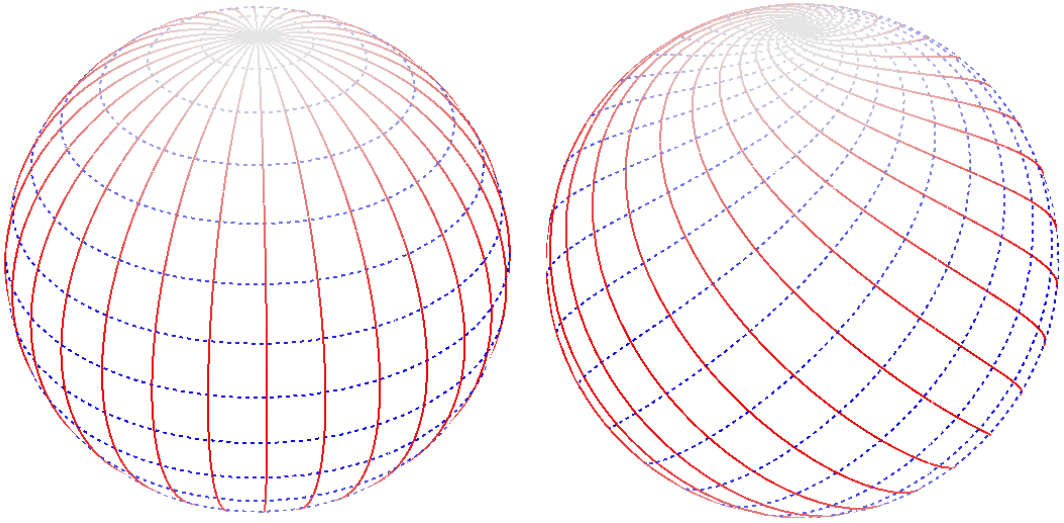

Figure 3.8: Tendex lines (left) and vortex lines (right) for the gravitational waves that would arise from the merger of equal-mass black holes falling together along the z axis. The positive tendicity and vorticity lines are shown in blue (dashed) and the negative lines are depicted in red (solid). Each line's intensity is proportional to its tendicity (or vorticity), which varies over the sphere as the dominant spin-weighted spherical harmonic, ${}_{-2}Y_{2,0}(\theta,\phi) \propto \sin^2\theta$. Dark red and blue near the equator correspond to large-magnitude tendicity and vorticity, and light nearly white colors at the poles indicate that the tendicity and vorticity are small there.

parts of the Weyl tensor are given by

$$\mathcal{E}_{\hat{a}\hat{b}} = \frac{1}{2}\left(\begin{array}{c|cc} 0 & 0 & 0 \\ \hline 0 & \Re(\Psi_4) & 0 \\ 0 & 0 & -\Re(\Psi_4) \end{array}\right), \qquad \mathcal{B}_{\hat{a}\hat{b}} = \frac{1}{2}\left(\begin{array}{c|cc} 0 & 0 & 0 \\ \hline 0 & 0 & \Re(\Psi_4) \\ 0 & \Re(\Psi_4) & 0 \end{array}\right), \tag{3.61}$$

and the eigenvalues of both $\boldsymbol{\mathcal{E}}$ and $\boldsymbol{\mathcal{B}}$ are $\pm\Re(\Psi_4)/2$. The eigenvectors of $\boldsymbol{\mathcal{E}}$ are the unit vectors $\mathbf{e}_{\hat{\theta}}$ and $\mathbf{e}_{\hat{\phi}}$, and those of $\boldsymbol{\mathcal{B}}$ are $\mathbf{e}_{\hat{\theta}} \pm \mathbf{e}_{\hat{\phi}}$. Thus, the radiation is purely + polarized in this basis. The tendex lines are the lines of constant θ and ϕ on a sphere, and the vortex lines are rotated relative to the tendex lines by $\pi/4 = 45^{\circ}$.

We show these lines in Fig. 3.8: the tendex lines on the left, and the vortex lines on the right. As in Fig. 3.7, the red (solid) lines correspond to negative tendicity and vorticity, and the blue (dashed) lines denote positive values. The intensity of each line is proportional to the magnitude of its tendicity (or vorticity), which varies over the sphere as ${}_{-2}Y_{2,0}(\theta,\phi) \propto \sin^2\theta$ (the dominant spherical harmonic). Correspondingly, the dark blue and red regions near the equator represent strong tendicity and vorticity, whereas the light off-white colors near the poles indicate that the

tendicity and vorticity are small there.

We remark in passing that the duality of $\boldsymbol{\mathcal{E}}$ and $\boldsymbol{\mathcal{B}}$ implies that, if there were a source of gravitational waves which had a Ψ_4 that is purely imaginary and equal to the $i\Re[\Psi_4]$ for our colliding black holes, then those waves' vortex lines would be the same as the tendex lines of Fig. 3.8, and the tendex lines would be the same as the vortex lines of the same figure (but with the sign of the lines' vorticity flipped). One can see this because (i) Eq. (3.58) shows we would have a pure $\times$ polarized wave, and (ii) when we apply the rotation of basis (3.53) to (3.59) under the condition of $\Re(\Psi_4) = 0$ we get once again the matrices (3.61), but with $(\tilde{\boldsymbol{e}}_{\hat{2}}, \tilde{\boldsymbol{e}}_{\hat{3}})$ as basis vectors and with all instances of $\Re(\Psi_4)$ replaced by $\Im(\Psi_4)$. This duality does not address, however, how to construct a source with a purely imaginary Ψ_4.

3.6.3 Wave generation by a time-varying current quadrupole

A dynamical current-quadrupole moment $\mathcal{S}_{pq}(t)$ generates a metric perturbation described by the $\mathcal{S}_{pq}(t-r)/r$ terms in Eqs. (8.13) of [36]. It is straightforward to show that the corresponding frame-drag field is

$$\mathcal{B}_{ij} = \frac{2}{3}\left[-\left(\frac{\mathcal{S}_{pq}}{r}\right)_{,pqij} + \epsilon_{ipq}\left(\frac{{}^{(2)}\mathcal{S}_{pm}}{r}\right)_{,qn}\epsilon_{jmn} + 2\left(\frac{{}^{(2)}\mathcal{S}_{p(i}}{r}\right)_{,j)p} - \left(\frac{{}^{(4)}\mathcal{S}_{ij}}{r}\right)\right] . \quad (3.62)$$

Here $\mathcal{S}_{pq}$ is to be regarded as a function of retarded time, $t-r$, and the prefixes ${}^{(2)}$ and ${}^{(4)}$ mean two time derivatives and four time derivatives. This equation shows explicitly how $\mathcal{B}_{ij}$ in the near zone transitions into $\mathcal{B}_{ij}$ in the wave zone — or equivalently, how rotating (or otherwise time-changing) frame-drag vortexes in the near zone generate gravitational waves.

This transition from near zone to far zone can also be described by the linear approximation to the Maxwell-like equations for the frame-drag field $\boldsymbol{\mathcal{B}}$ and the tidal field $\boldsymbol{\mathcal{E}}$, Eqs. (3.14). These equations govern the manner by which the current-quadrupole near-zone frame-drag field (3.47) acquires an accompanying tidal field as it reaches outward into and through the transition zone, to the wave zone. That accompanying tidal field is most easily deduced from the $\mathcal{S}_{pq}(t-r)/r$ terms in the metric perturbation, Eqs. (8.13) of [36]. The result is:

$$\mathcal{E}_{ij} = \frac{4}{3}\epsilon_{pq(i}\left[-\left(\frac{{}^{(1)}\mathcal{S}_{pk}}{r}\right)_{,j)kq} + \left(\frac{{}^{(3)}\mathcal{S}_{j)p}}{r}\right)_{,q}\right] . \quad (3.63)$$

In the near zone, the current quadrupole's tidal field [first term of (3.63)] behaves differently from its frame-drag field [first term of (3.62)]: it has one additional time derivative and one fewer space derivative. As a result, *the tidal field is smaller than the frame-drag field in the near zone by a factor of* $r/\lambda\!\!\!^{-}$, where $\lambda\!\!\!^{-}$ is the reduced wavelength of the emitted gravitational waves.

As one moves outward through the near zone to the transition zone, where $r \sim \lambda\!\!\!^{-}$, the tidal field increases in magnitude to become the same strength as the frame-drag field. The frame-drag and tidal fields behave this way, because it is the near-zone vortexes that generate the gravitational waves, as discussed above.

In the wave zone, the general current-quadrupole (outgoing-wave) frame-drag field (3.62) reduces to

$$\mathcal{B}_{\hat{a}\hat{b}} = \frac{4}{3r}\left[{}^{(4)}S_{\hat{a}\hat{b}}(t-r)\right]^{\rm TT} \ . \tag{3.64}$$

Here the indices are confined to transverse directions (the surface of a sphere of constant r) in the orthonormal basis $\boldsymbol{e}_{\hat{\theta}}$, $\boldsymbol{e}_{\hat{\phi}}$, and "TT" means "take the transverse, traceless part". From the third of the Maxwell-like equations (3.14), or equally well from the general current-quadrupole tidal field, Eq. (3.63), we infer the wave-zone tidal field:

$$\mathcal{E}_{\hat{a}\hat{b}} = \frac{4}{3r}\left[\epsilon_{\hat{c}(\hat{a}}\,{}^{(4)}\mathcal{S}_{\hat{b})\hat{c}}(t-r)\right]^{\rm TT} \ , \tag{3.65}$$

where $\epsilon_{\hat{c}\hat{d}}$ is the 2-dimensional Levi-Civita tensor on the sphere. Since $\mathcal{E}_{\hat{a}\hat{b}} = \mathcal{R}_{\hat{a}\hat{0}\hat{b}\hat{0}} = -\frac{1}{2}{}^{(2)}h^{\rm TT}_{\hat{a}\hat{b}}$, where $h^{\rm TT}_{\hat{a}\hat{b}}$ is the transverse, traceless gravitational-wave field, our wave-zone tidal distortion (3.65) agrees with the standard result for the wave-zone current-quadrupole gravitational-wave field (Eq. (4.8) of [36]).

3.6.4 Rotating current quadrupole

In this section, we will discuss the vortex and tendex lines of a rotating current quadrupole.

A large rotating-current-quadrupole moment arises during the merger and ringdown of the extreme-kick configuration of a binary black hole (a quasicircular binary made of identical black holes, whose spins are antialigned and lie in the orbital plane). During the merger, the four vortexes associated with the initial holes' spins get deposited onto the merged horizon's equator, and they then rotate around the final Kerr hole's spin axis at the same rate as their separation vector rotates, generating a large, rotating-current-quadrupole moment (paper III in this series).

As a simple linearized-gravity model of this late time behavior, imagine that at an initial time $t = 0$, the two vortex-generating spins, of magnitude S, are separated by a distance a along the x axis and are pointing in the $\pm y$ direction — i.e. they have the same configuration as the static current quadrupole discussed in Sec. 3.5.3 above. Then at $t = 0$, the spins' current-quadrupole moment has as its nonzero components $\mathcal{S}_{xy} = \mathcal{S}_{yx} = Sa$ [Eq. (3.44) with the spin axes changed from z to y]. As time passes, the spins' separation vector and the spins' directions rotate at the same angular velocity ω so the configuration rotates rigidly. Then it is not hard to show that the

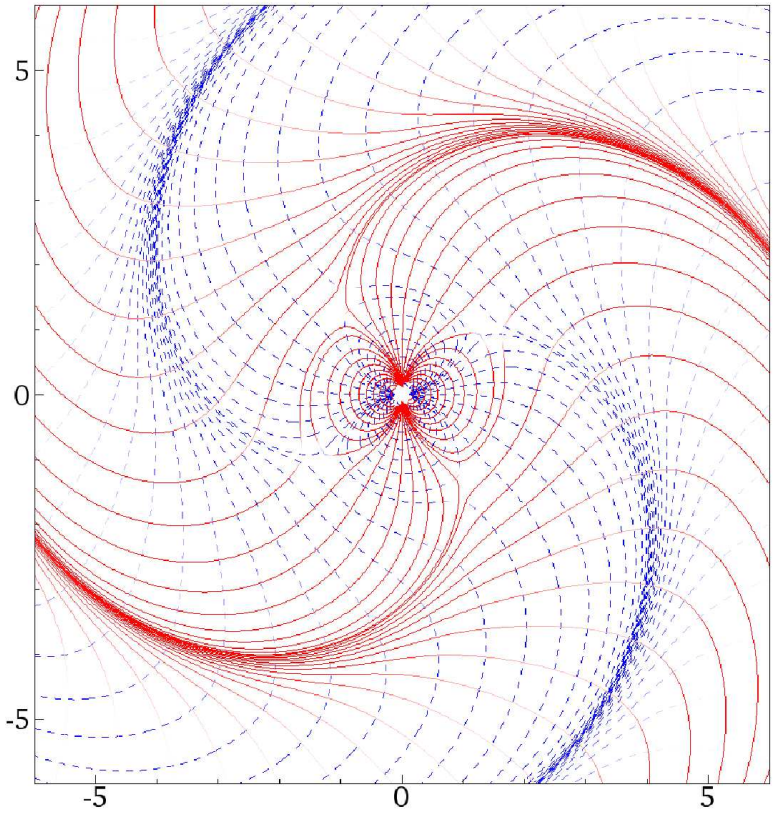

Figure 3.9: For a rotating current quadrupole in linearized theory, two families of vortex lines in the plane of reflection symmetry (the x-y plane). The red (solid) curves are lines with negative vorticity, and the blue (dashed) curves are lines of positive vorticity. The color intensity of the curves represents the strength of the vorticity, but rescaled by $(kr)^5/[1+(kr)^4]$ (with k the wave number) to remove the vorticity's radial decay. We see the quadrupolar near-zone pattern and the transition into the induction zone. In the induction zone, the pattern carries four "triradius" singular points [44] in each family of curves, necessitated for the transition from the static quadrupole pattern to the spiraling radiation pattern. This same figure also describes the tendex lines of a rotating mass quadrupole (see the end of Sec. 3.6.6).

current-quadrupole moment evolves as

$$\mathcal{S}_{xy} = \mathcal{S}_{yx} = Sa\cos(2\omega t)\,, \quad \mathcal{S}_{xx} = -\mathcal{S}_{yy} = -Sa\sin(2\omega t)\,. \tag{3.66}$$

It is straightforward to calculate the frame-drag field produced by this quadrupole moment using Eq. (3.62), and to then compute the vortex lines and their vorticities.

The explicit expressions for these lines are somewhat lengthy, and not particularly instructive; but the shapes of the vortex lines and the values of their vorticities are quite interesting.

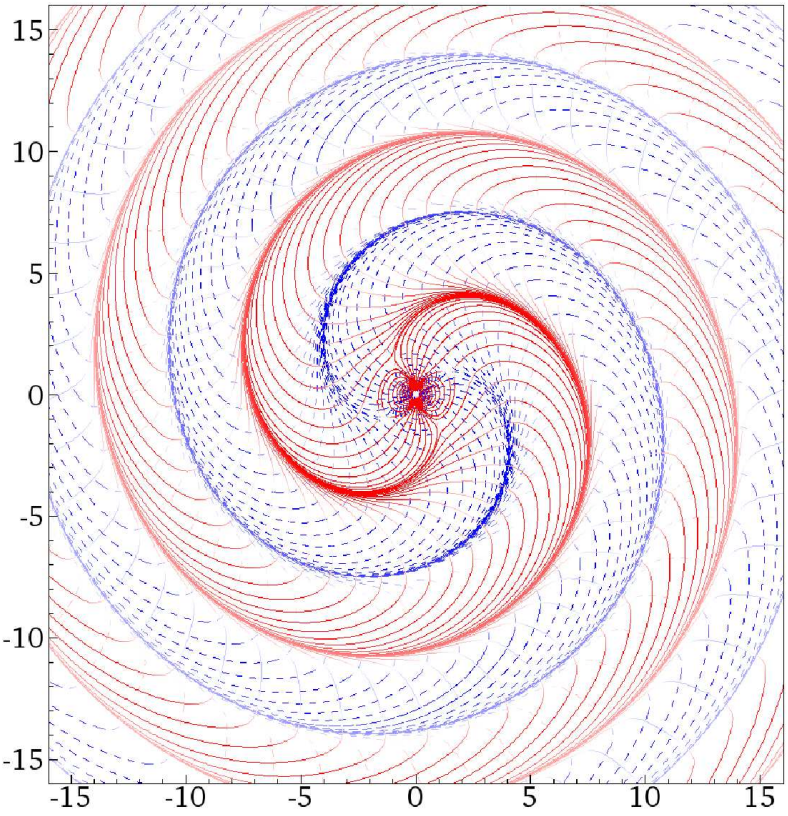

Figure 3.10: Same as Fig. 3.9 but zoomed out to show the wave zone. In the wave zone, the lines generically collect into spirals, which form the boundaries of vortexes (regions of concentrated vorticity).

3.6.4.1 Vortex and tendex lines in the plane of reflection symmetry

There are two sets of vortex lines that lie in the x-y plane (the plane of reflection symmetry) and one set that passes orthogonally through this plane. We show the in-plane vortex lines in Figs. 3.9 and 3.10. The two figures depict the negative-vorticity vortex lines by red (solid) curves and the positive-vorticity lines by blue (dashed) curves. The darkness of the lines is proportional to the vorticity; dark red (blue) indicates strong negative (positive) vorticity, and light red (blue) indicates weaker vorticity. To remove the effects of the radial dependence in the coloring, we have scaled the vorticity by $(kr)^5/[1+(kr)^4]$, where $k = 1/\lambda\!\!\!^{-} = 2\omega$ is the wave number of the radiation. Figure 3.9 shows the region of the near zone that is difficult to see in Fig. 3.10, an equivalent figure that spans a larger region of the x-y plane. As one can see from the figures, the two sets of lines have the same pattern, but are rotated with respect to each other by $\pi/2 = 90^{\rm o}$.

In the near zone (inner region of Fig. 3.9), the vortex-line pattern is the same as for the static current quadrupole of Fig. 3.6b. At the transition to the wave zone, the vortex lines fail to curve back into the central region and instead bend outward, joining a wave-zone spiral pattern.

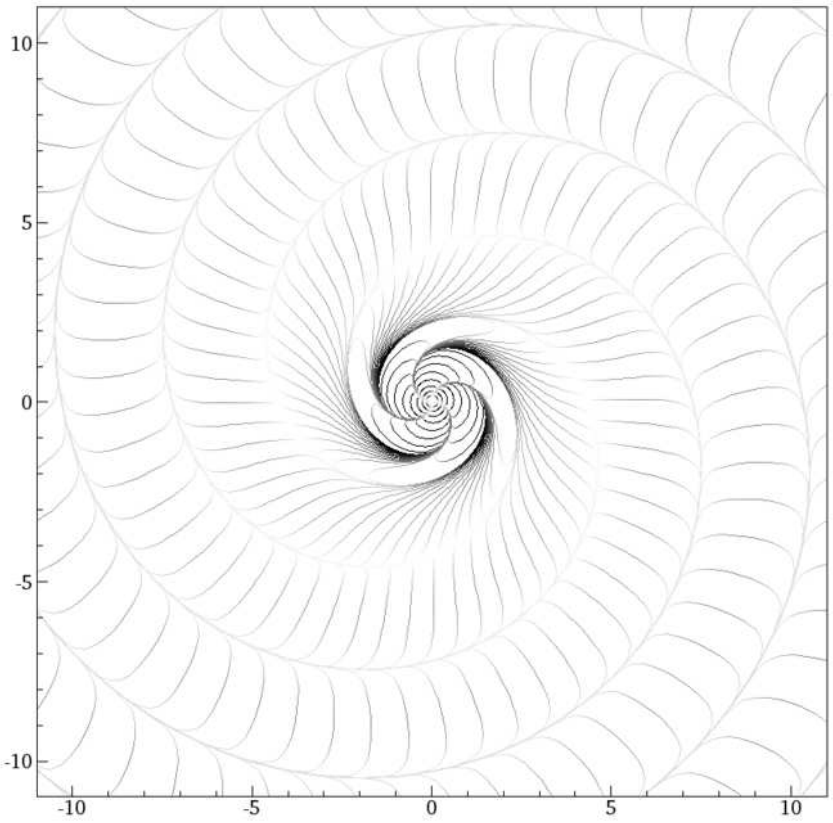

Figure 3.11: Tendex lines in the equatorial plane for a rotating current quadrupole in linearized theory. The curves shown are lines of identically zero tendicity, enforced by symmetry. The lines are shaded by the absolute value of the tendicity of the other two tendex lines that cross the lines shown, but are not tangent to the plane, and have equal and opposite tendicities.

That spiral pattern consists of four vortexes (regions of concentrated vorticity) that spiral outward and backward as the quadrupole rotates. These four regions of alternating positive and negative vorticity are bounded by tight clusters of vortex lines, just outside of which the sign of the dominant vorticity changes.

This same rotating vortex structure occurs in the case of an $l = 2$, $m = 2$, odd-parity (current-quadrupolar) perturbation of a Schwarzschild black hole (Paper II in this series). There the horizon vorticity pattern takes the place of the current quadrupole.

In Fig. 3.11 we indicate the structure of the tendex lines on the equatorial plane. Because the symmetry properties of the system imply different constraints on the tendex field than on the vortex field, some explanation is needed. The plane in which this and the previous two figures are drawn is a plane of reflection symmetry for the problem. However, because the source is a pure current quadrupole, it must be antisymmetric under reflection across this plane (as such a reflection is a parity inversion). The vorticity, which itself has an odd-parity relationship with its source, is symmetric under this reflection, constraining the vortex lines to be either tangent or orthogonal to

the plane, as noted above. The tendicity is antisymmetric under this reflection, so one family of lines can be tangent to the plane, so long as it has zero tendicity, and two other families of lines must cross the plane at equal and opposite inclinations, with equal and opposite tendicities, such that they are exchanged under the reflection. The diagram in Fig. 3.11 shows the single family of tendex lines tangent to the symmetry plane. As these curves have exactly zero tendicity, they are physically relevant only in that they denote the orientation of the other two families of tendex lines, which are not tangent to the plane, but whose projection onto the plane must be orthogonal to the curves shown (because all three curves are mutually orthogonal). The shading of the lines in Fig. 3.11 does not represent the tendicity of the lines drawn (which is identically zero), but rather of the other two tendex lines, which intersect the lines drawn with mutually equal and opposite tendicity. Again, this shading is rescaled by $(kr)^5/[1+(kr)^4]$. Though it is not apparent to the eye, the strength of the tendicity grows only as r^4 near the singular point (origin), rather than r^5 as for the vorticity. As argued early in Sec. 3.6.3, this can be interpreted intuitively as meaning that the vorticity is sourced directly from the current quadrupole, while the tendicity is sourced by induction from the time-varying vortex field.

For a rotating mass quadrupole (e.g. the quadrupole moment of an equal-mass binary), the tendex lines in the plane of reflection symmetry will have precisely the same form as the rotating-current-quadrupole vortex lines of Figs. 3.9 and 3.10; see Sec. 3.6.6.

3.6.4.2 Vortex lines outside the plane of reflection symmetry: Transition from near zone to wave zone

Outside the plane of reflection symmetry and in the wave zone, the extrema of the vorticity show a spiraling pattern that is the same at all polar angles. More specifically, at all polar angles θ, the magnitude of the vorticity, as a function of azimuthal angle ϕ, has four maxima, and the locations of those maxima are the same as in the equator ($\theta = \pi/2$). As in the equator, the maxima at fixed time t spiral around at an angular rate $d\phi_{\rm max}/dr = -\omega$ as one moves outward in radius, and as in the equator, vortex lines collect near these spiraling maxima, and those lines too undergo spiraling behavior.

Figure 3.12 shows the development of this spiraling structure as one moves outward from the near zone (innermost inset) into the wave zone (outer region of figure). This figure focuses on the family of vortex lines that pass orthogonally through the x-y plane of reflection symmetry. After entering the wave zone, the lines with nonnegligible vorticity (the blue and red lines) collect into a somewhat complicated spiral pattern, tangling among themselves a bit as they spiral. The gray lines with very low vorticity, by contrast, point radially outward. An animation of this rotating system can be seen at Ref. [26].

It should be noted Fig. 3.12, and the animation at Ref. [26], represent somewhat incomplete

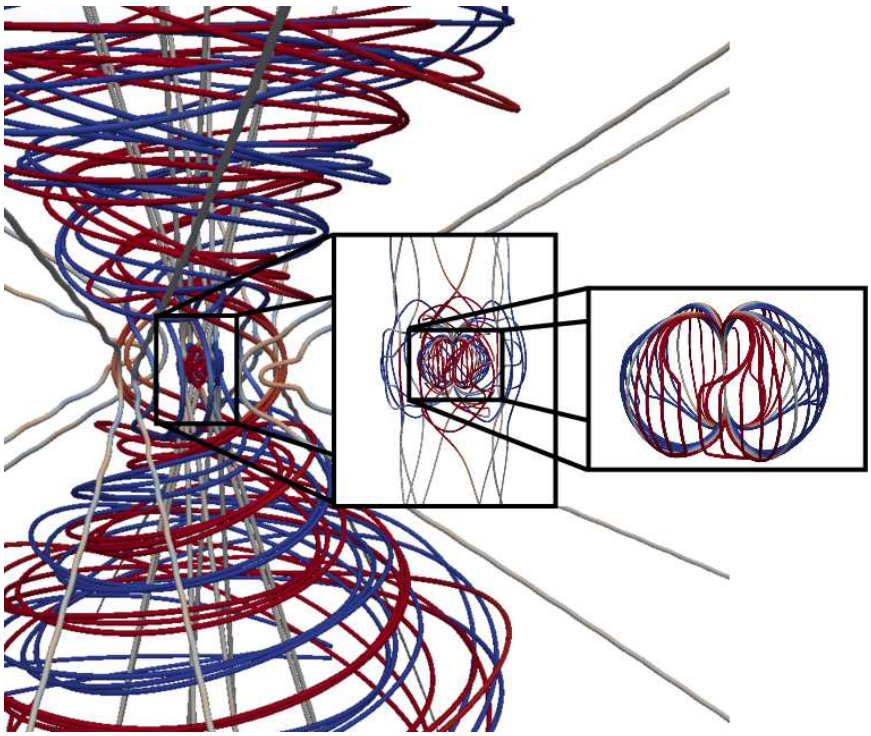

Figure 3.12: For the same rotating current quadrupole as in Figs. 3.9 and 3.10, the family of vortex lines that pass orthogonally through the x-y plane of reflection symmetry, color coded as in Fig. 3.9. In the wave zone, lines with approximately zero vorticity extend away from the source nearly radially, while lines with significant vorticity are dragged into tangled spirals by the rotation of the source. In the left inset, we see the transition between the near and wave zones. Here, lines with nearly zero vorticity escape to infinity as in the wave zone, but those with significant vorticity are drawn toward the source. The right inset delves down into the near zone, where the lines are approximately those of a stationary current quadrupole. This same figure also describes the tendex lines of a rotating mass quadrupole (see the end of Sec. 3.6.6).

descriptions of the structure of these field lines. The red and blue helical spirals shown in Fig. 3.12 do not cross one another. However, at any point in space, there must be three mutually orthogonal vortex lines, with vorticities summing to zero. Since at all points in the wave zone there is a field line of nearly zero vorticity directed in a nearly radial direction, through any point along these spirals of positive or negative vorticity, field lines of opposite vorticity must lie orthogonal to the spiral and to the approximately radial lines. As shown in the following subsection, these lines form closed loops in the far-field region.

3.6.4.3 Vortex lines in the far wave zone

In the far wave zone (strictly speaking at future null infinity), the frame-drag field becomes transverse and traceless, and takes the simple form (3.64). Of its three sets of vortex lines, one is radial (with vanishing vorticity) and the other two are tangent to a sphere of constant radius r (with vorticity of equal and opposite sign). The two sets of vortex lines on the sphere have an interesting angular

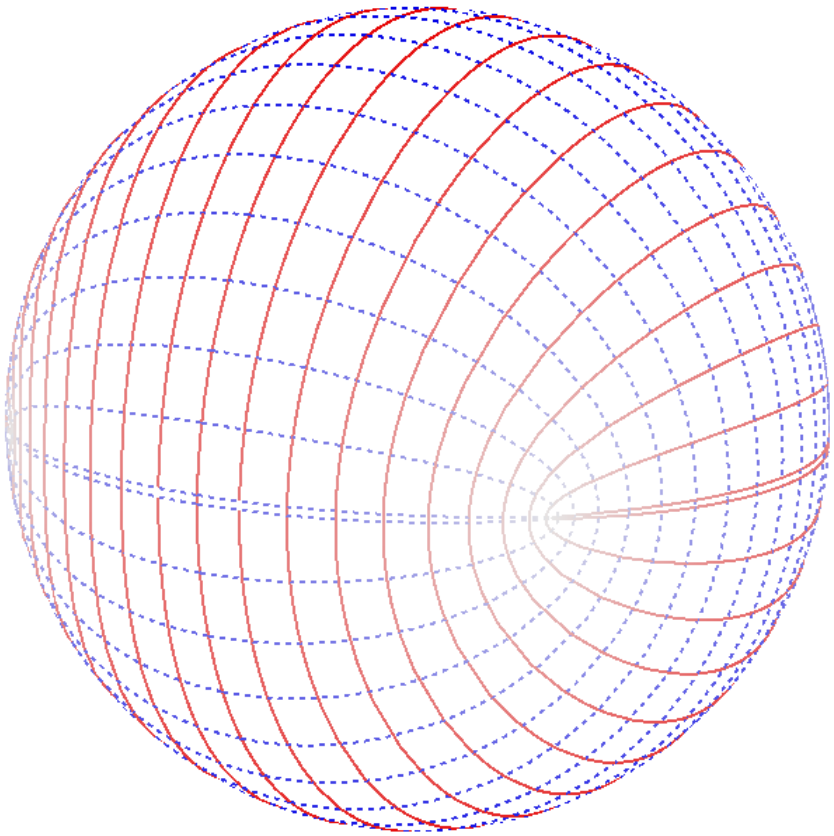

Figure 3.13: (color online). Vortex lines of a time-varying current quadrupole at very large r. The lines are colored by the vorticity scaled by r, to remove the $1/r$ falloff, but the color coding is the same as in previous figures. At very large distances from the source, the lines are transverse and live on a sphere. The third vortex line not shown is radial and has vanishing eigenvalue.

pattern that is shown in Fig. 3.13. The vortex line that lies in the equator alternates between positive and negative vorticity, going to zero at four points (one of which is shown at the front of the sphere). This line is just the limit of the spirals where vortex lines collect in Fig. 3.10 at very large r. [Further discussion of the vortex and tendex lines of radiation at large r is given in Chapter 4 (i.e. [28]), where the dual figure to Fig. 3.13 (tendex lines of a rotating mass quadrupole) is discussed in detail.]

How the vortex lines transition to the transverse pattern of Fig. 3.13 at very large r, from the spiraling pattern of Fig. 3.12 in the inner wave zone, is of considerable interest. We can explore this by examining the frame-drag field at sufficiently large radii that the $1/r$ piece dominates over all other components, and that the $1/r^2$ part of the frame-drag field may be thought of as a perturbation to the leading-order $1/r$ part. In this region, the vortex lines show two kinds of qualitative behavior. Some of the vortex lines continue to form spirals that meander out and do not close, as in Fig. 3.12. There also are lines that form closed loops similar to the leading-order vortex lines of Fig. 3.13. We show both of these types of lines in Fig. 3.14. The red, solid, spiraling lines continue to collect on

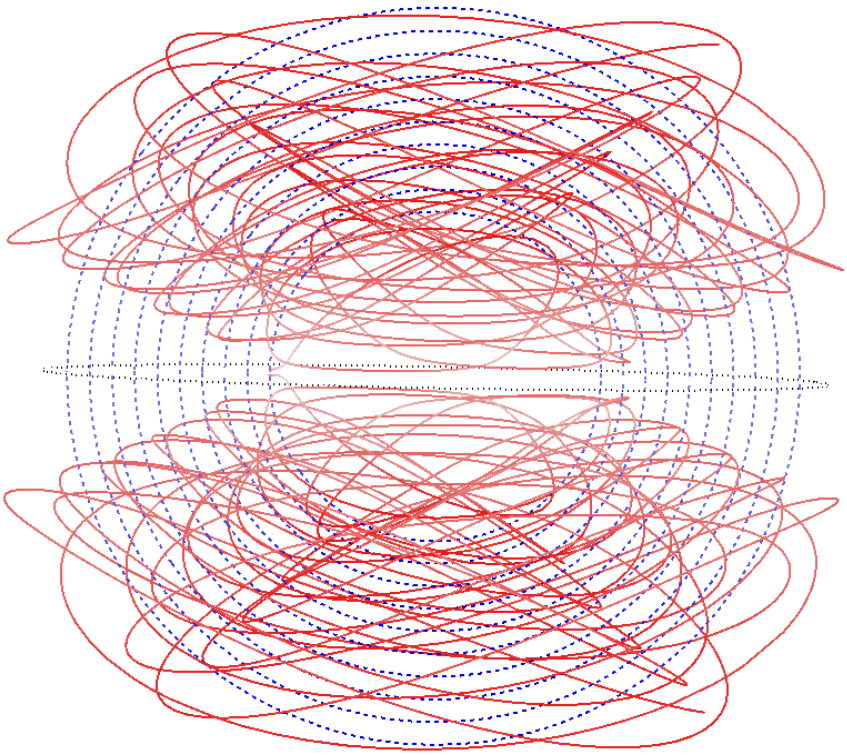

Figure 3.14: (color online). Vortex lines of a rotating current quadrupole at sufficiently large r that the $1/r^2$ part of the frame-drag field may be thought of as a perturbation to the transverse vortex lines of Fig. 3.13. The lines are colored by the vorticity as in that figure. We also show a black dotted circle in the equatorial plane to identify this plane. The red solid lines shown here continue to collect on the maximum-vorticity spiral, but they oscillate much more in polar angle than do the similar lines shown in the near wave zone in Fig. 3.12. The blue dashed lines shown here form closed loops that pass from one positive-vorticity spiral to the next. This family of lines more closely resembles the transverse lines of Fig. 3.13, though in the limit of infinite radius, the spiraling lines will also close to form transverse lines on the sphere. There are also spiraling positive-vorticity (blue) lines and closed-loop, negative-vorticity (red) lines, but to keep the figure from appearing muddled, we do not show them.

the maximum-vorticity spirals in the far wave zone. These lines begin to resemble the transverse lines of Fig. 3.13 more than the spiraling lines in the near wave zone of Fig. 3.12 do, because they rise and fall in polar angle as they wind around the maximum-vorticity spiral. It is only in the limit of infinite radius that these spirals close to form loops. The blue, dashed, closed lines, on the other hand, resemble the closed lines at infinity in Fig. 3.13 much more closely. The lines at finite r do have some subtle differences between the corresponding lines at infinity: At finite radii, each individual line passes from one maximum-vorticity spiral to the other; in doing so the line must slightly increase in radius and rotate in azimuthal angle. At the large radii shown in Fig. 3.14, this effect is very subtle. We finally note that there are also spiraling, positive-vorticity lines and closed, negative-vorticity lines that we do not show to avoid visual clutter.

3.6.5 Oscillating current quadrupole

The vortex lines of an oscillating current quadrupole (this section) have a very different structure from those of the rotating current quadrupole (last section). This should not be surprising, because the two quadrupoles arise from very different physical scenarios, e.g., for the oscillating quadrupole, the ringdown following a head-on collision of black holes with antialigned spins, and for the rotating quadrupole, the ringdown following the inspiral and merger of an extreme-kick black-hole binary. See Papers II and III of this series.

In linearized theory, one can envision an oscillating current quadrupole as produced by two particles, separated by a distance a along the x axis, whose spins, antialigned and pointing in the $\pm y$ direction, oscillate in magnitude as $S\cos\omega t$. The resulting quadrupole moment is [cf. Eq. (3.43)]

$$\mathcal{S}_{xy} = \mathcal{S}_{yx} = Sa\cos\omega t\,. \tag{3.67}$$

The frame-drag and tidal fields, and thence vortex and tendex lines, for this current quadrupole can be computed from Eqs. (3.62) and (3.63).

As for the rotating quadrupole, the x-y plane of reflection symmetry contains two families of vortex lines, and a third family passes orthogonally through that plane. The in-plane vortex lines are depicted in Figs. 3.15 and 3.16 using the same color conventions as for the rotating quadrupole (Figs. 3.9 and 3.10). Figure 3.15 shows the region of the near zone that is difficult to see in Fig. 3.16, an equivalent figure that spans a larger region of the x-y plane. As one can see from the figures, the two families of vortex lines, solid red (negative vorticity) and dashed blue (positive vorticity) have the same pattern, but are rotated by $\pi/2 = 90^{\rm o}$.

The way in which the gravitational waves are generated differs greatly from the rotating current quadrupole of the previous section. In the near zone, the two sets of vortex lines form a static quadrupole pattern (identical to the near-zone rotating quadrupole of Fig. 3.9, but rotated by $\pi/4$ due to the orientation of the spins). In the transition zone, the vortex lines form distorted loops that head away from the origin, along the lines $y = \pm x$, in alternating fashion. As they extend into the wave zone, the lines form two qualitatively different kinds of loops. The majority of the loops reside only in one of the four quadrants of the equatorial plane, but there are also loops that pass through all four quadrants, staying near the regions of maximum vorticity, where lines collect at the gravitational-wave crests. For both types of loops, they maintain the same wavelength, but the wave front becomes wider at larger radii, as they become gravitational waves. The portion of a loop transverse to the radial direction (the direction of propagation) has strong vorticity, as one would expect for a gravitational wave; in the radial portion of the loop, the vorticity is weak. Each cycle of the oscillating quadrupole casts off another set of vortex loops as the near-zone region passes through zero vorticity, and the loops travel outward towards infinity. This illustrates clearly the

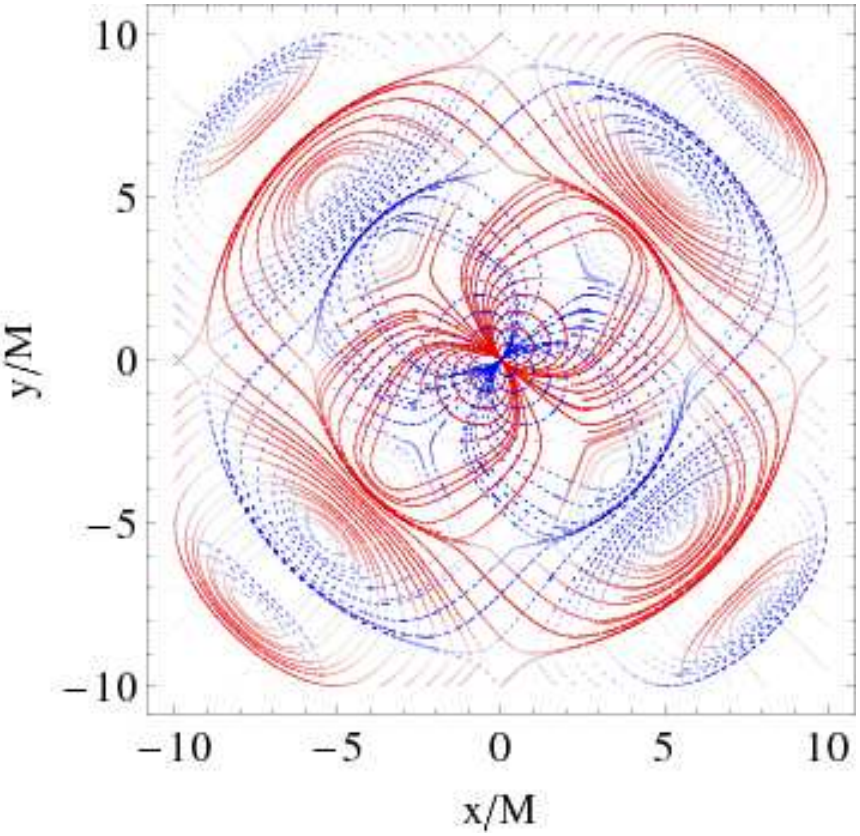

Figure 3.15: (color online). For an oscillating current quadrupole in linearized theory, two families of vortex lines in the plane of reflection symmetry (the x-y plane). The color coding is the same as for the rotating current quadrupole, Fig. 3.9. The vortex lines begin, near the origin, like the static quadrupole pattern of Fig. 3.6. The effects of time retardation cause the pattern to stretch making larger rectangular loops in the transition zone. As time passes and the quadrupole oscillates, these loops detach from the origin and propagate out into the wave zone. This same figure also describes the tendex lines of an oscillating mass quadrupole (see the end of Sec. 3.6.6).

manner in which the near-zone vortex pattern generates gravitational waves in the far zone through its dynamics.

As with the rotating current quadrupole, one can envision the equatorial vortex line of Fig. 3.13 as the limit of the wave fronts of the planar vortex lines in Fig. 3.16 at large distances. It is again of interest to understand how the vortex lines outside the equatorial plane become the remaining vortex lines in Fig. 3.13. To do so, we will make reference to Fig. 3.17, which shows the vortex lines at a distance sufficiently large that the $1/r^2$ portions of the frame-drag field can be thought of as a small perturbation to the transverse vortex lines of Fig. 3.13. We show only the three-dimensional analog of the lines that pass through all four quadrants in the equatorial plane, and do not show the lines that remain in just one octant (analogous to the loops that remain in one quadrant in the equatorial plane) to keep the figure as simple as possible.

Near the poles, these vortex lines have nearly the same structure as the purely transverse lines

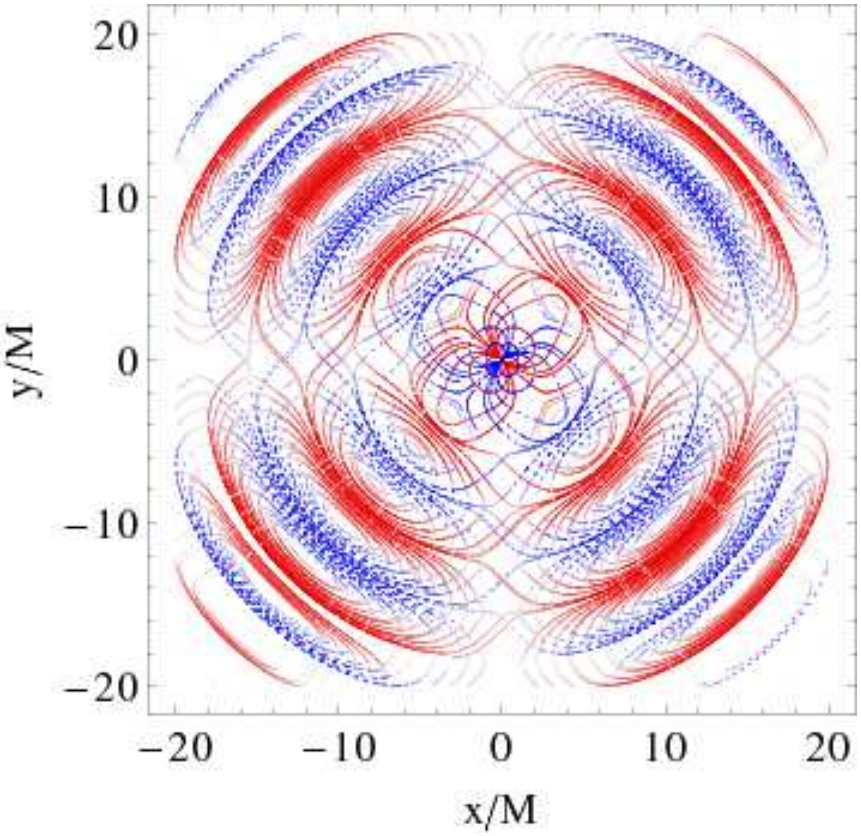

Figure 3.16: (color online). Same as Fig. 3.15, but zoomed out to show the wave zone. Farther from the source, the loops take on a more regular alternating pattern of gravitational waves. The coloring shows that the vorticity is strongest at the fronts and backs of the loops, where the vortex lines are transverse to the direction of propagation. In the regions of the closed loops that extend radially, the field is weak (as one would expect for a transverse gravitational wave).

of Fig. 3.13; it is only near the equator that the lines begin to differ. As the lines approach the equator, they also increase in radius, due to the $1/r^2$ parts of the frame-drag field. In doing so, they pass from one gravitational-wave crest to the next, and the lines sharply turn during their passage between successive crests. The portion of the line on this next crest runs nearly parallel to the equator, until it begins moving slightly inward (again due to the $1/r^2$ parts of the frame-drag field). As it then sharply turns again, it returns to the original crest and begins heading back toward the poles. This sharp turning happens on both sides of the sphere, which causes the lines to form the closed loops that reside in either the northern or the southern hemisphere in Fig. 3.17. Only in the limit that r goes to infinity do the radial perturbations vanish, and the loops in the northern and southern hemisphere connect to form the transverse pattern in Fig. 3.13.

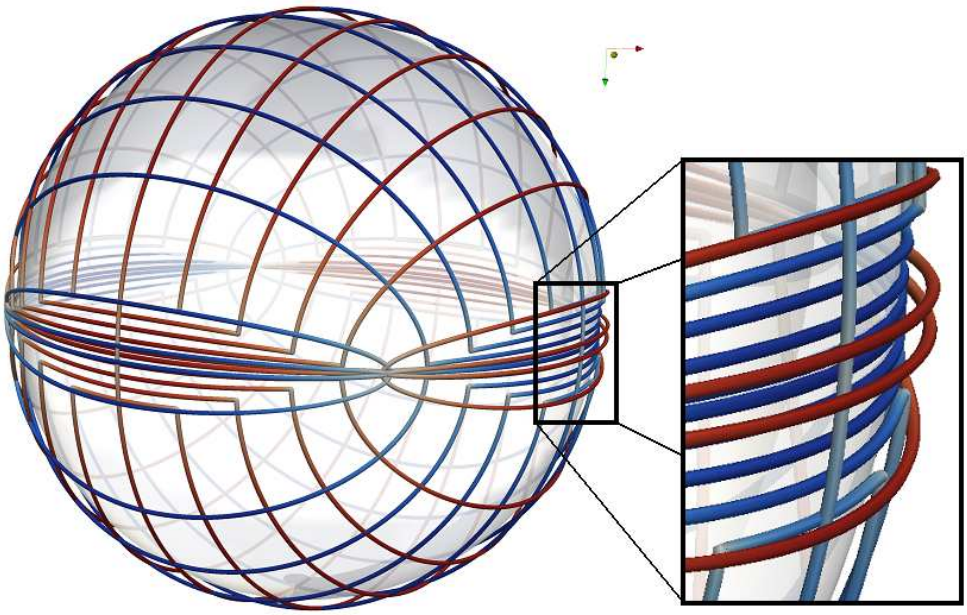

Figure 3.17: (color online). Vortex lines of an oscillating current quadrupole at sufficiently large r that the $1/r^2$ part of the frame-drag field may be thought of as a perturbation to the transverse vortex lines of Fig. 3.13. The lines are colored in the same way as that figure, and the pattern of the lines around the poles is nearly identical to the transverse lines of Fig. 3.13. Near the equator, the $1/r^2$ perturbation causes the lines to bend and form closed loops that reside in either the northern or the southern hemisphere. The blue horizontal lines in the blow-up inset should be compared with dense blue (dashed) bundles in Fig. 3.16, and red lines with the red bundles immediately outside of the blue ones.

3.6.6 Wave generation by a time-varying mass quadrupole

A time-varying mass-quadrupole moment $\mathcal{I}_{pq}(t)$ gives rise to metric perturbations of flat space given by the terms proportional to $\mathcal{I}_{pq}(t-r)/r$ and its derivatives in Eqs. (8.13) of [36]. It is straightforward to calculate that the frame-drag field for these metric perturbations is

$$\mathcal{B}_{ij} = \epsilon_{pq(i} \left[\left(\frac{{}^{(1)}\mathcal{I}_{pk}}{r} \right)_{,j)kq} - \left(\frac{{}^{(3)}\mathcal{I}_{j)p}}{r} \right)_{,q} \right] . \tag{3.68}$$

Notice that this mass-quadrupolar frame-drag field is the same as the current-quadrupolar tidal field (3.63), with the current-quadrupole moment $\mathcal{S}_{pq}$ replaced by $-\frac{3}{4}\mathcal{I}_{pq}$; cf. the duality relations (3.13) and (3.17). Correspondingly, the vortex lines of this mass quadrupole will be the same as the tendex lines of the equivalent current quadrupole.

The mass quadrupole's tidal field can be deduced from its frame-drag field (3.68) by using the

third of the Maxwell-like equations (3.14). The result is

$$\mathcal{E}_{ij} = \frac{1}{2}\left[-\left(\frac{\mathcal{I}_{pq}}{r}\right)_{,pqij} + \epsilon_{ipq}\left(\frac{{}^{(2)}\mathcal{I}_{pm}}{r}\right)_{,qn}\epsilon_{jmn} + 2\left(\frac{{}^{(2)}\mathcal{I}_{p(i}}{r}\right)_{,j)p} - \left(\frac{{}^{(4)}\mathcal{I}_{ij}}{r}\right)\right] . \quad (3.69)$$

Alternatively, this mass-quadrupolar tidal field can be deduced from the current-quadrupolar frame-drag field (3.62) by using the duality relation $\mathcal{S}_{pq} \to +\frac{3}{4}\mathcal{I}_{pq}$ [Eqs. (3.13) and (3.17)].

As a result, the tendex lines of this mass quadrupole will be the same as the vortex lines of the current quadrupole, Figs. 3.9 - 3.10 and 3.12 - 3.16, with the red (solid) lines describing tidal stretching, and the blue (dashed) lines, tidal squeezing.

3.6.7 Slow-motion binary system made of identical, nonspinning point particles

As a final example of a weakly gravitating system, we investigate the tendex lines of a Newtonian, equal-mass binary made of nonspinning point particles in a circular orbit. We assume a separation a between particles that is large compared to their mass M, so the orbital velocity $v = \frac{1}{2}\sqrt{M/a}$ is small compared to the speed of light ("slow-motion binary").

Close to the binary, where retardation effects are negligible, the tidal field is given by the Newtonian expression $\mathcal{E}_{jk} = \Phi_{,jk}$ [Eq. (3.33)], with Φ the binary's Newtonian gravitational potential

$$\Phi = -\frac{M_A}{|\boldsymbol{x} - \boldsymbol{x}_A|} - \frac{M_B}{|\boldsymbol{x} - \boldsymbol{x}_B|} . \quad (3.70)$$

Here $M_A = M_B = M/2$ are the particles' masses with M the total mass, and $\boldsymbol{x}_A$ and $\boldsymbol{x}_B$ are the locations of particles, which we take to be on the x axis, separated by a distance a.

In Fig. 3.18, we show the near-zone tendex lines associated with this potential's tidal field, color coded in the usual way (see the figure's caption). Close to each particle, the tendex lines resemble those of a static, spherically symmetric object. Moving farther from the particle, one can see the effects of the particle's companion, bending and compressing the lines. At radii $r \gtrsim a$, the Newtonian potential and tidal field can be expanded in multipole moments with the monopole and quadrupole dominating. At $r >> a$, the monopole dominates and the tendex lines become those of a single spherical body.

The binary's orbital angular velocity is $\omega = \sqrt{M/a^3}$ (Kepler's formula), and the binary emits gravitational waves with angular frequency 2ω, reduced wavelength $\lambda\!\!\!^{-} = 1/(2\omega) = \frac{1}{2}\sqrt{a^3/M}$, and wavelength $\lambda = 2\pi\lambda\!\!\!^{-}$. As a concrete example, we choose the particles' separation to be $a = 20M$; then $\lambda\!\!\!^{-} = \sqrt{5}a \simeq 2.24a$, and $\lambda = 2\pi\sqrt{5}a \simeq 14a$.

Figure 3.19 shows tendex lines in this binary's orbital plane, focusing on the transition and wave

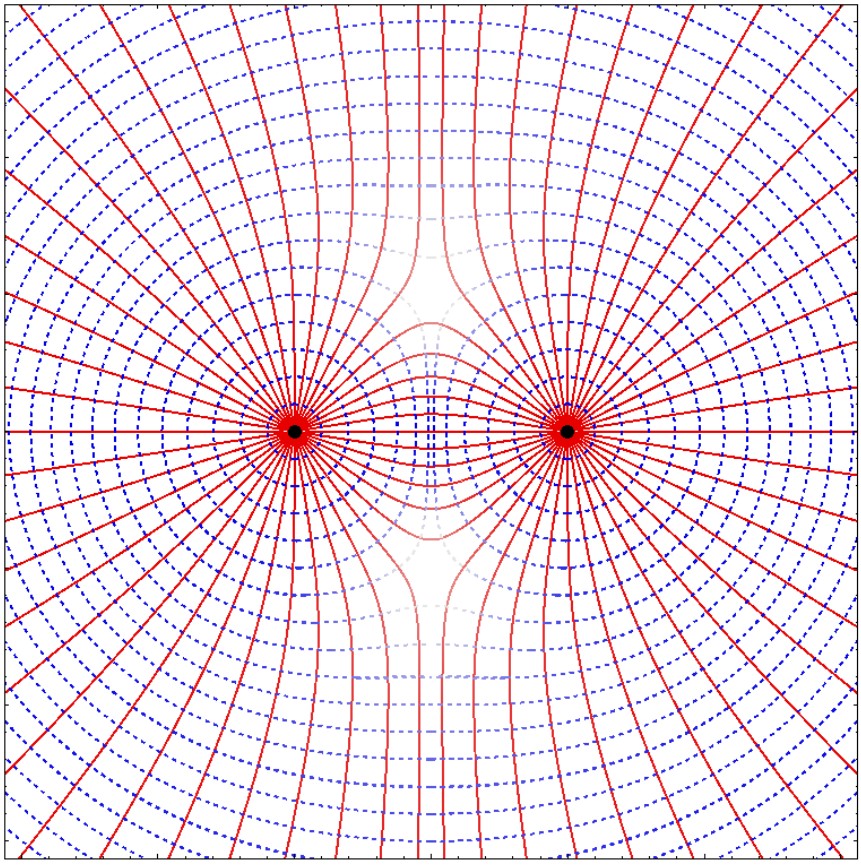

Figure 3.18: (color online). For a weak-gravity binary made of identical nonspinning point particles, in the near zone where retardation is negligible, two families of tendex lines lying in a plane that passes through the two particles (e.g. the orbital plane). The red (solid) curves are lines with negative tendicity, and the blue (dashed) curves have positive tendicity. The color intensity of the curves represents the magnitude of the tendicity, rescaled by $r_A^3 r_B^3/[M^3(r_A^3+r_B^3)]$, where r_A and r_B are the distances to the particles, to remove the tendicity's radial die out. Near each particle, the tendex lines resemble those of an isolated spherical body; as one moves closer to the particle's companion, the lines bend in response to its presence. At radii large compared to the particles' separation a, the binary's monopole moment comes to dominate, and the tendex lines resemble those of a single isolated spherical body.

zones $r \gtrsim \lambda\!\!\!^{-} = 2.24a$ (outside the solid black circle). The shapes and colors of the tendex lines in this figure can be understood in terms of the binary's multipole moments:

In the transition zone and wave zone, $r \gtrsim \lambda\!\!\!^{-}$, the tidal field is the sum of a nonradiative monopolar piece with magnitude $\mathcal{E}_M \simeq M/r^3$, and a quadrupolar piece with magnitude $(1/r)\partial^4\mathcal{I}/\partial t^4 \simeq (2\omega)^4(\frac{1}{4}Ma^2)/r \simeq 4M^3/a^4 r$; higher order moments are negligible. The two moments contribute about equally at radius $r = \frac{1}{2}a^2/M = 10a$ (dotted black circle in the figure). The (nonradiative) monopole moment, with its red radial and blue circular tendex lines, dominates inside this circle. The (radiative) quadrupole moment dominates outside the circle, so there the tendicity is significant (strong red and blue) only when the tendex lines are transverse; strong red alternates, radially, with

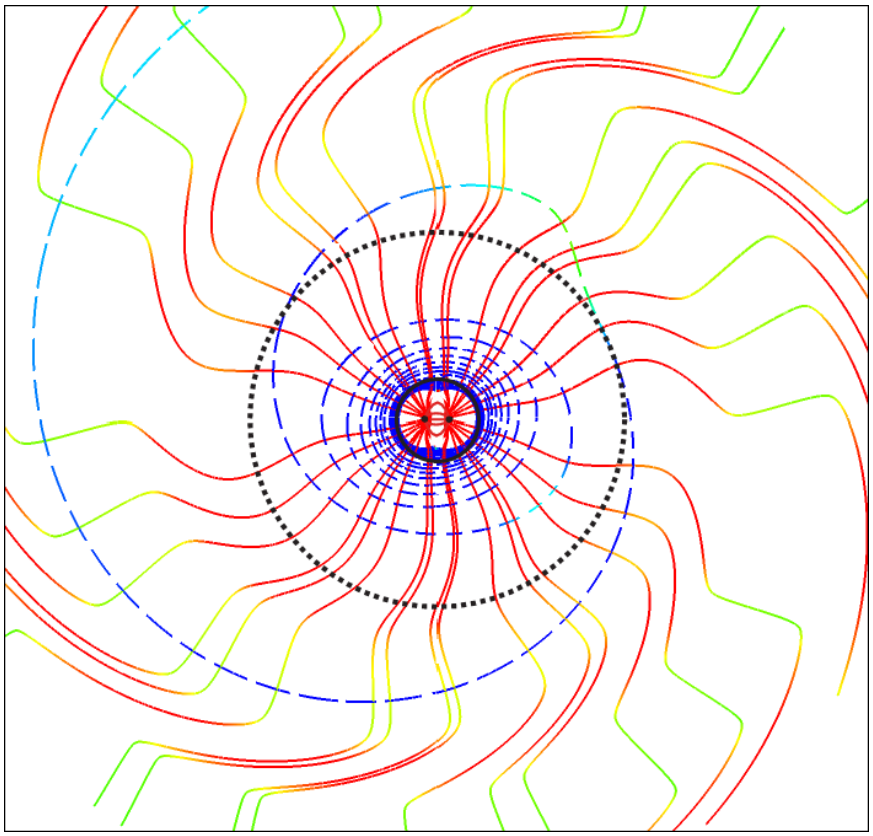

Figure 3.19: (color online). Tendex lines in the orbital plane of the same binary as Fig. 3.18, with separation $a = 20M$ (where M is the total mass), focusing on the transition and wave zones $r \gtrsim \lambda\!\!\!^{-} = 2.24a$. The solid black circle has radius $\lambda\!\!\!^{-}$. The colors are fixed by the tendicity weighted by ωr so as to scale out the $1/r$ falloff in the wave zone (with dark blue strongly positive, dark red strongly negative, and light green near zero). Inside the dotted black curve ($r = \frac{1}{2}a^2/M = 10a$), the binary's (nonradiative) monopole moment dominates, $\mathcal{E} \simeq M/r^3$, and the red (stretching) tendex lines are nearly radial. Outside the dotted black curve, the (radiative) quadrupole moment dominates, $\mathcal{E} \simeq 4M^3/a^4 r$, and the tendex lines are strong (significant tendicity) only where they are approximately transverse to the radial direction.

strong blue as the waves propagate radially. Ultimately, at very large radii (far outside the domain of Fig. 3.19), the quadrupole moment will totally dominate, and the tendex-line pattern will become that of a rotating quadrupole, depicted in Fig. 3.10.

Figure 3.20 shows the tendex lines for this same binary, with the same parameters, in three dimensions, i.e. above and below the equatorial plane. In the inner region, the monopole moment dominates so the red (stretching) tendex lines are nearly radial, and the blue (squeezing) tendex lines are nearly circular, centered on the binary. As one moves outward, the radiative quadrupole moment begins to distort these radial and circular tendex lines, and then at large radii, the now-dominant quadrupole moment drives them into the same spiraling pattern as we have seen in Fig. 3.12 for the tendex lines of a rotating, pure mass quadrupole.

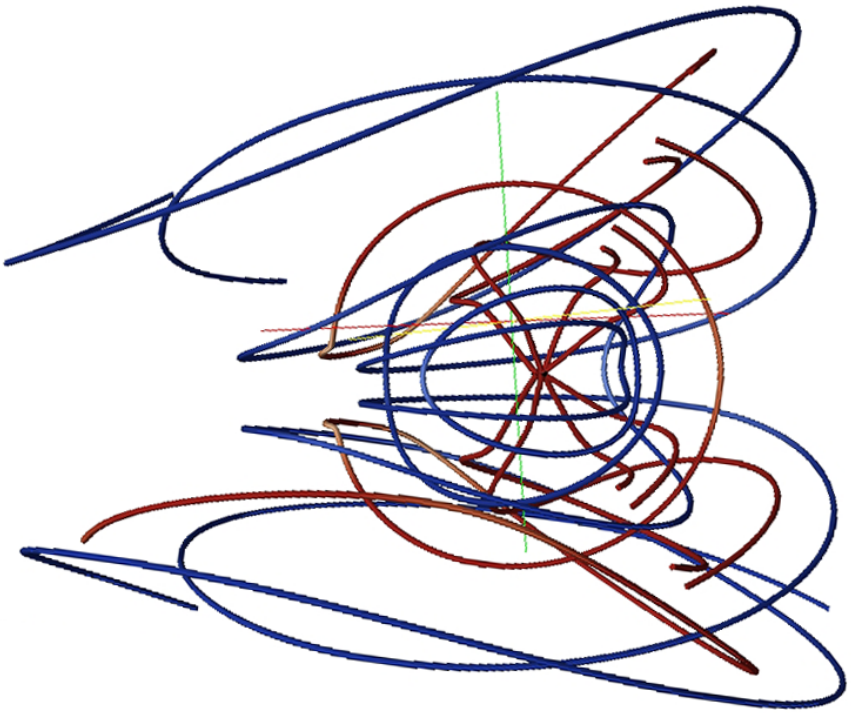

Figure 3.20: (color online). Tendex lines outside the (central, horizontal) orbital plane, for the same binary and parameters as Fig. 3.19. In the inner region, the binary's monopole moment dominates, $\mathcal{E} \simeq M/r^3$, so the red (stretching) tendex lines are nearly radial and the blue (squeezing) tendex lines are nearly circular. At larger radii, the (radiative) quadrupole moment begins to be significant and then dominate, so the tendex lines begin to spiral outward as for the rotating quadrupole of Fig. 3.12.

3.7 Conclusions

In this paper, we have focused on the electric and magnetic parts of the Weyl curvature tensor, $\mathcal{E}_{ij}$ and $\mathcal{B}_{ij}$, and have given them the names *tidal field* and *frame-drag field*, based on their roles in producing tidal gravitational accelerations and differential frame dragging. Being parts of the Riemann tensor, these fields are well defined (though slicing dependent) in strong-gravity situations such as the near zone of colliding black holes. For this reason, and because they embody the full vacuum Riemann tensor and are easily visualized, $\mathcal{E}_{ij}$ and $\mathcal{B}_{ij}$ are powerful tools for exploring the nonlinear dynamics of spacetime curvature (geometrodynamics).

As tools for visualizing $\mathcal{E}_{ij}$ and $\mathcal{B}_{ij}$, we have introduced tendex and vortex lines (the integral curves of the eigenvectors of $\mathcal{E}_{ij}$ and $\mathcal{B}_{ij}$), along with their tendicities and vorticities (the eigenvectors' eigenvalues). The tendex and vortex lines are gravitational analogs of electric and magnetic field lines. Moreover, just as the electromagnetic field tensor is fully determined by its electric and magnetic field lines, together with their field-line densities (which encode the lengths of the electric and magnetic vectors), so the vacuum Riemann curvature tensor is fully determined by its tendex

and vortex lines, together with their colors (which encode the tendicities and vorticities as in Fig. 3.19).

In terms of their transformation properties, the ($\mathcal{E}_{ij}$, $\mathcal{B}_{ij}$) pair is strictly analogous to the pair of electric and magnetic 3-vector fields: they are components of a 4-tensor, divided into two groups in a slicing dependent manner. We are confident that this mild and transparent form of frame dependence will not prevent our tendex and vortex concepts from becoming useful tools for studying geometrodynamics, any more than the frame dependence of electric and magnetic fields and field lines have been impeded these fields from being useful tools for studying electromagnetism in flat or curved spacetime.

Using various examples from linearized gravity, for which analytical formulas are available, we have plotted color-coded tendex and vortex lines, and thereby we have gained insight into the behaviors of the tidal and frame-drag fields. This intuition from weak-gravity examples will be of great value when studying strongly gravitating systems in asymptotically flat spacetimes, e.g. binary black holes. This is because, in the weak-gravity region of spacetime outside such strong-gravity systems, linearized gravity is a good approximation. More specifically:

For stationary, strongly gravitating systems (e.g., stationary black holes and neutron stars), the tendex and vortex lines in their asymptotic, weak-gravity regions will be well approximated by our linearized-theory results in Sec. 3.5 (and, perhaps in some cases, extensions to higher multipoles).

For oscillatory, strongly gravitating systems (e.g., binary black holes and oscillating neutron stars), the wave zones' tendex and vortex lines will be well approximated by those of our examples in Sec. 3.6, and their extensions. Whether the system has strong gravity or weak gravity, its wave-zone field lines are controlled by radiative multipole moments that are tied to the system's near-zone dynamics.

As one moves inward through the weak-gravity wave zone into the near zone and the region of strong gravity, the details of the field lines and the system's dynamics may be quite different for strong-gravity systems than for our weak-gravity examples. Nevertheless it seems likely that in *all* cases, the gravitational waves will be generated by dynamical motions of near-zone tendexes and vortexes (regions of strong tendicity and vorticity). By exploring that near-zone tendex/vortex dynamics, we can gain deep physical insight into nonlinear spacetime curvature. This will be a central theme of Papers II and III in this series.

Whatever may be a source's strong-field dynamics, it will be useful to focus on the imprints that the strong-field dynamics leaves on the tendex/vortex structures in the strong-to-weak-gravity transition region. Those transition-region tendex/vortex imprints will govern spacetime curvature throughout the asymptotic, weak-gravity region, and in particular will govern the radiative multipole moments that control the emitted gravitational waves. Moreover, the imprinted structures in the strong-to-weak-gravity transition region may turn out to have some sort of effective dynamics

that can be captured by simple analytical models and can become a powerful tool for generating approximate gravitational waveforms, e.g. for use in gravitational-wave data analysis.

3.8 Appendix: The Newman-Penrose Formalism

In this appendix we give the connection between the electric and magnetic parts of the Weyl tensor $\boldsymbol{\mathcal{E}}$ and $\boldsymbol{\mathcal{B}}$, and the five Newman-Penrose (NP) curvature scalars [46].

The NP formalism [46] is especially useful for expressing the gravitational-wave content of a dynamical spacetime at asymptotic null infinity. It is also a crucial foundation for the study of black-hole perturbations and for the Petrov classification of vacuum spacetimes, both of which will naturally make contact with the study of vortexes and tendexes. In order to make contact with numerical simulations, we will need to understand the connection between the NP formalism and gravitational waves propagating on a flat background, as discussed in Sec. 3.6.1.

Because we use the opposite metric signature to that of the original Newman-Penrose paper [46] and the widely used Penrose-Rindler book [32], our sign conventions for the NP quantities and for Eqs. (3.73) and (3.78) below differ from theirs. Ours are the same as in [33].

To begin with, we define an orthonormal tetrad $\vec{e}_{\hat{\alpha}} = (\vec{e}_{\hat{0}}, \vec{e}_{\hat{1}}, \vec{e}_{\hat{2}}, \vec{e}_{\hat{3}})$ with time basis vector $\vec{e}_{\hat{0}} = \vec{u}$ orthogonal to our chosen foliation's spacelike hypersurfaces, and with the spatial basis vectors $\vec{e}_{\hat{1}}, \vec{e}_{\hat{2}}, \vec{e}_{\hat{3}}$ lying in those hypersurfaces. We use this tetrad to build a complex null tetrad for use in the NP formalism:

$$\begin{aligned} \vec{l} &= \frac{1}{\sqrt{2}}(\vec{e}_{\hat{0}} + \vec{e}_{\hat{1}})\,, \qquad \vec{n} = \frac{1}{\sqrt{2}}(\vec{e}_{\hat{0}} - \vec{e}_{\hat{1}})\,, \\ \vec{m} &= \frac{1}{\sqrt{2}}(\vec{e}_{\hat{2}} + i\vec{e}_{\hat{3}})\,, \qquad \vec{m}^* = \frac{1}{\sqrt{2}}(\vec{e}_{\hat{2}} - i\vec{e}_{\hat{3}})\,. \end{aligned} \tag{3.71}$$

By projecting the Weyl tensor onto this null basis, we construct the complex Weyl scalars,

$$\Psi_0 = C_{\mu\nu\rho\sigma} l^\mu m^\nu l^\rho m^\sigma\,, \tag{3.72a}$$

$$\Psi_1 = C_{\mu\nu\rho\sigma} l^\mu n^\nu l^\rho m^\sigma\,, \tag{3.72b}$$

$$\Psi_2 = C_{\mu\nu\rho\sigma} l^\mu m^\nu m^{*\rho} n^\sigma\,, \tag{3.72c}$$

$$\Psi_3 = C_{\mu\nu\rho\sigma} l^\mu n^\nu m^{*\rho} n^\sigma\,, \tag{3.72d}$$

$$\Psi_4 = C_{\mu\nu\rho\sigma} n^\mu m^{*\nu} n^\rho m^{*\sigma}\,. \tag{3.72e}$$

Using the null tetrad (3.71) built from our orthonormal tetrad, we can express the spatial orthonormal components of the electric and magnetic parts of the Weyl tensor in terms of the Weyl scalars

as follows:

$$\mathcal{E}_{\hat{a}\hat{b}} + i\mathcal{B}_{\hat{a}\hat{b}} = \begin{bmatrix} 2\Psi_2 & -(\Psi_1 - \Psi_3) & i(\Psi_1 + \Psi_3) \\ * & \frac{\Psi_0 + \Psi_4}{2} - \Psi_2 & -\frac{i}{2}(\Psi_0 - \Psi_4) \\ * & * & -\frac{\Psi_0 + \Psi_4}{2} - \Psi_2 \end{bmatrix}, \tag{3.73}$$

(cf. Eq (3.65) of [33], where the differences are due to differing conventions on both $\boldsymbol{\mathcal{B}}$ and our null tetrad). In Eq. (3.73), the rows and columns are ordered as $\hat{1}, \hat{2}, \hat{3}$ and the entries indicated by $*$ are given by the symmetry of the matrix.

The entries in Eq. (3.73) can be derived in a straightforward manner from the definitions of $\boldsymbol{\mathcal{E}}$ and $\boldsymbol{\mathcal{B}}$, Eqs. (3.2a) and (3.2b), and the definitions of the Weyl scalars, Eqs. (3.72a)-(3.72e). For example, we have

$$\mathcal{E}_{\hat{1}\hat{1}} = R_{\hat{1}\hat{0}\hat{1}\hat{0}} = \frac{1}{2}(R_{\hat{r}l\hat{r}l} + 2R_{\hat{r}l\hat{r}n} + R_{\hat{r}n\hat{r}n}) = \frac{1}{4}(R_{nlnl} - 2R_{nlln} + R_{lnln}) = R_{lnln}\ , \tag{3.74}$$

where we have used the symmetry properties of the Riemann tensor to eliminate and combine many terms. This result is not obviously equal to any of the Weyl scalars, but note that

$$\begin{aligned} R_{lnln} &= -R^{n}{}_{nln} = R^{n}{}_{nnl} = -(R^{l}{}_{nll} + R^{m}{}_{nml} + R^{m^*}{}_{nm^*l}) \\ &= -R_{m^*nml} - R_{mnm^*l} = R_{lmm^*n} + R_{lm^*mn} \\ &= \Psi_2 + \Psi_2^*\,, \end{aligned} \tag{3.75}$$

where we have used the fact that in the null tetrad basis $\{\vec{l}, \vec{n}, \vec{m}, \vec{m}^*\}$, indices are raised and lowered with the metric components

$$g_{\alpha\beta} = g^{\alpha\beta} = \begin{pmatrix} 0 & -1 & 0 & 0 \\ -1 & 0 & 0 & 0 \\ 0 & 0 & 0 & 1 \\ 0 & 0 & 1 & 0 \end{pmatrix}, \tag{3.76}$$

and the fact that the Ricci tensor vanishes in vacuum spacetimes. Similar manipulations give

$$B_{\hat{1}\hat{1}} = \frac{1}{2}\epsilon_{\hat{1}}{}^{\hat{p}\hat{q}} R_{\hat{p}\hat{q}\hat{1}\hat{0}} = R_{\hat{2}\hat{3}\hat{1}\hat{0}} = -iR_{m^*mln} = i(R_{lmnm^*} + R_{lm^*mn}) = i(-\Psi_2 + \Psi_2^*)\,, \tag{3.77}$$

so we see that $\mathcal{E}_{\hat{1}\hat{1}} + i\mathcal{B}_{\hat{1}\hat{1}} = 2\Psi_2$. Similar computations give all of the entries of Eq. (3.73).

We will often have reason to consider the "horizon tendicity" and "horizon vorticity." These are the values of $\boldsymbol{\mathcal{E}}$ and $\boldsymbol{\mathcal{B}}$ projected normal to the 2-dimensional event horizon of a spacetime containing a black hole, evaluated at the horizon. If the inward normal to the horizon is denoted $\boldsymbol{N}$ and we

choose the vector $\boldsymbol{e}_{\hat{1}}$ such that it coincides with $-\boldsymbol{N}$ at the horizon, then we immediately have the useful result

$$\Psi_2 = \frac{1}{2}(\mathcal{E}_{NN} + i\mathcal{B}_{NN}) = \frac{1}{2}(\mathcal{E}_{ij} + i\mathcal{B}_{ij})N^i N^j \,, \tag{3.78}$$

which we will use in our studies of analytic and numerical spacetimes containing horizons (papers II and III in this series).

Bibliography

[1] R. Owen, J. Brink, Y. Chen, J. D. Kaplan, G. Lovelace, K. D. Matthews, D. A. Nichols, M. A. Scheel, F. Zhang, A. Zimmerman, et al., Phys. Rev. Lett. **106**, 151101 (2011).

[2] J. A. Wheeler, *Geometrodynamics* (Academic Press, New York, 1963).

[3] J.A. Wheeler, in *Relativity, Groups and Topology (Les Houches Summer School, 1963)*, edited by B. DeWitt and C. DeWitt (Gordon and Breach, New York, 1964), pp. 325–520.

[4] C. W. Misner, Phys. Rev. **118**, 1110 (1960).

[5] D. R. Brill and R. W. Lindquist, Phys. Rev. **131**, 471 (1963).

[6] S. Hahn and R. Lindquist, Ann. Phys. (NY) **29**, 304 (1964).

[7] J. Weber, Phys. Rev. **117**, 306 (1960).

[8] J. Centrella, J. G. Baker, B. J. Kelly, and J. R. van Meter, Rev. Mod. Phys. **82**, 3069 (2010).

[9] B. C. Barish and R. Weiss, Phys. Today **52**, 44 (1999), ISSN 00319228, URL `http://dx.doi.org/10.1063/1.882861`.

[10] D. Sigg and the LIGO Scientific Collaboration, Class. Quantum Grav. **25**, 114041 (2008), ISSN 0264-9381, 1361-6382, URL `http://iopscience.iop.org/0264-9381/25/11/114041`.

[11] F. Acernese, M. Alshourbagy, P. Amico, F. Antonucci, S. Aoudia, et al., Class.Quant.Grav. **25**, 184001 (2008).

[12] K. Kuroda and the LCGT Collaboration, Class. Quantum Grav. **27**, 084004 (2010), ISSN 0264-9381, URL `http://iopscience.iop.org/0264-9381/27/8/084004`.

[13] G. M. Harry (for the LIGO Scientific Collaboration), Class. Quantum Grav. **27**, 084006 (2010).

[14] C. W. Misner, K. S. Thorne, and J. A. Wheeler, *Gravitation* (Freeman, New York, New York, 1973).

[15] L. Smarr, Phys. Rev. D **7**, 289 (1973).

[16] D. Marolf, Gen. Rel. Grav. **31**, 919 (1999).

[17] U. Jacob and T. Piran, Class. Quantum Grav. **23**, 4035 (2006).

[18] J. D. Romano and R. H. Price, Class. Quantum Grav. **12**, 875 (1995).

[19] M. Bondarescu, M. Alcubierre, and E. Seidel, Class. Quantum Grav. **19**, 375 (2002).

[20] H. Chan, Class. Quantum Grav. **23**, 225 (2006).

[21] L. Rezzolla, R. P. Macedo, and J. L. Jaramillo, Phys. Rev. Lett. **104**, 221101 (2010), `arxiv:1003.0873`.

[22] J. L. Jaramillo, R. P. Macedo, P. Moesta, and L. Rezzolla (2011), `arxiv:1108.0060`.

[23] J. L. Jaramillo, R. P. Macedo, P. Moesta, and L. Rezzolla (2011), `arxiv:1108.0061`.

[24] J. L. Jaramillo (2011), `arxiv:1108.2408`.

[25] J. W. Belcher and S. Olbert, Am. J. Phys. **71**, 220 (2003).

[26] `http://www.black-holes.org/curQuadVortex.html`.

[27] `http://www.black-holes.org/antiAliPoints.html`.

[28] A. Zimmerman, D. A. Nichols, and F. Zhang, Phys. Rev. D **84**, 044037 (2011).

[29] F. B. Estabrook and H. D. Wahlquist, Journal of Mathematical Physics **5**, 1629 (1964).

[30] C. Schmid, Phys. Rev. D **79**, 064007 (2009).

[31] R. Maartens and B. A. Bassett, Class. Quantum Grav. **15**, 705 (1998).

[32] R. Penrose and W. Rindler, *Spinors and Space-time, Volume 1* (Cambridge University Press, Cambridge, 1992).

[33] H. Stephani, D. Kramer, M. MacCallum, C. Hoenselaers, and E. Herlt, *Exact solutions of Einstein's field equations* (Cambridge University Press, Cambridge, UK, 2003).

[34] H. Friedrich, Class. Quantum Grav. **13**, 1451 (1996).

[35] A. Anderson, Y. Choquet-Bruhat, and J. W. York, Jr., Topol. Meth. Nonlin. Anal. **10**, 353 (1997).

[36] K. S. Thorne, Rev. Mod. Phys. **52**, 299 (1980).

[37] R. D. Blandford and K. S. Thorne, *Applications of Classical Physics* (California Institute of Technology, 2008), URL `http://www.pma.caltech.edu/Courses/ph136/yr2011/`.

[38] J. D. Kaplan, D. A. Nichols, and K. S. Thorne, Phys. Rev. D **80**, 124014 (2009).

[39] R. L. Forward, Proc. IRE **49**, 892 (1961).

[40] D. Keppel, D. A. Nichols, Y. Chen, and K. S. Thorne, Phys. Rev. D **80**, 124015 (2009), arXiv:0902.4077.

[41] G. Lovelace, Y. Chen, M. Cohen, J. D. Kaplan, D. Keppel, K. D. Matthews, D. A. Nichols, M. A. Scheel, and U. Sperhake, Phys. Rev. D **82**, 064031 (2010), arXiv:0907.0869.

[42] K. S. Thorne, R. H. Price, and D. A. MacDonald, *Black Holes: The Membrane Paradigm* (Yale University Press, New Haven and London, 1986).

[43] D. R. Fiske, J. G. Baker, J. R. van Meter, D.-I. Choi, and J. M. Centrella, Phys. Rev. D **71**, 104036 (2005).

[44] R. Penrose, Ann. Hum. Genet., Lond. **42**, 435 (1979).

[45] http://www.black-holes.org/SpEC.html.

[46] E. Newman and R. Penrose, Journal of Mathematical Physics **3**, 566 (1962).

Chapter 4

Frame-Drag Vortexes and Tidal Tendexes II. Classifying the Isolated Zeros of Asymptotic Gravitational Radiation

Originally published as
Aaron Zimmerman, David A. Nichols, Fan Zhang
Phys. Rev. D 84, 044037 (2011)

4.1 Introduction

A recent study [1] (i.e. Chapter 1.2) proposed a method for visualizing spacetime curvature that is well-suited for studying spacetimes evolved from initial data using numerical-relativity codes. The method first projects the Riemann curvature tensor $R_{\mu\nu\sigma\rho}$ into a spatial slice, thereby splitting it into two symmetric, trace-free spatial tensors, $\boldsymbol{\mathcal{E}}$ and $\boldsymbol{\mathcal{B}}$ (see e.g. [2] and the references therein). These tensors are the spacetime-curvature analogs of the electric and magnetic fields in Maxwell's theory. The electric tensor $\boldsymbol{\mathcal{E}}$ is familiar; it is the tidal field in the Newtonian limit. The frame-drag field $\boldsymbol{\mathcal{B}}$ (the magnetic curvature tensor) describes the differential frame dragging of spacetime. The eigenvectors of the tidal field provide the preferred directions of strain at a point in spacetime, and its eigenvalues give the magnitude of the strain along those axes. Similarly, the eigenvectors of the frame-drag field give preferred directions of differential precession of gyroscopes, and their eigenvalues give the magnitude of this precession [1, 3, 4].

The study in Chapter 1.2 (i.e. [1]) then proposed using the integral curves of these eigenvectors as a way to visualize the curvature of spacetime. Three orthogonal curves associated with $\boldsymbol{\mathcal{E}}$, called tendex lines, pass through each point in spacetime. Along each tendex line there is a corresponding eigenvalue, which is called the tendicity of the line. For the tensor $\boldsymbol{\mathcal{B}}$, there is a second set of three orthogonal curves, the vortex lines, and their corresponding eigenvalues, the vorticities. These six curves are analogous to the field lines of electromagnetism, and the six eigenvalues to the electric and magnetic field strengths. The tendex and vortex lines, with their corresponding vorticities and tendicities, represent very different physical phenomena from field lines of electromagnetism; they allow one to visualize the aspects of spacetime curvature associated with tidal stretching and differential frame-dragging. In addition, each set of curves satisfies the constraint that its eigenvalues sum to zero at every point, since $\boldsymbol{\mathcal{E}}$ and $\boldsymbol{\mathcal{B}}$ are trace-free.

Wherever the eigenvector fields are well-behaved, the tendex and vortex lines form extended, continuous fields of lines in a spatial slice. At points where two (or more) eigenvectors have the same eigenvalue, the eigenvectors are said to be degenerate. Any linear combination of the degenerate eigenvectors at these points is still an eigenvector with the same eigenvalue; therefore, the span of these eigenvectors forms a degenerate subspace. Singular features can appear at points of degeneracy, where many lines intersect, terminate, or turn discontinuously. The topology of unoriented fields of lines and their singular points has been studied both in the context of general relativity and elsewhere. For example, Delmarcelle and Hesselink [5] studied the theory of these systems and applied them to real, symmetric two-dimensional tensors. In the context of relativity, Penrose and Rindler [6] examined the topology of unoriented lines, or ridge systems, to characterize the principle null directions about single points in spacetime. Finally, Penrose [7] also applied the study of ridge systems to human handprint and fingerprint patterns.

In this paper, we focus on the vortex and tendex lines and their singular points far from an isolated, radiating source. In Sec. 4.2, we show that two of the vortex and tendex lines lie on a sphere (the third, therefore, is normal to the sphere), and that the vortex and tendex lines have the same eigenvalues. Moreover, the two eigenvalues on the sphere have opposite sign, and the eigenvalue normal to the sphere has zero eigenvalue. This implies that the only singular points in the lines occur when all eigenvalues vanish (i.e. when the curvature is exactly zero at the point, and all three eigenvectors are degenerate).

In Sec. 4.3 we employ a version of the Poincaré-Hopf theorem for fields of integral curves to argue that there must be singular points where the curvature vanishes. Penrose, in a 1965 paper [8], made a similar observation. There, he notes in passing that gravitational radiation must vanish for topological reasons, although he does not discuss the point any further. Here we show that the topological classification of singular points of ridge systems can be applied to the tendex and vortex lines of gravitational radiation. This allows us to make a topological classification of the zeros of

the radiation field.

In Sec. 4.4, we visualize the tendex and vortex lines of radiating systems in linearized gravity. We begin with radiation from a rotating mass-quadrupole moment, the dominant mode in most astrophysical gravitational radiation. We then move to an idealized model of the "extreme-kick" configuration (an equal-mass binary-black-hole merger with spins antialigned in the orbital plane [9]). As we vary the magnitude of the spins in the extreme-kick configuration, we can relate the positions of the singular points of the tendex and vortex patterns to the degree of beaming of gravitational waves. We also visualize the radiation fields of individual higher-order multipole moments, which serve, primarily, as examples of patterns with a large number of singularities. Astrophysically, these higher multipoles would always be accompanied by a dominant quadrupole moment; we also, therefore, look at a superposition of multipoles. Since the tendex lines depend nonlinearly upon the multipoles, it is not apparent, *a priori*, how greatly small higher multipoles will change the leading-order quadrupole pattern. Nevertheless, we see that for an equal-mass black-hole binary, higher multipoles make only small changes to the tendex line patterns. Finally, we discuss our results in Sec. 4.5.

Throughout this paper we use Greek letters for spacetime coordinates in a coordinate basis and Latin letters from the beginning of the alphabet for spatial indices in an orthonormal basis. We use a spacetime signature $(-+++)$ and a corresponding normalization condition for our tetrad. We will use geometric units, in which $G = c = 1$.

We will also specialize to vacuum spacetimes, where the Riemann tensor is equal to the Weyl tensor $C_{\mu\nu\rho\sigma}$. To specify our slicing and to compute $\boldsymbol{\mathcal{E}}$ and $\boldsymbol{\mathcal{B}}$, we use a hypersurface-orthogonal, timelike unit vector, $\boldsymbol{e}_0$, which we choose to be part of an orthonormal tetrad, $(\boldsymbol{e}_0, \boldsymbol{e}_1, \boldsymbol{e}_2, \boldsymbol{e}_3)$. We then perform a $3+1$ split of the Weyl tensor by projecting it and its Hodge dual ${}^*C_{\mu\nu\rho\sigma} = \frac{1}{2}\epsilon_{\mu\nu}{}^{\alpha\beta}C_{\alpha\beta\sigma\rho}$ into this basis,

$$\mathcal{E}_{ab} = C_{a\mu b\nu} e_0{}^{\mu} e_0{}^{\nu} , \tag{4.1}$$

$$\mathcal{B}_{ab} = -{}^*C_{a\mu b\nu} e_0{}^{\mu} e_0{}^{\nu} . \tag{4.2}$$

Here our convention for the alternating tensor is that $\epsilon_{0123} = +1$ in an orthonormal basis. Note that, while the sign convention on $\boldsymbol{\mathcal{B}}$ is not standard (see e.g. [10]), it has the advantage that $\boldsymbol{\mathcal{E}}$ and $\boldsymbol{\mathcal{B}}$ obey constraints and evolution equations under the $3+1$ split of spacetime that are directly analogous to Maxwell's equations in electromagnetism [2, 4]. After the projection, we will solve the eigenvalue problem for the tensors $\boldsymbol{\mathcal{E}}$ and $\boldsymbol{\mathcal{B}}$ in the orthonormal basis,

$$\mathcal{E}_{ab} v^b = \lambda v_a , \tag{4.3}$$

and we will then find their streamlines in a coordinate basis via the differential equation relating a curve to its tangent vector,

$$\frac{dx^\mu}{ds} = v^a {e_a}^\mu \,. \tag{4.4}$$

Here s is a parameter along the streamlines.

4.2 Gravitational Waves Near Null Infinity

Consider a vacuum, asymptotically flat spacetime that contains gravitational radiation from an isolated source. We are specifically interested in the transverse modes of radiation on a large sphere S near future null infinity. To describe these gravitational waves, we use an orthonormal tetrad $(\boldsymbol{e}_0, \boldsymbol{e}_1, \boldsymbol{e}_2, \boldsymbol{e}_3)$, with $\boldsymbol{e}_0$ timelike and $\boldsymbol{e}_2, \boldsymbol{e}_3$ tangent to the sphere, and we associate with this tetrad a corresponding complex null tetrad,

$$\begin{aligned} \boldsymbol{l} &= \frac{1}{\sqrt{2}}(\boldsymbol{e}_0 + \boldsymbol{e}_1)\,, & \boldsymbol{n} &= \frac{1}{\sqrt{2}}(\boldsymbol{e}_0 - \boldsymbol{e}_1)\,, \\ \boldsymbol{m} &= \frac{1}{\sqrt{2}}(\boldsymbol{e}_2 + i\boldsymbol{e}_3)\,, & \bar{\boldsymbol{m}} &= \frac{1}{\sqrt{2}}(\boldsymbol{e}_2 - i\boldsymbol{e}_3)\,. \end{aligned} \tag{4.5}$$

Here, $\boldsymbol{l}$ is tangent to outgoing null rays that pass through S and strike a sphere at null infinity. We enforce that the null tetrad is parallelly propagated along these rays, and that it is normalized such that $l_\mu n^\mu = -m_\mu \bar{m}^\mu = -1$ (all other inner products of the null tetrad vanish). With these rays, we can associate Bondi-type coordinates (see e.g. [11, 12]) on a sphere at future null infinity with those on S. The timelike vector $\boldsymbol{e}_0$ specifies our spatial slicing in this asymptotic region. When the orthonormal and null tetrads are chosen as in Eq. (4.5), $\boldsymbol{\mathcal{E}}$ and $\boldsymbol{\mathcal{B}}$ are related to the complex Weyl scalars [13]. With the Newman-Penrose conventions appropriate to our metric signature (see, e.g., [10]), and our convention in Eq. (4.2), one can show that

$$\mathcal{E}_{ab} + i\mathcal{B}_{ab} = \begin{pmatrix} 2\Psi_2 & \Psi_3 - \Psi_1 & i(\Psi_1 + \Psi_3) \\ * & \frac{\Psi_0+\Psi_4}{2} - \Psi_2 & \frac{i(\Psi_4-\Psi_0)}{2} \\ * & * & -\frac{\Psi_0+\Psi_4}{2} - \Psi_2 \end{pmatrix}, \tag{4.6}$$

where $*$ indicates entries that can be inferred from the symmetry of $\boldsymbol{\mathcal{E}}$ and $\boldsymbol{\mathcal{B}}$.

In an asymptotically flat spacetime, the peeling theorem [13] ensures that $\Psi_4 \sim r^{-1}$ (with r an affine parameter along the rays), and that the remaining Weyl scalars fall off with progressively higher powers of r, $\Psi_3 \sim r^{-2}, \Psi_2 \sim r^{-3}, \Psi_1 \sim r^{-4}$, and $\Psi_0 \sim r^{-5}$. Asymptotically, only Ψ_4

contributes to $\boldsymbol{\mathcal{E}}$ and $\boldsymbol{\mathcal{B}}$,

$$\mathcal{E}_{ab} + i\mathcal{B}_{ab} = \frac{1}{2}\begin{pmatrix} 0 & 0 & 0 \\ 0 & \Psi_4 & i\Psi_4 \\ 0 & i\Psi_4 & -\Psi_4 \end{pmatrix} . \tag{4.7}$$

We see immediately that one eigenvector of both $\boldsymbol{\mathcal{E}}$ and $\boldsymbol{\mathcal{B}}$ is the "radial" basis vector $\boldsymbol{e}_1$, with vanishing eigenvalue. The remaining 2×2 block is transverse and traceless, and the eigenvectors in this subspace have a simple analytical solution. The eigenvalues are $\lambda_\pm = \pm|\Psi_4|/2$ for both tensors, and the eigenvectors of $\boldsymbol{\mathcal{E}}$ have the explicit form

$$\boldsymbol{v}_\pm = \frac{-\mathcal{E}_{23}\boldsymbol{e}_2 + (\mathcal{E}_{22} - \lambda_\pm)\boldsymbol{e}_3}{\sqrt{\mathcal{E}_{23}^2 + (\mathcal{E}_{22} - \lambda_\pm)^2}} = \frac{\mathrm{Im}\Psi_4\boldsymbol{e}_2 + (\mathrm{Re}\Psi_4 \mp |\Psi_4|)\boldsymbol{e}_3}{\sqrt{(\mathrm{Im}\Psi_4)^2 + (\mathrm{Re}\Psi_4 \mp |\Psi_4|)^2}} . \tag{4.8}$$

The eigenvectors of $\boldsymbol{\mathcal{B}}$ are locally rotated by $\pm\pi/4$ with respect to those of $\boldsymbol{\mathcal{E}}$ [4]. As a result, although the global geometric pattern of vortex and tendex lines may differ, their local pattern and their topological properties on S will be identical. Moreover, when the eigenvalues of $\boldsymbol{\mathcal{E}}$ (the tendicity of the corresponding tendex line) vanish, so must those of $\boldsymbol{\mathcal{B}}$ (the vorticity of the vortex lines). In arguing that the radiation must vanish, we can, therefore, focus on the tendex lines on S without loss of generality. Physically, however, both the vortex and the tendex lines are of interest. Similarly, since the two sets of tendex lines on S have equal and opposite eigenvalue and are orthogonal, we need only consider the properties of a single field of unoriented lines on S in order to describe the topological properties of all four tendex and vortex lines on the sphere. Note that thus far we leave the coordinates (x^2, x^3) on S unspecified. We will assume that these coordinates are everywhere nonsingular, for instance by being constructed from two smooth, overlapping charts on S.

4.3 The Topology of Tendex Patterns Near Null Infinity

Before investigating the properties of the tendex lines on S, we first recall a few related properties of vector fields on a 2-sphere. A well-known result regarding vector fields on a sphere is the "hairy-ball theorem." This result states, colloquially, that if a sphere is covered with hairs at each point, the hair cannot be combed down everywhere without producing cowlicks or bald spots. The hairy-ball theorem is a specific illustration of the Poincaré-Hopf theorem, applied to a 2-sphere. On a 2-sphere, this theorem states that the sum of the indices of the zeros of a vector field must equal the Euler characteristic, χ, of the sphere, specifically $\chi = 2$. The index of a zero of a vector field (also called a singular point) can be found intuitively by drawing a small circle around the point and traveling once around the circle counterclockwise. The number of times the local vector field rotates counterclockwise through an angle of 2π during this transit is the index. More precisely, we can form a map from the points near a zero of the vector field to the unit circle. To do this consider

a closed, oriented curve in a neighborhood of the zero, and map each point on the curve to the unit circle by associating the direction of the vector field at that point with a particular point on the unit circle. The index is the degree of the map (the number of times the map covers the circle in a positive sense). For the zero of a vector field, the index is a positive or negative integer, because we must return to the starting point on the unit circle as we finish our circuit of the curve around the zero.

The concept of an index and the formal statement of the Poincaré-Hopf theorem generalizes naturally to ridge systems, fields of unoriented lines such as the tendex lines on S. For ridge systems on the sphere, the index of a singular point can be a half-integer [5]. Intuitively, this can occur because fields of lines do not have orientation. As one traverses counterclockwise about a small circle around a singular point, the local pattern of lines can rotate through an angle of $\pm\pi$ during the transit. We illustrate the two fundamental types of singularity in Fig. 4.1, which, following [6], we call loops for index $i = 1/2$ and triradii for $i = -1/2$. One can argue that the Poincaré-Hopf Theorem holds for ridge systems, by noting that we can create a singular point with integer index by bringing two half-index singularities together (see Fig. 4.2 for a schematic of the creation of a singularity of index $i = 1$ from two loop singularities). Ridge patterns near singularities with integer index $i = \pm 1$ can be assigned orientations consistently; they must, therefore, have the same topological properties as streamlines of vector fields (which, in turn, have the same properties as the underlying vector fields themselves). By arguing that one can always deform a ridge system so that its singular points have integer index, one can see that the sum of the indices of a ridge system on a sphere must equal the Euler characteristic of the surface, $\chi = 2$ (see [5] and the references therein for a more formal statement and proof of this theorem). In Fig. 4.3 we show several other ridge singularities with integer index for completeness. In the top row, we show three patterns with index $i = 1$, and in the bottom left, we sketch a saddle type singularity with index $i = -1$. All of these patterns can be consistently assigned an orientation and, thus, have the same topological properties as vector field singularities.

Having arrived at the result that the tendex lines on S must have singular points in a general, asymptotically flat vacuum spacetime, we now recall the fact that the singular points appear where there is a degenerate eigenvalue of the tidal tensor. From the result of Sec. 4.2, the only degeneracies occur where the curvature vanishes completely, and it follows therefore that there must be points of vanishing curvature on S. In general we would expect the radiation to vanish at a minimum of four points, as Penrose [8] had previously noted. In this case there would be four loop singularities with index $i = 1/2$, whose index sums to $\chi = 2$. As we highlight in Sec. 4.4, where we show several examples of multipolar radiation in linearized theory, the number of singular points, the types of singularities, and the pattern of the tendex lines contains additional information.

Additional symmetry, however, can modify the structure of the singular points, as we see in the

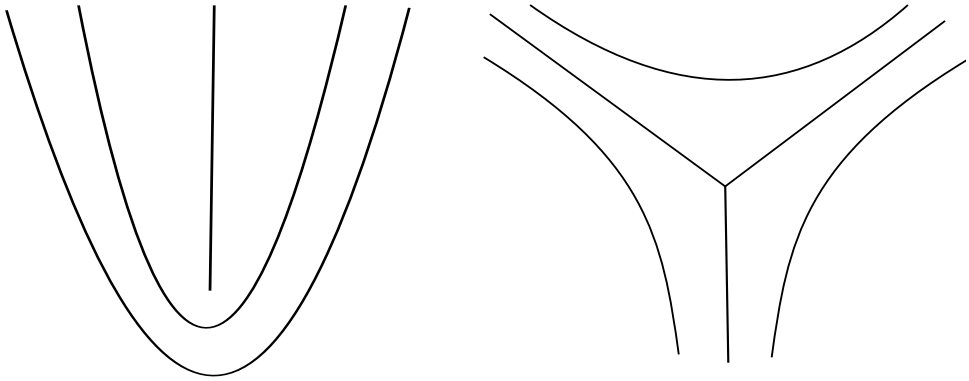

Figure 4.1: Illustrations of the two types of half-index singularities for ridge systems on a two-dimensional space. On the left is a loop singularity with index $i = 1/2$, and on the right is a triradius with $i = -1/2$.

simple example of an axisymmetric, head-on collision of two nonspinning black holes. Axisymmetry guarantees that the Weyl scalar Ψ_4 is purely real when we construct our tetrad, Eq. (4.5), by choosing $\mathbf{e}_2$ and $\mathbf{e}_3$ to be the orthonormal basis vectors of spherical polar coordinates on S, $\boldsymbol{e}_\theta$ and $\boldsymbol{e}_\phi$ [14]. Using the relation $\Psi_4 = -\ddot{h}_+ + i\ddot{h}_\times$, we see that the waves are purely + polarized. By substituting this relationship into (4.7), we also see that $\boldsymbol{e}_\theta$ and $\boldsymbol{e}_\phi$ are the eigenvectors whose integral curves are the tendex lines. The tendex lines, therefore, are the lines of constant latitude and longitude, and the singular points reside on the north and south poles of S. Their index must be $i = 1$, and the local pattern at the singularity will resemble the pattern at the top left of Fig. 4.3 for one set of lines, and the image on the top right of Fig. 4.3 for the other set (see also [4]). In this special situation, axisymmetry demands that there be two singular points on the axis, rather than four (or more). Moreover, these singular points are each generated from the coincidence of two loop singularities, with one singular point at each end of the axis of symmetry. Similarly, if Ψ_4 were purely imaginary, then the radiation would only contain the $\times$ polarization. The $\pi/4$ rotations of the unit spherical vectors would then be the eigenvectors of the tidal field, and the two singularities at the poles would resemble that illustrated at the top middle of Fig. 4.3.

It is even conceivable that four loops could merge into one singular point. This singularity would have the dipolelike pattern illustrated at the bottom right of Fig. 4.3, and it would have index $i = 2$. Though this situation seems very special, we show in the next section how a finely tuned linear combination of mass and current multipoles can give rise to this pattern. Because there is only one zero, the radiation is beamed in the direction opposite the zero, resulting in a net flux of momentum opposite the lone singular point.

Before concluding this section, we address two possible concerns. The scalar $\Psi_4 = C_{\mu\nu\rho\sigma} n^\mu \bar{m}^\nu n^\rho \bar{m}^\sigma$ depends both on the curvature and on the chosen tetrad. We first emphasize that the singular points we have discussed have nothing to do with tetrad considerations, in particular with the behavior of

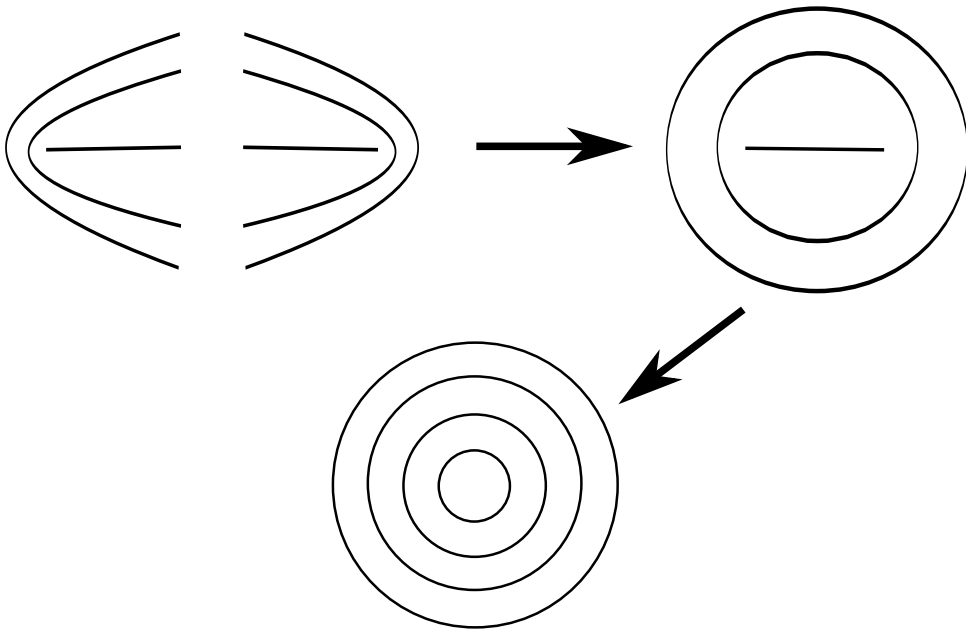

Figure 4.2: An illustration of the formation of a singularity with index $i = 1$ from two loop singularities with index $i = 1/2$. The local structure of the two loops is shown in the top left, and the arrow represents, schematically, how they might join together into the extended pattern at the top right. Finally, the two loop singularities can be brought together until they coincide (which we represent by an arrow pointing to the image at the bottom). This resulting local pattern can be assigned an orientation and is equivalent to the singular point of a vector field.

the vectors tangent to the sphere, $\boldsymbol{m}$, and $\bar{\boldsymbol{m}}$. Though these vectors will also become singular at points on the sphere, we are free to use a different tetrad on S in these regions, just as we can cover the sphere everywhere with smooth coordinates using overlapping charts. Secondly, the vanishing of radiation does not occur due to the null vector $\boldsymbol{n}$ coinciding with a principle null direction of the spacetime. We note that, if Ψ_4 vanishes at a point on S, then a change of basis cannot make Ψ_4 (or any of the other curvature scalars) nonvanishing. For example, a rotation about $\boldsymbol{l}$ by a complex parameter a induces a transformation on the other basis vectors,

$$\boldsymbol{l}' = \boldsymbol{l}\,, \quad \boldsymbol{m}' = \boldsymbol{m} + a\boldsymbol{l}\,, \quad \bar{\boldsymbol{m}}' = \bar{\boldsymbol{m}} + \bar{a}\boldsymbol{l}\,, \quad \boldsymbol{n}' = \boldsymbol{n} + a\bar{\boldsymbol{m}} + \bar{a}\boldsymbol{m} + a\bar{a}\boldsymbol{l}\,. \tag{4.9}$$

Under this rotation, Ψ_4 transforms as

$$\Psi_4' \;=\; \Psi_4 + 4\bar{a}\Psi_3 + 6\bar{a}^2\Psi_2 + 4\bar{a}^3\Psi_1 + \bar{a}^4\Psi_0\,, \tag{4.10}$$

which vanishes when the Weyl scalars are zero in the original basis. The remaining scalars transform analogously, and the other independent tetrad transformations are also homogeneous in the Weyl scalars (see e.g. [10]).

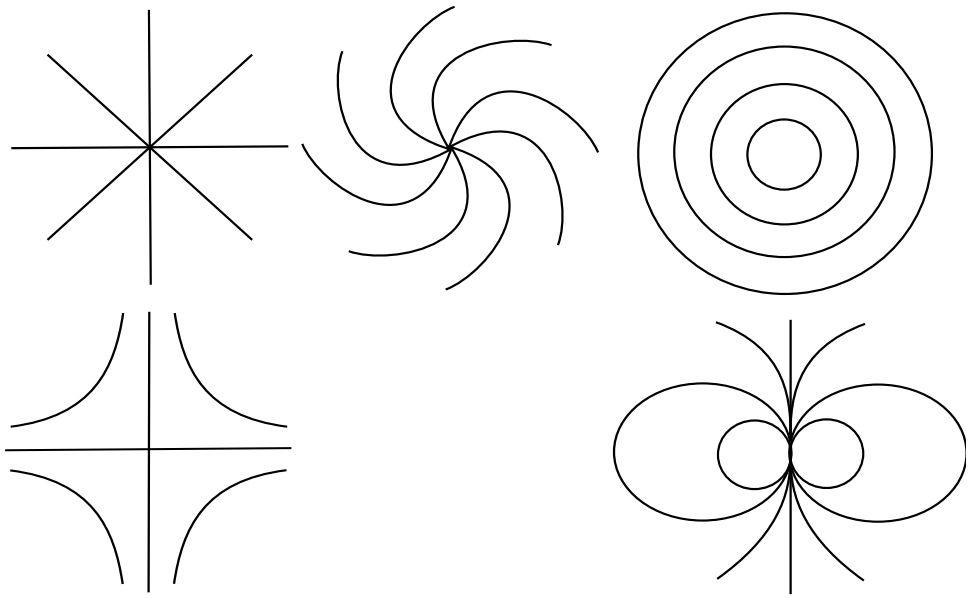

Figure 4.3: Top row: Diagrams of three orientable ridge patterns, which can be made from a combination of two loops, all with index $i = 1$. Bottom row: On the left is an orientable ridge pattern with index $i = -1$ (which is identical to a saddle point of a vector field). It can be constructed by joining two triradii singularities. The figure on the right shows a dipolelike pattern with index $i = 2$, which can come from the coincidence of four loops.

4.4 Examples from Linearized Gravity

We now give several examples of the tendex and vortex patterns on S from weak-field, multipolar sources. We first investigate quadrupolar radiation, produced by a time-varying quadrupole moment. For many astrophysical sources, such as the inspiral of comparable mass compact objects, the gravitational radiation is predominantly quadrupolar. As a result, our calculations will capture features of the radiation coming from these astrophysical systems. We will then study a combination of rotating mass- and current-quadrupole moments that are phase-locked. The locking of these moments was observed by Schnittman et al. in their multipolar analysis of the extreme-kick merger [15]. We conclude this section by discussing isolated higher multipoles. Although it is unlikely that astrophysical sources will contain only higher multipoles, it is of interest to see what kinds of tendex patterns occur. More importantly, while the tidal tensor is a linear combination of multipoles, the tendex lines will depend nonlinearly on the different moments. Actual astrophysical sources will contain a superposition of multipoles, and it is important to see how superpositions of multipoles change the leading-order quadrupole pattern.

We perform our calculations in linearized theory about flat space, and we use spherical polar coordinates and their corresponding unit vectors for our basis. One can compute from the multipolar metric in [16] that for a symmetric, trace-free (STF) quadrupole moment $\mathcal{I}_{ab}$, the leading-order

contributions to $\boldsymbol{\mathcal{E}}$ and $\boldsymbol{\mathcal{B}}$ on S are

$$\mathcal{E}_{ab}^{(\ell=2)} = -\frac{1}{2r}\left[{}^{(4)}\mathcal{I}_{ab}(t-r) + \epsilon_{ac}{}^{(4)}\mathcal{I}_{cd}(t-r)\epsilon_{db}\right]^{\rm TT}, \tag{4.11}$$

$$\mathcal{B}_{ab}^{(\ell=2)} = -\frac{1}{r}\left[\epsilon_{c(a}{}^{(4)}\mathcal{I}_{b)c}(t-r)\right]^{\rm TT}. \tag{4.12}$$

Here, the superscript ${}^{(4)}$ indicates four time derivatives, TT means to take the transverse-traceless projection of the expression, and ϵ_{ac} is the antisymmetric tensor on a sphere. In this expression, and in what follows, the Latin indices run only over the basis vectors $\boldsymbol{e}_\theta$ and $\boldsymbol{e}_\phi$, and repeated Latin indices are summed over even when they are both lowered.

4.4.1 Rotating Mass Quadrupole

As our first example, we calculate the STF quadrupole moment of two equal point masses (with mass $M/2$) separated by a distance a in the equatorial plane, and rotating at an orbital frequency Ω. We find that

$$\begin{aligned}
{}^{(4)}\mathcal{I}_{\theta\theta}(t-r) &= Ma^2\Omega^4(1+\cos^2\theta)\cos\{2[\phi-\Omega(t-r)]\}\,,\\
{}^{(4)}\mathcal{I}_{\theta\phi}(t-r) &= -2Ma^2\Omega^4\cos\theta\sin\{2[\phi-\Omega(t-r)]\}\,,\\
{}^{(4)}\mathcal{I}_{\phi\phi}(t-r) &= -{}^{(4)}\mathcal{I}_{\theta\theta}(t-r)\,.
\end{aligned} \tag{4.13}$$

By substituting these expressions into Eqs. (4.11) and (4.8), we find the eigenvectors of the tidal field. We can then calculate the tendex lines on the sphere by solving Eq. (4.4) with a convenient normalization of the parameter along the curves,

$$\frac{d\theta}{ds} = \frac{1}{r}{}^{(4)}\mathcal{I}_{\theta\phi}\,, \tag{4.14}$$

$$\frac{d\phi}{ds} = \frac{1}{r\sin\theta}(-{}^{(4)}\mathcal{I}_{\theta\theta}-\lambda_+)\,. \tag{4.15}$$

Here, λ_+ is the positive eigenvalue. The differential equation for the vortex lines [found from the corresponding frame-drag field of Eq. (4.12)], has the same form as those of the tendex lines above; however, one must replace ${}^{(4)}\mathcal{I}_{\theta\phi}$ in the first equation by ${}^{(4)}\mathcal{I}_{\theta\theta}$ and ${}^{(4)}\mathcal{I}_{\theta\theta}$ by $-{}^{(4)}\mathcal{I}_{\theta\phi}$ in the second equation.

We show the tendex and vortex lines corresponding to the positive eigenvalues in Figs. 4.4 and 4.5, respectively, at a retarded time $t-r=0$. We also plot the magnitude of the eigenvalue on the sphere, using a color scheme in which purple (darker) regions at the poles correspond to large eigenvalues and yellow (lighter) colors near the equator are closer to zero. Both the tendex and vortex lines have four equally spaced loop singularities on the equator at the points where the field

is zero (the two on the back side of the sphere are not shown). Because the vortex and tendex lines must cross each other at an angle of $\pi/4$, the global geometric patterns are quite different.

We note here that these two figures also provide a visualization for the transverse-traceless, "pure-spin" tensor spherical harmonics [16]. For example, we can see that the mass-quadrupole tendex lines are the integral curves of the eigenvectors of the real part of the $\ell = 2,\ m = 2$ electric-type transverse-traceless tensor harmonic. First, the tendex lines correspond to the electric-type harmonic, because the tidal tensor is even under parity. Second, the radiation pattern will not contain an $\ell = 2,\ m = 0$ harmonic, because the overall magnitude of the quadrupole moment of the source is not changing in time; also, the $\ell = 2,\ m = \pm 1$ harmonics are absent because the source is an equal-mass binary and is symmetric under a rotation of π. Finally, the $\ell = 2,\ m = -2$ moment is equal in magnitude to the $m = 2$ harmonic, since the tidal tensor is real. By similar considerations, we can identify the vortex lines of the mass quadrupole as a visualization of the real parts of the $\ell = 2,\ m = 2$ magnetic-type tensor harmonics.

In addition, the eigenvalue (the identical color patterns of Figs. 4.4 and 4.5) is given by the magnitude of the sum of spin-weighted spherical harmonics,

$$\lambda_+ \propto \left| {}_{-2}Y_{22} + {}_{-2}Y_{2-2} \right| . \tag{4.16}$$

One can see this most easily by using the symmetries described above, the expression for the eigenvalue $\lambda_+ = |\Psi_4|/2$, and the spin-weighted spherical harmonic decomposition of Ψ_4. It is also possible to verify this expression using the tensor harmonics above and the standard relations between tensor spherical harmonics and spin-weighted spherical harmonics (see e.g. [16]). Radiation from numerical spacetimes is usually decomposed into spin-weighted spherical harmonics, and, as a result, the pattern of the eigenvalue is familiar. The tendex lines, however, also show the polarization pattern of the waves on S (a feature that numerical simulations rarely explicitly highlight). Figure 4.4 (and the accompanying negative-tendicity lines not shown) gives the directions of preferred strain on S, and hence the wave polarization that can be inferred from gravitational-wave-interferometer networks such as LIGO/VIRGO. Thus, visualizations such as Fig. 4.4 give complete information about the gravitational waves passing through S.

4.4.2 Rotating Mass and Current Quadrupoles in Phase

As our second example, we will consider a source that also has a time-varying current-quadrupole moment, $\mathcal{S}_{ab}$. In linearized theory, one can show that the tidal tensor and frame-drag field of a current quadrupole are simply related to those of a mass quadrupole. In fact, $\mathcal{B}_{ab}$ of the current quadrupole has exactly the same form as $\mathcal{E}_{ab}$ of a mass quadrupole, Eq. (4.11), when one replaces ${}^{(4)}\mathcal{I}_{ab}$ by $(4/3){}^{(4)}\mathcal{S}_{ab}$. Similarly, $\mathcal{E}_{ab}$ of the current quadrupole is identical to $\mathcal{B}_{ab}$ of a mass quadrupole, Eq.

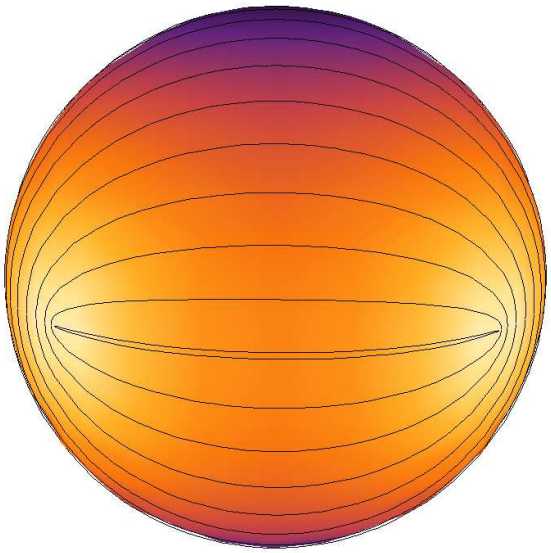

Figure 4.4: (color online). The positive tendex lines on S generated by a rotating quadrupole moment in linearized gravity. The sphere is colored by the magnitude of the eigenvalue; purple (darker) areas at the poles corresponding to a large eigenvalue, and yellow (lighter) areas near the equator indicate a value closer to zero. Four loop singularities appear equally spaced on the equator at the points of vanishing tendicity.

(4.12), when ${}^{(4)}\mathcal{I}_{ab}$ is replaced by $-(4/3){}^{(4)}\mathcal{S}_{ab}$.

We impose that the source's mass- and current-quadrupole moments rotate in phase, with frequency Ω, and with the current quadrupole lagging in phase by $\pi/2$. This arrangement of multipoles

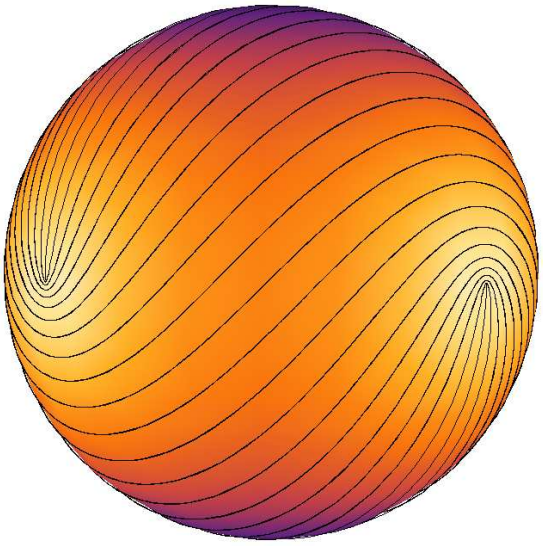

Figure 4.5: (color online). As in Fig. 4.4, we show the positive vortex lines and their magnitude of the eigenvalue on S (using the same coloring as in that figure). The loop singularities lie at the same locations as they do for the tendex lines, but they are locally rotated by $\pi/4$.

models the lowest multipoles during the merger and ringdown of the extreme-kick configuration (a collision of equal-mass black holes in a quasicircular orbit that have spins of equal magnitude lying in the orbital plane, but pointing in opposite directions), when the mass- and current-quadrupole moments rotate in phase [15]. The relative amplitude of the mass- and current-multipoles depends upon, among other variables, the amplitude of the black-holes' spin. We, therefore, include a free parameter C in the strength of the current quadrupole which represents the effect of changing the spin. An order-of-magnitude estimate based on two fast-spinning holes orbiting near the end of their inspiral indicates that that their amplitudes could be nearly equal, $C = O(1)$. To determine the exact relative amplitude of the mass- and current-quadrupole moments of the radiation would require comparison with numerical relativity results.

We calculate the current-quadrupole moment by scaling the mass quadrupole by the appropriate factor of C and letting the term $2[\phi - \Omega(t-r)]$ in the equations for $\mathcal{I}_{ab}(t-r)$ become $2[\phi - \Omega(t-r)] - \pi/2$ in the corresponding expressions for $\mathcal{S}_{ab}(t-r)$. In linearized theory, the tidal tensor and frame-drag fields of the different multipoles add directly. As a result, the equations for the tendex lines have the same form as Eqs. (4.14) and (4.15), but one must now replace the mass quadrupole ${}^{(4)}\mathcal{I}_{\theta\phi}$ by ${}^{(4)}\mathcal{I}_{\theta\phi} - (4/3){}^{(4)}\mathcal{S}_{\theta\theta}$ in the first expression and ${}^{(4)}\mathcal{I}_{\theta\theta}$ by ${}^{(4)}\mathcal{I}_{\theta\theta} + (4/3){}^{(4)}\mathcal{S}_{\theta\phi}$ in the second.

First, we allow the current quadrupole to be half as large as the mass quadrupole, $C = 1/2$. We show the positive tendex lines and positive eigenvalue in Fig. 4.6. Because of the relative phase and amplitude of the two moments, the tensors add constructively in the northern hemisphere and destructively in the southern hemisphere on S. This is evident in the eigenvalue on the sphere in Fig. 4.6, which, one can argue, is now given by an unequal superposition of spin-weighted spherical harmonics,

$$\lambda_+ \propto \left| {}_{-2}Y_{22} + b\,{}_{-2}Y_{2-2} \right| , \tag{4.17}$$

with $b < 1$. As in previous figures, dark colors (black and purple) represent where the eigenvalue is large, and light colors (white and yellow) show where it is nearly zero. While the singular points are still equally spaced on a line of constant latitude, they no longer reside on the equator; they now fall in the southern hemisphere. This is a direct consequence of the beaming of radiation toward the northern pole.

The case shown above has strong beaming, but it is possible to make the beaming more pronounced. To get the greatest interference of the multipoles, the mass and current quadrupoles must have equal amplitude in the tidal field. Because the tidal field of the current quadrupole is $4/3$ as large as the tidal field of the mass quadrupole, setting $C = 3/4$ gives the strongest constructive interference in the tidal fields. In this case, the eigenvalue vanishes at just one point, the south pole, and the eigenvalue can be shown to be proportional to just a single spin-weighted spherical

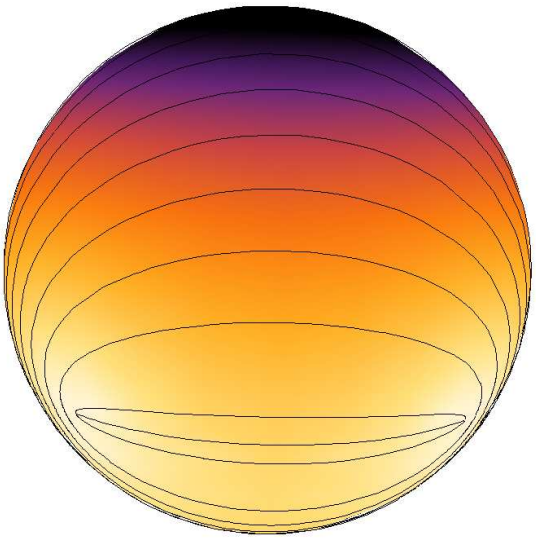

Figure 4.6: (color online). The positive tendex lines on S generated by the superposition of rotating mass- and current-quadrupole moments, $\pi/2$ out of phase, in linearized gravity. The sphere is colored by the tendicity as in Fig. 4.4. Interference between the moments leads to beaming of the radiation toward the north pole. Similarly, the singular points of the tendex lines now fall on a line of constant latitude in the southern hemisphere.

harmonic,

$$\lambda_+ \propto |{}_{-2}Y_{22}| \,. \tag{4.18}$$

As a result, the four equally spaced singular points of the tendex lines must coincide at one singular point whose index must be $i = 2$. This is precisely the dipolelike pattern depicted in Fig. 4.3. We show the tendex lines around the south pole in Fig. 4.7. The vortex lines are identical to the tendex lines, but they are globally rotated by $\pi/4$ in this specific case.

We see that the beaming can be maximized by carefully tuning the phase and amplitude of the mass- and current-quadrupole moments. Interestingly, the maximally beamed configuration corresponds with the coincidence of all singular points at the south pole in the radiation zone. Whether this degree of beaming could occur from astrophysical sources is an open question.

4.4.3 Higher Multipoles of Rotating Point Masses

We also investigate the effect of including higher multipoles on the tendex lines on S. For the orbiting, nonspinning, point masses of the first example the next two lowest multipoles arise from the current octopole (the $\ell = 3$ STF moment [16]) and the mass hexadecapole (the $\ell = 4$ STF moment). From

the multipolar metric in [16], one can show that the tidal field for these two moments are

$$\mathcal{E}^{\ell=3}_{ab} = -\frac{1}{2r}\left[\epsilon_{c(a}{}^{(5)}\mathcal{S}_{b)cr}(t-r)\right]^{\rm TT}, \tag{4.19}$$

$$\mathcal{E}^{\ell=4}_{ab} = -\frac{1}{24r}\left[{}^{(6)}\mathcal{I}_{abrr}(t-r) + \epsilon_{ac}\epsilon_{db}{}^{(4)}\mathcal{I}_{cdrr}(t-r)\right]^{\rm TT}, \tag{4.20}$$

where the index r indicates contraction with the radial basis vector $\boldsymbol{e}_r$, and so repeated r indices do not indicate summation. The STF current-octopole moment, can be expressed compactly as $\mathcal{S}_{ijk} = (L^i_N x^j_A x^k_A)^{\rm STF}$, where L^i_N is the Newtonian angular momentum and x^j_A is the position of one of the point masses. The superscript STF indicates that all indices should be symmetrized, and all traces removed. In Cartesian coordinates, the vectors have the simple forms $\mathbf{L}_N = (0, 0, Mav/4)$ and $\mathbf{x}_A = (a/2)(\cos[\Omega t], \sin[\Omega t], 0)$, where Ω is the Keplerian frequency and v is the relative velocity. Similarly, one can write the STF mass-hexadecapole moment as $\mathcal{I}_{ijkl} = M(x^i_A x^j_A x^k_A x^l_A)^{\rm STF}$, for the same vector x^j_A as above. Because these tensors have many components, we shall only list those that are relevant for finding the tendex lines. We will also define $\alpha = \phi - \Omega(t-r)$ for convenience.

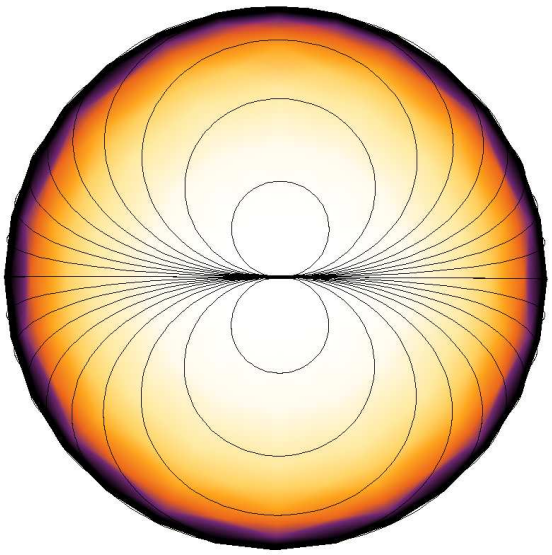

Figure 4.7: (color online). South polar region of the tendex line pattern of a gravitational wave generated by rotating mass- and current-quadrupole moments. The amplitude and phase of the moments are chosen so that the radiation vanishes only at the south pole. The purple (darker) areas indicate a positive eigenvalue, while yellow (lighter) areas are values closer to zero. The singularity at the pole has index $i = 2$.

For the current octopole the relevant components are

$$\begin{aligned}
{}^{(5)}\mathcal{S}_{\theta\theta r}(t-r) &= -\frac{Ma^3v\Omega^5}{24}(5\cos\theta+3\cos 3\theta)\sin 2\alpha\,,\\
{}^{(5)}\mathcal{S}_{\theta\phi r}(t-r) &= -\frac{Ma^3v\Omega^5}{3}\cos 2\theta\cos 2\alpha\,,\\
{}^{(5)}\mathcal{S}_{\phi\phi r}(t-r) &= -{}^{(5)}\mathcal{S}_{\theta\theta r}(t-r)\,,
\end{aligned} \tag{4.21}$$

and for the mass hexadecapole they are

$$\begin{aligned}
{}^{(6)}\mathcal{I}_{\theta\theta rr}(t-r) &= \frac{Ma^4\Omega^6}{8}[(\cos^2\theta+\cos 4\theta)\cos 2\alpha\\
&\quad -128\sin^2\theta(1+\cos^2\theta)\cos 4\alpha]\,,\\
{}^{(6)}\mathcal{I}_{\theta\phi rr}(t-r) &= -\frac{Ma^4\Omega^6}{4}[\cos 3\theta\sin 2\alpha\\
&\quad -128\sin^2\theta\cos\theta\sin 4\alpha]\,,\\
{}^{(6)}\mathcal{I}_{\phi\phi rr}(t-r) &= -{}^{(6)}\mathcal{I}_{\theta\theta rr}(t-r)\,.
\end{aligned} \tag{4.22}$$

The tendex lines of the current octopole can be found by solving the system of differential equations in Eqs. (4.14) and (4.15) by substituting ${}^{(4)}\mathcal{I}_{\theta\phi}$ by ${}^{(5)}\mathcal{S}_{\theta\theta r}/2$ and ${}^{(4)}\mathcal{I}_{\theta\theta}$ by $-{}^{(5)}\mathcal{S}_{\theta\phi r}/2$ Similarly, for the mass hexadecapole, one must make the substitutions of ${}^{(4)}\mathcal{I}_{\theta\phi}$ by ${}^{(6)}\mathcal{I}_{\theta\phi rr}/12$ and ${}^{(4)}\mathcal{I}_{\theta\theta}$ by ${}^{(6)}\mathcal{I}_{\theta\theta rr}/12$ in the same equations.

In Fig. 4.8 we show the tendex line pattern for the current octopole, and in Fig. 4.9 we show the pattern for the mass hexadecapole. Together with the mass quadrupole, Fig. 4.4, these are the three lowest multipole moments for the equal-mass circular binary. For the current octopole, there are eight triradius singular points and 12 loop singularities (and thus the net index is two). Four of the loop singularities remain equally spaced on the equator, at the same position of those of the quadrupole, but the remaining singularities appear at different points on S. The mass hexadecapole has eight loop singularities equally spaced on the equator, and there are integer-index saddle-point-like singularities at each pole.

Gravitational radiation from astrophysical sources will likely not be dominated by these higher multipoles. Nevertheless, these figures are of interest as examples of tendex lines with many singular points and as visualizations of tensor harmonics. By analyzing the symmetries in a way analogous to that discussed in Sec. 4.4.1, we can identify the current-octopole tendex lines with the integral curves of $\ell = 3,\ m = 2$ magnetic-type harmonics, and we can associate the mass-hexadecapole lines with those of the $\ell = 4,\ m = 4$ electric-type harmonics. In the case of the mass hexadecapole, the $m = 2$ moment is not ruled out by symmetry, but it is suppressed relative to the $m = 4$ moment. This occurs because the $m = 4$ moment oscillates at twice the frequency of the $m = 2$ moment, and the tidal tensor for this higher-order moment is given by taking six time derivatives of the

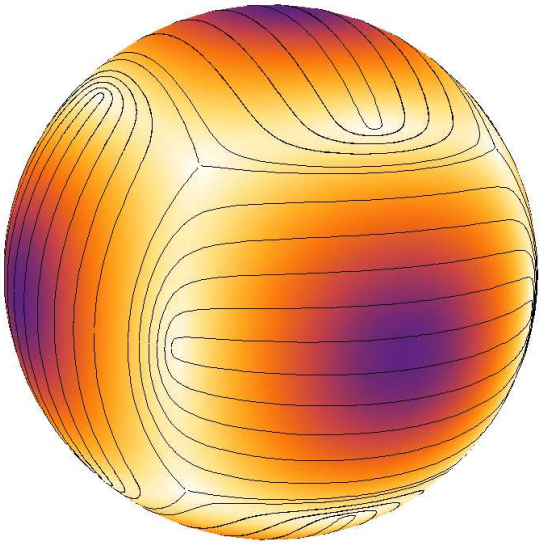

Figure 4.8: (color online). The tendex lines of a current-octopole moment of an equal-mass, circular binary of point masses. The colors on the sphere represent the tendicity, with the same scale described in Fig. 4.4. The current octopole also has four loop singularities on the equator (at the same position of those of the rotating quadrupole), but it has eight additional loops and eight triradius singularities off of the equator. Only half of the singular points are visible on the sphere; the other half appear on the back side.

STF moment, Eq. (4.22). This enhances the $m = 4$ radiation by a factor of 2^6 over the $m = 2$ contribution. Similarly, we can relate the eigenvalue to the magnitude of the corresponding sum of $s = -2$ spin-weighted spherical harmonics, and the tendex line patterns to the the polarization directions that could be inferred from networks of gravitational-wave interferometers.

Finally, we show the pattern generated from the linear combination of the three lowest multipole moments in Fig. 4.10. Any astrophysical source will contain several multipoles, with the quadrupole being the largest. The tendex lines depend nonlinearly on the multipoles, and it is important, therefore, to see to what extent higher multipoles change the overall pattern. We find the total tidal tensor by linearly combining the tidal tensor of each individual moment, and we then find the eigenvectors and tendex lines of the total tidal tensor. The pattern formed from the combination of multipoles depends upon the parameters of the binary; in making this figure we assumed (in units in which $M = 1$) a separation of $a = 15$, an orbital frequency $\Omega = a^{-3/2}$, and a velocity $v = a\Omega = a^{-1/2}$. When these higher moments are combined with the mass quadrupole, the tendex line structure resembles that of the mass quadrupole. The pattern is deformed slightly, however, by the presence of the higher multipoles. The loop singularities on the equator are no longer evenly spaced; rather, the pair illustrated (and the corresponding pair which is not visible) are pushed slightly closer together.

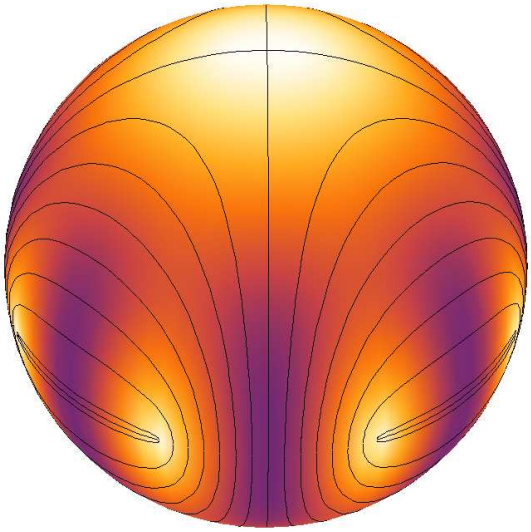

Figure 4.9: (color online). The tendex lines on S of the mass hexadecapole of an equal-mass, circular binary of point masses, with the sphere colored by the tendicity as in Fig. 4.4. The hexadecapole has eight loop singularities equally spaced on the equator and two saddle-point-like singularities (from the coincidence of two triradius singularities at a point) at the poles. Again, only half are visible in the figure. Four of the singular points on the equator coincide with those of the quadrupole, but the remaining four appear at different locations.

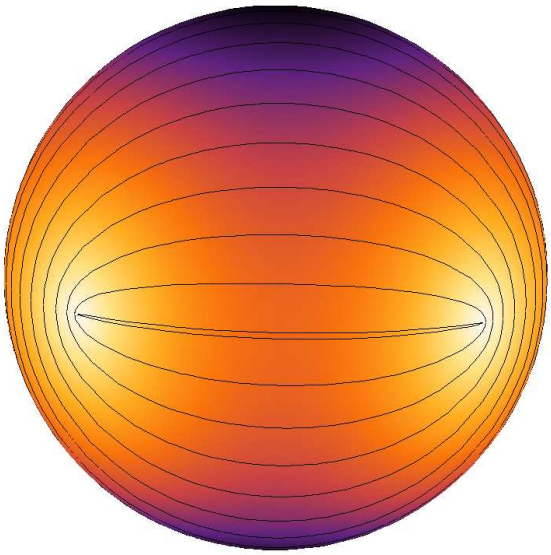

Figure 4.10: (color online). The tendex lines of a superposition of mass-quadrupole, current-octopole, and mass-hexadecapole moments of an equal-mass circular binary. It assumes a total mass $M = 1$, a separation $a = 15$, an orbital frequency $\Omega = a^{-3/2}$ and a velocity $v = a\Omega = a^{-1/2}$. The sphere is colored by the tendicity in an identical way to that of Fig. 4.4. When the tidal tensors of the three multipoles are combined, the net pattern is dominated by the quadrupole and contains only the four loops. The loop singularities are no longer equally spaced on the equator; the two pairs are pushed closer together due to the influence of the higher multipoles.

4.5 Conclusions

Tendex and vortex lines provide a new tool with which to visualize and study the curvature of spacetime. Fundamentally, they allow for the visualization of the Riemann tensor, through its decomposition into two simpler, trace-free and symmetric spatial tensors. These tensors, $\boldsymbol{\mathcal{E}}$ and $\boldsymbol{\mathcal{B}}$, can be completely characterized by their eigenvectors and corresponding eigenvalues. The integral curves of these eigenvector fields are easily visualized, and their meaning is well understood; physically, the lines can be interpreted in terms of local tidal strains and differential frame-dragging. Here, the simple nature of these lines allows us to apply well-known topological theorems to the study of radiation passing through a sphere near null infinity.

Tendex line patterns must develop singularities (and thus have vanishing tendicity) on a closed surface. When we applied this fact to the tendex lines of gravitational radiation near null infinity from arbitrary physical systems, we could easily show that the gravitational radiation must at least vanish in isolated directions. Although this result is somewhat obvious in retrospect and has been noted before [8], the result does not appear to be well-known. We also began exploring the manner in which these singular points can provide a sort of fingerprint for radiating spacetimes. The essential elements of this fingerprint consist of the zeros of the curvature on the sphere, together with the index and the tendex line pattern around these zeros. We studied these patterns for a few specific examples, such as the four equally spaced loops of a rotating mass quadrupole. A more interesting case is that of a radiating spacetime composed of locked, rotating mass and current quadrupoles, which can be thought of as a simplified model of the late stages of the extreme-kick black-hole-binary merger. Here, the shifted positions of the singular points of the tendex pattern provide a direct illustration of gravitational beaming for this system. By seeking the most extreme topological arrangement of singular points, we also described a maximally beaming configuration of this system.

The radiation generated by higher-order STF multipole moments gives more complex examples of tendex and vortex patterns, with many singular points of varied types. Additionally, we argued that their tendex and vortex patterns provide a visualization of the tensor spherical harmonics on the sphere; the eigenvalue illustrates the magnitude of these harmonics, and the lines show the tensor's polarization in an intuitive manner. The sum of the three multipoles illustrated in Fig. 4.10 shows how including higher-order multipoles slightly deforms the pattern of quadrupole radiation to make a more accurate total radiation pattern of the equal-mass binary. Similar illustrations of complete radiation patterns could be readily produced from numerical spacetimes, when Ψ_4 is extracted asymptotically using a tetrad with appropriate peeling properties. Such visualizations, and their evolution in time, could provide a useful method for visualizing the gravitational emission from these systems.

This study of the tendex and vortex lines (and their singular points) of asymptotic radiation

fields is one of several [4] exploring and developing this new perspective on spacetime visualization. Naturally, it would be of interest to extend the two-dimensional case here to a larger study of the singular points in the full, three-dimensional tendex and vortex fields. Methods to find and visualize the singular points (and singular lines) of 3D tensors have been discussed preliminarily in [17], though there is still room for further work. We suspect that singular points will be important in visualizing and studying the properties of numerical spacetimes with these methods. Further, we expect that there is still much to be learned from the study of the vortexes and tendexes of dynamical spacetimes.

Bibliography

[1] R. Owen et al., Phys. Rev. Lett. **106**, 151101 (2011).

[2] R. Maartens and B. A. Bassett, Classical Quantum Gravity **15**, 705 (1998).

[3] F. B. Estabrook and H. D. Wahlquist, J. Math. Phys. **5**, 1629 (1964).

[4] R. Owen et al., in preparation.

[5] T. Delmarcelle and L. Hesselink, in *Proceedings of the Conference on Visualization '94.* (1994), VIS '94, pp. 140–147.

[6] R. Penrose and W. Rindler, *Spinors and Space-time. Volume 2: Spinor and Twistor Methods in Space-time Geometry.* (Cambridge University Press, London, 1986).

[7] R. Penrose, Ann. Hum. Genet., Lond. **42**, 435 (1979).

[8] R. Penrose, Proc. R. Soc. A **284**, 159 (1965).

[9] M. Campanelli, C. O. Lousto, Y. Zlochower, and D. Merritt, Phys. Rev. Lett. **98**, 231102 (2007).

[10] H. Stephani, D. Kramer, M. MacCallum, C. Hoenselaers, and E. Herlt, *Exact Solutions of Einstein's Field Equations* (Cambridge University Press, London, 2003).

[11] H. Bondi, M. G. J. van der Burg, and A. W. K. Metzner, Proc. R. Soc. A **269**, 21 (1962).

[12] L. A. Tamburino and J. H. Winicour, Phys. Rev. **150**, 1039 (1966).

[13] E. Newman and R. Penrose, J. Math. Phys. **3**, 566 (1962).

[14] D. R. Fiske, J. G. Baker, J. R. van Meter, D.-I. Choi, and J. M. Centrella, Phys. Rev. D **71**, 104036 (2005).

[15] J. D. Schnittman, A. Buonanno, J. R. van Meter, J. G. Baker, W. D. Boggs, J. Centrella, B. J. Kelly, and S. T. McWilliams, Phys. Rev. D **77**, 044031 (2008).

[16] K. S. Thorne, Rev. Mod. Phys. **52**, 299 (1980).

[17] J. Weickert, and H. Hagen, ed., *Visualization and Processing of Tensor Fields* (Springer Verlag, Berlin, 2006).

Chapter 5

Frame-Drag Vortexes and Tidal Tendexes III. Stationary Black Holes

---

Originally published as

Fan Zhang, Aaron Zimmerman, David A. Nichols, Yanbei Chen, Geoffrey Lovelace, Keith D. Matthews, Robert Owen, Kip S. Thorne

Phys. Rev. D 86, 084049 (2012)

5.1 Motivation and Overview

It has long been known that, when one performs a 3+1 split of spacetime into space plus time, the Weyl curvature tensor $C_{\alpha\beta\gamma\delta}$ gets split into two spatial, symmetric, traceless tensors: the so-called "electric" part, $\boldsymbol{\mathcal{E}}$, which we call the *tidal field* (because it is responsible for the gravitational stretching and squeezing that generates tides), and the so-called "magnetic" part $\boldsymbol{\mathcal{B}}$, which we call the *frame-drag field* (because it generates differential frame dragging, i.e., differential precession of gyroscopes).

Recently [1, 2] (i.e. Chapters 1.2 and 3), we and colleagues have proposed visualizing the tidal field by means of the integral curves of its three eigenvector fields, which we call *tendex lines*, and each line's eigenvalue, which we call its *tendicity*. These are very much like electric field lines and the magnitude of the electric field. Similarly, we have proposed visualizing the frame-drag field by integral curves of its three eigenvector fields, which we call *vortex lines*, and each curve's eigenvalue, which we call its *vorticity*. These are analogous to magnetic field lines and the magnitude of the magnetic field.

In our initial presentation in Chapter 1.2 (i.e. [1]) of these new concepts and their applications,

we demonstrated that they can be powerful tools for visualizing the nonlinear dynamics of curved spacetime that is triggered by the inspiral, collision, and merger of binary black holes. We expect them also to be powerful visualization tools in other venues of nonlinear spacetime dynamics (geometrodynamics).

After our initial presentation Chapter 1.2 (i.e. [1]), we have turned to a methodical exploration of these tools, in a series of papers in this journal. We are beginning in Papers I–III by applying these tools to "analytically understood" spacetimes, in order to gain intuition into the relation between their visual pictures and the analytics. Then in Paper IV and thereafter, we shall apply them to numerical spacetimes, looking for types of features we have already found, and retrieving their analytical origin.

In Chapter 3 (i.e. [2], henceforth Paper I), using examples of nearly flat (linearized) spacetimes, we have shown that tendex lines and vortex lines can illustrate very well the spacetime dynamics around oscillating multipole sources, and we have connected various features of the field lines to physical understanding, and to the analytics. We found that, in the near zone of an oscillating multipole, the field lines are attached to the source; in the transition zone, retardation effects cause the field lines to change character in understandable ways; and in the wave zone, the field lines approach those of freely propagating plane waves. In a supplementary study [3] (i.e. Chapter 4), some of us have classified the tendex and vortex lines of asymptotically flat space times at future null infinity according to the lines' topological features.

Recently, Dennison and Baumgarte [4] computed the tendex and vortex fields of approximate analytical solutions of boosted, non-spinning black holes (both isolated holes and those in binaries). Specifically, they computed an analytical initial-data solution of the Einstein constraint equations (in the form of that of Bowen and York [5]) that is accurate through leading order in a boost-like parameter of the black holes. Their results are an important analytical approximation to the vortex and tendex fields of a strong-field binary, and will likely be useful for understanding aspects of numerical-relativity simulations of binary black holes.

In Paper III, we shall explore the tendex and vortex lines, and their tendicities and vorticities, for quasinormal-mode oscillations of black holes—and shall see very similar behaviors to those we found, in the linearized approximation, in Paper I [2] (i.e. Chapter 3). In preparation for this, we must explore in depth the application of our new tools to stationary (Schwarzschild and Kerr) black holes. That is the purpose of this Paper II.

In Paper IV we shall apply our tools to numerical simulations of binary-black-hole inspiral, collision, and merger, and shall use our linearized visualizations (Paper I), our stationary-black-hole visualizations (Paper II), our quasinormal-mode visualizations (Paper III), and Dennison and Baumgarte's visualizations [4] to gain insight into the fully nonlinear spacetime dynamics that the binary black holes trigger.

This paper is organized as follows: In Sec. 5.2, we briefly review the underlying theory of the 3+1 split of spacetime and our definitions of the tidal field $\boldsymbol{\mathcal{E}}$ and frame-drag field $\boldsymbol{\mathcal{B}}$ in Chapters 1.2 and 3 (i.e. [1, 2]). In Sec. 5.3, we introduce the concepts of *horizon tendicity* (the normal-normal component of $\boldsymbol{\mathcal{E}}$ on a black-hole horizon) and *horizon vorticity* (the normal-normal component of $\boldsymbol{\mathcal{B}}$), which, for stationary black holes, can be related to the real and imaginary parts of the Newman-Penrose Weyl scalar Ψ_2 and are the horizon's scalar intrinsic curvature and scalar extrinsic curvature (aside from simple multiplicative factors).

In Sec. 5.4, we give formulae for the eigenvector and eigenvalue fields for the tidal field around a static (Schwarzschild) black hole, we draw pictures of the black hole's corresponding tendex lines, and we discuss the connection to the tidal stretching and squeezing felt by observers near a Schwarzschild hole. (The frame-drag field vanishes for a Schwarzschild hole.)

In Sec. 5.5, we turn on a slow rotation of the hole, we compute the frame-drag field $\boldsymbol{\mathcal{B}}$ generated by that rotation, we visualize $\boldsymbol{\mathcal{B}}$ via color-coded pictures of the horizon vorticity and the vortex lines, and we discover a spiraling of azimuthal tendex lines that is created by the hole's rotation. In this section, we restrict ourselves to time slices (and the fields on those time slices) that have constant ingoing Eddington-Finklestein time, and that therefore penetrate the horizon smoothly. (For the Schwarzschild black hole of Sec. 5.4, the tendex lines are the same in Schwarzschild slicing as in Eddington-Finklestein slicing; the hole's rotation destroys this.)

In Sec. 5.6, we turn to rapidly rotating (Kerr) black holes, and explore how the vortex and tendex lines and the horizon vorticities and tendicities change when a hole is spun up to near maximal angular velocity. In these explorations, we restrict ourselves to horizon-penetrating slices, specifically: slices of constant Kerr-Schild time $\tilde{t}$, and the significantly different slices of constant Cook-Scheel, harmonic time $\bar{t}$. By using the same spatial coordinates in the two cases, we explore how the time slicing affects the tendex and vortex lines and the horizon tendicities and vorticities. There is surprisingly little difference, for the two slicings; the field lines and horizon properties change by only modest amounts when one switches from one slicing to the other (top row of Fig. 5.6 compared with bottom row). By contrast, when we use non-horizon-penetrating Boyer-Lindquist slices (Appendix 5.8), the field lines are noticeably changed. In Sec. 5.6 we also explore how the vortex and tendex lines (plotted on a flat computer screen or flat sheet of paper) change, when we change the spatial coordinates with fixed slicing (Fig. 5.5). We find only modest changes, and they are easily understood and quite obvious once one understands the relationship between the spatial coordinate systems.

In Sec. 5.7, we briefly summarize our results. In three Appendices, we present mathematical details that underlie some of the results in the body of the paper.

Throughout this paper we use geometrized units, with $G = c = 1$. Greek indices are used for 4D spacetime quantities, and run from 0 to 3. Latin indices are used for spatial quantities, and run

from 1 to 3. Hatted indices indicate components on an orthonormal tetrad. Capital Latin indices from the start of the alphabet are used for angular quantities defined on spheres of some constant radius, and they generally run over θ, ϕ. We use signature $(-+++)$ for the spacetime metric, and our Newman-Penrose quantities are defined appropriately for this signature, as in [6].

5.2 Tendex and Vortex Lines

In this section we will briefly review the $3+1$ split and the definition of our spatial curvature quantities. A more detailed account is given in Paper I of this series [2] (i.e. Chapter 3). To begin with, we split the spacetime using a unit timelike vector $\vec{u}$, which is everywhere normal to the slice of constant time. This vector can be associated with a family of observers who travel with four-velocity $\vec{u}$, and will observe the corresponding time slices as moments of simultaneity. We consider only vacuum spacetimes, where the Riemann tensor $R_{\mu\nu\rho\sigma}$ is the same as the Weyl tensor $C_{\mu\nu\rho\sigma}$. The Weyl tensor has ten independent degrees of freedom, and these are encoded in two symmetric, traceless spatial tensors $\boldsymbol{\mathcal{E}}$ and $\boldsymbol{\mathcal{B}}$. These spatial tensors are formed by projection of the Weyl tensor $C_{\mu\nu\rho\sigma}$ and (minus) its Hodge dual ${}^*C_{\mu\nu\rho\sigma}$ onto the spatial slices using u^μ, and the spatial projection operator $\gamma_\alpha{}^\mu$. The projection operator is given by raising one index on the spatial metric of the slice, $\gamma_{\mu\nu} = g_{\mu\nu} + u_\mu u_\nu$. The resulting spatial projection of the Weyl tensor is given by an even-parity field called the "electric" part of $C_{\mu\nu\rho\sigma}$ and also called the "tidal field",

$$\mathcal{E}_{\alpha\beta} = \gamma_\alpha{}^\rho \gamma_\beta{}^\sigma C_{\rho\mu\sigma\nu} u^\mu u^\nu \ , \quad \text{i.e. } \mathcal{E}_{ij} = C_{i\hat{0}j\hat{0}} \ , \tag{5.1a}$$

and an odd-parity field called the "magnetic" part of $C_{\mu\nu\rho\sigma}$ and also called the "frame-drag field",

$$\mathcal{B}_{\alpha\beta} = -\gamma_\alpha{}^\rho \gamma_\beta{}^\sigma {}^*C_{\rho\mu\sigma\nu} u^\mu u^\nu \ , \quad \text{i.e. } \mathcal{B}_{ij} = \frac{1}{2}\epsilon_{ipq} C^{pq}{}_{j\hat{0}}. \tag{5.1b}$$

Here, as usual, we give spatial (Latin) indices to quantities after projection onto the spatial slices using $\gamma_\alpha{}^\mu$. We note that our conventions on the antisymmetric tensors are, when expressed in an orthonormal basis, $\epsilon_{\hat{0}\hat{1}\hat{2}\hat{3}} = +1$ and $\epsilon_{\hat{1}\hat{2}\hat{3}} = +1$, with $\epsilon_{ijk} = \epsilon_{\hat{0}ijk}$.

The real, symmetric matrices, $\mathcal{E}_{ij}$ and $\mathcal{B}_{ij}$ are completely characterized by their orthogonal eigenvectors and corresponding eigenvalues. Note that, since each tensor is traceless, the sum of its three eigenvalues must vanish. Our program for generating field lines to visualize the spacetime curvature is to find these eigenvector fields by solving the eigenvalue problem,

$$\mathcal{E}^i{}_j v^j = \lambda v^i \, . \tag{5.2}$$

This results in three eigenvector fields for each of the two tensors $\boldsymbol{\mathcal{E}}$ and $\boldsymbol{\mathcal{B}}$. These fields are vector

fields on the spatial slice, and behave as usual under transformations of the spatial coordinates (but not changes of the slicing vector u^μ). By integrating the streamlines of these eigenvector fields, we arrive at a set of three *tendex* lines and three *vortex* lines. These lines are associated with the corresponding eigenvalues, the *tendicity* of each tendex line and *vorticity* of each vortex line. In visualizations, we color code each tendex or vortex line by its tendicity or vorticity.

This method of visualization represents physical information about the spacetime in a very natural way. It was shown in Paper I that the tidal field $\boldsymbol{\mathcal{E}}$ describes the local tidal forces between nearby points in the spacetime, and the less-familiar frame-drag field $\boldsymbol{\mathcal{B}}$ describes the relative precession of nearby gyroscopes. In the local Lorentz frame of two freely falling observers, separated by a spatial vector ξ^j, the differential acceleration experienced by the observers is

$$\Delta a^i = -\mathcal{E}^i{}_j \xi^j \,. \tag{5.3a}$$

If these same observers carry inertial guidance gyroscopes, each will measure the gyroscope of the other to precess (relative to her own) with a vectorial angular velocity dictated by $\boldsymbol{\mathcal{B}}$,

$$\Delta\Omega^i = \mathcal{B}^i{}_j \xi^j \,. \tag{5.3b}$$

In particular, note that if one observer measures a clockwise precession of the other observer's gyroscope, the second observer will also measure the precession of the first to be clockwise.

The physical meaning of the tendex and vortex lines is then clear: if two observers have a small separation along a tendex line, they experience an acceleration along that line with a magnitude (and sign, in the sense of being pushed together or pulled apart) given by the value of the tendicity of that line, as governed by Eqs. (5.3a) and (5.2). In the same way, two observers separated along a vortex line experience differential frame dragging as dictated by Eqs. (5.3b) and (5.2) (with $\mathcal{E}_{ij} \to \mathcal{B}_{ij}$).

5.3 Black-Hole Horizons; The Horizon Tendicity $\mathcal{E}_{NN}$ and Vorticity $\mathcal{B}_{NN}$

In many problems of physical interest, such as black-hole perturbations and numerical-relativity simulations using excision (as in the `SpEC` code [7]), black-hole interiors are not included in the solution domain. However, we are interested in structures defined on spacelike surfaces that penetrate the horizon, and, in order to retain the information describing the dynamics of spacetime in and near the black-hole region, we must define quasilocal quantities representing the tendicity and vorticity of the excised black-hole region.

We define the horizon tendicity and vorticity as follows: For a hypersurface-normal observer

with 4-velocity $\vec{u}$, passing through a worldtube such as an event horizon or a dynamical horizon, the worldtube has an inward pointing normal $\vec{N}$ orthogonal to $\vec{u}$, and two orthonormal vectors tangent to its surface, $\vec{e}_2$ and $\vec{e}_3$ (together these four vectors form an orthonormal tetrad). The horizon tendicity is defined as $\mathcal{E}_{NN} = \mathcal{E}_{ij}N^iN^j$ and the horizon vorticity is $\mathcal{B}_{NN} = \mathcal{B}_{ij}N^iN^j$. Physically, they represent the differential acceleration and differential precession of gyroscopes, respectively, as measured by the observer, for two points separated in the direction of $\vec{N}$, and projected along that direction.

The horizon tendicity and vorticity have several interesting connections with other geometric quantities of 2-surfaces. In particular, they fit nicely into the Newman-Penrose (NP) formalism [8]. Rather than describe spacetime in terms of the tetrad $\vec{u}$, $\vec{N}$, $\vec{e}_2$ and $\vec{e}_3$, the NP approach describes spacetime in terms of a null tetrad, with two null vectors $\vec{l}$, and $\vec{n}$, together with a complex spatial vector $\vec{m}$ and its complex conjugate $\vec{m}^*$. It is convenient to adapt this tetrad to the 2-surface so that it is given by

$$\vec{l} = \frac{1}{\sqrt{2}}(\vec{u} - \vec{N})\,, \quad \vec{n} = \frac{1}{\sqrt{2}}(\vec{u} + \vec{N})\,, \quad \vec{m} = \frac{1}{\sqrt{2}}(\vec{e}_2 + i\vec{e}_3)\,. \tag{5.4}$$

On an event horizon, $\vec{l}$ is tangent to the generators of the horizon and $\vec{n}$ is the ingoing null normal. It is not difficult to show that in this tetrad the complex Weyl scalar Ψ_2 is given by

$$\Psi_2 = C_{lmm^*n} = (\mathcal{E}_{NN} + i\mathcal{B}_{NN})/2\,, \tag{5.5}$$

where C_{lmm^*n} is the Weyl tensor contracted into the four different null vectors of the tetrad in the order of the indices.

Penrose and Rindler [9] relate the NP quantities to curvature scalars of a spacelike 2-surface in spacetime. In turn, we can then connect their results to the horizon tendicity and vorticity. More specifically: Penrose and Rindler define a complex curvature of a 2-surface that equals

$$\mathcal{K} = \frac{1}{4}\left(\mathcal{R} + i\mathcal{X}\right)\,. \tag{5.6}$$

Here $\mathcal{R}$ is the intrinsic Ricci curvature scalar of a the 2D horizon and $\mathcal{X}$ is a scalar extrinsic curvature (a curvature of the bundle of vector spaces normal to the two-surface in spacetime). This extrinsic curvature $\mathcal{X}$ is related to the Hájíček field [10] $\Omega_A = n^\mu \nabla_A l_\mu$ (where ∇_A denotes the covariant derivative projected into the 2D horizon) by $\mathcal{X} = \epsilon^{AB}\nabla_A\Omega_B$, where ϵ^{AB} is the antisymmetric tensor of the 2D horizon. In the language of differential forms, $\mathcal{X}$ is the dual of the exterior derivative of the Hájíček 1-form.

Penrose and Rindler [9] show that for a general, possibly dynamical black hole,

$$\mathcal{K} = -\Psi_2 + \mu\rho - \lambda\sigma\,, \tag{5.7}$$

where ρ, σ, μ, and λ are spin coefficients related to the expansion and shear of the null vectors $\vec{l}$ and $\vec{n}$, respectively. This means that the horizon tendicity and vorticity are given by

$$\mathcal{E}_{NN} = -\mathcal{R}/2 + 2\Re[\mu\rho - \lambda\sigma]\,, \tag{5.8a}$$

$$\mathcal{B}_{NN} = -\mathcal{X}/2 + 2\Im[\mu\rho - \lambda\sigma]\,. \tag{5.8b}$$

In the limit of a stationary black hole (this paper), ρ and σ vanish, so

$$\mathcal{E}_{NN} = -\mathcal{R}/2\,, \quad \text{and} \quad \mathcal{B}_{NN} = -\mathcal{X}/2\,. \tag{5.9}$$

The 2D horizon of a stationary black hole has spherical topology, and the Gauss-Bonnet theorem requires that the integral of the scalar curvature $\mathcal{R}$ over a spherical surface is 8π; accounting for factors of two, the integral of the horizon tendicity $\mathcal{E}_{NN}$ over the horizon is -4π (the average value of the horizon tendicity will be negative). Stokes's theorem states that the integral of an exact form such as $\mathcal{X}$ vanishes on a surface of spherical topology, and the horizon vorticity will also have zero average. In formulae:

$$\oint \mathcal{E}_{NN} dA = -4\pi\,, \quad \oint B_{NN} dA = 0 \tag{5.10}$$

for the horizon of a stationary black hole.

It is worth noting a few other examples in the literature where the complex curvature quantities (and as such, horizon tendicity and vorticity) have been used. The most common use of horizon vorticity (in a disguised form) is for computing the spin angular momentum associated with a quasilocal black-hole horizon. Following Refs. [11, 12, 13], it has become common to compute black hole spin in numerical-relativity simulations using the following integral over the horizon:

$$J = -\frac{1}{8\pi} \oint K_{ij} N^i \varphi^j dA, \tag{5.11}$$

where K_{ij} is the extrinsic curvature of the spatial slice embedded in spacetime, $\vec{N}$ is the inward-pointing unit normal vector to the horizon in the spatial slice, and $\vec{\varphi}$ is a rotation-generating vector field tangent to the two-dimensional horizon surface. If $\vec{\varphi}$ is a Killing vector, then one can show that J is conserved. In Ref. [14], this was applied to binary-black-hole simulations with $\vec{\varphi}$ given as a certain kind of approximate Killing vector that can be computed even on a deformed two-surface. In Ref. [15], and independently in Refs. [16, 17], this idea was refined. The quantity J can be

shown to be *boost invariant* (independent of boosts of the spatial slice in the direction of $\vec{N}$) if $\vec{\varphi}$ is divergence-free. Hence, in Refs. [15, 16, 17], $\vec{\varphi}$ is restricted to have the form $\varphi^A = \epsilon^{AB}\nabla_B\zeta$, where ζ is some scalar quantity on the two-surface (eventually fixed by a minimization problem for other components of the Killing equation). Once this substitution has been made, an integration by parts allows J to be written as:

$$J = \frac{1}{8\pi}\oint \mathcal{X}\zeta dA. \tag{5.12}$$

The quantity ζ is fixed by a certain eigenvalue problem on the horizon 2-surface. On a round 2-sphere, the operator in this eigenproblem reduces to the conventional Laplacian, and ζ can be shown to reduce to an $\ell = 1$ spherical harmonic. Thus the quasilocal black-hole spin defined in Refs. [15, 16, 17] can be thought of as the dipole part of the horizon vorticity.

There are simpler ways that one can distill a measure of black hole spin from the concepts of horizon vorticity and tendicity. In Ref. [17], an alternative measure of spin was made by comparing the maximum and minimum values of the horizon scalar curvature to formulae for a Kerr black hole. This method has roots in older techniques by which spin is inferred from the horizon's intrinsic geometry through measurements of geodesic path length (see, for example, Refs. [18, 19, 20]). The method of computing spin by comparing horizon curvature extrema to Kerr formulae could be extended to use the extrinsic scalar curvature, or the horizon vorticity or tendicity (which differ from the scalar curvatures in dynamical situations). While such methods have the benefit of relative simplicity, their practical value in numerical relativity is weakened by an empirical sensitivity of the inferred spin to effects such as "junk" radiation and black hole tides [17, 21].

In Ref. [22], it was shown that higher spherical-harmonic components of these horizon quantities provide natural definitions of *source multipoles* on axisymmetric isolated horizons. In Refs. [23] and [24], this formalism was extended to less symmetric cases for use with numerical-relativity simulations, while attempting to introduce as little gauge ambiguity as possible in the process. Related applications of this formalism can be found in Refs. [25, 26].

5.4 Schwarzschild Black Hole

In this section, we examine vortex and tendex lines for a non-rotating black hole with mass M. These lines, of course, depend on our choice of time slicing. As in the numerical simulations that are the focus of Paper IV, so also here, we shall use a slicing that penetrates smoothly through the black hole's horizon. The slices of constant Schwarzschild time t for the hole's Schwarzschild metric

$$ds^2 = -(1-2M/r)dt^2 + \frac{dr^2}{1-2M/r} + r^2 d\theta^2 + r^2\sin^2\theta d\phi^2 \tag{5.13}$$

do not penetrate the horizon smoothly; rather, they become singular as they approach the horizon. (Dennison and Baumgarte [4] compute the tidal and frame-drag fields of a Schwarzschild black hole in a slice of constant Schwarzschild time and in isotropic coordinates; see their paper for comparison.)

The simplest horizon-penetrating slices are those of constant ingoing Eddington-Finkelstein (EF) time

$$\tilde{t} = t + 2M \ln |r/2M - 1| \, . \tag{5.14}$$

The Schwarzschild metric (5.13), rewritten using EF coordinates $\{\tilde{t}, r, \theta, \phi\}$, takes the form

$$ds^2 \;=\; -\left(1 - \frac{2M}{r}\right) d\tilde{t}^2 + \frac{4M}{r} d\tilde{t} dr + \left(1 + \frac{2M}{r}\right) dr^2 + r^2 d\theta^2 + r^2 \sin^2\theta d\phi^2 \, . \tag{5.15}$$

The observers who measure the tidal and frame-drag fields that lie in a slice of constant $\tilde{t}$ have 4-velocities $\vec{u} = -\alpha_{\rm EF} \vec{\nabla} \tilde{t}$, where $\alpha_{\rm EF} = 1/\sqrt{1 + 2M/r}$ is the normalizing lapse function. These observers can be regarded as carrying the following orthonormal tetrad for use in their measurements:

$$\vec{u} = \frac{1}{\sqrt{1+2M/r}} \left[\left(1 + \frac{2M}{r}\right) \partial_{\tilde{t}} - \frac{2M}{r} \partial_r \right] , \quad \vec{e}_{\hat{r}} = \frac{1}{\sqrt{1+2M/r}} \partial_r \, , \quad \vec{e}_{\hat{\theta}} = \frac{1}{r} \partial_\theta \, , \quad \vec{e}_{\hat{\phi}} = \frac{1}{r \sin\theta} \partial_\phi \tag{5.16}$$

The nonzero components of the tidal field that they measure using this tetrad are

$$\mathcal{E}_{\hat{r}\hat{r}} = -\frac{2M}{r^3} \, , \quad \mathcal{E}_{\hat{\theta}\hat{\theta}} = \mathcal{E}_{\hat{\phi}\hat{\phi}} = \frac{M}{r^3} \, , \tag{5.17}$$

and the frame-drag field $\mathcal{B}_{\hat{a}\hat{b}}$ vanishes. (See, e.g., Eq. (31.4b) of [27]).

Note that the black hole's tidal field (5.17) has the same form as the Newtonian tidal tensor outside of a spherical source. Since the tidal field is diagonal in this tetrad, its eigenvalues and its unit-normed eigenvectors are

$$\vec{V}_r = \vec{e}_{\hat{r}} \, , \quad \vec{V}_\theta = \vec{e}_{\hat{\theta}} \, , \quad \vec{V}_\phi = \vec{e}_{\hat{\phi}} \, , \tag{5.18}$$

$$\lambda_r = -\frac{2M}{r^3} \, , \quad \lambda_\theta = \frac{M}{r^3} \, , \quad \lambda_\phi = \frac{M}{r^3} \, . \tag{5.19}$$

Because the two transverse eigenvalues λ_θ and λ_ϕ are degenerate, any vector in the transverse vector space spanned by $\vec{e}_{\hat{\theta}}$ and $\vec{e}_{\hat{\phi}}$ is a solution to the eigenvalue problem, and correspondingly, any curve that lies in a sphere of constant r can be regarded as a tendex line. However (as we shall see in the next section), when the black hole is given an arbitrarily small rotation about its polar axis $\theta = 0$, the degeneracy is broken, the non-degenerate transverse eigenvectors become $\vec{e}_{\hat{\theta}}$ and $\vec{e}_{\hat{\phi}}$, and the transverse tendex lines become circles of constant latitude and longitude.

In Figure 5.1, we plot a few of these transverse tendex lines (giving them a blue color corresponding to positive tendicity $\lambda_\theta > 0$ and $\lambda_\phi > 0$), and also a few of the radial tendex lines (colored

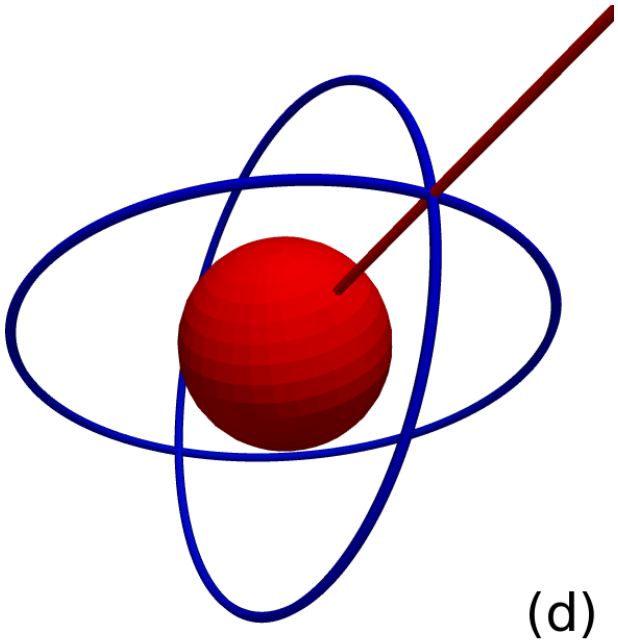

Figure 5.1: Tendex lines for a non-rotating (Schwarzschild) black hole. These lines are identical to those generated by a spherically symmetric mass distribution in the Newtonian limit. Also shown are observers who experience the tidal stretching and compression associated with the tendex lines.

red for negative tendicity $\lambda_r < 0$). Also shown are two human observers, one oriented along a blue tendex line (and therefore being squeezed by the tidal field) the other oriented along a red tendex line (and therefore being stretched).

5.5 Slowly Rotating Black Hole

5.5.1 Slicing and coordinates

When the black hole is given a slow rotation with angular momentum per unit mass a, its metric (5.13) in Schwarzschild coordinates acquires an off-diagonal $g_{t\phi}$ term:

$$ds^2 = -(1-2M/r)dt^2 + \frac{dr^2}{1-2M/r} + r^2 d\theta^2 + r^2 \sin^2\theta d\phi^2 - \frac{4aM}{r}\sin^2\theta dt d\phi \qquad (5.20)$$

[the Kerr metric in Boyer-Lindquist coordinates, Eq. (5.29) below, linearized in a]. The slices of constant EF time $\tilde{t} = t + 2M\ln|r/2M - 1|$ are still smoothly horizon penetrating, but the dragging of inertial frames (the off-diagonal $g_{t\phi}$ term in the metric) causes the Schwarzschild ϕ coordinate to become singular at the horizon. To fix this, we must "unwrap" ϕ, e.g., by switching to

$$\tilde{\phi} = \phi + (a/2M)\ln|1 - 2M/r| \,, \qquad (5.21)$$

thereby bringing the "slow-Kerr" metric (5.20) into the form

$$ds^2 = -\left(1-\frac{2M}{r}\right)d\tilde{t}^2 + \frac{4M}{r}d\tilde{t}dr + \left(1+\frac{2M}{r}\right)dr^2 + r^2d\theta^2 + r^2\sin^2\theta d\tilde{\phi}^2 - \frac{4aM}{r}\sin^2\theta d\tilde{t}d\tilde{\phi} \\ -2a\sqrt{1+2M/r}\sin^2\theta dr d\tilde{\phi} \tag{5.22}$$

[Eq. (5.46) below, linearized in a], which is well behaved at and through the horizon. The observers who move orthogonally to the slices of constant $\tilde{t}$ have 4-velocity $\vec{u}$ and orthonormal basis the same as for a non-rotating black hole, Eq. (5.16), except that $\vec{e}_{\hat{r}}$ is changed to

$$\vec{e}_{\hat{r}} = \frac{1}{\sqrt{1+2M/r}}\left[\partial_r + \frac{a}{r^2}(1+2M/r)\partial_{\tilde{\phi}}\right] \tag{5.23}$$

[Eq. (5.47) below, linearized in a].

5.5.2 Frame-drag field and deformed tendex lines

The slow rotation gives rise to a frame-drag field

$$\mathcal{B}_{\tilde{r}\tilde{r}} = \frac{-6aM\cos\theta}{r^4}\,, \quad \mathcal{B}_{\tilde{r}\tilde{\theta}} = \mathcal{B}_{\tilde{\theta}\tilde{r}} = \frac{-3aM\sin\theta}{r^4\sqrt{1+2M/r}}\,, \quad \mathcal{B}_{\tilde{\theta}\tilde{\theta}} = \mathcal{B}_{\tilde{\phi}\tilde{\phi}} = \frac{3aM\cos\theta}{r^4} \tag{5.24}$$

[Eq. (5.41b) linearized in a/M] that lives in the slices of constant EF time $\tilde{t}$. This field's vortex lines, shown in Fig. 5.2b, are poloidal and closely resemble those of a spinning point mass (a "current dipole") in the linearized approximation to general relativity (Fig. 3 of Paper I [2] or Chapter 3). At radii $r \gg M$, the field asymptotes to that of a linearized current dipole.

The rotating hole's horizon vorticity is $\mathcal{B}_{NN} = \mathcal{B}_{\hat{r}\hat{r}} = -6(aM/r^4)\cos\theta$, which is negative in the north polar regions and positive in the south polar regions. Correspondingly, there is a counterclockwise frame-drag vortex sticking out of the hole's north pole, and a clockwise one sticking out if its south pole. We identify the edge of each vortex, at radius r, as the location where the vorticities of the vortex lines that emerge from the hole at the base of the vortex, fall (as a function of θ at fixed r) to 90% of the on-pole vorticity. The vortex edges are shown, in Fig. 5.2, as semi-transparent surfaces; for comparison we also show where the vorticity has fallen to 85% and 80% of the on-pole vorticity at a given radius r.

The hole's (small) spin not only generates a frame-drag field $\mathcal{B}_{ij}$; it also modifies, slightly, the hole's tidal field $\mathcal{E}_{ij}$ and its tendex lines. However, the spin does not modify the field's tendicities, which (to first order in a/M) remain $\lambda^{\mathcal{E}}_r = -2M/r^3$, $\lambda^{\mathcal{E}}_\theta = \lambda^{\mathcal{E}}_\phi = M/r^3$ [Eq. (5.19)]. The modified unit tangent vectors to the tendex lines are

$$\vec{V}^{\mathcal{E}}_r = \vec{e}_{\hat{r}} - \frac{2Ma\sin\theta}{r^2\sqrt{1+2M/r}}\vec{e}_{\hat{\tilde{\phi}}}\,, \quad \vec{V}^{\mathcal{E}}_{\tilde{\phi}} = \vec{e}_{\hat{\tilde{\phi}}} + \frac{2Ma\sin\theta}{r^2\sqrt{1+2M/r}}\vec{e}_{\hat{r}}\,, \quad \vec{V}^{\mathcal{E}}_{\tilde{\theta}} = \vec{e}_{\hat{\tilde{\theta}}}\,. \tag{5.25}$$

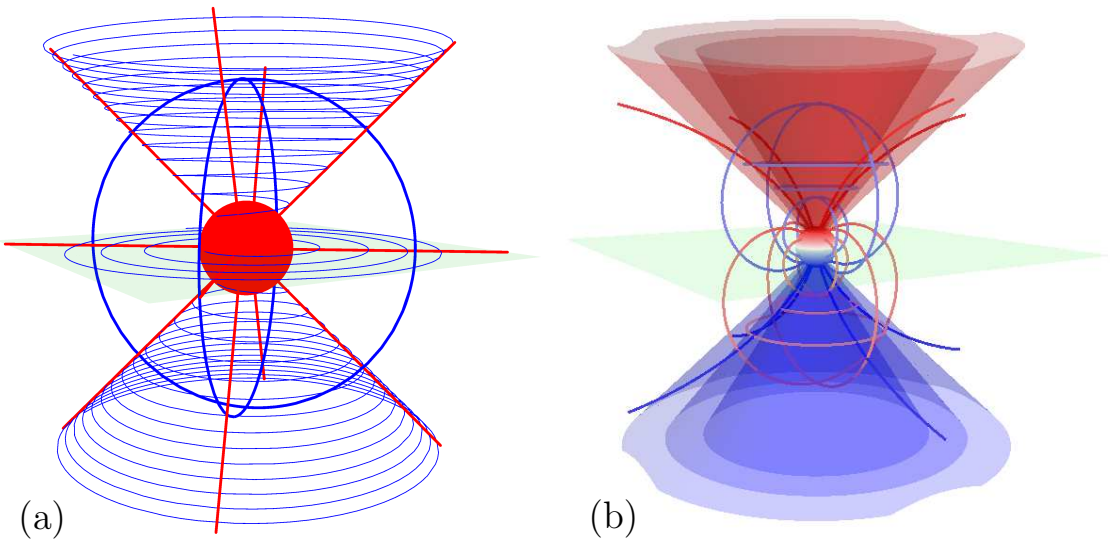

Figure 5.2: (a) Tendex lines, and (b) vortex lines for a slowly rotating (Kerr) black hole. Here we take $a/M = 0.1$. The horizon is color coded by its tendicity $\mathcal{E}_{NN}$ in (a) (uniformly red signifying negative tendicity) and vorticity $\mathcal{B}_{NN}$ in (b), and the field lines are color coded by the sign of their tendicity or vorticity (blue for positive, red for negative). That is, the radial tendex lines, the vortex lines emerging from the north pole and the azimuthal vortex lines on the bottom carry negative tendicity or vorticity, while all other lines have positive tendicity or vorticity.) In (a), the spiraling lines have been made to spiral more loosely by multiplying the rate of change in the r direction by five. The semi-transparent cone-like surfaces emerging from the horizon's north and south polar regions show where the magnitude of the vorticity at a given radius has fallen to 80% (outermost cones), 85%, and 90% (innermost cones) of the polar magnitude. We identify the innermost cone (the 90% contour) as the edge of the frame-drag vortex. The equatorial plane is shown for reference in both panels.

Correspondingly, there is a slight (though hardly noticeable) bending of the radial tendex lines near the black hole, and—more importantly—the azimuthal tendex lines (the ones tangent to $\vec{V}^{\mathcal{E}}_{\hat{\phi}}$) cease to close. Instead, the azimuthal tendex lines spiral outward along cones of fixed θ, as shown in Fig. 5.2a. Since these lines have been only slightly perturbed from closed loops, they spiral quite tightly, appearing as solid cones. In order to better visualize these spiraling lines, we have increased their outward (r directed) rate of change by a factor of five as compared to the axial rate of change in Fig. 5.2a.

5.5.3 Robustness of frame-drag field and tendex-line spiral

The two new features induced by the hole's small spin (the frame-drag field, and the spiraling of the azimuthal tendex lines) are, in fact, robust under changes of slicing. We elucidate the robustness of the tendex spiral in Appendix 5.10. We here elucidate the robustness of the frame-drag field and its vortex lines and vorticities:

Suppose that we change the time function $\tilde{t}$, which defines our time slices, by a small fractional amount of order a/M; i.e., we introduce a new time function

$$t' = \tilde{t} + \xi(r, \theta) \ , \tag{5.26}$$

where $\tilde{t}$ is EF time and ξ has been chosen axisymmetric and time-independent, so it respects the symmetries of the black hole's spacetime. Then "primed" observers who move orthogonal to slices of constant t' will be seen by the EF observers (who move orthogonal to slices of constant $\tilde{t}$) to have small 3-velocities that are poloidal, $\mathbf{v} = v^{\hat{r}}\mathbf{e}_{\hat{r}} + v^{\hat{\theta}}\mathbf{e}_{\hat{\theta}}$. The Lorentz transformation from the EF reference frame to the primed reference frame at some event in spacetime induces a change of the frame-drag field given by

$$\delta\boldsymbol{\mathcal{B}} = -2(\mathbf{v} \times \boldsymbol{\mathcal{E}})^S \tag{5.27}$$

[see, e.g., Eq. (B12) of [28], linearized in small $\mathbf{v}$], where the S means symmetrize. Inserting the EF tidal field (5.17) and the poloidal components of $\mathbf{v}$, we obtain as the only nonzero components of $\delta\mathcal{B}$

$$\delta\mathcal{B}_{\hat{r}\hat{\phi}\hat{}\hat{}} = \delta\mathcal{B}_{\hat{}\hat{}\hat{\phi}\hat{r}} = -(3M/r^3)v^{\hat{\theta}} \ . \tag{5.28}$$

This axisymmetric, slicing-induced change of the frame-drag field does not alter the nonzero components of the frame-drag field in Eq. (5.24); it only introduces a change in the component $\mathcal{B}_{\hat{r}\hat{\phi}\hat{}\hat{}}$. This is a sense in which we mean the frame-drag field is robust. A simple calculation can show that one vorticity is unchanged, $\mathcal{B}_{\hat{\phi}\hat{\phi}} = 3aM\cos\theta/r^4$, but the corresponding vortex line will no longer be a circle of constant (r, θ). Instead, it will wind on a sphere of constant r relative to these closed azimuthal circles with an angle whose tangent is given by $v^{\hat{\theta}}\csc\theta\sqrt{r^2 + 2Mr}$. The poloidal vortex lines must twist azimuthally to remain orthogonal to these spiralling azimuthal lines, as well.

Although we will not see this specific kind of spiraling vortex lines in the next section on rapidly rotating Kerr black holes, we will see a different spiraling of the azimuthal vortex lines: spiraling on cones of constant θ. We describe the reason for this in Appendix 5.10.

5.6 Rapidly Rotating (Kerr) Black Hole

We shall now explore a rapidly rotating black hole described by the precise Kerr metric.

5.6.1 Kerr metric in Boyer-Lindquist coordinates

The Kerr metric is usually written in Boyer-Lindquist (BL) coordinates $\{t, r, \theta, \phi\}$, where it takes the form

$$\begin{aligned} ds^2 &= -\left(1 - \frac{2Mr}{\Sigma}\right) dt^2 + \frac{\Sigma}{\Delta} dr^2 + \Sigma d\theta^2 + \frac{\sin^2\theta}{\Sigma} A d\phi^2 \\ &\quad - \frac{4Mar\sin^2\theta}{\Sigma} dt d\phi \,, \\ \Sigma &= r^2 + a^2\cos^2\theta \,, \\ \Delta &= r^2 - 2Mr + a^2 \,, \\ A &= (r^2 + a^2)^2 - a^2\Delta\sin^2\theta \,, \end{aligned} \tag{5.29}$$

Because the slices of constant t are singular at the horizon (and therefore not of much interest to us), we relegate to Appendix 5.8 the details of their tidal and frame-drag fields, and their vortex and tendex lines.

5.6.2 Horizon-penetrating slices

In our study of Kerr black holes, we shall employ two different slicings that penetrate the horizon smoothly: surfaces of constant Kerr-Schild time coordinate $\tilde{t}$, and surfaces of constant Cook-Scheel time coordinate $\bar{t}$. By comparing these two slicings' tendex lines with each other, and also their vortex lines with each other, we shall gain insight into the lines' slicing dependence.

The Kerr-Schild ([29, 30], see also, e.g., Exercise 33.8 of [27]) time coordinate (also sometimes called ingoing-Kerr time) is defined by

$$\tilde{t} = t + r_* - r \,, \quad \text{where } \frac{dr_*}{dr} = \frac{r^2 + a^2}{\Delta} \,. \tag{5.30}$$

The Cook-Scheel [31] time coordinate is

$$\bar{t} = t + \frac{r_+^2 + a^2}{r_+ - r_-} \ln\left|\frac{r - r_+}{r - r_-}\right| = \tilde{t} + 2M \ln\left|\frac{2M}{r - r_-}\right| \,, \tag{5.31}$$

(see Eqs. (19) and (20) of [31]) where r_+ is the value of the Boyer-Lindquist radial coordinate r at the event horizon, and r_- is its value at the (inner) Cauchy horizon:

$$r_\pm = M \pm \sqrt{M^2 - a^2} \,. \tag{5.32}$$

Figure 5.3 shows the relationship between these slicings for a black hole with $a/M = 0.95$. In this figure, horizontal lines are surfaces of constant Kerr-Schild time $\tilde{t}$. Since t, $\bar{t}$ and $\tilde{t}$ differ solely

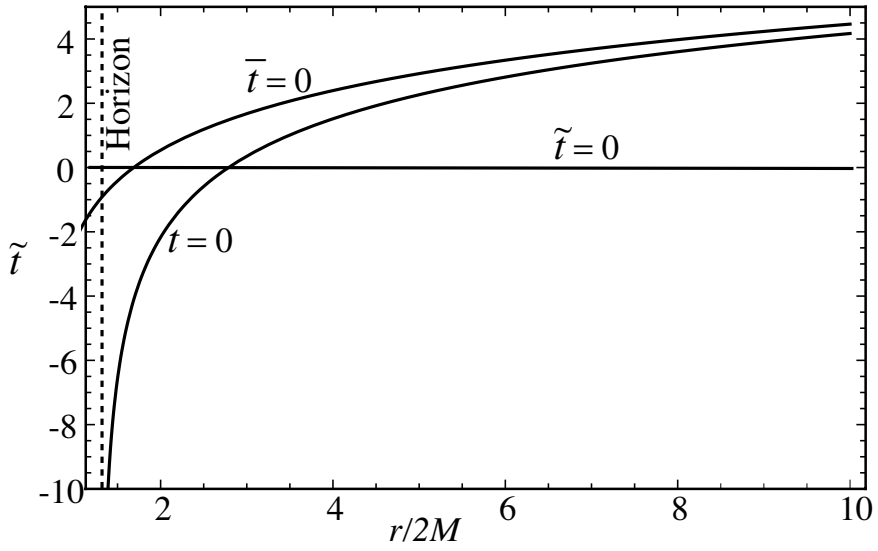

Figure 5.3: Slices of constant Boyer-Lindquist time t, Kerr-Schild time $\tilde{t}$, and Cook-Scheel time $\bar{t}$, drawn in a Kerr-Schild spacetime diagram for a black hole with $a/M = 0.95$.

by functions of r, the surfaces of constant Cook-Scheel time $\bar{t}$ are all parallel to the $\bar{t} = 0$ surface shown in the figure, and the surfaces of constant Boyer-Lindquist time t are all parallel to the $t = 0$ surface. The Kerr-Schild and Cook-Scheel surfaces penetrate the horizon smoothly. By contrast, the Boyer-Lindquist surfaces all asymptote to the horizon in the deep physical past, never crossing it; i.e., they become physically singular at the horizon.

5.6.3 Horizon-penetrating coordinate systems

Not only is the Boyer-Lindquist time coordinate t singular at the event horizon; so is the Boyer-Lindquist azimuthal angular coordinate ϕ. It winds around an infinite number of times as it asymptotes to the horizon. We shall use two different ways to unwind it, associated with two different horizon-penetrating angular coordinates: The ingoing-Kerr coordinate

$$\tilde{\phi} = \phi + \frac{a}{r_+ - r_-} \ln \left| \frac{r - r_+}{r - r_-} \right| = \phi + \int_r^\infty \frac{a}{\Delta} dr \ , \tag{5.33}$$

and the Kerr-Schild coordinate

$$\varphi = \tilde{\phi} - \tan^{-1}(a/r) \ . \tag{5.34}$$

Figure 5.4 shows the relationship of these angular coordinates for a black hole with $a/m = 0.95$. Notice that: (i) all three angular coordinates become asymptotically the same as $r \to \infty$; (ii) the two horizon-penetrating coordinates, ingoing-Kerr $\tilde{\phi}$ and Kerr-Schild φ, differ by less than a radian as

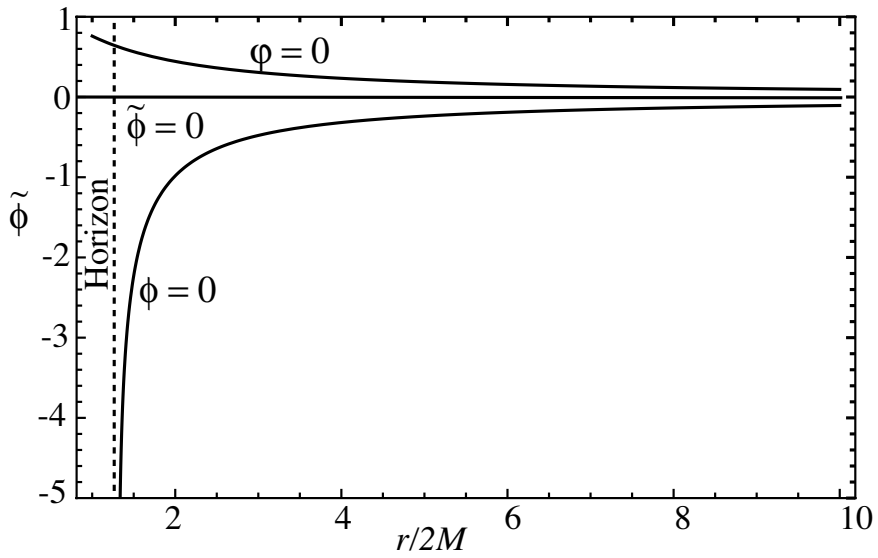

Figure 5.4: Curves of constant Boyer-Lindquist angle ϕ, Kerr-Schild angle φ, and ingoing-Kerr angle $\tilde{\phi}$ for a black hole with $a/M = 0.95$.

one moves inward to the horizon; and (iii) the Boyer-Lindquist coordinate ϕ plunges to $-\infty$ (relative to horizon-penetrating coordinates) as one approaches the horizon, which means it wraps around the horizon an infinite number of times.

In the literature on Kerr black holes, four sets of spacetime coordinates are often used:

- ***Boyer-Lindquist coordinates***, $\{t, r, \theta, \phi\}$. These are the coordinates in Sec. 5.6.1.
- ***Ingoing-Kerr coordinates***, $\{\tilde{t}, r, \theta, \tilde{\phi}\}$. Often in this case $\tilde{t}$ is replaced by a null coordinate, $v = \tilde{t} + r$ (curves $v =$ const, $\theta =$ const, and $\tilde{\phi} =$ const are ingoing null geodesics).
- Quasi-Cartesian ***Kerr-Schild coordinates***, $\{\tilde{t}, x, y, z\}$ and their cylindrical variant $\{\tilde{t}, \varpi, z, \varphi\}$. Here

$$\begin{aligned} x + iy &= (r + ia)e^{i\tilde{\phi}} \sin\theta \ , \quad z = r\cos\theta \ , \\ \varpi &= \sqrt{x^2 + y^2} = \sqrt{r^2 + a^2}\sin^2\theta \ , \\ \varphi &= \arctan(y/x) = \tilde{\phi} + \arctan(a/r) \ . \end{aligned} \tag{5.35}$$

The Kerr-Schild spatial coordinates $\{x, y, z\}$ resemble the coordinates typically used in numerical simulations of binary black holes at late times, when the merged hole is settling down into its final, Kerr state. These coordinate systems resemble each other in the senses that (i) both are quasi-Cartesian, and (ii) for a fast-spinning hole, the event horizon in both cases, when

plotted in the coordinates being used, looks moderately oblate. For this reason, in our study of Kerr black holes, we shall focus our greatest attention on Kerr-Schild coordinates. The Kerr metric, written in Kerr-Schild coordinates, has the form

$$\begin{aligned} ds^2 &= \left(\eta_{\mu\nu} + \frac{2Mr^3}{r^4 + a^2 z^2} k_\mu k_\nu\right) dx^\mu dx^\nu \,, \\ k_\mu &= \left(1, \frac{rx + ay}{r^2 + a^2}, \frac{ry - ax}{r^2 + a^2}, \frac{z}{r}\right) \,, \end{aligned} \tag{5.36}$$

where r is the Boyer-Lindquist radial coordinate, and is the larger root of

$$x^2 + y^2 + z^2 = r^2 + a^2 \left(1 - \frac{z^2}{r^2}\right) \,, \tag{5.37}$$

and $\eta_{\mu\nu}$ is the usual flat Minkowski metric.

- ***Cook-Scheel harmonic coordinates*** [31], $\{\bar{t}, \bar{x}, \bar{y}, \bar{z}\}$ where $\bar{t}$ is given by Eq. (5.31), while the spatial coordinates are defined by

$$\bar{x} + i\bar{y} = [r - M + ia]\, e^{i\tilde{\phi}} \sin(\theta) \tag{5.38}$$

$$\bar{z} = [r - M] \cos(\theta) \tag{5.39}$$

These coordinates are harmonic in the sense that the scalar wave operator acting on them vanishes. In these coordinates, the event horizon of a spinning black hole is more oblate than in Kerr-Schild coordinates—and much more oblate for a/M near unity.

5.6.4 Computation of tendex and vortex lines, and their tendicities and vorticities

Below we show pictures of tendex and vortex lines, color coded with their tendicities and vorticities, for our two horizon-penetrating slicings and using our three different sets of spatial coordinates. In all cases we have computed the field lines and their eigenvalues numerically, beginning with analytical formulas for the metric. More specifically, after populating a numerical grid using analytical expressions for the metric, we numerically compute $\mathcal{E}_{ij}$ and $\mathcal{B}_{ij}$, as well as their eigenvalues and eigenvectors. A numerical integrator is then utilized to generate the tendex and vortex lines. Finally, we apply analytical transformations that take these lines to whatever spatial coordinate system we desire.

Although not required for the purpose of generating the figures in the following sections, it is nevertheless possible to find analytical expressions for $\mathcal{E}_{ij}$ and $\mathcal{B}_{ij}$, and subsequently their eigenvalues and eigenvectors. These expressions provide valuable insights into the behavior of the tendex and

vortex lines, and we present such results for the ingoing-Kerr coordinates in Appendix 5.9.

5.6.5 Kerr-Schild slicing: Tendex and vortex lines in several spatial coordinate systems

Once the slicing is chosen, the tidal and frame-drag fields, and also the tendex and vortex lines and their tendicities and vorticities, are all fixed as geometric, coordinate-independent entities that live in a slice. If we could draw an embedding diagram showing the three-dimensional slice isometrically embedded in a higher-dimensional flat space, then we could visualize the tendex and vortex lines without the aid of a coordinate system. However, the human mind cannot comprehend embedding diagrams in such high-dimensional spaces, so we are forced to draw the tendex and vortex lines in some coordinate system for the slice, in a manner that makes the coordinate system look like it is one for flat space.

Such a coordinate-diagram plot of the lines makes them look coordinate dependent—i.e., their shapes depend on the coordinate system used. Nevertheless, the lines themselves are geometrically well-defined, independent of coordinate system, and they map appropriately between them. The visual features of these lines are also qualitatively similar in reasonable coordinate systems.

Figure 5.5 is an important example. It shows the tendex lines (left column of plots) and vortex lines (right column of plots) for a fast-spinning Kerr black hole, with $a = 0.95M$. We have also colored the horizon of the black hole according to its horizon tendicity and vorticity, respectively. In all cases the slicing is Kerr-Schild; i.e., the lines lie in a slice of constant $\tilde{t}$. The three rows of figures are drawn in three different spatial coordinate systems: ingoing-Kerr, Kerr-Schild, and Cook-Scheel.

Notice the following important features of this figure:

- As expected, the qualitative features of the tendex lines are independent of the spatial coordinates. The only noticeable differences from one coordinate system to another are a flattening of the strong-gravity region near the hole as one goes from ingoing-Kerr coordinates (upper row of panels) to Kerr-Schild coordinates (center row of panels) and then a further flattening for Cook-Scheel coordinates (bottom row of panels).

- The azimuthal (toroidal) tendex and vortex lines (those that point predominantly in the $\vec{e}_{\hat{\tilde{\phi}}}$ direction) spiral outward from the horizon along cones of constant θ, as for the tendex lines of a slowly spinning black hole [cf. the form of $\vec{V}_{\hat{\tilde{\phi}}}$ in Eqs. (5.51)]. As we shall discuss in Appendix 5.10, this is a characteristic of a large class of commonly used, horizon-penetrating slicings of spinning black holes.

- All the poloidal tendex and vortex lines have (small) azimuthal ($\tilde{\phi}$) components, which do not show up in this figure; see the $\vec{e}_{\hat{\tilde{\phi}}}$ components of the eigenvectors $\vec{V}^{\mathcal{E}}_r$, $\vec{V}^{\mathcal{E}}_\theta$, $\vec{V}^{\mathcal{B}}_-$ and $\vec{V}^{\mathcal{B}}_+$ in Eqs. (5.51) and (5.52).

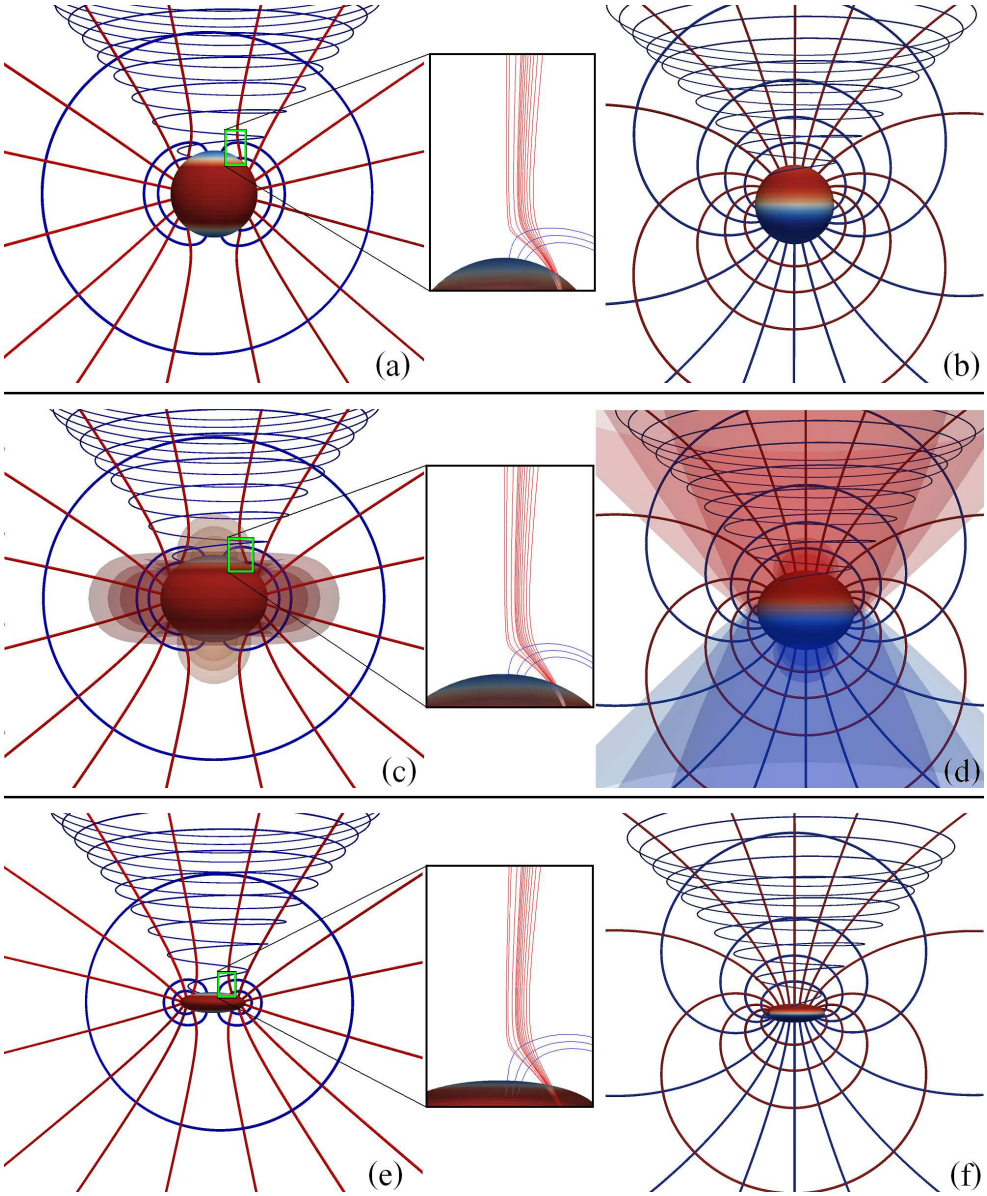

Figure 5.5: Kerr black hole with $a/M = 0.95$ in ***Kerr-Schild slicing***, drawn in three different spatial coordinate systems. The left and center columns of drawings [panels (a), (c), (e)] show tendex lines; the right column of drawings [panels (b), (d), (f)] show vortex lines. The three rows, from top downward, use ingoing-Kerr spatial coordinates $\{r, \theta, \tilde{\phi}\}$ [panels (a) and (b)], Kerr-Schild spatial coordinates $\{x, y, z\}$ [panels (c) and (d)], and Cook-Scheel spatial coordinates $\{\bar{x}, \bar{y}, \bar{z}\}$ [panels (e) and (f)]. In all cases, the lines with positive tendicity or vorticity are colored blue; those with negative tendicity or vorticity are colored red. (The radial tendex lines and vortex lines emerging from the top half of the horizon are red, while all other lines are blue.) The horizon is shown with its horizon tendicity (left column of drawings) and horizon vorticity (right column) color coded from dark blue for strongly positive to dark red for strongly negative. (Horizon tendicity is negative near the equator and positive near the poles. Vorticity on the other hand transitions from being negative on top to positive on the bottom.) In Kerr-Schild coordinates [panels (c) and (d)], we have also shown as semi-transparent surfaces, contours of $\tilde{r}^3$ times tendicity and $\tilde{r}^4$ times vorticity, where $\tilde{r}^2 = x^2 + y^2 + z^2$ for Kerr-Schild spatial coordinates. In panel (c), the innermost equatorial contour has the most negative tendicity while the others have $90\%, 80\%, 30\%, 20\%$, and 10% this value, and the innermost polar contour has the least negative tendicity. In panel (d) the contour with the most negative vorticity consists of the innermost red cone and the outermost red bubble (at the north pole), and the others are at 90% and 80% this value. The blue contours of panel (d) (at the bottom half of that panel) are arranged similarly but with positive vorticity.

- Left column of drawings: For this rapidly spinning black hole, the horizon tendicity is positive (blue) in the north and south polar regions, and negative (red) in the equatorial region, by contrast with a slowly spinning hole, where the horizon tendicity is everywhere negative (Fig. 5.2). Correspondingly, a radially oriented person falling into a polar region of a fast-spinning hole gets *squeezed* from head to foot, rather than stretched, as conventional wisdom demands. The relationship $\mathcal{E}_{NN} = -\mathcal{R}/2$ between the horizon's tendicity and its scalar curvature tells us that this peculiar polar feature results from the well-known fact that, when the spin exceeds $a/M = \sqrt{3}/2 \approx 0.8660$, the scalar curvature goes negative near the poles, at angles θ satisfying $2(a/M)^2 \cos^2\theta > 1 + \sqrt{1-(a/M)^2}$. This negative scalar curvature is also responsible for the fact that is it impossible to embed the horizon's 2-geometry in a 3-dimensional Euclidean space when the spin exceeds $a/M = \sqrt{3}/2$ [32].

- Left column of drawings: The blue (positive tendicity) tendex lines that emerge from the north polar region sweep around the hole, just above the horizon, and descend into the south polar region. In order to stay orthogonal to these blue (squeezing) tendex lines, the red (stretching) lines descending from radial infinity get deflected away from the horizon's polar region until they reach a location with negative tendicity (positive scalar curvature), where they can attach to the horizon; see the central panels, which are enlargements of the north polar region for the left panels.

- Right column of drawings: The vortex-line structure for this fast-spinning black hole is very similar to that for the slow-spinning hole of Fig. 5.2, and similar to that for a spinning point mass in the linear approximation to general relativity (Fig. 3 of Paper I [2], or Chapter 3). The principal obvious change is that the azimuthal vortex lines are not closed; instead, they spiral away from the black hole, like the azimuthal tendex lines.

- Right column of drawings: Most importantly, as for a slow-spinning black hole, there are two vortexes (regions of strong vorticity): as a counterclockwise vortex emerging from the north polar region, and a clockwise vortex emerging from the south polar region. As we shall see in Paper IV, when two spinning black holes collide and merge, these vortexes sweep around, emitting gravitational waves. In Fig. 5.5(d), these vortexes are indicated by contours of $\tilde{r}^4$ times vorticity, where $\tilde{r}^2 = x^2 + y^2 + z^2$ for Kerr-Schild coordinates $\{x, y, z\}$. Notice in particular that each contour consists of one cone together with one bubble attached to the horizon, with the bubbles enclosing the polar regions excluding them from the vortexes. This is a feature not seen for the slow-spinning case.

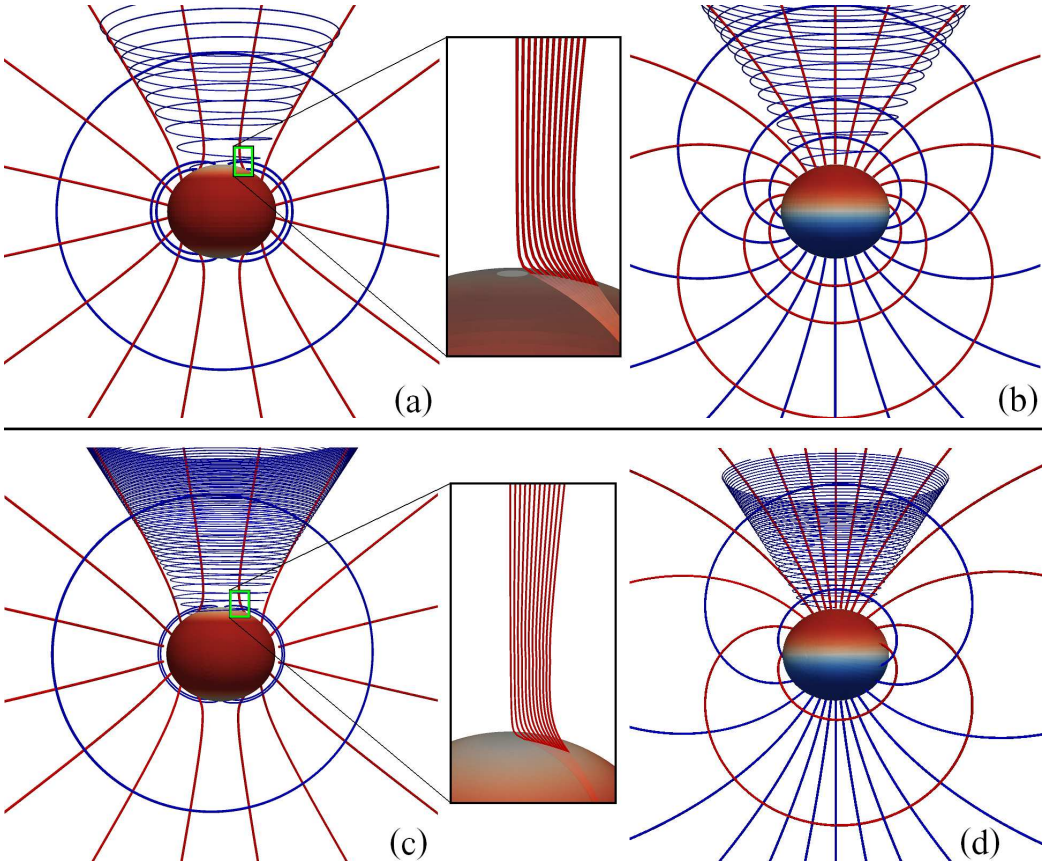

Figure 5.6: Tendex lines and vortex lines for a Kerr black hole with $a/M = 0.875$ in ***Kerr-Schild spatial coordinates***, for two different slicings: ***Kerr-Schild*** $\tilde{t}$ =constant, and ***Cook-Scheel*** $\bar{t}$ =constant. The left and center columns of drawings [panels (a) and (c)] show tendex lines; the right column of drawings [panels (b) and (d)] show vortex lines. The top row of drawings [panels (a) and (b)] is for Kerr-Schild slicing; the bottom row [panels (c) and (d)] is for Cook-Scheel slicing. Since the slicings are different, it is not possible to focus on the same sets of field lines in the Kerr-Schild (upper panels) and Cook-Scheel (lower panels) cases. However, we have attempted to identify similar field lines by ensuring they pass through the same Kerr-Schild spatial coordinate locations on selected surfaces. (The color of the lines and horizon are similar to Fig. 5)

5.6.6 Slicing-dependence of tendex and vortex lines

To explore how a Kerr black hole's vortex and tendex lines depend on the choice of slicing, we focus in Fig. 5.6 on a black hole with $a/M = 0.875$, viewed in a slice of constant Kerr-Schild time, $\tilde{t}$ =constant, and in a slice of constant Cook-Scheel harmonic time, $\bar{t}$ =constant. In the two slices, we use the same spatial coordinates: Kerr-Schild. (We chose $a/M = 0.875$, rather than the 0.95 that we used for exploring spatial coordinate dependence, because it is simpler to handle numerically in the Cook-Scheel slicing.)

The most striking aspect of Fig. 5.6 is the close similarity of the tendex lines (left column of drawings) in the two slicings (upper and lower drawings), and also the close similarity of the vortex lines (right column of drawings) in the two slicings (upper and lower). There appears to be very

little slicing dependence when we restrict ourselves to horizon-penetrating slicings.

By contrast, if we switch from a horizon-penetrating to a horizon-avoiding slice, there are noticeable changes in the field lines: Compare the top row of Fig. 5.6 ($a/M = 0.875$ for a Kerr-Schild, horizon-penetrating slice) with Fig. 5.7 (the same hole, $a/M = 0.875$, for a Boyer-Lindquist, horizon-avoiding slice), concentrating for now on panels (a) and (b) depicting tendex and vortex lines in Boyer-Lindquist spatial coordinates. The most striking differences are (i) the radial tendex lines' failure to reach the horizon for horizon-avoiding slices, contrasted with their plunging through the horizon for horizon-penetrating slices, and (ii) the closed azimuthal tendex and vortex lines for Boyer-Lindquist horizon-avoiding slices, contrasted with the outward spiraling azimuthal lines for horizon-penetrating slices. In Appendix 5.10 we show that this outward spiral is common to a class of horizon-penetrating slices. Lastly, we note that Fig. 5.7 (a) and (b) are plotted using Boyer-Lindquist spatial coordinates in order to compare with analytical expressions given in that appendix. When we use Kerr-Schild spatial coordinates, as is done in Fig. 5.6, in order to facilitate a more appropriate comparison, we observe that the Boyer-Lindquist azimuthal coordinate singularity depicted in Fig. 5.4 causes the tendex and vortex lines in Boyer-Lindquist slicing to wind in ϕ direction when close to horizon. This feature is clearly visible in Fig. 5.7 (c) and (d), where we display the tendex and vortex lines in Kerr-Schild spatial coordinates.

Based on our comparison of Kerr-Schild and Cook-Scheel slicings (Fig. 5.6), and our analysis of the ubiquity of azimuthal spiraling lines in horizon-penetrating slices (Appendix 5.10), we conjecture that horizon-penetrating slicings of any black-hole spacetime will generically share the same qualitative and semi-quantitative structures of tendex and vortex lines. This conjecture is of key importance for our use of tendex and vortex lines to extract intuition into the dynamical processes observed in numerical simulations. More specifically:

Numerical spacetimes have dynamically chosen slicings, and the primary commonality from simulation to simulation is that the time slicing must be horizon penetrating, to prevent coordinate singularities from arising on the numerical grid near the horizon. Our conjecture implies that, regardless of the precise slicing used in a simulation, we expect the tendex and vortex lines to faithfully reveal the underlying physical processes. We will build more support for this conjecture in Paper III, by comparing the final stages of a numerical black-hole merger with a perturbed Kerr black hole, using very different slicing prescriptions.

We conclude this section with a digression from its slicing-dependence focus:

When we compare the $a/M = 0.875$ black hole of Fig. 5.6 with the $a/M = 0.95$ hole of Fig. 5.5, the most striking difference is in the tendex lines very near the horizon. The value $a/M = 0.875$ is only slightly above the critical spin $a/M = \sqrt{3}/2 = 0.8660$ at which the horizon's poles acquire negative scalar curvature. Correspondingly, for $a/M = 0.875$, the blue tendex lines that connect the two poles emerge from a smaller region at the poles than for $a/M = 0.95$, and they hug the horizon

more tightly as they travel from one pole to the other; and the red, radial tendex lines near the poles suffer much smaller deflections than for $a/M = 0.95$ as they descend into the horizon (see insets).

5.7 Conclusion

Using vortex and tendex lines and their vorticities and tendicities, we have visualized the spacetime curvature of stationary black holes. Stationary black-hole spacetimes are a simple arena in which to learn about the properties of these visualization tools in regions of strong spacetime curvature. From the features of the vortex and tendex lines and their vorticities and tendicities that we describe below, we have gained an understanding of these visualization tools and made an important stride toward our larger goal of using these tools to identify geometrodynamical properties of strongly curved spacetimes—particularly those in the merger of binary black holes.

Black hole spacetimes have an event horizon (a feature that was absent in our study of weakly gravitating systems in Paper I). To understand our visualization tools on the horizon, we defined and discussed the *horizon tendicity* and *horizon vorticity* of stationary black holes. The horizon tendicity and vorticity are directly proportional to the intrinsic and extrinsic curvature scalars of a two-dimensional horizon. As a result, the average value of the horizon tendicity must be negative, and the horizon vorticity must average to zero. Any region of large vorticity on the horizon (a horizon vortex), therefore, must be accompanied by an equivalent vortex of the opposite sign, but there is not an analogous constraint for horizon tendexes.

Outside the horizon, we also visualized the tendex lines and vortex lines, the tendicities and vorticities, and the regions of large tendicity (*tendexes*) and large vorticity (*vortexes*) for Schwarzschild and Kerr black holes (the latter both slowly and rapidly spinning). In particular, we investigated how the vortex and tendex lines of Kerr black holes changed when they were drawn in different time slices and with different spatial coordinates—within the set of those time slices that smoothly pass through the horizon and spatial coordinates that are everywhere regular. We found our visualizations are quite similar between two commonly used, though rather different, horizon-penetrating time functions: Kerr-Schild and Cook-Scheel. The spatial-coordinate dependence was also mild, and was easily understandable in terms of the relation between the different coordinate systems. Because the coordinate systems used in numerical simulations of black holes are also horizon penetrating, this suggests that the vortex and tendex lines will not be very different, even though the dynamical coordinates of the simulation may be.

This study is a foundation for future work on computing the tendexes and vortexes of black-hole spacetimes. A recent work by Dennison and Baumgarte [4]—in which the authors calculated the tendex and vortex fields of approximate initial data representing non-spinning, boosted black holes, and also black-hole binaries—will also be helpful for understanding binaries. In addition, our

investigations of the slicing and coordinate dependence of tendexes and vortexes is complemented by another recent study of Dennison and Baumgarte [33], where expressions are given for computing curvature invariants in terms of the vorticities, tendicities, and the eigenvector fields which give the tendex and vortex lines. These expressions will likely be of use in future analytic and numerical studies of tendexes and vortexes.

In a companion paper (Paper III), we turn to perturbed black holes. We aim to deepen our understanding of tendex and vortex lines in these well-understood situations and to see what new insights we can draw from these spacetimes by using vortex and tendex lines. Ultimately, we will apply these visualization techniques and our intuition from simpler analytical spacetimes to study numerical simulations of strongly curved and dynamic spacetimes and their geometrodynamics. In Paper IV, we will do just this, focusing on binary-black-hole mergers.

5.8 Appendix: Kerr Black Hole in Boyer-Lindquist Slicing and Coordinates

For a rapidly rotating Kerr black hole in Boyer-Lindquist (BL) coordinates $\{t, r, \theta, \phi\}$, the metric is given by Eq. (5.29) above. A "BL observer", who moves orthogonally to the slices of constant BL time t, has a 4-velocity $\vec{u}$ and orthonormal tetrad given by

$$\begin{aligned}
\vec{u} &= \sqrt{\frac{A}{\Sigma\Delta}}\left(\partial_t - \frac{2Mar}{A}\partial_\phi\right), & \vec{e}_{\hat{r}} &= \sqrt{\frac{\Delta}{\Sigma}}\partial_r, \\
\vec{e}_{\hat{\theta}} &= \frac{1}{\sqrt{\Sigma}}\partial_\theta, & \vec{e}_{\hat{\phi}} &= \sqrt{\frac{\Sigma}{A}}\frac{1}{\sin\theta}\partial_\phi.
\end{aligned} \tag{5.40}$$

This tetrad is also often called the locally nonrotating frame [34, 35]. In this orthonormal basis, the tidal and frame-drag fields are given by (cf. Eqs. (6.8a-6.9d) of [36])

$$\mathcal{E}_{\hat{a}\hat{b}} = \begin{pmatrix} -Q_e\frac{2+\xi}{1-\xi} & \mu Q_m & 0 \\ * & Q_e\frac{1+2\xi}{1-\xi} & 0 \\ * & * & Q_e \end{pmatrix}, \tag{5.41a}$$

$$\mathcal{B}_{\hat{a}\hat{b}} = \begin{pmatrix} -Q_m\frac{2+\xi}{1-\xi} & -\mu Q_e & 0 \\ * & Q_m\frac{1+2\xi}{1-\xi} & 0 \\ * & * & Q_m \end{pmatrix}, \tag{5.41b}$$

with entries denoted by $*$ fixed by the symmetry of the tensors, and where

$$Q_e = \frac{Mr(r^2 - 3a^2\cos^2\theta)}{\Sigma^3}\,, \tag{5.41c}$$

$$Q_m = \frac{Ma\cos\theta(3r^2 - a^2\cos^2\theta)}{\Sigma^3}\,, \tag{5.41d}$$

$$\xi = \frac{\Delta a^2\sin^2\theta}{(r^2+a^2)^2}\,, \tag{5.41e}$$

$$\mu = \frac{3a\sqrt{\Delta}(r^2+a^2)\sin\theta}{A} = \frac{3\sqrt{\xi}}{1-\xi}\,. \tag{5.41f}$$

The functions Q_e and Q_m are related to the real and imaginary parts of the complex Weyl scalar Ψ_2 calculated using the Kinnersley null tetrad by $\Psi_2 = -Q_e + iQ_m$. Note that there is a duality between the electric and the magnetic curvature tensors: namely, by replacing $Q_e \to Q_m$ and $Q_m \to -Q_e$, the tensor transforms as $\mathcal{E}_{\hat{a}\hat{b}} \to \mathcal{B}_{\hat{a}\hat{b}}$.

The block diagonal forms of $\mathcal{E}_{\hat{a}\hat{b}}$ and $\mathcal{B}_{\hat{a}\hat{b}}$ imply that one of the eigenvectors for each will be $\vec{e}_{\phi}$. When integrated, this gives toroidal tendex and vortex lines (i.e., lines that are azimuthal, closed circles). The other two sets of lines for each tensor are poloidal (i.e., they lie in slices of constant ϕ).

More specifically, the eigenvectors of the tidal field are

$$\begin{aligned}
\vec{V}^{\mathcal{E}}_r &= \frac{(\lambda^{\mathcal{E}}_r - \mathcal{E}_{\hat{\theta}\hat{\theta}})\vec{e}_{\hat{r}} + \mathcal{E}_{\hat{r}\hat{\theta}}\vec{e}_{\hat{\theta}}}{\sqrt{(\lambda^{\mathcal{E}}_r - \mathcal{E}_{\hat{\theta}\hat{\theta}})^2 + (\mathcal{E}_{\hat{r}\hat{\theta}})^2}}\,,\\
\vec{V}^{\mathcal{E}}_\theta &= \frac{(\lambda^{\mathcal{E}}_\theta - \mathcal{E}_{\hat{\theta}\hat{\theta}})\vec{e}_{\hat{r}} + \mathcal{E}_{\hat{r}\hat{\theta}}\vec{e}_{\hat{\theta}}}{\sqrt{(\lambda^{\mathcal{E}}_\theta - \mathcal{E}_{\hat{\theta}\hat{\theta}})^2 + (\mathcal{E}_{\hat{r}\hat{\theta}})^2}}\,,\\
\vec{V}^{\mathcal{E}}_\phi &= \vec{e}_{\hat{\phi}}\,.
\end{aligned} \tag{5.42}$$

The labeling of these eigenvectors is such that, as $a \to 0$, they limit to the corresponding eigenvectors (5.19) of a Schwarzschild black hole. The tendicities (eigenvalues) associated with these three eigenvectors, which appear in the above formulas, are

$$\begin{aligned}
\lambda^{\mathcal{E}}_r &= -\frac{Q_e}{2} - \sqrt{\left(\frac{3Q_e}{2}\right)^2\left(\frac{1+\xi}{1-\xi}\right)^2 + \mu^2 Q_m^2}\,,\\
\lambda^{\mathcal{E}}_\theta &= -\frac{Q_e}{2} + \sqrt{\left(\frac{3Q_e}{2}\right)^2\left(\frac{1+\xi}{1-\xi}\right)^2 + \mu^2 Q_m^2}\,,\\
\lambda^{\mathcal{E}}_\phi &= Q_e\,,
\end{aligned} \tag{5.43}$$

The eigenvectors of the frame-drag field are

$$\begin{aligned}
\vec{V}^{\mathcal{B}}_\pm &= \frac{(\lambda^{\mathcal{B}}_\pm - \mathcal{B}_{\hat{\theta}\hat{\theta}})\vec{e}_{\hat{r}} + \mathcal{B}_{\hat{r}\hat{\theta}}\vec{e}_{\hat{\theta}}}{\sqrt{(\lambda^{\mathcal{B}}_\pm - \mathcal{B}_{\hat{\theta}\hat{\theta}})^2 + (\mathcal{B}_{\hat{r}\hat{\theta}})^2}}\,,\\
\vec{V}^{\mathcal{B}}_\phi &= \vec{e}_{\hat{\phi}}\,.
\end{aligned} \tag{5.44}$$

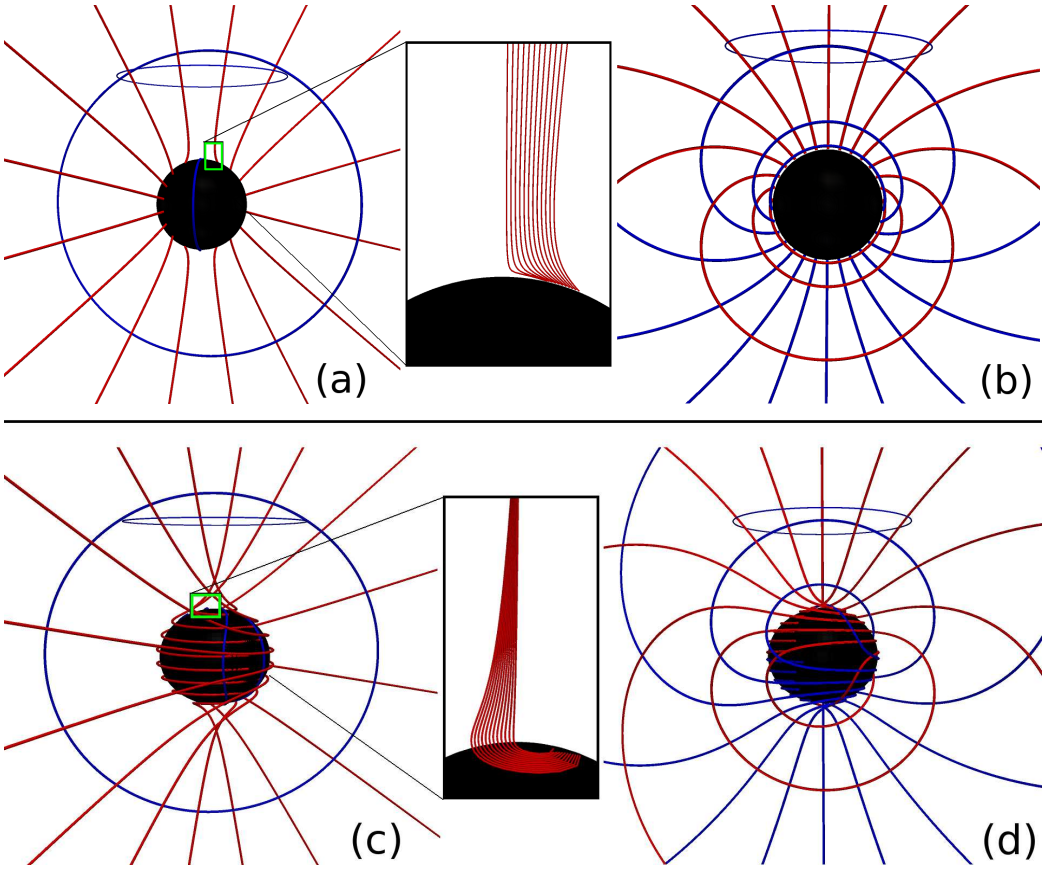

Figure 5.7: (a) Tendex lines for a Kerr black hole with $a/M = 0.875$ on a slice of constant Boyer-Lindquist time t, plotted in ***Boyer-Lindquist spatial coordinates***. The lines with positive tendicity are colored blue and negative are colored red. (b) Vortex lines for this same black hole, slicing and coordinates, with lines of positive vorticity colored blue and negative colored red. (c) and (d) Tendex and vortex lines for the same black hole and same Boyer-Lindquist slicing, but drawn in the ***Kerr-Schild spatial coordinates***. (The color of the lines and horizon are similar to Fig. 5)

Here the labeling + and − of the poloidal eigenvectors corresponds to the signs of their eigenvalues (vorticities). The eigenvalues are

$$\begin{aligned} \lambda^{\mathcal{B}}_{\pm} &= -\frac{Q_m}{2} \pm \sqrt{\left(\frac{3Q_m}{2}\right)^2 \left(\frac{1+\xi}{1-\xi}\right)^2 + \mu^2 Q_e^2}\,, \\ \lambda^{\mathcal{B}}_{\phi} &= Q_m\,. \end{aligned} \tag{5.45}$$

The tendex and vortex lines tangent to the eigenvectors (5.42) and (5.44) are shown in Fig. 5.7 for a rapidly rotating black hole, $a/M = 0.875$. The lines with positive eigenvalues (tendicity or vorticity) are colored blue, and those with negative eigenvalues are colored red. Far from the black hole, the tendex lines resemble those of a Schwarzschild black hole, and the vortex lines resemble those of a slowly spinning hole. However, near the horizon the behavior is quite different. The nearly radial tendex lines in the inset of Fig. 5.7 are bent sharply as they near the horizon, because of the

black hole's spin.

Before closing this appendix, we describe the behavior of the eigenvalues near the poles. From Eqs. (5.43), we see that as $\theta \to 0$ and $\theta \to \pi$, $\lambda^{\mathcal{E}}_{\theta} \to \lambda^{\mathcal{E}}_{\phi}$. Along the polar axis, therefore, the poloidal and axial eigenvectors of $\mathcal{E}_{\hat{a}\hat{b}}$ become degenerate, and any vector in the plane spanned by these directions is also an eigenvector at the axis. Meanwhile, for $\mathcal{B}_{\hat{a}\hat{b}}$, Eqs. (5.45) show that as $\theta \to 0$, $\lambda^{\mathcal{B}}_{+} \to \lambda^{\mathcal{B}}_{\phi}$, and as $\theta \to \pi$, $\lambda^{\mathcal{B}}_{-} \to \lambda^{\mathcal{B}}_{\phi}$. Once again there is a degenerate plane spanned by two eigenvectors at the polar axis. In Paper III, in which we study the tendex and vortex lines of perturbed Kerr black holes, the degenerate regions have a strong influence on the perturbed tendex and vortex lines (see Appendix F of Paper III).

5.9 Appendix: Kerr Black Hole in Kerr-Schild Slicing and Ingoing-Kerr Coordinates

In ingoing-Kerr coordinates $\{\tilde{t}, r, \theta, \tilde{\phi}\}$ [Eqs. (5.30) and (5.33)], the Kerr metric takes the form (see, e.g., Chapter 33 of [27], though we use the Kerr-Schild time $\tilde{t}$ [29, 30], or Eq. (D.4) of [37])

$$\begin{aligned} ds^2 &= -\left(1-\frac{2Mr}{\Sigma}\right)d\tilde{t}^2 + \frac{4Mr}{\Sigma}dr d\tilde{t} - \frac{4Mar\sin^2\theta}{\Sigma}d\tilde{t}d\tilde{\phi} \\ &\quad + H^2 dr^2 + \Sigma d\theta^2 - 2aH\sin^2\theta dr d\tilde{\phi} + \frac{A\sin^2\theta}{\Sigma}d\tilde{\phi}^2\,, \\ H^2 &= 1+\frac{2Mr}{\Sigma}\,, \end{aligned} \tag{5.46}$$

where Σ and A are defined in Eq. (5.29). The 4-velocities of ingoing-Kerr observers, who move orthogonally to slices of constant $\tilde{t}$, and the orthonormal tetrads they carry, are given by

$$\begin{aligned} \vec{u} &= H\partial_{\tilde{t}} - \frac{2Mr}{H\Sigma}\partial_r\,, & \vec{e}_{\hat{r}} &= \frac{\sqrt{A}}{H\Sigma}\partial_r + \frac{aH}{\sqrt{A}}\partial_{\tilde{\phi}}\,, \\ \vec{e}_{\hat{\theta}} &= \frac{1}{\sqrt{\Sigma}}\partial_\theta\,, & \vec{e}_{\hat{\tilde{\phi}}} &= \sqrt{\frac{\Sigma}{A}}\frac{1}{\sin\theta}\partial_{\tilde{\phi}} \end{aligned} \tag{5.47}$$

(see, e.g., [38] or [37]).

The components of the tidal field in this orthonormal basis are

$$\mathcal{E}_{\hat{a}\hat{b}} = \begin{pmatrix} -Q_e\frac{2+\xi}{1-\xi} & Q_m\frac{3a(r^2+a^2)\sin\theta}{H\sqrt{A\Sigma}} & Q_e\frac{6aMr(r^2+a^2)\sin\theta}{HA\sqrt{\Sigma}} \\ * & Q_e\left(1+\frac{3a^2\sin^2\theta}{H^2\Sigma}\right) & -Q_m\frac{6a^2Mr\sin^2\theta}{H^2\Sigma\sqrt{A}} \\ * & * & Q_e\frac{2+\xi}{1-\xi} - Q_e\left(1+\frac{3a^2\sin^2\theta}{H^2\Sigma}\right) \end{pmatrix}, \tag{5.48}$$

where Q_e, Q_m, and ξ are defined in Eqs. (5.41c), (5.41d), and (5.41e). Just as in Boyer-Lindquist slicing and coordinates (Appendix 5.8), so also here, the components $\mathcal{B}_{\hat{a}\hat{b}}$ of the frame-drag field can

be deduced from $\mathcal{E}_{\hat{a}\hat{b}}$ by the duality relation

$$\mathcal{B}_{\hat{a}\hat{b}} = \mathcal{E}_{\hat{a}\hat{b}}|_{Q_e \to Q_m,\, Q_m \to -Q_e} \,. \tag{5.49}$$

The eigenvalues of the tidal field (5.48), i.e. the tendicities, and their corresponding eigenvectors are

$$\begin{aligned}
\lambda^{\mathcal{E}}_r &= -\frac{3\zeta}{2H^2\Sigma} - \frac{Q_e}{2}\,, \\
\lambda^{\mathcal{E}}_\theta &= \frac{3\zeta}{2H^2\Sigma} - \frac{Q_e}{2}\,, \\
\lambda^{\mathcal{E}}_\phi &= Q_e\,, \\
\zeta^2 &= Q_e^2(H^2\Sigma)^2 + \frac{(2Ma\sin\theta)^2 F}{\Sigma^3}\,, \\
F &= r^2 + 2Mr + a^2\,;
\end{aligned} \tag{5.50}$$

$$\begin{aligned}
\vec{V}^{\mathcal{E}}_r &= \frac{1}{v_r}\left(H\sqrt{\Sigma}(r^2+a^2)\vec{e}_{\hat{r}} + \frac{\sqrt{A}}{2Q_m a\sin\theta}\left[Q_e(F + a^2\sin^2\theta) - \zeta\right]\vec{e}_{\hat{\theta}} - 2Mar\sin\theta\vec{e}_{\hat{\tilde{\phi}}}\right), \\
\vec{V}^{\mathcal{E}}_\theta &= \frac{1}{v_\theta}\left(H\sqrt{\Sigma}(r^2+a^2)\vec{e}_{\hat{r}} + \frac{\sqrt{A}}{2Q_m a\sin\theta}\left[Q_e(F + a^2\sin^2\theta) + \zeta\right]\vec{e}_{\hat{\theta}} - 2Mar\sin\theta\vec{e}_{\hat{\tilde{\phi}}}\right), \\
\vec{V}^{\mathcal{E}}_{\tilde{\phi}} &= \frac{1}{v_{\tilde{\phi}}}\left(2Mar\sin\theta\vec{e}_{\hat{r}} + H\sqrt{\Sigma}(r^2+a^2)\vec{e}_{\hat{\phi}}\right).
\end{aligned} \tag{5.51}$$

Here the quantities v_r, v_θ, and $v_{\tilde{\phi}}$ are the norms of the vectors in large parentheses (which give the eigenvectors $\vec{V}^{\mathcal{E}}$ unit norms). As for Boyer-Lindquist slicing, our r, θ, ϕ labels for the eigenvectors and eigenvalues are such that as $a \to 0$, they limit to the corresponding Schwarzschild quantities in Eddington-Finkelstein slicing. Note that although the expressions for $\vec{V}^{\mathcal{E}}_r$ and $\vec{V}^{\mathcal{E}}_\theta$ appear nearly identical, the coefficient of the term in front of $\vec{e}_{\hat{\theta}}$ for $\vec{V}^{\mathcal{E}}_r$ includes $-\zeta$, and that in front of $\vec{e}_{\hat{\theta}}$ for $\vec{V}^{\mathcal{E}}_\theta$ includes $+\zeta$. This seemingly small difference determines whether the eigenvectors are predominantly radial or poloidal. Note also that the limit $a \to 0$ must be taken carefully with the vectors written in this form in order to recover the eigenvectors of a Schwarzschild hole.

As for Boyer-Lindquist slicing, so also here, the eigenvectors and eigenvalues (vorticities) for $\mathcal{B}_{\hat{a}\hat{b}}$ can be derived from those for $\mathcal{E}_{\hat{a}\hat{b}}$ using the Kerr duality relations:

$$\{\vec{V}^{\mathcal{B}}_-, \vec{V}^{\mathcal{B}}_+, \vec{V}^{\mathcal{B}}_{\tilde{\phi}}\} = \{\vec{V}^{\mathcal{E}}_r, \vec{V}^{\mathcal{E}}_\theta, \vec{V}^{\mathcal{E}}_{\tilde{\phi}}\}|_{Q_e \to Q_m,\, Q_m \to -Q_e} \tag{5.52}$$

$$\{\lambda^{\mathcal{B}}_-, \lambda^{\mathcal{B}}_+, \lambda^{\mathcal{B}}_{\tilde{\phi}}\} = \{\lambda^{\mathcal{E}}_r, \lambda^{\mathcal{E}}_\theta, \lambda^{\mathcal{E}}_{\tilde{\phi}}\}|_{Q_e \to Q_m\,, Q_m \to -Q_e} \tag{5.53}$$

As in the case of Boyer-Lindquist slicing, so also for Kerr-Schild slicing, the transverse (nonradial) eigenvectors are degenerate on the polar axis. This can be seen, for example, from the form of $\mathcal{E}_{\hat{a}\hat{b}}$ in Eq. (5.48), or from the corresponding eigenvalues in Eqs. (5.50): as $\sin\theta \to 0$, the matrix becomes

diagonal with two equal eigenvalues, λ_θ and λ_ϕ. This is an inevitable consequence of axisymmetry.

5.10 Appendix: Spiraling Axial Vortex and Tendex Lines for Kerr Black Holes in Horizon-Penetrating Slices

In Figs. 5.5, 5.6, and 5.7, the azimuthal tendex and vortex lines of a Kerr black hole in horizon-avoiding Boyer-Lindquist slices are closed circles, while those in horizon-penetrating Kerr-Schild and Cook-Scheel slices are outward spirals. In this section, we argue that outward spirals are common to a wide class of horizon-penetrating slices, including ingoing-Kerr and Cook-Scheel slicings.

The class of time slices that we will investigate are those that differ from Boyer-Lindquist slices, t, by a function of Boyer-Lindquist r,

$$t' = t + f(r)\,. \tag{5.54}$$

For example, both ingoing Kerr and Cook-Scheel times fall into this category. By computing the normal to a slice of constant t' [when expressed in terms of the locally non-rotating frame of Eq. (5.40)] we find that

$$\vec{u}' = \sqrt{\frac{g^{tt}}{g^{t't'}}}\left(\vec{u} + \sqrt{\frac{g^{rr}}{g^{tt}}}\frac{df(r)}{dr}\vec{e}_{\hat{r}}\right)\,. \tag{5.55}$$

Here g^{tt} and g^{rr} are the contravariant components of the metric in Boyer-Lindquist coordinates, and $g^{t't'}$ are those in coordinates that use t' instead. Defining

$$\gamma = \sqrt{\frac{g^{tt}}{g^{t't'}}}\,, \quad v = \sqrt{\frac{g^{rr}}{g^{tt}}}\frac{df(r)}{dr}\,, \tag{5.56}$$

we can see that the above transformation has the form of a set of local Lorentz transformations between the locally non-rotating frame and the new frame, and that $\gamma^2 = 1/(1-v^2)$. This implies that we can express the timelike normal and the new radial vector as

$$\vec{u}' = \gamma(\vec{u} + v\vec{e}_{\hat{r}})\,, \tag{5.57a}$$

$$\vec{e}_{\hat{r}'} = \gamma(v\vec{u} + \vec{e}_{\hat{r}})\,, \tag{5.57b}$$

and that we need not change the vectors $\vec{e}_{\hat{\theta}}$ and $\vec{e}_{\hat{\phi}}$ in making this transformation.

From the expressions for how the tidal and frame-drag fields transform under changes of slicing (see Appendix B of [28]), we find that we can compute the new components of the tidal field in the transformed slicing and tetrad from the tidal and frame-drag fields in the Boyer-Lindquist slicing and tetrad [Eq. (5.41a) and (5.41b)]. For a change in slicing corresponding to a radial boost, these

general transformation laws simplify to

$$\mathcal{E}_{\hat{r}'\hat{r}'} = \mathcal{E}^{\rm BL}_{\hat{r}\hat{r}}\,, \tag{5.58a}$$

$$\mathcal{E}_{\hat{r}'\hat{A}'} = \gamma(\mathcal{E}^{\rm BL}_{\hat{r}\hat{A}} - v\epsilon_{\hat{A}\hat{r}\hat{C}}\mathcal{B}^{\rm BL}_{\hat{C}\hat{r}})\,, \tag{5.58b}$$

$$\mathcal{E}_{\hat{A}'\hat{B}'} = \gamma^2[(1+v^2)\mathcal{E}^{\rm BL}_{\hat{A}\hat{B}} + v^2\mathcal{E}^{\rm BL}_{\hat{r}\hat{r}}\delta_{\hat{A}\hat{B}} - 2v\epsilon_{\hat{r}\hat{C}(\hat{A}}\mathcal{B}^{\rm BL}_{\hat{B})\hat{C}}]\,, \tag{5.58c}$$

where $\hat{A}$, $\hat{B}$, and $\hat{C} = \hat{\theta}$ and $\hat{\phi}$, and where repeated lowered index $\hat{C}$ is summed over its two values. To understand how $\boldsymbol{\mathcal{B}}$ is transformed, we use the duality $\boldsymbol{\mathcal{E}} \to \boldsymbol{\mathcal{B}}$ and $\boldsymbol{\mathcal{B}} \to -\boldsymbol{\mathcal{E}}$ in the transformation laws (5.58a)–(5.58c).

By substituting the explicit expressions for the Boyer-Lindquist slicing and tetrad tidal fields and the definition of μ in Eq. (5.41f), we see

$$\mathcal{E}_{\hat{a}'\hat{b}'} = \begin{pmatrix} -\left(\frac{2+\xi}{1-\xi}\right)Q_e & \gamma\left(\frac{3\sqrt{\xi}}{1-\xi}\right)Q_m & \gamma v\left(\frac{3\sqrt{\xi}}{1-\xi}\right)Q_e \\ * & \gamma^2\left(\frac{1+2\xi}{1-\xi} - v^2\right)Q_e & -\gamma^2 v\left(\frac{3\xi}{1-\xi}\right)Q_m \\ * & * & \gamma^2\left(1 - v^2\frac{1+2\xi}{1-\xi}\right)Q_e \end{pmatrix}. \tag{5.59}$$

In calculating $\boldsymbol{\mathcal{B}}$, we could again use the duality in Eq. (5.49).

To compute the tendex lines and the tendicity, we express Eq. (5.59) in a new basis given by

$$\vec{e}_{\hat{r}''} = \frac{1}{\sqrt{1+\gamma^2v^2\xi}}(\vec{e}_{\hat{r}'} - \gamma v\sqrt{\xi}\vec{e}_{\hat{\phi}})\,, \tag{5.60a}$$

$$\vec{e}_{\hat{\phi}''} = \frac{1}{\sqrt{1+\gamma^2v^2\xi}}(\gamma v\sqrt{\xi}\vec{e}_{\hat{r}'} + \vec{e}_{\hat{\phi}})\,, \tag{5.60b}$$

and where $\vec{e}_{\hat{\theta}}$ is again unchanged. In this basis, the tidal field becomes block diagonal

$$\mathcal{E}_{\hat{a}''\hat{b}''} = \begin{pmatrix} \gamma^2\left(2v^2 - \frac{2+\xi}{1-\xi}\right)Q_e & \frac{3\gamma\sqrt{\xi(1+\gamma^2v^2\xi)}}{1-\xi}Q_m & 0 \\ * & \gamma^2\left(\frac{1+2\xi}{1-\xi} - v^2\right)Q_e & 0 \\ * & * & Q_e \end{pmatrix}. \tag{5.61}$$

We then see that the tendicities are

$$\lambda_{r''} = -\frac{Q_e}{2} - \frac{3}{2(1-\xi)}\sqrt{[(1+\gamma^2v^2\xi)+\gamma^2\xi]^2Q_e^2 + 4\gamma^2\xi(1+\gamma^2v^2\xi)Q_m^2}\,, \tag{5.62a}$$

$$\lambda_{\theta''} = -\frac{Q_e}{2} + \frac{3}{2(1-\xi)}\sqrt{[(1+\gamma^2v^2\xi)+\gamma^2\xi]^2Q_e^2 + 4\gamma^2\xi(1+\gamma^2v^2\xi)Q_m^2}\,, \tag{5.62b}$$

$$\lambda_{\phi''} = Q_e\,, \tag{5.62c}$$

and the corresponding vectors have an identical form to those in Eq. (5.42), when one replaces the components of the tidal field, the tendicities, and the unit vectors there with the equivalent (primed)

quantities in Eqs. (5.60)–(5.62):

$$\vec{V}_{r''} = \frac{(\lambda_{r''} - \mathcal{E}_{\hat{\theta}''\hat{\theta}''})\vec{e}_{\hat{r}''} + \mathcal{E}_{\hat{r}''\hat{\theta}''}\vec{e}_{\hat{\theta}}}{\sqrt{(\lambda_{r''} - \mathcal{E}_{\hat{\theta}''\hat{\theta}''})^2 + (\mathcal{E}_{\hat{r}''\hat{\theta}''})^2}}\,, \tag{5.63a}$$

$$\vec{V}_{\theta''} = \frac{(\lambda_{\theta''} - \mathcal{E}_{\hat{\theta}''\hat{\theta}''})\vec{e}_{\hat{r}''} + \mathcal{E}_{\hat{r}''\hat{\theta}''}\vec{e}_{\hat{\theta}}}{\sqrt{(\lambda_{\theta''} - \mathcal{E}_{\hat{\theta}''\hat{\theta}''})^2 + (\mathcal{E}_{\hat{r}''\hat{\theta}''})^2}}\,, \tag{5.63b}$$

$$\vec{V}_{\phi''} = \vec{e}_{\hat{\phi}''}\,. \tag{5.63c}$$

From the expressions for the eigenvectors, we can explain several features of the tendex lines in Figs. 5.5, 5.6, and 5.7. When $v = 0$ [i.e., when $f(r) = 0$ and the slicing is given by the horizon-avoiding, Boyer-Lindquist time], the azimuthal lines formed closed loops, and the radial and polar lines live within a plane of constant ϕ. For all other slicings in this family [i.e., $v \neq 0$ and $f(r) \neq 0$], the azimuthal lines pick up a small radial component, and they will spiral outward on a cone of constant θ with a pitch angle whose tangent is proportional to $\gamma v\sqrt{\xi}$; the radial and polar lines will also wind slightly in the azimuthal direction (an effect that is more difficult to see in Figs. 5.5 and 5.6). By duality, an identical result holds for the azimuthal vortex lines of $\boldsymbol{\mathcal{B}}$, and an analogous behavior holds for the poloidal vortex lines (in Boyer-Lindquist slicing, they remain in planes of constant ϕ, but in horizon-penetrating slicings, they twist azimuthally).

For this class of slices, the azimuthal eigenvector of the tidal field changes linearly in the velocity of the boost, but the tendicity along the corresponding tendex line is unchanged. The other eigenvectors also change linearly in the velocity, but their tendicities are quadratic in v; therefore, for small changes in the slicing, the tendicities change more weakly. This result is reminiscent of a similar qualitative result for perturbations of black holes in the next paper of this series: the tendex lines appear to be more slicing dependent than their corresponding tendicities.

In the relatively general class of slicings investigated here, we showed that the generic behavior of the azimuthal lines in horizon-penetrating slices is to spiral outward radially (and the other lines must also wind azimuthally as well). This, however, is not the most general set of slicings that still respect the symmetries of the Kerr spacetime [e.g., those of the form $t' = t + g(r, \theta)$ are]. These slicings will have a θ component to their boost velocities, and (based on the argument for slowly spinning black holes in Sec. 5.5.3), the azimuthal vortex lines will also wind in the polar direction. A more generic, behavior, therefore, would be azimuthal lines that no longer wind on cones of constant θ. Because we were not aware of any simple analytical slicings of this form, we did not investigate here; however, we suspect that this more general behavior of the lines may appear in numerical simulations.

Before concluding, we note that by choosing

$$\gamma = \sqrt{\frac{A}{H^2\Delta\Sigma}}\,, \quad v = \frac{2Mr}{\sqrt{A}}\,, \tag{5.64}$$

we can recover the results given in Appendix 5.9 for the tidal field (and by duality, the frame-drag field). Similarly, if we choose

$$\gamma = \sqrt{\frac{A(r-r_-)}{\Delta[(r-r_-)\Sigma + 2M(r^2+r_+r+r_+^2+a^2)]}}\,, \tag{5.65a}$$

$$v = \frac{r_+^2+a^2}{\sqrt{A}}\,, \tag{5.65b}$$

then we can use Eq. (5.59) to calculate the tidal and frame-drag fields in time-harmonic Cook-Scheel slicing (and its associated tetrad). The expressions were not as simple as those in Appendix 5.9, and for this reason, we do not give them here. Because the velocity in Cook-Scheel slicing falls off more rapidly in radius than that in ingoing-Kerr slicing the azimuthal lines should have a tighter spiral (a feature that we observe in Fig. 5.6).

Bibliography

[1] R. Owen, J. Brink, Y. Chen, J. D. Kaplan, G. Lovelace, K. D. Matthews, D. A. Nichols, M. A. Scheel, F. Zhang, A. Zimmerman, et al., Phys. Rev. Lett. **106**, 151101 (2011).

[2] D. A. Nichols, R. Owen, F. Zhang, A. Zimmerman, J. Brink, Y. Chen, J. Kaplan, G. Lovelace, K. D. Matthews, M. A. Scheel, et al. (2011), `1108.5486`.

[3] A. Zimmerman, D. A. Nichols, and F. Zhang, Phys. Rev. D **84**, 044037 (2011).

[4] K. A. Dennison and T. W. Baumgarte, Phys.Rev. **D86**, 084051 (2012), `1207.2431`.

[5] J. M. Bowen and J. W. York, Jr., Phys. Rev. D **21**, 2047 (1980).

[6] H. Stephani, D. Kramer, M. MacCallum, C. Hoenselaers, and E. Herlt, *Exact solutions of Einstein's field equations* (Cambridge University Press, Cambridge, UK, 2003).

[7] `http://www.black-holes.org/SpEC.html`.

[8] E. Newman and R. Penrose, J. Math. Phys. **3**, 566 (1962), URL `http://link.aip.org/link/?JMP/3/566/1`.

[9] R. Penrose and W. Rindler, *Spinors and Space-time, Volume 1* (Cambridge University Press, Cambridge, 1992).

[10] T. Damour, in *Proceedings of the Second Marcel Grossman Meeting on General Relativity*, edited by R. Ruffini (North-Holland Publishing Company, Amsterdam, 1982), pp. 587–606.

[11] J. D. Brown and J. W. York, Phys. Rev. D **47**, 1407 (1993).

[12] A. Ashtekar, C. Beetle, and J. Lewandowski, Phys. Rev. D **64**, 044016 (2001), `gr-qc/0103026`.

[13] A. Ashtekar and B. Krishnan, Phys. Rev. D **68**, 104030 (2003).

[14] O. Dreyer, B. Krishnan, D. Shoemaker, and E. Schnetter, Phys. Rev. D **67**, 024018 (2003).

[15] G. B. Cook and B. F. Whiting, Phys. Rev. D **76**, 041501(R) (2007).

[16] R. Owen, Ph.D. thesis, California Institute of Technology (2007), URL http://resolver.caltech.edu/CaltechETD:etd-05252007-143511.

[17] G. Lovelace, R. Owen, H. P. Pfeiffer, and T. Chu, Phys. Rev. D **78**, 084017 (2008).

[18] P. Anninos, D. Bernstein, S. R. Brandt, D. Hobill, E. Seidel, and L. Smarr, Phys. Rev. D **50**, 3801 (1994).

[19] S. R. Brandt and E. Seidel, Phys. Rev. D **52**, 870 (1995).

[20] M. Alcubierre, B. Brügmann, P. Diener, F. Guzmán, I. Hawke, S. Hawley, F. Herrmann, M. Koppitz, D. Pollney, E. Seidel, et al., Phys. Rev. D **72**, 044004 (2005).

[21] T. Chu, H. P. Pfeiffer, and M. A. Scheel, Phys. Rev. D **80**, 124051 (2009), 0909.1313.

[22] A. Ashtekar, J. Engle, T. Pawlowski, and C. V. D. Broeck, Class. Quantum Grav. **21**, 2549 (2004).

[23] E. Schnetter, B. Krishnan, and F. Beyer, Phys. Rev. D **74**, 024028 (2006), gr-qc/0604015.

[24] R. Owen, Phys. Rev. D **80**, 084012 (2009).

[25] N. Vasset, J. Novak, and J. L. Jaramillo, Phys. Rev. D **79**, 124010 (2009).

[26] M. Jasiulek, Class. Quantum Grav. **26**, 254008 (2009).

[27] C. W. Misner, K. S. Thorne, and J. A. Wheeler, *Gravitation* (Freeman, New York, New York, 1973).

[28] R. Maartens, prd **58**, 124006 (1998), arXiv:astro-ph/9808235.

[29] R. P. Kerr, Physical Review Letters **11**, 237 (1963).

[30] R. H. Boyer and R. W. Lindquist, Journal of Mathematical Physics **8**, 265 (1967).

[31] G. B. Cook and M. A. Scheel, Phys. Rev. D **56**, 4775 (1997).

[32] L. Smarr, Phys. Rev. D **7**, 289 (1973).

[33] K. A. Dennison and T. W. Baumgarte (2012), 1208.1218.

[34] J. M. Bardeen, Astrophys. J. **162**, 71 (1970).

[35] J. M. Bardeen, W. H. Press, and S. A. Teukolsky, Astrophys. J. **178**, 347 (1972).

[36] K. S. Thorne, R. H. Price, and D. A. MacDonald, *Black Holes: The Membrane Paradigm* (Yale University Press, New Haven and London, 1986).

[37] E. Gourgoulhon and J. L. Jaramillo, Phys. Rep. **423**, 159 (2006), gr-qc/0503113.

[38] A. R. King, J. P. Lasota, and W. Kundt, Phys. Rev. D **12**, 3037 (1975).

Chapter 6

Frame-Drag Vortexes and Tidal Tendexes IV. Quasinormal Pulsations of Schwarzschild and Kerr Black Holes

---

Originally published as

David A. Nichols, Aaron Zimmerman, Yanbei Chen, Geoffrey Lovelace, Keith D. Matthews, Robert Owen, Fan Zhang, Kip S. Thorne

Phys. Rev. D 86, 104028 (2012)

6.1 Motivations, Foundations and Overview

6.1.1 Motivations

This is the third in a series of papers that introduce a new set of tools for visualizing the Weyl curvature tensor (which, in vacuum, is the same as the Riemann tensor), and that develop, explore, and exploit these tools.

We gave a brief overview of these new tools and their applications in an initial Physical Review Letter [1] (i.e. Chapter 1.2). Our principal motivation for these tools was described in that Letter, and in greater detail in Sec. I of our first long, pedagogical paper [2] (Paper I or Chapter 3). In brief: We are motivated by the quest to understand *the nonlinear dynamics of curved spacetime* (what John Wheeler has called *geometrodynamics*).

The most promising venue, today, for probing geometrodynamics is numerical simulations of the

collisions and mergers of binary black holes [3]. Our new tools provide powerful ways to visualize the results of those simulations. As a byproduct, our visualizations may motivate new ways to compute the gravitational waveforms emitted in black-hole mergers—waveforms that are needed as templates in LIGO's searches for and interpretation of those waves.

We will apply our tools to black-hole binaries in Paper IV of this series. But first, in Papers I–III, we are applying our tools to analytically understood spacetimes, with two goals: (i) to gain intuition into the relationships between our tools' visual pictures of the vacuum Riemann tensor and the analytics, and (ii) to gain substantial new insights into phenomena that were long thought to be well understood. Specifically, in Paper I [2] (i.e. Chapter 3), after introducing our tools, we applied them to weak-gravity situations ("linearized theory"); in Paper II [4] (i.e. Chapter 5), we applied them to stationary (Schwarzschild and Kerr) black holes; and here in Paper III we will apply them to weak perturbations (quasinormal modes) of stationary black holes.

6.1.2 Our new tools, in brief

In this section, we briefly summarize our new tools. For details, see Secs. II, III, and IV of Paper I [2] (i.e. Chapter 3), and Secs. II and III of Paper II [4] (i.e. Chapter 5).

When spacetime is foliated by a family of spacelike hypersurfaces (surfaces on which some time function t is constant), the electromagnetic field tensor $F_{\mu\nu}$ splits up into an electric field $E_{\hat{i}} = F_{\hat{i}\hat{0}}$ and a magnetic field $B_{\hat{i}} = \frac{1}{2}\epsilon_{\hat{i}\hat{j}\hat{k}}F_{\hat{j}\hat{k}}$, which are 3-vector fields living in the spacelike hypersurfaces. Here the indices are components in proper reference frames (orthonormal tetrads) of observers who move orthogonally to the hypersurfaces, and $\epsilon_{\hat{i}\hat{j}\hat{k}}$ is the Levi-Civita tensor in those hypersurfaces.

Similarly, the Weyl (and vacuum Riemann) tensor $C_{\mu\nu\lambda\rho}$ splits up into: (i) a *tidal field* $\mathcal{E}_{\hat{i}\hat{j}} = C_{\hat{i}\hat{0}\hat{j}\hat{0}}$, which produces the tidal gravitational accelerations that appear, e.g., in the equation of geodesic deviation, $\Delta a_{\hat{j}} = -\mathcal{E}_{\hat{j}\hat{k}}\Delta x^{\hat{k}}$ [Eq. (3.3) of Paper I]; and (ii) a *frame-drag field* $\mathcal{B}_{\hat{i}\hat{j}} = \frac{1}{2}\epsilon_{\hat{i}\hat{p}\hat{q}}C_{\hat{j}\hat{0}\hat{p}\hat{q}}$, which produces differential frame-dragging (differential precession of gyroscopes), $\Delta\Omega_{\hat{j}} = \mathcal{B}_{\hat{j}\hat{k}}\Delta x^{\hat{k}}$ [Eq. (3.11) of Paper I].

We visualize the tidal field $\boldsymbol{\mathcal{E}}$ by the integral curves of its three eigenvector fields, which we call *tendex lines*, and also by the eigenvalue of each tendex line, which we call the *tendicity* of the line and we depict using colors. Similarly, we visualize the frame-drag field $\boldsymbol{\mathcal{B}}$ by frame-drag *vortex lines* (integral curves of its three eigenvector fields) and their *vorticities* (eigenvalues, color coded). See Figs. 6.2 and 6.3 below for examples. Tendex and vortex lines are analogs of electric and magnetic field lines. Whereas through each point in space there pass just one electric and one magnetic field line, through each point pass three orthogonal tendex lines and three orthogonal vortex lines, which identify the three principal axes of $\boldsymbol{\mathcal{E}}$ and $\boldsymbol{\mathcal{B}}$.

A person whose body is oriented along a tendex line gets stretched or squeezed with a relative head-to-foot gravitational acceleration that is equal to the person's height times the line's tendicity

(depicted blue [dark gray] in our figures for squeezing [positive tendicity] and red [light gray] for stretching [negative tendicity]). Similarly, if the person's body is oriented along a vortex line, a gyroscope at her feet precesses around her body axis, relative to inertial frames at her head, with an angular velocity equal to her height times the line's vorticity (depicted blue [dark gray] for clockwise precession [positive vorticity] and red [light gray] for counterclockwise [negative vorticity]).

We color code the horizon of a black hole by the normal-normal component of the tidal field, $\mathcal{E}_{NN}$, to which we give the name *horizon tendicity*, and also by the normal-normal component of the frame-drag field, $\mathcal{B}_{NN}$, the *horizon vorticity*; see, e.g., Fig. 6.9 below. These quantities are boost-invariant along the normal direction $\mathbf{N}$ to the horizon in the foliation's hypersurfaces.

A person hanging radially above the horizon or falling into it experiences head-to foot squeezing (relative acceleration) equal to the horizon tendicity times the person's height, and a differential head-to-foot precession of gyroscopes around the person's body axis with an angular velocity equal to the horizon vorticity times the person's height.

For any black hole, static or dynamic, the horizon tendicity $\mathcal{E}_{NN}$ and vorticity $\mathcal{B}_{NN}$ are related to the horizon's Newman-Penrose Weyl scalar Ψ_2, and its scalar intrinsic curvature $\mathcal{R}$ and scalar extrinsic curvature $\mathcal{X}$ by

$$\mathcal{E}_{NN} + i\mathcal{B}_{NN} = 2\Psi_2 = -\frac{1}{2}(\mathcal{R} + i\mathcal{X}) + 2(\mu\rho - \lambda\sigma) \; ; \tag{6.1}$$

[5], and Sec. III of [4] (i.e. Chapter 5). Here ρ, σ, μ, λ are spin coefficients related to the expansion and shear of the null vectors $\vec{l}$ and $\vec{n}$ used in the Newman-Penrose formalism [with $(\vec{l}+\vec{n})/\sqrt{2} = \vec{u}$ the normal to the foliation's hypersurfaces, $(\vec{l}-\vec{n})/\sqrt{2} = \vec{N}$ the normal to the horizon in the foliation's hypersurfaces, and $\vec{e}_2 = (\vec{m}+\vec{m}^*)/\sqrt{2}$ and $\vec{e}_3 = (\vec{m}-\vec{m}^*)/(i\sqrt{2})$ tangent to the instantaneous horizon in the foliation's hypersurfaces]. For stationary black holes, ρ and σ vanish, and $\mathcal{E}_{NN} = -\frac{1}{2}\mathcal{R}$ and $\mathcal{B}_{NN} = -\frac{1}{2}\mathcal{X}$.

For perturbations of Schwarzschild black holes, it is possible to adjust the slicing at first order in the perturbation, and adjust the associated null tetrad, so as to make the spin coefficient terms in Eq. (6.1) vanish at first order in the perturbation; whence $\mathcal{E}_{NN} = -\frac{1}{2}\mathcal{R}$ and $\mathcal{B}_{NN} = -\frac{1}{2}\mathcal{X}$. For perturbations of the Kerr spacetime, however, this is not possible. See App. 6.11 for details. Following a calculation by Hartle [6], we show in this appendix that for Kerr one can achieve $\mathcal{R} + i\mathcal{X} = -4(\Psi_2 + \lambda^{(0)}\sigma^{(1)})$ on the horizon, accurate through first order. Here, and throughout this paper, the superscripts $^{(i)}$ (or subscripts $_{(i)}$) indicate orders in the perturbation.

For the dynamical black holes described in [1] (i.e. Chapter 1.2) and for the weakly perturbed holes in this paper, we found that the spin terms in Eq. (6.1) are numerically small compared to the other terms, so $\mathcal{E}_{NN} \simeq -\frac{1}{2}\mathcal{R}$ and $\mathcal{B}_{NN} \simeq -\frac{1}{2}\mathcal{X}$. In addition, in a recent study of the tendexes and vortexes of approximate black hole initial data, Dennison and Baumgarte [7] found that these spin

terms vanish to a high order in the small velocities of their black holes, giving further evidence that these terms are typically negligible.

Because $\mathcal{X}$ is the 2-dimensional curl of a 2-dimensional vector (the Hájíček field) [8], its integral over the black hole's 2D horizon vanishes; and by virtue of the Gauss-Bonnet theorem, the horizon integral of $\mathcal{R}$ is equal to 8π. Correspondingly, for fully dynamical black holes as well as weakly perturbed black holes, the horizon integrals of $\mathcal{E}_{NN}$ and B_{NN} have the approximate values [1] (i.e. Chapter 1.2)

$$\int_{\mathcal{H}} \mathcal{B}_{NN} \simeq 0 \ , \quad \int_{\mathcal{H}} \mathcal{E}_{NN} \simeq -4\pi \ . \tag{6.2}$$

6.1.3 Overview of this paper's results

6.1.3.1 Slicing, coordinates and gauges

Throughout this paper, we use slices of constant Kerr-Schild time $\tilde{t}$ (which penetrate smoothly through the horizon) to decompose the Weyl tensor into its tidal and frame-drag fields; and we express our quasinormal perturbations, on the slices of constant $\tilde{t}$, in Kerr-Schild spatial coordinates (Secs. 6.2.1 and 6.2.2, and also Paper II [4] (i.e. Chapter 5)). In the zero-spin (Schwarzschild) limit, the Kerr-Schild slices become slices of constant ingoing Eddington-Finkelstein time $\tilde{t}$ and the spatial coordinates become those of Schwarzschild. Our choice of Kerr-Schild is dictated by these coordinates' resemblance to the coordinates that are typically used in numerical-relativity simulations of binary black holes, at late times, when the merged hole is settling down into its final Kerr-black-hole state; see, e.g., Fig. 6.15 below.

For a perturbed black hole, the slices and coordinates get modified at perturbative order in ways that depend on the *gauge* used to describe the perturbations (i.e., the slicing and spatial coordinates at perturbative order); see Sec. 6.2.3.

For spinning black holes, we perform all our computations in ingoing radiation gauge (Sec. 6.2.1 and App. 6.9). For non-spinning (Schwarzschild) black holes, we explore gauge dependence by working with two gauges that appear to be quite different: ingoing radiation gauge (App. 6.9), and Regge-Wheeler gauge (App. 6.7). Remarkably, for each mode we have explored, the field-line visualizations that we have carried out in these two gauges look nearly the same to the human eye; visually we see little gauge dependence. We discuss this and the differences in the gauges, in considerable detail, in Sec. 6.2.3 and App. 6.10.

For a Schwarzschild black hole, we have explored somewhat generally the influence of perturbative slicing changes and perturbative coordinate changes on the tidal and frame-drag fields, and on their tendex and vortex lines, and tendicities and vorticities (Sec. 6.2.3). We find that the tendicities and vorticities are less affected by perturbative slicing changes, than the shapes of the tendex and vortex lines. We also find that while coordinate changes affect the shapes of the tendex and vortex lines, the

tendicity and vorticity along a line is unchanged, and that in the wave zone a perturbative change in coordinates affects the tendicity and vorticity at a higher order than the effect of gravitational radiation.

For this reason, in this paper we pay considerable attention to vorticity and tendicity contours, as well as to the shapes of vortex and tendex lines.

6.1.3.2 Classification of quasinormal modes

As is well known, the quasinormal-mode, complex eigenfrequencies of Schwarzschild and Kerr black holes can be characterized by three integers: a poloidal quantum number $l = 2, 3, ...$, an azimuthal quantum number $m = -l, -l+1, ...+l$, and a radial quantum number n. For each $\{n, l, m\}$ and its eigenfrequency ω_{nlm}, there are actually two different quasinormal modes (a two-fold degeneracy). Of course, any linear combination of these two modes is also a mode. We focus on those linear combinations of modes that have *definite parity* (App. 6.9).

We define a tensor field to have positive parity if it is unchanged under reflections through the origin, and negative parity if it changes sign. A quasinormal mode of order (n, l, m) is said to have *electric parity* [or *magnetic parity*] if the parity of its metric perturbation is $(-1)^l$ [or $(-1)^{l+1}$]. The parity of the tidal-field perturbation is the same as that of the metric perturbation, but that of the frame-drag field is opposite. In much of the literature the phrase "even parity" is used in place of "electric parity", and "odd parity" in place of "magnetic parity"; we avoid those phrases because of possible confusion with positive parity and negative parity.

In this paper, we focus primarily on the most slowly damped ($n = 0$) quadrupolar ($l = 2$) modes, for various azimuthal quantum numbers m and for electric- and magnetic-parity. Since we discuss exclusively the $n = 0$ modes, we will suppress the n index and abbreviate mode numbers as (l, m).

6.1.3.3 The duality of magnetic-parity and electric-parity modes

In vacuum, the exact Bianchi identities for the Riemann tensor become, under a slicing-induced split of spacetime into space plus time, a set of Maxwell-like equations for the exact tidal field and frame-drag field [Eqs. (2.15) of Paper I [2] (i.e. Chapter 3) in a local Lorentz frame; Eqs. (2.13) and (2.4) of Paper I in general]. These Maxwell-like equations exhibit an exact duality: If one takes any solution to them and transforms $\boldsymbol{\mathcal{E}} \to \boldsymbol{\mathcal{B}}$, $\boldsymbol{\mathcal{B}} \to -\boldsymbol{\mathcal{E}}$, they continue to be satisfied (Sec. II B 1 of Paper I [2] (i.e. Chapter 3)).

This duality, however, is broken by the spacetime geometry of a stationary black hole. A Schwarzschild black hole has a monopolar tidal field $\boldsymbol{\mathcal{E}}$ and vanishing frame-drag field $\boldsymbol{\mathcal{B}}$; and a Kerr black hole has a monopolar component to its tidal field (as defined by a spherical-harmonic analysis at large radii or at the horizon), but only dipolar and higher-order components to its frame-drag field.

When a Schwarzschild or Kerr black hole is perturbed, there is a near duality between its electric-parity mode and its magnetic-parity mode of the same (l, m); but the duality is not exact. The unperturbed hole's duality breaking induces (surprisingly weak) duality-breaking imprints in the quasinormal modes. We explore this duality breaking in considerable detail in this paper (Secs. 6.2, 6.3.1, 6.3.2.3, and 6.3.3.2, and Apps. 6.9 and 6.11.2).

If one tries to see the duality between electric-parity and magnetic-parity modes, visually, in pictures of the perturbed hole's tendex and vortex lines, the duality is hidden by the dominant background tidal field and (for a spinning hole) the background frame-drag field. To see the duality clearly, we must draw pictures of tendex and vortex lines for the perturbative parts $\delta\boldsymbol{\mathcal{E}}$ and $\delta\boldsymbol{\mathcal{B}}$ of the tidal and frame-drag fields, with the unperturbed fields subtracted off. We draw many such pictures in this paper.

We have made extensive comparisons of the least damped ($n = 0$) electric-parity and magnetic-parity modes with ($l = 2$, $m = 2$). These two $(2, 2)$ modes (for any chosen black-hole mass M and spin parameter a) have identically the same complex eigenfrequency, i.e., they are degenerate (as has long been known and as we discussed above). This frequency degeneracy is an unbroken duality.

Pictures of the perturbative vortex and tendex lines and their color-coded vorticities and tendicities show a strong but not perfect duality: For a non-spinning hole, the perturbative vortex lines and their vorticities for the magnetic-parity mode (e.g., Fig. 6.2) look almost the same as the perturbative tendex lines and their tendicities for the electric-parity mode (Fig. 6.12); and similarly for the other pair of lines and eigenvalues. As the hole's spin is increased, the duality becomes weaker (the corresponding field lines and eigenvalues begin to differ noticeably); but even for very high spins, the duality is strikingly strong; see bottom row of Fig. 6.12 below. The duality remains perfect on the horizon in ingoing radiation gauge for any spin, no matter how fast (Sec. 6.3.1 and App. 6.11), and there is a sense in which it also remains perfect on the horizon of Schwarzschild in Regge-Wheeler gauge (last paragraph of App. 6.7.5).

6.1.3.4 Digression: Electromagnetic perturbations of a Schwarzschild black hole

As a prelude to discussing the physical character of the gravitational modes of a black hole, we shall discuss electromagnetic (EM) modes, i.e., quasinormal modes of the EM field around a black hole. The properties of EM modes that we shall describe can be derived from Maxwell's equations in the Schwarzschild and Kerr spacetimes, but we shall not give the derivations.

Because the unperturbed hole has no EM field and the vacuum Maxwell equations exhibit a perfect duality (they are unchanged when $\boldsymbol{E} \to \boldsymbol{B}$ and $\boldsymbol{B} \to -\boldsymbol{E}$), the EM modes exhibit perfect duality. For any magnetic-parity EM mode, the magnetic field pierces the horizon, so its normal component B_N is nonzero, while E_N vanishes. By duality, an electric-parity EM mode must have $E_N \neq 0$ and $B_N = 0$. For a magnetic-parity mode, the near-zone magnetic fields that stick out of

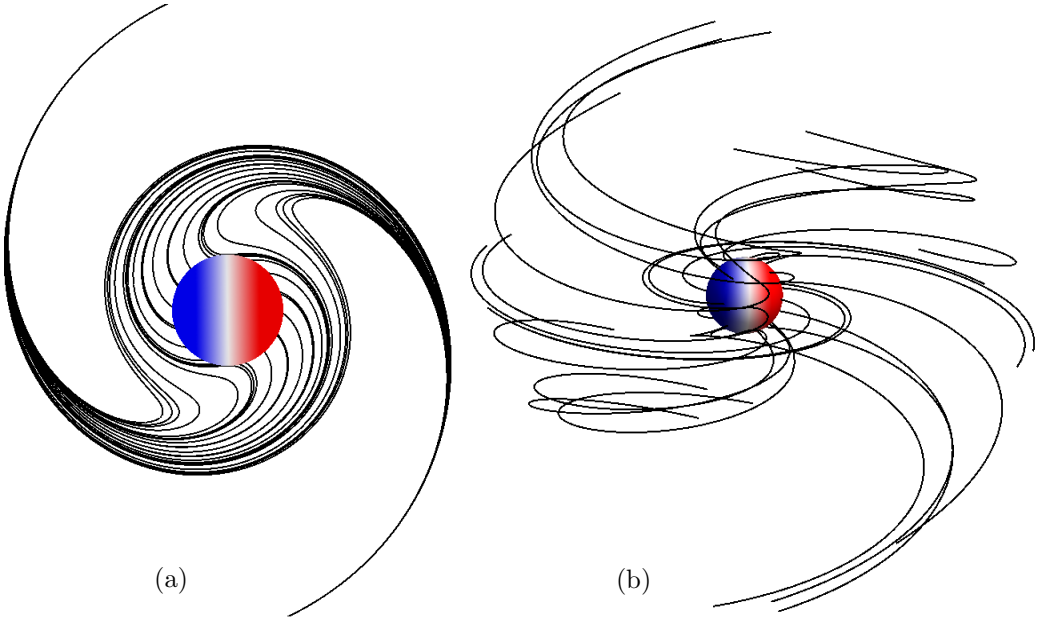

Figure 6.1: (color online). (a) Some magnetic field lines in the equatorial plane for the $(1,1)$ quasinormal mode of the electromagnetic field around a Schwarzschild black hole, with Eddington-Finklestein slicing. The horizon is color coded by the sign of the normal component of the magnetic field. The configuration rotates counterclockwise in time. (b) Some magnetic field lines for this same quasinormal mode, in 3 dimensions.

the horizon can be thought of as the source of the mode's emitted EM waves. We make this claim more precise by focusing on the fundamental ($n = 0$), magnetic-parity, $l = 1$, $m = 1$ mode:

Figure 6.1 shows magnetic field lines for this (1,1) mode, on the left (a) in the hole's equatorial plane, and on the right (b) in 3 dimensions with the equatorial plane horizontal. On the left, we see a bundle of magnetic field lines that thread through the horizon and rotate counterclockwise. As they rotate, the field lines spiral outward and backward, like water streams from a whirling sprinkler, becoming the magnetic-field component of an outgoing electromagnetic wave. The electric field lines for this mode (not shown) are closed circles that represent the electric part of electromagnetic waves traveling outward at radii $r \gg 2M$ and inward at radii $r \simeq 2M$. This mode's waves, we claim, are generated by the near-zone, rotating magnetic field lines that thread the hole (Fig. 6.1a). An analogy will make this clear.

Consider a rotating (angular velocity σ), perfectly conducting sphere in which is anchored a magnetic field with the same dipolar normal component $B_N \propto \Re[Y^{11}(\theta,\phi)e^{-i\sigma t}]$ as the horizon's B_N for the (1,1) quasinormal mode (the red [light gray] and blue [dark gray] coloring on the horizon in Fig. 6.1). At some initial moment of time, lay down outside the conducting sphere, a magnetic-field configuration that (i) has this B_N at the sphere, (ii) satisfies the constraint equation $\boldsymbol{\nabla}\cdot\boldsymbol{B} = 0$, (iii) resembles the field of Fig. 6.1 in the near zone, i.e., at $r \lesssim \lambda\!\!\!^{-} = c/\sigma$ and at larger radii has some arbitrary form that is unimportant; and (iv) (for simplicity) specify a vanishing initial electric

field. Evolve these initial fields forward in time using the dynamical Maxwell equations. It should be obvious that the near-zone, rotating magnetic field will not change much. However, as it rotates, via Maxwell's dynamical equations it will generate an electric field, and those two fields, interacting, will give rise to the outgoing electromagnetic waves of a $l = 1$, $m = 1$ magnetic dipole. Clearly, the ultimate source of the waves is the rotating, near-zone magnetic field that is anchored in the sphere. (Alternatively, one can regard the ultimate source as the electric currents in the sphere, that maintain the near-zone magnetic field.)

Now return to the magnetized black hole of Fig. 6.1, and pose a similar evolutionary scenario: At some initial moment of time, lay down a magnetic-field configuration that (i) has the same normal component at the horizon as the (1,1) mode, (ii) satisfies the constraint equation $\boldsymbol{\nabla}\cdot\boldsymbol{B} = 0$, and (iii) resembles the field of Fig. 6.1 in the near zone. In this case, the field is not firmly anchored in the central body (the black hole), so we must also specify its time derivative to make sure it is rotating at the same rate as the (1,1) quasinormal mode. This means (by a dynamical Maxwell equation) that we will also be giving a nonvanishing electric field that resembles, in the near zone, that of the (1,1) mode and in particular does not thread the horizon. Now evolve this configuration forward in time. It will settle down, rather quickly, into the (1,1) mode, with outgoing waves in the wave zone, and ingoing waves at the horizon. This is because the (1,1) mode is the most slowly damped quasinormal mode that has significant overlap with the initial data.

As for the electrically conducting, magnetized sphere, so also here, the emitted waves are produced by the rotation of the near-zone magnetic field. But here, by contrast with there, the emitted waves act back on the near-zone magnetic field, causing the field lines to gradually slide off the horizon, resulting in a decay of the field strength at a rate given by the imaginary part of the mode's complex frequency.

This backaction can be understood in greater depth by splitting the electric and magnetic fields, *near the horizon*, into their *longitudinal* (radial) and *transverse* pieces. The longitudinal magnetic field is B_N and it extends radially outward for a short distance; the tangential magnetic field is a 2-vector $\boldsymbol{B}^{\rm T}$ parallel to the horizon; and similarly for the electric field, which has $E_N = 0$ and so is purely transverse. The tangential fields actually only look like ingoing waves to observers who, like the horizon, move outward at (almost) the speed of light: the observers of a Schwarzschild time slicing. As one learns in the Membrane Paradigm for black holes (Secs. III.B.4 and III.C.2 of [9]), such observers can map all the physics of the event horizon onto a *stretched horizon*—a spacelike 2-surface of constant lapse function $\alpha = \sqrt{1-2M/r} \ll 1$ very close in spacetime to the event horizon. On the stretched horizon, these observers see $\boldsymbol{E}^{\rm T} = \boldsymbol{N}\times\boldsymbol{B}^{\rm T}$ (ingoing-wave condition), and the tangential magnetic field acts back on the longitudinal field via

$$\frac{\partial B_N}{\partial t} +^{(2)} \boldsymbol{\nabla}\cdot(\alpha\boldsymbol{B}^{\rm T}) = 0\ . \tag{6.3}$$

Here ${}^{(2)}\boldsymbol{\nabla}\cdot(\alpha\boldsymbol{B}^{\rm T})$ is the 2-dimensional divergence in the stretched horizon, and the lapse function in this equation compensates for the fact that the Schwarzschild observers see a tangential field that diverges as $1/\alpha$ near the horizon, due to their approach to the speed of light.

Equation (6.3) is a conservation law for magnetic field lines on the stretched horizon. The density (number per unit area) of field lines crossing the stretched horizon is B_N, up to a multiplicative constant; the flux of field lines (number moving through unit length of some line in the stretched horizon per unit time) is $\boldsymbol{B}^{\rm T}$, up to the same multiplicative constant; and Eq. (6.3) says that the time derivative of the density plus the divergence of the flux vanishes: the standard form for a conservation law.

Return to Fig. 6.1; the dynamics embodied in this scenario are summarized as follows: *The longitudinal magnetic field $B_N(\theta,\phi)$ is laid down as an initial condition (satisfying the magnetic constraint condition). As it rotates, it generates the ingoing-wave near-horizon transverse fields embodied in $\boldsymbol{E}^{\rm T}$ and $\boldsymbol{B}^{\rm T}$ (and also the outgoing electromagnetic waves far from the hole); and the divergence of $\alpha\boldsymbol{B}^{\rm T}$, via Eq. (6.3), then acts back on the longitudinal field that produced it, pushing the field lines away from the centers of the blue (dark gray) and red (light gray) spots on the stretched horizon toward the white ring. Upon reaching the white ring, each field line in the red region attaches onto a field line from the blue region and slips out of the horizon. Presumably, the field line then travels outward away from the black hole and soon becomes part of the outgoing gravitational waves. The gradual loss of field lines in this way is responsible for the mode's exponential decay.*

6.1.3.5 The physical character of magnetic-parity and electric-parity modes

For a Schwarzschild black hole, the physical character of the gravitational modes is very similar to that of the electromagnetic modes:

Just as a magnetic-parity EM mode has nonzero B_N and vanishing E_N, so similarly: *for a Schwarzschild black hole, the **magnetic-parity** modes of any (l,m) have nonzero (solely perturbative) horizon vorticity $\delta\mathcal{B}_{NN}=\mathcal{B}_{NN}$, and vanishing perturbative horizon tendicity $\delta E_{NN}=0$; and correspondingly, from the horizon there emerge nearly normal vortex lines that are fully perturbative and no nearly normal, perturbative tendex lines.*

Just as in the EM case, the near-zone magnetic fields that emerge from the horizon are the source of the emitted electromagntic waves, so also in the gravitational case, *for a magnetic-parity mode the emerging, near-zone, vortex lines and their vorticities can be thought of as the source of the emitted magnetic-parity gravitational waves* (see the next subsection). In this sense, magnetic-parity modes can be thought of as fundamentally frame-drag in their physical origin. Figure 6.2 below depicts a $(2,2)$ example. We will discuss this example in Sec. 6.1.3.6.

For a Schwarzschild black hole, *the **electric-parity** modes of any (l,m) have nonzero perturbative horizon tendicity $\delta\mathcal{E}_{NN}\neq 0$, and vanishing horizon vorticity $\delta B_{NN}=B_{NN}=0$; and correspond-*

ingly, from the horizon there emerge nearly normal perturbative tendex lines and no nearly normal vortex lines. The emerging, near-zone, perturbative tendex lines can be thought of as the source of the mode's emitted electric-parity gravitational waves. In this sense, electric-parity modes can be thought of as fundamentally tidal in their physical origin.

There is a close analogy, here, to the tidal and frame-drag fields of dynamical multipoles in linearized theory (Paper I [2] (i.e. Chapter 3)): Electric-parity (mass) multipoles have a tidal field that rises more rapidly, as one approaches the origin, than the frame-drag field, so these electric-parity multipoles are fundamentally tidal in physical origin. By contrast, for magnetic-parity (current) multipoles it is the frame-drag field that grows most rapidly as one approaches the origin, so they are fundamentally frame-drag in physical origin.

When a black hole is spun up, the horizon vorticities of its electric-parity modes become nonzero, and the horizon tendicities of its magnetic-parity modes acquire nonzero perturbations. However, these spin-induced effects leave the modes still predominantly tidal near the horizon for electric-parity modes, and predominantly frame-drag near the horizon for magnetic-parity modes (Sec. 6.3).

6.1.3.6 The $(2,2)$ magnetic-parity mode of a Schwarzschild hole

In this and the next several subsections, we summarize much of what we have learned about specific $n = 0$, $l = 2$ modes (the least-damped quadrupolar modes), for various m. We shall focus primarily on magnetic-parity modes, since at the level of this discussion the properties of electric-parity modes are the same, after a duality transformation $\delta\boldsymbol{\mathcal{E}} \to \delta\boldsymbol{\mathcal{B}}$, $\delta\boldsymbol{\mathcal{B}} \to -\delta\boldsymbol{\mathcal{E}}$.

It is a remarkable fact that, for a magnetic-parity mode of a Schwarzschild black hole, all gauges share the same slicing, and the mode's frame-drag field is unaffected by perturbative changes of spatial coordinates; therefore, the frame-drag field is fully gauge invariant. See Sec. 6.2.3. This means that Figs. 6.2–6.8 are fully gauge invariant.

We begin with the $(2,2)$ magnetic-parity mode of a Schwarzschild black hole. Figure 6.2 depicts the negative-vorticity vortex lines (red) and contours of their vorticity (white and purple [dark gray]), in the hole's equatorial plane. Orthogonal to the red (solid) vortex lines (but not shown) are positive-vorticity, vortex lines that also lie in the equatorial plane. Vortex lines of the third family pass orthogonally through the equatorial plane. The entire configuration rotates counterclockwise, as indicated by the thick dashed arrow. The dotted lines, at radii $r = \lambda\!\!\!^{-}$ and $r = \pi\lambda\!\!\!^{-}$ (where $\lambda\!\!\!^{-}$ is the emitted waves' reduced wavelength), mark the approximate outer edge of the near zone, and the approximate inner edge of the wave zone.

Just as the near-zone electromagnetic (1,1) perturbations are dominated by radial field lines that thread the black hole and have a dipolar distribution of field strength, so here the *near-zone gravitational perturbations* are dominated by (i) the radial vortex lines that thread the hole and have a quadrupolar distribution of their horizon vorticity $\mathcal{B}_{NN} = \delta\mathcal{B}_{NN}$, and also by (ii) a transverse,

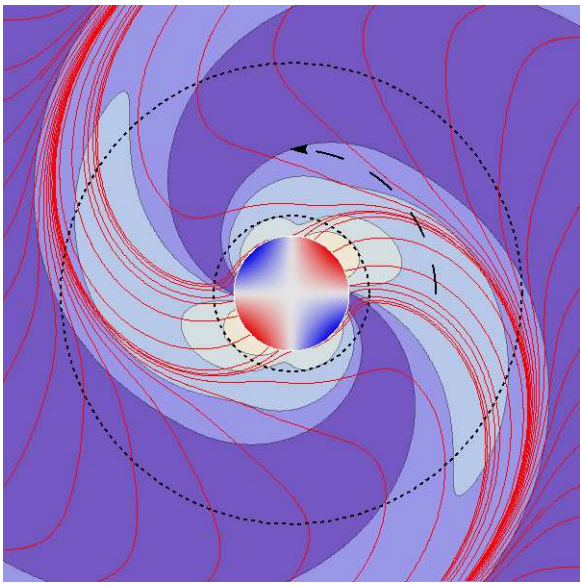

Figure 6.2: (color online). Some vortex lines (solid, red lines) and contours of vorticity (shaded regions) in the equatorial plane for the $(2,2)$ *magnetic-parity* quasinormal mode of a non-rotating, Schwarzschild black hole, with complex eigenfrequency $\omega = (0.37367 - 0.08896i)/M$ where M is the hole's mass. The horizon (central circle) is color coded by the horizon vorticity $\mathcal{B}_{NN}$ as seen by someone looking down on the black hole; this vorticity is entirely perturbative. The thick, solid red curves are one set of vortex lines in the equatorial plane—the set with negative vorticity. These lines include some that emerge from the horizon in the negative-vorticity (red) regions, and some that never reach the horizon. The other, positive-vorticity, equatorial vortex lines are orthogonal to the ones shown, and are identical to those shown but rotated through 90 degrees around the hole so some of them emerge from the horizon in the positive-vorticity (blue) regions. The contours represent the vorticity of the red (negative-vorticity) vortex lines, with largest magnitude of vorticity white and smallest purple (dark gray); the contours mark where the vorticity has fallen to 50%, 25%, 10%, and 5% of the maximum value attained at the center of the horizon vortex. The two dotted circles are drawn at Schwarzschild radii $r = \lambda$ and $r = \pi\lambda = \lambda/2$. They mark the approximate outer edge of the near zone and the approximate inner edge of the wave zone. The arrow marks the direction of rotation of the perturbation.

isotropic frame-drag field $\mathcal{B}_{\hat{\theta}\hat{\theta}} = \mathcal{B}_{\hat{\phi}\hat{\phi}} = -\frac{1}{2}\delta\mathcal{B}_{NN}$ that is tied to $\mathcal{B}_{NN}$ in such a way as to guarantee that this dominant part of $\boldsymbol{\mathcal{B}}$ is traceless.

This full structure, the normal-normal field and its accompanying isotropic transverse field, makes up the *longitudinal, nonradiative frame-drag field* $\boldsymbol{\mathcal{B}}^{\rm L}$ near the horizon. (As we shall discuss below, this longitudinal structure is responsible for generating the mode's gravitational waves, and all of the rest of its fields.) Somewhat smaller are (i) the longitudinal-transverse components of $\boldsymbol{\mathcal{B}}$ ($\mathcal{B}_{\hat{r}\hat{\theta}}$ and $\mathcal{B}_{\hat{r}\hat{\phi}}$), which together make up the *longitudinal-transverse* part of the frame-drag field, a 2-vector $\boldsymbol{\mathcal{B}}^{\rm LT}$ parallel to the horizon, and give the horizon-piercing vortex lines small non-normal components; and (ii) transverse-traceless components $\mathcal{B}_{\hat{\theta}\hat{\theta}} = -\mathcal{B}_{\hat{\phi}\hat{\phi}}$, which make up the *transverse-traceless* part of the frame-drag field, a 2-tensor $\boldsymbol{\mathcal{B}}^{\rm TT}$ parallel to the horizon, and are ingoing gravitational waves as seen by Schwarzschild observers. (This decomposition into L, LT, and TT parts is useful only

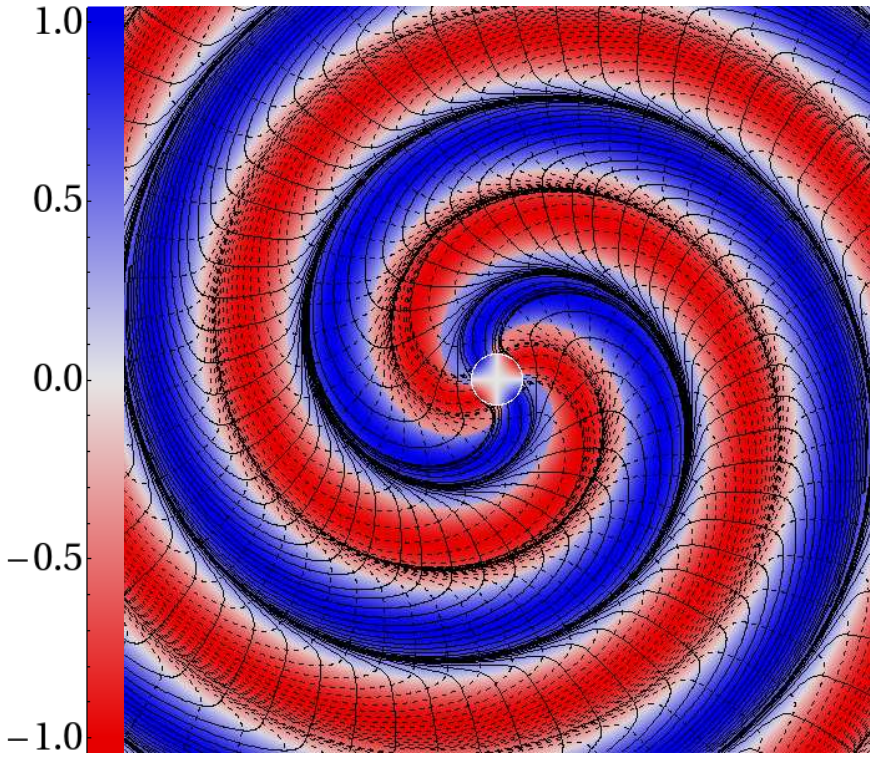

Figure 6.3: (color online). The vortex lines (solid black for clockwise; dashed black for counterclockwise) and color-coded vorticities in the equatorial plane for the same magnetic-parity $(2, 2)$ mode as in Fig. 6.2. This figure differs from Fig. 6.2 in ways designed to give information about the emitted gravitational waves: (i) It extends rather far out into the wave zone. (ii) It shows the angular structure of the vorticity for the dominant vortex lines in each region of the equatorial plane. More specifically: the color at each point represents the vorticity of the equatorial vortex line there which has the largest magnitude of vorticity, with radial variations of vorticity normalized away (so the linear color code on the left indicates vorticity relative to the maximum at any given radius). The regions of large positive vorticity (blue [dark gray]) are *clockwise vortexes*; those of large negative vorticity (red [light gray]) are *counterclockwise vortexes*.

near the horizon and in the wave zone, where there are preferred longitudinal directions associated with wave propagation.)

As the near-zone, longitudinal frame-drag field $\boldsymbol{\mathcal{B}}^{\rm L}$ rotates, it generates a near-zone longitudinal-transverse (LT) perturbative frame-drag field $\boldsymbol{\mathcal{B}}^{\rm LT}$ via $\boldsymbol{\mathcal{B}}$'s propagation equation (the wave equation for the Riemann tensor), and it generates a LT tidal field $\delta\boldsymbol{\mathcal{E}}^{\rm LT}$ via the Maxwell-like Bianchi identity which says, in a local Lorentz frame (for simplicity), $\partial\boldsymbol{\mathcal{E}}/\partial t = (\boldsymbol{\nabla}\times\boldsymbol{\mathcal{B}})^{\rm S}$, where the superscript S means "symmetrize" [Eq. (2.15) of Paper I]. These three fields, $\boldsymbol{\mathcal{B}}^{\rm L}$, $\boldsymbol{\mathcal{B}}^{\rm LT}$, and $\delta\boldsymbol{\mathcal{E}}^{\rm LT}$ together maintain each other during the rotation via this Maxwell-like Bianchi identity and its (local-Lorentz-frame) dual $\partial\boldsymbol{\mathcal{B}}/\partial t = -(\boldsymbol{\nabla}\times\boldsymbol{\mathcal{E}})^{\rm S}$. They also generate the transverse-traceless parts of both fields, $\boldsymbol{\mathcal{B}}^{\rm TT}$, and $\delta\boldsymbol{\mathcal{E}}^{\rm TT}$, which become the outgoing gravitational waves in the wave zone and ingoing gravitational waves at the horizon.

In the equatorial plane, this outgoing-wave generation process, described in terms of vortex and

tendex structures, is quite pretty, and is analogous to the (1,1) magnetic-field mode of Fig. 6.1 and Sec. 6.1.3.4: As one moves outward into the induction zone and then the wave zone, the equatorial vortex lines bend backward into outgoing spirals (Fig. 6.2) and gradually acquire accompanying tendex lines. The result, locally, in the wave zone, is the standard pattern of transverse, orthogonal red and blue vortex lines; and (turned by 45 degrees to them) transverse, orthogonal red and blue tendex lines, that together represent plane gravitational waves (Fig. 7 of Paper I).

It is instructive to focus attention on regions of space with large magnitude of vorticity. We call these regions *vortexes*. Figure 6.3 shows that the equatorial frame-drag field consists of four outspiraling vortexes, two red ([light gray] counterclockwise) and two blue ([dark gray] clockwise).

The solid black lines in the figure are clockwise vortex lines. In the clockwise vortexes of the wave zone, they have the large magnitude of vorticity that is depicted as blue (dark gray), and they are nearly transverse to the radial wave-propagation direction; so they represent crests of outgoing waves. In the counterclockwise vortexes (red [light gray] regions), these clockwise vortex lines have very small magnitude of vorticity and are traveling roughly radially, leaping through a red vortex (a wave trough) from one blue vortex (wave crest) to the next. These clockwise vortex lines accumulate at the outer edges of the clockwise (blue) vortexes.

The dashed black lines are counterclockwise vortex lines, which are related to the red (light gray), counterclockwise vortexes in the same way as the solid clockwise vortex lines are related to the blue (dark gray), clockwise vortexes.

Outside the equatorial plane, this mode also represents outgoing gravitational waves, once one gets into the wave zone. We depict the strengths of the vortexes which become those waves in Fig. 6.4. The blue (dark gray) regions are locations where one vortex line has vorticity at least 85% of the maximum at that radius; in this sense, they are clockwise vortexes. In the near zone, two (blue) clockwise vortexes emerge radially from the horizon parallel to the plane of the picture, and two (red) counterclockwise vortexes emerge radially toward and away from us. These are 3-dimensional versions of the four vortexes emerging from the horizon in the equatorial plane of Fig. 6.3. In the wave zone, the "85%" vortexes are concentrated in the polar regions, because this mode emits its gravitational waves predominantly along the poles. The waves are somewhat weaker in the equatorial plane, so although there are spiraling vortexes in and near that plane (Fig. 6.3), they do not show up at the 85% level of Fig. 6.4. The off-white, spiral-arm structures in the equatorial plane represent the four regions where the wave strength is passing through a minimum.

Turn attention from the wave zone to the horizon. There the ingoing waves, embodied in $\boldsymbol{\mathcal{B}}^{\rm TT}$ and $\delta\boldsymbol{\mathcal{E}}^{\rm TT}$ (which were generated in the near and transition zones by rotation of $\boldsymbol{\mathcal{B}}^{\rm L}$), act back on $\boldsymbol{\mathcal{B}}^{\rm L}$, causing its vortex lines to gradually slide off the horizon and thereby producing the mode's exponential decay.

Just as this process in the electromagnetic case is associated with the differential conservation

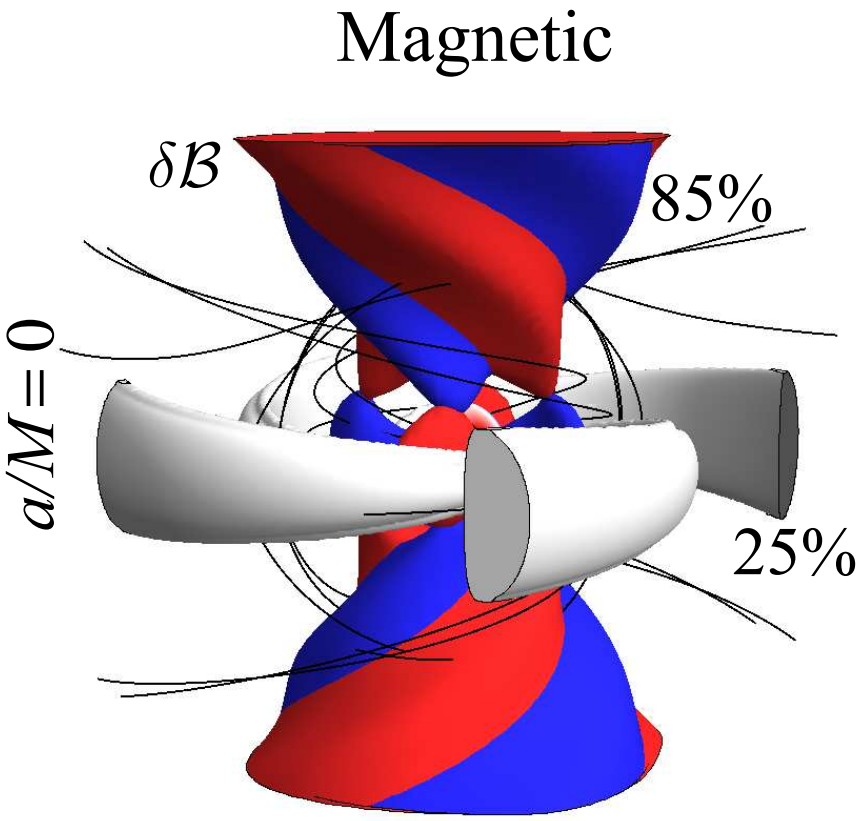

Figure 6.4: (color online). Some 3-dimensional clockwise vortex lines (shown black) and regions of large vorticity (vortexes, shown blue [dark gray] and red [light gray]) and small vorticity (shown off-white), for the same magnetic-parity mode of a Schwarzschild black hole as in Figs. 6.2 and 6.3. More specifically: the inner sphere is the horizon, color coded by its vorticity. The blue region is a clockwise vortex in which one vortex line has vorticity at least 85% of the maximum value at that radius, and similarly for the counterclockwise red region. The four off-white regions are locations where no vortex line has magnitude of vorticity in excess of 25% of the maximum at that radius.

law (6.3) for magnetic field lines threading the horizon, $\partial B_N/\partial t + {}^{(2)}\boldsymbol{\nabla}\cdot(\alpha \boldsymbol{B}^{\rm T})$, so also here it is associated with an analogous (approximate) conservation law and an accompanying driving equation, given in terms of two Newman Penrose equations (6.113) of Appendix 6.11 and the perturbative parts of the Weyl scalars Ψ_0, Ψ_1, and $\Psi_2^{(0)}$:

$$\mathbf{D}\Psi_2^{(1)} = (\boldsymbol{\delta}^* + 2\pi - 2\alpha)\Psi_1\,, \tag{6.4a}$$

$$(\mathbf{D} - 2\epsilon)\Psi_1 = (\boldsymbol{\delta}^* + \pi - 4\alpha)\Psi_0\,. \tag{6.4b}$$

(Note that only Ψ_2 is nonzero for the background spacetime with our tetrad choice.) Here the notation is that of Newman and Penrose: $\mathbf{D}$ is a time derivative on the horizon, $\Psi_2^{(1)}$ is the mode's $\delta\boldsymbol{\mathcal{E}}^{\rm L} + i\boldsymbol{\mathcal{B}}^{\rm L}$ (equivalently $\delta\mathcal{E}_{NN} + i\mathcal{B}_{NN}$ in disguise), with $\delta\boldsymbol{\mathcal{E}}^{\rm L}$ and $\delta\mathcal{E}_{NN}$ vanishing for our mode; Ψ_1 is the LT field $\delta\boldsymbol{\mathcal{E}}^{\rm LT} + i\delta\boldsymbol{\mathcal{B}}^{\rm LT}$ (as measured by Schwarzschild observers) in disguise; Ψ_0 is the

ingoing-wave $\delta\boldsymbol{\mathcal{E}}^{\rm TT}+i\delta\boldsymbol{\mathcal{B}}^{\rm TT}$ (as measured by Schwarzschild observers) in disguise; $\boldsymbol{\delta}^*$ is a divergence in disguise; and ϵ, π and α are NP spin coefficients. Equation (6.4b) says that the ingoing waves embodied in $\delta\boldsymbol{\mathcal{E}}^{\rm TT}+i\boldsymbol{\mathcal{B}}^{\rm TT}$ drive the evolution of the quantity Ψ_1, and Equation (6.4a) is an approximate differential conservation law in which this Ψ_1 plays the role of the flux of longitudinal vortex lines (number crossing a unit length per unit time) and Ψ_2 (i.e., $\mathcal{B}_{NN}$) is the density of longitudinal vortex lines. This differential conservation law says that the time derivative of the vortex-line density plus the divergence of the vortex-line flux is equal to some spin-coefficient terms that, we believe, are generally small. (By integrating this approximate conservation law over the horizon $\mathcal{H}$, we see that $\int_{\mathcal{H}} B_{NN}dA$ must be nearly conserved, in accord with Eq. (6.2) above, which tells us that the horizon integral is nearly zero. In both cases, the integral conservation law (6.2) and the differential conservation law (6.4a), it is numerically small spin coefficients that slightly spoil the conservation for vacuum perturbations of black holes. In Eq. (6.28), for a magnetic-parity mode of Schwarzschild and Eddington-Finkelstein slicing, we make this conservation law completely concrete and find that in this case it is precise; there are no small spin coefficients to spoil it. We plan to investigate this conservation law in numerical simulations as well, in which there may be additional subtleties related to the formation of caustics.

Returning to the evolution of the (2,2) magnetic-parity mode: The ingoing waves, via Eqs. (6.4), push the longitudinal vortex lines away from the centers of the horizon vortexes toward their edges (toward the white horizon regions in Figs. 6.2 and 6.3. At the edges, clockwise vortex lines from the blue (dark gray) horizon vortex and counterclockwise from the red (light gray) horizon vortex meet and annihilate each other, leading to decay of the longitudinal part of the field and thence the entire mode.

We expect to explore this evolutionary process in greater detail and with greater precision in future work.

Turn, next, to spinning black holes. In this case, the $(2,2)$ magnetic-parity mode has qualitatively the same character as for a non-spinning black hole. The principal change is due to the spin raising the mode's eigenfrequency, and the near zone thereby essentially disappearing, so the perturbed vortex lines that emerge from the horizon have a significant back-spiral-induced tilt to them already at the horizon. See Fig. 6.12 below.

6.1.3.7 The (2,1) magnetic-parity mode of a Schwarzschild hole

For the (2,1) magnetic-parity mode of a Schwarzschild black hole, there are two horizon vortexes in the hole's northern hemisphere (one counterlockwise, the other clockwise), and two in the southern hemisphere. From these emerge the longitudinal part of the frame-drag field, in the form of four 3D vortexes (Fig. 6.5).

These four vortexes actually form two spiral arms, each of which contains vortex lines of both

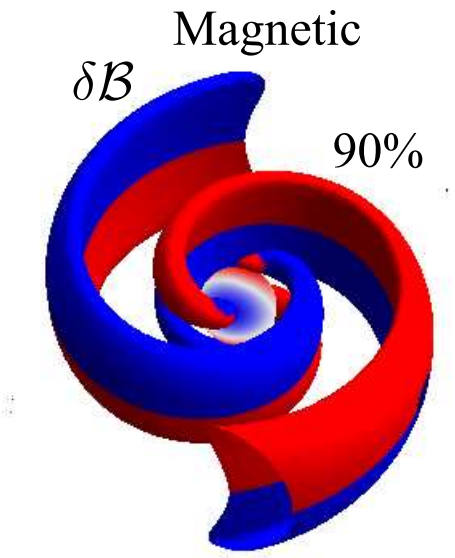

Figure 6.5: (color online). Three-dimensional vortexes for the magnetic-parity, (2,1) mode of a Schwarzschild black hole. The colored surfaces enclose the region where, for each radius, the vorticity of at least one vortex line exceeds 90% of the maximum for that radius. In the blue and red (dark and light gray) regions, the clockwise and counterclockwise vortex lines, respectively, have the larger vorticity.

signs (clockwise and counterclockwise). The surface of each arm is color coded by the sign of the vorticity that is largest in magnitude in that region of the arm. This dominant vorticity flips sign when one passes through the equatorial plane—from positive (i.e., blue [dark gray]; clockwise) on one side of the equator to negative (i.e., red [light gray]; clockwise) on the other side. The reason for this switch is that for $m = 1$ the $e^{im\phi}$ angular dependence means reflection antisymmetry through the polar axis, which combined with the positive parity of the $l = 2$ frame-drag field implies reflection antisymmetry through the equatorial plane. The (2,2) mode of the previous section, by contrast, was reflection symmetric through both the polar axis and the equatorial plane.

By contrast with the (2,2) mode, whose region of largest vorticity switched from equatorial in the near zone to polar in the wave zone (Fig. 6.3), for this (2,1) mode, the region of largest vorticity remains equatorial in the wave zone. In other words, this mode's gravitational waves are stronger in near-equator directions than in near-polar directions. (Recall that in the wave zone, the vortexes are accompanied by tendexes with tendicities equal in magnitude to the vorticities at each event, so we can discuss the gravitational-wave strengths without examining the tidal field.)

Close scrutiny of the near-horizon region of Fig. 6.5 reveals a surprising feature: Within the 90% vortexes (colored surfaces), the sign of the largest vorticity switches as one moves from the near zone into the transition zone—which occurs not very far from the horizon; see the inner dashed circle in

Fig. 6.2 above). This appears to be due to the following: The near-zone vortexes are dominated by the longitudinal part of the frame-drag field $\delta\mathcal{B}^{\rm L}$, which generates all the other fields including $\delta\boldsymbol{\mathcal{B}}^{\rm LT}$ via its rotation [see discussion of the (2,2) mode above]. The longitudinal-transverse field $\delta\boldsymbol{\mathcal{B}}^{\rm LT}$ is strong throughout the near zone and comes to dominate over $\delta\boldsymbol{\mathcal{B}}^{\rm L}$ as one moves into the transition zone. Its largest vorticity has opposite sign from that of $\delta\boldsymbol{\mathcal{B}}^{\rm L}$, causing the flip of the dominant vorticity and thence the color switch as one moves into the transition zone. (Note that a similar switch in the sign of the strongest vorticity occurs for the magnetic-parity (2,2) mode vortexes illustrated in Fig. 6.4, although there the transition occurs farther out, at the edge of the wave zone.)

In Secs. 6.5.1 and 6.5.2, we explore in considerable detail this magnetic-parity (2,1) mode and also its near dual, the electric-parity (2,1) mode, focusing especially on the shapes of their vortexes.

6.1.3.8 The (2,0) magnetic-parity mode of a Schwarzschild hole

The (2,0) magnetic-parity mode has very different dynamical behavior from that of the (2,1) and (2,2) modes. Because of its axisymmetry, this mode cannot be generated by longitudinal, near-zone vortexes that rotate around the polar axis, and its waves cannot consist of outspiraling, intertwined vortex and tendex lines.

Instead, this mode is generated by longitudinal, near-zone vortexes that oscillate, and its waves are made up of intertwined vortex lines and tendex lines that wrap around deformed tori. These gravitational-wave tori resemble smoke rings and travel outward at the speed of light. More specifically:

Because of axisymmetry, the (2,0) magnetic-parity mode has one family of vortex lines that are azimuthal circles of constant r and θ, and two families that lie in surfaces $\mathcal{S}_\phi$ of constant ϕ. Figure 6.6 is a plot in one of these $\mathcal{S}_\phi$ surfaces. (The plot for any other ϕ will be identical to this, by axisymmetry.) This plot shows the vortex lines that lie in $\mathcal{S}_\phi$, and by color coding at each point, the vorticity of the strongest of those lines.

Notice that, at this phase of oscillation, there are clockwise (solid) vortex lines sticking nearly radially out of the horizon's polar regions and counterclockwise (dashed) vortex lines sticking nearly radially out of the horizon's equatorial region. A half cycle later the poles will be red (light gray) and equator blue (dark gray). These near-zone vortex lines are predominantly the longitudinal part of the frame-drag field $\delta\boldsymbol{\mathcal{B}}^{\rm L}$, which we can regard as working hand in hand with the near-zone, longitudinal-transverse tidal field $\delta\boldsymbol{\mathcal{E}}^{\rm LT}$ to generate the other fields.

As we shall see in Sec. 6.5.3 (and in more convincing detail for a different oscillatory mode in Sec. 6.4.3), the dynamics of the oscillations are these: Near-zone energy [1] oscillates back and forth

[1] We use the term *energy* in a generalized and descriptive sense here and elsewhere in this paper. We note, however, that with a suitable (nonunique) definition of local energy, we can make these notions more precise. For example, the totally symmetric, traceless Bel-Robinson tensor serves as one possible basis for this. In vacuum it is

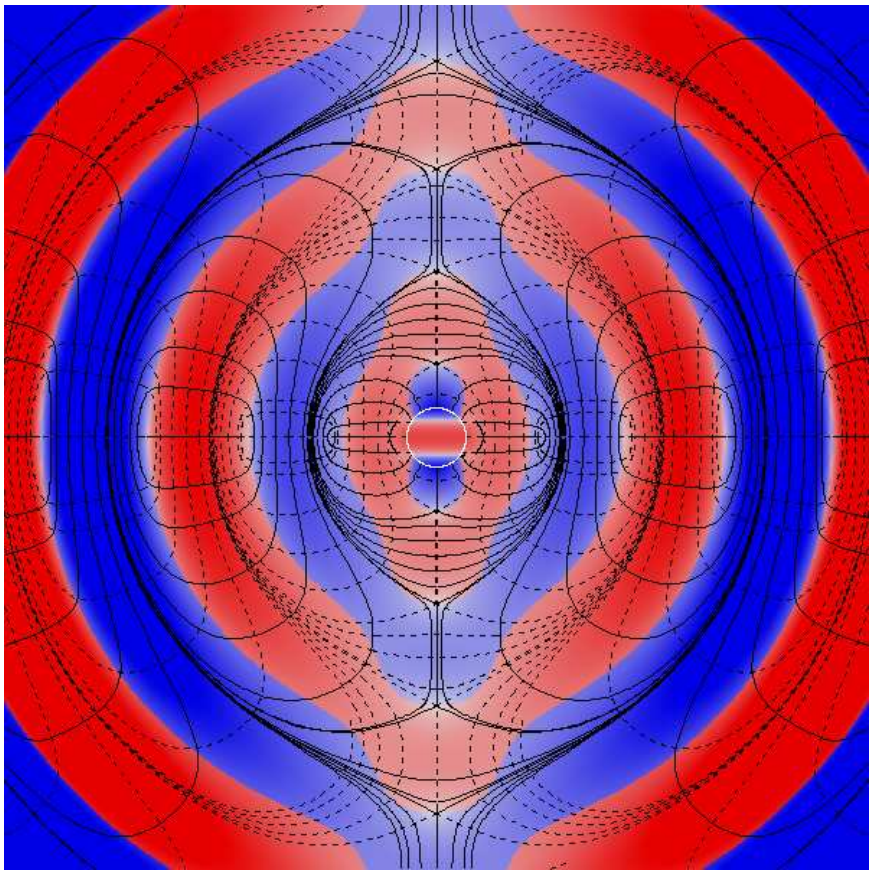

Figure 6.6: (color online). Vortex lines and vorticities for magnetic-parity (2,0) mode of Schwarzschild in a surface $\mathcal{S}_\phi$ of constant ϕ. The line and coloring conventions are the same as in Fig. 6.3 (solid lines for clockwise, dashed for counterclockwise; color shows vorticity of the vortex line with largest magnitude of vorticity, with radial variations removed and intensity of color as in the key on right edge of Fig. 6.3). The central circle is the horizon, color coded by the horizon vorticity.

between the near-zone $\delta\boldsymbol{\mathcal{B}}^{\rm L}$, and the near-zone $\delta\boldsymbol{\mathcal{B}}^{\rm LT}$ and $\delta\boldsymbol{\mathcal{E}}^{\rm LT}$. As $\delta\boldsymbol{\mathcal{B}}^{\rm L}$ decays, its vortex lines slide off the hole and (we presume) form closed loops, lying in $\mathcal{S}_\phi$, which encircle outgoing deformed tori of perturbed tendex lines that become the transverse-traceless gravitational waves. Only part of the energy in $\delta\boldsymbol{\mathcal{B}}^{\rm L}$ goes into the outgoing waves. Some goes into the TT ingoing waves, and the rest (a

$T_{\mu\nu\rho\sigma} = 1/2(C_{\mu\alpha\nu\beta}C_\rho{}^\alpha{}_\sigma{}^\beta + C^*_{\mu\alpha\nu\beta}C^{*\alpha}_\rho{}_\sigma{}^\beta)$ with $*$ denoting the Hodge dual, and it is completely symmetric and obeys the *differential* conservation law $\nabla_\mu T^\mu{}_{\nu\rho\sigma} = 0$. Given a unit timelike slicing vector $\vec{u}$ we conveniently have $W(\vec{u}) = T_{\mu\nu\rho\sigma}u^\mu u^\nu u^\rho u^\sigma = 1/2(E_{ij}E^{ij} + B_{ij}B^{ij}) \geq 0$ as a positive-definite *superenergy* built from the squares of the tidal and frame-drag fields in a given slice (see the reprint of Bel's excellent paper [10] for motivation and definition, e.g., Penrose and Rindler [5] for the spinor representation of the Bel-Robinson tensor, and e.g., [11] for its relation to notions of quasilocal energy). As another example, magnetic-parity modes of Schwarzschild are describable by the Regge-Wheeler function $Q(r_*,t)$ which satisfies the Sturm-Liouville equation $Q_{,r_*r_*} - Q_{,tt} - \mathcal{V}(r_*)Q = 0$ [Eq. (6.33) but with the $e^{-i\omega t}$ time dependence absorbed into Q]. The *integral* conservation law associated with this Sturm-Liouville equation is $\partial/\partial t \int_a^b \left(Q^2_{,r_*} + Q^2_{,t} + \mathcal{V}Q^2\right) dr_* = 2Q_{,r_*}Q_{,t}\big|_a^b$. The quantity inside the integral can be regarded as an energy density, and the quantity on the right hand side an energy flux. For the $(2,m)$ magnetic-parity mode, Eqs. (6.40a) and (6.40d) express Q in terms of the time derivative of the longitudinal part of $\delta\boldsymbol{\mathcal{B}}$ with its angular dependence Y^{2m} removed: $Q = (r^3/12)\partial\delta\mathcal{B}_{\hat{r}\hat{r}}/\partial t$. Others of Eqs. (6.40) and (6.54) relate $Q_{,r_*}$ to the LT parts of $\delta\boldsymbol{\mathcal{B}}$ and $\delta\boldsymbol{\mathcal{E}}$. This could be the foundation for a second way to make more precise the notion of energy fed back and forth between the various parts of $\delta\boldsymbol{\mathcal{B}}$ and $\delta\boldsymbol{\mathcal{E}}$.

substantial fraction of the total energy) goes into $\delta\boldsymbol{\mathcal{B}}^{\rm LT}$ and $\delta\boldsymbol{\mathcal{E}}^{\rm LT}$, which then use it to regenerate $\delta\boldsymbol{\mathcal{B}}^{\rm L}$, with its horizon-penetrating vortex lines switched in sign (color), leading to the next half cycle of oscillation.

The vortex lines that encircle the gravitational-wave tori are clearly visible in Fig. 6.6. Each solid (clockwise) line is tangential (it points nearly in the θ direction) when it is near the crest (the maximum-vorticity surface) of a blue (dark gray), lens-shaped gravitational-wave vortex. As it nears the north or south pole, it swings radially outward becoming very weak (low vorticity) and travels across the red trough of the wave, until it nears the next blue crest. There it swings into the transverse, θ direction and travels toward the other pole, near which it swings back through the red trough and joins onto itself in the original blue crest.

Each dashed (counterclockwise) closed vortex line behaves in this same manner, but with its transverse portions lying near red (light gray) troughs (surfaces of most negative vorticity). Near the red troughs, there are blue azimuthal vortex lines (not shown) that encircle the hole in the ϕ direction, and near the blue crests, there are red azimuthal lines.

Figure 6.7 sheds further light on these gravitational-wave tori. It shows in three dimensions some of the perturbative tendex lines for the (2,0) magnetic-parity mode that we are discussing. (For this mode, two families of perturbative tendex lines, one red [counterclockwise] and the other blue [clockwise], have nonzero tendicity and the third family has vanishing tendicity.) As is required by the structure of a gravitational wave (transverse tendex lines rotated by 45 degrees relative to transverse vortex lines), these perturbative tendex lines wind around tori with pitch angles of 45 degrees; one family winds clockwise and the other counterclockwise, and at each point the two lines have the same magnitude of vorticity.

A close examination of Fig. 6.7 reveals that the tori around which the perturbative tendex lines wrap are half as thick as the tori around which the vortex lines wrap. Each tendex-line torus in Fig. 6.7 is centered on a single node of the gravitational-wave field; the thick red torus in the upper right panel reaches roughly from one crest of the wave to an adjacent trough. By contrast, each vortex-line torus (Fig. 6.6 and black poloidal curves in Fig. 6.7) reach from crest to crest or trough to trough and thus encompass two gravitational-wave nodes.

Each node in the wave zone has a family of nested tendex-line tori centered on it. The four tendex-line tori shown in Fig. 6.7 are taken from four successive families, centered on four successive nodes. The second thin torus is from near the center of one nested family; it tightly hugs a node and therefore has near vanishing tendicity. The two thick tori are from the outer reaches of their nested families.

For further details of the (2,0) modes, see Secs. 6.5.3 and 6.5.4 below.

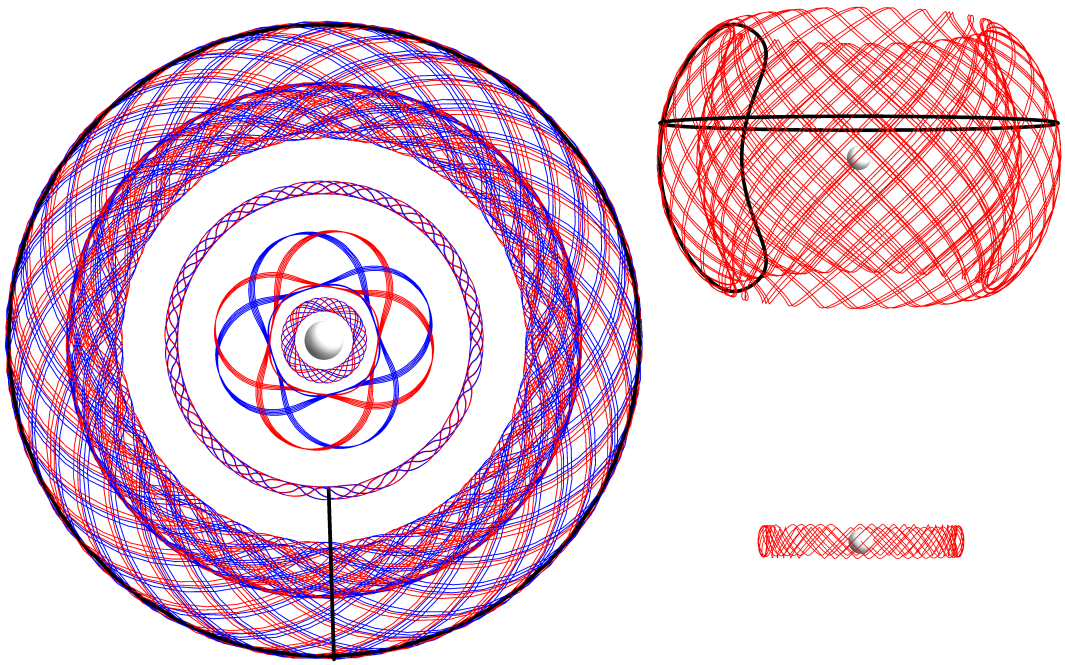

Figure 6.7: (color online). Positive-tendicity (blue) and negative-tendicity (red) perturbative tendex lines of a $(2, 0)$ magnetic-parity perturbation of a Schwarzschild black hole. These lines spiral around deformed tori of progressively larger diameter. The viewpoint is looking down onto the equatorial plane from the positive symmetry axis. *Upper right inset*: The negative tendex line spiraling around the outermost torus, viewed in cross section from the equatorial plane. *Lower right inset*: The negative tendex line spiraling around the small torus third from the center, viewed in cross section from the equatorial plane. Also shown, in black in the main drawing and the large inset, are two of this mode's vortex lines, one from Fig. 6.6 wrapping around the outermost torus in a $\mathcal{S}_\phi$ plane; the other an azimuthal circle wrapping around that torus in the ϕ direction. This figure was actually drawn depicting vortex lines of the electric-parity mode discussed in Sec. 6.5.4; but by duality (which is excellent in the wave zone), it also represents the tendexes of the magnetic-parity mode discussed in this section.

6.1.3.9 The superposed $(2, 2)$ and $(2, -2)$ magnetic-parity mode of a Schwarzschild hole

As we have seen, the magnetic-parity, $(2, 2)$ mode of a Schwarzschild black hole represents vortexes that rotate counterclockwise around the hole, spiraling outward and backward (Figs. 6.2, 6.3 and 6.4 above). If we change the sign of the azimuthal quantum number to $m = -2$, the vortexes rotate in the opposite direction, and spiral in the opposite direction. If we superpose these two modes (which, for Schwarzschild, have the same eigenfrequency), then, naturally, we get a non-rotating, oscillatory mode—whose dynamics are similar to those of the (2,0) mode of the last subsection. See Sec. 6.4 for details.

Figure 6.8 is a snapshot of the two families of vortex lines that lie in this mode's equatorial plane. The plane is colored by the vorticity of the dashed vortex lines; they are predominantly counterclockwise (red), though in some regions they are clockwise (blue).

The red (light gray) regions form *interleaved rings* around the black hole, that expand outward at

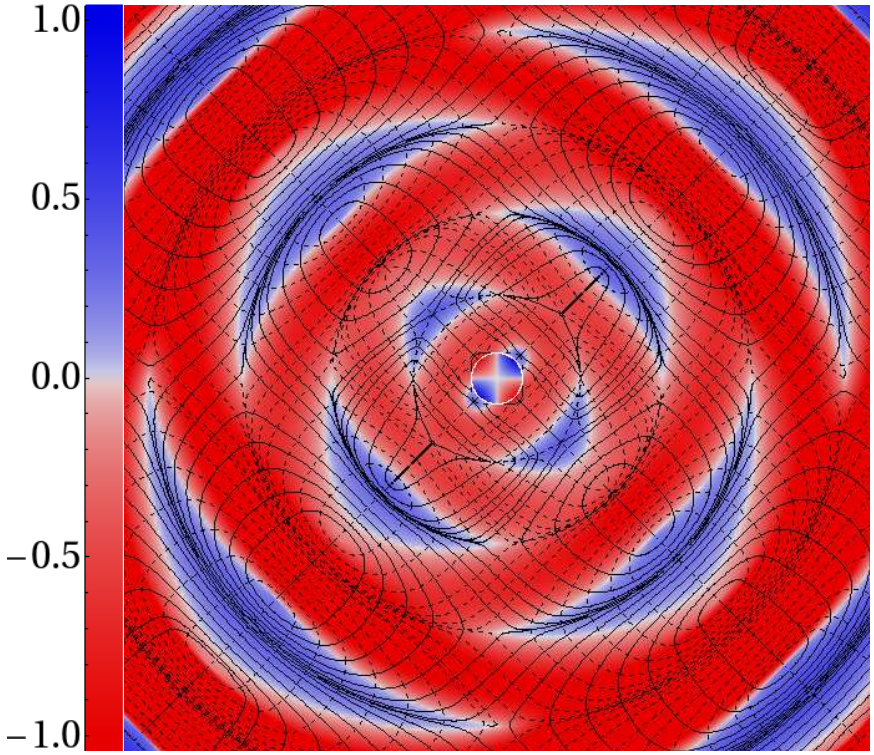

Figure 6.8: (color online). Equatorial vortex structure of the superposed $(2, 2)$ and $(2, -2)$, magnetic-parity, fundamental modes of a Schwarzschild black hole. The colors encode the vorticity of the dashed vortex lines. The vorticity of the solid lines is not shown, but can be inferred from the fact that under a 90° rotation, the dashed lines map into solid and the solid into dashed.

the speed of light, along with their dashed vortex lines. These rings are not tori in three dimensions because [by contrast with the $(2, 0)$ mode] the frame drag field grows stronger as one moves up to the polar regions, rather than weakening. As the mode oscillates, the longitudinal near-zone frame-drag field $\boldsymbol{\mathcal{B}}^{\rm L}$, which drives the mode, generates new interleaved rings, one after another and sends them outward.

During the oscillations, there are phases at which the longitudinal field $\boldsymbol{\mathcal{B}}^{\rm L}$ threading the hole goes to zero, and so the hole has vanishing horizon vorticity. The near-zone oscillation energy, at these phases, is locked up in the near-zone, longitudinal-transverse fields $\boldsymbol{\mathcal{B}}^{\rm LT}$ and $\delta\boldsymbol{\mathcal{E}}^{\rm LT}$, which, via the Maxwell-like Bianchi identities (and the propagation equation that they imply), then feed energy into the longitudinal near-zone frame-drag field $\boldsymbol{\mathcal{B}}^{\rm L}$, thereby generating new horizon-threading vortex lines, which will give rise to the next ejected interleaved ring.

We explore these dynamics in greater detail in Sec. 6.4.3.

6.1.4 This paper's organization

The remainder of this paper is organized as follows: In Sec. 6.2, we introduce the time slicing and coordinates used throughout this paper for the background Schwarzschild and Kerr spacetimes, we introduce the two gauges that we use for Schwarzschild perturbations (Regge-Wheeler-Zerilli and ingoing radiation gauges) and the one gauge (ingoing radiation) we use for Kerr, we discuss how our various results are affected by changes of gauge, and we discuss how we perform our computations. In Secs. 6.3, 6.4, and 6.5, we present full details of our results for the fundamental (most slowly damped) quadrupolar modes of Schwarzschild and Kerr: (2,2) modes in Sec. 6.3; superposed (2,2) and (2,-2) modes in Sec. 6.4, and both (2,1) and (2,0) modes in Sec. 6.5. In Sec. 6.3.4, we compare vortex lines computed in a numerical-relativity simulation of a binary black hole at a late time, when the merged hole is ringing down, with the vortex lines from this paper for the relevant quasinormal mode; we obtain good agreement. In Sec. 6.6, we make a few concluding remarks. And in six appendices, we present mathematical details that underlie a number of this paper's computations and results.

6.2 Slicings, Gauges and Computational Methods

When calculating the tidal and frame-drag fields of perturbed black-hole spacetimes, we must choose a slicing and also spatial coordinates on each slice, for both the background spacetime and at first order in the perturbations ("perturbative order"). The perturbative-order choices of slicing and spatial coordinates are together called the chosen *gauge*. We will always use the same choice of background slicing and coordinates in this study, but we will use different choices for our gauge.

This section describes the choices we make, how they influence the vortex and tendex lines and their vorticities and tendicities (which together we call the "vortex and tendex structures"), and a few details of how, having made our choices, we compute the perturbative frame-drag and tidal fields and the vortex and tendex structures. Most of the mathematical details are left to later sections and especially appendices.

In Sec. 6.2.1, we describe our choices of slicing and spatial coordinates. In Sec. 6.2.2, we sketch how we calculate the perturbative frame-drag and tidal fields and visualize their vortex and tendex structures. In Sec. 6.2.3, we explore how those structures change under changes of gauge, i.e., changes of the perturbative slicing and perturbative spatial coordinates.

6.2.1 Slicing, spatial coordinates, and gauge

Throughout this paper, for the background (unperturbed) Kerr spacetime, we use slices of constant Kerr-Schild (KS) time $\tilde{t}$, which is related to the more familiar Boyer-Lindquist time by

$$\tilde{t} = t + r_* - r \ , \quad \text{where} \quad \frac{dr_*}{dr} = \frac{r^2 + a^2}{\Delta} \tag{6.5}$$

(Eq. (6.2) of Paper II [4] (i.e. Chapter 5)). Here t and r are the Boyer-Lindquist time and radial coordinates, a is the black hole's spin parameter (angular momentum per unit mass), and $\Delta \equiv r^2 - 2Mr + a^2$, with M the black-hole mass. Our slices of constant $\tilde{t}$ penetrate the horizon smoothly, by contrast with slices of constant t, which are singular at the horizon. In the Schwarzschild limit $a \to 0$, t and r become Schwarzschild's time and radial coordinates, and $\tilde{t}$ becomes ingoing Eddington-Finkelstein time, $\tilde{t} = t + 2M \ln|r/2M - 1|$.

On a constant-$\tilde{t}$ slice in the background Kerr spacetime, we use Cartesian-like KS (Kerr-Schild) spatial coordinates, when visualizing vortex and tendex structures; but in many of our intermediary computations, we use Boyer-Lindquist spatial coordinates $\{r, \theta, \phi\}$ (which become Schwarzschild as $a \to 0$). The two sets of coordinates are related by

$$x + iy = (r + ia)e^{i\tilde{\phi}} \sin\theta \ , \quad z = r\cos\theta \ , \tag{6.6}$$

[Eq. (6.7) of Paper II]. Here

$$\tilde{\phi} = \phi + \int_r^\infty \frac{a}{\Delta} dr \tag{6.7}$$

[Eq. (6.5) of Paper II] is an angular coordinate that, unlike ϕ, is well behaved at the horizon. In the Schwarzschild limit, the KS $\{x, y, z\}$ coordinates become the quasi-Cartesian $\{x, y, z\}$ associated with Eddington-Finkelstein (EF) spherical coordinates $\{r, \theta, \phi\}$.

Our figures (e.g., 6.2–6.8 above) are drawn as though the KS $\{x, y, z\}$ were Cartesian coordinates in flat spacetime—i.e., in the Schwarzschild limit, as though the EF $\{r, \theta, \phi\}$ were spherical polar coordinates in flat spacetime.

We denote by $g^{(0)}_{\mu\nu}$ the background metric in KS spacetime coordinates [Eq. (6.8) of Paper II] (or EF spacetime coordinates in the Schwarzschild limit). When the black hole is perturbed, the metric acquires a perturbation $h_{\mu\nu}$ whose actual form depends on one's choice of gauge—i.e., one's choice of slicing and spatial coordinates at perturbative order.

For Schwarzschild black holes, we use two different gauges, as a way to assess the gauge dependence of our results: (i) *Regge-Wheeler-Zerilli (RWZ) gauge*, in which $h_{\mu\nu}$ is a function of two scalars (Q for magnetic parity and Z for electric parity) that obey separable wave equations in the Schwarzschild spacetime and that have spin-weight zero (see App. 6.7 for a review of this formalism), and (ii) *ingoing radiation (IR) gauge*, in which $h_{\mu\nu}$ is computed from the Weyl scalar Ψ_0 (or Ψ_4) that

obeys the separable Bardeen-Press equation. The method used to compute the metric perturbation from Ψ_0 is often called *the Chrzanowski-Cohen-Kegeles (CCK) procedure of metric reconstruction* (see App. 6.9).

In App. 6.10, we exhibit explicitly the relationship between the RWZ and IR gauges, for electric- and magnetic-parity perturbations. The magnetic-parity perturbations have different perturbative spatial coordinates, but the same slicing. (In fact, *all* gauges related by a magnetic-parity gauge transform have identically the same slicing for magnetic-parity perturbations of Schwarzschild [although the same is not true for Kerr]; see Sec. 6.2.3). For electric-parity perturbations, the two gauges have different slicings and spatial coordinates.

For all the perturbations that we visualize in this paper, the tendexes and vortexes show quite weak gauge dependence. See, e.g., Sec. 6.3, where we present results from both gauges. The results in Secs. 6.4 and 6.5 are all computed in RWZ gauge.

For Kerr black holes, there is no gauge analogous to RWZ; but the IR gauge and the CCK procedure that underlies it are readily extended from Schwarzschild to Kerr. In this extension, one constructs the metric perturbation from solutions to the Teukolsky equation (see App. 6.8) for the perturbations to the Weyl scalars Ψ_0 and Ψ_4, in an identical way to that for a Schwarzschild black hole described above. Our results in this paper for Kerr black holes, therefore, come solely from the IR gauge.

6.2.2 Sketch of computational methods

This section describes a few important aspects of how we calculate the tidal and frame-drag fields, and their vortex and tendex structures which are visualized and discussed in Secs. 6.3, 6.4, and 6.5.

We find it convenient to solve the eigenvalue problem in an orthonormal basis (orthonormal tetrad) given by the four-velocities of the Kerr-Schild (KS) or Eddington-Finkelstein (EF) observers, and a spatial triad, $\vec{e}_{\hat{a}}$, carried by these observers.

The background EF tetrad for the Schwarzschild spacetime, expressed in terms of Schwarzschild coordinates, is

$$\begin{aligned}
\vec{u}^{\,(0)} &= \frac{1}{\sqrt{1+2M/r}}\left(\frac{1}{\alpha^2}\frac{\partial}{\partial t} - \frac{2M}{r}\frac{\partial}{\partial r}\right) , \\
\vec{e}^{\,(0)}_{\hat{r}} &= \frac{1}{\sqrt{1+2M/r}}\left(\frac{\partial}{\partial r} - \frac{2M}{\alpha^2 r}\frac{\partial}{\partial t}\right) , \\
\vec{e}^{\,(0)}_{\hat{\theta}} &= \frac{1}{r}\frac{\partial}{\partial \theta} , \qquad \vec{e}^{\,(0)}_{\hat{\phi}} = \frac{1}{r\sin\theta}\frac{\partial}{\partial \phi}
\end{aligned} \tag{6.8}$$

[cf. Eqs. (4.4) of Paper II, which, however, are written in terms of the EF coordinate basis rather than Schwarzschild]. The background orthonormal tetrad for KS observers (in ingoing Kerr coordinates

$\{\tilde{t}, r, \theta, \tilde{\phi}\}$; see Paper II, Sec. VI C) is

$$\vec{u}^{(0)} = H\partial_{\tilde{t}} - \frac{2Mr}{H\Sigma}\partial_r\,, \qquad \vec{e}^{(0)}_{\hat{r}} = \frac{\sqrt{A}}{H\Sigma}\partial_r + \frac{aH}{\sqrt{A}}\partial_{\tilde{\phi}}\,,$$
$$\vec{e}^{(0)}_{\hat{\theta}} = \frac{1}{\sqrt{\Sigma}}\partial_\theta\,, \qquad \vec{e}^{(0)}_{\hat{\phi}} = \sqrt{\frac{\Sigma}{A}}\frac{1}{\sin\theta}\partial_{\tilde{\phi}}\,, \tag{6.9a}$$

where we have defined

$$\Sigma = r^2 + a^2\cos^2\theta\,, \tag{6.9b}$$
$$H = 1 + \frac{2Mr}{\Sigma}\,, \tag{6.9c}$$
$$A = (r^2+a^2)^2 - a^2(r^2 - 2Mr + a^2)\sin^2\theta \tag{6.9d}$$

[see Eq. (B2) of Paper II].

When the black hole is perturbed, the tetrad $\{\vec{u}^{(0)}, \vec{e}^{(0)}_{\hat{r}}, \vec{e}^{(0)}_{\hat{\theta}}, \vec{e}^{(0)}_{\hat{\phi}}\}$ acquires perturbative corrections that keep it orthonormal with respect to the metric $g_{\mu\nu} = g^{(0)}_{\mu\nu} + h_{\mu\nu}$. We choose the perturbative corrections to the observers' 4-velocity so as to keep it orthogonal to the space slices, i.e., so as to keep $\vec{u} = -\alpha\vec{\nabla}\tilde{t}$. (Here $\alpha = d\tau/d\tilde{t}$, differentiating along the observer's world line, is the observer's lapse function.) A straightforward calculation using the perturbed metric gives the following contravariant components of this $\vec{u}$:

$$u^\mu = u^\mu_{(0)} + u^\mu_{(1)}\,, \quad u^\mu_{(1)} = -\frac{1}{2}h_{\hat{0}\hat{0}}u^\mu_{(0)} - h^{\mu\nu}u^{(0)}_\nu\,. \tag{6.10}$$

where $h_{\hat{0}\hat{0}} = h_{\mu\nu}u^\mu_{(0)}u^\nu_{(0)}$, and $u^\mu_{(0)}$ is the four-velocity of the background observers.

We choose the perturbative corrections to the spatial triad $\{\vec{e}_{\hat{j}}\}$ so the radial vector stays orthogonal to surfaces of constant r in slices of constant $\tilde{t}$, the $\hat{\theta}$ direction continues to run orthogonal to curves of constant θ in surfaces of constant r and $\tilde{t}$, and the $\hat{\phi}$ vector changes only in its normalization.

When written in terms of the unperturbed tetrad and projections of the metric perturbation into the unperturbed tetrad, the perturbation to the tetrad then takes the form

$$\vec{u}_{(1)} = \frac{1}{2}h_{\hat{0}\hat{0}}\vec{u}_{(0)} - h_{\hat{0}\hat{i}}\vec{e}^{\hat{i}}_{(0)}\,, \tag{6.11a}$$
$$\vec{e}^{(1)}_{\hat{r}} = -\frac{1}{2}h_{\hat{r}\hat{r}}\vec{e}^{(0)}_{\hat{r}} - h_{\hat{r}\hat{A}}\vec{e}^{\hat{A}}_{(0)}\,, \tag{6.11b}$$
$$\vec{e}^{(1)}_{\hat{\theta}} = -\frac{1}{2}h_{\hat{\theta}\hat{\theta}}\vec{e}^{(0)}_{\hat{\theta}} - h_{\hat{\theta}\hat{\phi}}\vec{e}^{\hat{\phi}}_{(0)}\,, \tag{6.11c}$$
$$\vec{e}^{(1)}_{\hat{\phi}} = -\frac{1}{2}h_{\hat{\phi}\hat{\phi}}\vec{e}^{(0)}_{\hat{\phi}}\,, \tag{6.11d}$$

where $\hat{i}$ is summed over $\hat{r}$, $\hat{\theta}$, and $\hat{\phi}$, and $\hat{A}$ is summed over only $\hat{\theta}$ and $\hat{\phi}$.

In Appendices 6.7 (RWZ gauge) and 6.9 (IR gauge), we give the details of how we compute the

components

$$\mathcal{E}_{\hat{i}\hat{j}} = \mathcal{E}^{(0)}_{\hat{i}\hat{j}} + \mathcal{E}^{(1)}_{\hat{i}\hat{j}} , \quad \mathcal{B}_{\hat{i}\hat{j}} = \mathcal{B}^{(0)}_{\hat{i}\hat{j}} + \mathcal{B}^{(1)}_{\hat{i}\hat{j}} . \tag{6.12}$$

of the tidal and frame-drag field in this perturbed tetrad. The background portions $\mathcal{E}^{(0)}_{\hat{i}\hat{j}}$ and $\mathcal{B}^{(0)}_{\hat{i}\hat{j}}$ are the stationary fields of the unperturbed black hole, which were computed and visualized in Paper II. The perturbative pieces, $\mathcal{E}^{(1)}_{\hat{i}\hat{j}}$ and $\mathcal{B}^{(1)}_{\hat{i}\hat{j}}$ are the time-dependent, perturbative parts, which carry the information about the quasinormal modes, their geometrodynamics, and their gravitational radiation.

As part of computing the perturbative $\mathcal{E}^{(1)}_{\hat{i}\hat{j}} \equiv \delta\mathcal{E}_{\hat{i}\hat{j}}$ and $\mathcal{B}^{(1)}_{\hat{i}\hat{j}} \equiv \delta\mathcal{B}_{\hat{i}\hat{j}}$ for a chosen quasinormal mode of a Kerr black hole, we have to solve for the mode's Weyl-scalar eigenfunctions $\Psi^{(1)}_0$ and $\Psi^{(1)}_4$ and eigenfrequency ω. To compute the frequencies, we have used, throughout this paper, Emanuele Berti's elegant computer code [12], which is discussed in [13] and is an implementation of Leaver's method [14]. To compute the eigenfunctions, we our own independent code (which also uses the same procedure as that of Berti). In App. 6.9, we describe how we extract the definite-parity (electric or magnetic) eigenfunctions from the non-definite-parity functions.

To best visualize each mode's geometrodynamics and generation of gravitational waves in Secs. 6.3, 6.4, and 6.5, we usually plot the tendex and vortex structures of the perturbative fields $\mathcal{E}^{(1)}_{\hat{i}\hat{j}}$ and $\mathcal{B}^{(1)}_{\hat{i}\hat{j}}$. However, when we compare our results with numerical-relativity simulations, it is necessary to compute the tendex and vortex structures of the full tidal and frame-drag fields (background plus perturbation), because of the difficulty of unambiguously removing a stationary background field from the numerical simulations. As one can see in Figs. 6.15 and 6.26, in this case much of the detail of the geometrodynamics and wave generation is hidden behind the large background field.

In either case, the tendex and vortex structure of the perturbative fields or the full fields, we compute the field lines and their eigenvalues in the obvious way: At selected points on a slice, we numerically solve the eigenvalue problem

$$\mathcal{E}_{\hat{i}\hat{j}} V_{\hat{j}} = \lambda V_{\hat{i}} \tag{6.13}$$

for the three eigenvalues λ and unit-normed eigenvectors $V_{\hat{i}}$ of $\mathcal{E}_{\hat{i}\hat{j}}$, and similarly for $\mathcal{B}_{\hat{i}\hat{j}}$; and we then compute the integral curve (tendex or vortex line) of each eigenvector field by evaluating its coordinate components V^j in the desired coordinate system (KS or EF) and then numerically integrating the equation

$$\frac{dx^j}{ds} = V^j , \tag{6.14}$$

where s is the proper distance along the integral curve.

6.2.3 Gauge changes: Their influence on tidal and frame-drag fields and field lines

For perturbations of black holes, a perturbative gauge change is a change of the spacetime coordinates, $x^{\alpha'} = x^\alpha + \xi^\alpha$, that induces changes of the metric that are of order the metric perturbation; when dealing with definite parity perturbation, we split the generator of the transform ξ^α into definite electric- and magnetic-parity components. The gauge change has two parts: A change of slicing generated by ξ^0, and a change of spatial coordinates

$$\tilde{t}' = \tilde{t} + \xi^0 \quad x^{j'} = x^j + \xi^j \ . \tag{6.15}$$

Here all quantities are to be evaluated at the same event, $\mathcal{P}$, in spacetime.

Because ξ^0 is a scalar under rotations in the Schwarzschild spacetime—and all scalar fields in Schwarzschild have electric parity—for a magnetic-parity ξ^α, ξ^0 vanishes, and *the slicings for magnetic-parity quasinormal modes of Schwarzschild are unique. For these modes, all gauges share the same slicing* (see Appendix 6.10).[2]

6.2.3.1 Influence of a perturbative slicing change

For (electric-parity) changes of slicing, the new observers, whose world lines are orthogonal to the new slices, $\tilde{t}'$ =const, move at velocity

$$\Delta \boldsymbol{v} = -\alpha \boldsymbol{\nabla} \xi^0 \tag{6.16}$$

with respect to the old observers, whose world lines are orthogonal to the old slices $\tilde{t}$ =const). Here $\boldsymbol{\nabla}$ is the gradient in the slice of constant $\tilde{t}$, and $\alpha = (d\tau/d\tilde{t})$ is the lapse function, evaluated along the observer's worldline. In other words, $\Delta \boldsymbol{v}$ is the velocity of the boost that leads from an old observer's local reference frame to a new observer's local reference frame. Just as in electromagnetic theory, this boost produces a change in the observed electric and magnetic fields for small $\Delta \boldsymbol{v}$ given by $\Delta \boldsymbol{B} = \Delta \boldsymbol{v} \times \boldsymbol{E}$ and $\Delta \boldsymbol{E} = -\Delta \boldsymbol{v} \times \boldsymbol{B}$, so also it produces a change in the observed tidal and frame-drag fields given by

$$\Delta \boldsymbol{\mathcal{B}} = (\Delta \boldsymbol{v} \times \boldsymbol{\mathcal{E}})^{\rm S} \ , \quad \Delta \boldsymbol{\mathcal{E}} = -(\Delta \boldsymbol{v} \times \boldsymbol{\mathcal{B}})^{\rm S} \tag{6.17}$$

[2] In the Kerr spacetime, however, there are magnetic-parity changes of slicing, because ξ^0 no longer behaves as a scalar under rotations. To understand this more clearly, consider, as a concrete example, a vector in Boyer-Lindquist coordinates with covariant components $\xi_\mu = (0, 0, X^{lm}_\theta, X^{lm}_\phi) f(r) e^{-i\omega t}$, where X^{lm}_A are the components of a magnetic-parity vector spherical harmonic [see Eq. (6.88a)]. This vector's contravariant components are $\xi^\mu = (g^{t\phi} X^{lm}_\phi, 0, g^{\theta\theta} X^{lm}_\theta, g^{\phi\phi} X^{lm}_\phi) f(r) e^{-i\omega t}$, where $g^{t\phi}$, $g^{\theta\theta}$, and $g^{\phi\phi}$ are the contravariant components of the Kerr metric (which have positive parity). The vector ξ^μ, has magnetic parity and a nonvanishing component ξ^0; therefore, it is an example of a magnetic-parity gauge-change generator in the Kerr spacetime that changes the slicing.

(e.g., Eqs. (A12) and (A13) of [15], expanded to linear order in the boost velocity). Here the superscript S means symmetrize.

6.2.3.2 Example: Perturbative slicing change for Schwarzschild black hole

For a Schwarzschild black hole, because the unperturbed frame-drag field vanishes, $\Delta\boldsymbol{\mathcal{E}}$ is second order in the perturbation and thus negligible, so *the tidal field is invariant under a slicing change.* By contrast, the (fully perturbative) frame-drag field *can* be altered by a slicing change; $\Delta\boldsymbol{\mathcal{B}} = (\Delta\boldsymbol{v}\times\boldsymbol{\mathcal{E}})^{\rm S}$ is nonzero at first order.

Since the unperturbed tidal field is isotropic in the transverse (θ,ϕ) plane, the radial part of $\Delta\boldsymbol{v}$ produces a vanishing $\Delta\boldsymbol{\mathcal{B}}$. The transverse part of $\Delta\boldsymbol{v}$, by contrast, produces a radial-transverse $\Delta\boldsymbol{\mathcal{B}}$ (at first-order in the perturbation). In other words, *a perturbative slicing change in Schwarzschild gives rise to a vanishing $\Delta\boldsymbol{\mathcal{E}}$ and an electric-parity $\Delta\boldsymbol{\mathcal{B}}$ whose only nonzero components are*

$$\Delta\mathcal{B}_{\hat{r}\hat{\theta}} = \Delta\mathcal{B}_{\hat{\theta}\hat{r}} \quad \text{and} \quad \Delta\mathcal{B}_{\hat{r}\hat{\phi}} = \Delta\mathcal{B}_{\hat{\phi}\hat{r}} \ . \tag{6.18}$$

For a Schwarzschild black hole that is physically unperturbed, the first-order frame-drag field is just this radial-transverse $\Delta\boldsymbol{\mathcal{B}}$, and its gauge-generated vortex lines make 45 degree angles to the radial direction.

6.2.3.3 Influence of perturbative change of spatial coordinates

Because $\boldsymbol{\mathcal{E}}$ and $\boldsymbol{\mathcal{B}}$ are tensors that live in a slice of constant $\tilde{t}$, the perturbative change of spatial coordinates, which is confined to that slice, produces changes in components that are given by the standard tensorial transformation law, $\mathcal{E}_{i'j'}(x^{k'}[\mathcal{P}]) = \mathcal{E}_{pq}(x^k[\mathcal{P}])(\partial x^q/\partial x^{i'})(\partial x^p/\partial x^{j'})$. To first order in the gauge-change generators x^k, this gives rise to the following perturbative change in the tidal field

$$\Delta\mathcal{E}_{ij} \quad = \quad -\mathcal{E}_{ij,k}\xi^k - \mathcal{E}_{ik}\xi^k{}_{,j} - \mathcal{E}_{jk}\xi^k{}_{,i} = -\mathcal{E}_{ij|k}\xi^k - \mathcal{E}_{ik}\xi^k{}_{|j} - \mathcal{E}_{jk}\xi^k{}_{|i} \ , \tag{6.19}$$

and similarly for the frame-drag field $\mathcal{B}$. Here the subscript "|" denotes covariant derivative with respect to the background metric, in the slice of constant $\tilde{t}$. The two expressions in Eq. (6.19) are equal because the connection coefficients all cancel.

The brute-force way to compute the influence of a spatial coordinate change $x^{j'} = x^j + \xi^j$ on the coordinate shape $x^j(s)$ of a tendex line (or vortex line) is to (i) solve the eigenequation to compute the influence of $\Delta\mathcal{E}_{ij}$ [Eq. (6.19)] on the line's eigenvector, and then (ii) compute the integral curve of the altered eigenvector field.

Far simpler than this brute-force approach is to note that the tendex line, written as location

$\mathcal{P}(s)$ in the slice of constant $\tilde{t}$ as a function of spatial distance s along the curve, is unaffected by the coordinate change. Therefore, if the old coordinate description of the tendex line is $x^j(s) = x^j[\mathcal{P}(s)]$, then the new coordinate description is $x^{j'}(s) = x^j[\mathcal{P}(s)] + \xi^j[\mathcal{P}(s)]$; i.e., $x^{j'}(s) = x^j(s) + \xi^j[x^j(s)]$. In other words, *as seen in the new (primed) coordinate system, the tendex line appears to have been moved from its old coordinate location, along the vector field ξ^j, from its tail to its tip; and similarly for any vortex line.*

6.2.3.4 Example: Perturbative spatial coordinate change for a Schwarzschild black hole

Because the frame-drag field of a perturbed Schwarzschild black hole is entirely perturbative, it is unaffected by a spatial coordinate change. This, together with $\Delta\boldsymbol{\mathcal{B}} = 0$ for magnetic-parity modes implies that the frame-drag field of any magnetic-parity mode of Schwarzschild is fully gauge invariant!

By contrast, a spatial coordinate change (of any parity) mixes some of the background tidal field into the perturbation, altering the coordinate locations of the tendex lines.

As an example, consider an electric-parity (2,2) mode of a Schwarzschild black hole. In RWZ gauge and in the wave zone, the tidal field is given by

$$\begin{aligned}
\mathcal{E}_{\hat{\phi}\hat{\phi}} &= \frac{M}{r^3} + \frac{A}{r}\cos[2(\phi-\phi_o) - \omega(t-r_*)] \,, \\
\mathcal{E}_{\hat{\theta}\hat{\theta}} &= \frac{M}{r^3} - \frac{A}{r}\cos[2(\phi-\phi_o) - \omega(t-r_*)] \\
\mathcal{E}_{\hat{r}\hat{\phi}} &= \frac{2A}{\omega r^2}\cos[2(\phi-\phi_o) - \omega(t-r_*)] \,, \\
\mathcal{E}_{\hat{r}\hat{r}} &= -\frac{2M}{r^3} + \mathrm{O}\left(\frac{A}{\omega^2 r^3}\right) \,,
\end{aligned} \tag{6.20}$$

where A is the wave amplitude

Focus on radii large enough to be in the wave zone, but small enough that the wave's tidal field is a small perturbation of the Schwarzschild tidal field. Then the equation for the shape of the nearly circular tendex lines that lie in the equatorial plane, at first order in the wave's amplitude, is

$$\frac{1}{r}\frac{dr}{d\phi} = \frac{\mathcal{E}_{\hat{r}\hat{\phi}}}{(\mathcal{E}_{\hat{\phi}\hat{\phi}} - \mathcal{E}_{\hat{r}\hat{r}})} = \frac{2rA}{3M\omega}\cos[2(\phi-\phi_o) - \omega(t-r_*)] \tag{6.21}$$

(an equation that can be derived using the standard perturbation theory of eigenvector equations). Solving for $r(\phi)$ using perturbation theory, we obtain for the tendex line's coordinate location

$$\begin{aligned}
r(\phi,t) &= r_o + \rho(\phi, r_o, t) \,, \\
\rho(\phi, r_o, t) &\equiv r_o \frac{A r_o}{3M\omega}\sin[2(\phi-\phi_o) - \omega(t-r_{o*})] \,.
\end{aligned} \tag{6.22}$$

Here r_o is the radius that the chosen field line has when $\phi = \phi_o$. Notice that the field line undergoes a quadrupolar oscillation, in and out, as it circles around the black hole, and it is closed—i.e., it is an ellipse centered on the hole. The ellipticity is caused by the gravitational wave. As time passes, the ellipse rotates with angular velocity $d\phi/dt = \omega/2$, and the phasing of successive ellipses at larger and larger radii r_o is delayed by an amount corresponding to speed-of-light radial propagation.

Now, consider an unperturbed Schwarzschild black hole. We can produce this same pattern of elliptical oscillations of the equatorial-plane tendex lines, in the absence of any gravitational waves, by simply changing our radial coordinate: Introduce the new coordinate

$$r' = r + \xi^r, \quad \text{where} \quad \xi^r = \rho(\phi, r, t) \,, \tag{6.23}$$

with ρ the function defined in Eq. (6.22). In Schwarzschild coordinates, the equatorial tendex lines are the circles $r = r_o$ =constant. In the new coordinate system, those tendex lines will have precisely the same shape as that induced by our gravitational wave [Eq. (6.22)]: $r' = r_o + \rho(\phi, r_o, t)$. Of course, a careful measurement of the radius of curvature of one of these tendex lines will show it to be constant as one follows it around the black hole (rather than oscillating), whereas the radius of curvature of the wave-influenced tendex line will oscillate. In fact, if we follow along with the tendex line and measure the tendicity *along* the line, we find that the tendicity of the line is unchanged by the change in coordinates. To be explicit, consider the tendicity, which we denote λ_ϕ, along one of the lines $r = r_o$. Enacting the coordinate transform on the tendicity but continuing to evaluate it along the perturbed line, we have the identity

$$\lambda_\phi(r)|_{r=r_o} = \lambda_\phi(r' - \xi^r)|_{r'=r_o+\rho} = \lambda_\phi(r_o + \rho - \rho) = \lambda_\phi(r_o) \,. \tag{6.24}$$

Nevertheless, if one just casually looks at the Schwarzschild tendex lines in the new, primed, coordinate system, one will see a gravitational-wave pattern.

The situation is a bit more subtle for the perturbed black hole. In this case, the tendex lines are given by Eq. (6.22), and we can change their ellipticity by again changing radial coordinates, say to

$$r' = r + \alpha\rho(\phi, r, t) \,. \tag{6.25}$$

The radial oscillations $\Delta r'$ of the elliptical tendex lines in the new (r', ϕ, t) coordinate system will have amplitudes $1 + \alpha$ times larger than in the original (r, ϕ, t) coordinates, and in the presence of the gravitational waves it may not be easy to figure out how much of this amplitude is due to the physical gravitational waves and how much due to rippling of the coordinates.

On the other hand, the tendicities of these tendex lines are unaffected by rippling of the coordinates. They remain equal to $\lambda_\phi = \mathcal{E}_{\hat{\phi}\hat{\phi}} = M/r^3 + (A/r)\cos[2(\phi - \phi_o) - \omega(t - r_*)] = M/(r')^3 +$

$(A/r')\cos[2(\phi-\phi_o)-\omega(t-r'_*)]$ at leading order, which oscillates along each closed line by the amount $\Delta\mathcal{E}_{\hat{\phi}\hat{\phi}} = (A/r)\cos[2(\phi-\phi_o)-\omega(t-r_*)]$ that is precisely equal to the gravitational-wave contribution to the tendicity. Note that in this example, even without evaluating the tendicity along the perturbed lines to cancel the coordinate change, the change in the tendicity due to the coordinate change enters at a higher order than the contribution from the gravitational wave.

Therefore, in this example, the tendicity and correspondingly the structures of tendexes capture the gravitational waves cleanly, whereas the tendex-line shapes do not do so; the lines get modified by spatial coordinate changes. This is why we pay significant attention to tendexes and also vortexes in this paper, rather than focusing solely or primarily on tendex and vortex lines.

6.3 $(2,2)$ Quasinormal Modes of Schwarzschild and Kerr Black Holes

In Sec. 6.1.3.6, we described the most important features of the fundamental, (2,2) quasinormal modes of Schwarzschild black holes. In this section, we shall explore these modes in much greater detail and shall extend our results to the (2,2) modes of rapidly spinning Kerr black holes. For binary-black-hole mergers, these are the dominant modes in the late stages of the merged hole's final ringdown (see, e.g., [16]).

6.3.1 Horizon vorticity and tendicity

We can compute the horizon tendicity $\mathcal{E}_{NN}$ and vorticity $\mathcal{B}_{NN}$ [or equivalently $\Psi_2 = \frac{1}{2}(\mathcal{E}_{NN} + i\mathcal{B}_{NN})$] using two methods: first, we can directly evaluate them from the metric perturbations, and second, we can calculate them, via Eq. (6.116) in the form (6.118), from the ingoing-wave curvature perturbation Ψ_0, which obeys the Teukolsky equation (App. 6.8). For perturbations of Schwarzschild black holes, both methods produce simple analytical expressions for the horizon quantities; they both show that the quantities are proportional to a time-dependent phase times a scalar spherical harmonic, $e^{-i\omega t}Y_{lm}$ [see, e.g., Eq. (6.123)]. For Kerr holes, the simplest formal expression for the horizon quantities is Eq. (6.118), and there is no very simple analytical formula. Nevertheless, from these calculations one can show that there is an exact duality between $\mathcal{E}_{NN}$ and $\mathcal{B}_{NN}$ in ingoing radiation gauge for quasinormal modes with the same order parameters (n,l,m) but opposite parity, for both Schwarzschild and Kerr black holes; see App. 6.11.2. For Schwarzschild black holes in RWZ gauge, there is also a duality for the horizon quantities, although it is complicated by a perturbation to the position of the horizon in this gauge; see Appendices. 6.7.4 and 6.7.5 for further discussion.

In Fig. 6.9, we show $\delta\mathcal{E}_{NN}$ and $\delta\mathcal{B}_{NN}$ for the $(2,2)$ modes with both parities, of a Schwarzschild black hole (upper row) and a rapidly rotating Kerr black hole (bottom row).

The duality is explicit in the labels at the top: the patterns are identically the same for $\delta\mathcal{E}_{NN}$ (tendexes) of electric-parity modes and $\delta\mathcal{B}_{NN}$ (vortexes) of magnetic-parity modes [left column]; and also identically the same when the parities are switched [right column] The color coding is similar to Fig. 6.3 above (left-hand scale). The red (light gray) regions are stretching tendexes or counterclockwise vortexes (negative eigenvalues); the blue (dark gray), squeezing tendexes or clockwise vortexes (positive eigenvalues).

For the Schwarzschild hole, the electric-parity tendex pattern and magnetic-parity vortex pattern (upper left) is that of the spherical harmonic $Y^{22}(\theta,\phi)$, and the perturbative electric-parity vorticity and magnetic-parity tendicity vanish (upper right).

For the rapidly spinning Kerr hole, the electric-parity tendexes and magnetic-parity vortexes (lower left) are concentrated more tightly around the plane of reflection symmetry than they are for the Schwarzschild hole, and are twisted; but their patterns are still predominantly Y^{22}. And also for Kerr, the (perturbative) electric-parity vorticity and magnetic-parity tendicity have become nonzero (lower right), they appear to be predominantly $Y^{32}(\theta,\phi)$ in shape, they are much less concentrated near the equator and somewhat weaker than the electric-parity tendicity and magnetic-parity vorticity (lower left).

6.3.2 Equatorial-plane vortex and tendex lines, and vortexes and tendexes

As for the weak-field, radiative sources of Paper I, so also here, the equatorial plane is an informative and simple region in which to study the generation of gravitational waves.

For the (2,2) modes that we are studying, the $\delta\mathcal{E}_{jk}$ of an electric-parity perturbation and the $\delta\mathcal{B}_{jk}$ for magnetic parity are symmetric about the equatorial plane. This restricts two sets of field lines (tendex lines for electric-parity $\delta\mathcal{E}_{jk}$; vortex lines for magnetic-parity $\delta\mathcal{B}_{jk}$) to lie in the plane and forces the third to be normal to the plane. By contrast, the electric-parity $\delta\mathcal{B}_{jk}$ and magnetic-parity $\delta\mathcal{E}_{jk}$ are reflection antisymmetric. This requires that two sets of field lines cross the equatorial plane at 45° angles, with equal and opposite eigenvalues (tendicities or vorticities), and forces the third set to lie in the plane and have zero eigenvalue; this third set of zero-vorticity vortex lines have less physical interest and so we will not illustrate them.

In this section, we shall focus on the in-plane field lines and their vorticities and tendicities.

6.3.2.1 Magnetic-parity perturbations of Schwarzschild black holes

In Sec. 6.1.3.6 and Figs. 6.2 and 6.3, we discussed some equatorial-plane properties of the magnetic-parity $(2,2)$ mode. Here we shall explore these and other properties more deeply. Recall that for the magnetic-parity mode, the frame-drag field, and hence also the vortex lines and their vorticities,

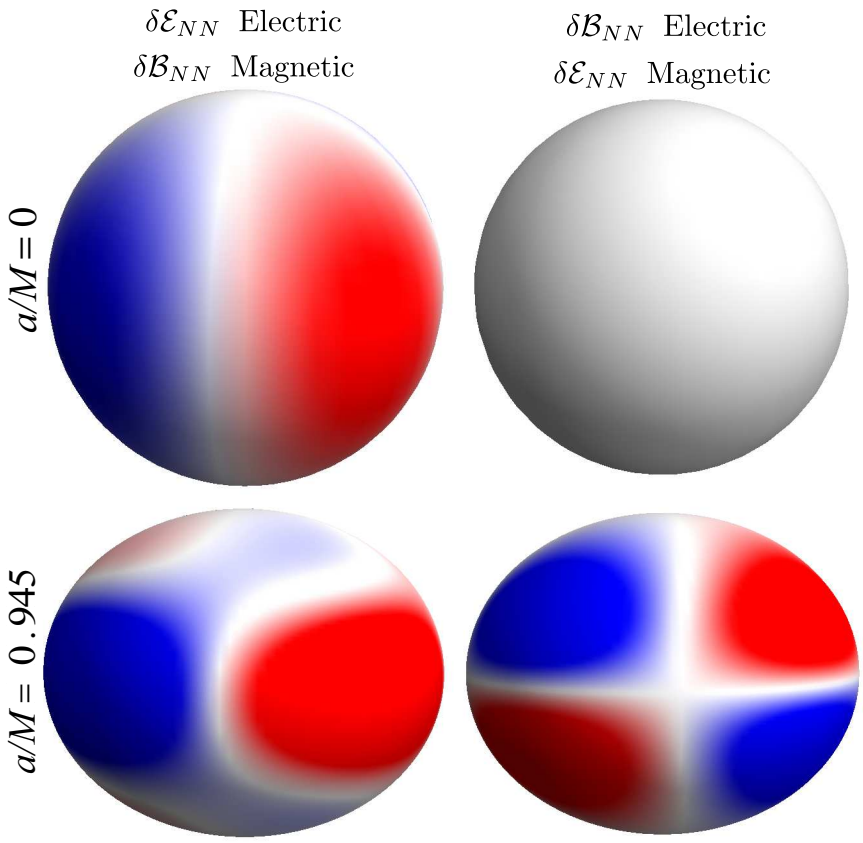

Figure 6.9: (color online). Perturbative horizon tendicities $\delta\mathcal{E}_{NN}$ and vorticities $\delta\mathcal{B}_{NN}$ for the $(2,2)$ quasinormal modes with electric and magnetic parities (see column labels at the top). The top row is for a Schwarzschild black hole, $a = 0$; the bottom for a rapidly spinning Kerr black hole, $a/M = 0.945$. The color intensity is proportional to the magnitude of the tendicity or vorticity, with blue (dark gray) for positive and red (light gray) for negative. For discussion, see Sec. 6.3.1 of the text.

are fully gauge invariant.

In Fig. 6.10, we show six different depictions of the vortex lines and their vorticities in the equatorial plane, each designed to highlight particular issues. See the caption for details of what is depicted.

The radial variation of vorticity is not shown in this figure, only the angular variation. The vorticity actually passes through a large range of values as a function of radius: from the horizon to roughly $r = 4M \simeq 1.5\lambda$ (roughly the outer edge of the near zone), the vorticity rapidly decreases; between $r \simeq 4M$ and $12M$ (roughly the extent of the transition zone), it falls off as $1/r$; and at $r \gtrsim 12M$ (the wave zone), it grows exponentially due to the damping of the quasinormal mode as time passes. (The wave field at larger radii was emitted earlier when the mode was stronger.) In the figure, we have removed these radial variations in order to highlight the angular variations.

By comparing the left panels of Fig. 6.10 with Fig 9 of Sec. VI D of Paper I, we see a strong resemblance between the vortex lines of our $(2,2)$, magnetic-parity perturbation of a Schwarzschild

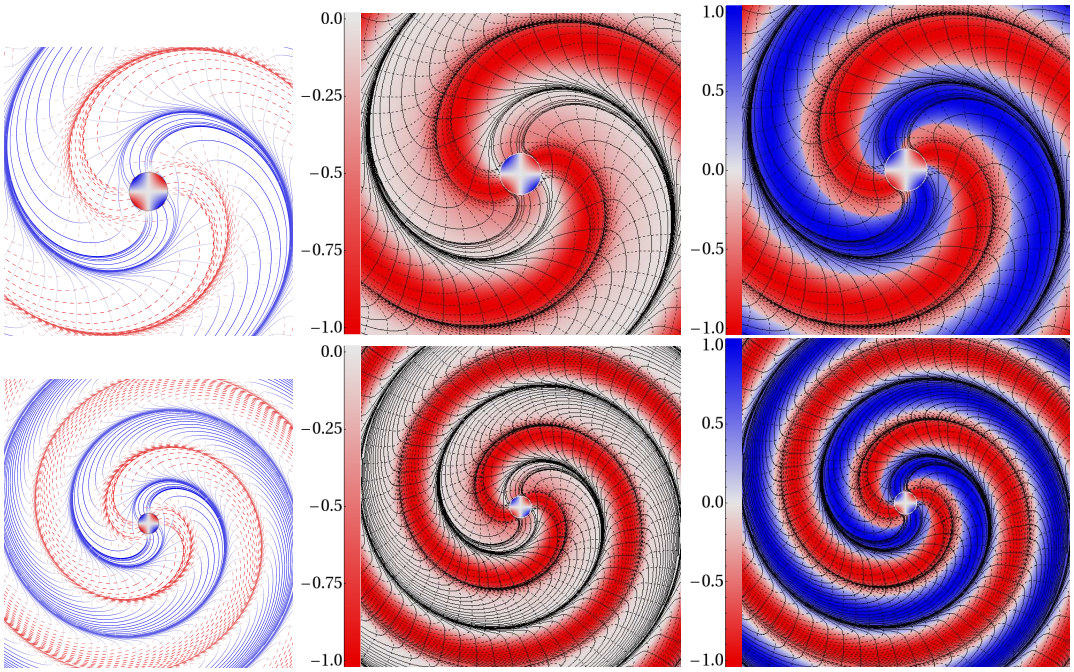

Figure 6.10: (color online). Three representations of the vortex lines and vortexes in the equatorial plane of a Schwarzschild black hole perturbed by a magnetic-parity $(2, 2)$ quasinormal mode. The bottom panels span a region $56M$ on each side, and the top panels are a zoom-in of the lower panels, $30M$ on each side. All panels show positive-vorticity lines as solid and negative-vorticity lines as dashed. In all panels, blue (dark gray) corresponds to positive and red (light gray) to negative; the intensity of the color indicates the strength of the vorticity at that point normalized by the maximum of the vorticity at that radius (darker shading indicates a larger strength and lighter, weaker). Similarly, in all panels, the central circle surrounded by a narrow white line is the horizon colored by its vorticity as described above. *Left column*: Vortex lines colored and shaded by their scaled vorticity. *Middle column*: Negative vorticity coloring the plane with black vortex lines. *Right column*: Vorticity with the larger absolute value coloring the plane and black vortex lines. For discussion of this figure, see Sec. 6.3.2.1.

black hole, and those of a rotating current quadrupole in linearized theory. As in linearized theory, when the radial (or, synonymously, longitudinal) vortex lines in the near zone rotate, the effects of time retardation cause the lines, in the transition and wave zones, to collect around four backspiraling regions of strong vorticity (the vortexes) and to acquire perturbative tendex lines as they become transverse-traceless gravitational waves. The most important difference is that, for the black-hole perturbations, the positive vortex lines emerge from the blue, clockwise horizon vortexes and spiral outward (and the negative vortex lines emerge from the counterclockwise horizon vortexes) rather than emerging from a near-zone current quadrupole.

Although the left panels of Fig. 6.10 highlight most clearly the comparison with figures in Paper I, the middle and right panels more clearly show the relationship between the vortex lines (in black) and the vorticities, throughout the equatorial plane. In the middle panels (which show only the negative vorticity), the negative vortex lines that emerge longitudinally from the horizon stay in

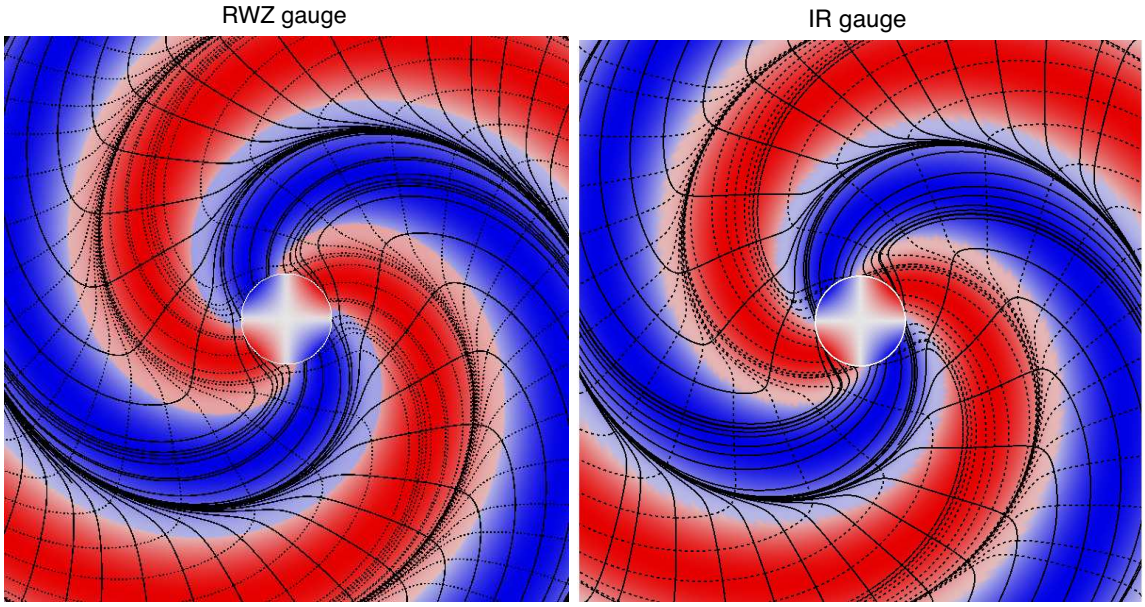

Figure 6.11: (color online). The equatorial-plane, electric-parity tendexes and tendex lines of a $(2, 2)$ perturbation of a Schwarzschild black hole in RWZ gauge (left panel) and IR gauge (right panel). The conventions for the lines, the coloring and the shading are identical to those in the right panels of Fig. 6.10.

the center of their vortex in the near zone, and then collect onto the outer edge of the vortex in the transition and wave zones. Interestingly, near the horizon, there are also two weaker regions of negative vorticity between the two counterclockwise vortexes, regions associated with the tangential negative vortex lines that pass through this region without attaching to the horizon (and that presumably represent radiation traveling into the horizon).

In the right panels of Fig. 6.10 (which show the in-plane vorticity with the larger absolute value), a clockwise vortex that extends radially from the horizon takes the place of the weaker region of counterclockwise vorticity. From these panels, it is most evident that the vortexes and vortex lines of opposite signs are identical, though rotated by 90°. These panels also highlight that there are four spirals of nearly zero vorticity that separate the vortexes in the wave zone, which the spiraling vortex lines approach. All three vorticities nearly vanish at these spirals; in the limit of infinite radius, they become vanishing points for the radiation, which must exist for topological reasons [17] (i.e. Chapter 4).

6.3.2.2 Gauge dependence of electric-parity tendexes for a Schwarzschild black hole

In this subsection, we explore the gauge dependence of the (2,2) modes for a Schwarzschild black hole. In Sec. 6.2.3, we showed that for magnetic-parity modes, all gauges share the same slicing. Therefore, to maximize any gauge dependence that there might be, we focus on the electric-parity (2,2) mode.

Because the frame-drag field of the unperturbed Schwarzschild black hole vanishes, this mode's perturbative frame-drag field will be unaffected by perturbative changes of the spatial coordinates. Therefore, we focus on the perturbative tidal field $\delta\boldsymbol{\mathcal{E}}$ of the electric-parity mode, which is sensitive to *both* perturbative slicing changes and perturbative spatial coordinate changes.

In Fig. 6.11, we plot this field's perturbative equatorial tendexes and tendex lines for the electric-parity (2,2) mode in RWZ gauge (left panel) and IR gauge (right panel)—which differ, for this mode, in both slicing and spatial coordinates. The tendex lines for the two gauges were seeded at the same coordinate points, so all the differences between the panels can be attributed to the gauge differences.

The two panels are almost identical. Therefore, these maximally sensitive tendexes and tendex lines are remarkably unaffected by switching from one gauge to the other. The primary differences are that (i) the tendex lines of IR gauge which are near the black hole tend to be pulled closer to the horizon as compared to RWZ gauge (ii) the lines falling onto the attracting spiral are bunched even more tightly in IR gauge than in RWZ gauge; however, more lines reach the spiral in RWZ gauge in this figure, and (iii) the four tendex spirals wind more tightly in IR gauge, which is most easily seen by comparing the lower right and upper left corners of the two panels.

One subtlety that must be remarked upon is that the central circle colored by the normal-normal component of the tidal field (surface tendicity) in the RWZ gauge (left panel of Fig. 6.11) is simply the surface $r = 2M$, and not the true event horizon. The location of the event horizon is affected by the perturbations in a gauge-dependent manner, as discussed by Vega, Poisson, and Massey [18]. We rely on the results of this article in the brief discussion that follows. In RWZ gauge, the horizon is at $r_H = 2M + \delta r(\tilde{t}, \theta, \phi)$, where the function δr can be solved for by ensuring that the vector tangent to the perturbed generators (in our case, $l^\mu = \partial x^\mu / \partial \tilde{t}$) remains null [18]. We give an expression for δr in Appendix 6.7.5. There we also discuss the correction to the horizon tendicity in RWZ gauge. One key result is that the horizon tendicity has the same angular distribution in RWZ gauge as in IR gauge (given by the Y^{22} spherical harmonic), so that the normal-normal tendicity on the horizon and on the surface at $r = 2M$ differ only by an amplitude and phase in RWZ gauge. Meanwhile, in IR gauge the horizon remains at $r_H = 2M$ and so the colored central circle is in fact the horizon, colored by its horizon tendicity.

However, the bulk tendexes and tendex lines are determined completely independently of these horizon considerations, and so Fig. 6.11 provides an accurate comparison of them in the two gauges.

6.3.2.3 Duality and influence of spin in the equatorial plane

In this subsection, we use Fig. 6.12 to explore duality and the influence of spin, for the fundamental $(2, 2)$ mode.

By comparing the left and center panels in the top row of Fig. 6.12, we see *visually* the near duality between the electric- and magnetic-parity modes for a Schwarzschild hole. This near duality

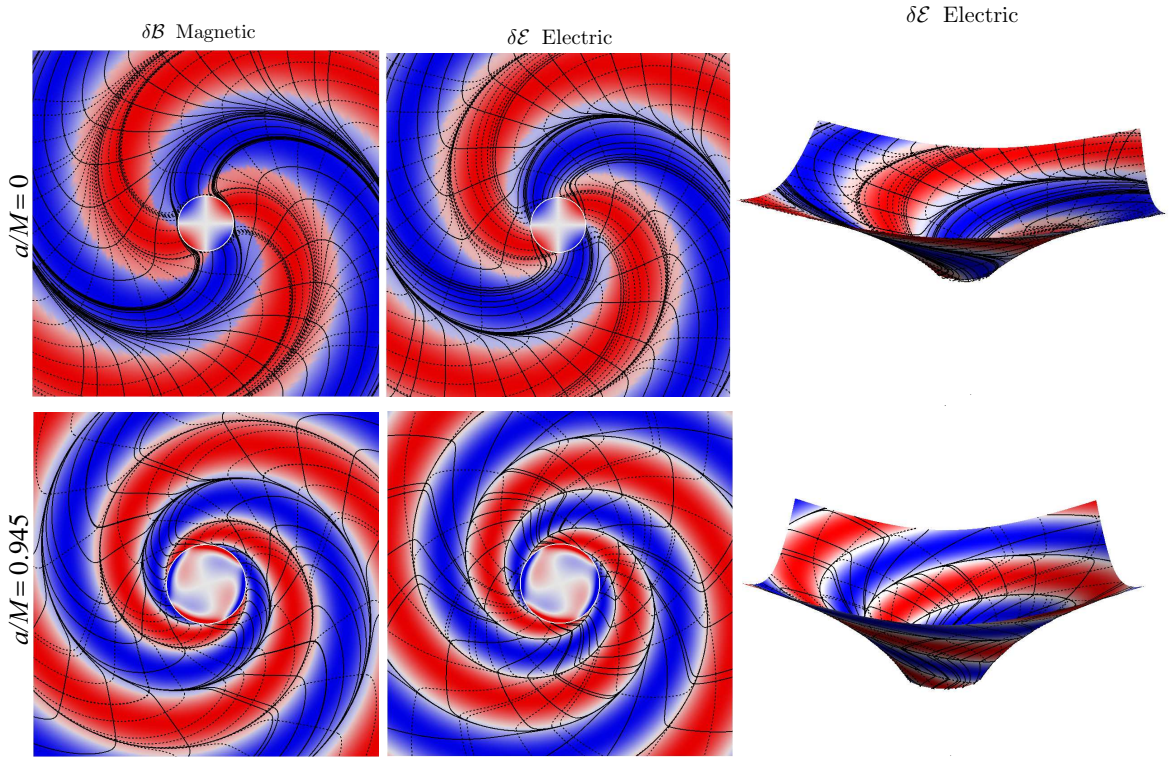

Figure 6.12: (color online). Vortexes and tendexes and their field lines in the equatorial plane for $(2, 2)$ modes of Schwarzschild and Kerr black holes. The lines, the coloring and the shading are identical to those in the right panels of Fig. 6.10. The upper row is for a Schwarzschild black hole ($a = 0$); the lower row, for a rapidly spinning Kerr black hole ($a = 0.945$); see labels on the left. The left column shows the vortex lines and vorticities for magnetic parity (which are gauge invariant for the perturbations of a Schwarzschild hole); the middle and right columns show the tendex lines and tendicities for the electric-parity mode in IR gauge; see labels at the top. In the right column, the equatorial plane is isometrically embedded in three-dimensional Euclidean space. The top panels are $24M$ across; the bottom, $14M$. This figure elucidates duality and the influence of black-hole spin; see the discussion in Sec. 6.3.2.3.

is explored *mathematically* in App. 6.9. Specifically, the vortexes and their lines for the magnetic-parity mode (left) are nearly identical to the tendexes and their lines for the electric-parity mode. The only small differences appear in the size of the nearly zero-vorticity (or tendicity) regions, and the curvatures of the lines.

For the fast-spinning Kerr black hole (the bottom left and center panels of Fig. 6.12), the near duality is still obvious, especially in the colored vortexes and tendexes; but it is less strong than for Schwarzschild, especially in the field lines. The vortex lines (on the left) continue to look like those of a Schwarzschild black hole, but the tendex lines (in the middle) curve in the opposite direction, which makes some lines reach out from the horizon and connect back to it instead of spiraling away from the horizon.

By comparing the top and bottom panels in the left and center columns of Fig. 6.12, we see the influence of the background black hole's spin on the dynamics of the perturbative vortexes and

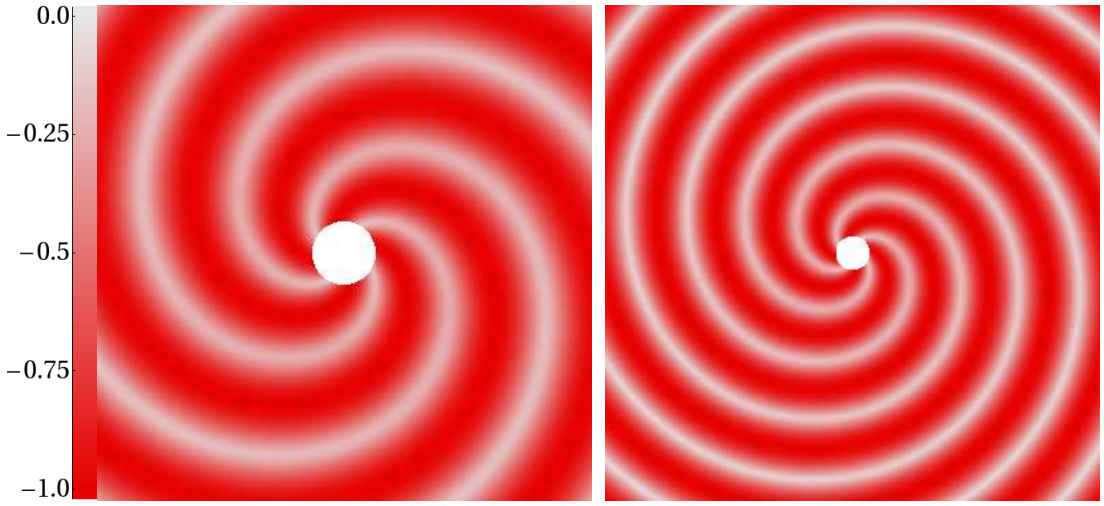

Figure 6.13: (color online). For an electric-parity (2,2) mode of a Schwarzschild black hole: the vorticity of the counterclockwise vortex lines that pass through the equatorial plane at a 45 degree angle. The clockwise vortex lines that pass through the plane have equal and opposite vorticity. By near duality, this figure also depicts the perturbative tendex structure for the magnetic-parity (2,2) mode. The conventions for coloring and shading are the same as in Fig. 6.10. Because the horizon vorticity is exactly zero for this mode, the horizon is shown as a white disk. The left panel, a region $30M$ across, is a zoom in of the right panel, which is $56M$ across.

tendexes. For fast Kerr (bottom), the vortexes and tendexes near the horizon look more transverse (less radial) than for Schwarzschild, because the size of the near zone is much smaller. (The frequency of the waves is nearly twice that for a perturbed Schwarzschild hole.) The higher frequency also explains why the spirals of the vortexes and tendexes are tighter.

In the isometric embedding diagrams in the right column of Fig. 6.12, we see that proper radial distance in the near zone is somewhat larger than it appears in the flat, planar drawing. Taking this into account, we conclude that, aside from a few small differences, the qualitative ways in which waves are generated for fast Kerr and for Schwarzschild are the same: two pairs of vortexes or tendexes emerge longitudinally from horizon vortexes, and twist into backward spirals that eventually form the transverse-traceless gravitational waves.

6.3.2.4 Vortexes of electric-parity mode, and perturbative tendexes of magnetic-parity mode for a Schwarzschild black hole

In Fig. 6.13, we visualize the vortexes of the electric-parity $(2, 2)$ mode of a Schwarzschild hole. (By near duality, the perturbative tendexes of the magnetic-parity mode must look nearly the same.)

As noted at the beginning of Sec. 6.3.2, reflection antisymmetry of the frame-drag field for this electric-parity mode dictates that through each point in the plane there will pass one zero-vorticity vortex line lying in the plane, and two vortex lines with equal and opposite vorticities that pass through the plane at 45 degree angles and are orthogonal to each other and to the zero-vorticity

line. The vorticity plotted in Fig. 6.13 is that of the counterclockwise, 45 degree line. For the clockwise line, the vorticity pattern is identically the same, but blue instead of red.

There are again four regions of strong vorticity (four vortexes), which spiral outward from the horizon, becoming gravitational waves. In this case, the four regions look identical, whereas for the tendexes of this same electric-parity mode (middle column of Fig. 6.12) there is an alternation between blue and red. There is actually an alternation here, too, though it does not show in the figure: The relative tilt of the lines (in the sense of the ϕ direction) rotates, such that in one tendex, the red tendex lines pass through the plane with a forward 45 degree tilt on average, and in the next tendex, with a backward 45 degree tilt; and conversely for the blue tendex lines.

6.3.3 Three-Dimensional vortexes and tendexes

In this section, we shall explore the 3-dimensional vortexes and tendexes of the $(2, 2)$ modes of Schwarzschild and Kerr black holes, which are depicted in Fig. 6.14. In the first subsection, we shall focus on what this figure tells us about the generation of gravitational waves, and in the second, what it tells us about duality.

6.3.3.1 Physical description of gravitational-wave generation

In Sec. 6.1.3.6 of the Introduction, we summarized in great detail what we have learned about gravitational-wave generation from our vortex and tendex studies. There we focused on the $(2, 2)$ magnetic-parity mode, and among other things we scrutinized the upper left panel of Fig. 6.14 (which we reproduced as Fig. 6.4). Here, instead, we shall focus on the $(2, 2)$ electric-parity mode as depicted in the right half of Fig. 6.14.

We begin with the perturbative tendexes of the electric-parity, (2,2) mode of a Schwarzschild black hole (third panel on top row of Fig. 6.14). The 3-D tendexes emerge from the horizon as four deformed-cylinder structures, two red (light gray) and two blue (dark gray). These are the extensions into the third dimension of the four near-zone, equatorial-plane tendexes of the center panel in Fig. 6.12 above. As we enter the transition zone, the four 3D tendexes lengthen vertically (parallel to the poles), and then as we enter the wave zone, they spiral upward and downward around the poles; they have become gravitational waves. They are concentrated near the poles because the (2,2)–mode gravitational waves are significantly stronger in polar directions than in the equator.

In this panel, we also see black tendex lines that emerge from the horizon and spiral upward and downward alongside the polar-spiraling tendexes, becoming nearly transverse at large radii—part of the outgoing gravitational waves. Of course, there are similar tendex lines, not shown, inside the spiraling tendexes. In addition, we also see tendex lines in the inner part of the wave zone that are approximately polar circles; these are also part of the outgoing waves.

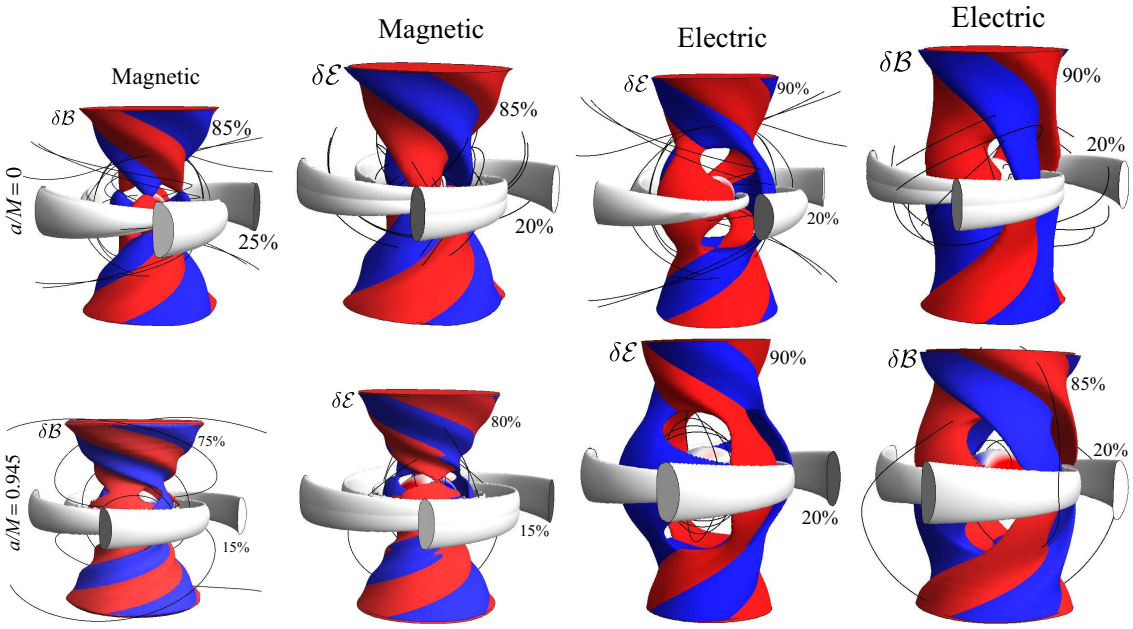

Figure 6.14: (color online). Three-dimensional vortexes and tendexes of the same four modes as are shown in Fig. 6.12. As there, so here, the top row is for a Schwarzschild black hole, and the bottom for fast-spin Kerr, $a = 0.945$; the left two columns (one in Fig. 6.12) are for a magnetic-parity (2,2) mode (with the vortexes in IR coordinates), and the right two columns (one in Fig. 6.12) are for electric parity in IR gauge. For each parity, the first column shows structures of the field that generates the waves ($\delta\mathcal{B}$ for magnetic parity; $\delta\mathcal{E}$ for electric parity) and the second column shows structures of the other field (not included in the equatorial-plane drawings of Fig. 6.12). In each panel, the colored surfaces show the outer faces of vortexes (for $\delta\mathcal{B}$) or tendexes (for $\delta\mathcal{E}$), defined as the locations, for a given radius, where the largest-in-magnitude eigenvalue of the field being plotted ($\delta\mathcal{B}$ or $\delta\mathcal{E}$) has dropped to a certain percentage (90, 85, 80 or 75) of its maximum for that radius; that percentage is shown alongside the colored surfaces. As in previous figures, the surface is red (light gray) if that largest-in-magnitude eigenvalue is negative and blue (dark gray) if positive. The off-white regions are surfaces where the largest-in-magnitude eigenvalue has dropped to 15%, 20% or 25% of the maximum at that radius. In each panel the black lines are a few of the vortex lines (for $\delta\mathcal{B}$ panels) or tendex lines (for $\delta\mathcal{E}$ panels) that become transverse when they reach large radii, and thereby produce the tidal or frame-drag force of an emitted gravitational wave. For discussion of this figure, see Sec. 6.3.3.

The top rightmost panel depicts the vortexes associated with this electric-parity mode. The horizon vorticity vanishes, so the horizon is white. The vortexes near the horizon are dominated by the longitudinal-transverse part of the frame-drag field $\boldsymbol{\mathcal{B}}^{\rm LT}$, which interacts with $\delta\boldsymbol{\mathcal{E}}^{\rm L}$ and $\delta\boldsymbol{\mathcal{E}}^{\rm LT}$ to maintain their joint near-zone structure as they rotate (cf. the description of the dual magnetic-parity mode in Sec. 6.1.3.6). However, of course, there is also a $\boldsymbol{\mathcal{B}}^{\rm TT}$ associated with the ingoing gravitational waves. At large radii, in the outgoing-wave zone, the vortexes, like the tendexes of the third panel top row, spiral upward and downward around the polar axis; they have joined with the tendexes to form the full gravitational-wave structure.

For insight into how (we think) the near-zone tendexes of this electric-parity mode, extending radially out of the horizon, generate these outgoing gravitational waves, and how the ingoing waves,

that they also generate, act back on them and drive their gradual decay, see the description of this mode's dual in Sec. 6.1.3.6.

For the rapid-spin Kerr black hole, the tendex and vortex structures (last two panels of second row of Fig. 6.14) are quite similar to those for the Schwarzschild black hole. The detailed differences are similar to those in the equatorial plane (see discussion in Sec. 6.3.2.3 above): smaller near zone and tighter spiraling for the tendexes because of the higher eigenfrequency; nonvanishing horizon vorticity with a predominantly $Y^{32}(\theta, \phi)$ angular structure. In the near zone, the 3D vortexes seem to have acquired a longitudinal (radial) part, emerging from the Y^{32} horizon vortexes (though this is largely hidden behind the off-white structures). Thus, for a Kerr black hole, one might intuitively describe the generation of gravitational waves as being produced by a superposition of near-zone tendexes that induce vortexes by their motions, and near-zone vortexes that induce tendexes by their motions. However, because the near-zone vortexes are weaker than the tendexes, the tendexes still play the dominant role for gravitational-wave generation in this electric-parity mode.

6.3.3.2 Approximate duality

By comparing the magnetic-parity left half of Fig. 6.14 with the electric-parity right half, we can visually assess the degree to which there is a duality between the modes in three dimensions. For the perturbations of Schwarzschild black holes (top row), the most notable difference between the magnetic- and electric-parity perturbations is that the transition between the longitudinal near-zone and spiraling wave-zone vortexes of the magnetic-parity perturbation is more abrupt, and happens closer to the horizon than it does in the electric-parity perturbations. The reason for this is encoded in Eqs. (6.91), (6.92), and (6.93), but we do not have a simple physical explanation for why this occurs. This difference is magnified for perturbations of the rapidly rotating Kerr black hole (bottom row). Thus, the small breaking of duality quantified in App. 6.9 for Schwarzschild black holes seems to be more pronounced in three-dimensions than in two, and stronger for rapidly rotating black holes than for non-rotating ones.

Nevertheless, the qualitative picture of wave generation by longitudinal near-zone tendexes and vortexes is essentially dual for perturbations of the two parities.

6.3.4 Comparing vortex lines of a perturbed Kerr black hole and a binary-black-hole-merger remnant

As a conclusion to this section and a prelude to future work, in Fig. 6.15 we compare the vortex lines found using our analytic methods to those found in a numerical ringdown of a fast-spinning Kerr black hole.

More specifically, we compare an electric-parity, $(2, 2)$ quasinormal-mode perturbation of a Kerr

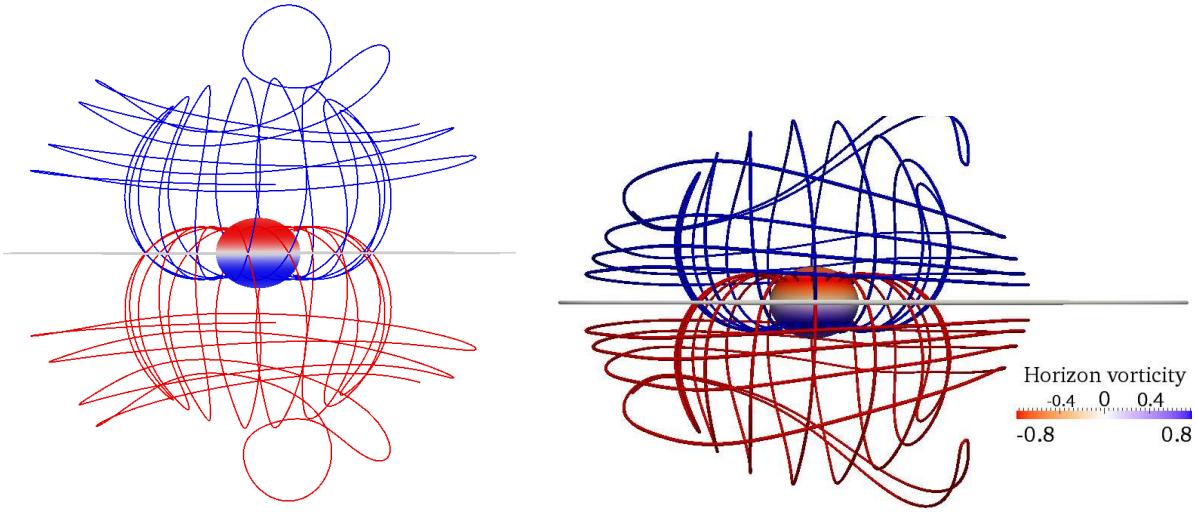

Figure 6.15: (color online). *Left:* Vortex lines of a $a/M = 0.945$ Kerr black hole perturbed by an electric-parity $(2,2)$ quasinormal-mode in IR gauge. *Right:* Vortex lines from a $a/M = 0.945$ ringing down Kerr black hole obtained from a numerical simulation [19] of two identical merging black holes with spins of magnitude 0.97 aligned parallel to the orbital angular momentum. In the simulation, we chose a late enough time that the common apparent horizon is essentially that of a single, perturbed black hole, and we computed the vortex lines using methods summarized in Ref. [1] (i.e. Chapter 1.2).

black hole with dimensionless spin $a/M = 0.945$, to a ringing-down Kerr black hole of the same spin formed in a numerical simulation [19] of the merger of two equal-mass black holes with equal spins of magnitude 0.97 aligned with the orbital angular momentum. (Note that because of the symmetry of this configuration, during the ringdown there is no magnetic-parity $(2,2)$ mode excited.)

For both the analytical and numerical calculations, the vortex lines are those of the full frame-drag tensor. To describe the magnitude of the perturbation in the analytical calculation, we write the frame-drag field as $\mathcal{B}_{\hat{i}\hat{j}} = \mathcal{B}^{(0)}_{\hat{i}\hat{j}} + \mathcal{B}^{(1)}_{\hat{i}\hat{j}}$, including the background part $\mathcal{B}^{(0)}_{\hat{i}\hat{j}}$ and the perturbation $\mathcal{B}^{(1)}_{\hat{i}\hat{j}} \equiv \delta\mathcal{B}_{\hat{i}\hat{j}}$ (as in App. 6.12). We choose the ratio of the maximum of the perturbation of the horizon vorticity, $\mathcal{B}^{(1)}_{NN}$ to the background horizon vorticity $\mathcal{B}^{(0)}_{NN}$ to be of order 10^{-3}. This amplitude of the perturbation produces lines that agree qualitatively with those from the numerical simulation.

The lines of the full frame-drag field look quite different from those for just $\delta\mathcal{B}_{\hat{i}\hat{j}}$ depicted in Figs. 6.12 and 6.14. Near the equator, the vortex lines in both panels look like those of an unperturbed Kerr black hole (see Paper II). Closer to the axis of rotation, the background vortex lines become degenerate, and the perturbations break the degeneracy by picking the principal axes of the perturbative field. Correspondingly, near the rotation axis and at large enough radii to be in or near the wave zone, the vortex lines resemble those of transverse-traceless gravitational waves, which are emitted symmetrically above and below the hole.

Although the vortex lines from these similar physical situations were computed using very different methods and gauge conditions, the results are qualitatively similar (see Fig. 6.15). The lines

in the two figures are not identical, but they were selected to intersect the horizon in approximately the same places; a careful inspection shows there are small differences, for example very near the horizon.

This comparison ultimately gives us confidence that our analytical methods can guide our understanding of the vortexes and tendexes in the late stages of numerical simulations.

6.4 Superposed $(2,2)$ and $(2,-2)$ Quasinormal Modes of Schwarzschild

6.4.1 Magnetic-parity superposed modes

In Sec. 6.1.3.9, we summarized the properties of the quasinormal mode of Schwarzschild that is obtained by superposing the magnetic-parity $(2,2)$ and $(2,-2)$ modes. Here we give details. The vortex lines and vorticities for this superposed mode are depicted in Fig. 6.16 using the three types of visualizations in Fig. 6.10.

The left column of Fig. 6.16 shows the two families of vortex lines that lie in the equatorial plane, color coded by their vorticities. The solid-line family has predominantly positive (clockwise) vorticity, but in some regions its vorticity becomes weakly negative (counterclockwise). The dashed-line family has predominantly negative vorticity, but in some regions it is weakly positive. A rotation around the hole by angle $\pi/2$ maps each family into the other.

In the center column of Fig. 6.16, the vortex lines are drawn black and the equatorial plane is colored by the vorticity of the dashed lines. To deduce the coloring for the solid lines, just rotate the colored plane (but not the lines) by $\pi/2$ and interchange red (light gray) and blue (dark gray). By contrast with most previous figures, the radial variation of the vorticity is not scaled out of this figure; so in the wave zone (roughly, the outer half of right panel) the coloring oscillates radially, in color and intensity, in the manner of a gravitational wave. At large radii, there is also a growth of intensity (and saturation of the color scale) due to the waves emitted earlier having larger amplitude.

In the right column of Fig. 6.16, the vortex lines are again drawn black, and the equatorial plane is now colored by the larger of the two vorticities in amplitude.

Together, the columns of Fig. 6.16 provide the following picture: For each family of lines, the equatorial-plane vortexes form interleaved rings (dashed lines and red [light gray] vortexes for center column). Most of the family's vortex lines form closed, distorted ellipses that, when tangential, lie in a single vortex (red for dashed lines), and when more nearly radial, travel from one vortex to another. In the wave zone, these line and vortex structures grow longer tangentially as they propagate outward, and they maintain fixed radial thickness. When one looks at both families simultaneously, focusing on the strongest at each point (right column), one sees vortexes of alternating red and blue vorticity (light and dark gray). The angular oscillations are those of a quadrupolar structure; the radial oscillations are those of a propagating wave.

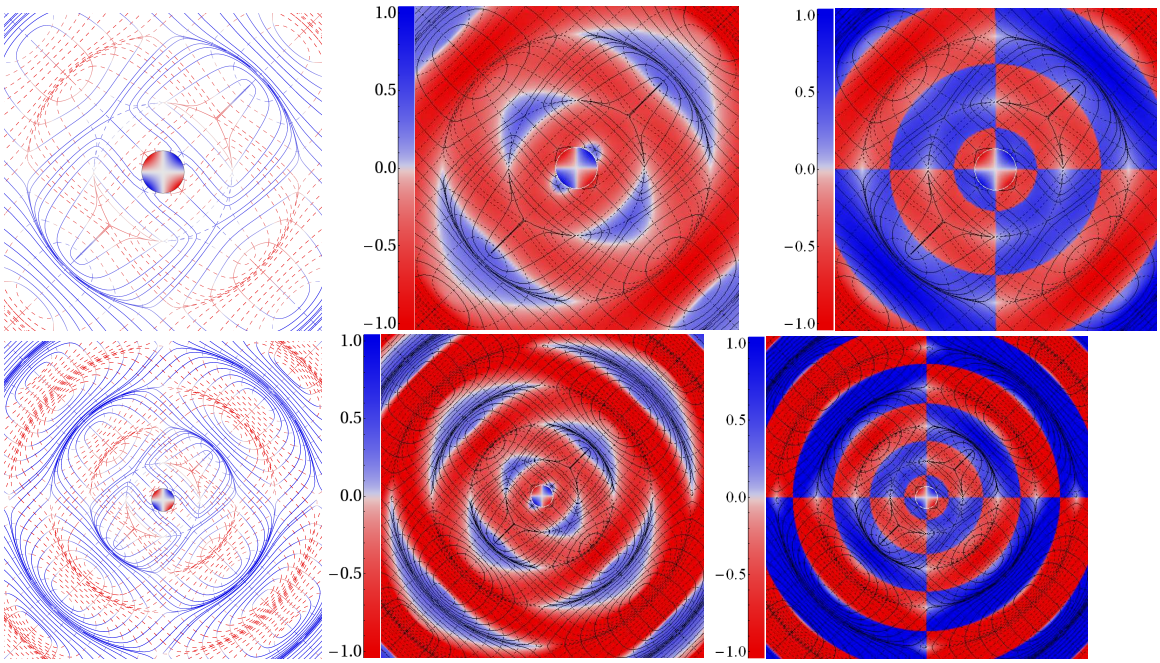

Figure 6.16: (color online). The vorticities and vortex lines in the equatorial plane of a Schwarzschild black hole, for the fundamental magnetic-parity $(2,2)$ mode superposed on the fundamental magnetic-parity $(2,-2)$ mode, depicted using the same three visualization techniques as in Fig. 6.10. Here, however, we do not scale the vorticity by any function, but the numbers on the vorticity scale on the left of the panels are equal to $\sqrt{\text{vorticity} \times r}$ (where r is radius), in units of the maximum value of this quantity, which occurs on the horizon at $\phi = 3\pi/4$ and $\phi = 7\pi/4$. The top panels cover a region $30M$ across, and the bottom panels are a zoom-out of the upper panels, $56M$ across. The central circle in all panels is the horizon as viewed from the polar axis, colored by its vorticity. *Left column*: The two families of vortex lines (one shown dashed, the other solid) with each line colored, at each point, by the sign of its vorticity (blue [dark gray] for positive, i.e., clockwise; red (light gray) for negative, i.e., counterclockwise), and each line has an intensity proportional to the magnitude of its vorticity. *Center column*: The same vortex lines are colored black, and the equatorial plane is colored by the vorticity of the dashed family of lines. *Right column*: The same as the center column, but the equatorial plane is colored by the vorticity with the larger magnitude.

In the near zone, the vortex lines have rather sharp, right angled features associated with the quadrupolar nature of the near-zone perturbation; this is to be compared to the oscillating current quadrupole in linearized gravity (Paper I, Sec. VI, Fig. 15). There are multiple singular points in the lines, degenerate points where three lines cross with sharp bends, and where both families of vortex lines take on the same eigenvalue. (The third eigenvalue, that of the lines perpendicular to the plane, must then be minus twice the vorticity of these lines, in order for the sum of the eigenvalues to vanish).

We shall discuss the dynamics of these vortex lines and vortexes in Sec. 6.4.3 below, after first gaining insight into the electric-parity superposed mode (whose vortexes will teach us about this magnetic-parity mode's tendexes through the near duality).

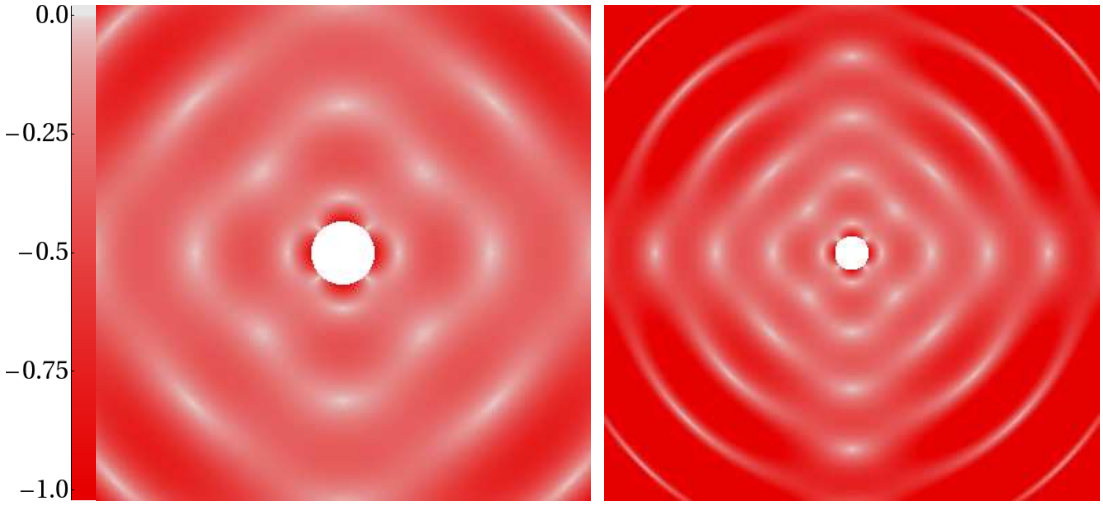

Figure 6.17: (color online). For the electric-parity, superposed (2,2) and (2,-2) fundamental modes of Schwarzschild: the vorticity of the counterclockwise vortex lines that pass through the equatorial plane at 45° angles. By near duality, this figure also depicts the perturbative tendex structure for the magnetic-parity superposed mode. The intensity scale of the red color (left edge of figure) is the same as that in the center column of Fig. 6.16. The left panel, a region $30M$ across, is a zoom-in of the right panel, which is $56M$ across. This figure is the superposed-mode analog of Fig. 6.13.

6.4.2 Electric-parity superposed mode

For the mode constructed by superposing electric-parity (2,2) and (2,-2) modes of Schwarzschild, as for the electric-parity (2,2) mode itself (Sec. 6.3.2.4), symmetry considerations dictate that: (i) one family of vortex lines lies in the equatorial plane and has vanishing vorticity, (ii) two families pass through the equatorial plane at 45° angles, with equal and opposite vorticities, and (iii) the horizon vorticity vanishes.

In Fig. 6.17 [analog of Fig. 6.13 for the (2,2) electric-parity mode], we show the vorticity of the family of counterclockwise vortex lines, as they pass through the equatorial plane.

In the near zone of this figure, we see again a distinct quadrupolar structure, with four lobes of strong vorticity present near the horizon (four near-zone vortexes). Beyond these near-zone lobes, there is a ring of vanishing vorticity, followed by an annulus where the cast-off vortexes of a previous cycle have begun to deform into an annulus of stronger vorticity. In the wave zone, the vortexes have transitioned into outward traveling transverse waves, with regions of vanishing vorticity between the crests and troughs of each wave. The waves are strongest along the diagonals, though in the near zone the (LT) frame-drag field is strongest in the up, down, left and right directions.

By (near) duality, the tendexes of the magnetic-parity superposed mode will have the same form as these electric-parity-mode vortexes. Accordingly, in the next section, we will use this figure to elucidate the magnetic-parity mode's dynamics — and by duality, also the dynamics of this electric-parity mode.

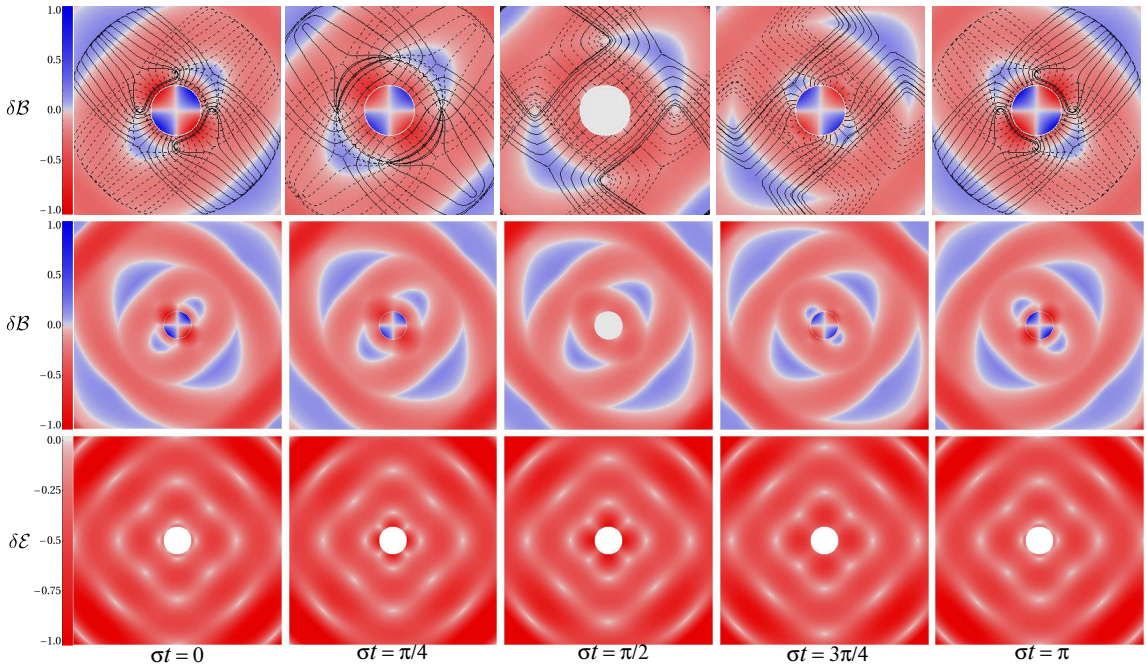

Figure 6.18: (color online). Time evolution of the equatorial vortexes (top and middle rows) and equatorial perturbative tendexes (bottom row) for the superposed $(2, 2)$ and $(2, -2)$ magnetic-parity mode of Schwarzschild in RWZ gauge. The color scale is the same as the center column of Fig. 6.16, and the gravitational-wave-induced exponential decay of the vorticity and tendicity has been removed. *Top row*: Equatorial vortex lines and their vorticity plotted in a region near the horizon ($16M$ across) followed over time t. The real part of the eigenfrequency is denoted σ, so the successive panels, left to right cover half a cycle of the mode's oscillation. *Middle row*: The vorticity of the equatorial vortex lines in the near, intermediate and beginning of wave zone ($30M$ across) at the same time steps as the top row. *Bottom row*: Tendicity of the counterclockwise tendex lines passing through the equatorial plane (which is dual to the left panel of Fig. 6.17), plotted at the same time steps as the top row.

6.4.3 Dynamics of the magnetic-parity superposed mode

We now turn to the dynamics of the magnetic-parity superposed mode, which we studied in Sec. 6.4.1

In Fig. 6.18 for this mode we show, in the equatorial plane, the time evolution of (i) the vortex lines and their vorticities near the black hole (top row), and (ii) on a larger scale that extends into the wave zone, the mode's vortexes (middle row) and perturbative tendexes (bottom row). The five panels in the top row are stills from a movie at [20]. To be absolutely clear, the vortexes and tendexes are those of the same magnetic-parity mode. As in the center column of Fig. 6.16, the top and middle rows show only one family of vortexes, that for the dashed vortex lines which have predominantly negative vorticity; and as in Fig. 6.17, the bottom row shows only the tendicity of the negative-tendicity perturbative tendexes that pass through the equatorial plane at 45°. Time $t = 0$ (left panels of Fig. 6.18) is chosen at a moment when the horizon vorticity is maximum, whereas Figs. 6.16 and 6.17 are snapshots at the slightly earlier time $\sigma t \approx -\pi/3$ (which gives nearly the same

vortex structures as the fourth column, after a rotation by $\pi/2$).

In interpreting Fig. 6.18, especially the top row, we emphasize that there is no unique way of following a single vortex or tendex line in time. The same is true of electric and magnetic field lines in Maxwell's theory (cf. [21]). While we hope to elucidate this issue in future work, here, in constructing the panels in the top row of Fig. 6.18, we have simply started the integration of the vortex lines from the same points at each time step, *making no attempt to identify and follow individual lines from moment to moment.* Correspondingly, in order to interpret Fig. 6.18 and gain insight into the dynamics of the superposed mode, instead of trying to follow individual lines, we will focus on the lines' evolving shapes, and the structures of the vortexes and tendexes and the equations governing their evolution on the horizon.

As a foundation for understanding the near-zone dynamics depicted in this figure, we write down explicit expressions for the longitudinal and longitudinal-transverse parts of the frame-drag and tidal fields *on the horizon*:

$$\mathcal{B}_{\hat{r}\hat{r}} = \Re\left[\frac{3}{2i\omega M^3}e^{-i\omega(\tilde{t}+2M)}\right]\mathcal{Y}(\theta,\phi)\ , \tag{6.26a}$$

$$\mathcal{B}_{\hat{r}\hat{A}} = \Re\left[\frac{1}{2\sqrt{2}M^2}(1-\beta)e^{-i\omega(\tilde{t}+2M)}\right]D_{\hat{A}}\mathcal{Y}\ , \tag{6.26b}$$

$$\delta E_{\hat{r}\hat{A}} = \Re\left[\frac{1}{2\sqrt{2}M^2}(1+\beta)e^{-i\omega(\tilde{t}+2M)}\right]\left(-\epsilon_{\hat{A}}{}^{\hat{B}}D_{\hat{B}}\right)\mathcal{Y}\ , \tag{6.26c}$$

where

$$\beta \equiv \frac{3}{2i\omega M(1-4i\omega M)}\ . \tag{6.26d}$$

Here the normalization is that of App. 6.7, $\omega = (0.37367 - 0.08896i)/M$ is the mode's eigenfrequency, $\epsilon_{\hat{A}}{}^{\hat{B}}$ is the Levi-Civita tensor on the horizon,

$$\mathcal{Y} \equiv Y^{22} + Y^{2\,-2} = \sqrt{15/8\pi}\sin^2\theta\cos 2\phi \tag{6.26e}$$

is this mode's scalar spherical harmonic, and $D_{\hat{A}}$ is the covariant derivative on the unit 2-sphere (related to the covariant derivative on the horizon by $D_{\hat{A}} = 2M\boldsymbol{\nabla}_{\hat{A}}$). [Equations (6.26) follow from Eqs. (6.40), (6.41), (6.54) of App. 6.7, the vector-spherical-harmonic definitions (6.84a) and (6.88a), and definition (6.5) of the EF time coordinate.]

Equations (6.26) are the fields measured by Eddington-Finkelstein observers. The conservation law (6.4a) for longitudinal field lines threading the horizon (which we shall need below) involves, by contrast, the LT frame-drag field measured by Schwarzschild observers on the "stretched horizon" (very close to the event horizon). Since the Schwarzschild observers move outward with velocity $\boldsymbol{v} = (2M/r)\boldsymbol{N} \simeq \boldsymbol{N}$ with respect to the EF observers, and with $\gamma \equiv 1/\sqrt{1-v^2} \simeq 1/(\sqrt{2}\alpha)$, the field

they measure is $\boldsymbol{\mathcal{B}}^{\rm LT}_{\rm Sch} = \gamma(\boldsymbol{\mathcal{B}}^{\rm LT} - \boldsymbol{N}\times\delta\boldsymbol{\mathcal{E}}^{\rm LT})$. This field diverges as $1/\alpha$ as the stretched horizon is pushed toward the event horizon; to remove that divergence, in the Membrane Paradigm [9]) we renormalize by multiplying with α:

$$\mathcal{B}^{\rm H}_{\hat r\hat A} \equiv \alpha\boldsymbol{\mathcal{B}}^{\rm LT}_{\rm Sch} = \alpha\gamma(\boldsymbol{\mathcal{B}}^{\rm LT} - \boldsymbol{N}\times\delta\boldsymbol{\mathcal{E}}^{\rm LT}) = \Re\left[\frac{1}{4M^2}e^{-i\omega(\tilde t+2M)}\right] D_{\hat A}\mathcal{Y}\ . \tag{6.27}$$

The second line is obtained by inserting the EF fields (6.26a) and (6.26b), and $\gamma = 1/\sqrt{2}\alpha$, into the first line. The conservation law for longitudinal vortex lines threading the horizon (actually, one of the Maxwell-like Bianchi identities in disguise) says that

$$\partial\mathcal{B}_{NN}/\partial\tilde t + \nabla_{\hat A}(-\mathcal{B}^{\rm H}_{\hat r\hat A}) = 0\ ; \tag{6.28}$$

cf. Eq. (6.4a) and subsequent discussion. (In this Schwarzschild-perturbation-theory case, there are no small spin-coefficient terms to spoil the perfection of the conservation law.) The vortex-line density and flux expressions (6.26a) and (6.27) do, indeed, satisfy this conservation law, by virtue of the fact that the 2-dimensional Laplacian acting on the quadrupolar spherical harmonic $\mathcal{Y}$ gives $D_{\hat A}D^{\hat A}\mathcal{Y} = -6\mathcal{Y}$.

Equations (6.26) and (6.28) tell us the following: (i) On and near the horizon, the LT fields $\boldsymbol{\mathcal{B}}^{\rm LT}$ [Eq. (6.26b)] and $\delta\boldsymbol{\mathcal{E}}^{\rm LT}$ [Eq. (6.26c)], and also $\mathcal{B}^{\rm H}_{\hat r\hat A}$ [Eq. (6.27)], all oscillate approximately out of phase with the longitudinal field $\boldsymbol{\mathcal{B}}^{\rm L}$ [Eq. (6.26a)].[3] Therefore, near-zone energy is fed back and forth between the L and LT fields as the black hole pulsates.

(ii) The conservation law (6.28) says that, if we regard $\mathcal{B}_{NN}$ as the density of vortex lines of $\boldsymbol{\mathcal{B}}^{\rm L}$ threading the horizon, and $-\mathcal{B}^{\rm H}_{\hat r\hat A}$ as the flux of vortex lines (number crossing a unit length in the horizon per unit time), then these horizon-threading vortex lines of $\boldsymbol{\mathcal{B}}^{\rm L}$ are conserved during the pulsation. More specifically:

(iii) As the mode evolves in Fig. 6.18 from $\sigma t = 0$ to $\sigma t = \pi$, the conserved vortex lines are pushed away from the center of each horizon vortex toward its white edges, and there the conserved lines from the red region (counterclockwise) annihilate with the conserved lines from the blue region (clockwise). The pushing is embodied in the vortex-line flux $-\mathcal{B}^{\rm H}_{\hat r\hat A}$, which grows stronger during this evolution.

(iv) As the mode evolves further from $\sigma t = \pi/2$ to $\sigma t = \pi$, conserved vortex lines of $\boldsymbol{\mathcal{B}}^{\rm L}$ are created in pairs (one clockwise, the other counterclockwise) at the white edges of the horizon vortexes, and move inward toward the center of each vortex.

[3] The longitudinal-transverse frame-drag field $\boldsymbol{\mathcal{B}}^{\rm LT}$ lags approximately $1.04 \approx \pi/3$ radians behind $\mathcal{B}_{NN}$ on the horizon, while the LT component of the tidal field, $\boldsymbol{\mathcal{E}}^{\rm LT}$, lags approximately $1.21 \approx 2\pi/5$ radians behind $\mathcal{B}_{NN}$. Most importantly for interpreting Fig. 6.18, the two nonzero tendicities of the tidal field are (in the equatorial plane) $\pm\sqrt{\mathcal{E}^2_{\hat r\hat\theta} + \mathcal{E}^2_{\hat\theta\hat\phi}}$, and on the horizon they lag nearly $\pi/2$ radians behind $\mathcal{B}_{NN}$; the damping of the perturbation adds slightly to the phase lag, so that it is actually $\pi/2 + \arctan[\Im(\omega)/\Re(\omega)] \simeq \pi/2 + 0.234$ out of phase with $\mathcal{B}_{NN}$.

Turn, now, from the conserved vortex lines of $\boldsymbol{\mathcal{B}}^{\rm L}$ piercing the horizon to the 3D vortex lines outside the horizon, depicted in the top row of Fig. 6.18. Because these are lines of the full 3D frame-drag field $\boldsymbol{\mathcal{B}}$ and not its longitudinal part $\boldsymbol{\mathcal{B}}^{\rm L}$, they do not obey a conservation law and there is no unique way of following individual lines from one panel to the next. However, their evolving shapes teach us much about the geometrodynamics of this superposed mode:

At time $\sigma t = 0$ (upper left panel), the horizon-piercing vortex lines of the full frame-drag field $\boldsymbol{\mathcal{B}}$ are almost perfectly radial, with clockwise (solid) tendex lines emerging from the two blue horizon tendexes, and counterclockwise (dashed) tendex lines emerging from the two red horizon tendexes. As time passes, the horizon piercing lines become less radial and the horizon vorticity decreases ($\sigma t = \pi/4$) until the lines' angles to the horizon are almost all near 45° and the horizon vorticity vanishes ($\sigma t = \pi/2$). Note that the lines that lie precisely on the diagonals, and which contact the horizon radially in the middle panel ($\sigma t = \pi/2$), have zero vorticity where they strike the horizon. This latter fact allows them to have a more radial angle of intersection than almost all other lines. The near-horizon frame-drag field has evolved at this time from being predominantly longitudinal, $\boldsymbol{\mathcal{B}}^{\rm L}$, to being predominantly longitudinal-transverse, $\boldsymbol{\mathcal{B}}^{\rm LT}$, but with some small admixture of transverse-traceless ingoing waves, $\boldsymbol{\mathcal{B}}^{\rm TT}$. As time moves onward from $\sigma t = \pi/2$ to $\sigma t = \pi$, the vortex lines in the outer part of each panel reach around on the horizon and attach to a quadrant on the side rather than directly below themselves—a quadrant that has newly acquired the color corresponding to the lines' own vorticity (blue for solid lines, red for dashed lines).

At $\sigma t = 0$ (upper left panel), the near-horizon, nearly circular vortex lines in each quadrant represent, predominantly, the transverse-isotropic part of $\boldsymbol{\mathcal{B}}^{\rm L}$ and keep it trace free. As time passes and $\boldsymbol{\mathcal{B}}^{\rm L}$ decreases,we can regard these lines as traveling outward, forming the distorted ellipses which become gravitational waves in the far zone. The manner in which these circular vortex lines are restored each cycle appears to be as follows: As discussed above, as the horizon vorticity oscillates through zero, formerly longitudinal lines are pushed away from their respective vortexes and become first more longitudinal-transverse, and then attach to a different quadrant of the horizon; meanwhile the $\boldsymbol{\mathcal{B}}^{\rm L}$ is being regenerated with opposite sign in each quadrant, which requires new transverse-isotropic lines of opposite vorticity. These lines run tangent to the horizon, hugging it while they cross through a vortex of strong opposite vorticity. At each edge of the vortex these isotropic-transverse lines link up with predominantly radial lines which have the same sign of vorticity (it appears that it is the degenerate points at these edges that allow for such a reconnection). This deforms the highly distorted, nearly circular arcs, which then lift off the horizon and propagate away as the cycle progresses.

This entire evolution is being driven by the oscillatory turn-off and turn-on of the longitudinal part of the frame-drag field $\boldsymbol{\mathcal{B}}^{\rm L}$.

Turn attention to the evolution of the mode's equatorial vortexes (middle row) and tendexes

(bottom row). In accord with our discussion above of the evolution of the horizon fields, Eqs. (6.26), these panels reveal (see below) that the vortexes and tendexes oscillate out of phase with each other. Near-zone energy (see footnote 1 in Sec. 6.1.3.8) gets fed back and forth between vortexes and tendexes in an oscillatory manner (though during this feeding, some of it leaks out into the transition zone and thence into gravitational waves). This oscillatory feeding enables the near-zone perturbative tendexes to store half of the oscillation energy (while the LT vortexes store the other half) when the longitudinal frame-drag field $\boldsymbol{\mathcal{B}}^{\rm L}$ is temporarily zero; and then use that energy to regenerate $\boldsymbol{\mathcal{B}}^{\rm L}$.

The evidence for this near-zone feeding, in Fig. 6.18, is the following: (i) The near-horizon vortexes are strongest along the diagonals, while the regions of strong near-zone tendicity always occur along the vertical and horizontal directions. Thus, the vortexes and tendexes tend to occupy different regions, with a $\pi/4$ rotation between the patterns [as one should expect from the angular dependences in Eqs. (6.26a) and (6.26c)]. (ii) There is a $\simeq \pi/2$ phase difference in the time evolution of the vortexes and tendexes. At those times when the horizon vorticity and near-horizon vortexes are strongest, the near-horizon tendexes are weak. As the horizon oscillates through zero vorticity, the tendexes are reaching their maximum strength.

A careful study of the phases of these time behaviors reveals that the dynamics are not precisely $\pi/2$ out of phase, as can be seen clearly in the first panel in the bottom row of Fig. 6.18: though the horizon vorticity is at it's maximum, the tendicities have just oscillated through zero in this region and are beginning to regenerate. As mentioned in footnote 3 above, this additional phase lag is due to the mode's damping, and in radians its magnitude is $\arctan[\Im(\omega)/\Re(\omega)] \simeq 0.234$.

The $\pi/4$ differences in spatial phase and $\simeq \pi/2$ differences in temporal phase are lost as the frame-drag and tidal fields travel outward through the intermediate zone and into the wave zone; an inspection of the outer edges of the time series plots shows bands of strong tendicity and vorticity *in phase* in time and space, propagating outward in synch. This must be the case, since for plane waves in linearized gravity, the vortex and tendex lines are in phase temporally and spatially (though the lines are rotated by $\pi/4$ with respect to each other at each event; see Paper I, Sec VI A).

By scrutinizing the middle and bottom rows of Fig. 6.18, (which extend from the near zone through the intermediate zone and into the inner parts of the wave zone), one can see visually how the oscillatory feeding of energy between near-zone vortexes and tendexes gives rise to outgoing vortexes and tendexes that represent gravitational waves.

6.5 $(2,1)$ and $(2,0)$ Quasinormal Modes of Schwarzschild

In this section we will complete our study of the quadrupolar perturbations of Schwarzschild black holes. Specifically, we will explore the vortex and tendex structures and the dynamics of the $(2,1)$

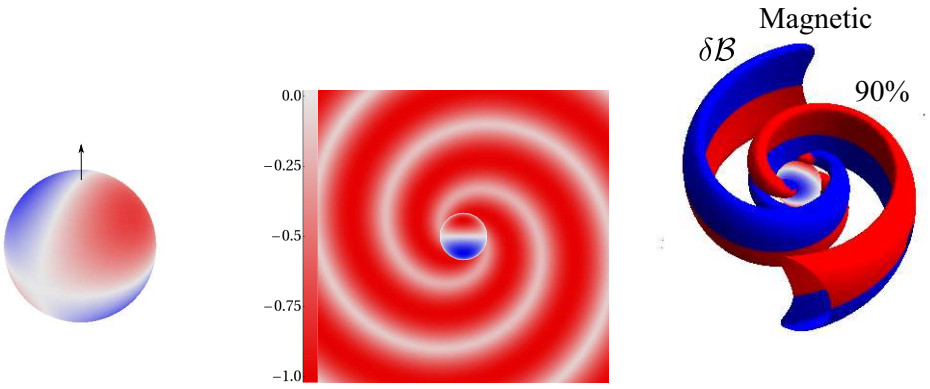

Figure 6.19: (color online). The $(2,1)$ magnetic-parity horizon vorticity and vortexes. *Left panel*: The horizon vorticity for the $(2,1)$ magnetic-parity perturbation of Schwarzschild, colored as in Fig. 6.9. There are four horizon vortexes, two clockwise (blue [dark gray]) and two counterclockwise (red [light gray]). The horizon vorticity vanishes at the equator and the poles. *Middle panel*: Vorticity of the counterclockwise vortex lines passing through the equatorial plane, colored and normalized as in the middle and right hand columns of Fig. 6.10 and plotted in a region $24M$ across. The (blue [dark gray]) vorticity of the clockwise vortex lines has precisely this same pattern, because the two families of lines pass through the equatorial plane with the same magnitude of vorticity at each point. *Right panel*: Three dimensional vortexes colored and labeled as in Fig. 6.14. By near duality, this figure also represents (to good accuracy) the tendicity and tendex structure of the (2,1) electric-parity mode.

and $(2,0)$ magnetic- and electric-parity perturbations of a Schwarzschild hole, in RWZ gauge.

6.5.1 Vortexes of $(2,1)$ magnetic-parity mode and perturbative tendexes of $(2,1)$ electric-parity mode

In Sec. 6.1.3.7, we summarized the most important properties of the (2,1) magnetic-parity mode of a Schwarzschild black hole. In this subsection and the next, we shall give additional details about this mode and its electric-parity dual. We begin with the vortex structure for magnetic parity.

The horizon vorticity of the magnetic-parity (2,1) mode has an angular dependence given by the spherical harmonic $Y^{21}(\theta,\phi)$ (of course). We display this horizon vorticity in the left panel of Fig. 6.19. There are four horizon vortexes, two of each sign, and vanishing horizon vorticity all along the equator.

As we noted in Sec. 6.1.3.7, this mode's symmetry dictates that the frame-drag field be reflection antisymmetric through the equatorial plane. As for the electric-parity (2,2) frame drag field, which also has this property (second paragraph of Sec. 6.3.2; also Sec. 6.3.2.4 and Fig. 6.13), this implies that one family of vortex lines lies in the equatorial plane with vanishing vorticity, and two cross through that plane at 45° with equal and opposite vorticities. The negative vorticities of the crossing lines are plotted in the middle panel of Fig. 6.19, along with the projected horizon vorticity, as if the horizon were viewed from above. The positive-vorticity pattern of the other family of crossing

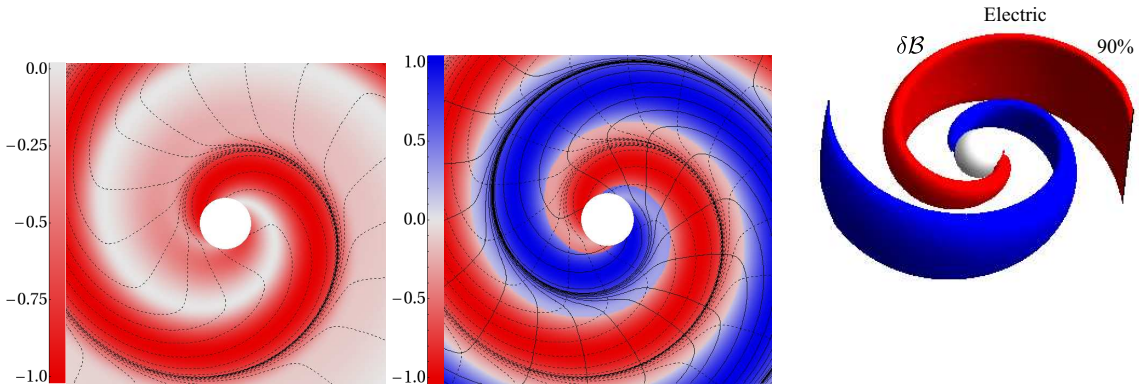

Figure 6.20: (color online). The $(2,1)$ electric-parity vortex lines, vorticities and vortexes in the equatorial plane. For this mode the horizon's vorticity vanishes, so the horizon is plotted as a white disk or sphere. *Left panel*: Counterclockwise vortex lines (dashed) and their vorticity (red [light gray] color) normalized as in Fig. 6.10, and plotted in a region $24M$ across. *Middle panel*: Both clockwise (solid) and counterclockwise (dashed) vortex lines, and the vorticity (color) of the line with the larger magnitude of vorticity, in a region $24M$ across. *Right Panel*: Three-dimensional vortexes colored and labeled as in Fig. 6.14. By near duality, this figure also represents to good accuracy the perturbative tendex lines, tendicities and tendexes for the magnetic-parity (2,1) mode.

lines is identical to this negative-vorticity pattern, since at each point the two lines have the same vorticity magnitude.

The fact that there are just two spiraling vortexes in this figure, by contrast with four for the (2,2) modes, is guaranteed by the modes' azimuthal orders, $m = 1$ here and $m = 2$ for (2,2).

The vortex structure outside the equatorial plane, depicted in the right panel of Fig. 6.19, was discussed in Sec. 6.1.3.7. The two red (light gray), 3D vortexes are the same ones depicted in the middle panel. They actually extend across the equatorial plane (via the 45° vortex lines) into the region occupied by the blue (dark gray) vortexes; but we do not see them there in the 3D drawing because the blue vortexes have larger vorticity and we have chosen to show at each point only the largest-vorticity vortex.

6.5.2 Vortexes of $(2,1)$ electric-parity mode and perturbative tendexes of $(2,1)$ magnetic-parity mode

Turn, next, to the vortex lines and vortex structure of the (2,1) electric-parity mode. [By near duality, the perturbative tendex lines and tendex structure of the (2,1) magnetic-parity mode will be the same.]

For this mode, with the parity reversed from the previous section, the frame-drag field is symmetric under reflection through the equatorial plane rather than antisymmetric. Therefore, there are two sets of vortex lines that remain in the equatorial plane, with the third set normal to it. In

this sense the vortexes structures are analogous to those of the magnetic-parity, $(2, 2)$ mode; and in fact they are strikingly similar, aside from having two arms rather than four.

We show the vortexes and vortex lines in Fig. 6.20. The left and middle panels of Fig. 6.20 show the lines that remain in the equatorial plane, along with color-intensity plots depicting the lines' vorticities.

The left panel of Fig. 6.20 shows the counterclockwise lines and their vorticities. As in the case of the $(2, 2)$ mode, we see a spiraling region of strong vorticity which contacts the horizon, and an accompanying spiral of low vorticity. At the horizon, the frame-drag field is primarily longitudinal-transverse, and correspondingly its vortex lines enter the horizon at a (nearly) 45° angle. As for the (2,2) mode, there is a limiting spiral that all the outspiraling vortex lines approach, near the edge of the vortex.

There is also a small region of strong vorticity near the horizon which forms a second spiral, opposite the primary spiral, although it quickly becomes weak; this second vortex coincides with the region of strong positive vorticity, as we see in the middle panel of Fig. 6.20, and we think its existence is due to the frame-drag field at the horizon being primarily longitudinal-transverse. It also should be compared to the similar regions of strong negative vorticity near the positive horizon vortexes of the magnetic-parity $(2, 2)$ mode in Fig. 6.10.

In the middle panel, we plot both the counterclockwise (dashed) and clockwise (solid) vortex lines, and we color each point by the vorticity that is strongest. We see two strong vortexes spiraling out to form gravitational waves, and we see that under a rotation through 180° the clockwise and counterclockwise vortex lines map into each other.

Finally, in the right panel of Fig. 6.20, we show the vortexes in three dimensions using the same conventions as in Fig. 6.14: the red (light gray) and blue (dark gray) surfaces are the locations where the vorticity of largest magnitude has fallen to 90% of its maximum at each radius. By contrast with the (2,1) magnetic-parity mode, where the 3D vortexes are antisymmetric through the equator (and so they flip colors; see Fig. 6.19), here they are symmetric and so have the same color above and below the equatorial plane.

By duality, for the (2,1) magnetic-parity mode, with its antisymmetric 3D vortexes (Fig. 6.19), the 3D perturbative tendexes are symmetric through the equatorial plane and have the form shown in this right panel of Fig. 6.20.

6.5.3 Vortexes of $(2, 0)$ magnetic-parity mode and perturbative tendexes of (2,0) electric-parity mode

In Sec. 6.1.3.8, we described in detail the dynamics of the axisymmetric (2,0) magnetic-parity mode of Schwarzschild and the gravitational waves it emits—waves in which the vortex and tendex lines

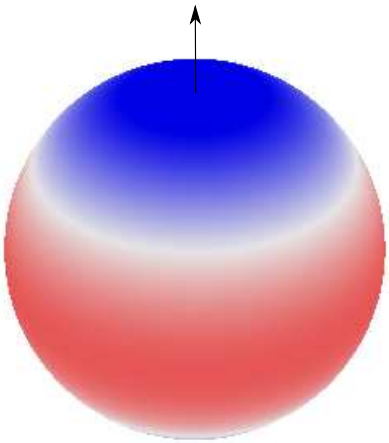

Figure 6.21: (color online). The horizon vorticities ($\delta\mathcal{B}_{NN}$) of the quadrupolar, $(2,0)$, magnetic-parity mode. As in Fig. 6.9, the color intensity is proportional to the magnitude of the vorticity with blue (dark gray) for positive and red (light gray) for negative. The arrow points along the polar axis. The vorticity oscillates sinusoidally in time, causing $\delta\mathcal{B}_{NN}$ first to vanish and then to change sign.

wrap around deformed tori. In this section and the next, we shall discuss some other details of this mode and its dual, the (2,0) electric-parity mode.

In Fig. 6.21, we show the horizon vorticity for this magnetic-parity mode. Of course, it is proportional to the scalar spherical harmonic $Y^{20}(\theta,\phi)$. At this moment of time, there are clockwise vortexes (blue [dark gray]) in the northern and southern hemispheres, and a band-shaped counter-clockwise vortex (red [light gray]) in the equatorial region. As time passes, the horizon vorticity oscillates, with red vortexes becoming blue and blue becoming red in each half cycle, while also decaying exponentially. The cause of these oscillations, as we discussed in Sec. 6.1.3.8, is exchange of energy between $\delta\boldsymbol{\mathcal{B}}^{\rm L}$ (whose normal-normal component is the horizon vorticity) and $\delta\boldsymbol{\mathcal{E}}^{\rm LT}$ (which we will visualize in the next section).

As we discussed in Sec. 6.1.3.8, symmetries dictate that this mode have two families of vortex lines lying in planes $\mathcal{S}_\phi$ of constant ϕ and a third family consisting of azimuthal circles of constant r and θ. In Fig. 6.6, we explored in detail the wave-zone wrap-around-torus shapes of the $\mathcal{S}_\phi$ vortex lines, and their vorticity patterns. In the near zone, the line shapes and vorticities are somewhat more complex. We elucidate them in Fig. 6.22, where, to make the figure more understandable and preserve some features lost in Fig. 6.6, we show the two families of vortex lines in separate panels, left and center.

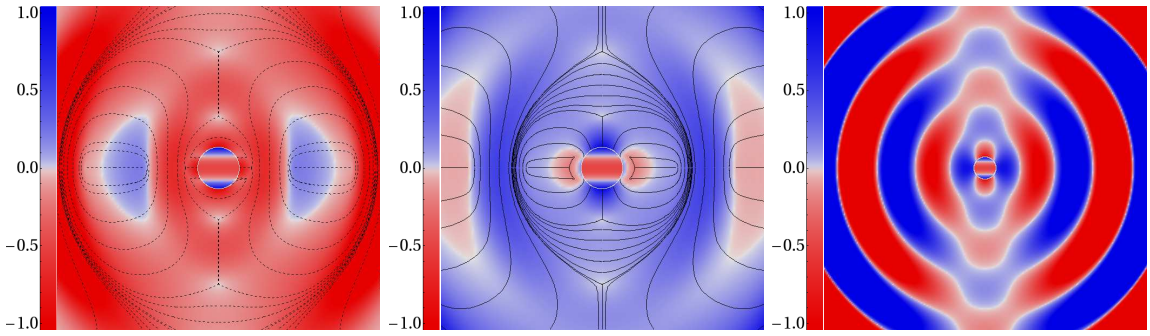

Figure 6.22: (color online). *Left and middle panels:* Near- and transition-zone vortex lines and their vorticities in an $\mathcal{S}_\phi$ plane of constant ϕ, for the axisymmetric (2,0) magnetic-parity mode of Schwarzschild in the near and transition zones ($30M$ across). *Left panel*: The predominantly counterclockwise family of vortex lines. *Middle panel*: The predominantly clockwise family of vortex lines. *Right panel*: Vorticity of the axial lines normal to an $\mathcal{S}_\phi$ plane, in near and wave zones ($56M$ across). The color intensity in each panel gives the vorticity of the lines, scaled as in Fig. 6.16.

As for the superposed $(2, 2)$ and $(2, -2)$ perturbations of Sec. 6.4, each family takes on both positive and negative vorticities, but is predominantly one or the other. And unlike the (2,2) mode and the superposed mode, the (2,0) line families do not map into each other after a 90° rotation; rather, they have distinct patterns (as one might expect, since their plane is $\mathcal{S}_\phi$ rather than the equatorial plane). On the other hand, because of this mode's oscillating nature, the predominantly positive lines are the same as the predominantly negative lines a half-cycle previous (with signs reversed). For this reason, we illustrate the two families at the same moment in time, the moment when the horizon vorticity reaches a maximum with blue (dark gray) near the poles and red (light gray) near the equator.

One striking feature of Fig. 6.22 is a set of isolated points where six lines meet, three from each family (three in each panel). These are nodes (zeros) of the frame-drag field, as one can see from the fact that the coloring there is white. These are also points where, dynamically, the field lines can reconnect, changing their topologies.

Let us focus on the near-horizon, predominantly negative vortex lines (dashed lines) in the left panel of Fig. 6.22. The lines that emerge from the counterclockwise horizon vortex in the equatorial region loop over the north or south pole of the black hole, and reconnect to the opposite side of that horizon vortex. We think that, as the mode oscillates, these lines will merge at the equator then slide off the horizon and form closed loops surrounding the hole, of the sort that we see in the outer parts of the lenticular blue (dark gray) region of the center panel, and these will then expand and deform and reconnect to form the set of wrap-around-deformed-torus lines of the left panel, which lie in the outer part of the transition zone and are becoming outgoing gravitational waves.

Next focus on the near-horizon, predominantly positive vortex lines (solid lines) in the middle panel of Fig. 6.22. The lines, that emerge from the clockwise horizon vortex in the north polar

region, swing around the equator and descend into the south polar horizon vortex. We think that, as the oscillation proceeds, these lines will slide off the horizon and immediately form closed loops that wrap around deformed tori, which expand to become like those near the left and right edges of the left panel (outer part of transition zone), and then continue their expansion, becoming the gravitational-wave wrap-around-torus lines whose inner parts are at the left and right edges of the right panel.

Notice, in the middle panel near the equator, two regions of weakly negative (pink [light gray]) vorticity, and their near-zone lines that appear to have just disconnected from the horizon but are mostly radially directed. And notice similarly the pink regions near the left and right edges of this panel, again with vortex lines that are traveling roughly radially. These pink regions are actually toroidal, because of the rotation symmetry around the vertical axis. In the outer transition zone and the wave zone, they are the regions in which this family's wrap-around-torus, gravitational-wave vortex lines are crossing over from one clockwise vortex (wave crest) to another. This feature of crossover lines with weakly reversed vorticity appears to be a robust feature of oscillatory modes. For other examples, see the weakly blue regions in the left panel, and see the superposed (2,2) and (2,-2) mode in Fig. 6.16, where the dashed vortex lines, with predominantly counterclockwise (red [light gray]) vorticity, become weakly blue (darker gray) in the crossover regions.

The right panel of Fig 6.22 shows the vorticity of the axial lines (constant r, θ circles) in both near zone and wave zone. Near the horizon, these lines are largely part of the transverse, isotropic piece of the longitudinal field $\delta\boldsymbol{\mathcal{B}}^{\rm L}$; they have opposite color to the horizon vortexes at the horizon, as they must, in order to keep $\delta\boldsymbol{\mathcal{B}}^{\rm L}$ trace-free. Near the horizon, these lines also contain a smaller component of the ingoing-wave transverse-traceless field $\delta\boldsymbol{\mathcal{B}}^{\rm TT}$. In the wave zone, they are fully outgoing-wave $\delta\boldsymbol{\mathcal{B}}^{\rm TT}$.

6.5.4 Vortex lines of $(2,0)$ electric-parity mode and perturbative tendex lines of (2,0) magnetic-parity mode

For the (2,0) electric-parity mode of Schwarzschild in RWZ gauge, the only nonzero components of the frame-drag field are $\delta\mathcal{B}_{\hat{r}\hat{\phi}}$ and $\delta\mathcal{B}_{\hat{\theta}\hat{\phi}}$. Near the horizon, where decomposition into longitudinal, longitudinal-transverse, and transverse-traceless parts is meaningful, $\delta\boldsymbol{\mathcal{B}}^{\rm L}$ vanishes (and hence the horizon vorticity vanishes), $\delta\mathcal{B}_{\hat{r}\hat{\phi}}$ is the sole component of $\delta\boldsymbol{\mathcal{B}}^{\rm LT}$, and $\delta\mathcal{B}_{\hat{\theta}\hat{\phi}}$ is the sole component of $\delta\boldsymbol{\mathcal{B}}^{\rm TT}$.

By (near) duality, the same is true for the (2,0) magnetic-parity mode of the last subsection, with $\delta\boldsymbol{\mathcal{B}}$ replaced by $\delta\boldsymbol{\mathcal{E}}$.

Because the only nonzero components are $\delta\mathcal{B}_{\hat{r}\hat{\phi}}$ and $\delta\mathcal{B}_{\hat{\theta}\hat{\phi}}$ and because of the axisymmetry, there is a family of zero-vorticity vortex lines which lie in a plane $\mathcal{S}_\phi$ of constant ϕ, and the other two

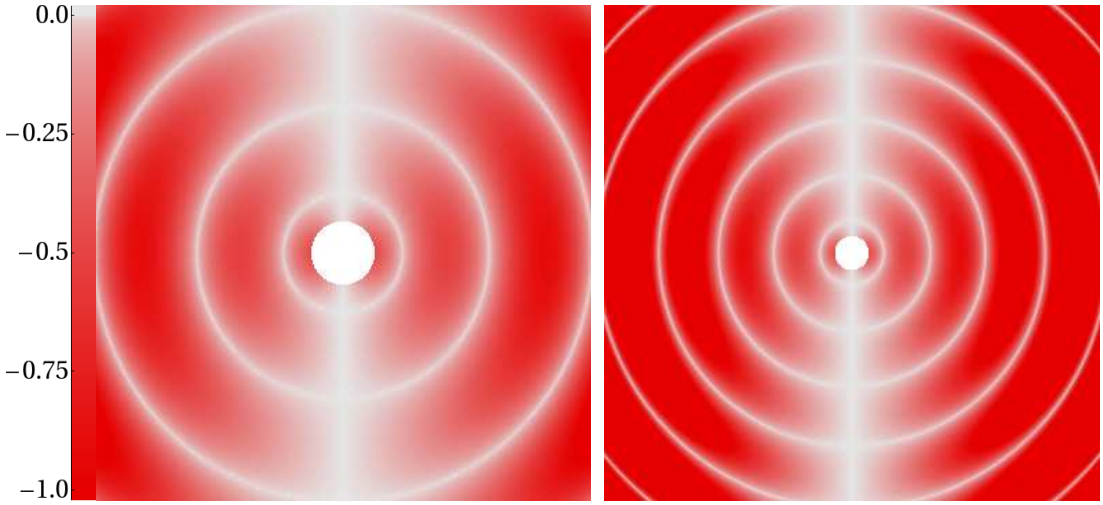

Figure 6.23: (color online). For the (2,0) electric-parity mode of Schwarzschild in RWZ gauge: the vorticity of the counterclockwise vortex lines that pass through the plane $\mathcal{S}_\phi$ of constant ϕ. The color intensity (scale on left) is scaled as in Fig. 6.16. *Left panel*: $30M$ across, showing the near and intermediate zones and beginning of the wave zone. *Right panel*: $56M$ across.

sets of vortex lines have equal and opposite vorticity and pass through $\mathcal{S}_\phi$ at 45 degree angles. In Fig. 6.23, we show in $\mathcal{S}_\phi$ the vorticity of the counterclockwise lines that pass through it. A plot for the clockwise lines would be identical, but with blue changed into red.

Notice the remarkable absence of structure in the near zone. All we see is toroidal vortexes separated by circular null surfaces and a polar null line. (Recall the axisymmetry around the vertical polar axis). The absence of structure is presumably due to the fact that this mode is sourced by the longitudinal perturbative tendex field, and not by this frame-drag field (though its longitudinal-transverse part plays a key role of periodically storing near-zone energy during the oscillations; cf. the discussion of the dual mode below). The vorticity vanishes along the polar axis because of axisymmetry and the fact that the radial-radial part of the frame-drag field vanishes.

For greater insight into this frame-drag field, we show in the left panel of Fig. 6.24 several of its three-dimensional vortex lines in the near zone and innermost part of the transition zone. These vortex lines wind densely around axisymmetric deformed tori.

Note that the large torus is attached to the horizon. Its vortex lines intersect the horizon at the approximately 45° angles characteristic of the longitudinal-transverse part of the field, which is these lines' dominant component.

For the dual, magnetic-parity (2,0) mode, this torus depicts the perturbative tendex lines of the near zone, and those lines predominantly belong to the longitudinal-transverse part of the tidal field, $\delta\boldsymbol{\mathcal{E}}^{\rm LT}$. This is the part that stores the mode's near-zone oscillation energy when $\delta\boldsymbol{\mathcal{B}}^{\rm L}$ is passing through zero and its perturbative vortex lines are detached from the horizon (see the discussion of this mode's dynamics in Sec. 6.1.3.8). Immediately after this snapshot, these tendex lines' $\delta\boldsymbol{\mathcal{E}}^{\rm LT}$

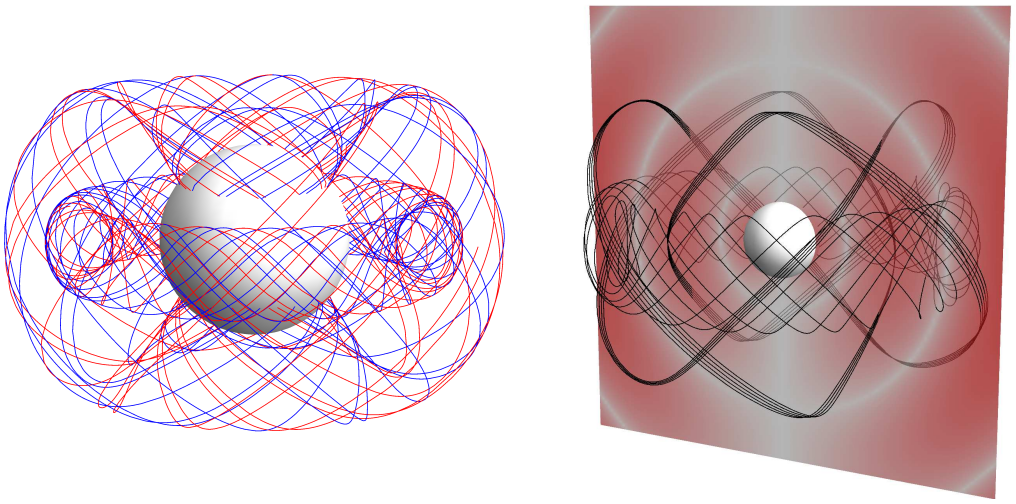

Figure 6.24: (color online). Vortex lines for the $(2, 0)$ electric-parity mode of Schwarzschild in RWZ gauge. *Left panel*: Two vortex lines of each sign in the near zone and innermost part of transition zone. The positive (blue lines) and negative (red) lines are identical but wind their tori in opposite directions. *Right panel*: Two counterclockwise vortex lines in the transition zone, with the vorticity shown in a semitransparent slice $\mathcal{S}_\phi$ of constant ϕ as a density plot. The vortex lines are plotted in black rather than red in this panel to aid the eye.

begin to regenerate the near-horizon longitudinal frame-drag field $\delta\boldsymbol{\mathcal{B}}^{\rm L}$ and its horizon vorticity. As it does so, these tendex lines and their torus (presumably) detach from the horizon and expand outward into the transition then wave zone, becoming the tendex-line component of a gravitational-wave torus like those displayed in Fig. 6.7 above.

The small torus in the left panel of Fig. 6.24 encircles the equatorial point on the innermost node of the field (innermost white circle in Fig. 6.23). It is also the innermost torus shown in Fig. 6.7 above.

In the right-hand panel of Fig. 6.24, for the (2,0) electric-parity mode we show two counterclockwise vortex lines in the transition zone. By chance, the larger of the selected lines nearly forms closed orbits, and so even after wrapping its torus four times it appears as a thin ribbon. While it is difficult to tell with this nearly closed line, extended integration reveals that it does wrap a (deformed) torus.

Notice that both lines (both tori) in the right panel straddle the second null of the frame-drag field (second-from-center white circle in Fig. 6.23).

6.6 Conclusions

Although the theory of black-hole quasinormal modes is roughly half a century old, most past studies of them have focused on their mathematical properties, their eigenfrequencies and emitted

gravitational waves, and their excitation by various physical processes. Aside from a geometric-optics interpretation of high-frequency modes (see, e.g., [22, 23, 24], the last one being Chapter 7), little was known, before this paper, about their geometrodynamic properties—e.g., the structure and dynamics of their spacetime curvature in the near zone and transition zone, and how the near-zone curvature generates gravitational waves.

In this paper we have used our new vortex and tendex tools to explore, in depth, the geometrodynamics of the quadrupolar modes for Schwarzschild and Kerr black holes. Most importantly, we have discovered that:

(i) There is a near duality between electric-parity modes and magnetic-parity modes, in which tendexes get mapped into vortexes and vortexes into tendexes.

(ii) The electric-parity $(l, m) = (2, 2)$ and (2,1) modes are generated by near-zone, longitudinal vortexes that extend out of the horizon and rotate (four tendexes for $m = 2$; two for $m = 1$). The vortexes' rotation generates outgoing and ingoing gravitational waves; the ingoing waves act back on the longitudinal vortexes, gradually pushing them off the horizon, which results in the mode's exponential attenuation.

(iv) By (near) duality, the electric-parity (2,2) and (2,1) modes are generated and attenuated in the same way, but with near-zone, longitudinal tendexes rather than vortexes playing the central role.

(v) The magnetic-parity (2,0) mode and superposed (2,2) & (2,-2) mode are generated by near-zone, longitudinal vortexes that extend out of the horizon and oscillate between clockwise and counterclockwise vorticity. In these oscillations, energy is fed back and forth between the longitudinal vortexes and longitudinal-transverse, near-zone tendexes that do not penetrate the horizon. In each oscillation, as the horizon vorticity passes through zero, the longitudinal vortex lines slide off the horizon and reconnect to form toroidal vortexes that travel outward, becoming gravitational waves; and the near-zone tendexes then regenerate the longitudinal vortexes (with reversed vorticity), thereby triggering the next half cycle of oscillation.

(vi) The electric-parity (2,0) mode and superposed (2,2) & (2,-2) mode exhibit these same geometrodynamics, but with the roles of the vortexes and tendexes reversed.

In future papers, these quasinormal-mode insights will be a foundation as we explore the geometrodynamics of merging binary black holes using numerical simulations.

While all analytic approximations fail near the time of merger, black-hole perturbation theory does approximate a binary-black-hole spacetime well in some epochs: the merged hole during its ringdown, each tidally deformed hole during inspiral, and each perturbed hole during the initial relaxation that causes spurious "junk" gravitational radiation. Before exploring the fully nonlinear vortex and tendex structures in simulations, we are likely first to compare numerical vortex and tendex structures during these epochs with the corresponding perturbative results (as in Fig. 6.15).

Such comparisons will allow us to determine to what degree the insights we have gained from our perturbative studies can also be applied to numerical simulations—particularly the relative insensitivity of vortexes and tendexes to changes in gauge and slicing.

Building on these comparisons, our future work will then include initial explorations of the fully nonlinear geometrodynamics of the warped spacetimes present in binary-black-hole simulations. For example, Kamaretsos, Hannam, and Sathyaprakash [25] have recently observed relationships between the properties (masses and spins) of the initial holes in a binary-black-hole merger and the particular quasinormal modes that are excited in the remnant (modes which generate the ringdown portion of the gravitational waves). By examining the vortex and tendex structures of a variety of binary-black-hole mergers, we hope to gain insight into the origin of such relationships. Also, following Dennison and Baumgarte's recent exploration [7] of the vortex and tendex structures in approximate, perturbative initial data, we intend to explore the vortex and tendex structures of constraint-satisfying binary-black-hole initial data, which could give insight into the initial perturbations (and the corresponding spurious "junk" gravitational radiation) that appear in all currently used, binary-black-hole initial-data schemes.

Ultimately, we plan to use vortexes and tendexes to explore the geometrodynamics of binary-black-hole spacetimes throughout the entire simulated inspiral, merger, and ringdown. We expect that these tools will provide insights into the behavior of these spacetimes and perhaps also motivate new ways of constructing phenomenological waveform templates for use in gravitational-wave data analysis.

6.7 Appendix: Quasinormal Modes of a Schwarzschild Black Hole in Regge-Wheeler Gauge

In this appendix, we review the Regge-Wheeler-Zerilli (RWZ) formalism for black-hole perturbations, and we discuss the calculations that underlie the results reported in Secs. 6.3, 6.4, and 6.5 for quadrupolar perturbations of non-spinning black holes in the RWZ gauge.

6.7.1 Regge-Wheeler-Zerilli formalism

Here we review the equations governing quasinormal modes for a non-rotating black hole in the Regge-Wheeler-Zerilli gauge [27, 28].[4] We write the metric in Schwarzschild coordinates with a

[4] There are many errors in the original paper of Regge and Wheeler [27], most of which were corrected by Edelstein and Vishveshwara [29]. We use the corrected equations without further comment.

small perturbation $h_{\mu\nu}$,

$$\begin{aligned} ds^2 &= -\alpha^2 dt^2 + \frac{dr^2}{\alpha^2} + r^2(d\theta^2 + \sin^2\theta d\phi^2) + h_{\mu\nu}dx^\mu dx^\nu \,, \\ \alpha^2 &= 1 - 2M/r \,. \end{aligned} \tag{6.29}$$

The components of $h_{\mu\nu}$ obey separable differential equations, and importantly $h_{\mu\nu}$ can be split into definite-parity perturbations (electric and magnetic) which do not couple to each other.

For magnetic-parity perturbations, the only nonzero components of $h_{\mu\nu}$ in Regge-Wheeler gauge are

$$h_{tA} = h_0(r)e^{-i\omega t}X_A^{lm}(\theta,\phi) \,, \quad h_{rA} = h_1(r)e^{-i\omega t}X_A^{lm}(\theta,\phi) \,. \tag{6.30}$$

Here ω is the mode's complex QNM eigenfrequency, and X_A^{lm} is the magnetic-parity vector spherical harmonic on the unit two-sphere,

$$X_\theta^{lm} = -\csc\theta\, Y^{lm}{}_{,\phi} \,, \qquad X_\phi^{lm} = \sin\theta\, Y^{lm}{}_{,\theta} \,, \tag{6.31}$$

with $Y^{lm}(\theta,\phi)$ denoting the scalar spherical harmonics. Regge and Wheeler [27, 29] showed that the radial parts of the metric perturbation, $h_0(r)$ and $h_1(r)$, can be expressed in terms of a single scalar radial eigenfunction $Q(r)$ as

$$h_0 = -\frac{\alpha^2}{i\omega}(rQ)_{,r} \,, \quad h_1 = \frac{rQ}{\alpha^2} \,, \tag{6.32}$$

which satisfies the eigenequation

$$Q_{,r_*r_*} + \omega^2 Q = \mathcal{V}_Q(r)Q \,, \;\; \mathcal{V}_Q(r) = \alpha^2\left(\frac{l(l+1)}{r^2} - \frac{6M}{r^3}\right) \,. \tag{6.33}$$

Here r_* is the tortoise coordinate

$$dr_* = \frac{dr}{\alpha^2} \,, \quad r_* = r + 2M\ln(\alpha^2 r/2M) \,, \tag{6.34}$$

which goes to $+\infty$ far from the hole and $-\infty$ at the hole's horizon. This eigenequation must be solved subject to the boundary conditions of outgoing waves at infinity, $Q \sim e^{i\omega r_*}$ as $r_* \to +\infty$, and ingoing waves at the horizon, $Q \sim e^{-i\omega r_*}$ as $r_* \to -\infty$.

For electric-parity modes, the nonzero components of $h_{\mu\nu}$ in RWZ gauge are [28]

$$\begin{aligned} h_{tt} &= \alpha^2 H_0(r)e^{-i\omega t}Y^{lm} \,, \qquad h_{rr} = \frac{H_0(r)}{\alpha^2}e^{-i\omega t}Y^{lm} \,, \\ h_{tr} &= H_1(r)e^{-i\omega t}Y^{lm} \,, \qquad h_{AB} = r^2\Omega_{AB}K(r)e^{-i\omega t}Y^{lm} \,. \end{aligned} \tag{6.35}$$

Here Ω_{AB} denotes the metric on the unit 2-sphere. We can write the metric perturbation functions in terms of the Zerilli function $Z(r)$ as[5]

$$\begin{aligned} K &= \left[\frac{\lambda(\lambda+1)r^2+3\lambda Mr+6M^2}{r^2(\lambda r+3M)}\right] Z+\alpha Z_{,r}\ , \\ H_1 &= -i\omega\left[\frac{\lambda r^2-3\lambda Mr-3M^2}{(r-2M)(\lambda r+3M)}\right] Z-i\omega r Z_{,r}\ , \\ H_0 &= \left[\frac{\lambda r(r-2M)-\omega^2 r^4+M(r-3M)}{(r-2M)(\lambda r+3M)}\right] K+\left[\frac{(\lambda+1)M-\omega^2 r^3}{i\omega r(\lambda r+3M)}\right] H_1\ . \end{aligned} \tag{6.36}$$

Here we have used Zerilli's notation

$$\lambda=\frac{1}{2}(l-1)(l+2)\ . \tag{6.37}$$

The Zerilli function satisfies the eigenequation

$$Z_{,r_*r_*}+\omega^2 Z=\mathcal{V}_z(r)Z\ , \tag{6.38}$$

where

$$\mathcal{V}_z(r)=\alpha^2\left[\frac{2\lambda^2(\lambda+1)r^3+6\lambda^2Mr^2+18\lambda M^2r+18M^3}{r^3(\lambda r+3M)^2}\right]. \tag{6.39}$$

The slices of constant Schwarzschild time t do not intersect the black hole's horizon, so in performing our 3+1 split, we use slices of constant Eddington-Finklestein time $\tilde{t}=t+2M\ln(r/2M-1)$. Written in Schwarzschild coordinates, the perturbed tetrad for the EF observers is given by Eqs. (6.8) and (6.11). For any chosen mode, we compute the frame-drag and tidal fields by (i) computing, from the metric-perturbation components $h_{\mu\nu}$, the perturbation $\delta R_{\alpha\beta\gamma\delta}$ to the Riemann tensor (same as Weyl) in Schwarzschild coordinates; (ii) projecting the total Riemann tensor $R_{\alpha\beta\gamma\delta}=R^{(0)}_{\alpha\beta\gamma\delta}+\delta R_{\alpha\beta\gamma\delta}$ (where $R^{(0)}_{\alpha\beta\gamma\delta}$ is the unperturbed Riemann tensor) onto the perturbed EF tetrad; (iii) reading off $\mathcal{E}_{\hat{a}\hat{b}}=R_{\hat{a}\hat{0}\hat{b}\hat{0}}$ and $\mathcal{B}_{\hat{a}\hat{b}}=\frac{1}{2}\epsilon_{\hat{a}\hat{p}\hat{q}}R_{\hat{p}\hat{q}\hat{0}\hat{b}}$ and splitting them into their unperturbed and perturbed parts.

6.7.2 Magnetic-parity $(2,m)$ mode: Frame-drag field

We first focus on the $(2,m)$ quadrupolar modes for magnetic-parity perturbations. Carrying out the above computation, expressing the answer for the frame-drag field in terms of the Regge-Wheeler function $Q(r)$ and the electric-parity scalar, vector, and tensor harmonics (see discussion in App. 6.9.3), and simplifying using Eq. (6.33), we obtain:

[5] In H_1 we have corrected a term in the numerator of the fraction: the last term, $-3M^2$, was incorrectly written as $-3M$ by Zerilli, an error that should be obvious on dimensional grounds.

$$\mathcal{B}^{(1)}_{\hat{r}\hat{r}} = \Re\left[B_{1(\mathrm{m})}e^{-i\omega t}Y^{2m}\right] , \tag{6.40a}$$

$$\mathcal{B}^{(1)}_{\hat{r}\hat{A}} = \Re\left[B_{2(\mathrm{m})}e^{-i\omega t}Y^{2m}_{\hat{A}}\right] , \tag{6.40b}$$

$$\mathcal{B}^{(1)}_{\hat{A}\hat{B}} = \Re\left[\left(-\frac{1}{2}B_{1(\mathrm{m})}\delta_{\hat{A}\hat{B}}Y^{2m} + B_{3(\mathrm{m})}Y^{2m}_{\hat{A}\hat{B}}\right)e^{-i\omega t}\right] , \tag{6.40c}$$

$$B_{1(\mathrm{m})}(r) = -\frac{12Q}{i\omega r^3} , \tag{6.40d}$$

$$B_{2(\mathrm{m})}(r) = -\frac{4iM\omega Q + 2\alpha^2 rQ'}{i\omega r^3\alpha^2\sqrt{1+2M/r}} , \tag{6.40e}$$

$$B_{3(\mathrm{m})}(r) = -\frac{1}{i\omega r^5\alpha^4(r+2M)}\Big(\left[3\alpha^2(r-M)(r^2+4M^2) + 4iM\omega r^2(r-3M) - r^3\omega^2(r^2+4M^2)\right]Q + r\alpha^2\left[(r-3M)(r^2+4M^2) + 4iM\omega r^3\right]Q'\Big) , \tag{6.40f}$$

where a prime denotes a derivative with respect to r, Y^{lm}_{A} and Y^{lm}_{AB} are given by Eqs. (6.85), and $\delta_{\hat{A}\hat{B}}$ is the Kronecker delta.

We have solved the Regge-Wheeler equation (6.33) numerically for the most slowly damped, quadrupolar normal mode. When the numerical solution is inserted into the above expressions for $\mathcal{B}^{(1)}_{\hat{a}\hat{b}}$, numerical errors cause problems with delicate cancellations in the transverse-traceless and radial-transverse components near the horizon. To deal with this, we have derived the following asymptotic formula for $Q(r)$ near the horizon, $r_*/M \ll -1$:

$$\begin{aligned} Q &= Y^{-2iM\omega}\left[1 + \frac{3Y}{(1-4iM\omega)e} + \frac{9iM\omega Y^2}{(1-4iM\omega)(1-2iM\omega)e^2}\right. \\ &\quad \left. -\frac{3(1+12iM\omega+40M^2\omega^2)Y^3}{2(1-4iM\omega)(1-2Mi\omega)(3-4iM\omega)e^3} + O(Y^4)\right] \end{aligned} \tag{6.41}$$

where $Y = e^{r_*/2M}$. Inserting this into Eqs. (6.40), we find, of course, that all components of $\mathcal{B}_{\hat{a}\hat{b}}$ are finite at the horizon.

Using Eqs. (6.40) for the frame-drag field, our analytic formula (6.41) for $Q(r)$ near the horizon, and our numerical solution for $Q(r)$ at larger radii, and the $(2,2)$ harmonics, we compute the vortex lines and their vorticities for the fundamental $(2,2)$ quasinormal mode. We illustrate them in Figs. 6.2, 6.3, 6.4 and 6.10.

For our superposition of the $(2,2)$ and $(2,-2)$ modes we can simply sum the $(2,2)$ and $(2,-2)$ harmonics in the above expressions. We plot the vortex lines for the resulting frame-drag field in Figs. 6.8, 6.16, and the top row of Fig. 6.18. We use the $(2,1)$ harmonics for generating the vortexes

of the magnetic-parity, $(2,1)$ perturbations that are illustrated in Fig. 6.19. Finally, we use the $(2,0)$ harmonics to produce the vortexes and vortex lines of the $(2,0)$ magnetic-parity perturbation. We note that $Y^{20}_{\hat{\phi}} = Y^{20}_{\hat{\theta}\hat{\phi}} = 0$ for this mode. This means that $\mathcal{B}^{(1)}_{\hat{a}\hat{b}}$ is block-diagonal, and the vortex lines split into a pair of lines which remains in a slice of constant ϕ and a single, axial line that runs in circles of constant (r,θ). In a slice of constant ϕ, we illustrate the two sets of vortex lines in the slice and their voticity together in Fig. 6.6 and separately in the left and middle panels of Fig. 6.22. We also plot the vorticity of the axial lines in a slice in the right panel of Fig. 6.22.

6.7.3 Electric-parity $(2,m)$ modes: Frame-drag field

Carrying out the calculation described at the end of Sec. 6.7.1 using the electric-parity metric perturbation (6.35), expressing the result in terms of the Zerilli function Z with the aid of Eqs. (6.36), and simplifying using Zerilli's differential equation (6.38), we obtain for the frame-drag field of a $(2,m)$ electric-parity perturbation

$$\mathcal{B}^{(1)}_{\hat{r}\hat{r}} = 0\,, \tag{6.42a}$$

$$\mathcal{B}^{(1)}_{\hat{r}\hat{A}} = \Re\left[B_{1(\mathrm{e})} e^{-i\omega t} X^{2m}_{\hat{A}}\right]\,, \tag{6.42b}$$

$$\mathcal{B}^{(1)}_{\hat{A}\hat{B}} = \Re\left[B_{2(\mathrm{e})} e^{-i\omega t} X^{2m}_{\hat{A}\hat{B}}\right]\,, \tag{6.42c}$$

where

$$B_{1(\mathrm{e})} = \frac{\left[6M^2\alpha^2 - i\omega r^2(2r+3M)\right] Z - 2Mr\alpha^2(2r+3M)Z'}{2r^5\alpha^2\sqrt{1+2M/r}}\,, \tag{6.42d}$$

$$\begin{aligned} B_{2(\mathrm{e})} = \frac{1}{2r^4\alpha^4(2r+3M)(r+2M)}\Big(&\left[-12M\alpha^2(M^2+4r\beta_1) - i\omega(r^2+4M^2)\beta_2 + 4M\omega^2 r^3(2r+3M)\right] Z \\ &- r\alpha^2\left[4M\beta_2 + i\omega r(2r+3M)(r^2+4M^2)\right] Z'\Big)\,. \end{aligned} \tag{6.42e}$$

Here a prime denotes a derivative with respect to r, and X^{lm}_A and X^{lm}_{AB} are the magnetic-parity vector and tensor spherical harmonics given by Eqs. (6.88) (see discussion in App. 6.9.3). We have defined here for convenience the functions

$$\beta_1 = \frac{r^2+Mr+M^2}{2r+3M}\,, \qquad\qquad \beta_2 = (2r^2-6Mr-3M^2)\,. \tag{6.42f}$$

We note again that the horizon vorticity, $\mathcal{B}^{(1)}_{NN}$, vanishes. With this $\mathcal{B}^{(1)}_{\hat{a}\hat{b}}$ we can again compute the eigenvector fields and eigenvalues for the perturbed spacetime, and from them compute the vortex lines. We use these expressions to calculate the vortex lines and their vorticities generated by electric-parity perturbations. In order to compute the vortex lines for these modes, once again we expand Z around the horizon in terms of $Y = e^{r_*/2M}$ up to $O(Y^3)$. We use this series to match to

a numerical solution of the Zerilli equation subject to ingoing-wave boundary conditions. Because the Zerilli potential $\mathcal{V}_z$ is more complicated than the Regge-Wheeler potential $\mathcal{V}_Q$, the coefficients of the expansion of Z in powers of Y are lengthy, but easily computed using algebraic computing software such as Mathematica. For this reason, we do not give the coefficients here.

For an electric-parity $(2,2)$ perturbation, the only set of vortex lines that are confined to the equatorial plane have vanishing vorticity (and are of less physical interest). Instead, we used the above frame-drag field to compute, and then plot in Fig. 6.13, the vorticity of one of the sets of vortex lines that pass through the equatorial plane at a 45 degree angle: the set with negative vorticity. Just as with the magnetic-parity modes, we superpose a $(2,2)$ perturbation with a $(2,-2)$ perturbation by a simple sum of the harmonics. The vorticity of these lines passing through the equatorial plane (the analog of Fig. 6.13) is plotted in Fig. 6.17.

For the vortex lines of the $(2,1)$ mode, there is a reflection symmetry about the equatorial plane, which implies that there are two sets of vortex lines confined to the plane, with a third normal to it. We illustrate the vortex lines and 3D vortexes of this mode in Fig. 6.20. Finally, when we use the $(2,0)$ harmonics, we note that $X^{20}_{\hat{\theta}} = X^{20}_{\hat{\theta}\hat{\theta}} = X^{20}_{\hat{\phi}\hat{\phi}} = 0$. While this means that the frame drag field is simple, it is not block-diagonal and its nonzero vortex lines pass through all three dimensions. There is a single set of axial vortex lines with zero vorticity, and two sets with equal and opposite vorticity that wind around deformed tori. We illustrate the vorticity in a slice of constant ϕ for the negative lines in Fig. 6.23. In addition, we illustrate some 3D vortex lines in Figs. 6.7 and 6.24.

6.7.4 Electric-parity $(2,2)$ mode: Tidal field

To help understand the slicing dependence of our results, we compare fields generated by electric-parity perturbations, because the slicings are identical for all magnetic-parity perturbations. In particular, we focused on the perturbed tidal field for the electric-parity, $(2,2)$ mode. Carrying out the calculation of this mode as above when using the electric-parity metric perturbation (6.35), we obtain

$$\mathcal{E}^{(1)}_{\hat{r}\hat{r}} = \Re\left[E_{1(\mathrm{e})} e^{-i\omega t} Y^{22}\right] \tag{6.43a}$$

$$\mathcal{E}^{(1)}_{\hat{r}\hat{A}} = \Re\left[E_{2(\mathrm{e})} e^{-i\omega t} Y^{22}_{\hat{A}}\right] , \tag{6.43b}$$

$$\mathcal{E}^{(1)}_{\hat{A}\hat{B}} = \Re\left[\left(-\frac{1}{2} E_{1(\mathrm{e})} \delta_{\hat{A}\hat{B}} Y^{22} + E_{3(\mathrm{e})} Y^{22}_{\hat{A}\hat{B}}\right) e^{-i\omega t}\right] , \tag{6.43c}$$

$$E_{1(\mathrm{e})}(r) = -\frac{3\mathcal{Z}}{2r^3}\,, \tag{6.43d}$$

$$E_{2(\mathrm{e})}(r) = \frac{\left[3M\alpha^2 - 2iM\omega(2r+3M)\right]Z - \alpha^2 r(2r+3M)Z'}{2r^4\alpha^2\sqrt{1+2M/r}}\,, \tag{6.43e}$$

$$\begin{aligned} E_{3(\mathrm{e})}(r) = \frac{1}{2r^4\alpha^4(r+2M)}\Bigg(\Bigg[&-\frac{3\alpha^2(3M^3+6M^2r+4Mr^2+4r^3)(4M+r\alpha^2)}{(2r+3M)^2} + \frac{4iM\omega r(3M^2+6Mr-2r^2)}{(2r+3M)} \\ &+ \omega^2 r^3(4M+r\alpha^4)\Bigg]Z + \alpha^2 r\left[\frac{(3M^2+6Mr-2r^2)(4M+r\alpha^2)}{2r+3M} - 4iM\omega r^2\right]Z'\Bigg)\,, \end{aligned} \tag{6.43f}$$

where $\mathcal{Z}$ is a function which obeys the same Regge-Wheeler equation (6.33) as Q and can be built from the Zerilli function Z as, (see, e.g., Ch. 4, Eq. (156) of [30])

$$\mathcal{Z} = \left[\frac{\lambda^2(\lambda+1)}{3M} + \frac{3M\alpha^2}{r(\lambda r+3M)}\right]Z - \frac{Z_{,r_*}}{\lambda}\,, \tag{6.44}$$

for integers $l \geq 2$. This implies there is an exact duality between $\mathcal{E}_{\hat{r}\hat{r}}$ for electric-parity perturbations and $\mathcal{B}_{\hat{r}\hat{r}}$ magnetic-parity perturbations [in fact for any (l,m) mode] in RWZ gauge. This follows from the facts that these radial-radial components have the same time, radial, and angular dependence (but not necessarily the same amplitude and phase). However, we can fix the relative normalization of the Regge-Wheeler function Q and Zerilli function Z such that $Q = -\omega\mathcal{Z}/8$, in which case we have for Eqs. (6.40d) and (6.43a)

$$B_{1(\mathrm{m})}(r) = iE_{1(\mathrm{e})}(r)\,. \tag{6.45}$$

Substituting $\mathcal{Z}$ into Eqs. (6.43b)—(6.43c) does not illustrate the near-duality of the other components of $\boldsymbol{\mathcal{E}}^{(1)}$ and $\boldsymbol{\mathcal{B}}^{(1)}$ in an obvious manner, so we leave these equations in terms of Z.

As we discuss in the next section, however, the exact duality of $\mathcal{E}^{(1)}_{\hat{r}\hat{r}}$ and $\mathcal{B}^{(1)}_{\hat{r}\hat{r}}$ does not immediately correspond to an exact duality of the horizon tendicity and vorticity. This happens because in RWZ gauge, the electric-parity perturbations deform the horizon, which changes the horizon tendicity.

For the electric-parity, $(2,2)$ perturbation, the tidal field is symmetric about the equatorial plane, and there are two sets of tendex lines that remain in the equatorial plane (just as the vortex lines of the $(2,2)$ magnetic-parity mode did). The tendex lines are illustrated in the left-hand panel of Fig. 6.11

6.7.5 Perturbed horizon and horizon tendicity for electric-parity modes

We discuss here the correction to the position of the horizon and its influence on the perturbed horizon tendicity for the electric-parity $(2,2)$ modes. First, we calculate the correction to the horizon position δr using the same procedure as that of Vega, Poisson, and Massey [18]. The horizon

generators, $\vec{l}$, for the perturbed spacetime are given by

$$l^\mu = \frac{\partial x^\mu}{\partial \tilde{t}} = (1 + \delta\dot{t}, \delta\dot{r}, \delta\dot{\theta}, \delta\dot{\phi}) \,, \tag{6.46}$$

with an overdot represents a derivative with respect to $\tilde{t}$. The functions $\delta\theta$ and $\delta\phi$ change the location of individual generators, but do not alter the shape of the surface defined by the instantaneous horizon. We will not treat them here, but they are described in [18]. By requiring that the generators remain null to first order in the perturbation, we find

$$\delta r - 4M\delta\dot{r} = 2Mh_{ll} \,. \tag{6.47}$$

For IR gauge, $h_{ll} = 0$ and the only physical solution of Eq. (6.47) is $\delta r = 0$. Magnetic-parity RWZ perturbations also have $h_{ll} = 0$, and, therefore, the coordinate location of the horizon does not change in this gauge either. For electric-parity perturbations in RWZ gauge, we use the fact that $h_{ll} = h_{\tilde{t}\tilde{t}}$ on the horizon to solve for the perturbation to the horizon's shape. For a general electric-parity perturbation of indices (l, m), Eqs. (6.35) allow us to write

$$\delta r = \Re \left[\frac{e^{-2iM\omega}}{\kappa + i\omega} e^{-i\omega\tilde{t}} Y_{lm} \lim_{r\to 2M} \left(\frac{H_1 - H_0}{r - 2M} e^{i\omega r^*} \right) \right] , \tag{6.48}$$

where $\kappa = (4M)^{-1}$ is the horizon's unperturbed surface gravity. We evaluate these quantities on the horizon using the near-horizon expansion of the Zerilli function Z, and they are finite.

The perturbation to the position of the horizon corrects the perturbative horizon tendicity in two ways: First, the background horizon tendicity $\mathcal{E}^{(0)}_{\hat{r}\hat{r}}$, when evaluated at $r = 2M + \delta r$, becomes, through first order in δr,

$$\mathcal{E}^{(0)}_{\hat{r}\hat{r}}(r = r_H) = -\frac{1}{4M^2} + \frac{3}{8M^3}\delta r \,. \tag{6.49}$$

Next, we recall that $\vec{e}_{\hat{r}} = \vec{e}^{(0)}_{\hat{r}} + \vec{e}^{(1)}_{\hat{r}}$ is normal to surfaces of constant r through perturbative order. Now that the horizon's surface is deformed, however, the normal to the horizon $\vec{N}$ is no longer precisely the same as $\vec{e}_{\hat{r}}$. It receives a correction such that

$$N^\mu = \frac{1}{N}\gamma^{\mu\nu}\nabla_\nu(r + \delta r) = e^{(0)\mu}_{\hat{r}} + e^{(1)\mu}_{\hat{r}} + \delta N^\mu - \left(\delta N_\nu e^{(0)\nu}_{\hat{r}}\right) e^{(0)\mu}_{\hat{r}} \,, \tag{6.50}$$

where $N = N^{(0)} + N^{(1)}$ is a normalization factor and $\delta N^\mu = (\gamma^{\mu\nu}_{(0)}\nabla_\nu\delta r)/N^{(0)}$ deforms $\vec{N}$ away from $\vec{e}_{\hat{r}}$. Note that the leading-order normal remains $\vec{N}^{(0)} = \vec{e}^{(0)}_{\hat{r}}$. The deformation of the horizon normal

produces additional modifications to the horizon tendicity,

$$\mathcal{E}_{NN} = \mathcal{E}_{\mu\nu}(2M+\delta r)N^\mu N^\mu = \mathcal{E}^{(0)}_{\hat{r}\hat{r}} + \mathcal{E}^{(1)}_{\hat{r}\hat{r}} + \frac{3}{8M^3}\delta r + 2\mathcal{E}^{(0)}_{\hat{r}\mu}\delta N^\mu - 2\mathcal{E}^{(0)}_{\hat{r}\hat{r}}\delta N_\nu e^{(0)\nu}_{\hat{r}}\,, \tag{6.51}$$

where, as usual, $\mathcal{E}^{(1)}_{\hat{r}\hat{r}}$ includes the effects of both the perturbation to the tidal field and to $\vec{e}^{(1)}_{\hat{r}}$ (and where all quantities are evaluated at the unperturbed horizon position $r = 2M$). The new contributions [the last three terms on the right-hand side of Eq. (6.51)] come from the displacement of the position of the horizon δr and the deformation to the normal $\delta\vec{N}$.

In RWZ gauge, the $(\tilde{t}, r)$ components of $\delta\vec{N}$ vanish, although $\delta\vec{N}$ does have angular components; this means that the deformation to the normal to the horizon $\delta\vec{N}$ does not affect the horizon tendicity in RWZ gauge. [To show this, note first that when the deformation to the normal has no $(\tilde{t}, r)$ components $\delta N_\nu e^{(0)\nu}_{\hat{r}} = 0$. Then observe that the (projected) spatial tidal field $\mathcal{E}^{(0)}_{\alpha\beta}$ is diagonal and that $\delta\vec{N}$ has only angular components; therefore, the term $\mathcal{E}^{(0)}_{\hat{r}\mu}\delta N^\mu = 0$ and all terms involving $\delta\vec{N}$ in Eq. (6.51) vanish as well.] Only the shifted coordinate location of the horizon, changes the horizon tendicity, and we find

$$\mathcal{E}^{(1)}_{NN} = \mathcal{E}^{(1)}_{\hat{r}\hat{r}} + \frac{3}{8M^3}\delta r\,. \tag{6.52}$$

From Eq. (6.48), we see that the angular distribution of $\mathcal{E}^{(1)}_{NN}$ in RWZ gauge is the same as in IR gauge [it is $Y^{22}(\theta,\phi)$].

With the angular dependence of the horizon tendicity well understood, let us focus on the amplitude and time dependence of the horizon tendicity. Using a notation analogous to that in Eq. (6.43a), we write the horizon tendicity in the form

$$\mathcal{E}^{(1)}_{NN} = E_{1(\mathrm{e})}(r=2M)e^{-i\omega\tilde{t}}Y^{22}\,, \tag{6.53}$$

for some amplitude $E_{1(\mathrm{e})}$ [we can do this because both terms in Eq. (6.52) have the same time dependence]. This amplitude has two contributions: one from the amplitude (and phase) of $\mathcal{E}^{(1)}_{\hat{r}\hat{r}}$, and the other from the correction to the radial perturbation of the generators [second term on the right hand side of Eq. (6.52)]. We plot these contributions to $E_{1(\mathrm{e})}e^{-i\omega\tilde{t}}$ of Eq. (6.53) in Fig. 6.25, as a function of $\tilde{t}$ and normalized by the maximum of the (perturbed) horizon tendicity. We also plot the amplitude of total perturbation to the horizon tendicity, $E_{1(\mathrm{e})}e^{-i\omega\tilde{t}}$ (the sum of the two contributions). The two contributions are of roughly the same magnitude, but are out of phase. The influence of the change in horizon position (dot-dashed line) is slightly larger than $\mathcal{E}^{(1)}_{\hat{r}\hat{r}}$ (dashed line).

That $\mathcal{E}^{(1)}_{NN}$ differs from $\mathcal{E}^{(1)}_{\hat{r}\hat{r}}$ only by an amplitude and phase means that, in some sense, the duality between the horizon tendicity and vorticity (which is exact in IR gauge) is still intact; however, they

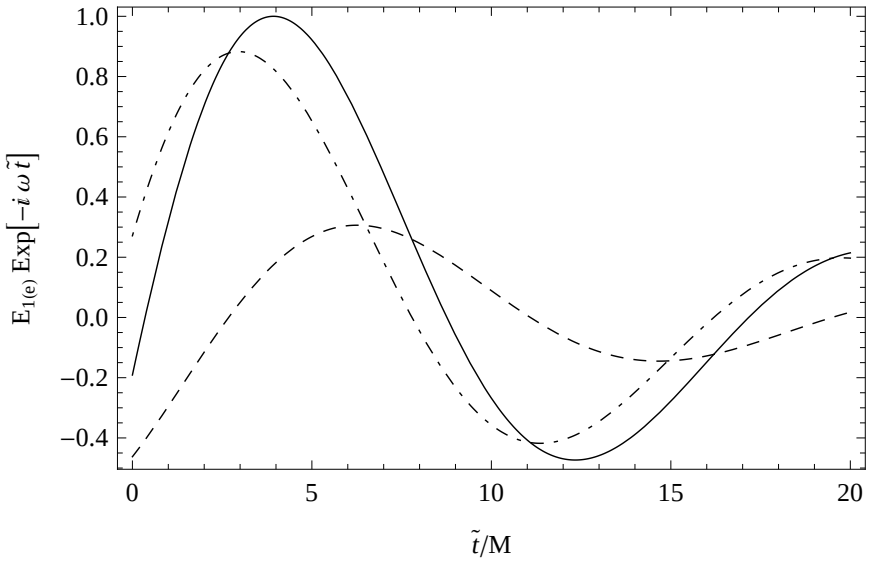

Figure 6.25: Plot illustrating the contributions to the amplitude $E_{1(e)}e^{-i\omega\tilde{t}}$ [Eq. (6.53)] of the perturbed horizon tendicity $\mathcal{E}^{(1)}_{NN}$, in RWZ gauge for the electric-parity, (2,2) perturbation. Plotted agianst $\tilde{t}$ are the amplitude contributions from $\mathcal{E}^{(1)}_{\hat{r}\hat{r}}$ (dashed line), and from the perturbative shift of the horizon generators [dot-dashed line; see Eqs. (6.49) and (6.52)]. The time-dependent amplitude of the total perturbed horizon tendicity is the solid line.

are no longer related by the simple phase shift of i. In fact, we could choose a different normalization between the Regge-Wheeler function Q and the Zerilli function Z than we did in App. 6.7.4 to restore this duality relation, but this would only hold for the horizon tendicity and vorticity [and the duality in Eq. (6.45) would be more complicated, with a complex amplitude replacing the factor of i].

6.7.6 Magnetic-parity, superposed $(2,2)$ and $(2,-2)$ modes: Tidal field

In order to understand better the dynamics and interaction of the tendexes and vortexes, we compute the perturbations to the tidal field that must accompany the frame-drag field of a magnetic-parity perturbation for the superposed $(2,2)$ and $(2,-2)$ modes. These tidal perturbations are much like the frame-drag perturbations of an electric-parity metric perturbation, as expected by the near-duality. Their odd parity ensures that they must be reflection antisymmetric about the equatorial plane. If we consider the tendex lines of $\boldsymbol{\mathcal{E}}^{(1)}$ alone, there must be a zero tendicity set of tendex lines in the plane, and two sets which pass through the plane at 45° with equal and opposite tendicity. We are also assured that $\mathcal{E}^{(1)}_{NN} = 0$. From the calcultion described at the beginning of Sec. 6.7.1

above, we obtain:

$$\mathcal{E}^{(1)}_{\hat{r}\hat{r}} = 0\,, \tag{6.54a}$$

$$\mathcal{E}^{(1)}_{\hat{r}\hat{A}} = \Re\left[E_{1(\mathrm{m})}e^{-i\omega t}\left(X^{22}_{\hat{A}} + X^{2-2}_{\hat{A}}\right)\right]\,, \tag{6.54b}$$

$$\mathcal{E}^{(1)}_{\hat{A}\hat{B}} = \Re\left[E_{2(\mathrm{m})}e^{-i\omega t}\left(X^{22}_{\hat{A}\hat{B}} + X^{2-2}_{\hat{A}\hat{B}}\right)\right], \tag{6.54c}$$

$$E_{1(\mathrm{m})} = \frac{2i\omega rQ + 4M\alpha^2 Q'}{i\omega r^3\alpha^2\sqrt{1+2M/r}}\,, \tag{6.54d}$$

$$\begin{aligned} E_{2(\mathrm{m})} =& \frac{\left[6M\alpha^2(\alpha^2+1) + i\omega(r^2 - 3Mr - 2M^2 + 6M^2\alpha^2) - 4M\omega^2 r^2\right]Q}{i\omega r^4\alpha^4(1+2M/r)} \\ &+ \frac{\alpha^2\left[-12M^2 + 4r(M + iM^2\omega) + i\omega r^3\right]Q'}{i\omega r^4\alpha^4(1+2M/r)} \end{aligned} \tag{6.54e}$$

We illustrate the tendicity of the predominantly negative tendex lines in the equatorial plane in the time series of Fig. 6.18 (bottom row), which shows the evolution over a half period of oscillation of the metric perturbation.

6.8 Appendix: Teukolsky's Equation and Black-Hole Perturbations in the Newman-Penrose Formalism

The results in this appendix appear in many places in the literature (see, for example, Teukolsky's paper [31]). We summarize them here because we will need them in Apps. 6.9 and 6.11.

Teukolsky's equation relies on the Newman-Penrose (NP) formalism using Kinnersley's tetrad, which is the principal complex null tetrad in the Schwarzschild and Kerr spacetimes. For Kerr, in the Boyer-Lindquist coordinate basis $\{\partial_t, \partial_r, \partial_\theta, \partial_\phi\}$ [Eq. (6.1) of Paper II], this tetrad's contravariant components are given by

$$\begin{aligned} l^\mu &= \frac{1}{\Delta}(r^2 + a^2, \Delta, 0, a)\,, \quad n^\mu = \frac{1}{2\Sigma}(r^2 + a^2, -\Delta, 0, a)\,, \\ m^\mu &= \frac{1}{\sqrt{2}(r + ia\cos\theta)}(ia\sin\theta, 0, 1, i\csc\theta)\,, \end{aligned} \tag{6.55}$$

with the final leg given by $\vec{m}^*$, the complex conjugate of $\vec{m}$. Here

$$\Delta = r^2 + 2Mr + a^2\,, \quad \Sigma = r^2 + a^2\cos^2\theta\,. \tag{6.56}$$

When a is taken to zero, we recover the Kinnersley tetrad for Schwarzschild spacetime in the Schwarzschild coordinate basis [Eq. (4.1) of Paper II]. The Teukolsky equation also requires the NP

spin coefficients, certain contractions of covariant derivatives of the tetrad above given by Eq. (4.1a) of [32] (though with the opposite signs because of differing metric-signature conventions). The nonzero spin coefficients in this tetrad are

$$\rho = -\frac{1}{r - ia\cos\theta}\,, \quad \pi = \frac{ia}{\sqrt{2}}\rho^2\sin\theta\,, \quad \beta = -\frac{1}{2\sqrt{2}}\rho^*\cot\theta\,, \quad \alpha = \pi - \beta^*\,,$$
$$\mu = \frac{\rho^*\Delta}{2\Sigma}\,, \quad \gamma = \mu + \frac{r-M}{2\Sigma}\,, \quad \tau = -\frac{ia}{\sqrt{2}\Sigma}\sin\theta\,. \tag{6.57}$$

The Weyl scalars Ψ_0 and Ψ_4 are defined in terms of the Weyl tensor by $\Psi_0 = C_{\mu\nu\rho\sigma}l^\mu m^\nu l^\rho m^\sigma$ and $\Psi_4 = C_{\mu\nu\rho\sigma}n^\mu m^{*\nu} n^\rho m^{*\sigma}$. These both vanish in the background when using the Kinnersley tetrad, and are gauge invariant at first order in the perturbation theory [31], consequently. At that perturbative order, they satisfy decoupled, linear, second-order partial-differential equations. Teukolsky's big breakthrough [31] was to show that, when those equations are re-expressed in terms of

$$\psi_2 \equiv \Psi_0 \quad \text{and} \quad \psi_{-2} \equiv \rho^{-4}\Psi_4\,, \tag{6.58}$$

they take on a unified form (the *Teukolsky equation*) that depends on the spin-weight $s = +2$ for ψ_2 and $s = -2$ for ψ_{-2}, and that is separable; i.e., it has a solution of the form $\psi_s^{lm\omega} = {}_sR_{lm\omega}(r)\,{}_sS_{lm\omega}(\theta)e^{i(m\phi-\omega t)}$. The Teukolsky equation implies for the radial function ${}_sR_{lm\omega}$ the following ordinary differential equation (in vacuum)

$$0 = \Delta^{-s}\frac{d}{dr}\left(\Delta^{s+1}\frac{d\,{}_sR_{lm\omega}}{dr}\right) \tag{6.59}$$
$$+\left(\frac{K^2 - 2is(r-M)K}{\Delta} + 4is\omega r + 2am\omega - a^2\omega^2 - {}_sA_{lm}\right){}_sR_{lm\omega}\,, \tag{6.60}$$

where ${}_sA_{lm}$ is a separation constant that is a function of $a\omega$ [i.e., ${}_sA_{lm} = {}_sA_{lm}(a\omega)$], and $K \equiv (r^2+a^2)\omega - am$. The radial function has the symmetries ${}_sR_{lm\omega} = (-1)^m\,{}_sR_{l-m-\omega^*}$. The angular function, ${}_{-2}S_{lm\omega}(\theta)$, (called the spin-weighted spheroidal harmonic) satisfies the ordinary differential equation (in vacuum)

$$0 = \csc\theta\frac{d}{d\theta}\left(\sin\theta\frac{d\,{}_sS_{lm\omega}}{d\theta}\right) + (a^2\omega^2\cos^2\theta - m^2\csc^2\theta$$
$$- 2a\omega s\cos\theta - 2ms\cot\theta\csc\theta - s^2\cot^2\theta + s + {}_sA_{lm})\,{}_sS_{lm\omega}\,. \tag{6.61}$$

This angular function has the symmetries ${}_sS_{lm\omega}(\pi-\theta) = (-1)^{(m+l)}\,{}_{-s}S_{lm\omega}(\theta)$ and ${}_sS^*_{lm\omega}(\theta) = (-1)^{m+s}\,{}_{-s}S_{l-m-\omega^*}(\theta)$, where we are using a phase convention such that the angular functions agree with the usual convention for spin-weighted spherical harmonics in the limit that spin parameter, a, goes to zero.

It is often useful, in working with the perturbation equations, to change variables from the

separation constants ${}_sA_{lm}$ to Chandrasekhar's [30]

$$ {}_s\lambda_{lm} \equiv {}_sA_{lm} + s + |s| - 2am\omega + a^2\omega^2 \ , \tag{6.62} $$

which are the same for positive and negative spin weights, $\pm s$.

6.9 Appendix: The Chrzanowski-Cohen-Kegeles Procedure and the Ingoing-Radiation-Gauge Metric

In this appendix, we will review the formalism used for computing the ingoing-radiation-gauge (IR gauge) metric, using what is known as the Chrzanowski-Cohen-Kegeles (CCK) procedure. We will also connect the CCK procedure to Chrzanowski's original calculation of definite-parity harmonics, which we find useful for our calculations.

Although Chrzanowski conjectured that "the conceptual benefits of having found the perturbed Kerr metric potentials surpass the usefulness of these potentials for doing future computations" [33], the procedure he helped to formulate has found several applications in the past few years. Lousto and Whiting [34] revisited Chrzanowski's construction and found explicit expressions for computing the Hertz potential corresponding to specific perturbations of the Weyl curvature scalars Ψ_0 and Ψ_4 in the Schwarzschild spacetime. Ori then derived a similar result for Kerr black holes, using a frequency-domain calculation [35]. Yunes and Gonzalez were the first to explicitly compute the metric of a perturbed Kerr black hole from the Hertz potential [36], and Keidl, Friedman, and Wiseman were the first to use the procedure to calculate the metric perturbation from a static point particle in the Schwarzschild spacetime [37]. More recently, Keidl, Shah, and their collaborators articulated a formalism for computing the gravitational self-force of a point particle in the Schwarzschild or Kerr spacetimes using the metric constructed from a Hertz potential [38]. They were then able to compute the conservative piece of the self-force from this metric perturbation in the Schwarzschild spacetime [39]. In the first article [38], they gave a concise summary of constructing metric perturbations from a Hertz potential, and they called this process the Chrzanowski-Cohen-Kegeles (CCK) procedure or formalism (names we will also adopt).

In the first part of this appendix, we will review the CCK formalism in a similar manner to how Keidl summarized it in [38]. While the metric we ultimately compute in this paper is nearly identical to that described by Chrzanowski [33], we find it helpful to put Chrzanowski's original calculation into the context of the more recent work on the CCK procedure. Furthermore, we review the CCK procedure here, rather than simply referring the interested reader to [38], because there are several differences between our calculation and that set forth in [38]: we use a metric of the opposite signature, we calculate the metric corresponding to quasinormal modes with complex

frequencies, we construct the metric in a different radiation gauge, and (like Chrzanowski's original calculation) we are interested in metric perturbations of definite parities.

Because the CCK formalism relies heavily on the Newman-Penrose formalism and Teukolsky's equation for perturbations of Weyl curvature scalars, we review these in Appendix 6.8. In the second part of this appendix, we will describe how to use the CCK procedure to compute definte-parity metric perturbations corresponding to quasinormal modes. In the third part of this appendix, we compute the metric perturbations in a notation in which they can be compared more easily with those of the RWZ formalism (a calculation originally performed by [33]), and we also give explicit analytial expressions for the tidal and frame-drag fields for $(2, 2)$ perturbations, which highlight a near duality between the perturbative pieces of these fields for perturbations of opposite parities. In the final part, we summarize how we numerically calculate the IR gauge metric perturbations that we use in the visualizations in Figs. 6.4, 6.12, 6.14, 6.15, and 6.26.

6.9.1 The CCK procedure

The purpose of the CCK procedure is to construct a metric perturbation, $h_{\mu\nu}$, from a given solution to Teukolsky's equation, either $\psi_2 = \Psi_0$ or $\psi_{-2} = \rho^{-4}\Psi_4$ (see Appendix 6.8 for a summary of the Teukolsky formalism). As part of the calculation, it is necessary to relate the solutions of the Teukolsky equation to a Hertz potential from which the metric perturbation is directly constructed [see Eq. (6.67) for the general relationship, Eq. (6.73) for the relationship for the radial functions for their harmonics, and Eq. (6.80) for the relationship of the radial functions of definite-parity perturbations].

The CCK procedure can construct a metric in either ingoing-radiation (IR) gauge,

$$h_{\mu\nu} l^\nu = 0 \,, \quad h_{\mu\nu} g^{\mu\nu}_{(0)} = 0 \,, \tag{6.63}$$

or outgoing-radiation gauge

$$h_{\mu\nu} n^\nu = 0 \,, \quad h_{\mu\nu} g^{\mu\nu}_{(0)} = 0 \,, \tag{6.64}$$

for Schwarzschild and Kerr black holes. Here l^ν and n^ν are two vectors of a Newman-Penrose null tetrad [for our calculations, we will use the Kinnersley tetrad, Eq. (6.55)], and $g^{\mu\nu}_{(0)}$ is the background Schwarzschild or Kerr metric. Because our goal is to compute vacuum perturbations of Kerr that are regular on the future event horizon, we will construct the metric perturbation in IR gauge, and we will be able to compute it by algebraically inverting a differential relationship between the harmonics of the Hertz potential and those of ψ_{-2} [the result is in Eq. (6.73)].

The Hertz potential is tensor with the same symmetries as the Riemann tensor, whose double coordinate divergence is a harmonic coordinate metric. Stewart [40] showed that in Type D space-

times, there is sufficient gauge freedom that one can represent the independent degrees of freedom of the perturbative part of the Hertz potential as a single complex scalar; furthermore, if one applies a coordinate transformation from harmonic gauge into IR gauge, the Hertz potential, which we will denote by Ψ_H, is a solution of the vacuum Teukolsky equation for scalars of spin weight $s = -2$ (the same as ψ_{-2}). One can then construct a metric perturbation from the Hertz potential by applying several differential operators to Ψ_H,

$$\begin{aligned} h_{\mu\nu} &= \{-l_\mu l_\nu(\boldsymbol{\delta} + \alpha^* + 3\beta - \tau)(\boldsymbol{\delta} + 4\beta + 3\tau) \\ &\quad -m_\mu m_\nu(\mathbf{D} - \rho + 3\epsilon - \epsilon^*)(\mathbf{D} + 3\rho + 4\epsilon) \\ &\quad +l_{(\mu}m_{\nu)}\left[(\mathbf{D} + \rho^* - \rho + \epsilon^* + 3\epsilon)(\boldsymbol{\delta} + 4\beta + 3\tau)\right. \\ &\quad \left.+(\boldsymbol{\delta} + 3\beta - \alpha^* - \pi^* - \tau)(\mathbf{D} + 3\rho + 4\epsilon)\right]\} \Psi_H \\ &\quad +\text{c.c.} \end{aligned} \tag{6.65}$$

(see, e.g., Eqs. (93) and (94) of [37]). The differential operators are defined by $\mathbf{D} = l^\mu \nabla_\mu$ and $\boldsymbol{\delta} = m^\mu \nabla_\mu$. The last term in Eq. (6.65), denoted by "c.c.," means to take the complex conjugate of the entire expression, so that the metric perturbation is real.

When computing perturbations of black holes, it is helpful to be able to relate a given Hertz potential Ψ_H to a specific perturbation of the Weyl scalar Ψ_4. It is possible to do this by computing the components of the perturbative Riemann tensor from the metric perturbations (6.65 that correspond to the Weyl scalar

$$\Psi_4 = C_{\alpha\beta\mu\nu} n^\alpha m^{*\beta} n^\mu m^{*\nu} \,. \tag{6.66}$$

The result can be expressed compactly as

$$\psi_{-2} = \frac{1}{8}\left(\mathcal{L}^{\dagger 4}\Psi_H^* - 12M\partial_t \Psi_H\right) \tag{6.67}$$

[see, e.g., Table I of the paper by Keidl [38], where our $\mathcal{L}^\dagger$ is their $\tilde{\mathcal{L}}$]. We have used the shorthand that $\mathcal{L}^{\dagger 4} = \mathcal{L}^\dagger_{-1}\mathcal{L}^\dagger_0\mathcal{L}^\dagger_1\mathcal{L}^\dagger_2$ where

$$\mathcal{L}^\dagger_s = -\left(\partial_\theta + s\cot\theta - i\csc\theta\partial_\phi\right) + ia\sin\theta\partial_t \,. \tag{6.68}$$

In general, solving for the Hertz potential Ψ_H that corresponds to a perturbed Weyl scalar Ψ_4 involves inverting the fourth-order partial differential equation (6.67); however, when Ψ_H and ψ_{-2} are expanded in harmonics in the frequency domain, it is possible to perform the inversion algebraically.

The algebraic inversion can be completed by expanding ψ_{-2} in harmonics,

$$\psi_{-2} = \sum_{lm\omega} \psi_{-2}^{(lm\omega)} = \sum_{lm\omega} {}_{-2}R_{lm\omega}(r)\, {}_{-2}S_{lm\omega}(\theta) e^{i(m\phi-\omega t)}\,, \tag{6.69}$$

where ${}_{-2}R_{lm\omega}(r)$ and ${}_{-2}S_{lm\omega}(\theta)$ satisfy Eqs. (6.60) and (6.61). In the IR gauge, the Hertz potential is a solution to the Teukolsky equation with spin $s = -2$; consequently, it can also be expanded in the same harmonics

$$\Psi_H = \sum_{lm\omega} \Psi_H^{(lm\omega)} = \sum_{lm\omega} {}_{-2}X_{lm\omega}(r)\, {}_{-2}S_{lm\omega}(\theta) e^{i(m\phi-\omega t)}\,. \tag{6.70}$$

The radial function of the Hertz potential's harmonics ${}_{-2}X_{lm\omega}(r)$ also satisfies the vacuum Teukolsky radial equation, but because it is not the same radial function as in the harmonics of ψ_{-2}, we denote it with a different function. The radial functions of the harmonics of Ψ_H and ψ_{-2} can be related by substituting Eqs. (6.69) and (6.70) into Eq. (6.67) and using the Teukolsky-Starobinsky identity

$$\mathcal{L}^{\dagger 4}{}_2S_{lm\omega} = D\, {}_{-2}S_{lm\omega} \tag{6.71}$$

(Eq. (59) of Ch. 9 of [30], after noting that our $\mathcal{L}_s^\dagger$ is equivalent to $-\mathcal{L}_s$ there), and the identity

$${}_{-2}S^*_{lm\omega} = (-1)^m {}_2S_{l-m-\omega^*}\,. \tag{6.72}$$

Then, it is necessary to equate the full radial function for a given angular and time harmonic of the Hertz potential to the radial functions ${}_{-2}R_{lm\omega}$ of ψ_{-2}. After this relationship is inverted, the individual radial harmonics of the Hertz potential can be written as

$${}_{-2}X_{lm\omega} = 8\frac{(-1)^m D^*\, {}_{-2}R^*_{l-m-\omega^*} - 12iM\omega\, {}_{-2}R_{lm\omega}}{D^{*2} + 144M^2\omega^2}\,. \tag{6.73}$$

The constant $D^* \equiv D^*_{lm\omega} = D_{l-m-\omega^*}$ is defined by

$$\begin{aligned} D^2 &= \lambda^2(\lambda+2)^2 - 8\lambda(5\lambda+6)(a^2\omega^2 - am\omega) + 96\lambda a^2\omega^2 + 144(a^2\omega^2 - am\omega)^2\,, \end{aligned} \tag{6.74}$$

where λ is the separation constant (6.62) used by Chandrasekhar [30] (a choice of the separation constant that is the same for both the angular and the radial equations). Although the Teukolsky-Starobinsky identities are usually derived assuming real frequencies, they have been shown to hold for complex frequencies as well (for a recent derivation, see [41]).

The general description of the CCK formalism is now complete: (i) For a vacuum perturbation of Ψ_4, we can find the Hertz potential Ψ_H that corresponds to this perturbation by expanding Ψ_H

in harmonics [Eq. (6.70)], and expressing the radial functions of this expansion in terms of those of $\psi_{-2} = \rho^{-4}\Psi_4$ via Eq. (6.73). (ii) From the resulting Ψ_H, we can then compute the metric perturbations via Eq. (6.65).

Next, we will show that if we choose the radial function of the Hertz potential to correspond to a perturbation of ψ_{-2} with definite parity, then the result of this calculation is equivalent to Chrzanowski's original calculation of definite-parity metric perturbations [33].

6.9.2 Definite-parity harmonics and Chrzanowski's calculation

Let us now connect this CCK procedure with Chrzanowski's original calculation of metric perturbations of definite parities. We shall begin by showing that, if the perturbations have definite parity (electric or magnetic), then the Hertz potential must itself transform as $\Psi_H \to \pm(-1)^l \Psi_H^*$ under parity (the plus and minus correspond to electric- and magnetic-parity perturbations, respectively), and its radial harmonics must satisfy ${}_{-2}X^*_{l-m-\omega^*} = \pm(-1)^m {}_{-2}X_{lm\omega}$. In turn, this implies that the radial harmonics of ψ_{-2} must satisfy the same relationship ${}_{-2}R^*_{l-m-\omega^*} = \pm(-1)^m {}_{-2}R_{lm\omega}$.

To deduce these relationships, we discuss the parity of the terms that appear in Eq. (6.65). The Newman-Penrose tetrad and spin coefficients of the background spacetime transform in several different ways under parity: $\vec{l}$ and $\vec{n}$ have positive parity, and $\vec{m}$ does not have a definite parity, $\vec{m} \to -\vec{m}^*$. Similarly, the differential operator $\mathbf{D} = l^\mu \nabla_\mu$ has positive parity, and $\boldsymbol{\delta} = m^\mu \nabla_\mu$ again does not have a definite parity, $\boldsymbol{\delta} \to -\boldsymbol{\delta}^*$. Three of the nonzero spin coefficients map to their complex conjugates under parity ($\rho \to \rho^*$, $\mu \to \mu^*$, and $\gamma \to \gamma^*$), and the remaining four spin coefficients become minus their complex conjugates under parity ($\alpha \to -\alpha^*$, $\beta \to -\beta^*$, $\pi \to -\pi^*$, and $\tau \to -\tau^*$). These relationships hold true for both Schwarzschild and Kerr, although in the former case, the spin coefficients are real and, therefore, have definite parity.

When applying a parity transformation to the perturbative metric tensor, $h_{\mu\nu} dx^\mu dx^\nu$, where $h_{\mu\nu}$ is given by Eq. (6.65), we can show that the tensor differential operator in Eq. (6.65) becomes its complex conjugate by using the parity transformations for the spin coefficients, NP tetrad, and differential operators above. As a result, the metric perturbation will have either electric or magnetic parity when the Hertz potential transforms as

$$\Psi_H \to \pm(-1)^l \Psi_H^* \tag{6.75}$$

under parity. The plus sign corresponds to an electric-parity perturbation, and the minus sign describes a magnetic-parity perturbation. The condition this implies on the harmonics is also quite simple, which we can determine by applying a parity transformation to the Hertz potential expanded in harmonics [Eq. (6.70)] and equating it to its complex conjugate. Then using the properties of the

Teukolsky angular functions

$$
\begin{aligned}
{}_sS_{lm\omega}(\pi-\theta) &= (-1)^{m+l}\,{}_{-s}S_{lm\omega}(\theta) && (6.76)\\
{}_sS^*_{lm\omega}(\theta) &= (-1)^{m+s}\,{}_{-s}S_{l-m-\omega^*}(\theta) && (6.77)
\end{aligned}
$$

(see Appendix 6.8) and equating the radial function of each time and angular harmonic, we obtain the following condition on its radial functions,

$$
{}_{-2}X^*_{l-m-\omega^*} = \pm(-1)^m\,{}_{-2}X_{lm\omega}\,. \tag{6.78}
$$

Similarly by substituting Eq. (6.73) into the expression above, we find an analogous relationship for the radial function of the Weyl scalar ψ_{-2},

$$
{}_{-2}R^*_{l-m-\omega^*} = \pm(-1)^m\,{}_{-2}R_{lm\omega}\,. \tag{6.79}
$$

For these definite-parity perturbations, the relationship between the radial functions of the Hertz potential and ψ_{-2}, Eq. (6.73) also simplifies,

$$
{}_{-2}X_{lm\omega} = \pm 8(D^* \pm 12iM\omega)^{-1}\,{}_{-2}R_{lm\omega}\,; \tag{6.80}
$$

namely, for definite-parity perturbations, the radial functions of ψ_{-2} and Ψ_H differ by only a complex constant. Because Eq. (6.80) shows that the two radial functions ${}_{-2}X_{lm\omega}$ and ${}_{-2}R_{lm\omega}$ differ only by a constant multiple, we will express both Ψ_H and ψ_{-2} in terms of the radial function of ψ_{-2}, ${}_{-2}R_{lm\omega}$, for simplicity.

In the next part (and also for all other IR gauge calculations in this paper), we will compute a metric perturbation that corresponds to a perturbation of ψ_{-2} of the form

$$
\begin{aligned}
\psi_{-2} &= \pm\frac{1}{8}(D^* \pm 12iM\omega)\,{}_{-2}R_{lm\omega}e^{i(m\phi-\omega t)}\,{}_{-2}S_{lm\omega}\\
&\quad +\frac{1}{8}(-1)^m(D \mp 12iM\omega^*)\,{}_{-2}R^*_{lm\omega}e^{-i(m\phi-\omega^* t)}\,{}_{-2}S_{l-m-\omega^*}\,. && (6.81)
\end{aligned}
$$

The corresponding Hertz potential is

$$
\Psi_H = {}_{-2}R_{lm\omega}e^{i(m\phi-\omega t)}\,{}_{-2}S_{lm\omega} \pm (-1)^m\,{}_{-2}R^*_{lm\omega}{}_2e^{-i(m\phi-\omega^* t)}\,{}_{-2}S_{l-m-\omega^*}\,. \tag{6.82}
$$

We choose the prefactors on the modes of ψ_{-2} so as to make the Hertz potential (and, therefore, the metric) as simple as possible. Furthermore, this choice gives the same definite-parity metric as that of Chrzanowski (when we take the real part of his expressions).

6.9.3 Definite-parity CCK metric perturbations and tidal and frame-drag fields for Schwarzschild black holes

In the first two parts of this section, we will calculate electric- and magnetic-parity perturbations of Schwarzschild black holes in IR gauge. Because Chrzanowski performed this calculation in Table III of reference [33], and our results agree with his, we do not go into great detail describing the calculations; instead, we aim show the results here so as to be able to compare with the RWZ formalism in Appendix 6.7. In the third part, we will compute the tidal and frame-drag fields corresponding to these metric perturbations and show a near duality of the tidal and frame-drag fields of opposite parity perturbations for the $(2, 2)$ mode.

6.9.3.1 Electric-parity metric perturbations

We begin this part by comparing the metric produced by the CCK procedure to that of the RWZ formalism. We will write the RWZ metric using the covariant notation described by Martel and Poisson [42]. Martel and Poisson write the electric-parity perturbations as

$$h^{(\mathrm{e})}_{ab} = \sum_{lm} h^{lm}_{ab} Y^{lm} \,, \tag{6.83a}$$

$$h^{(\mathrm{e})}_{aB} = \sum_{lm} j^{lm}_{a} Y^{lm}_{B} \,, \tag{6.83b}$$

$$h^{(\mathrm{e})}_{AB} = r^2 \sum_{lm} \left(K^{lm} \Omega_{AB} Y^{lm} + G^{lm} Y^{lm}_{AB} \right) \,, \tag{6.83c}$$

where the lowercase indices run over the radial and time coordinates (e.g., $a, b = t, r$), and uppercase indices run over the angular coordinates as before, $A, B = \theta, \phi$. The angular functions Y^{lm} are scalar spherical harmonics, Y^{lm}_B are the electric-parity Regge-Wheeler harmonics, and Y^{lm}_{AB} are transverse-traceless, electric-parity tensor harmonics; the term Ω_{AB} is the metric on a 2-sphere. The vector and tensor harmonics are defined by

$$Y^{lm}_{A} = D_A Y^{lm} \,, \tag{6.84a}$$

$$Y^{lm}_{AB} = \left[D_A D_B + \frac{1}{2} l(l+1) \Omega_{AB} \right] Y^{lm} \,, \tag{6.84b}$$

where D_A is the covariant derivative on a 2-sphere.

Because the Schwarzschild spacetime is spherically symmetric, we can see, intuitively, that the CCK metric, Eq. (6.65), corresponding to an electric-parity quasinormal-mode perturbation [the plus sign in Eq. (6.82)] will have a relatively simple form. The angular operators acting on the Hertz potential in Eq. (6.65) become the spin-weight raising and lowering operators, and the angular functions become the spin-weighted spherical harmonics; furthermore, and when the spin-weighted

harmonics are combined with the appropriate factors of $\vec{m}$ and $\vec{m}^*$ the angular functions become proportional to the scalar, vector, and tensor harmonics described above. When performing the calculation, we will need to use the following identities, which can be found, for example, by adapting Eqs. (2.22a) and (2.38e) in the review by Thorne [43] to the notation used here,

$$Y^{lm}_A = \sqrt{\frac{l(l+1)}{2}}({}_{-1}Y_{lm} m_A - {}_1Y_{lm} m^*_A)\,, \tag{6.85a}$$

$$Y^{lm}_{AB} = \frac{\sqrt{D}}{2}({}_{-2}Y_{lm} m_A m_B + {}_2Y_{lm} m^*_A m^*_B)\,. \tag{6.85b}$$

The Teukolsky-Starobinsky constant for spin-weighted spherical harmonics is $D = (l+2)!/(l-2)!$. We can then find that the metric coefficients are given by

$$h^{(\mathrm{e})}_{tt} = -\alpha^2 h^{(\mathrm{e})}_{tr} = \alpha^4 h^{(\mathrm{e})}_{rr} = -\frac{2\sqrt{D}}{r^2}\Re[{}_{-2}R_{lm} e^{-i\omega t} Y^{lm}]\,, \tag{6.86a}$$

$$h^{(\mathrm{e})}_{tA} = -\alpha^2 h^{(\mathrm{e})}_{rA} = \frac{\sqrt{D}}{2l(l+1)\alpha^2}\Re\left\{\left[\frac{d}{dr_*}{}_{-2}R_{lm} - \left(i\omega + \frac{2\alpha^2}{r}\right){}_{-2}R_{lm}\right] Y^{lm}_A e^{-i\omega t}\right\}\,, \tag{6.86b}$$

$$h^{(\mathrm{e})}_{AB} = \frac{2}{\sqrt{D}\alpha^4}\Re\left\{\left[(i\omega r^2 - M)\frac{d}{dr_*}{}_{-2}R_{lm} - [\tfrac{1}{2}\mu^2\alpha^2 - i\omega(-3r+7M) - r^2\omega^2]{}_{-2}R_{lm}\right] Y^{lm}_{AB} e^{-i\omega t}\right\}\,. \tag{6.86c}$$

In the last equation we have used the radial Teukolsky equation to eliminate the second-derivative term, and we have defined $\mu^2 = (l-1)(l+2)$ (which is also equal to $l(l+1) - s(s+1)$ for $s = -2$).

There are a few noteworthy differences between the IR gauge electric-parity perturbations, and the electric-parity RWZ-gauge metric. The CCK metric has a strictly angular part of the perturbation which is proportional to the transverse-traceless harmonics, and the trace portion of the angular block vanishes; conversely, the angular block of the RWZ metric perturbation has a trace part, but no transverse-traceless perturbation. The $h^{(\mathrm{e})}_{tr}$ part of the metric perturbation also has a simpler relationship with the $h^{(\mathrm{e})}_{tt}$ and $h^{(\mathrm{e})}_{rr}$ components in IR gauge than in RWZ gauge; one reason for this is that the IR gauge metric has electric-parity vector perturbations, whereas the RWZ metric sets these to zero. Finally, the IR gauge metric is finite on the future event horizon for ingoing radiation. One can see this by noting that both ${}_{-2}R_{lm}$ and $d{}_{-2}R_{lm}/dr_*$ scale as $\alpha^4 e^{-i\omega r_*}$ near the horizon, which will cancel any negative powers of α^2 in the expressions for the metric coefficients. The same is not as manifest for the RWZ perturbations (see Appendix 6.7 for more details on the RWZ formalism).

6.9.3.2 Magnetic-parity metric perturbations

The magnetic-parity perturbations are given by

$$h^{(\mathrm{m})}_{ab} = 0\,, \tag{6.87a}$$

$$h^{(\mathrm{m})}_{aB} = \sum_{lm} h^{lm}_{a} X^{lm}_{B}\,, \tag{6.87b}$$

$$h^{(\mathrm{m})}_{AB} = \sum_{lm} h^{lm}_{2} X^{lm}_{AB}\,, \tag{6.87c}$$

where the magnetic-parity harmonics are defined by

$$X^{lm}_{A} = -\epsilon_{A}{}^{B} D_{B} Y^{lm}\,, \tag{6.88a}$$

$$X^{lm}_{AB} = -\frac{1}{2}(\epsilon_{A}{}^{C} D_{B} + \epsilon_{B}{}^{C} D_{A}) D_{C} Y^{lm}\,, \tag{6.88b}$$

and ϵ_{AB} is the Levi-Civita tensor on a unit 2-sphere. As in the previous part, we can compute the CCK metric (6.65), which is relativitely simple for a Schwarzschild black hole. The reason for the simplification is the same, but we will need the following two identities that relate the spin-weighted spherical harmonics to magnetic-parity vector and tensor harmonics

$$X^{lm}_{A} = -i\sqrt{\frac{l(l+1)}{2}}({}_{-1}Y_{lm} m_{A} + {}_{1}Y_{lm} m^{*}_{A})\,, \tag{6.89a}$$

$$X^{lm}_{AB} = -i\frac{\sqrt{D}}{2}({}_{-2}Y_{lm} m_{A} m_{B} - {}_{2}Y_{lm} m^{*}_{A} m^{*}_{B})\,. \tag{6.89b}$$

These relationships can found in Eqs. (2.22b) and (2.38f) of [43]. The magnetic-parity metric perturbations have the same radial and time dependence as the electric-parity perturbations for the vector and tensor parts,

$$-h^{(\mathrm{m})}_{tA} = \alpha^{2} h^{(\mathrm{m})}_{rA} = \frac{\sqrt{D}}{2l(l+1)\alpha^{2}} \Im\left\{\left[\frac{d}{dr_{*}} {}_{-2}R_{lm} - \left(i\omega + \frac{2\alpha^{2}}{r}\right) {}_{-2}R_{lm}\right] X^{lm}_{A} e^{-i\omega t}\right\}\,. \tag{6.90a}$$

$$h^{(\mathrm{m})}_{AB} = -\frac{2}{\sqrt{D}\alpha^{4}} \Im\left\{\left[(i\omega r^{2} - M)\frac{d}{dr_{*}} {}_{-2}R_{lm} - [\tfrac{1}{2}\mu^{2}\alpha^{2} - i\omega(-3r + 7M) - r^{2}\omega^{2}]_{-2}R_{lm}\right] X^{lm}_{AB} e^{-i\omega t}\right\}\,. \tag{6.90b}$$

Because they have the same radial dependence as the electric-parity metric, the magnetic-parity peturbations will also be well-behaved on the future event horizon.

The major difference between the RWZ formalism's magnetic-parity metric and the IR gauge metric is that in IR gauge, the transverse-traceless metric perturbation is no longer required to be zero.

6.9.3.3 Tidal and frame-drag fields of the (2,2) mode

In this part, we calculate the tidal and frame-drag fields for a $(2,2)$ mode in IR gauge of both electric and magnetic parities. We find an interesting near duality between the tidal and frame-drag fields of opposite-parity peturbations that we noted in Secs. 6.1.3.3, 6.3.2.3 and 6.3.3.2.

We compute the tidal and frame-drag fields from the metric by evaluating the components of the Weyl tensor and its dual in the tetrad (6.8) including the perturbative corrections to the tetrad (6.11a)–(6.11d). We find that for an electric-parity mode, the tidal and frame-drag fields can be written as

$$\mathcal{E}^{(1,\mathrm{e})}_{\hat{r}\hat{r}} = 2\Re[E_{\mathrm{I(e)}}(r)Y^{22}e^{-i\omega t}]\,, \tag{6.91a}$$

$$\mathcal{E}^{(1,\mathrm{e})}_{\hat{r}\hat{A}} = 2\Re[E_{\mathrm{II(e)}}(r)Y^{22}_{\hat{A}}e^{-i\omega t}]\,, \tag{6.91b}$$

$$\mathcal{E}^{(1,\mathrm{e})}_{\hat{A}\hat{B}} = 2\Re\left[\left(-\frac{1}{2}E_{\mathrm{I(e)}}(r)\delta_{\hat{A}\hat{B}}Y^{22} + E_{\mathrm{III(e)}}(r)Y^{22}_{\hat{A}\hat{B}}\right)e^{-i\omega t}\right]\,, \tag{6.91c}$$

$$\mathcal{B}^{(1,\mathrm{e})}_{\hat{r}\hat{r}} = 0\,, \tag{6.91d}$$

$$\mathcal{B}^{(1,\mathrm{e})}_{\hat{r}\hat{A}} = 2\Re[B_{\mathrm{I(e)}}(r)X^{22}_{\hat{A}}e^{-i\omega t}]\,, \tag{6.91e}$$

$$\mathcal{B}^{(1,\mathrm{e})}_{\hat{A}\hat{B}} = 2\Re[B_{\mathrm{II(e)}}(r)X^{22}_{\hat{A}\hat{B}}e^{-i\omega t}]\,. \tag{6.91f}$$

The symbol $\delta_{\hat{A}\hat{B}}$ is the Kronecker delta function, and the traceless property of $\mathcal{E}$ requires that the radial function in front of the Kronecker delta must be minus one-half that of $\mathcal{E}^{(1)}_{\hat{r}\hat{r}}$ [i.e., $-(1/2)E_{I(\mathrm{e})}(r)$].

For the magnetic-parity perturbation, the frame-drag and tidal fields are

$$\mathcal{B}^{(1,\mathrm{m})}_{\hat{r}\hat{r}} = 2\Re[B_{\mathrm{I(m)}}(r)Y^{22}e^{-i\omega t}]\,, \tag{6.92a}$$

$$\mathcal{B}^{(1,\mathrm{m})}_{\hat{r}\hat{A}} = 2\Re[B_{\mathrm{II(m)}}(r)Y^{22}_{\hat{A}}e^{-i\omega t}]\,, \tag{6.92b}$$

$$\mathcal{B}^{(1,\mathrm{m})}_{\hat{A}\hat{B}} = 2\Re\big[\big(-\frac{1}{2}B_{\mathrm{I(m)}}(r)\delta_{\hat{A}\hat{B}}Y^{22} + B_{\mathrm{III(m)}}(r)Y^{22}_{\hat{A}\hat{B}}\big)e^{-i\omega t}\big]\,, \tag{6.92c}$$

$$\mathcal{E}^{(1,\mathrm{m})}_{\hat{r}\hat{r}} = 0\,, \tag{6.92d}$$

$$\mathcal{E}^{(1,\mathrm{m})}_{\hat{r}\hat{A}} = 2\Re[E_{\mathrm{I(m)}}(r)X^{22}_{\hat{A}}e^{-i\omega t}]\,, \tag{6.92e}$$

$$\mathcal{E}^{(1,\mathrm{m})}_{\hat{A}\hat{B}} = 2\Re[E_{\mathrm{II(m)}}(r)X^{22}_{\hat{A}\hat{B}}e^{-i\omega t}]\,. \tag{6.92f}$$

Interestingly, the radial functions of the tidal and frame-drag fields of the opposite-parity per-

turbations are nearly identical

$$B_{\mathrm{I(m)}}(r) = iE_{\mathrm{I(e)}}(r) \tag{6.93a}$$

$$B_{\mathrm{II(m)}}(r) = iE_{\mathrm{II(e)}}(r) - i\frac{M\sqrt{3(r+2M)}}{r^5\alpha^4\sqrt{2r}}\left[-(2\alpha^2+i\omega r){}_{-2}R_{22} + r\frac{d}{dr_*}{}_{-2}R_{22}\right], \tag{6.93b}$$

$$B_{\mathrm{III(m)}}(r) = iE_{\mathrm{III(e)}}(r) + \frac{\sqrt{3}(r+2M)}{r^5\alpha^4\sqrt{2}}M\omega\,{}_{-2}R_{22}\,, \tag{6.93c}$$

$$E_{\mathrm{I(m)}}(r) = -iB_{\mathrm{I(e)}}(r) + i\frac{M\sqrt{3(r+2M)}}{r^5\alpha^4\sqrt{2r}}\left[-(2\alpha^2+i\omega r){}_{-2}R_{22} + r\frac{d}{dr_*}{}_{-2}R_{22}\right], \tag{6.93d}$$

$$E_{\mathrm{II(m)}}(r) = -iB_{\mathrm{II(e)}}(r) - \frac{\sqrt{3}(r+2M)}{r^5\alpha^4\sqrt{2}}M\omega\,{}_{-2}R_{22}\,. \tag{6.93e}$$

In fact, there is an exact duality of the radial-radial components, which implies that the horizon vorticity of a magnetic-parity perturbation is the same as the horizon tendicity of an electric-parity perturbation. For completeness, we list the expressions for the radial functions for the electric-parity perturbations, which are lengthy, but will be needed in the next appendix.

$$E_{\mathrm{I(e)}}(r) = -\frac{2\sqrt{6}}{r^6\alpha^4}\left\{r^2(r-3M+i\omega r^2)\frac{d}{dr_*}{}_{-2}R_{22} + [-5r^2+16Mr-12M^2-i\omega r^2(4r-9M)+r^4\omega^2]{}_{-2}R_{22}\right\}, \tag{6.94a}$$

$$\begin{aligned}E_{\mathrm{II(e)}}(r) = \frac{1}{r^6\sqrt{6r(r+2M)}\alpha^4}\Big\{&r^2[3r^2+6M^2+i\omega r^2(r-3M)+r^4\omega^2]\frac{d}{dr_*}{}_{-2}R_{22}\\ &+[(-9r^3+18Mr^2-12M^2r+24M^3)-i\omega r^2(8r^2-16Mr+18M^2)+2\omega^2r^4(4r-9M)\\ &+ir^6\omega^3]{}_{-2}R_{22}\Big\},\end{aligned} \tag{6.94b}$$

$$\begin{aligned}E_{\mathrm{III(e)}}(r) = \frac{1}{r^5(r+2M)\alpha^4\sqrt{6}}\Big\{&ir^2\omega(-2r^2+3Mr+3M^2+r^4\omega^2)\frac{d}{dr_*}{}_{-2}R_{22}+[6(r^2+4M^2)\\ &+i\omega(4r^3-11Mr^2+12M^2r+12M^3)-\omega^2r^2(4r^2-4Mr-9M^2)-3i\omega^3r^5\alpha^2+r^6\omega^4]{}_{-2}R_{22}\Big\},\end{aligned} \tag{6.94c}$$

$$\begin{aligned}B_{\mathrm{I(e)}}(r) = \frac{\sqrt{2}}{r^5\sqrt{3r(r+2M)}\alpha^4}\Big\{&r^2[9M-i\omega r(r-3M)+r^3\omega^2]\frac{d}{dr_*}{}_{-2}R_{22}\\ &+[-24Mr\alpha^2+i\omega r(12M^2-25Mr+5r^2)-\omega^2r^3(4r-9M)-ir^5\omega^3]{}_{-2}R_{22}\Big\},\end{aligned} \tag{6.94d}$$

$$\begin{aligned}B_{\mathrm{II(e)}}(r) = \frac{1}{r^4(r+2M)\alpha^4\sqrt{6}}\Big\{&i\omega r(-2r^2+3Mr+3M^2+r^4\omega^2)\frac{d}{dr_*}{}_{-2}R_{22}\\ &+[-24M+2i\omega r(2r-7M)+\omega^2r(-4r^2+4Mr+9M^2)-3i\omega^3r^4\alpha^2+r^5\omega^4]{}_{-2}R_{22}\Big\}.\end{aligned} \tag{6.94e}$$

From these expressions, it is clear that the tidal and frame drag-fields are regular on the horizon,

because, as noted above ${}_{-2}R_{lm}$ and $d_{-2}R_{lm}/dr_*$ scale as $\alpha^4 e^{-i\omega r_*}$ near the horizon; consequently, they will cancel the corresponding powers of α in the denominators of these functions.

6.9.4 Analytical and numerical methods for computing metric perturbations and tidal and frame-drag fields in IR gauge

The procedures for calculating the metric perturbations and their tidal and frame-drag fields are identical for Schwazschild and Kerr black holes; however, because the analytical expressions for the Newman-Penrose quantities, the angular Teukolsky function, and the metric derived from these mathematical objects are significantly simpler for Schwarzschild black holes, the amount of work we can perform analytically differs for rotating and non-rotating black holes. Even for Schwarzschild black holes, however, we will not be able to compute all aspects of the metric perturbation analytically. We calculate the the least-damped $l = 2$, $m = 2$ quasinormal-mode frequencies for both Schwarzschild and Kerr black holes using the Mathematica notebook associated with [13], an implementation of Leaver's method [14]. Similarly, we compute the radial Teukolsky functions ${}_{-2}R_{lm\omega}$ corresponding to a quasinormal-mode solution for both Schwarzschild and Kerr black holes numerically. We compute it in two ways, which give comparable results: we solve the boundary-value problem for a quasinormal mode solution to the radial Teukolsky equation, Eq. (6.59), using a shooting method, and we compare the result with a series solution given by Leaver [14] (as is also done in the notebook of [13]). For Kerr black holes, the numerical solution requires the angular eigenvalue, ${}_sA_{lm}$ associated with the quasinormal mode frequency, which we again compute from the implementation of Leaver's method in [13].

The most significant difference between the calculations of quasinormal modes of Schwarzschild and Kerr black holes arises from differences in the Teukolsky angular function, and the angular operators used in computing the metric (6.65). First, the spin-weighted spheroidal harmonics in the expression for the Hertz potential, Eq. (6.82), reduce to spin-weighted spherical harmonics for Schwarzschild black holes. Second, the angular operators in Eq. (6.65) reduce to spin-weight lowering operators, in the non-spinning limit. As a result, the metric perturbation can be expressed, analytically, in terms of electric- or magnetic-parity scalar, vector, and tensor spherical harmonics of a single l, for Schwarzschild black holes. For perturbations of Kerr black holes, there are not these additional simplifications. First, we must calculate the spin-weighted spheroidal harmonics numerically, which we do using a series solution put forward by Leaver [14] (the same method as that implemented in [13]). Second, the angular operators are no longer the spin-weight lowering operators. The metric perturbation computed from these functions, therefore, is not nearly as simple as that of the Schwarzschild limit. In fact, for our calculations with spinning black holes, we find it easier to work with a numerical fit to the analytical expression for the metric.

Once we calculate the metric perturbation, we construct the perturbation to the Weyl tensor in the same way for both rotating and non-rotating black holes. We can then calculate the tetrad components of the tidal field, $\mathcal{E}_{\hat{a}\hat{b}}$, and frame-drag field, $\mathcal{B}_{\hat{a}\hat{b}}$, using the background tetrad in Eq. (6.8 for Schwarzschild holes or Eq. (6.9a) for Kerr holes and its perturbative corrections in Eqs. (6.11a)–(6.11d). From these fields, we can solve the eigenvalue problem and compute tendex and vortex lines, and their corresponding tendicities and vorticities.

6.10 Appendix: Relationship Between Regge-Wheeler-Zerilli and Ingoing-Radiation Gauges

In this appendix, we construct generators of infinitesimal coordinate transformations between RWZ and IR gauges, for both magnetic- and electric-parity perturbations of Schwarzschild black holes.

6.10.1 Magnetic-parity gauge transformation

In this part, we compute the gauge-change generator that transforms the magnetic-parity metric in IR gauge to the same metric in Regge-Wheeler gauge. We show, as noted in Sec. 6.2.3, that this infinitesimal magnetic-parity coordinate transformations does not change the time function that specifies the slicing (into surfaces of constant $\tilde{t}$). In addition, perturbative changes of the spatial coordinates will not alter the coordinate (or tetrad) components of the frame-drag field; therefore, the fields in both gauges will be equal.

The calculation that shows these facts is relatively straightforward. Regge and Wheeler showed in Eq. (17) of [27] that, beginning in any gauge, it is possible to remove the transverse-traceless part of the magnetic-parity metric perturbation [Eq. (6.87c) in the notation used in Appendix 6.9.3] by an infinitesimal coordinate transformation of the form

$$\vec{\xi}^{(\mathrm{m})} = -\frac{1}{2}\sum_{lm} h_2^{lm}(0, 0, \mathbf{X}^{lm})\,, \tag{6.95}$$

where $\mathbf{X}^{lm}$ is a magnetic-parity, vector spherical harmonic. This follows from the fact that the perturbation to the metric transforms under this change of coordinates by

$$h_{\mu\nu} \to h_{\mu\nu} + 2\xi_{(\mu|\nu)}\,, \tag{6.96}$$

(where $|$ denotes a covariant derivative with respect to the background metric, and parenthesis around the indices means the expression is symmetrized) and from the definition of the magnetic-parity, transverse-traceless tensor harmonics (6.88b). The result can also be found from Eqs. (5.5) and (5.6) of [42].

For a multipolar perturbation with indices (l,m) in IR gauge, the function $-\frac{1}{2}\sum_{lm} h_2^{lm}/2$ is given by the radial function in Eq. (6.90b) multiplied by $e^{-i\omega t}$, and the full coordinate transformation vector is therefore

$$\xi_t^{(\mathrm{m})} = \xi_r^{(\mathrm{m})} = 0\,, \tag{6.97a}$$

$$\xi_A^{(\mathrm{m})} = \frac{1}{\sqrt{D}\alpha^4}\Im\left\{\left[(i\omega r^2 - M)\frac{d}{dr_*}{}_{-2}R_{lm} - [\tfrac{1}{2}\mu^2\alpha^2 - i\omega(-3r+7M) - r^2\omega^2]_{-2}R_{lm}\right]X_A^{lm}e^{-i\omega t}\right\}. \tag{6.97b}$$

A short calculation can verify that h_{tA} and h_{rA} are the only nonzero components of the metric after this transformation (the same as in RWZ gauge) and they are given by

$$h_{tA} = \Im\left\{\frac{1}{\sqrt{l(l+1)D}r\alpha^4}\left[[-\tfrac{1}{2}\mu^2 r\alpha^2 + (iM\omega + r^2\omega^2)]\frac{d}{dr_*}{}_{-2}R_{lm} + [\alpha^2(\alpha^2 + i\omega r) - \omega^2 r(3r-7M) - i\omega^3 r^3]_{-2}R_{lm}\right]X_A^{lm}e^{-i\omega t}\right\}, \tag{6.98a}$$

$$h_{rA} = \Im\left\{\frac{-i\omega}{\sqrt{l(l+1)D}\alpha^6}\left[(r - 3M + i\omega r^2)\frac{d}{dr_*}{}_{-2}R_{lm} + [-\alpha^2(\tfrac{1}{2}\mu^2 + 3\alpha^2) - i\omega(4r-9M) + \omega^2 r^2]_{-2}R_{lm}\right]X_A^{lm}e^{-i\omega t}\right\}. \tag{6.98b}$$

It is not immediately apparent, however, that this gauge is RWZ gauge, because it is expressed in terms of the radial function of ψ_{-2}, $({}_{-2}R_{lm})$, rather than the Regge-Wheeler function Q.

To show that this transformation did bring the metric into Regge-Wheeler gauge, it is necessary to use the relationship between Q and ${}_{-2}R_{lm}$ given in, e.g., Eq. (319) of Ch. 4 of [30][6]

$$Q = \frac{-2i\omega}{r\alpha^4(D - 12iM\omega)}\left\{(r - 3M + i\omega r^2)\frac{d}{dr_*}{}_{-2}R_{lm} + [-\alpha^2(\tfrac{1}{2}\mu^2 + 3\alpha^2) - i\omega(4r-9M) + r^2\omega^2]_{-2}R_{lm}\right\}. \tag{6.99}$$

After substituting this relationship into Eqs. (6.32) and (6.30) and taking its imaginary part—so that the RWZ metric is real and is expressed in terms of ${}_{-2}R_{lm}$—it becomes apparent that the transformation brings the IR gauge metric into RWZ gauge.

Because the gauge change from IR to RWZ is generated by a strictly spatial $\vec{\xi}^{(\mathrm{m})}$ and because $\boldsymbol{\mathcal{B}}$ is a strictly first-order quantity for perturbations of Schwarzschild holes, the frame-drag analog

[6] Aside from several differences in notation (the radial function used by Chandrasekhar, $Z^{(-)}$, is related to the Regge-Wheeler function by $Q = i\omega Z^{(-)}$, and his radial function for the Teukolsky equation, Y_{-2} is related to that of this paper by ${}_{-2}R_{lm} = r^3 Y_{-2}$), there is one additional subtle point about using this equation. This equation is expressed as a relationship between Y_{+2} (proportional to the radial function of Ψ_0) and $Z^{(-)}$. Because the time dependence of Ψ_0 is given by $e^{+i\sigma t}$ in [30], then the Y_{+2} there is equivalent to Y_{+2}^* of Ψ_0 with a time dependence given by $e^{-i\omega t}$. In addition, because Y_{-2} satisfies the same equation as Y_{+2}^*, then this equation is valid for Y_{-2} when σ is replaced by ω.

of Eq. (6.19) guarantees that the frame-drag field must be identically the same in the two gauges:

$$\mathcal{B}^{\rm IRG}_{\hat{i}\hat{j}} = \mathcal{B}^{\rm RW}_{\hat{i}\hat{j}} \,. \tag{6.100}$$

This can be confirmed explicitly for the $(2,2)$ mode by substituting Eq. (6.99) into the tetrad components of the RWZ frame-drag field in Eqs. (6.40a)–(6.40f) and finding that they are identical to the IR gauge frame-drag field of Eqs. (6.92), (6.93), and (6.94).

When thought of as abstract tensors without reference to any coordinate system, it is also the case that the tidal fields are equal,

$$\boldsymbol{\mathcal{E}}^{\rm IRG} = \boldsymbol{\mathcal{E}}^{\rm RW} \,. \tag{6.101}$$

Because there is a background tidal field, perturbative differences in the coordinates enter into the components of the tidal field and the components are no longer equal; see Eq. (6.19). Therefore, visualizations of the tendex lines or tendicity in the two coordinate systems (when the coordinates are drawn as though they were flat) look different.

6.10.2 Electric-parity gauge transformation

In this part, we construct an infinitesimal generator of an electric-parity coordinate transformation that brings the electric-parity IR gauge to RWZ gauge. The transformation changes the time function (and hence how we define the slicing) in addition to the spatial coordinates. This implies that neither the frame-drag fields nor the coordinate components of the tidal field will equal in the two gauges (but the tidal field written without coordinates will be); see Eqs. (6.18) and (6.19), respectively.

The gauge-change generator that connects the two gauges is somewhat more complex for the electric-parity perturbations than it was for the magnetic-parity ones. The transformation can be found by using Eq. (19) of [27] or Eqs. (4.6)–(4.9) of [42]. The general approach to find the transformation is to use $\xi^{(\rm e)}_A$ to remove the transverse-traceless part of the IRG metric, and then use $\xi^{(\rm e)}_t$ and $\xi^{(\rm e)}_r$ to annul the transverse metric coefficients. After a short calculation, it is possible

to express the generator as

$$\xi_t^{(\mathrm{e})} = \frac{1}{2\mu^2 r^2\alpha^4}\Re\Big\{\Big[-r^2[\mu^3\alpha^2 - 4i\omega(M-r^2\omega)]\frac{d}{dr_*}{}_{-2}R_{lm} + [\mu^3 r\alpha^4 + i\omega r^2\mu^2\alpha^2(\mu-2) - 4rM\omega^2 r^2(3r-7M) - 4i\omega^3 r^4]_{-2}R_{lm}\Big]Y^{lm}e^{-i\omega t}\Big\} \tag{6.102a}$$

$$\xi_r^{(\mathrm{e})} = \frac{1}{2\mu^2 r^3\alpha^6}\Re\Big\{\Big[r^3[\alpha^2\mu^2(\mu+2) + 4i\omega(r-3M) - 4r^2\omega^2]\frac{d}{dr_*}{}_{-2}R_{lm} + \{-r\mu^2\alpha^2(\mu+2)(2r\alpha^2 + ir^2\omega) - 2r^2(\mu+2) - 2i\omega r[(\mu^2+\mu-2)r^2 + 2Mr(\mu-8) + 24M^2] + 4\omega^2 r^3(4r-9M) + 4i\omega^3 r^5\}_{-2}R_{lm}\Big]Y^{lm}e^{-i\omega t}\Big\} \tag{6.102b}$$

$$\xi_A^{(\mathrm{e})} = \frac{-1}{\sqrt{D}\alpha^4}\Re\Big\{\Big[(i\omega r^2 - M)\frac{d}{dr_*}{}_{-2}R_{lm} - [\tfrac{1}{2}\mu^2\alpha^2 - i\omega(-3r+7M) - r^2\omega^2]_{-2}R_{lm}\Big]Y^{lm}_A e^{-i\omega t}\Big\}, \tag{6.102c}$$

where we used Eq. (6.59) to reduce second-order radial derivatives to first-order ones.

To confirm that this gauge-change generator does bring the IR-gauge metric to the RWZ metric, we again use the relation between the Zerilli function and the radial Teukolsky function encoded in Eq. (319) of Ch. 4 of [30]:

$$Z = \frac{1}{r^2\alpha^4(D+12iM\omega)(\mu^2 r+6M)}\Big\{2r[i\omega r^2(\mu^2 r+6M) + (\mu^2 r^2 - 3\mu^2 Mr - 6M^2)]\frac{d}{dr_*}{}_{-2}R_{lm} + \{\alpha^2(\mu^2 r+6M)^2 + 2(3\alpha^2 + i\omega r)[\mu^2 r^2 - 3\mu^2 Mr - 6M^2 + i\omega r^2(\mu^2 r+6M)]\}_{-2}R_{lm}\Big\}. \tag{6.103}$$

This allows us to confirm that the IR metric was brought to RWZ gauge through the transformation vector $\vec{\xi}^{(\mathrm{e})}$.

With this expression, we can also compare the frame-drag fields in the two gauges for the $(2,2)$ mode. By expressing the radial functions for the frame-drag field of a $(2,2)$, electric-parity mode in RWZ gauge [$B_{1(\mathrm{e})}(r)$ and $B_{2(\mathrm{e})}(r)$ of Eqs. (6.42d) and (6.42e)] in terms of the radial Teukolsky function ${}_{-2}R_{22}$, we find

$$B_{1(\mathrm{e})}(r) = B_{\mathrm{I}(\mathrm{e})}(r) + \frac{\sqrt{3}}{2r^5\alpha^4\sqrt{2r(r+2M)}}\Big\{[-4r\alpha^2 - 2i\omega(2r^2 - 5Mr + 6M^2) + 3r^2\omega^2(r-3M) + ir^4\omega^3]_{-2}R_{22} - r^2\alpha^2(r^2\omega^2 + 3iM\omega - 2)\frac{d}{dr_*}{}_{-2}R_{22}\Big\}, \tag{6.104a}$$

$$B_{2(\mathrm{e})}(r) = B_{\mathrm{II}(\mathrm{e})}(r)\,, \tag{6.104b}$$

where $B_{\mathrm{I(e)}}(r)$ and $B_{\mathrm{II(e)}}(r)$ are the equivalent radial functions of the IR-gauge frame-drag field in Eqs. (6.94). Because the functions $B_{1\mathrm{(e)}}(r)$ and $B_{\mathrm{I(e)}}(r)$ determine the radial dependence of the transverse part of the frame-drag field (and $B_{2\mathrm{(e)}}(r)$ and $B_{\mathrm{II(e)}}(r)$ do the same for the transverse-traceless part), we see a particular illustration of the result of Eq. (6.18) of Sec. 6.2.3.2: namely, a change in slicing from an electric-parity gauge change will induce a change in the longitudinal-transverse components of the frame-drag field (but not the longitudinal or transverse-traceless parts).

6.11 Appendix: Horizon Tendicity and Vorticity Calculated from the Weyl Scalar Ψ_0

In this appendix, we modify a calculation by Hartle [6] to compute the horizon tendicity and vorticity by applying differential operators of the background spacetime to a perturbation of $\Psi_0 \equiv \psi_2$ (where ψ_2 satisfies Teukolsky's equation; see Appendix 6.8). Using this result, we derive the duality between the horizon vorticity and tendicity of opposite-parity perturbation mentioned in Sec. 6.3.1, for both Schwarzschild and Kerr black holes. We also relate the horizon quantities to the complex curvature and show that they are proportional for Schwarzschild holes and differ only by the product of spin coefficients $\lambda^{(0)}\sigma^{(1)}$ for Kerr holes. This proves these claims made in Sec. 6.1.2.

6.11.1 Constructing a hypersurface-orthogonal tetrad on the horizon

As in Hartle's calculation, we must work in a NP tetrad in which the null vector $\vec{l}$ is tangent to the horizon, $\vec{n}$ is normal to the horizon, and $\vec{m}$ and its complex conjugate lie in the instantaneous horizon (constant $v = \tilde{t} + r$ for Hartle, though we will use constant $\tilde{t}$). This NP tetrad must also satisfy additional constraints

$$\vec{u} = \frac{1}{\sqrt{2}}(\vec{l} + \vec{n}) \tag{6.105a}$$

$$\vec{N} = \frac{1}{\sqrt{2}}(\vec{l} - \vec{n}) \tag{6.105b}$$

$$\vec{m} = \frac{1}{\sqrt{2}}(\vec{e}_2 + i\vec{e}_3) \tag{6.105c}$$

[with the associated non-null tetrad given by Eqs. (6.9a) and (6.11)], which ensure that the slicing vector $\vec{u}$ associated with this NP tetrad is hypersurface-orthogonal on the horizon and the spatial basis vectors are tied to our coordinate system in the desired way.

To describe the unperturbed NP tetrad, it is useful to first construct Hartle's tetrad, which can be obtained from Kinnersley's tetrad (6.55), by a boost followed by a null rotation about $\vec{l}$ (also

called class III and I transformations, respectively):

$$\vec{l}_{\rm H} = \frac{\Delta}{2(r^2+a^2)}\vec{l}_{\rm K}\,, \tag{6.106a}$$

$$\vec{m}_{\rm H} = \vec{m}_{\rm K} - \frac{ia\sin\theta}{\sqrt{2}(r+ia\cos\theta)}\vec{l}_{\rm H}\,, \tag{6.106b}$$

$$\vec{n}_{\rm H} = \frac{2(r^2+a^2)}{\Delta}\vec{n}_{\rm K} + \frac{ia\sin\theta}{\sqrt{2}(r+ia\cos\theta)}\vec{m}_{\rm K} - \frac{ia\sin\theta}{\sqrt{2}(r+ia\cos\theta)}\vec{m}^*_{\rm K} + \frac{a^2\sin^2\theta}{2\Sigma}\vec{l}_{\rm H}\,. \tag{6.106c}$$

The quantites Δ and Σ are defined in Eq. (6.56). Then, we can construct an unperturbed tetrad from Hartle's tetrad using the following spin-boost transformation (also called class III):

$$\vec{l}_{(0)} = N_l\vec{l}_{\rm H}\,, \quad \vec{m}_{(0)} = e^{i\Theta}\vec{m}_{\rm H}\,, \quad \vec{n}_{(0)} = N_l^{-1}\vec{n}_{\rm H}\,, \tag{6.107a}$$

where

$$N_l = \sqrt{\frac{\Sigma+2Mr}{2\Sigma}}\,, \quad e^{i\Theta} = \frac{r+ia\cos\theta}{\sqrt{\Sigma}}\,. \tag{6.107b}$$

One can verify that the resulting orthonormal tetrad

$$\vec{u}^{\,(0)} = \frac{1}{\sqrt{2}}(\vec{l}_{(0)} + \vec{n}_{(0)})\,, \tag{6.108a}$$

$$\vec{N}^{\,(0)} \equiv \vec{e}^{\,(0)}_{\hat{r}} = \frac{1}{\sqrt{2}}(\vec{l}_{(0)} - \vec{n}_{(0)})\,, \tag{6.108b}$$

$$\vec{e}^{\,(0)}_{\hat{\theta}} = \frac{1}{\sqrt{2}}(\vec{m}_{(0)} + \vec{m}^*_{(0)})\,, \tag{6.108c}$$

$$\vec{e}^{\,(0)}_{\hat{\theta}} = \frac{1}{i\sqrt{2}}(\vec{m}_{(0)} - \vec{m}^*_{(0)})\,, \tag{6.108d}$$

is exactly the ingoing-Kerr tetrad (6.9a), when evaluated on the horizon, though away from the horizon it is not.

For the NP null tetrad to correspond, on the horizon, to the hypersurface-orthogonal $\{\vec{u}, \vec{e}_{\hat{r}}, \vec{e}_{\hat{\theta}}, \vec{e}_{\hat{\phi}}\}$ of Eqs. (6.9a) and (6.11) via Eqs. (6.105), we must choose the perturbative corrections to the tetrad to satisfy

$$\vec{l}_{(1)} = \frac{1}{2\sqrt{2}}[(h_{\hat{0}\hat{0}}\vec{u}_{(0)} - h_{\hat{r}\hat{r}}\vec{e}^{\,(0)}_{\hat{r}}) - 2h_{\hat{0}\hat{i}}\vec{e}^{\,\hat{i}}_{(0)} - 2h_{\hat{r}\hat{A}}\vec{e}^{\,\hat{A}}_{(0)}]\,, \tag{6.109a}$$

$$\vec{n}_{(1)} = \frac{1}{2\sqrt{2}}[(h_{\hat{0}\hat{0}}\vec{u}_{(0)} + h_{\hat{r}\hat{r}}\vec{e}^{\,(0)}_{\hat{r}}) - 2h_{\hat{0}\hat{i}}\vec{e}^{\,\hat{i}}_{(0)} + 2h_{\hat{r}\hat{A}}\vec{e}^{\,\hat{A}}_{(0)}]\,, \tag{6.109b}$$

$$\vec{m}_{(1)} = -\frac{1}{2\sqrt{2}}[(h_{\hat{\theta}\hat{\theta}}\vec{e}^{\,(0)}_{\hat{\theta}} + ih_{\hat{\phi}\hat{\phi}}\vec{e}^{\,(0)}_{\hat{\phi}}) + 2h_{\hat{\theta}\hat{\phi}}\vec{e}^{\,(0)}_{\hat{\phi}}]\,. \tag{6.109c}$$

Because $\vec{e}_{\hat{r}}$ is normal to surfaces of constant r in slices of constant $\tilde{t}$ through perturbative order, we will need to choose our gauge so that the coordinate position of the horizon does not move from the constant value $r = r_+$. Although Poisson [44] has shown that there are a wide class of gauges that

satisfy this property (horizon-locking gauges), for our calculation, we find it convenient to work in an ingoing radiation gauge based on the unperturbed tetrad vector $\vec{l}_{(0)}$,

$$h_{\mu\nu} l^{\nu}_{(0)} = 0\,, \quad g^{\mu\nu} h_{\mu\nu} = 0\,. \tag{6.110}$$

On the horizon, these gauge conditions imply that

$$h_{\hat{0}\hat{0}} = h_{\hat{r}\hat{r}} = -h_{\hat{0}\hat{r}}\,, \tag{6.111a}$$

and that the null vector $\vec{l}$ undergoes a perturbative boost,

$$\vec{l}_{(1)} = \frac{1}{2} h_{\hat{0}\hat{0}} \vec{l}_{(0)}\,. \tag{6.111b}$$

[To derive this, one should split $-2h_{\hat{0}\hat{i}}\vec{e}^{\,\hat{i}}_{(0)}$ into a sum of two terms $-2(h_{\hat{0}\hat{r}}\vec{e}^{\,\hat{r}}_{(0)} + h_{\hat{0}\hat{A}}\vec{e}^{\,\hat{A}}_{(0)})$ and use the relation in Eq. (6.105).] In addition to keeping the horizon at a constant coordinate position $r = r_+$ (see [44]), using this gauge condition allows us to calculate the perturbation to Ψ_2 in a much simpler way, as we describe in the next subsection.

6.11.2 Computing the horizon tendicity and vorticity from Ψ_0

Although the explicit expressions for spin coefficients in this tetrad are somewhat lengthy (and, as a result, we do not give them here), through a direct calculation we can verify that on the horizon

$$\rho_{(0)} = \sigma_{(0)} = \kappa_{(0)} = 0\,, \quad \epsilon_{(0)} \in \mathbb{R}\,. \tag{6.112a}$$

Moreover, because in this ingoing radiation gauge the perturbation to the vector $\vec{l}$ can be obtained by applying a boost (Class III) transformation to the tetrad, the perturbed value of κ will also vanish,

$$\kappa_{(1)} = 0\,. \tag{6.112b}$$

From Eq. (310a) of Ch. 1 of [30] (which describes the components of the Riemann tensor in the Newman-Penrose formalism), we see that the perturbation to the spin-coefficient ρ satisfies an equation

$$\mathbf{D}_{(0)}\rho_{(1)} = 2\epsilon_{(0)}\rho_{(1)}\,,$$

where $\epsilon_{(0)} > 0$. If $\rho_{(1)}$ is not zero, then the separated solution to this equation, $\rho_{(1)} = f(r,\theta)e^{-i(\omega\tilde{t} - m\tilde{\phi})}$, implies the constraint that $2\epsilon_{(0)} + iN_l(\omega - m\omega_+) = 0$ [here $\omega_+ = a/(2Mr_+)$ is the horizon angular velocity]. This condition is not satisfied for constant frequencies ω, so the perturbation to the spin

coefficient must vanish:

$$\rho_{(1)} = 0\,. \tag{6.112c}$$

From these conditions on the spin coefficients, and the fact that $\Psi_0^{(0)} = \Psi_1^{(0)} = 0$, we can write the Bianchi identities (see, e.g., Eqs. (321a) and (321b) of Ch. 1 of [30]) as

$$(\mathbf{D} - 2\epsilon)\Psi_1 = (\boldsymbol{\delta}^* + \pi - 4\alpha)\Psi_0\,, \tag{6.113a}$$

$$\mathbf{D}\Psi_2^{(1)} = (\boldsymbol{\delta}^* + 2\pi - 2\alpha)\Psi_1\,, \tag{6.113b}$$

where we have dropped the superscripts indicating perturbative orders on all differential operators and spin coeffients (because they are all background quantities) and the Weyl scalars Ψ_0 and Ψ_1 (because they are strictly perturbative quantities). Note that we do not need the term of the form $\mathbf{D}_{(1)}\Psi_2^{(0)}$, because on the horizon the differential operator $\mathbf{D}_{(1)}$ contains only time and azimuthal-angle derivatives, but the background Weyl scalar $\Psi_2^{(0)}$ is only a function of r and θ.

By applying the differential operator $(\mathbf{D} - 2\epsilon)$ to the second Bianchi identity and using the identity (valid on the horizon) that $\boldsymbol{\delta}^*\mathbf{D} - \mathbf{D}\boldsymbol{\delta}^* = (\alpha + \beta^* - \pi)\mathbf{D}$, we find that

$$(\mathbf{D} - 2\epsilon)\mathbf{D}\Psi_2^{(1)} = [\boldsymbol{\delta}^* + 3(\pi - \alpha) - \beta^*)](\boldsymbol{\delta}^* + \pi - 4\alpha)\Psi_0 - (\mathbf{D} - 2\epsilon)(\lambda\Psi_0)\,, \tag{6.114}$$

Using Geroch-Held-Penrose [45] notation, and the equation for a component of the Riemann tensor (Eq. (310g) of Ch. 1 of [30]) restricted to the horizon

$$\mathbf{D}\lambda - \boldsymbol{\delta}^*\pi = -2\epsilon\lambda + \pi(\pi + \alpha - \beta^*)\,, \tag{6.115}$$

we find that

$$\text{þ}\text{þ}\Psi_2^{(1)} = (\eth'\eth' + 4\pi\eth' + 2\pi^2 - \lambda\text{þ})\Psi_0\,. \tag{6.116}$$

Note that the Ψ_0 here is related to that which satisfies Teukolsky's equation in the Kinnersley tetrad by

$$\Psi_0 = \frac{N_l^2 e^{2i\Theta}\Delta^2}{(r^2+a^2)^2}\Psi_0^{\rm K} \equiv A\Psi_0^{\rm K}\,. \tag{6.117}$$

Starting from a modal solution for the Kinnersley Ψ_0 (denoted by $\Psi_{0\,lm\omega}^{\rm K}$), then we see that the corresponding perturbation to Ψ_2 is given by

$$\Psi_{2\,lm\omega}^{(1)} = \frac{\eth'\eth' + 4\pi\eth' + 2\pi^2 + \lambda(iN_l\Omega + 4\epsilon)}{N_l\Omega(2i\epsilon - N_l\Omega)}(A\Psi_{0\,lm\omega}^{\rm K})\,, \tag{6.118}$$

where $\Omega = \omega - m\omega_+$, and where we have used the fact that $\mathbf{D} = N_l(\partial_{\tilde{t}} + \omega_+\partial_{\tilde{\phi}})$ on the horizon.

A Weyl scalar, Ψ_0 formed from the superposition of modes $\Psi_{0\,lm\omega}^{\rm K} \pm (-1)^m\Psi_{0\,l-m-\omega^*}^{\rm K}$, with radial functions that obey ${}_2R_{l-m-\omega^*} = \pm(-1)^m{}_2R_{lm\omega}^*$, transforms under parity as $\Psi_0 \to \pm(-1)^l\Psi_0^*$. The

perturbation of Ψ_2 formed from superimposing Eq. (6.118) for the individual modes of $\Psi_0^{\rm K}$ above also transforms under parity as $\Psi_2 \to \pm(-1)^l \Psi_2^*$. Using the relation $2\Psi_2 = \mathcal{E}_{NN} + i\mathcal{B}_{NN}$ and taking the real and imaginary parts of Ψ_2, it becomes clear that $\mathcal{E}_{NN}$ and $\mathcal{B}_{NN}$ have definite parity. Moreover, it is not difficult to see that $\mathcal{E}_{NN}$ of an electric-parity mode is equal to $i\mathcal{B}_{NN}$ of a magnetic-parity mode of $i\Psi^{\rm K}_{0\,lm\omega}$, and $\mathcal{E}_{NN}$ of a magnetic-parity mode is $-i\mathcal{B}_{NN}$ of an electric-parity mode of $i\Psi^{\rm K}_{0\,lm\omega}$.

This demonstrates a perfect duality between electric-parity modes and magnetic-parity modes, on the horizon of a Kerr black hole.

6.11.3 Relationship between Ψ_2 and the complex curvature

As a final part of this appendix, we discuss how the relationship between the complex curvature and Ψ_2,

$$\frac{1}{4}(\mathcal{R} + i\mathcal{X}) = -\Psi_2 + \mu\rho - \lambda\sigma\,, \tag{6.119}$$

simplifies for perturbations of Schwarzschild and Kerr black holes in the tetrad and gauge discussed in the sections of this appendix above. First, we note that the spin coefficient λ has as its unperturbed value on the horizon

$$\lambda_{(0)} = -\frac{Mr_+\omega_+^2 \sin^2\theta e^{-2i\Theta}}{N_l(r - ia\cos\theta)^3}[4Mr_+ + (r_+ - M)(r_+ - ia\cos\theta)]\,, \tag{6.120}$$

where we have made use of the fact that on the horizon $r_+^2 + a^2 = 2Mr_+$. For a Schwarzschild black hole, ω_+ vanishes, and, therefore, the background values of all four spin coefficients μ, ρ, λ, and σ all vanish. Through first-order in perturbation theory, therefore,

$$\mathcal{R} = -2\mathcal{E}_{NN}\,, \quad \mathcal{X} = -2\mathcal{B}_{NN}\,. \tag{6.121}$$

[We briefly digress here to note that for Schwarzschild black hole, the spin coefficient π also vanishes, and Eq. (6.116) reduces to

$$\text{þ}\text{þ}\Psi_2^{(1)} = \text{ð}'\text{ð}'\Psi_0\,. \tag{6.122}$$

For a modal solution, Eq. (6.118) also simplifies to

$$\Psi^{(1)}_{2\,lm\omega} = \frac{4M\sqrt{2D}\alpha^4}{\omega(i - 4M\omega\sqrt{2})}\,{}_2R_{lm}Y_{lm}e^{-i\omega t}\,, \tag{6.123}$$

where $\alpha^2 = 1 - 2M/r$, $D = (l+2)!/(l-2)!$, $\omega = \Omega$ (because $\omega_+ = 0$), and the radial function of ψ_2, ${}_2R_{lm}$, is evaluated at the horizon $r = 2M$. We have also used the fact that $\epsilon = 1/(8M)$ in this tetrad. Because the spin coefficients vanish in Eq. (6.119) for this perturbed Schwarzschild hole, the above expression is equivalent to minus one quarter of the complex curvature.]

For a Kerr black hole $\lambda_{(0)} \neq 0$, and we must compute the perturbation to σ. It satisfies the differential equation

$$(\mathbf{D} - 2\epsilon)\sigma_{(1)} = \Psi_0 \tag{6.124}$$

[Eq. (310b) of Ch. 1 of [30] specialized to our tetrad and gauge]. For a modal solution of $\sigma_{(1)}$, we can solve this to find

$$\sigma_{(1)} = -\frac{\Psi_0}{iN_l\Omega + 2\epsilon}\,, \tag{6.125}$$

which implies that the perturbation to σ does not vanish. Thus, for a Kerr black hole,

$$\frac{1}{4}(\mathcal{R}_{(1)} + i\mathcal{X}_{(1)}) = -\Psi_2^{(1)} - \lambda_{(0)}\sigma_{(1)}\,, \tag{6.126}$$

so the horizon tendicity and vorticity are no longer exactly equal the horizon's intrinsic and extrinsic scalar curvatures.

6.12 Appendix: Vortex and Tendex Lines of $(2,2)$ Perturbations of Schwarzschild and Kerr Black Holes with the Background Frame-Drag and Tidal Fields

In this appendix, we show the tendex and vortex lines of Schwarzschild and Kerr black holes when we plot a small $(2,2)$ perturbation of either electric or magnetic parity on top of the background tidal or frame-drag fields in Fig. 6.26. Specifically, we plot the vortex and tendex lines of

$$\boldsymbol{\mathcal{E}} = \boldsymbol{\mathcal{E}}^{(0)} + \epsilon\boldsymbol{\mathcal{E}}^{(1)}\,, \quad \boldsymbol{\mathcal{B}} = \boldsymbol{\mathcal{B}}^{(0)} + \epsilon\boldsymbol{\mathcal{B}}^{(1)}\,, \tag{6.127}$$

where $\boldsymbol{\mathcal{E}}^{(0)}$ and $\boldsymbol{\mathcal{B}}^{(0)}$ are the stationary, unperturbed background fields (visualized in Paper II), $\boldsymbol{\mathcal{E}}^{(1)}$ and $\boldsymbol{\mathcal{B}}^{(1)}$ are the perturbations (visualized by themselves in Fig. 6.14), and ϵ is a constant that sets the scale of the perturbation. To describe the strength of the perturbation, we will compare the perturbative horizon tendicity or vorticity to the background tendicity (for Schwarzschild holes) and the tendicity or vorticity (for Kerr black holes). For the Schwarzschild black holes in Fig. 6.26, we chose $\mathcal{E}^{(1)}_{NN}/\mathcal{E}^{(0)}_{NN} \approx 2\times10^{-4}$ for the electric-parity perturbations and $\mathcal{B}^{(1)}_{NN}/\mathcal{E}^{(0)}_{NN} \approx 2\times10^{-4}$ for the magnetic-parity perturbations. For electric-parity perturbations of Kerr holes, we chose $\mathcal{E}^{(1)}_{NN}/\mathcal{E}^{(0)}_{NN} \approx 3.5\times10^{-3}$ and $\mathcal{B}^{(1)}_{NN}/\mathcal{B}^{(0)}_{NN} \approx 3\times10^{-3}$, and for the magnetic-parity perturbations the ratios we selected were $\mathcal{E}^{(1)}_{NN}/\mathcal{E}^{(0)}_{NN} \approx 2.5\times10^{-3}$ and $\mathcal{B}^{(1)}_{NN}/\mathcal{B}^{(0)}_{NN} \approx 5\times10^{-3}$. We anticipate that these images may be useful for comparing with the results of numerical-relativity simulations, in which there is more ambiguity about how to separate a spacetime into a stationary background and dynamical perturbations, and for which it may be more useful to visualize the full frame-drag and

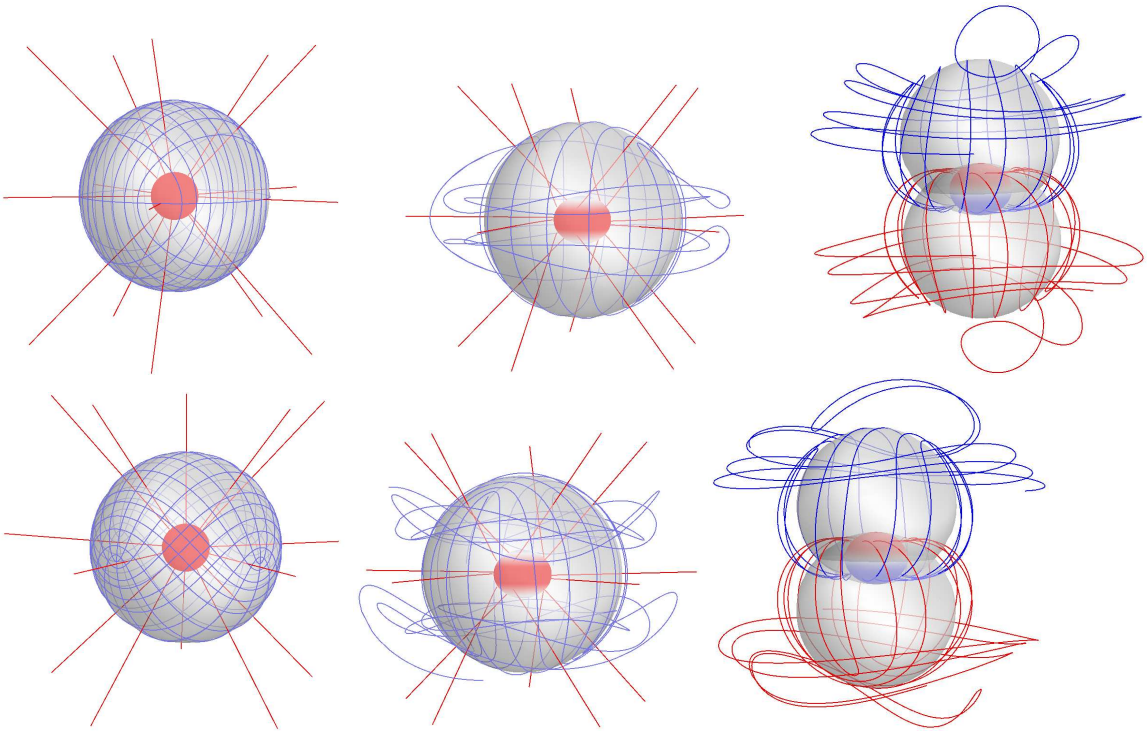

Figure 6.26: (color online). Tendex and vortex lines of Schwarzschild and Kerr black holes (of spin $a/M = 0.945$) perturbed by a $(2, 2)$ mode of either electric or magnetic parity, without removing the background tidal or frame-drag fields. The tendex lines and vortex lines are colored by the signs of their respective tendicities and vorticities (blue [dark gray] for positive and red [light gray] for negative). The horizons are colored and shaded by their vorticities or tendicities, and the transparent spheres have no physical significance, but they help to add perspective to the figures. The top panels are electric-parity perturbations and the bottom panels are magnetic-parity ones. *Left column*: Tendex lines of Schwarzschild black holes. *Middle column*: Tendex lines of Kerr black holes. *Right column*: Vortex lines of Kerr black holes.

tidal fields.

In the top panels of Fig. 6.26 are electric-parity perturbations, and the bottom panels are magnetic-parity perturbations. The left column of images are tendex lines of Schwarzschild black holes, the center column are tendex lines of Kerr black holes of spin $a/M = 0.945$, and the right column are the corresponding vortex lines of the perturbed Kerr black holes. The lines are colored by the sign of their tendicity or vorticity (blue [dark gray] for positive and red [light gray] for negative) and the horizons are colored by their tendicity or vorticity. The transparent spheres are placed in the figures to help guide the eye, and do not indicate any feature of the vortexes or tendexes.

In these figures, we must choose an amplitude for the perturbation (described in the first paragraph above). For the all the black holes, we make the perturbation sufficiently small that one cannot see the effect of the perturbation in either the horizon tendicity, or the red (light gray) radial tendex lines. For the Kerr holes, we also require that the amplitude of the perturbation is less than the difference of the tendicities of the two non-radial tendex lines at the equatorial plane and around

the radius at which the angular lines reach closest to the horizon. With this choice, the angular tendex lines will retain some features of the unperturbed lines before they become more distorted by the perturbation in the regions near the poles.

First, we will describe the tendex lines of the Schwarzschild black holes. An unperturbed Schwarzschild black hole is spherically symmetric, the tendicity on a sphere of constant radius is constant, and, therefore, any direction tangent to the sphere is a valid tendex line. For a weakly perturbed Schwarzschild black hole, although the perturbation may be small, the perturbation restricted to a sphere of constant r completely determines the variation in the tendicity, and, furthermore, it will determine the directions of the tendex lines. This is analogous to degenerate perturbation theory in quantum mechanics, in which the eigenstates of the perturbing Hamiltonian restricted to the subspace spanned by the degenerate eigenstates are treated as the unperturbed states within the degenerate subspace. In directions that are not degenerate, however, its effects are negligible.

We can now use these facts about degeneracy to understand the tendex lines in the angular direction. The tidal field in the strictly angular directions, Eq. (6.91c) will determine the structure of the tendex lines on the sphere. The angular dependence is determined by the transverse-traceless, electric-parity tensor harmonic (for the top-left panel), because the trace term in Eq. (6.91c) is proportional to the identity and will not lift the degeneracy of the tendex lines. We would expect, therefore, that the tendex lines in the angular direction would resemble those of transverse-traceless, $l = 2$, $m = 2$, gravitational waves generated by a time-dependent mass quadrupole. These were shown in [17, 2] (i.e. Chapters 4 and 3), and the pattern of the lines is nearly identical. The tendicity along the lines is quite different from those of a gravitational wave, because for the perturbed Schwarzschild black hole, the tendicity is primarily determined by the constant unperturbed value on the sphere. Nevertheless, the tendex lines on the sphere show a striking similarity to those of gravitational waves at infinity.

For the magnetic-parity perturbation (the bottom-left panel), the tendex lines are determined by an $l = 2$, $m = 2$, magnetic-parity tensor harmonic; consequently, we would expect that the lines would resemble those of transverse-traceless gravitational waves at infinity, produced by a time-dependent, current-quadrupole source. Those lines were shown in [17] (i.e. Chapter 4), and they appear identical. Once more, though, the value of the tendicity along the lines is set by the background Schwarzschild black hole for the lines in bottom-left panel of Fig. 6.26 (unlike the tendicity of the lines studied in [17] (i.e. Chapter 4)).

The degeneracy between the angular tendex and vortex lines can also be used to explain the tendex and vortex lines in the middle and right columns of Fig. 6.26, respectively. For both the tendex and vortex lines, when the lines are near the equatorial plane ($\theta = \pi/2$) they resemble the unperturbed lines, but as they head toward the poles, they begin to become perturbed. This happens because the perturbation is small compared to the difference in the eigenvalues near the

equatorial plane, and the perturbations have little effect on the tendex or vortex lines. Near the poles, however, the background vorticities and tendicities in the angular directions become degenerate (see the discussion at the end of Apps. A and B of Paper II), and the perturbation restricted to the degenerate subspace controls the lines' directions. In the vicinity of the poles, the degenerate subspace is a plane parallel to the equatorial plane, and the perturbative tendex lines must form a regular grid around these points. When we combine this observation with the parity of the perturbation, we see that the lines at the opposite poles must be either parallel or orthogonal. Thus, these few simple constraints combine to explain the relatively simple pattern of the vortex and tendex lines of the perturbation plus the background frame-drag and tidal fields.

Bibliography

[1] R. Owen, J. Brink, Y. Chen, J. D. Kaplan, G. Lovelace, K. D. Matthews, D. A. Nichols, M. A. Scheel, F. Zhang, A. Zimmerman, et al., Phys. Rev. Lett. **106**, 151101 (2011).

[2] D. A. Nichols, R. Owen, F. Zhang, A. Zimmerman, J. Brink, Y. Chen, J. Kaplan, G. Lovelace, K. D. Matthews, M. A. Scheel, et al. (2011), 1108.5486.

[3] J. Centrella, J. G. Baker, B. J. Kelly, and J. R. van Meter, Rev. Mod. Phys. **82**, 3069 (2010).

[4] F. Zhang, A. Zimmerman, D. A. Nichols, Y. Chen, G. Lovelace, K. D. Matthews, R. Owen, and K. S. Thorne, Phys. Rev. D **86**, 084049 (2012).

[5] R. Penrose and W. Rindler, *Spinors and Space-time, Volume 1* (Cambridge University Press, Cambridge, 1992).

[6] J. Hartle, Phys. Rev. D **9**, 2749 (1974).

[7] K. A. Dennison and T. W. Baumgarte, Phys.Rev. **D86**, 084051 (2012), 1207.2431.

[8] T. Damour, in *Proceedings of the Second Marcel Grossman Meeting on General Relativity*, edited by R. Ruffini (North-Holland Publishing Company, Amsterdam, 1982), pp. 587–606.

[9] K. S. Thorne, R. H. Price, and D. A. MacDonald, *Black Holes: The Membrane Paradigm* (Yale University Press, New Haven and London, 1986).

[10] L. Bel, General Relativity and Gravitation **32**, 2047 (2000), URL http://dx.doi.org/10.1023/A:1001958805232.

[11] J. D. Brown, S. R. Lau, and J. W. York, Phys. Rev. D **59**, 064028 (1999), URL http://link.aps.org/doi/10.1103/PhysRevD.59.064028.

[12] http://www.phy.olemiss.edu/ berti/qnms.html.

[13] E. Berti, V. Cardoso, and A. O. Starinets, Class. Quantum Grav. **26**, 163001 (2009), 0905.2975.

[14] E. W. Leaver, Proc. R. Soc. Lond. A **402**, 285 (1985).

[15] R. Maartens, T. Gebbie, and G. F. Ellis, Phys. Rev. D **59**, 083506 (1999), astro-ph/9808163.

[16] J. D. Schnittman, A. Buonanno, J. R. van Meter, J. G. Baker, W. D. Boggs, J. Centrella, B. J. Kelly, and S. T. McWilliams, Phys. Rev. D **77**, 044031 (2008), arXiv:0707.0301v2.

[17] A. Zimmerman, D. A. Nichols, and F. Zhang, Phys. Rev. D **84**, 044037 (2011).

[18] I. Vega, E. Poisson, and R. Massey, Class. Quant. Grav. **28**, 175006 (2011), 1106.0510.

[19] G. Lovelace, M. Boyle, M. A. Scheel, and B. Szilágyi, Class. Quant. Grav. **29**, 045003 (2012), arXiv:1110.2229.

[20] http://www.black-holes.org/oscillateQuadVortex.html.

[21] J. W. Belcher and S. Olbert, Am. J. Phys. **71**, 220 (2003).

[22] V. Ferrari and B. Mashhoon, Phys. Rev. D **30**, 295 (1984).

[23] S. R. Dolan, Phys. Rev. D **82**, 104003 (2010), URL http://link.aps.org/doi/10.1103/PhysRevD.82.104003.

[24] H. Yang, D. A. Nichols, F. Zhang, A. Zimmerman, Z. Zhang, and Y. Chen (2012), arXiv:1207.4253.

[25] I. Kamaretsos, M. Hannam, and B. Sathyaprakash (2012), 1207.0399.

[26] http://www.black-holes.org/SpEC.html.

[27] T. Regge and J. A. Wheeler, Phys. Rev. **108**, 1063 (1957).

[28] F. J. Zerilli, Phys. Rev. D **2**, 2141 (1970).

[29] L. A. Edelstein and C. V. Vishveshwara, Phys. Rev. D **1**, 3514 (1970).

[30] S. Chandrasekhar, *The Mathematical Theory of Black Holes* (Oxford University Press, Oxford, 1983).

[31] S. Teukolsky, Astrophys. J. **185**, 635 (1973).

[32] E. Newman and R. Penrose, J. Math. Phys. **3**, 566 (1962), URL http://link.aip.org/link/?JMP/3/566/1.

[33] P. L. Chrzanowski, Phys. Rev. D **11**, 2042 (1975).

[34] C. O. Lousto and B. F. Whiting, Phys. Rev. D **66**, 024026 (2002).

[35] A. Ori, Phys. Rev. D **67**, 124010 (2003).

[36] N. Yunes and J. Gonzalez, Phys. Rev. D **73**, 024010 (2006).

[37] T. S. Keidl, J. L. Friedman, and A. G. Wiseman, Phys. Rev. D **75**, 124009 (2007).

[38] T. S. Keidl, A. G. Shah, J. L. Friedman, D.-H. Kim, and L. R. Price, Phys. Rev. D **82**, 124012 (2010).

[39] A. G. Shah, T. S. Keidl, J. L. Friedman, D.-H. Kim, and L. R. Price, Phys. Rev. D **83**, 064018 (2011).

[40] J. M. Stewart, Proc. R. Soc. Lond. A **367**, 527 (1979).

[41] P. P. Fiziev, Phys. Rev. D **80**, 124001 (2009).

[42] K. Martel and E. Poisson, Phys. Rev. D **71**, 104003 (2005).

[43] K. S. Thorne, Rev. Mod. Phys. **52**, 299 (1980).

[44] E. Poisson, Phys. Rev. D **70**, 084044 (2004), URL `http://link.aps.org/abstract/PRD/v70/e084044`.

[45] R. Geroch, A. Held, and R. Penrose, J. Math. Phys. **14**, 874 (1973).

Chapter 7

Quasinormal-mode spectrum of Kerr black holes and its geometric interpretation

---

Originally published as

Huan Yang, David A. Nichols, Fan Zhang, Aaron Zimmerman, Zhongyang Zhang, Yanbei Chen

Phys. Rev. D 86, 104006 (2012)

7.1 Introduction

Quasinormal modes (QNMs) of black-hole spacetimes are the characteristic modes of linear perturbations of black holes that satisfy an outgoing boundary condition at infinity and an ingoing boundary condition at the horizon (they are the natural, resonant modes of black-hole perturbations). These oscillatory and decaying modes are represented by complex characteristic frequencies $\omega = \omega_R - i\omega_I$, which are typically indexed by three numbers, n, l, and m. The overtone number n is proportional to the decay rate of the perturbation, and l and m are multipolar indexes of the angular eigenfunctions of the QNM.

7.1.1 Overview of quasinormal modes and their geometric interpretation

Since their discovery, numerically, in the scattering of gravitational waves in the Schwarzschild spacetime by Vishveshwara [1], QNMs have been thoroughly studied in a wide range of spacetimes, and they have found many applications. There are several reviews [2, 3, 4, 5, 6] that summarize the many discoveries about QNMs. They describe how QNMs are defined, the many methods used to calculate QNMs (e.g., estimating them from time-domain solutions [7], using shooting methods

in frequency-domain calculations [8], approximating them with inverse-potential approaches [9] and WKB methods [10, 11], and numerically solving for them with continued-fraction techniques [12, 13]), and the ways to quantify the excitation of QNMs (see, e.g., [14, 15]). They also discuss the prospects for detecting them in gravitational waves using interferometric gravitational-wave detectors, such as LIGO [16] and VIRGO [17], and for inferring astrophysical information from them (see, e.g., [18, 19] for finding the mass and spin of black holes using QNMs, [20, 21] for quantifying the excitation of QNMs in numerical-relativity simulations binary-black-hole mergers, and [22, 23] for testing the no-hair theorem with QNMs). There have also been several other recent applications of QNMs. For example, Zimmerman and Chen [24] (based on work by Mino and Brink [25]) study extensions to the usual spectrum of modes generated in generic ringdowns. Dolan and Ottewill use eikonal methods to approximate the modal wave function, and they use these functions to study the Green's function and to help understand wave propagation in the Schwarzschild spacetime [26, 27, 28].

Although QNMs are well-understood and can be calculated quite precisely, it remains useful to develop intuitive and analytical descriptions of these modes. An important calculation in this direction was performed by Ferrari and Mashhoon [9], who showed that for a Schwarzschild black hole, the QNM frequency (which depends only on a multipolar index l and an overtone index n) can be written in the eikonal (or geometric-optics) limit, $l \gg 1$, as

$$\omega \approx (l + 1/2)\Omega - i\gamma_L(n + 1/2)\,. \tag{7.1}$$

The quantities Ω and γ_L are, respectively, the Keplerian frequency of the circular photon orbit and the Lyapunov exponent of the orbit, the latter of which characterizes how quickly a congruence of null geodesics on the circular photon orbit increases its cross section under infinitesimal radial perturbations [29, 28]. Equation (7.1) hints at an intriguing physical description of QNMs: for modes with wavelengths much shorter than the background curvature, the mode behaves as if it were sourced by a perturbation that orbits on and diffuses away from the light ring on the time scale of the Lyapunov exponent.

Ferrari and Mashhoon [9] also derived an analogous result to Eq. (7.1) for slowly rotating black holes. They showed for $l \gtrsim m \gg 1$, the real part of the frequency is given by

$$\Omega \approx \omega_{\rm orb} + \frac{m}{l + 1/2}\omega_{\rm prec}\,, \tag{7.2}$$

where $\omega_{\rm orb}$ is now the Keplerian orbital frequency for the circular photon orbit and $\omega_{\rm prec}$ is the Lense-Thiring-precession frequency of the orbit (which arises because of the slow rotation of the black hole). The term proportional to $\omega_{\rm prec}$ also has a simple geometric-optics interpretation. Inertial frames near the high-frequency wave at the light ring are dragged with respect to inertial frames at infinity, and this frame dragging causes the perturbation's orbit to precess about the spin axis of the black

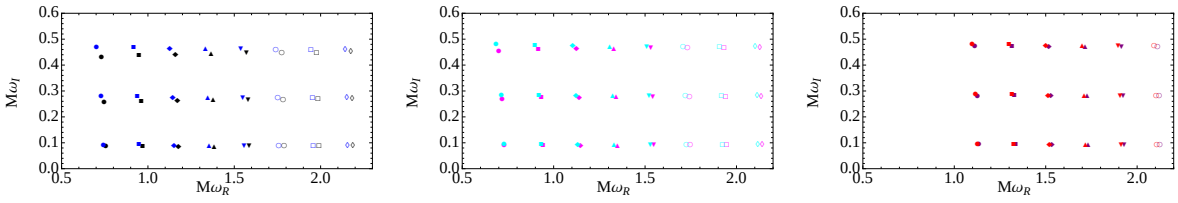

Figure 7.1: Low-overtone QNM spectrum of three Kerr black holes of different spins with approximate degeneracies in their spectra. From left to right, we plot the three lowest-overtone QNM excitations for (i) $a/M = 0.69$ in which $(l, m) = (j, 2)$ are black symbols and $(l', m') = (j + 1, -2)$ are blue symbols, where $j = 3, \ldots, 9$; (ii) $a/M = 0.47$ in which $(l, m) = (j, 3)$ are magenta symbols and $(l', m') = (j + 1, -3)$ are cyan symbols, where $j = 3, \ldots, 9$; (iii) $a/M = 0.35$ in which $(l, m) = (j, 4)$ are red symbols and $(l', m') = (j + 1, -4)$ are purple symbols, where $j = 5, \ldots, 10$. For these spin parameters, the mode with positive values of m and ω_R (a corotating mode) of index l is approximately degenerate with the mode with $m' = -m$, and ω_R (a counterrotating mode) of index $l' = l + 1$.

hole with a frequency, $\omega_{\rm prec}$. If the orbit is inclined at an angle of $\sin^2\theta = m^2/l(l+1)$ (the ratio of angular momenta L_z^2/L^2 for quantized waves in flat space), then the projection of the precessional velocity onto the orbital plane scales the precessional frequency by a factor of $\sim m/(l + 1/2)$.

Why the QNM frequency is multiplied by $(l+1/2)$ is a feature that we will explain in greater detail in this paper. Intuitively, this term arises because the in the high-frequency limit, any wavefront traveling on null orbits will have an integral number of oscillations in the θ and ϕ directions. For the wave to be periodic and single-valued, there must be m oscillations in the ϕ direction. For the θ direction, it is a Bohr-Sommerfeld quantization condition that requires $l - |m| + 1/2$ oscillations in this direction, which implies that there should be a net spatial frequency of roughly $(l + 1/2)$. This increases the frequency of the radiation seen far from the hole by the same factor.

From this intuitive argument, we expect that the real part of the mode should be

$$\omega_R = L\left(\omega_{\rm orb} + \frac{m}{L}\omega_{\rm prec}\right) , \tag{7.3}$$

where we define $L = l + 1/2$. In this paper, we will show that an equation of the form of Eq. (7.3) does, in fact, describe the QNM frequencies of Kerr black holes of arbitrary astrophysical spins (and it recovers the result of Ferrari and Mashhoon for slowly spinning black holes). As we mention in the next part of this section, the exact details of the correspondence between QNMs and photon orbits is richer for rapidly rotating black holes than for slowly rotating or static black holes.

7.1.2 Methods and results of this article

To derive Eq. (7.3) requires that we develop a geometric-optics interpretation of the QNMs of Kerr black holes with arbitrary astrophysical spins. Finding the correspondence requires two steps: first, we need to calculate the approximate frequencies using the WKB method; next, we must

articulate a connection between the mathematics of waves propagating in the Kerr spacetime in the geometric-optics approximation and those of the WKB approximation (the first step). Finally, with the geometric-optics description of QNMs, we can make a physical interpretation of the spectrum (for example, the degeneracy or the lack of damping in the extremal limit).

In Sec. 7.2, we describe how we solve the eigenvalue problem that arises from separating the Teukolsky equation [30] (a linear partial differential equation that describes the evolution of scalar, vector, and gravitational perturbations of Kerr black holes) into two nontrivial linear ordinary differential equations. The two differential equations, the radial and angular Teukolsky equations, share two unknown constants—the frequency, ω, and the angular separation constant, A_{lm}—that are fixed by the boundary conditions that the ordinary differential equations must satisfy (ingoing at the horizon and outgoing at infinity for the radial equation, and well-behaved at the poles for the angular equation). The goal of the WKB method is to compute the frequency and separation constant approximately.

Although there has been work by Kokkotas [31] and Iyer and Seidel [32] using WKB methods to compute QNM frequencies of rotating black holes, their results were limited to slowly rotating black holes, because they performed an expansion of the angular separation constant, A_{lm}, for small, dimensionless spin parameters, a/M, and only applied the WKB method to the radial Teukolsky equation to solve for the frequency. In a different approach, Dolan developed a matched-expansion formalism for Kerr black holes of arbitrary spins that can be applied to compute the frequency of QNMs, but only for modes with $l = |m|$ and $m = 0$ [27].

Therefore, it remains an outstanding problem to compute a WKB approximation to the quasi-normal modes of Kerr black holes of large spins and for any multipolar index m. In Sec. 7.2, we solve the joint eigenvalue problem of the radial and angular Teukolsky equations by applying a change of variables to the angular equation that brings it into the form of a bound-state problem in quantum mechanics. Applying the WKB method to the angular equation, we arrive at a Bohr-Sommerfeld condition that constrains the angular constant in terms of the frequency (and the indices l and m). Simultaneously, we can analyze the radial equation in the WKB approximation, and the two equations together define an system of integral equations, which can be solved for the eigenvalues. When we expand the Bohr-Sommerfeld condition in a Taylor series in terms of the numerically small parameter, $a\omega/l$, the system of integral equations reduces to an algebraic system (which, in turn, leads to a simpler expression for the frequency). The approximate frequency agrees very well with the result that includes all powers of $a\omega/l$, and, in the eikonal limit, it is accurate to order $1/l$ for Kerr black holes of arbitrary spins, for modes with any value of m, and for both the real and the imaginary parts of the frequency.

To interpret the WKB calculation of Sec. 7.2 in the language of propagating waves in the geometric-optics limit within the Kerr spacetime, we analyze waves around a Kerr black hole in

Sec. 7.3 using the geometric-optics approximation and the Hamilton-Jacobi formalism. We confirm that the leading-order pieces of the WKB frequencies and angular constants correspond to the conserved quantities of the leading-order, geodesic behavior of the geometric-optics approximation (specifically, the real part of ω, the index m, and the real part of A_{lm} are equivalent to the energy $\mathcal{E}$, the z-component of the specific angular momentum L_z, and Carter's constant $\mathcal{Q}$ plus L_z^2, respectively). The specific geodesics corresponding to a QNM are, in fact, spherical photon orbits. The next-to-leading-order WKB quantities (the imaginary parts of ω and A_{lm}) correspond to dispersive, wavelike corrections to the geodesic motion (they are the Lyapunov exponent and the product of this exponent with the change in Carter's constant with respect to the energy). Table 7.1 in Sec. 7.3 summarizes this geometric-optics correspondence.

In Sec. 7.4, we make several observations about features of the QNM spectrum of Kerr black holes that have simple geometric interpretations. First, we find that for extremal Kerr black holes, a significant fraction of the QNMs have a real frequency proportional to the angular frequency of the horizon and a decay rate that rapidly falls to zero; we explain this in terms of a large number of spherical photon orbits that collect on the horizon for extremal Kerr holes. Second, we expand the WKB expression for the real part of the frequency as in Eq. (7.3), and we interpret these terms as an orbital and a precessional frequency of the corresponding spherical photon orbit. These two frequencies depend on the spin of the black hole and the value of m/L very weakly for slowly-rotating black holes, though quite strongly when the spin of the black hole is nearly extremal. Finally, we use the geometric-optics interpretation given by Eq. (7.3) to explain a degeneracy in the QNM spectrum of Kerr black holes, in the eikonal limit, which also manifests itself, approximately, for small l (see Fig. 7.1). The degeneracy occurs when the orbital and precession frequencies, $\omega_{\rm orb}$ and $\omega_{\rm prec}$ are rationally related (i.e., $\omega_{\rm orb}/\omega_{\rm prec} = p/q$ for integers p and q) for a hole of a specific spin parameter, and when the corresponding spherical photon orbits close. By substituting this result into Eq. (7.3) one can easily see that modes with multipolar indexes l and m become degenerate with those of indexes $l' = l + kq$ and $m' = m - kp$ for any non-negative integer k, in the eikonal limit (note that in Fig. 7.1, we show an approximate degeneracy for $k = 1$ and for three spin parameters, such that $q/p = 1/4$, $1/6$, and $1/8$, respectively.)

To conclude this introduction, we briefly summarize the organization of this paper: In Sec. 7.2, we review the Teukolsky equations, and we then describe the WKB formalism that we use to calculate an accurate approximation to the angular eigenvalues $A_{lm} = A_{lm}^R + iA_{lm}^I$ and QNM frequencies $\omega = \omega_R - i\omega_I$, in the eikonal limit $L \gg 1$ and for holes of arbitrary spins. We verify the accuracy of our expressions in Sec. 7.2.4 by comparing the WKB frequencies to exact, numerically calculated frequencies. In Sec. 7.3, we develop a correspondence between the WKB calculation and mathematics of wave propagation within the Kerr spacetime in the geometric-optics limit, using the geometric-optics approximation and the Hamilton-Jacobi formalism. At leading-order, the QNM frequencies

and angular eigenvalues correspond to the conserved quantities of motion in the Kerr spacetime for spherical photon orbits; at next-to-leading order in the geometric-optics approximation, we connect the the decaying behavior of the QNMs to dispersive behaviors of the waves. Finally, in Sec. 7.4, we interpret aspects of the QNM spectrum geometrically, such as the vanishing of the damping rate for many modes of extremal black holes, the decomposition of the frequency into orbital and precessional parts, and the degeneracies in the QNM frequency spectrum. Finally, in Sec. 7.5, we conclude. We use geometrized units in which $G = c = 1$ and the Einstein summation convention throughout this paper.

7.2 WKB Approximation for the Quasinormal-Mode Spectrum of Kerr Black Holes

In this section, we will derive expressions for the frequencies of quasinormal modes of Kerr black holes using the WKB approximation. We will need to compute the real and imaginary parts to an accuracy of $O(1)$ in terms of $l \gg 1$, which implies that we must calculate ω_R to leading and next-to-leading order and ω_I to leading order. Here, we will focus on obtaining an analytic approximation to the frequency spectrum, and we will leave the geometrical interpretation of our results until the next section.

Before specializing our results to the angular and radial Teukolsky equations, we will review a basic result about the WKB expansion that we will use frequently throughout this paper; a more complete discussion of WKB methods can be found in [11]. Given a wave equation for $\psi(x)$

$$\epsilon^2 \frac{d^2\psi}{dx^2} + U(x)\psi = 0\,, \tag{7.4}$$

we will expand the solution as $\psi = e^{S_0/\epsilon + S_1 + \epsilon S_2 + \cdots}$, where the leading and next-to-leading action variables are given by

$$S_0 = \pm i \int^x \sqrt{U(x)} dx\,, \tag{7.5a}$$

$$S_1 = -\frac{1}{4}\log U(x)\,. \tag{7.5b}$$

The formulas above will be the basis for our analysis of the radial and angular Teukolsky equations in the next sections.

7.2.1 The Teukolsky equations

Teukolsky showed that scalar, vector, and tensor perturbations of the Kerr spacetime all satisfy a single master equation for scalar variables of spin weight s; moreover, the master equation can

be solved by separation of variables [30]. We will use u to denote our scalar variable, and we will separate this scalar wave as

$$u(t, r, \theta, \phi) = e^{-i\omega t} e^{im\phi} u_r(r) u_\theta(\theta) \,. \tag{7.6}$$

Then, at the relevant order in $l \gg 1$, the angular equation for $u_\theta(\theta)$ can be written as

$$\frac{1}{\sin\theta} \frac{d}{d\theta} \left[\sin\theta \frac{du_\theta}{d\theta} \right] + \left[a^2\omega^2 \cos^2\theta - \frac{m^2}{\sin^2\theta} + A_{lm} \right] u_\theta = 0 \,, \tag{7.7}$$

where A_{lm} is the angular eigenvalue of this equation. The equation obeyed by the radial function $u_r(r)$ is

$$\frac{d^2 u_r}{dr_*^2} + \frac{K^2 - \Delta\lambda^0_{lm}}{(r^2+a^2)^2} u_r = 0 \,, \quad \frac{d}{dr_*} \equiv \frac{\Delta}{r^2+a^2} \frac{d}{dr} \tag{7.8a}$$

with

$$K = -\omega(r^2+a^2) + am \,, \tag{7.8b}$$

$$\lambda^0_{lm} = A_{lm} + a^2\omega^2 - 2am\omega \,, \tag{7.8c}$$

$$\Delta = r^2 - 2Mr + a^2 \,. \tag{7.8d}$$

Here we have used the facts that $\omega_R \sim O(l)$, $\omega_I \sim O(1)$, $m \sim O(l)$ to drop terms that are of higher orders in the expansion than those that we treat. Note that the spin s of the perturbation no longer enters into these equations after neglecting the higher-order terms.

7.2.2 The angular eigenvalue problem

We will first find an expression for A_{lm} in terms of ω, l, and m, by analyzing the angular equation in the WKB approximation. By defining

$$x = \log\left(\tan\frac{\theta}{2} \right) \tag{7.9}$$

and $dx = d\theta/\sin\theta$, we can write the angular equation as

$$\frac{d^2 u_\theta}{dx^2} + V^\theta u_\theta = 0 \,, \tag{7.10a}$$

where

$$V^\theta = a^2\omega^2 \cos^2\theta \sin^2\theta - m^2 + A_{lm} \sin^2\theta \,. \tag{7.10b}$$

When written in this form, it is clear that u_θ must satisfy a boundary condition that it be 0 as $x \to \pm\infty$ (which corresponds to $\theta \to 0, \pi$). Furthermore, the angular equation is now in a form that is amenable to a WKB analysis (which will be the subject of the next part).

First, however, we outline how we will perform the calculation. Because the frequency $\omega = \omega_R - i\omega_I$ is complex, the angular eigenvalue A_{lm}, a function of ω, must also be complex. We will write

$$A_{lm} = A^R_{lm} + iA^I_{lm}\,, \tag{7.11}$$

to indicate the split between real and imaginary parts. We will treat a real-valued $\omega = \omega_R$ in the first part of this section, and, therefore, a real-valued $A^R_{lm}(\omega_R)$; we shall account for $-i\omega_I$ by including it as an additional perturbation in the next part of this section.

7.2.2.1 Real part of A_{lm} for a real-valued ω

For $\omega_R \in \mathbb{R}$, we will compute the eigenvalues $A^R_{lm}(\omega_R)$, of Eq. (7.10a) for standing-wave solutions that satisfy physical boundary conditions. At the boundary, $\theta = 0, \pi$ (or $x = \mp\infty$) the potential satisfies $V^\theta = -m^2$ independent of the value of A^R_{lm}; this implies that the solutions to Eq. (7.10a) behave like decaying exponential functions at these points (i.e., the wave does not propagate). For there to be a region where the solutions oscillate (i.e., where the wave would propagate), A_{lm} must be sufficiently large to make $V^\theta > 0$ in some region. Depending on the relative amplitudes of A_{lm} and $a^2\omega^2$, V^θ either has one maximum at $\theta = \pi/2$ (when $A_{lm} \geq a^2\omega^2$), or two identical maxima at two locations at symmetrically situated around $\theta = \pi/2$ (when $A_{lm} < a^2\omega^2$). It turns out that the region where the maximum of $V^\theta > m^2$ is centered around $\pi/2$; therefore, all solutions fall into the former category rather than the latter.

The length scale over which the function u_θ varies is $1/\sqrt{V^\theta}$, and the WKB approximation is valid only if the potential V^θ does not vary much at this scale. Therefore, to use the WKB approximation, we require that

$$\left|\frac{1}{\sqrt{V^\theta}}\frac{dV^\theta}{d\theta}\right| \ll |V^\theta|\,. \tag{7.12}$$

This condition applies regardless of the sign of V^θ. Empirically, we find this condition to hold for V^θ in Eq. (7.10a), except around points at which $V^\theta = 0$. We will refer to these as *turning points*, and they can be found by solving for the zeros of the potential,

$$a^2\omega_R^2\cos^2\theta_\pm \sin^2\theta_\pm - m^2 + A^R_{lm}\sin^2\theta_\pm = 0\,, \tag{7.13}$$

which are given by

$$\sin^2\theta_\pm = \frac{2m^2}{A_{lm} + a^2\omega^2_{lm} \mp \sqrt{(A_{lm} + a^2\omega^2_{lm})^2 + 4m^2}}\,. \tag{7.14}$$

Using the leading and next-to-leading WKB approximation, we can write the solution to the wave

equation in the propagative region, $x_- < x < x_+$, as

$$u_\theta(x) = \frac{a_+ e^{i\int_0^x dx'\sqrt{V^\theta(x')}} + a_- e^{-i\int_0^x dx'\sqrt{V^\theta(x')}}}{[V^\theta(x)]^{1/4}}\,, \tag{7.15}$$

where $a_\pm$ are constants that must be fixed by the boundary conditions that the solution approach zero at $\theta = 0, \pi$. For $x > x_+$, we find

$$u_\theta(x) = \frac{c_+ e^{-\int_{x_+}^x dx'\sqrt{-V^\theta(x')}}}{[V^\theta(x)]^{1/4}}\,, \tag{7.16a}$$

and $x < x_-$,

$$u_\theta(x) = \frac{c_- e^{-\int_x^{x_-} dx'\sqrt{-V^\theta(x')}}}{[V^\theta(x)]^{1/4}}\,, \tag{7.16b}$$

with $c_\pm$ also being constants set by the boundary conditions. Note that outside of the turning points, we have only allowed the solution that decays towards $x \to \pm\infty$.

Around the turning points $x_\pm$, the WKB approximation breaks down, but u_θ can be solved separately by using the fact that $V_\theta(x \sim x_\pm) \propto x - x_\pm$. Solutions obtained in these regions can be matched to Eqs. (7.15)–(7.16b); the matching condition leads to the Bohr-Sommerfeld quantization condition

$$\int_{\theta_-}^{\theta_+} d\theta \sqrt{a^2\omega_R^2\cos^2\theta - \frac{m^2}{\sin^2\theta} + A_{lm}^R} = (L - |m|)\,\pi\,. \tag{7.17}$$

Here we have defined

$$L \equiv l + \frac{1}{2}\,, \tag{7.18}$$

which will be used frequently throughout this paper. The limits of the integration are the values of θ where the integrand vanishes [the turning points of Eq. (7.14)].

If we define

$$\mu \equiv \frac{m}{L}\,,\quad \alpha_R(a,\mu) \equiv \frac{A_{lm}^R}{L^2}\,,\quad \Omega_R(a,\mu) \equiv \frac{\omega_R}{L}\,, \tag{7.19}$$

then all three of these quantities are $O(1)$ in our expansion in L. From these definitions, we can re-express the limits of integration as

$$\sin^2\theta_\pm = \frac{2\mu^2}{\alpha + a^2\Omega^2 \mp \sqrt{(\alpha + a^2\Omega_R^2)^2 + 4\mu^2}}\,, \tag{7.20}$$

and the integral as

$$\int_{\theta_-}^{\theta_+} d\theta \sqrt{\alpha_R - \frac{\mu^2}{\sin^2\theta} + a^2\Omega^2\cos^2\theta} = (1 - |\mu|)\pi\,. \tag{7.21}$$

For each set of quantities $(\alpha_R, \mu, \Omega_R)$, we can express α_R as an implicit function involving elliptic integrals; however, if we treat $a\Omega_R$ as a small parameter, then the first two terms in the expansion

are

$$\alpha_R \approx 1 - \frac{a^2\Omega_R^2}{2}\left(1 - |\mu|^2\right) . \tag{7.22}$$

We derive and discuss this approximation in greater detail in Appendix 7.6. For $a = 0$, we note that this is accurate with a relative error of $O(1/L^2)$, because for a Schwarzschild black hole

$$A_{lm}^{\rm Schw} = l(l+1) - s(s+1) . \tag{7.23}$$

As we will confirm later in Figs. 7.2 and 7.4, Eq. (7.22) is an excellent approximation even for highly spinning black holes.

To understand intuitively why the approximation works so well, we will focus on corotating modes (i.e., those with positive and large m, or μ near unity), which have the highest frequencies and, therefore, the largest possible values for $a\Omega_R$. For a fixed value of (l, m), ω_R is a monotonically increasing function of a, and

$$\omega_R^{lm}(a) \leq \omega_R^{lm}(a = M) = m\Omega_H^{a=1} = \frac{m}{2M} . \tag{7.24}$$

In setting this upper bound, we have used the result that the low-overtone QNM frequencies approach $m\Omega_H$ for $m > 0$ and for extremal black holes (first discussed by Detweiler [33]); we have also used Ω_H to denote the horizon frequency of the Kerr black hole,

$$\Omega_H = \frac{a}{2Mr_+} , \tag{7.25}$$

and r_+ to indicate the position of the horizon [note that $r_+(a = M) = M$]. Normalizing Eq. 7.24 by L, we find

$$a\Omega_R \leq (\mu/2)(a/M) \leq 1/2 . \tag{7.26}$$

Even for the upper bound $a\Omega_R = 1/2$, the relative accuracy of Eq. (7.22) is still better than 0.2%.

7.2.2.2 Complex A_{lm} for a complex ω

To solve for the next-to-leading-order corrections to A_{lm}, we must compute the imaginary part A_{lm}^I. Because $\omega_I \ll \omega_R$, when we allow $\omega = \omega_R - i\omega_I$ to be a complex number in the angular eigenvalue problem (7.7), we can treat the term linear in ω_I as a perturbation to the angular equation. Using the perturbation theory of eigenvalue equations, we find that

$$A_{lm}^I = -2a^2\omega_R\omega_I\langle\cos^2\theta\rangle , \tag{7.27}$$

where

$$\langle \cos^2\theta \rangle = \frac{\int \cos^2\theta |u_\theta|^2 \sin\theta d\theta}{\int |u_\theta|^2 \sin\theta d\theta} = \frac{\int_{\theta_-}^{\theta_+} \frac{\cos^2\theta}{\sqrt{a^2\omega_R^2\cos^2\theta - \frac{m^2}{\sin^2\theta} + A_{lm}^R}} d\theta}{\int_{\theta_-}^{\theta_+} \frac{1}{\sqrt{a^2\omega_R^2\cos^2\theta - \frac{m^2}{\sin^2\theta} + A_{lm}^R}} d\theta} . \tag{7.28}$$

By taking the derivative of both sides of the Bohr-Sommerfeld condition (7.17) with respect to the variable $z = a\omega_R$ and by treating A_{lm} as a function of z, we can rewrite the above expression as

$$\langle \cos^2\theta \rangle = -\frac{1}{2z} \frac{\partial A_{lm}^R(z)}{\partial z}\bigg|_{z=a\omega_R} . \tag{7.29}$$

Substituting this expectation value into Eq. (7.27), we find

$$A_{lm}^I = a\omega_I \left[\frac{\partial A_{lm}^R(z)}{\partial z}\right]_{z=a\omega_R} . \tag{7.30}$$

Equation (7.30) defines a numerical prescription for computing $A_{lm} = A_{lm}^R + iA_{lm}^I$. This approach is quite natural: as ω becomes complex, A_{lm} is the analytic function whose value on the real axis is given by A_{lm}^R. The approximate formula (7.22), therefore, becomes

$$A_{lm} \approx L^2 - \frac{a^2\omega^2}{2}\left[1 - \frac{m^2}{L^2}\right] , \tag{7.31a}$$

or

$$\alpha \approx 1 - \frac{a^2\Omega^2}{2}\left(1 - |\mu|^2\right) , \tag{7.31b}$$

for a complex frequency ω.

7.2.3 The radial eigenvalue problem

Now that we have solved for the angular eigenvalues A_{lm} in terms of ω, we turn to the radial Teukolsky equation. From Eq. (7.8a), we see that the radial equation is already in the form

$$\frac{d^2u_r}{dr_*^2} + V^r u_r = 0 , \tag{7.32a}$$

if we define

$$V^r(r,\omega) = \frac{[\omega(r^2+a^2) - ma]^2 - \Delta\left[A_{lm}(a\omega) + a^2\omega^2 - 2ma\omega\right]}{(r^2+a^2)^2} . \tag{7.32b}$$

Note here that V^r is an analytic function of ω, and that it is real-valued when ω is real.

In general, the WKB approximant for u_r is given at leading order by

$$u_r = b_+ e^{i\int^{r_*}\sqrt{V^r(r'_*)}dr'_*} + b_- e^{-i\int^{r_*}\sqrt{V^r(r'_*)}dr'_*}\,, \tag{7.33}$$

although in order to obtain a mode which is outgoing at $r_* \to +\infty$ (the same as $r \to \infty$) and ingoing at $r_* \to -\infty$ ($r \to r_+$), we must have

$$u_r = b_+ e^{i\int^{r_*}\sqrt{V^r(r'_*)}dr'_*}\,, \tag{7.34a}$$

for the region containing $r \to +\infty$, and

$$u_r = b_- e^{-i\int^{r_*}\sqrt{V^r(r'_*)}dr'_*}\,, \tag{7.34b}$$

for the region containing $r_* \to -\infty$. Intuitively speaking, a solution to Eq. (7.32a) will satisfy the asymptotic behavior above if $V^r \approx 0$ around a point $r = r_0$, and $V_r > 0$ on both sides. Then, the WKB expansion (7.33) is valid in the two regions on both sides of $r = r_0$, and the solution in the vicinity of r_0 must be obtained separately by matching to the WKB approximation. The matching will constrain the frequency, thereby giving a method to determine ω. A detailed calculation of this procedure has been carried out by Iyer and Will [11] to high orders in the WKB approximation; the only difference between our calculation and their result at lower orders comes from the more complex dependence of V^r on ω in our case (particularly because A_{lm} depends on ω in a more involved way).

7.2.3.1 Computing ω_R

From Iyer and Will [11], the conditions at the leading and next-to-leading order that must be solved to find ω_R are

$$V^r(r_0, \omega_R) = \left.\frac{\partial V^r}{\partial r}\right|_{(r_0,\omega_R)} = 0\,. \tag{7.35}$$

After a short calculation, these conditions can be expressed as

$$\Omega_R = \frac{\mu a}{r_0^2 + a^2} \pm \frac{\sqrt{\Delta(r_0)}}{r_0^2 + a^2}\beta(a\Omega_R)\,, \tag{7.36a}$$

$$0 = \frac{\partial}{\partial r}\left[\frac{\Omega_R(r^2+a^2) - \mu a}{\sqrt{\Delta(r)}}\right]_{r=r_0}\,, \tag{7.36b}$$

where we have defined

$$\beta(z) = \sqrt{\alpha(z) + z^2 - 2\mu z} \tag{7.37a}$$

$$\approx \sqrt{1 + \frac{z^2}{2} - 2\mu z + \frac{\mu^2 z^2}{2}}\,. \tag{7.37b}$$

In deriving Eq. (7.36b), we have used the fact that at $r > r_+$, $(r^2+a^2)^2/\Delta$ is a monotonically increasing function, and, therefore the extrema of V^r are the same as those of $V^r(r^2+a^2)^2/\Delta$; we then also used the fact that the quantity within the square brackets in Eq. (7.36b) is always nonzero at points at which $V^r = 0$.

One method of jointly solving Eqs. (7.36a) and (7.36b) would be to use Eq. (7.36b) to express Ω_R in terms of r_0

$$\Omega_R = \frac{(M-r_0)\mu a}{(r_0-3M)r_0^2+(r_0+M)a^2}\,, \tag{7.38}$$

and then insert this into Eq. (7.36a) to obtain r_0; finally Ω_R can be obtained by substituting this r_0 back into Eq. (7.38). If we use the approximate formula (7.37b) in this process, the equation for r_0 becomes a sixth-order polynomial in $x = r_0/M$, the roots of which can be found efficiently. For conveninece, we write this polynomial here

$$\begin{aligned} &2x^4(x-3)^2 + 4x^2[(1-\mu^2)x^2 - 2x - 3(1-\mu^2)](a/M)^2 \\ &+(1-\mu^2)[(2-\mu^2)x^2 + 2(2+\mu^2)x + (2-\mu^2)](a/M)^4\,. \end{aligned} \tag{7.39}$$

For each pair $(\mu, a/M)$, there are in general two real roots for x, which correspond to the two possible values of r_0/M (and the two real frequencies with opposite signs).

Note that the procedure above will not work when $m = 0$ (when both the numerator and denominator of Eq. (7.38) vanish). In this case, we can directly require that

$$(r_p - 3M)r_p^2 + (r_p+M)a^2 = 0\,. \tag{7.40}$$

The solution, r_p can be inserted into Eq. (7.36a) and the result can be expressed in terms of elliptic integrals

$$\Omega_R(a, \mu=0) = \pm\frac{\pi\sqrt{\Delta(r_p)}}{(r_p^2+a^2)\mathrm{EllipE}\left[\dfrac{a^2\Delta(r_p)}{(r_p^2+a^2)^2}\right]}\,, \tag{7.41}$$

where EllipE denotes an elliptic integral of the second kind. Here we have used the subscript p for this special case, because this mode will turn out to correspond to polar orbits.

We plot in Fig. 7.2 the relative error in Ω_R that comes from using the approximate expression for A_{lm} [Eq. (7.31a)] rather than the exact Bohr-Sommerfeld condition. The error is always less than $\sim 10^{-4}$ (we scale the quantity plotted on the vertical axis by 10^5), and therefore, we will use the approximate expression for A_{lm} for the remaining calculations involving Ω_R throughout this paper. In Fig. 7.3, we plot Ω_R for $a/M = 0$, 0.3, 0.5, 0.9, 0.99, and 1 (the flat curve corresponds to $a/M = 0$, and those with increasing slopes are the increasing values of a/M). While for low values of a/M below ~ 0.5, Ω_R depends roughly linearly upon μ, for higher values of a/M (and for $\mu > 0$), Ω_R grows more rapidly than linearly. For $a/M = 1$, $\Omega_R \to 1/2$ when $\mu \to 1$, as anticipated.

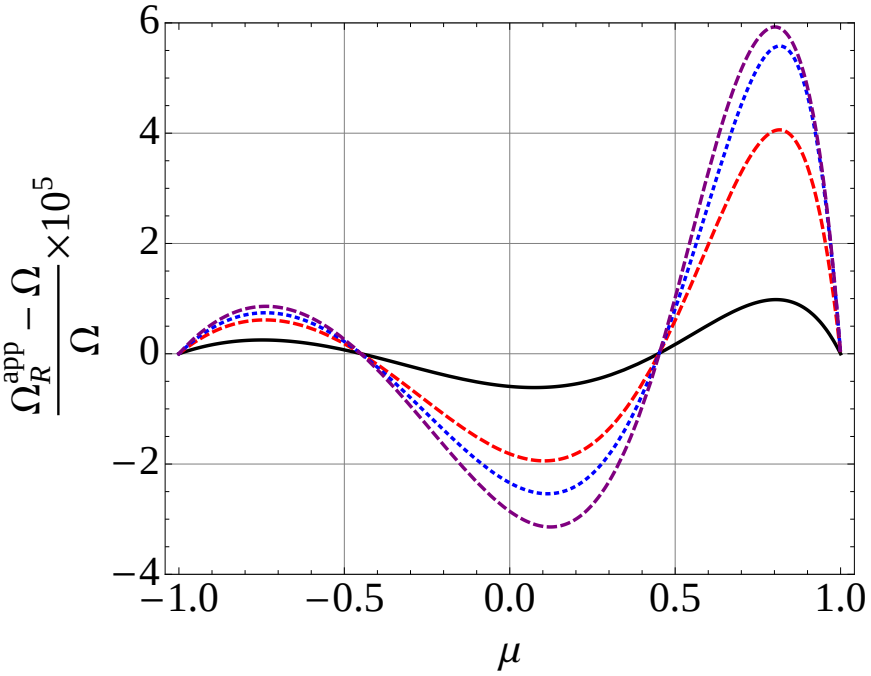

Figure 7.2: Difference in $\Omega_R(a,\mu)$ [Eq. (7.38)] that arises from using the approximate formula for A_{lm} [Eq. (7.31a)] as opposed to the exact formula. Here $a/M = 0.7$, 0.9,0.95, and 0.99 correspond to black solid, red dashed, blue dotted, and purple long-dashed curves, respectively. The quantity plotted on the vertical axis has been scaled by 10^5.

7.2.3.2 Computing ω_I

At leading order, the imaginary part ω_I can be calculated using the same procedure set forth by Iyer and Will [11]. They find that

$$\omega_I = -(n+1/2)\frac{\sqrt{2\left(\frac{d^2V^r}{dr_*^2}\right)_{r_0,\omega_R}}}{\left(\frac{\partial V^r}{\partial\omega}\right)_{r_0,\omega_R}} = -(n+1/2)\Omega_I(a,\mu)\,. \tag{7.42}$$

In our calculation, we must also take into account that V^r also depends on ω through the angular eigenvalue's dependence on ω. If we use the approximate formula for α, we obtain a reasonably compact expression for Ω_I:

$$\Omega_I = \Delta(r_0)\frac{\sqrt{4(6r_0^2\Omega_R^2-1)+2a^2\Omega_R^2(3-\mu^2)}}{2r_0^4\Omega_R - 4aMr_0\mu + a^2r_0\Omega_R[r_0(3-\mu^2)+2M(1+\mu^2)]+a^4\Omega_R(1-\mu^2)}\,. \tag{7.43}$$

In Fig. 7.4, we plot the relative error in Ω_I from using the approximate formula for A_{lm} identically to that in Fig. 7.2 (although here we scale the quantity plotted on the vertical axis by 10^4). Because the error is always less than $\sim 10^{-3}$, we will use the approximate expression for A_{lm} for computing Ω_I in the remainder of this paper. In Fig. 7.5, we plot $\Omega_I(a,\mu)$ for several values of a/M (the same as those in Fig. 7.3, though not $a/M = 0.3$). The curve for $a/M = 0$ is flat, and those with larger

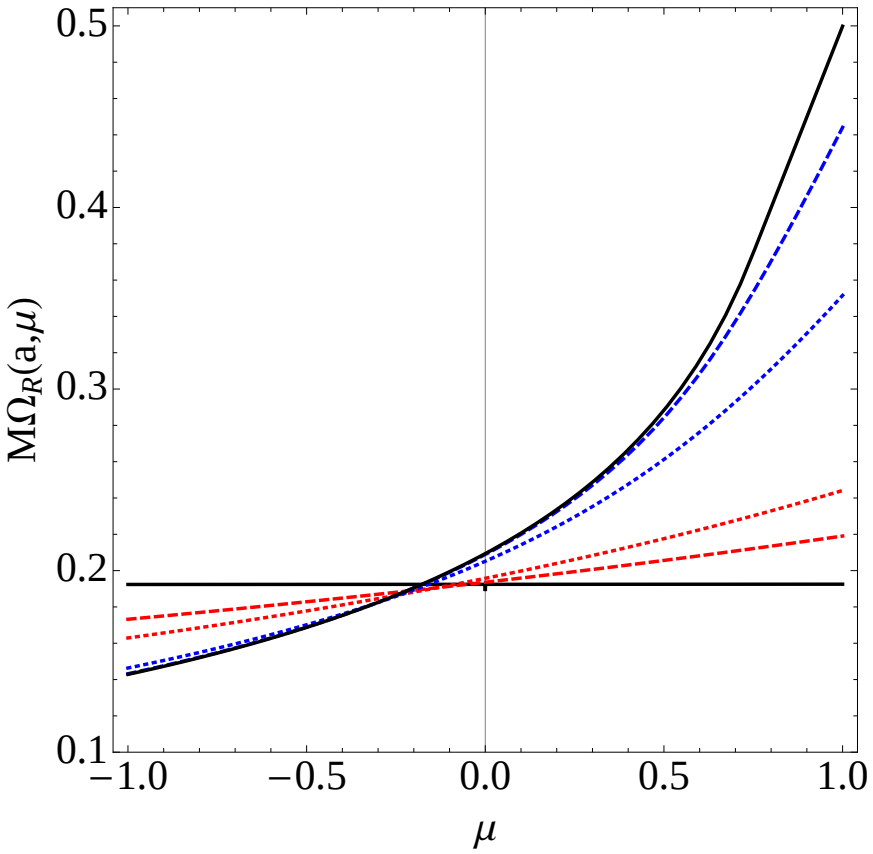

Figure 7.3: Real part of the QNM spectra from the WKB approximation. Black solid curves show Ω for $a/M = 0$ (the flat curve) and $a/M = 1$ (the curve that increases towards 0.5); red (light gray) dashed and dotted curves show $a/M = 0.3$ and 0.5, while blue (dark gray) dotted and dashed curves show $a/M = 0.9$ and 0.99.

spins have more rapidly decreasing slopes for increasing values of a/M. It is interesting to note that in the limit $a \to 1$, Ω_I becomes zero for values of μ in a finite interval $0.74 \lesssim \mu \leq 1$ (not only for $\mu = 1$ does Ω_I vanish). We will put forward an explanation for this phenomenon in Sec. 7.4, after we make connections between QNMs and wave propagation in the Kerr spacetime.

7.2.4 Accuracy of the WKB approximation

Because we calculated the leading and next-to-leading orders in the WKB approximation to ω_R, we expect that the relative error for increasing L should scale as $O(1/L^2)$. For the imaginary part, we computed only the leading-order expression, and we would expect that the relative error might scale as $O(1/L)$. In addition, because at this order of approximation, we do not account for the spin of the wave, we anticipate that the error for the gravitational modes may be larger than those for scalar modes. In Figs. 7.6–7.9, we confirm most of these expectations, but we find the somewhat unexpected result that the relative error for the imaginary part also scales as $O(1/L^2)$.

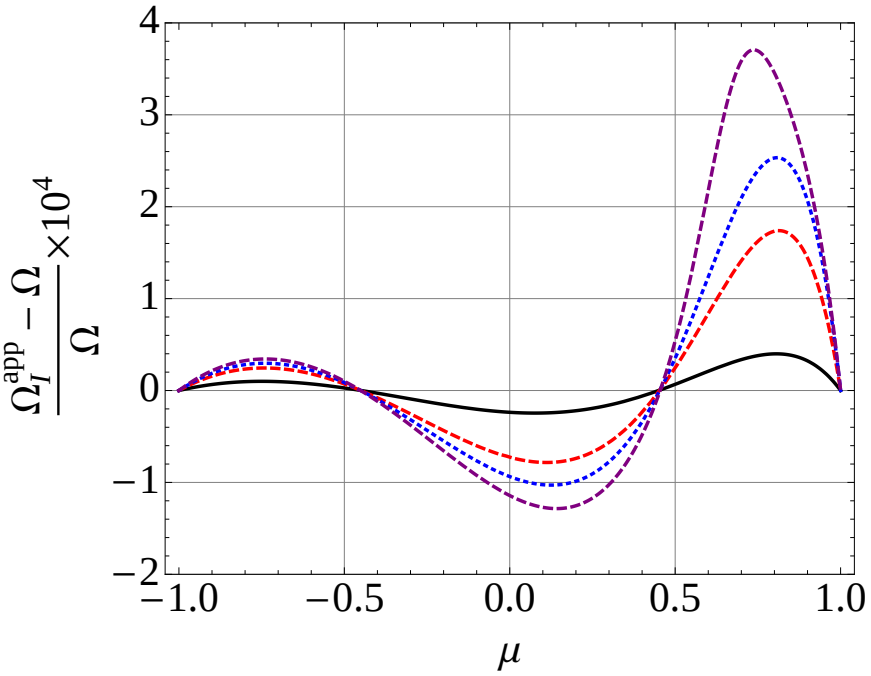

Figure 7.4: Difference in $\Omega_I(a,\mu)$ [Eq. (7.42)] from using the approximate formula for A_{lm} [Eq. (7.31a)] rather than the exact formula. Here $a/M = 0.7$, 0.9, 0.95, and 0.99 correspond to black solid, red dashed, blue dotted, and purple long-dashed curves, respectively. We scale the quantity plotted along the vertical axis by 10^4 in this figure.

In Fig. 7.6, we compare the WKB approximation to ω_R with numerical computations of the $s = 2$, gravitational-wave, quasinormal-mode spectra; specifically, we plot the fractional error against $\mu = m/L$, for $l = 2, 3, \ldots, 14$, and for black holes of spins $a/M = 0.3$, 0.5, 0.9, and 0.95. The relative error clearly converges to $O(L^2)$. Even for $l = 2$, the relative error tends to be $\lesssim 30\%$, and at $l \geq 3$ the relative error stays below $\sim 1.5L^{-2}$ (this means error is $\lesssim 10\%$ for $l = 3$ and higher).

In Fig. 7.7, we compare the WKB spectra with $s = 0$ scalar quasinormal-mode spectra, for the same values of l and the same black-hole spins. We find a much better agreement. For all $l \geq 2$ modes, the relative error stays below $4 \times 10^{-2}L^{-2}$. This suggests that coupling between the spin of the wave (i.e., its tensor polarization) and the background curvature of the Kerr black hole is the main source of error in our WKB approximation.

In Figs. 7.8 and 7.9, we perform the same comparisons as in Figs. 7.6 and 7.7 for the imaginary part of frequency. Surprisingly, we find that for both $s = 0$ and 2, the relative error in ω_I is $O(L^{-2})$. For $s = 0$, the relative error is $\lesssim 6 \times 10^{-2}L^{-2}$, while for $s = 2$, the error is $\lesssim L^{-2}$.

With this comparison, we conclude our direct calculation of the QNM spectrum by WKB techniques. We will discuss additional features of the QNM spectrum in Sec. 7.4, but before doing so, we will develop a geometric interpretation of our WKB results. Doing so will help us to develop more intuition about our WKB expressions.

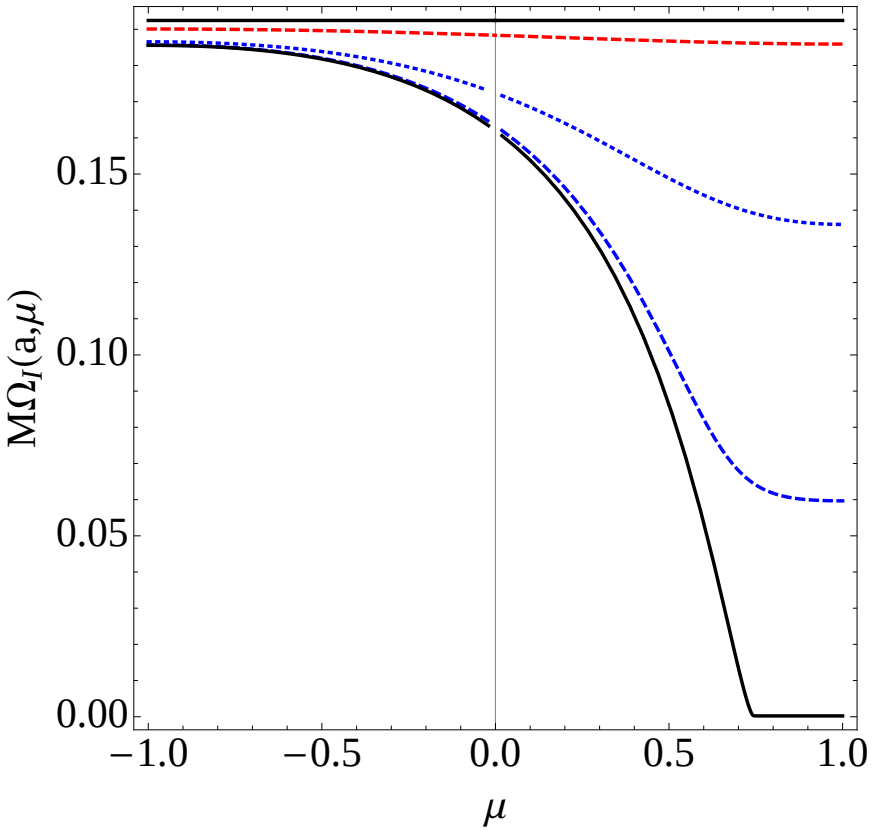

Figure 7.5: Imaginary part of the QNM spectrum computed in the WKB approximation. Black solid curves show Ω_I for $a/M = 0$ (again the flat curve) and $a/M = 1$ the curve that decreases and heads to zero. The red dashed curve shows $a/M = 0.5$, while blue dotted and dashed curves show $a/M = 0.9$ and 0.99, respectively. For $a/M = 1$, modes with $\mu \gtrsim 0.74$ approach zero (modes that do no decay), while others still decay.

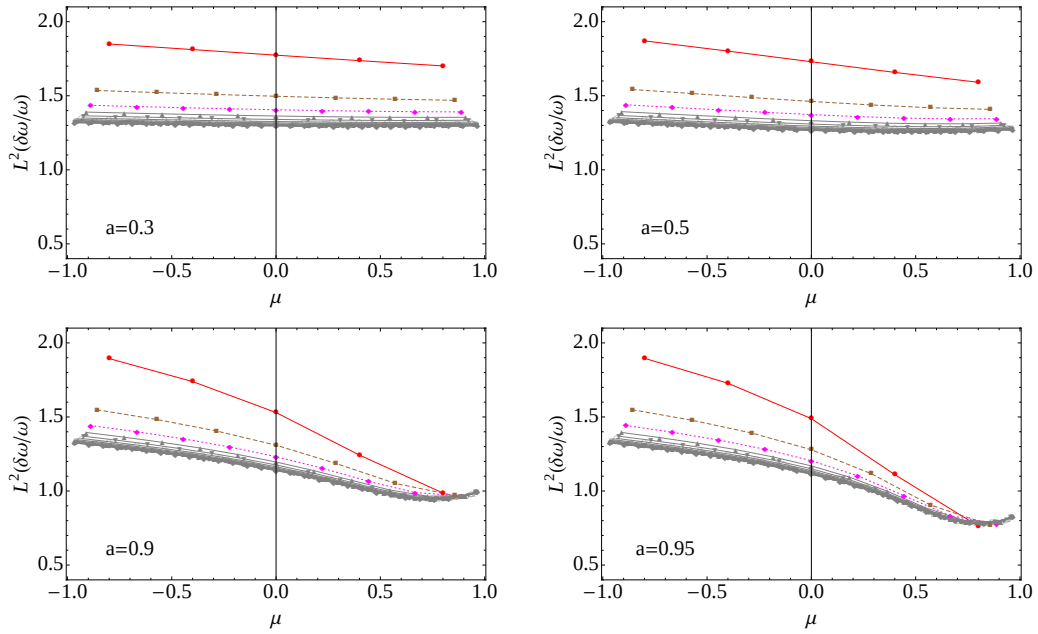

Figure 7.6: Fractional error, $\delta\omega_R/\omega_R$, of the WKB approximation to the $s = 2$, gravitational-wave, quasinormal-mode spectrum, multiplied by L^2. The four panels correspond to four different spins which (going clockwise from the top left) are $a/M = 0.3$, 0.5, 0.95, and 0.9. Errors for $l = 2, 3, 4$ are highlighted as red solid, brown dashed, and pink dotted lines, while the rest ($l = 5, \ldots, 14$) are shown in gray. This shows that the relative error approaches the $O(1/L^2)$ scaling quite quickly.

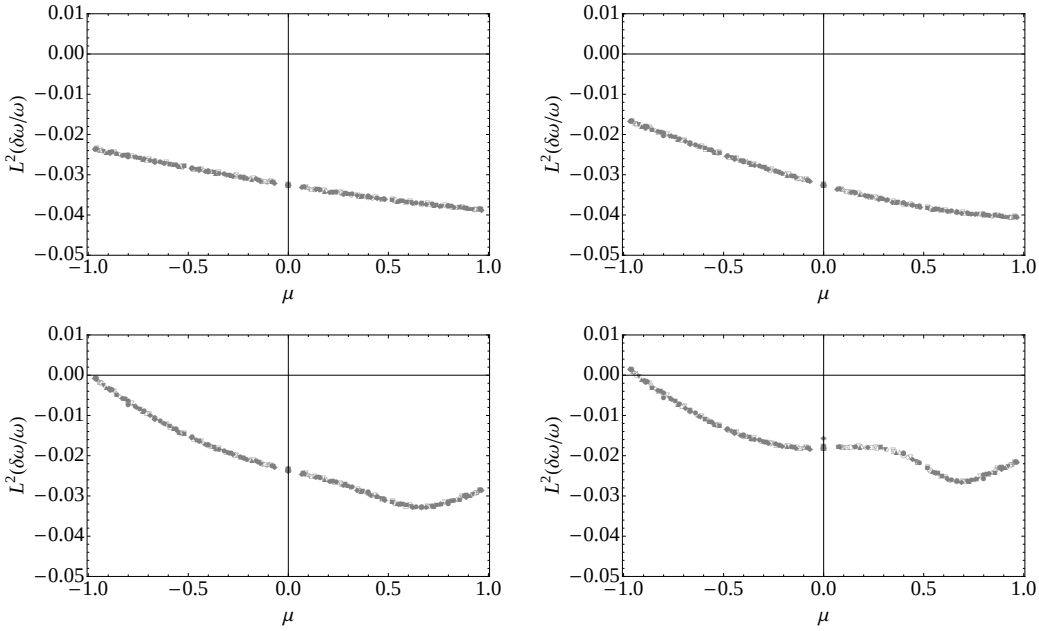

Figure 7.7: Fractional error, $\delta\omega_R/\omega_R$, of the WKB approximation to the $s = 0$, scalar-wave, quasinormal-mode spectrum, again scaled by L^2. The four panels correspond to the same four spins in Fig. 7.6. The points shown in the four panels are for values of l in the range $l = 2, 3, \ldots, 14$. Because all values of l nearly lie on the same curve, the relative error has converged at an order $O(1/L^2)$ even for very low l. The overall error is also significantly lower than that for the $s = 2$ modes.

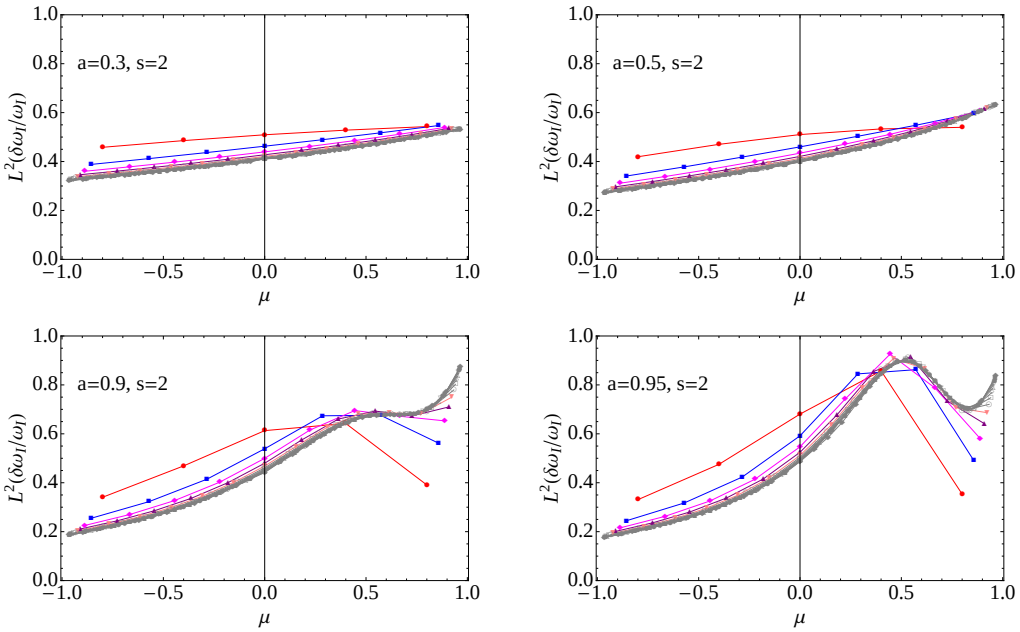

Figure 7.8: Fractional error, $\delta\omega_I/\omega_I$, of the WKB approximation to the $s = 2$, gravitational-wave, quasinormal-mode spectrum, also scaled by L^2. The panels and the curves are plotted in the same way as in Fig. 7.6, and the error scales similarly.

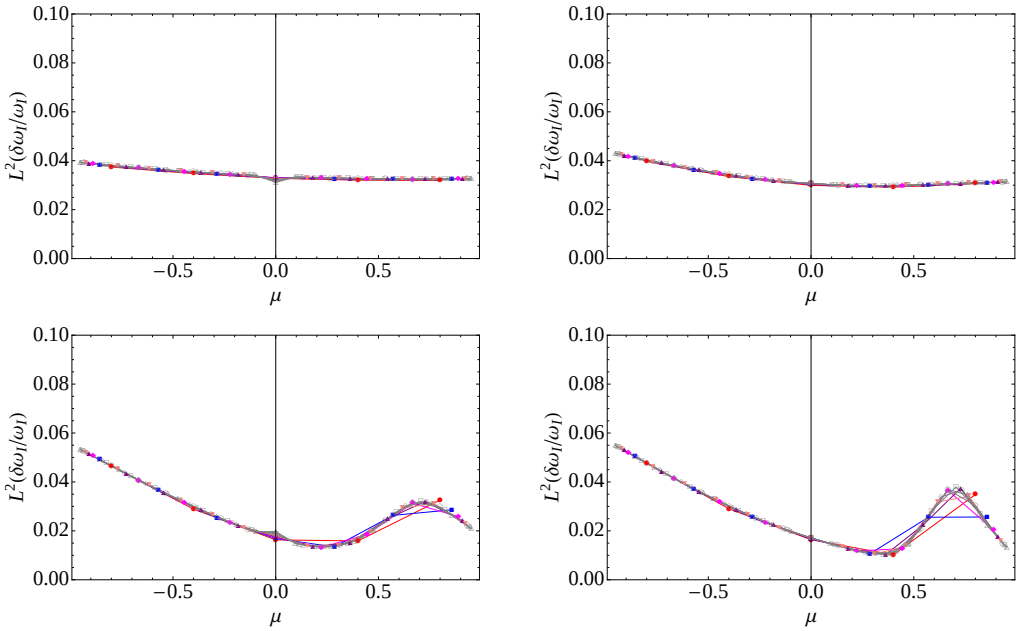

Figure 7.9: Fractional error, $\delta\omega_I/\omega_I$, of the WKB approximation to the $s = 0$, scalar-wave, quasinormal-mode spectrum, again multiplied by L^2. The four panels and the points are shown in the same way as in Fig. 7.7, and there is a similar rapid convergence of the error.

7.3 Geometric Optics in the Kerr Spacetime

In this section, we first briefly review the formalism of geometric optics, which describes the propagation of waves with reduced wavelengths $\lambda\!\!\!^{-}$ that are much shorter than the spacetime radius of curvature, R, and the size of the phase front, $\mathcal{L}$. In the geometric-optics approximation, the phase of the waves remains constant along null geodesics (rays), while the amplitude can be expressed in terms of the expansion and contraction of the cross-sectional area of bundles of null rays. We will then specialize the geometric-optics formalism to the Kerr spacetime, and we will write down the most general form of propagating waves in the geometric-optics approximation. Using the Hamilton-Jacobi method, we see that the waves' motion can be related to the null geodesics in the spacetime. By applying boundary conditions to the approximate wave, we obtain expressions for the quasinormal-mode waveforms and their corresponding complex frequency spectra and angular separation constants, in the eikonal limit.

7.3.1 Geometric optics: general theory

Here we briefly review the geometric-optics approximation to scalar-wave propagation (see, e.g., Section 22.5 of Ref. [35] for details). A massless scalar wave u propagating in curved spacetime satisfies the wave equation

$$g^{\mu\nu}\nabla_\mu\nabla_\nu u = 0\,. \tag{7.44}$$

If we write

$$u = Ae^{i\Phi}\,, \tag{7.45}$$

then at leading order in $\lambda\!\!\!^{-}/\mathcal{L}$, we have

$$g^{\mu\nu}k_\mu k_\nu = 0\,, \quad k_\mu \equiv \partial_\mu\Phi\,, \tag{7.46}$$

while at next-to-leading order,

$$2k^\mu\partial_\mu \log A + \nabla_\mu k^\mu = 0\,. \tag{7.47}$$

Note that Eq. (7.46) also implies that k^μ is geodesic,

$$k^\mu\nabla_\mu k_\nu = k^\mu\nabla_\mu\nabla_\nu\Phi = k^\mu\nabla_\nu\nabla_\mu\Phi = k^\mu\nabla_\nu k_\mu = 0\,. \tag{7.48}$$

Equations (7.45)–(7.48) encode information about the transport of the amplitude A and phase Φ along a null geodesic (or a *ray*). The phase should be kept constant, because Eq. (7.46) states

$$k^\mu\partial_\mu\Phi = 0\,, \tag{7.49}$$

while the amplitude is transported along the ray in a manner that depends upon the propagation of neighboring rays. Because the 2D area, $\mathcal{A}$, of a small bundle of null rays around the central ray satisfies the equation

$$\nabla_\mu k^\mu = k^\mu \partial_\mu \log \mathcal{A}\,, \tag{7.50}$$

it is possible to show from Eq. (7.47) that

$$k^\mu \partial_\mu \left(\mathcal{A}^{1/2} A\right) = 0\,, \tag{7.51}$$

which implies $A \propto \mathcal{A}^{-1/2}$.

The transport equations (7.49) and (7.51) provide a way to construct a wave solution from a single ray; therefore, any solution to the wave equation (7.44) in a 4D spacetime region can be found from a three-parameter family of null rays (with smoothly varying initial positions and wave vectors) by assigning smoothly varying initial values of (Φ, A) and then transporting these values along the rays. (We use the phrase "smoothly varying" to mean that the values of (Φ, A) must change on the scale of $\mathcal{L} \gg \lambda\!\!\!^{-}$.) We note it is often convenient to divide the three-parameter family of initial positions of the null rays into two-parameter families of rays with constant initial values of Φ. The constant-Φ surfaces are the initial phase fronts, which, upon propagation along the rays, become 3D phase fronts of the globally defined wave. The more usual 2D phase fronts, at a given time, are obtained if we take a particular time slicing of the spacetime and find the 2D cross sections of the 3D phase fronts in this slicing.

The above formalism describes wave propagation up to next-to-leading order in $\mathcal{L}/\lambda\!\!\!^{-}$, which will be enough for us to build a geometric correspondence for both the real frequency, the decay rate, and the angular separation constant of QNMs in the Kerr spacetime.

7.3.2 Null geodesics in the Kerr spacetime

Now let us review the description of null geodesics in the Kerr spacetime using the Hamilton-Jacobi formalism. In general, the Hamilton-Jacobi equation states

$$g^{\mu\nu}(\partial_\mu S)(\partial_\nu S) = 0\,, \tag{7.52}$$

where $S(x^\mu)$ is called the *principal function*. For the Kerr spacetime, the Hamilton-Jacobi equation can be solved via separation of variables (see, e.g., [34]), through which the principal function can be expressed as

$$S(t, \theta, \phi, r) = S_\theta(\theta) + L_z \phi + S_r(r) - \mathcal{E} t\,, \tag{7.53}$$

where $\mathcal{E}$ and L_z are constants that are conserved because of the the timelike and axial Killing vectors of the Kerr spacetime. Physically, $\mathcal{E}$ and L_z represent the energy and z-directed specific angular momentum of the massless scalar particle. The functions $S_r(r)$ and $S_\theta(\theta)$ are given by

$$S_r(r) = \int^r \frac{\sqrt{\mathcal{R}(r')}}{\Delta(r')} dr', \qquad S_\theta(\theta) = \int^\theta \sqrt{\Theta(\theta')} d\theta' \,, \tag{7.54a}$$

where $\mathcal{R}(r)$ and $\Theta(\theta)$ are given by

$$\mathcal{R}(r) = [\mathcal{E}(r^2+a^2) - L_z a]^2 - \Delta[(L_z - a\mathcal{E})^2 + \mathcal{Q}] \,, \tag{7.54b}$$

$$\Theta(\theta) = \mathcal{Q} - \cos^2\theta (L_z^2/\sin^2\theta - a^2\mathcal{E}^2) \,, \tag{7.54c}$$

and $\Delta(r)$ is given in Eq. (7.8d). The constant $\mathcal{Q}$ is the Carter constant of the trajectory, which is a third conserved quantity along geodesics in the Kerr spacetime.

The principal function $S(x^\mu; \mathcal{E}, L_z, \mathcal{Q})$ contains information about all null geodesics; equations of motion for individual null geodesics are given by first choosing a particular set of $(\mathcal{E}, L_z, \mathcal{Q})$, and then imposing

$$\frac{\partial S}{\partial \mathcal{E}} = 0 \,, \ \frac{\partial S}{\partial L_z} = 0 \,, \ \frac{\partial S}{\partial \mathcal{Q}} = 0 \,. \tag{7.55}$$

These conditions lead to at set of first-order differential equations

$$\frac{dt}{d\lambda} = \frac{r^2+a^2}{\Delta}\left[\mathcal{E}(r^2+a^2) - L_z a\right] - a(a\mathcal{E}\sin^2\theta - L_z) \,, \tag{7.56a}$$

$$\frac{d\phi}{d\lambda} = -\left(a\mathcal{E} - \frac{L_z}{\sin^2\theta}\right) + \frac{a\left[\mathcal{E}(r^2+a^2) - L_z a\right]}{\Delta} \,, \tag{7.56b}$$

$$\frac{dr}{d\lambda} = \sqrt{\mathcal{R}}, \qquad \frac{d\theta}{d\lambda} = \sqrt{\Theta} \,, \tag{7.56c}$$

where we have defined

$$\frac{d}{d\lambda} \equiv \Sigma \frac{d}{d\zeta} \,, \quad \Sigma = r^2 + a^2\cos^2\theta \,, \tag{7.57}$$

and ζ is an affine parameter along the null geodesics.

7.3.3 Correspondence with quasinormal modes

Table 7.1: Geometric-optics correspondence between the parameters of a quasinormal mode, (ω, A_{lm}, l, and m), and the conserved quantities along geodesics, ($\mathcal{E}$, L_z, and $\mathcal{Q}$). To establish a correspondence with the next-to-leading-order, geometric-optics approximation, the geodesic quantities $\mathcal{E}$ and $\mathcal{Q}$ must be complex.

Wave Quantity	Ray Quantity	Interpretation
ω_R	$\mathcal{E}$	Wave frequency is same as energy of null ray (determined by spherical photon orbit).
m	L_z	Azimuthal quantum number corresponds to z angular momentum (quantized to get standing wave in ϕ direction).
A^R_{lm}	$\mathcal{Q} + L_z^2$	Real part of angular eigenvalue related to Carter constant (quantized to get standing wave in θ direction).
ω_I	$\gamma = -\mathcal{E}_I$	Wave decay rate is proportional to Lyapunov exponent of rays neighboring the light sphere.
A^I_{lm}	$\mathcal{Q}_I$	Nonzero because $\omega_I \neq 0$ (see Secs. 7.2.2.2 and 7.3.3.3 for further discussion).

Here we will find connection between the general set of wave solutions in the previous section, and the particular solutions that correspond to a quasinormal modes, in the geometric-optics limit. Specifically, we will look for waves that propagate outwards at infinity and down the horizon. With this correspondence, we will be able to make a geometric interpretation of our WKB results from Sec. 7.2.

7.3.3.1 Leading order: conserved quantities of rays and the real parts of quasinormal-mode parameters

It is straightforward to note that the Hamilton-Jacobi equation (7.52) is identical to the leading-order geometric-optics equations, if we identify the phase, Φ, with the principal function, S. Therefore, at leading order, we can write

$$u = e^{iS} = e^{-i\mathcal{E}t} e^{iL_z\phi} e^{\pm iS_\theta} e^{\pm iS_r} \,, \tag{7.58}$$

where we recall that the amplitude A differs from unity only at next-to-leading order (we will treat it in the next subsections). Here, we have a chosen set of conserved quantities, $(\mathcal{E}, \mathcal{Q}, L_z)$, to identify the wave we wish to connect with a quasinormal-mode solution. The region in which the wave propagates is identical to the region in which geodesics with these conserved quantities can propagate. In addition, for each point in this region, there is one (and only one) geodesic passing through it; that we have $\pm$ in front of S_θ and S_r means only that either propagation direction could be a solution to the wave equation.

Now we note that u, a scalar wave in the Kerr spacetime, must separate as in Eq. (7.6). By comparing Eq. (7.6) and Eq. (7.58), we can immediately identify that

$$\mathcal{E} = \omega_R \,. \tag{7.59}$$

Because $\mathcal{E}$ is a real quantity (the conserved energy of the null geodesic), we see that at leading order, the wave does not decay. Next, we also observe that in order for u to be consistently defined in the azimuthal direction, L_z (of the null geodesics that S describes) must be an integer. This allows us to make the second identification

$$L_z = m \,. \tag{7.60}$$

Comparing S_θ from Eq. (7.54a) and u_θ from Eqs. (7.15) and (7.10b) (focusing on one direction of θ propagation, and ignoring next-to-leading-order terms), we can also conclude that

$$\mathcal{Q} = A^R_{lm} - m^2 \,. \tag{7.61}$$

At this stage, given any set of $(\mathcal{E}, \mathcal{Q}, L_z)$, we will be able to find a wave solution that exists in the region in which the geodesics travel. Not all such sets of conserved quantities correspond to quasinormal modes, however, because they may not satisfy the correct boundary conditions of QNMs.

We will first explain the conditions on the radial motion of the geodesics that will allow these particular geodesics to correspond to a wave that satisfies outgoing and downgoing conditions at $r_* \to \pm\infty$, respectively. If the radial geodesics satisfy $\mathcal{R} > 0$ everywhere, then there will be traveling waves across the entire r_* axis, which will not satisfy the boundary conditions; if there are two disconnected regions of traveling waves, however, waves will scatter off the potential on each side, and they will also fail to satisfy the boundary conditions. The only way to satisfy the boundary conditions is to have a point r_0 at which $\mathcal{R} = 0$ and $\mathcal{R}' = 0$, in which case there will be a family of geodesics on each side of $r = r_0$ (with each member a *homoclinic orbit* which has $r \to r_0$ on one end) and a *spherical orbit* with constant $r = r_0$. The corresponding wave has zero radial spatial frequency at $r = r_0$, and this frequency increases towards $r < r_0$ and decreases towards $r > r_0$. Noting that

$$\mathcal{R} = V^r \left(r^2 + a^2\right)^2 , \tag{7.62}$$

the condition

$$\mathcal{R} = \mathcal{R}' = 0 \tag{7.63}$$

is the same as the condition, Eq. (7.35), which determines ω_R in terms of L and m in the WKB approximation. It is worth mentioning that although the condition of Eq. (7.63) imposed on $(\mathcal{E}, \mathcal{Q}, L_z)$ can be interpreted most easily as the condition for a spherical photon orbit, the wave function for the quasinormal mode we are considering is *not* localized around that orbit. The wave function at leading order, in fact, has a constant magnitude at every location that homoclinic orbits reach (i.e., the entire r axis). We will derive the amplitude corrections in the next section.

The quantization of the frequency ω_R in terms of the multipolar indices l and m arises from the quantization of the motion in the angular directions. For the azimuthal direction, it is easy to see that for the wave function to be single-valued, we need to impose $L_z = m \in \mathbb{Z}$. For the θ direction, we note that

$$\Theta = V^\theta \sin^2\theta , \tag{7.64}$$

and the θ-quantization condition for the wave, Eq. (7.17), is

$$\int_{\theta_-}^{\theta_+} \sqrt{\Theta}\, d\theta = (L - |m|)\pi . \tag{7.65}$$

This corresponds to the Bohr-Sommerfeld condition for a particle moving in a potential given by Θ.

Consequently, the condition for a standing wave along the θ direction (at leading order) is equivalent to

$$\mathcal{Q} = A_{lm}(\omega_R a) - m^2 \approx L^2 - m^2 - \frac{a^2\omega_R^2}{2}\left[1 - \frac{m^2}{L^2}\right] . \tag{7.66}$$

In summary, we connected the QNM's wave function to the Hamilton-Jacobi principal function of homoclinic null geodesics (at leading order). These geodesics have the same energy, Carter constant, and z-component of its angular momentum as a spherical photon orbit; however only spherical orbits with *quantized* Carter constants and z-angular momenta correspond to quasinormal modes. In Table 7.1, we summarize our geometric-optics correspondence; so far we have identified the first three entries on the table. We can find the next two correspondences by investigating next-to-leading-order geometric optics in the next part.

7.3.3.2 Next-to-leading order: radial amplitude corrections and the imaginary part of the frequency

We showed in the previous part that the conserved quantities of a spherical photon orbit, $(\mathcal{E}, \mathcal{Q}, L_z)$, correspond simply to the real parts of the quasinormal-mode parameters, (ω_R, A^R_{lm}, m), which are the leading-order quantities of a quasinormal mode. Here, we will show that the behavior of the homoclinic orbits—namely, how the orbits propagate away from the spherical orbit, and how they move between $\theta_\pm$—reveals the spatiotemporal variation of the wave (i.e, the decay rate and the shape of its wave function in space). In Fig. 7.10, we plot the trajectory of a particular series of homoclinic orbits on the r-θ plane, to which we will refer at several points in the discussion below.

With the appropriate values of $(\mathcal{E}, \mathcal{Q}, L_z)$, the function u in Eq. (7.58) solves the wave equation to leading order and satisfies the required boundary conditions. To recover the decaying behavior of quasinormal modes, however, we make corrections to the amplitude of the wave, which appear at next-to-leading order in the geometric-optics approximation. Because of symmetry, there should not be any correction to the amplitude in the ϕ direction, and the correction in the t direction should be a simple decay; therefore, we write

$$u = A\exp(iS) = \underbrace{e^{-\gamma t}A_r(r)A_\theta(\theta)}_{A(t,r,\theta)}\, e^{-i\mathcal{E}t}e^{iL_z\phi}e^{\pm iS_\theta}e^{\pm iS_r} . \tag{7.67}$$

This general expression contains four possible directions that the wave could be propagating: the $\pm\theta$ direction and the $\pm r$ direction (depending on the signs in front of S_r and S_θ). Because the boundary conditions require that the waves propagate towards $r_* \to +\infty$ for $r > r_0$ and $r_* \to -\infty$ for $r < r_0$, the sign in front of S_r should be positive for $r > r_0$ and negative for $r < r_0$. For θ motion, however, we insist that both directions (signs) be present, because a quasinormal mode is a standing wave in

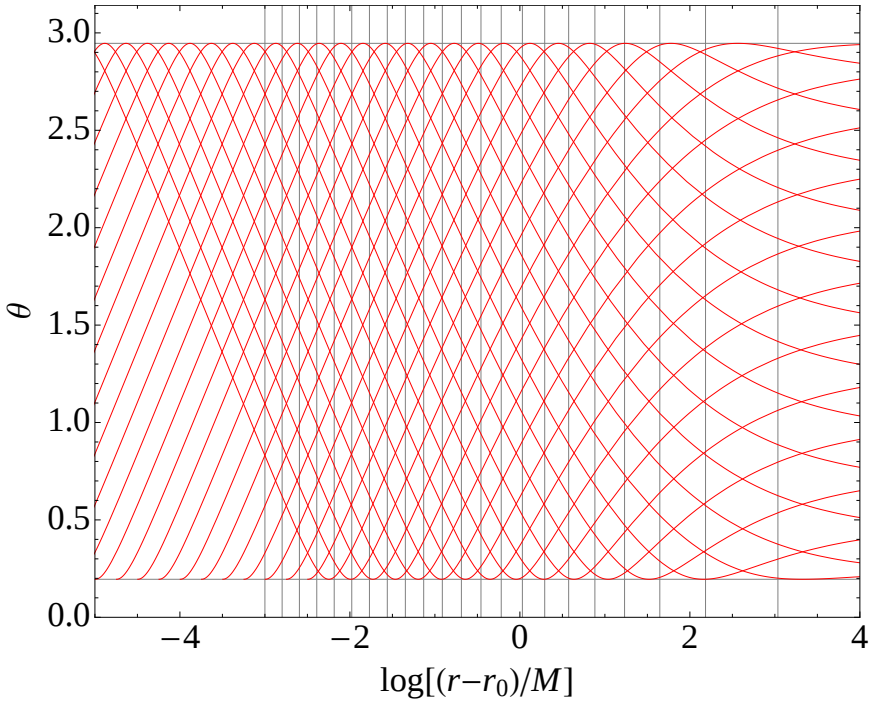

Figure 7.10: Schematic plot of trajectories in the r-θ plane of homoclinic orbits outside of the peak of the potential (specifically for a black hole with spin $a/M = 0.7$ and a photon orbit with radius $r_0/M = 2.584$). The two horizontal grid lines mark the turning points, $\theta = \theta_\pm$; between these turning points, there are two homoclinic orbits passing through every point, while at turning points only one orbit passes through. Vertical grid lines indicate when the value of parameter λ has changed along the orbit by (an arbitrarily chosen value) $\Delta\lambda = 0.046M$. Near the spherical photon orbit, each homoclinic orbit undergoes an infinite number of periodic oscillations in θ while $r - r_0$ is growing exponentially as a function of λ.

the θ direction. Focusing on $r > r_0$, we write

$$\begin{aligned} u &= e^{-\gamma t} A_r(r) \left[A_\theta^+ e^{iS_\theta} + A_\theta^- e^{-iS_\theta} \right] e^{-i\mathcal{E}t + iL_z\phi + iS_r} \\ &\equiv u_+ + u_- \,. \end{aligned} \tag{7.68}$$

We will next require that both u_+ and u_- satisfy the wave equation to next-to-leading order, separately. By explicitly computing Eq. (7.47) (or $A\sqrt{\mathcal{A}} = \text{const}$) in the Kerr spacetime, we find the amplitude satisfies the relation

$$\Sigma \frac{d\log A}{d\zeta} = -\frac{1}{2}\left[\partial_r(\Delta(r)\partial_r S_r) + \frac{1}{\sin\theta}\partial_\theta(\sin\theta\partial_\theta S_\theta) \right] . \tag{7.69}$$

Here ζ is an affine parameter along the geodesic specified by $(\mathcal{E}, \mathcal{Q}, \mathcal{L}_z)$. If we use the parameter λ

defined by $d/d\lambda = \Sigma d/d\zeta$ then we can separate the left-hand side of the equation as

$$\Sigma \frac{d\log A}{d\zeta} = \frac{d}{d\lambda}\log A_r(r) + \frac{d}{d\lambda}\log A_\theta(\theta) - \gamma\frac{dt}{d\lambda}\,. \tag{7.70}$$

Because the right-hand side of Eq. (7.56a) for $dt/d\lambda$, separates into a piece that depends only upon r and one that depends only upon θ, we will write Eq. (7.56a) schematically as

$$\frac{dt}{d\lambda} = \bar{\dot{t}} + \tilde{\dot{t}}\,, \tag{7.71}$$

where $\bar{\dot{t}}$ is only a function of r and $\tilde{\dot{t}}$ is only a function of θ. Unlike in Eq. (7.56a), we will require that $\tilde{\dot{t}}$ average to zero when integrating over λ for half a period of motion in the θ direction (i.e., from θ_- to θ_+). We can ensure this condition is satisfied by subtracting an appropriate constant from $\tilde{\dot{t}}$ and adding it to $\bar{\dot{t}}$. Combining Eqs. (7.69)–(7.71) and performing a separation of variables, we obtain

$$\sqrt{\mathcal{R}}\frac{d\log A_r}{dr} - \gamma\bar{\dot{t}} = -\frac{\mathcal{R}'}{4\sqrt{\mathcal{R}}}\,, \tag{7.72a}$$

$$\sqrt{\Theta}\frac{d\log A_\theta^\pm}{d\theta} \mp \gamma\tilde{\dot{t}} = -\frac{1}{2\sin\theta}(\sqrt{\Theta}\sin\theta)'\,, \tag{7.72b}$$

where a prime denotes a derivative with respect to r for functions of r only, and a derivative with respect to θ for functions of θ only (whether it is a θ or r derivative should be clear from the context). While it might at first seem possible to add a constant to the definition of $\bar{\dot{t}}$, and subtract it from $\tilde{\dot{t}}$ and still have both u_+ and u_- satisfy the next-to-leading order geometric optics, because we have already chosen to have $\tilde{\dot{t}}$ average to zero,

$$\int_{\theta_-}^{\theta_+} \gamma\tilde{\dot{t}}\frac{d\theta}{\sqrt{\Theta}} = \int \gamma\tilde{\dot{t}}d\lambda = 0\,, \tag{7.73}$$

this separation is the only way to guarantee that $|A_\theta^\pm|$ match each other at both ends. We will discuss the angular wave function in greater detail in the next part of this section.

Let us now turn to the radial equation, from which we will be able to compute the decay rate. Close to r_0, we can expand $\mathcal{R}(r)$ to leading order as

$$\mathcal{R}(r) \approx \frac{(r-r_0)^2}{2}\mathcal{R}''(r_0)\,. \tag{7.74}$$

Substituting this result into Eq. (7.72a), we find

$$\frac{d\log A_r}{dr} = \frac{1}{r-r_0}\left[\gamma\bar{\dot{t}}\sqrt{\frac{2}{\mathcal{R}_0''}} - \frac{1}{2}\right]\,, \tag{7.75}$$

where we used the notation $\mathcal{R}_0'' \equiv \mathcal{R}''(r_0)$. For A_r to be a function that scales as $A_r \sim (r-r_0)^n$ around r_0 for some integer n (namely it scales like a well-behaved function), we need to have

$$\gamma = \left(n+\frac{1}{2}\right)\frac{\sqrt{\mathcal{R}_0''/2}}{\bar{\dot{t}}} = (n+1/2)\lim_{r\to r_0}\frac{1}{r-r_0}\frac{dr/d\lambda}{\langle dt/d\lambda\rangle_\theta}\,. \tag{7.76}$$

To arrive at the second line, we used Eq. (7.74), the fact that $dr/d\lambda = \sqrt{\mathcal{R}}$, and that $\bar{\dot{t}}$ is the part of $dt/d\lambda$ that does not vanish when averaging over one cycle of motion in the θ direction; the limit in the expression comes from the fact that the approximation in Eq. (7.74) becomes more accurate as $r \to r_0$.

The physical interpretation of the rate that multiplies $(n+1/2)$ is somewhat subtle. Because the θ motion is independent from r motion, a bundle of geodesics at the same r slightly larger than r_0, but at different locations in θ, will return to their respective initial values of θ with a slightly increased value of r after one period of motion in the θ direction. The area of this bundle increases in the process, and by Eq. 7.51, the amplitude of the wave must decay; the rate of decay is governed by the quantity that multiplies $(n+1/2)$ in Eq. (7.76).

In addition, as shown in Fig. 7.10, the homoclinic orbits do pass through an infinite number of such oscillations near r_0, because the radial motion is indefinitely slower than the θ motion as r approaches r_0. It is clear from Fig. 7.10 that

$$\frac{1}{r-r_0}\frac{\Delta r}{\Delta\lambda} = \frac{\Delta\log(r-r_0)}{\Delta\lambda} \tag{7.77}$$

approaches a constant as $r \to r_0$. By multiplying the above equation by the constant value of $(\Delta\lambda)/(\Delta t)$ over one orbit of motion in the θ direction,

$$\frac{1}{r-r_0}\frac{\Delta r}{\Delta t} = \frac{\Delta\log(r-r_0)}{\Delta t} \equiv \gamma_L \tag{7.78}$$

also approaches a constant. This is usually defined as the *Lyapunov exponent* of one-dimensional motion; here, however, we emphasize that it is defined only after averaging over entire cycle of θ motion. By comparing Eq. (7.78) with the second line of Eq. (7.76), and bearing in mind that the Lyapunov exponent is defined after averaging over one period of θ motion, one can write Eq. (7.76) as

$$\gamma = (n+\tfrac{1}{2})\gamma_L\,. \tag{7.79}$$

To put Eq. (7.76) into a form that relates more clearly to Eq. (7.42), we use the conditions on the phase function,

$$\frac{\partial S}{\partial\mathcal{E}} = 0\,, \quad \frac{\partial S}{\partial\mathcal{Q}} = 0\,, \tag{7.80}$$

which hold for any point on the trajectory of the particle. We will apply this condition to two points

on the particle's trajectory: one at (t, r, θ, ϕ) and the second at $(t + \Delta t, r + \Delta r, \theta, \phi + \Delta\phi)$, where Δt is chosen such that the particle completes a cycle in θ in this time (and it moves to a new location shifted Δr and $\Delta\phi$). Substituting in the explicit expressions for the principal function in Eqs. (7.53) and (7.54a), we find

$$\frac{\partial}{\partial \mathcal{E}}\left[\int_r^{r+\Delta r} \frac{\sqrt{\mathcal{R}(r')}}{\Delta(r')} dr' + \Delta S_\theta\right] = \Delta t \tag{7.81a}$$

$$\frac{\partial}{\partial \mathcal{Q}}\left[\int_r^{r+\Delta r} \frac{\sqrt{\mathcal{R}(r')}}{\Delta(r')} dr' + \Delta S_\theta\right] = 0\ . \tag{7.81b}$$

where we have defined

$$\Delta S_\theta \equiv 2\int_{\theta_-}^{\theta_+} \sqrt{\Theta(\theta')} d\theta' \equiv \oint \sqrt{\Theta(\theta')} d\theta'. \tag{7.82}$$

Because the change Δr is infinitesimal for r near r_0, the integrand is roughly constant, and the r-dependent part of the integral becomes the product of the integrand with Δr. Then, one can use Eq. (7.74) to write Eqs. (7.81a) and (7.81b) as

$$\frac{1}{\sqrt{2\mathcal{R}_0''}\Delta_0}\frac{\partial \mathcal{R}}{\partial \mathcal{E}}\frac{\Delta r}{r - r_0} + \frac{\partial \Delta S_\theta}{\partial \mathcal{E}} = \Delta t\,, \tag{7.83a}$$

$$\frac{1}{\sqrt{2\mathcal{R}_0''}\Delta_0}\frac{\partial \mathcal{R}}{\partial \mathcal{Q}}\frac{\Delta r}{r - r_0} + \frac{\partial \Delta S_\theta}{\partial \mathcal{Q}} = 0\,. \tag{7.83b}$$

Now, we also note that for a given fixed $L_z = m$, the angular Bohr-Sommerfeld condition in Eq. (7.65) makes $\mathcal{Q}$ a function of $\mathcal{E}$ through the condition that $\Delta S_\theta = (L - |m|)\pi$. Because ΔS_θ is a function of $\mathcal{E}$, its total derivative with respect to $\mathcal{E}$ must vanish,

$$\frac{\partial \Delta S_\theta}{\partial \mathcal{E}} + \frac{\partial \Delta S_\theta}{\partial \mathcal{Q}}\left(\frac{d\mathcal{Q}}{d\mathcal{E}}\right)_{\rm BS} = 0\,. \tag{7.84}$$

Therefore, when we multiply Eq. (7.83b) by $(d\mathcal{Q}/d\mathcal{E})_{\rm BS}$ and add it to Eq. (7.83a), we obtain the condition that

$$\frac{1}{\sqrt{2\mathcal{R}_0''}\Delta_0}\left[\frac{\partial \mathcal{R}}{\partial \mathcal{E}} + \frac{\partial \mathcal{R}}{\partial \mathcal{Q}}\left(\frac{d\mathcal{Q}}{d\mathcal{E}}\right)_{\rm BS}\right]\frac{\Delta r}{r - r_0} = \Delta t\,. \tag{7.85}$$

Combining this fact with the definition of the Lyapunov exponent in Eq. (7.78) and Eq. (7.79), we find that

$$\gamma = \left(n + \frac{1}{2}\right)\frac{\sqrt{2\mathcal{R}_0''}\Delta_0}{\left[\dfrac{\partial \mathcal{R}}{\partial \mathcal{E}} + \dfrac{\partial \mathcal{R}}{\partial \mathcal{Q}}\left(\dfrac{d\mathcal{Q}}{d\mathcal{E}}\right)_{\rm BS}\right]_{r_0}}\,, \tag{7.86}$$

where we recall that the quantities should be evaluated at r_0. Equation (7.86) is equivalent to Eq. (7.42). Note, however, that in Eq. (7.86) we explicitly highlight the dependence of $\mathcal{Q}$ on $\mathcal{E}$ through the term $(d\mathcal{Q}/d\mathcal{E})_{\rm BS}$. There is an analogous term in Eq. (7.42) from the dependence of A_{lm} on ω in the expression for the potential V^r, which we must take into account when computing

$\partial V^r/\partial\omega$; however, we did not write it out explicitly in Eq. (7.42).

Summarizing the physical interpretation of the results in this subsection, we note that the Lyapunov exponent γ_L is the rate at which the cross-sectional area of a bundle of homoclinic rays expand, when averaged over one period of motion in the θ direction in the vicinity of r_0. The spatial Killing symmetry along ϕ means the extension of the ray bundle remains the same along that direction. This, therefore, allows us to write

$$\mathcal{A} \sim e^{\gamma_L t}\,. \tag{7.87}$$

Correspondingly, the $A\sqrt{\mathcal{A}} = \text{const}$ law requires that

$$A \sim e^{-\gamma_L t/2}\,, \tag{7.88}$$

which agrees with the decay rate of the least-damped QNM. The higher decay rates given by Eq. (7.76) come from an effect related to the intrinsic expansion of the area of a phase front. More specifically, if the amplitude is already nonuniform at points with different $r - r_0$ (but same θ), then shifting the spatial locations of the nonuniform distribution gives the appearance of additional decay.

7.3.3.3 Next-to-leading order: angular amplitude corrections and the imaginary part of Carter's constant

Having found a relation in Eq. (7.72a) between the imaginary part of the energy, ω_I, and the rate of divergence of rays, we now turn to Eq. (7.72b) to understand the geometric meaning of the complex part of A_{lm}. We recall from Sec. 7.3.3.1 that $\mathcal{Q} = A^R_{lm} - m^2$, at leading order, for a real Carter constant $\mathcal{Q}$. Because A_{lm} becomes complex at next to leading order (and because m remains unchanged), if the correspondence $\mathcal{Q} = A_{lm} - m^2$ holds for a complex A_{lm}, then the Carter constant should also be complex, and its imaginary part should be equivalent to A^I_{lm}. In this part, we argue that this relationship holds.

By integrating Eq. (7.72b), we find that

$$A^{\pm}_{\theta} = \sqrt{\frac{1}{\sin\theta\sqrt{\Theta}}}\exp\left[\pm\int_{\theta_-}^{\theta}\frac{\gamma\tilde{\dot{t}}}{\sqrt{\Theta}}d\theta'\right]\,. \tag{7.89}$$

To interpret this equation, we will assume that the orbit is sufficiently close to r_0 that the change in r over the course of a period of motion in θ is negligible. Under this assumption (and with the

fact that $d\lambda = d\theta/\sqrt{\Theta}$) we can write the integral in the exponent in Eq. (7.89) as

$$\int_{\theta_-}^{\theta} \frac{\gamma\tilde{\dot{t}}}{\sqrt{\Theta}} d\theta' = \gamma \left[[t(\theta) - t(\theta_-)] - \left(\frac{\Delta t}{\Delta \lambda} \right) [\lambda(\theta) - \lambda(\theta_-)] \right] , \tag{7.90}$$

where $\Delta t/\Delta\lambda$ is the average of $dt/d\lambda$ over a cycle of θ motion. We obtain this expression by using the fact that $dt/d\lambda$ is equivalent to $\tilde{\dot{t}}$ plus a constant when r (and hence $\bar{\dot{t}}$) does not change. Because $\tilde{\dot{t}}$ has zero average (by definition) over a period of θ motion, then when written in the form above, the constant must be $(\Delta t)/(\Delta\lambda)$. We can write this average rate of change in a useful form by noting that, from Eq. (7.56a) and Eqs. (7.54b),

$$\frac{dt}{d\lambda} = \frac{1}{2\Delta} \frac{\partial \mathcal{R}}{\partial \mathcal{E}} + a^2 \mathcal{E} \cos^2\theta \, . \tag{7.91}$$

Averaging this expression over a cycle of θ motion, noting that the first term on the right-hand side is independent of θ, and using Eq. (7.54b) gives

$$\begin{aligned} \frac{\Delta t}{\Delta \lambda} &= \frac{1}{2\Delta} \frac{\partial \mathcal{R}}{\partial \mathcal{E}} + a^2 \mathcal{E} \left(\int_{\theta_-}^{\theta^+} \frac{\cos^2\theta}{\sqrt{\Theta}} d\theta \right) \left(\int_{\theta_-}^{\theta^+} \frac{d\theta}{\sqrt{\Theta}} \right)^{-1} \\ &= \frac{1}{2\Delta} \frac{\partial \mathcal{R}}{\partial \mathcal{E}} + \frac{\partial \Delta S_\theta / \partial \mathcal{E}}{2 \partial \Delta S_\theta / \partial \mathcal{Q}} = \frac{1}{2\Delta} \frac{\partial \mathcal{R}}{\partial \mathcal{E}} - \frac{1}{2} \left(\frac{d\mathcal{Q}}{d\mathcal{E}} \right)_{\rm BS} . \end{aligned} \tag{7.92}$$

In the last step we have used the Bohr-Sommerfeld condition (7.84). Also according to Eq. (7.56a) and Eq. (7.56c), we can find

$$t(\theta) - t(\theta_-) = \frac{\partial}{\partial \mathcal{E}} \int_{\theta_-}^{\theta} \sqrt{\Theta(\theta')} d\theta' + \frac{1}{2\Delta} \frac{\partial \mathcal{R}}{\partial \mathcal{E}} (\lambda(\theta) - \lambda(\theta_-)) \, , \tag{7.93a}$$

$$\lambda(\theta) - \lambda(\theta_-) = 2 \frac{\partial}{\partial \mathcal{Q}} \int_{\theta_-}^{\theta} \sqrt{\Theta(\theta')} d\theta' \, , \tag{7.93b}$$

where to derive these two equations, we can again use the fact that $d\lambda = d\theta/\sqrt{\Theta}$ and the definition of Θ; for the first we also make use of Eq. (7.91).

Finally, we insert Eqs. (7.93a), (7.93b), and (7.92) into Eq. (7.90) to find

$$\int_{\theta-}^{\theta} \frac{\gamma\tilde{\dot{t}}}{\sqrt{\Theta}} d\theta' = (-i\gamma) \left[\frac{\partial}{\partial \mathcal{E}} + \left(\frac{d\mathcal{Q}}{d\mathcal{E}} \right)_{\rm BS} \frac{\partial}{\partial \mathcal{Q}} \right] [i S_\theta(\theta)] \, . \tag{7.94}$$

Substituting Eq. (7.94) into the solution for $A_\theta^\pm$ in Eq. (7.89) gives that

$$A_\theta^\pm = \frac{\exp\left\{ (\pm i\gamma) \left[\frac{\partial}{\partial \mathcal{E}} + \left(\frac{d\mathcal{Q}}{d\mathcal{E}} \right)_{\rm BS} \frac{\partial}{\partial \mathcal{Q}} \right] [i S_\theta(\theta)] \right\}}{\sqrt{\sin\theta \sqrt{\Theta}}} \, . \tag{7.95}$$

The phase in this equation, however, is precisely the correction to the leading-order expression for

the phase $e^{iS_\theta(\theta)}$ if we allow $\mathcal{E}$ and $\mathcal{Q}$ to be complex, where their imaginary parts are given by

$$\mathrm{Im}\mathcal{E} = -\gamma = -\omega_I\,, \quad \mathrm{Im}\mathcal{Q} = \left(\frac{d\mathcal{Q}}{d\mathcal{E}}\right)_{\mathrm{BS}}(-\gamma)\,. \tag{7.96}$$

Through next-to-leading order, therefore, the θ portion of the wave is given by

$$A^+_\theta e^{iS_\theta(\theta)} + A^-_\theta e^{-iS_\theta(\theta)} = \frac{e^{iS_\theta(\theta)} + e^{-iS_\theta(\theta)}}{\sqrt{\sin\theta\sqrt{\Theta}}}\,, \tag{7.97}$$

where $\mathcal{E}$ and $\mathcal{Q}$ used in S_θ are complex.

In the geometric-optics approximation, therefore, we have shown that we can account for the amplitude corrections to the wave by allowing the conserved quantities, $\mathcal{E}$ and $\mathcal{Q}$, to be complex [with their imaginary parts given in Eq. (7.96)]. Furthermore, through the geometric-optics correspondence, and the definition of A^I_{lm} in Eq. (7.30) we can confirm that $A^I_{lm} = \mathcal{Q}_I$; therefore, the relationship

$$\mathcal{Q} = A_{lm} - m^2\,, \tag{7.98}$$

is true for a complex $\mathcal{Q}$ and A_{lm}.

In closing, we note that at the same θ, the magnitude of the two components of the wave in Eq. (7.95) are not equal. More specifically, the integral involving $\tilde{\tilde{t}}$ makes A^+ have a larger amplitude at $\theta < \pi/2$ and a smaller amplitude at $\theta > \pi/2$; A^- has the opposite profile. Therefore, the net wave function remains symmetric about $\theta = \pi/2$.

7.4 Features of the Spectra of Kerr Black Holes

In this section, we will use the WKB formula and the geometric-optics correspondence in the first two sections of this paper to explain several aspects of the quasinormal-mode spectrum of Kerr black holes. Specifically, we will explain the absence of damping for a significant fraction of modes of extremal Kerr holes. We will also decompose the frequency into orbital and precessional parts and explain a degeneracy in the spectra of Kerr holes in terms of a rational relation of these frequencies when the corresponding photon orbits close.

7.4.1 Spherical photon orbits and extremal Kerr black holes

We will first review the properties of spherical photon orbits. These orbits can be found by setting $\mathcal{R}(r) = \mathcal{R}'(r) = 0$ (see, e.g., [34]), and their conserved quantities are fixed by the radius of the orbit

r and the spin of the black hole a to be

$$\mathcal{Q}/\mathcal{E}^2 = -\frac{r^3(r^3 - 6Mr^2 + 9M^2r - 4a^2M)}{a^2(r-M)^2} \ , \tag{7.99a}$$

$$L_z/\mathcal{E} = -\frac{r^3 - 3Mr^2 + a^2r + a^2M}{a(r-M)} \, . \tag{7.99b}$$

We will next discuss additional features of these orbits.

For a given spin parameter a, there is a unique spherical photon orbit with parameters $(\mathcal{E}, L_z, \mathcal{Q})$ for any radius between the outermost and innermost photon orbits (the retrograde and prograde equatorial photon orbits). Their radii (which we denote r_1 for retrograde and r_2 for prograde orbits) are given by

$$r_1 = 2M\left[1 + \cos\left(\frac{2}{3}\arccos\left(-\frac{|a|}{M}\right)\right)\right] \ , \tag{7.100a}$$

$$r_2 = 2M\left[1 + \cos\left(\frac{2}{3}\arccos\left(\frac{|a|}{M}\right)\right)\right] \, . \tag{7.100b}$$

At each $r_1 \leq r \leq r_2$, the spherical orbit's inclination angle reaches a maximum and minimum of $\theta_\pm$ (at which $\Theta = 0$). These angles are given by

$$\cos^2\theta_\pm = \frac{\left[2\sqrt{M\Delta(2r^3 - 3Mr^2 + Ma^2)} - (r^3 - 3M^2r + 2Ma^2)\right]r}{a^2(r-M)^2} \, , \tag{7.101}$$

which are equivalent to the turning points of the integral (7.17) (and, therefore, we use the same symbols for these angles).

Using the geometric-optics correspondence between $(\mathcal{E}, L_z, \mathcal{Q})$ and $(\Omega_R, \mu, \alpha^R_{lm})$, we see that equatorial orbits at r_1 and r_2 corresponds to modes with $\mu = -1$ and $+1$, respectively, or modes with $m = \pm l$ and $l \gg 1$ (strictly speaking, though, $\mu = m/(l+1/2)$ never precisely reaches ± 1). We can also relate r_p, the real root of Eq. (7.40), to the polar orbit and modes with $m = 0$. For orbits between the equatorial and polar ones, we can use Eqs. (7.36a) and (7.36b) to obtain a μ between -1 and $+1$. Then, only those modes that can be written as $m/(l + 1/2)$ with the allowed integer values of l and m correspond to a QNM (though the photon orbits that correspond to QNMs are a dense subset of all photon orbits).

Note in Fig. 7.11 that for $a \sim M$, a significant fraction of spherical photon orbits of different inclination angles all have nearly the same radius, $r \approx M$. Through the geometric-optics correspondence, a large fraction of modes (a finite range of values of μ) relate to this set of modes with $r \approx M$. In Fig. 7.12, we explicitly show the relation between modes characterized by μ and their corresponding spherical-photon-orbit radii (normalized by the horizon radius) for several values of a/M slightly less than unity. The radius exhibits an interesting transition between two kinds of

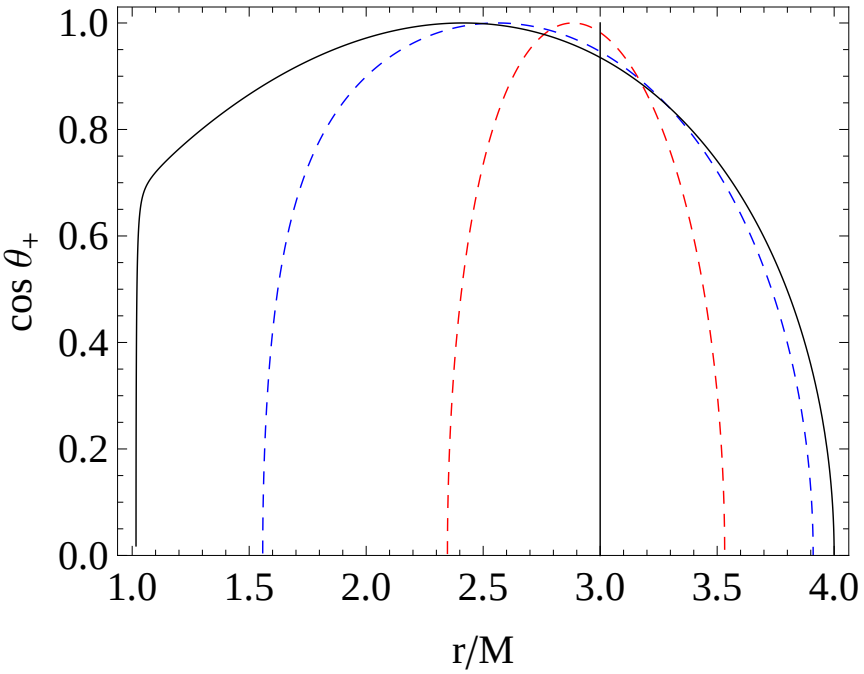

Figure 7.11: The values of r and $\cos\theta_+$ of spherical spherical orbits, for $a/M = 0$ (black, solid vertical line), 0.5 [red (light gray) dashed curve], 0.9 [blue (dark gray) dashed curve] and 0.99999 (black, solid curve). Note that for $a = 0$, all such orbits have $r = 3M$, while for $a = M$, a significant fraction reside at $r = M$.

behaviors: for $\mu > \mu_* \approx 0.744$, the value of r is very close to M (the horizon radius for an extremal Kerr black hole), and for $\mu < \mu_*$ the radii increase linearly. The orbits with $\mu > \mu_*$ have a range of inclination angles. Their $\sin\theta_\pm$ span from 0.731 (at μ_*, the most inclined orbit) to 1 (at $\mu = 1$, the prograde equatorial orbit).

For the extremal black holes, therefore, a nonzero fraction of corotating spherical photon orbits appear to coincide with the horizon in the Boyer-Lindquist coordinate system. Although the proper distance between these orbits will not vanish (see [36]), this does not seem to be a coordinate effect, because there is a definite physical change of the modes for these values of $\mu > \mu_*$. By comparing with Fig. 7.12 with Fig. 7.5, we see that these orbits also have $\Omega_I \approx 0$. A vanishing imaginary part of the frequency corresponds to a vanishing of the radial Lyapunov exponent for this entire nonzero region of spherical photon orbits. This, therefore, would lead to a curious effect for a highly spinning black hole: for perturbations with $\mu \geq \mu_*$, modes do not move away from or into the horizon very quickly. If we were to solve an initial-data problem containing these modes, we would find that they live for a long time; moreover, because these are nearly equatorial modes, we would see that the final, long-lived perturbations escape in the equatorial direction. This would imply that if we were to drive the black hole appropriately with equatorial incoming radiation, we would excite these nearly lossless modes with high amplitude (like optically exciting a resonant cavity with high finesse).

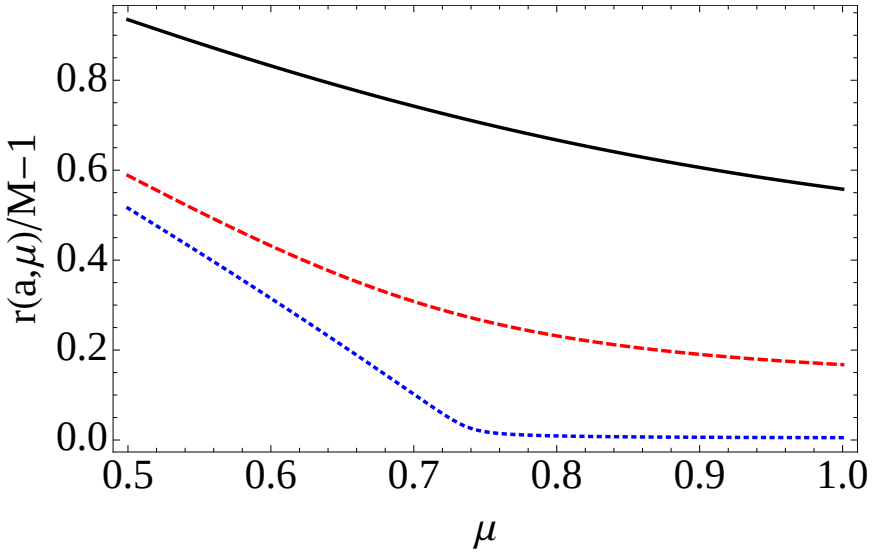

Figure 7.12: Radii of corotating spherical photon orbits as a function of μ, for $a/M = 0.9$ (black solid line), 0.99 (red dashed curve), 0.9999 (blue dotted line). For extremal Kerr black holes, a nonzero fraction of all spherical photon orbits are on the horizon.

7.4.2 A mode's orbital and precessional frequencies

In this part, we will define two frequencies associated with individual spherical photon orbits (the orbital and precessional frequencies) and understand their connection to the real part of the QNM frequency. We begin by noting that because spherical photon orbits have only two independent degrees of freedom describing their motion [see, e.g., Eq. (7.99)], the orbit can be characterized by two frequencies. The first is the θ-frequency, Ω_θ, the frequency at which the particle oscillates below and above the equatorial plane. During each θ-cycle, which takes an amount of time given by $T_\theta = 2\pi/\Omega_\theta$, the particle also moves in the azimuthal (or ϕ) direction. If this angle is 2π for a corotating orbit ($m > 0$) or -2π for a counterrotating orbit ($m < 0$), then there is no precession (and these simple, closed orbits have effectively one frequency describing their motion, as the spherical photon orbits of a Schwarzschild black hole do). The difference between the $\Delta\phi$ and $\pm 2\pi$ (its precession-free value) we will denote as the *precession angle*,

$$\Delta\phi_{\rm prec} \equiv \Delta\phi - 2\pi \,{\rm sgn}\, m\,, \tag{7.102}$$

where $\mathrm{sgn}\, m$ is the sign of m. We can also associate the rate of change of $\phi_{\rm prec}$ with a frequency,

$$\Omega_{\rm prec} \equiv \Delta\phi_{\rm prec}/T_\theta = \Delta\phi_{\rm prec}\Omega_\theta/(2\pi)\,. \tag{7.103}$$

Both T_θ and $\Delta\phi_{\rm prec}$ can be computed from geodesic motion [see the formulas for Ω_θ and $\Delta\phi_{\rm prec}$ in Eq. (7.106)].

It is possible to perform split of the real part of the QNM into two analogous frequencies. To derive this split, start from a single ray, along which the phase of the wave must be constant. Also suppose that the ray originates from θ_- and ends at θ_+ after traveling only one-half of a cycle of motion in the θ direction. During this time, the statement that the phase is unchanged is that

$$0 = -\omega_R T_\theta/2 + (L - |m|)\pi + m\Delta\phi/2\,. \tag{7.104}$$

Using (half of) Eq. (7.102), the real part of the frequency is

$$\omega_R = L\Omega_\theta(m/L) + m\Omega_{\rm prec}(m/L)\,. \tag{7.105}$$

Note that Ω_θ and $\Omega_{\rm prec}$ both depend on m/L.

More explicitly, given the orbital parameters $(\mathcal{E}, \mathcal{Q}, L_z)$, the quantities T_θ and $\Delta\phi$ can be obtained by computing

$$T_\theta = \frac{\partial}{\partial\mathcal{E}}\oint\sqrt{\Theta}d\theta + \frac{1}{2\Delta}\frac{\partial\mathcal{R}}{\partial\mathcal{E}}\oint\frac{d\theta}{\sqrt{\Theta}}\,, \tag{7.106a}$$

$$\Delta\phi = -\frac{1}{L_z}\left[1 - \frac{\partial}{\partial\log\mathcal{E}}\right]\oint\sqrt{\Theta}d\theta + \frac{1}{2\Delta}\frac{\partial\mathcal{R}}{\partial L_z}\oint\frac{d\theta}{\sqrt{\Theta}}\,, \tag{7.106b}$$

(expressions that hold for any spherical photon orbit—not simply orbits that satisfy the Bohr-Sommerfeld condition) and the two frequencies are given by

$$\Omega_\theta = 2\pi\left(\frac{\partial}{\partial\mathcal{E}}\oint\sqrt{\Theta}d\theta + \frac{1}{2\Delta}\frac{\partial\mathcal{R}}{\partial\mathcal{E}}\oint\frac{d\theta}{\sqrt{\Theta}}\right)^{-1} \tag{7.107a}$$

$$\Omega_{\rm prec} = \Omega_\theta\frac{\Delta\phi}{2\pi} - ({\rm sgn}L_z)\Omega_\theta\,. \tag{7.107b}$$

These can be expressed in terms of $(\mathcal{E}, \mathcal{Q}, L_z)$ using elliptic integrals (as was done in [37]), but we will not carry this out explicitly.

For very slowly spinning black holes, a short calculation shows that

$$\Omega_\theta \approx \frac{1}{\sqrt{27}M} = \sqrt{\frac{M}{r_0^3}}\,, \tag{7.108a}$$

$$\Omega_{\rm prec} \approx \frac{2a}{27M^2} = \frac{2S}{r_0^3}\,, \tag{7.108b}$$

where r_0 is the circular-photon-orbit radius for a Schwarzschild black hole, $r_0 = 3M$, and $S = aM$. The expression for Ω_θ is the Keplerian frequency of the spherical photon orbit, and $\Omega_{\rm prec} = 2S/r_0^3$ is the Lense-Thirring precessional frequency. In the slow-rotation limit, therefore, our formula recovers Ferrari and Mashhoon's result [9].

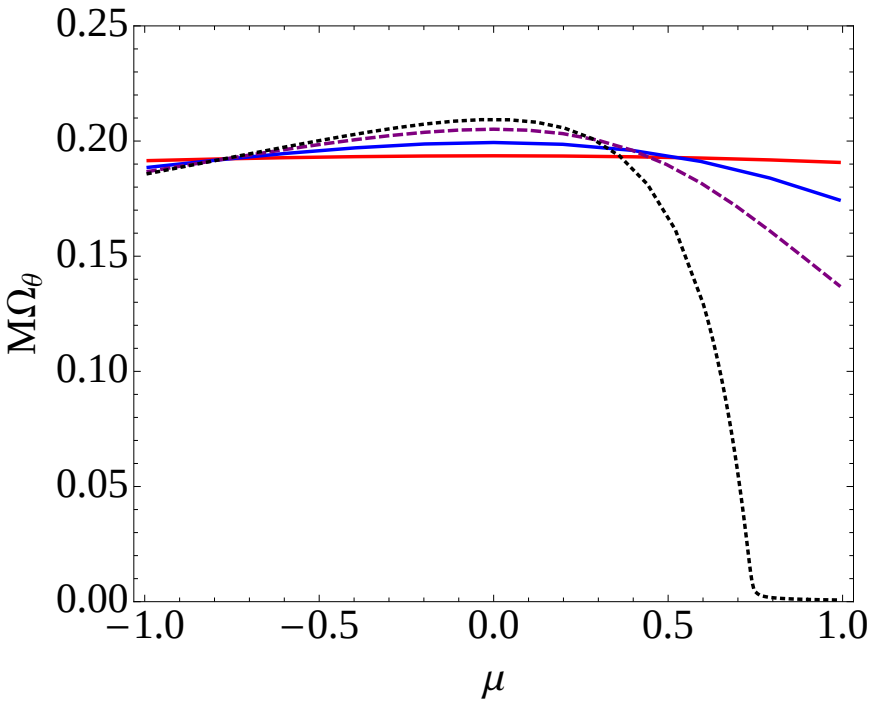

Figure 7.13: Orbital frequency, Ω_θ, plotted against μ, for $a/M = 0.3$ [red (light gray) solid curve], 0.7 [blue (dark gray) solid curve], 0.9 (purple dashed line), and 1 (black dotted line). The orbital frequency vanishes for a significant range of μ for extremal black holes.

For any value of a, we can normalize Eq. (7.105) by L, and write

$$\Omega_R(a,\mu) = \Omega_\theta(a,\mu) + \mu\Omega_{\rm prec}(a,\mu)\,. \tag{7.109}$$

In Figs. 7.13 and 7.14, we explore the two frequencies in the decomposition of Ω_R by separately plotting Ω_θ and $\Omega_{\rm prec}$, for different values of a.

For small values of a/M, Ω_θ and $\Omega_{\rm prec}$ are consistent with the constant values predicted by Eqs. (7.108a) and (7.108b). For larger values of a/M, Ω_θ does not vary much as a function of μ until $a \sim 0.7M$; for spins greater than this value, it is only for larger values of μ that Ω_θ changes significantly by decreasing from the equivalent values for $a = 0$. Finally, as $a \to M$, Ω_θ vanishes for $\mu \geq \mu_* \approx 0.744$. The precessional frequency, $\Omega_{\rm prec}$, on the other hand, monotonically increases as a function of μ even for small values of a/M; as $a \to M$, $\Omega_{\rm prec}$ grows to Ω_H at $\mu \sim \mu_*$, and stays there for all values of $\mu > \mu_*$. For $a \sim M$ and $\mu > \mu_*$, there is one additional feature worth noting: because $\Omega_\theta \sim 0$ and $\Omega_\phi \sim \Omega_H$, this gives rise to the interpretation of the mode as a ray that sticks on the horizon and corotates with the horizon at its angular frequency of Ω_H; moreover, there seems to be no restoring force along the θ direction.

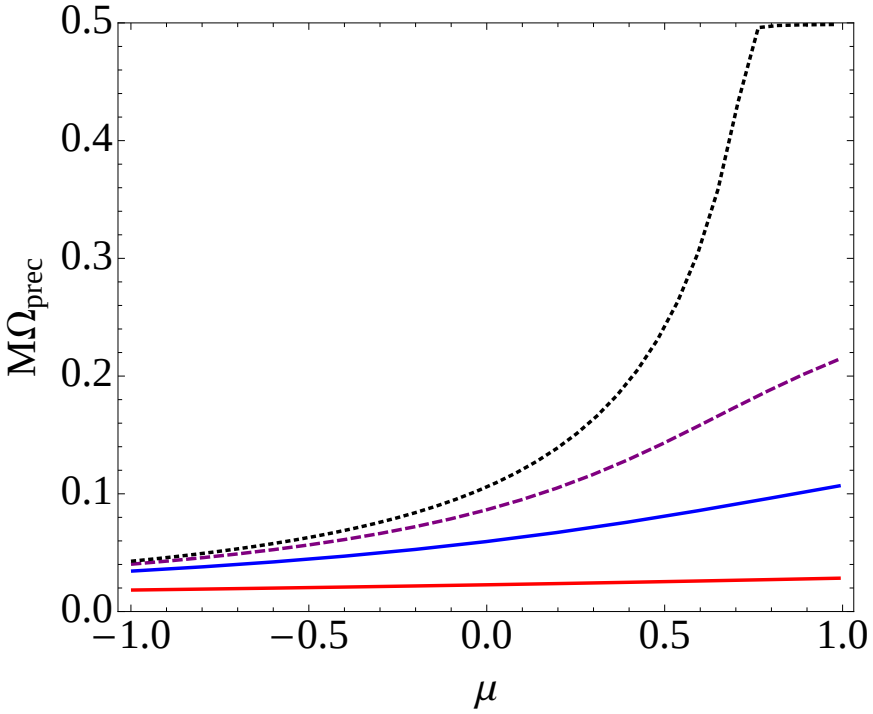

Figure 7.14: Precessional frequency, Ω_ϕ, versus μ plotted identically to those curves in Fig. 7.13 representing the same black-hole spins. The precessional frequency approaches the horizon frequency, Ω_H, for a range of values of μ for extremal black holes.

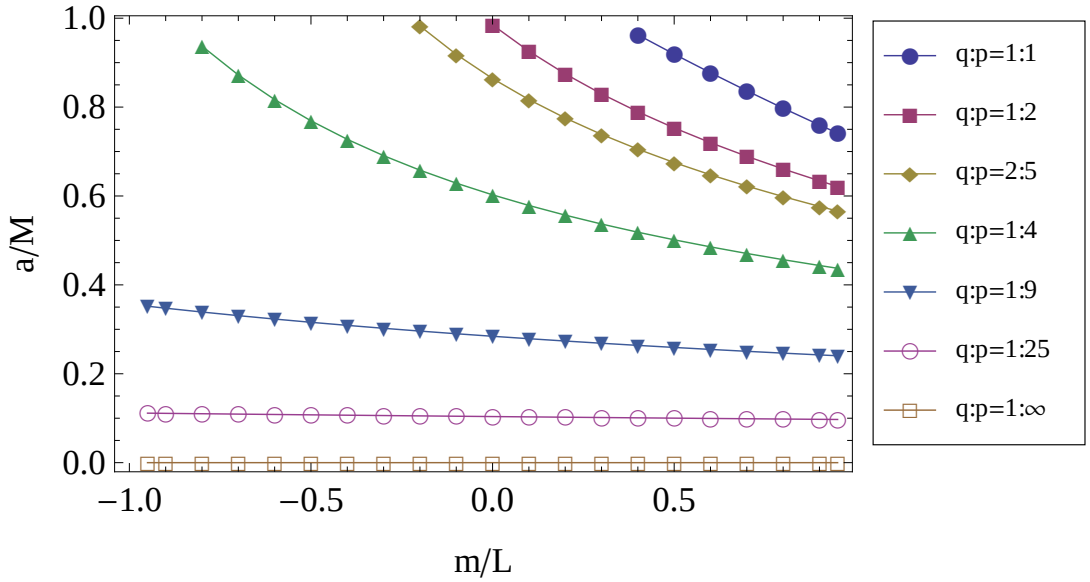

Figure 7.15: A diagram showing the spin parameters, a, and the ratios of the multipolar indexes m/L, at which the orbital and precessional frequencies have a ratio of p/q. Although we only perform our numerical calculations at a discrete set of m/L values (shown by the dots), in the eikonal limit, each set of points for a given ratio of p/q approaches a continuous curve.

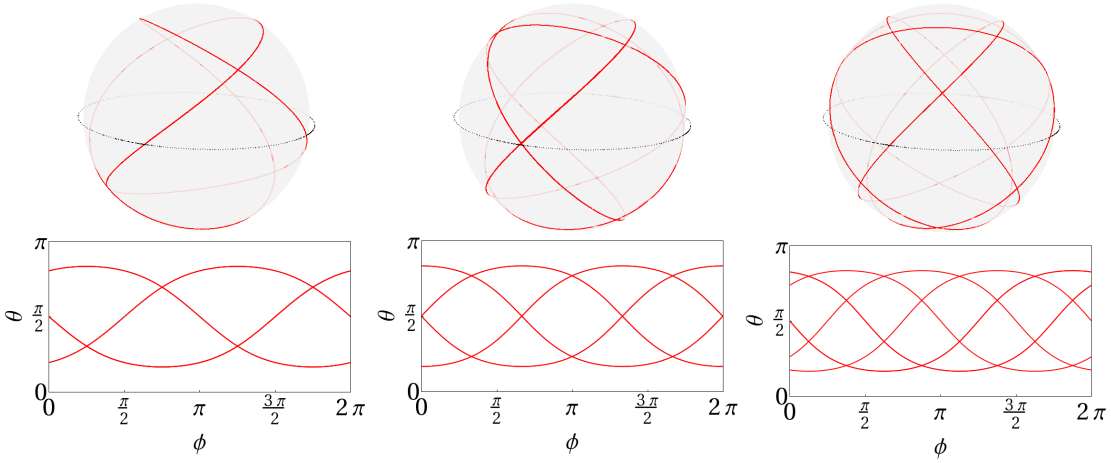

Figure 7.16: For black holes with spins $a/M = 0.768$, 0.612, and 0.502, the spherical photon orbits with $\omega_{\rm orb} = 2\omega_{\rm prec}$, on the left, $\omega_{\rm orb} = 3\omega_{\rm prec}$ in the center, and $\omega_{\rm orb} = 4\omega_{\rm prec}$ on the right, respectively. These orbits correspond to quasinormal modes in the eikonal limit with $m/L = 0.5$. The top figures show the photon orbit, the red, solid curve, on its photon sphere (represented by a transparent sphere). The dashed black line is the equatorial ($\theta = \pi/2$) plane, which was inserted for reference. The bottom figures are the same photon orbits, but plotted in the ϕ-θ plane, instead.

7.4.3 Degenerate quasinormal modes and closed spherical photon orbits

Finally, in this section, we interpret the degeneracy of QNM frequencies (of which Fig. 7.1 was an example). Recall that in that figure, for $a/M \approx 0.7$, we found pairs of modes such as $(2, 2)$ and $(3, -2)$, $(3, 2)$ and $(4, -2)$, $(4, 2)$ and $(5, -2)$, and so on, all have approximately the same frequency. For another, lower spin $a/M \approx 0.4$, pairs like $(3, 3)$ and $(4, -3)$, $(4, 3)$ and $(5, -3)$, et cetera, have approximately the same frequency.

The approximate degeneracy exists because the ratio between Ω_θ and $\Omega_{\rm prec}$ can be rational, and the photon orbits close. If for a certain mode of a black hole with spin a, with m and L, and for integers p and q,

$$q\Omega_\theta\left(a, \frac{m}{L}\right) = p\Omega_{\rm prec}\left(a, \frac{m}{L}\right) , \tag{7.110}$$

this means that there exists a closed spherical photon orbit that satisfies the conditions necessary to correspond to a QNM. Equation (7.110) implies that

$$L\Omega_\theta\left(a, \frac{m}{L}\right) + m\Omega_{\rm prec}\left(a, \frac{m}{L}\right) = (L + kq)\Omega_\theta\left(a, \frac{m}{L}\right) + (m - kp)\Omega_{\rm prec}\left(a, \frac{m}{L}\right) . \tag{7.111}$$

If Ω_θ and $\Omega_{\rm prec}$ do not change much from $\mu = m/L$ to $\mu' = (m - kp)/(L + kq)$ (either because spin is small—and therefore Ω_θ and $\Omega_{\rm prec}$ depend weakly on μ—or because $L \gg kq$ and $m \gg kp$), then

$$\omega_R^{l,m} \approx \omega_R^{l+kq,m-kp} . \tag{7.112}$$

Because Ω_I depends similarly on μ, under the same conditions,

$$\omega_I^{l,m} \approx \omega_I^{l+kq,m-kp}\,; \tag{7.113}$$

therefore, the modes are degenerate. It is also clear from Eq. (7.110) that the degeneracy happens at the same time that the corresponding orbit is closed. The three series mentioned at the beginning of the paper correspond to $p/q = 4$, 6, and 8, respectively (for $k = 1$).

7.4.3.1 Slowly spinning black holes

For $a/M \ll 1$, when Eqs. (7.108a) and (7.108b) apply, the condition for degenerate modes becomes

$$\frac{q\sqrt{27}}{2p} = \frac{a}{M} \ll 1 \tag{7.114}$$

(a statement that holds independent of μ). This implies that orbits of all inclinations close for these spins.

For these specific spins, the QNM spectrum is completely degenerate, by which we mean that all modes have the same decay rate, and all real parts of the frequencies are integer multiples of only one frequency (similar to those of a Schwarzschild black hole). Using this approximate formula to find a for the three instances of degeneracy in Fig. 7.1, we find

$$a_{4/1} \approx 0.65M, \quad a_{6/1} \approx 0.43M, \quad a_{8/1} \approx 0.32M. \tag{7.115}$$

These are not very far away from spins we found empirically.

7.4.3.2 Generic black holes

For a generic spin parameter a, we will explain degeneracies that exist around a mode with $L \gg 1$ and $|m| \gg 1$. If the condition in Eq. (7.110) holds for $p, q \ll \min(L, |m|)$, then there is a range of $|k| \ll \min(L, |m|)/\max(p, q)$ in which there is a degeneracy between all $(L+kq, m-kp)$ and (L, m). These modes must be those close to the mode of indices (L, m), because, strictly speaking, it is only the orbit corresponding to m/L which is precisely closed.

To find this degeneracy, we will search for spin parameters a for which Eq. (7.110) holds for any set of indexes (L, m) and integers (p, q) that satisfy $L, |m| \gg p, q$ (we generally either find one or zero solutions). To visualize this degeneracy, for each pair (p, q), we will mark all possible pairs of $(m/L, a)$ in a 2D plot; the values of the spins are sufficiently dense for each value of m/L that they form a smooth curve when plotted against m/L. Some of these curves are shown in Fig. 7.15. Because for a fixed p/q the degenerate spins for $a/M \lesssim 0.3$ are nearly independent of m/L, Eq. (7.114) should be an accurate prediction for spins less that that value. As a concrete illustration of the orbits

corresponding to these degenerate modes, we plot closed orbits for $m/L = 0.5$ and for $a/M \approx 0.5$, 0.61, and 0.77 in Fig. 7.16. The values of the spins agree quite well with those predicted in Fig. 7.15.

7.5 Conclusions and Discussion

In this paper, we extended the results of several earlier works [9, 27, 31, 32] to compute the quasinormal-mode frequencies and wave functions of a Kerr black hole of arbitrary astrophysical spins, in the eikonal limit ($l \gg 1$). We focused on developing a greater intuitive understanding of their behavior, but, in the process, we calculated expressions for large-l quasinormal-mode frequencies that are reasonably accurate even at low l. Specifically, we applied a WKB analysis to the system of equations defined by the angular and radial Teukolsky equations. Using a Bohr-Sommerfeld condition for the angular equation, we related the angular separation constant to the frequency; when we expanded the constraint to leading order in $a\omega/l$, we found an equally accurate and algebraically simpler relation between the frequency and angular eigenvalue. We then used a well-known WKB analysis on the radial Teukolsky equation to obtain expressions for the QNM frequencies and the angular separation constants. The accuracy of the approximate expressions for the QNM frequency are observed to be of order $O(L^{-2})$ even though we had only expected a $O(L^{-1})$ convergence for the imaginary part.

Next, we reviewed that a massless scalar wave in the leading-order, geometric-optics approximation obeys the Hamilton-Jacobi equations, which are very similar to the Teukolsky equations when $l \gg 1$. By identifying terms in the Hamilton-Jacobi equations and Teukolsky equations, we related the conserved quantities of the Hamilton-Jacobi equations to the eigenvalues of the separated Teukolsky equations. Specifically, we confirmed that the energy, angular momentum in the z direction, and Carter constant in the Hamilton-Jacobi equations correspond to the real frequency, the index m, and the angular eigenvalue minus m^2 in the Teukolsky equations, respectively. Furthermore, we found that the conditions that define a quasinormal mode in the WKB approximation are equivalent to the conditions in the geometric-optics approximation that determine a spherical photon orbit that satisfies an identical Bohr-Sommerfeld quantization condition.

By analyzing the next-to-leading-order, geometric-optics approximation, we showed that the corrections to the amplitude of the scalar wave correspond to the imaginary parts of the WKB quantities. Specifically, we saw that the imaginary part of the frequency is equal to a positive half-integer times the Lyapunov exponent averaged over a period of motion in the θ direction. The imaginary part of the angular eigenvalue is equal to the imaginary part of the Carter constant, which is, in turn, related to an amplitude correction to geometric-optics approximation to the angular function for θ.

We then applied these results to study properties of the QNM spectra of Kerr black holes. We

observed that for extremal Kerr black holes a significant fraction of the QNMs have nearly zero imaginary part (vanishing damping) and their corresponding spherical photon orbits are stuck on the horizon (in Boyer-Lindquist coordinates). We plan to study this unusual feature of extremal Kerr black holes in future work. In addition, we showed that for Kerr black holes of any spin, the modes' frequencies (in the eikonal limit) are a linear combination of the orbital and precession frequencies of the corresponding spherical photon orbits. This allows us to study an intriguing feature of the QNM spectrum: namely, when the orbital and precession frequencies are rationally related—i.e, when the spherical photon orbits are closed—then the corresponding quasinormal-mode frequencies are also degenerate.

We hope that the approximate expressions for the quasinormal-mode frequencies in this paper will prove helpful for understanding wave propagation in the Kerr spacetime. This not unreasonable to suppose, because Dolan and Ottewill have shown in [28, 26] that to calculate the Green's function analytically in the Schwarzschild spacetime, one needs to know analytical expressions for the frequency of the quasinormal modes (specifically, this comes from the fact that the frequencies of the quasinormal mode are the poles of the Green's function in the frequency domain). We, therefore, think that our approximate formulas could assist with the calculation of the Green's function in the Kerr spacetime, in future work.

7.6 Appendix: The Taylor expanded Bohr-Sommerfeld condition

The Bohr-Sommerfeld constraint (7.17) gives us a way to evaluate A_{lm} in terms of l, m, and ω; the error in this approximation scales as $1/l$. Because it is an integral equation, it is not particularly convenient to solve, and it is beneficial to have an approximate, but algebraic expression for the frequency of a QNM. With the benefit of hindsight, one can confirm through numerical calculations of exact QNM frequencies performed using Leaver's method that the parameter $a\omega/l$ is numerically a small number for all black hole spins. We can then expand the angular separation constant, A_{lm}, in a series in $a\omega/l$ as $A_{lm} = A^0_{lm} + \delta A_{lm}$, where A^0_{lm} satisfies the equation

$$\int_{\theta^0_-}^{\theta^0_+} \sqrt{A^0_{lm} - \frac{m^2}{\sin^2\theta}} = \pi\left(l + \frac{1}{2} - |m|\right) , \tag{7.116}$$

and at leading order, $\theta^0_+, \theta^0_- = \pm \arcsin[m/(l+1/2)]$. One can easily verify that the solution to this equation is the angular eigenvalue of a Schwarzschild black hole, $A^0_{lm} = (l+1/2)^2$ (note that we are assuming $l \gg 1$). Now we will compute the lowest-order perturbation in $a\omega/l$, which turns out to

be quadratic in this parameter [i.e., $(a\omega/l)^2$] below:

$$\int_{\theta^0_-}^{\theta^0_+} \frac{\delta A_{lm} + a^2\omega^2 \cos^2\theta}{\sqrt{(l+1/2)^2 - m^2/\sin^2\theta}} d\theta = 0\,. \tag{7.117}$$

The integration limits θ_+, θ_- also can be expanded in a series in $a\omega/l$, and the lowest-order terms of this series are given by θ^0_+, θ^0_-; The perturbation in θ_+, θ_- would result in some quartic corrections in $a\omega/l$ [i.e., $(a\omega/l)^4$] when we evaluate the integrals of Eqs. (7.117) and (7.116), because the integrand is of order $(a\omega/l)^2$ and the width of the correction in θ_+, θ_- are also of order $(a\omega/l)^2$. As a result, we will not need it here. Evaluating the integral in Eq. (7.117) is straightforward, and we find

$$A_{lm} = A^0_{lm} + \delta A_{lm} = l(l+1) - \frac{a^2\omega^2}{2}\left[1 - \frac{m^2}{l(l+1)}\right] \tag{7.118}$$

Interestingly, the above expression is consistent with the expansion of A_{lm} for small $a\omega$ given in [39], even in the eikonal limit, where $a\omega$ is large. The reason for this fortuitous agreement is again that for QNMs of Kerr black holes of any spin, $a\omega/l$ is small, and the expansion only involves even powers of this parameter, $(a\omega/l)^2$. Because the coefficients in the expansion of $a\omega$ scale as $1/l^k$ for even powers of $(a\omega)^k$ and $1/l^{k+1}$ for odd powers of $(a\omega)^k$, in the limit of large l, the two series actually are equivalent in the eikonal limit. In principle, one can also expand and solve Eq. (7.17) to higher orders in the parameter $a\omega/l$ and compare with the expansion in $a\omega$ in [39]; we expect that the two series should agree. This would be useful, because it would effectively let one use the small $a\omega$ expansion in the eikonal limit, where the series would, ostensibly, not be valid.

Bibliography

[1] C. V. Vishveshwara, Nature **227**, 936 (1970).

[2] K. D. Kokkotas and B. Schmidt, Living Rev. Relativity **2**, 2 (1999), http://www.livingreviews.org/lrr-1999-2.

[3] H.-P. Nollert, Classical Quantum Gravity **16**, R159 (1999).

[4] V. Ferrari and L. Gualtieri, Gen. Relativ. Gravit. **40**, 945 (2008).

[5] E. Berti, V. Cardoso, A. O. Starinets, Classical Quantum Gravity **26**, 163001 (2009).

[6] R. A. Konoplya and A. Zhidenko, Rev. Mod. Phys. **83**, 793 (2011).

[7] M. Davis, R. Ruffini, W. H. Press, and R. H. Price, Phys. Rev. Lett. **27**, 1466 (1971).

[8] S. Chandrasekhar and S. Detweiler, Proc. R. Soc. Lond. A **344**, 441 (1975).

[9] V. Ferrari and B. Mashhoon, Phys. Rev. D **30**, 295 (1984).

[10] B. F. Schutz and C. M. Will, Astrophys. J. **291**, L33 (1985).

[11] S. Iyer and C. M. Will, Phys. Rev. D **35**, 3621 (1987).

[12] E. W. Leaver, Proc. R. Soc. Lond. A **402**, 285 (1985).

[13] H.-P. Nollert, Phys. Rev. D **47**, 5253 (1993).

[14] E. W. Leaver, Phys. Rev. D **34**, 384 (1986).

[15] Y. Sun and R. H. Price, Phys. Rev. D **38**, 1040 (1988).

[16] http://www.ligo.caltech.edu/

[17] http://www.ego-gw.it/public/virgo/virgo.aspx

[18] F. Echeverria, Phys. Rev. D **40**, 3194 (1989).

[19] E. E. Flanagan, and S. A. Hughes, Phys. Rev. D **57**, 4566 (1998).

[20] A. Buonanno, G. B. Cook, and F. Pretorius, Phys. Rev. D **75**, 124018 (2007).

[21] E. Berti, V. Cardoso, J. A. Gonzalez, U. Sperhake, M. Hannam, S. Husa, and B. Brügmann, Phys. Rev. D **76**, 064034 (2007).

[22] O. Dreyer, B. Kelly, B. Krishnan, L. S. Finn, D. Garrison, and R. Lopez-Aleman, Classical Quantum Gravity **21**, 787 (2004).

[23] E. Berti, V. Cardoso, and C. M. Will, Phys. Rev. D **73**, 064030 (2006).

[24] A. Zimmerman and Y. Chen, Phys. Rev. D **84**, 084012 (2011).

[25] Y. Mino and J. Brink, Phys. Rev. D **78**, 124015 (2008).

[26] S. R. Dolan and A. C. Ottewill, Classical Quantum Gravity **26**, 225003 (2009).

[27] S. R. Dolan, Phys. Rev. D **82**, 104003 (2010).

[28] S. R. Dolan and A. C. Ottewill, Phys. Rev. D **84**, 104002 (2011).

[29] V. Cardoso, A. S. Miransa, E. Berti, H. Witek, V. T. Zanchin, Phys. Rev. D **79**, 064016 (2009).

[30] S. A. Teukolsky, Phys. Rev. Lett. **29**, 1114 (1972).

[31] K. D. Kokkotas, Classical Quantum Gravity **8**, 2217 (1991).

[32] E. Seidel and S. Iyer, Phys. Rev. D **41**, 374 (1990).

[33] S. Detweiler, Astrophys. J. **239**, 292 (1980).

[34] S. Chandrasekhar, *The Mathematical Theory of Black Holes* (Oxford University Press, Oxford, 1983).

[35] C. W. Misner, K. S. Thorne and J. A. Wheeler, *Gravitation*, (W. H. Freeman and Company, New York, 1973).

[36] J. M. Bardeen, W. H. Press, and S. A. Teukolsky, Astrophys. J. **178**, 347 (1972).

[37] E. Teo, Gen. Relativ. and Gravit. **35**, 1909 (2003).

[38] http://www.phy.olemiss.edu/ berti/qnms.html

[39] E. Berti, V. Cardoso, M. Casals, Phys. Rev. D **73**, 024013 (2006).

Chapter 8

Branching of quasinormal modes for nearly extremal Kerr black holes

---

Originally published as

Huan Yang, Fan Zhang, Aaron Zimmerman, David A. Nichols, Emanuele Berti, Yanbei Chen

Phys. Rev. D 87, 041502(R) (2013)

8.1 Introduction

Nearly extremal Kerr (NEK) black holes (BHs)—i.e., BHs for which the dimensionless angular momentum $a \approx 1$ in the geometrical units, $G = c = M = 1$, used in this paper—have drawn much attention recently. Besides the mounting evidence for fast-rotating BHs in astronomy [1], NEK BHs have considerable theoretical significance, e.g., in studies of weak cosmic censorship [2] and in calculations of black-hole entropy [3].

For extremal Kerr BHs ($a = 1$) the near-horizon geometry reduces to $\mathrm{AdS}_2 \times \mathrm{S}^2$ [4]. This observation led to the Kerr/CFT conjecture, which states that extremal Kerr BHs are dual to the chiral limit of a two-dimensional conformal field theory [5]. In the past few years the extremal Kerr spacetime and spacetimes violating the Kerr bound were shown to be unstable [6]. The stability of BHs depends on the sign of the imaginary part of their complex free vibration modes, called quasinormal modes (QNMs) [7]. Therefore the NEK QNM frequencies studied here can shed light on the onset of extremal Kerr instabilities and prove useful in quantum field theory (for example, in the calculation of two-point functions [8]).

Detweiler first used an approximation to the radial Teukolsky equation for NEK BHs (see also [9]) to show that QNMs with angular indices $l = m$ have a long decay time [10]. Using Detweiler's result,

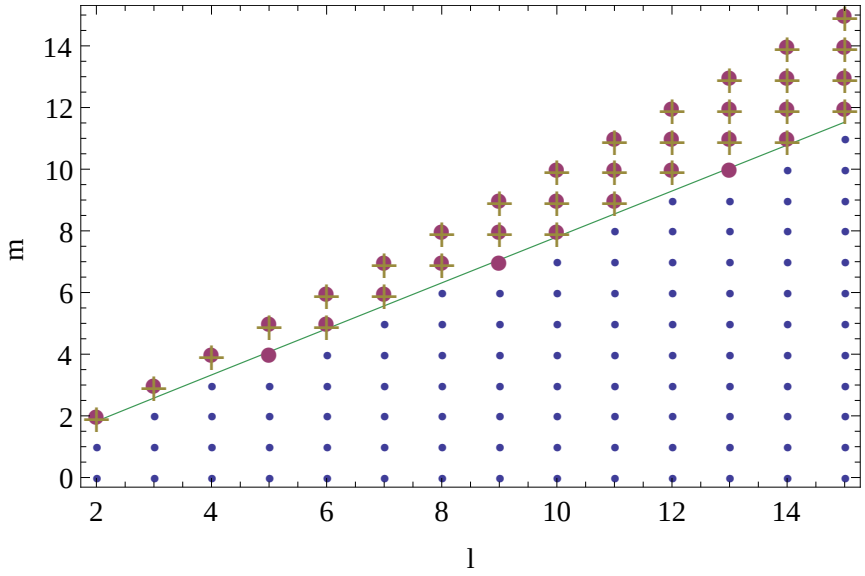

Figure 8.1: (Color online.) Phase diagram for the separation between the single- and double-branch regime for NEK BHs. Large purple dots and gold crosses correspond to (l, m) pairs with only ZDMs for perturbations with spin -2 and 0, respectively. Smaller blue dots correspond to (l, m) pairs with both ZDMs and DMs. The green line is the phase boundary, computed using the eikonal approximation.

Sasaki and Nakamura [11] calculated QNM frequencies analytically and Andersson and Glampedakis proposed long-lived emission from NEK BHs [12]. However, there remains a long-standing controversy in the literature about what set of QNMs decay slowly [13], whether long-lived radiation is possible [14], and whether the imaginary part of the QNM frequencies vanishes as $a \to 1$ (compare [11, 14] with [13]). Despite the importance of this problem, our present understanding of the QNM spectrum of NEK BHs is inconclusive.

In a recent paper [15] (i.e. Chapter 7), some of us used a WKB analysis to relate Kerr QNMs in the eikonal limit to spherical photon orbits around Kerr BHs. We pointed out that a subset of spherical photon orbits of extremal Kerr BHs reside on the horizon and that the corresponding QNMs have zero damping. This happens when the parameter $\mu \equiv m/(l + 1/2) \gtrsim \mu_c \simeq 0.74$. Hod [16] computed μ_c in the eikonal limit, finding an approximate analytical result in agreement with [15] (i.e. Chapter 7).

In this work, we will show that the NEK geometry has two distinct sets of QNMs: zero-damping modes (ZDMs) and damped modes (DMs). ZDMs are associated with the near-horizon geometry of the BH, and they exist for *all* allowed values of l and $m \geq 0$ (we classify modes using Leaver's conventions [17], but we use units in which the BH has mass $M = 1$). DMs are associated with peaks of the potential barrier; in the eikonal limit, they exist when $\mu \leq 0.74$. This implies that ZDMs and DMs coexist if $0 \leq \mu \leq 0.74$. Figure 8.1 is a "phase diagram" in QNM space, showing the regions where either the ZDMs or both the DMs and the ZDMs exist for scalar and gravitational

perturbations with $l \leq 15$. We will discuss this phase diagram further below. When the ZDMs and DMs coexist, and when the BH spin a is small, for each (l, m) there is only a single set of QNMs characterized by the overtone number n (where modes with larger n have stronger damping). For larger a, this set of QNMs appears to break into two branches. The DM branch originates from lower-overtone modes at smaller a, and its modes retain a finite decay rate as $a \to 1$. The ZDM branch originates from higher-overtone modes whose imaginary part becomes smaller than that of DMs as $a \to 1$, thereby forming the second branch. This is similar to the behavior of eigenmodes in quantum mechanics when we parametrically split a single potential well into two potential wells (cf. Fig. 8.2 below, as well as [18] for a somewhat analogous phenomenon in the theory of oscillations of ultracompact stars).

8.2 Matched expansions

For $\epsilon \equiv 1 - a \ll 1$ and $\omega - m/2 \ll 1$, the radial Teukolsky equation can be written in a self-similar form when $(r-1) \ll 1$ and in an asymptotic form (by setting $a = 1$) when $(r-1) \gg \sqrt{\epsilon}$ (cf. [9, 10, 19]). The solutions of the Teukolsky equation in these regions (hypergeometric and confluent hypergeometric functions, respectively) can be matched at $\sqrt{\epsilon} \ll (r-1) \ll 1$ to provide the following condition for QNM frequencies:

$$e^{-\pi\delta - 2i\delta\ln(m) - i\delta\ln(8\epsilon)} \frac{\Gamma^2(2i\delta)\Gamma(1/2+s-im-i\delta)}{\Gamma^2(-2i\delta)\Gamma(1/2+s-im+i\delta)} \times \frac{\Gamma(1/2-s-im-i\delta)\Gamma[1/2+i(m-\delta-\sqrt{2}\tilde{\omega})]}{\Gamma(1/2-s-im+i\delta)\Gamma[1/2+i(m+\delta-\sqrt{2}\tilde{\omega})]} = 1. \tag{8.1}$$

Here we denote the eigenvalues of the angular Teukolsky equation by ${}_sA_{lm}$, and we define $\delta^2 \equiv 7m^2/4 - (s+1/2)^2 - {}_sA_{lm}$ and $\tilde{\omega} \equiv (\omega - m\Omega_H)/\sqrt{\epsilon}$ [note that $\Omega_H = a/(r_+^2 + a^2)$ is the horizon frequency and $r_+ = 1 + \sqrt{1-a^2}$ is the horizon radius]. Scalar, electromagnetic, and gravitational perturbations correspond to spin $s = 0, -1, -2$, respectively. If we choose the conventions that $\mathcal{R}e(\delta) \geq 0$ and $\mathcal{I}m(\delta) \geq 0$ when δ^2 is positive and negative, respectively, then the left-hand side of Eq. (8.1) is usually a very small number, except when it is near the poles of the Γ-functions in the numerator. When $m \geq 0$, we can always find the solution near the poles at negative integers:

$$1/2 + i(m - \delta - \sqrt{2}\tilde{\omega}) \approx -n, \tag{8.2}$$

or

$$\omega \approx \frac{m}{2} - \frac{\delta\sqrt{\epsilon}}{\sqrt{2}} - i\left(n + \frac{1}{2}\right)\frac{\sqrt{\epsilon}}{\sqrt{2}}. \tag{8.3}$$

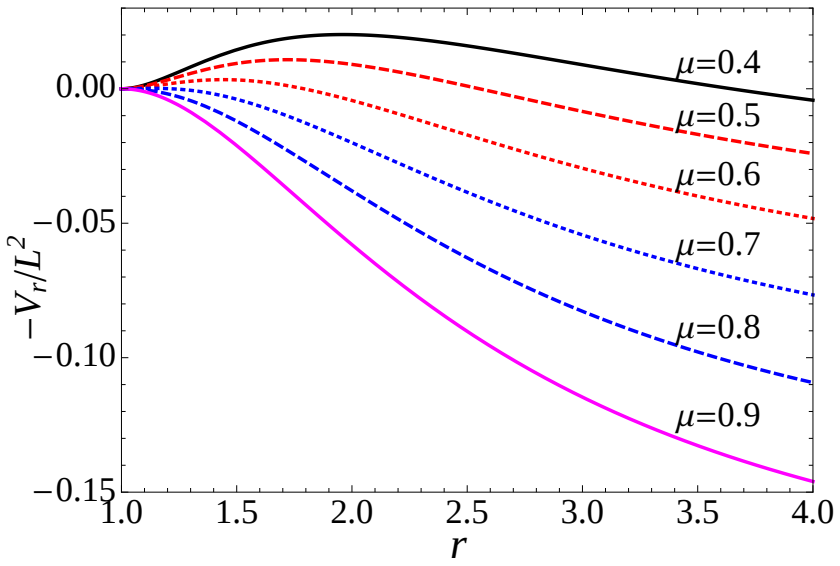

Figure 8.2: (Color online.) Plot of the potential term for $a = 1$, Eq. (8.6), for $\mu = 0.4$, 0.5, 0.6, 0.7, 0.8, and 0.9 (black-solid, red-dashed, red-dotted, blue-dotted, blue-dashed, and magenta-solid curves, respectively). The transition from single-branch to double-branch happens between $\mu = 0.7$ and $\mu = 0.8$.

Note that the overtone index n of these ZDM frequencies need not correspond precisely to the same overtone index of Kerr QNMs at lower spins. This set of solutions was first discovered by Hod [13]. The matched-expansion derivation shows that this set of modes depends on the near-horizon region of the Kerr BH. Equation (8.3) is quite accurate when $|\delta| \gg 1$, but when $|\delta| < 1$ it needs an additional correction [19]. However, the $\sqrt{\epsilon}$ scaling of the decay rate is still correct when $|\delta| < 1$. The solutions to Eq. (8.3) with $m < 0$ are those that arise from the symmetry $\omega_{l,m} = -\omega^*_{l,-m}$; there are no solutions with $m < 0$ and $\mathcal{R}e(\omega) > 0$, when $\omega - m/2$ is not small. Thus, the ZDMs only exist in the *corotating* regime $m \geq 0$.

Another set of solutions of Eq. (8.1) may exist when $\delta^2 < 0$ and $2i\delta \approx -n$, with n a positive integer. A more detailed analysis shows that, in this case, two nearly degenerate hypergeometric functions have comparable contribution to the near-horizon solution [19]. As a result, Eq. (8.1) is no longer valid when $2i\delta \approx -n$. As a consistency check, we looked for solutions with $2i\delta \approx -n$ using Leaver's method and we did not find any.

8.3 WKB analysis

The matched-expansion method assumes that $\omega \approx m/2$, but Eq. (8.1) does not hold for modes which do *not* meet this requirement (i.e., DMs). To compute these modes, we will instead use a WKB analysis in the eikonal limit $l \gg 1$. The radial Teukolsky equation when $l \gg 1$ is [15] (i.e. Chapter

7)

$$\frac{d^2u_r}{dr_*^2} + V_r u_r = \frac{d^2u_r}{dr_*^2} + \frac{K^2 - \Delta\lambda^0_{lm}}{(r^2+a^2)^2}u_r = 0\,, \tag{8.4a}$$

with

$$K = -\omega(r^2+a^2) + am, \quad \frac{d}{dr_*} \equiv \frac{\Delta}{r^2+a^2}\frac{d}{dr},$$
$$\lambda^0_{lm} = A_{lm} + a^2\omega^2 - 2am\omega, \quad \Delta = r^2 - 2r + a^2\,. \tag{8.4b}$$

We define $\omega \equiv \omega_R - i\omega_I$, and we note that the real and imaginary parts scale as $\omega_R \propto l$ and $\omega_I \propto l^0$, while the angular constant scales as $A_{lm} \propto l^2$. We only keep the leading-order terms in the eikonal limit in the following discussion (therefore all s-dependent terms are neglected, and the A_{lm} are real). In Fig. 8.2 and below, we will refer to $-V_r$ as "the potential". According to the WKB analysis and its geometric correspondence in [15] (i.e. Chapter 7), the position of the peak of the potential asymptotes the horizon as $a \to 1$ for some of the corotating modes. For this set of QNMs, one can verify that V_r'' (where primes denote derivatives with respect to r_*) scales as Δ^2; thus, the peak r_0 of the potential becomes broad as r_0 approaches the horizon. It then follows that $\omega_I \propto \sqrt{V_r''}/\partial_\omega V_r \to 0$, and $\omega_R \to m/2$ in order to satisfy $V_r(\omega_R, r_0) = 0$ for these modes. Assuming that $r_0 = 1 + c\sqrt{\epsilon}$ for the nearly extremal modes, where c is some constant, we can apply the eikonal equations in [15] (i.e. Chapter 7) and obtain

$$r_0 \approx 1 + \frac{m\sqrt{2\epsilon}}{\mathcal{F}_0},\ \omega_R \approx \frac{m}{2} - \frac{\mathcal{F}_0\sqrt{\epsilon}}{\sqrt{2}},\ \omega_I \approx \left(n + \frac{1}{2}\right)\frac{\sqrt{\epsilon}}{\sqrt{2}}\,, \tag{8.5}$$

with $\mathcal{F}_0 = \sqrt{7m^2/4 - A_{lm}(\omega = m/2)}$. Comparing this result with Eqs. (8.3) and (8.5), we can see the two sets of frequencies are essentially the *same* modes, although obtained in very different ways. Here $\mathcal{F}_0^2$ and δ^2 differ by 1/4, which is reasonable because in the eikonal limit $\mathcal{F}_0 \propto l$ and $\delta \propto l$ (making 1/4 a higher-order correction).

To build intuition about $\mathcal{F}_0$ and δ, we look at V_r for extreme Kerr BHs, with ω replaced by $m/2$:

$$V_r = L^2\frac{(r-1)^2}{(r^2+1)^2}\left[\frac{(r+1)^2}{4}\mu^2 - \alpha(\mu) + \frac{3}{4}\mu^2\right], \tag{8.6}$$

where $L \equiv l + 1/2$ and $\alpha(\mu) \equiv A_{lm}/L^2$. According to the WKB analysis of the radial Teukolsky equation [20], the QNM frequencies are determined by the peak of the potential. As shown in Fig. 8.2, when μ is large the maximum of the potential is at the horizon, $r = 1$, as expected for ZDMs. As μ decreases and falls below some critical value μ_c, the peak moves outside the horizon, and the horizon becomes a local minimum of the potential. At the peak ω_I is nonzero because

$d^2V_r/dr_*^2|_{r_0} \neq 0$, so we have DMs. The criterion for having no peak outside the horizon is

$$\frac{(r+1)^2}{4}\mu^2 - \alpha(\mu) + \frac{3}{4}\mu^2 > 0 \quad \text{for} \quad r = 1\,, \tag{8.7}$$

i.e., $\mathcal{F}_0^2 > 0$ (or $\delta^2 > 0$). The values at which $\mathcal{F}_0^2$ (or δ^2) vanish lead to the condition for the critical μ_c: $\alpha(\mu_c) = \frac{7}{4}\mu_c^2$. If we use the approximation $\alpha(\mu) \approx 1 - a^2\omega^2(1-\mu^2)/(2L^2)$ [15] (i.e. Chapter 7), this will reproduce Hod's approximate analytical result $\mu_c \approx [(15-\sqrt{193})/2]^{1/2}$ [16]. We can obtain the exact μ_c (in the eikonal limit) by inserting $\alpha(\mu_c) = \frac{7}{4}\mu_c^2$ into the Bohr-Sommerfeld condition for α derived in [15] (i.e. Chapter 7):

$$\int_{\theta_-}^{\theta_+} \sqrt{\alpha - \frac{\mu^2}{\sin^2\theta} + \frac{\mu^2}{4}\cos^2\theta}\,d\theta = (1-|\mu|)\pi, \tag{8.8}$$

where $\theta_+ = \pi - \theta_-$ and $\theta_- = \arcsin(\sqrt{3}-1)$ are the angles at which the integrand vanishes. Therefore we have

$$\mu_c = \frac{1}{1+\mathcal{I}/\pi}, \quad \mathcal{I} = \int_{\theta_-}^{\theta_+} d\theta \sqrt{\frac{7}{4} - \frac{1}{\sin^2\theta} + \frac{1}{4}\cos^2\theta}, \tag{8.9}$$

which yields the numerical value $\mu_c \simeq 0.74398$. In the eikonal limit, when $\mu > \mu_c$ NEK BHs have only ZDMs ("single-phase regime") ; when $0 \leq \mu \leq \mu_c$, both DMs and ZDMs exist ("double-phase regime").

8.4 Phase boundary

Although there is a clear criterion for determining the boundary between the single-phase regime and the double-phase regime in the eikonal limit (when $\mu < \mu_c$, the peak of the potential no longer resides on the horizon) it is not immediately clear if a similar criterion holds when l is small. For scalar perturbations, however, we can write the radial Teukolsky potential for extreme-Kerr BHs with generic l, m, under the assumption that $\omega = m/2$ (and, therefore, the ${}_0A_{lm}$ remain real for the ZDMs):

$$V_r = \frac{(r-1)^2}{(r^2+1)^2}\left[\frac{(r+1)^2}{4}m^2 - {}_0A_{lm}\right] + \frac{(r-1)^2}{(r^2+1)^2}\left[\frac{3}{4}m^2 + \frac{(r-1)(2r^2+3r-1)}{(1+r^2)^2}\right]. \tag{8.10}$$

It is not difficult to see that there is still no peak outside the horizon when $\frac{7}{4}m^2 > {}_0A_{lm}$, or $\mathcal{F}_0^2 > 0$. For electromagnetic and gravitational perturbations the potential terms $-V_r$ are complex functions, thereby making the positions of their extrema more difficult to define. Detweiler [21], however, has shown that the radial function can be transformed so that it satisfies a differential equation with a real potential. Using this potential, the criterion to exclude peaks outside the

horizon is [19]:

$$\mathcal{F}_s^2 \equiv \frac{7}{4}m^2 - s(s+1) - {}_sA_{lm}\left(\omega = \frac{m}{2}\right) > 0. \tag{8.11}$$

Note that this expression respects the pairing symmetry ${}_{-s}A_{lm} = {}_sA_{lm} + 2s$, and that for all s, $\mathcal{F}_s^2$ and δ^2 differ from each other only by 1/4. For $s = 0, -2$ and $2 \leq l \leq 100$, we have searched all QNMs numerically and have not found any mode simultaneously satisfying $\delta^2 < 0$ and $\mathcal{F}_s^2 > 0$; therefore, the sign of δ^2 also determines whether a peak exists outside the horizon. In addition, we have used Leaver's continued-fraction algorithm to determine the phase boundary numerically. As shown in Fig. 8.1, the actual phase boundary matches the criterion predicted by the eikonal limit, $\mu = \mu_c$. In addition, for scalar and gravitational perturbations, we find numerically that modes are in the single-phase regime when $\mathcal{F}_s^2 > 0$ for all $l \leq 15$. This reinforces our physical understanding that DMs are associated with a peak of the potential outside the horizon, while ZDMs are somewhat similar in nature to the s-modes in ultracompact stars [18].

8.5 Bifurcation

Schwarzschild and slowly spinning Kerr BHs have a single set of QNMs for each l, m that are characterized by their overtone number n. If the ZDMs originate from modes at higher-n than the DMs when the BH spin is low, then when the spin increases beyond a critical value $a_s = 1 - \epsilon_s$, a single set of QNMs may split into two branches.

We numerically investigate this bifurcation effect by examining the complex QNM frequency plane to search for solutions of Leaver's continued-fraction equations [17, 19]. In Fig. 8.3, we plot the contours of constant value of the logarithm of the continued-fraction expansion, truncating at $N = 800$ terms. The QNM frequencies correspond to the local minima of this sum, where the contours cluster. The shading indicates the value of the fraction, with darker values nearly zero.

When $\mu < \mu_c$, a single set of QNMs splits into two branches for increasing a (see the left-hand panels of Fig. 8.3, where $l = 10$, $m = 7$, as the spin increases from $a = 0.9990$ to $a = 0.9999$ from the upper panel to the lower). The ZDM branch is quite accurately described by Eq. (8.3); the imaginary part of the ZDMs scales like $\sqrt{\epsilon}$, and they move towards the real axis as $\epsilon \to 0$. The DM branch changes relatively little with increasing spin (it is expected that the WKB peak can only support a finite number of modes [19], and there are only 3 DMs in the lower-left panel). In this case, the WKB formulae of [15] (i.e. Chapter 7) are in good agreement with the lowest-overtone DM (marked with a $\times$ in the figure).

For $\mu > \mu_c$ there is no bifurcation, and the modes are predicted fairly well by Eq. (8.3). We can see this in the right-hand panels of Fig. 8.3, where $l = 10$, $m = 8$ and we again raise the spin from $a = 0.9990$ to $a = 0.9999$. For the $m = 8$ modes, we also mark the leading-order WKB prediction of Eq. (8.5) with a box. For the bifurcation effect, we can define a benchmark $a_c = 1 - \epsilon_c$ as the BH

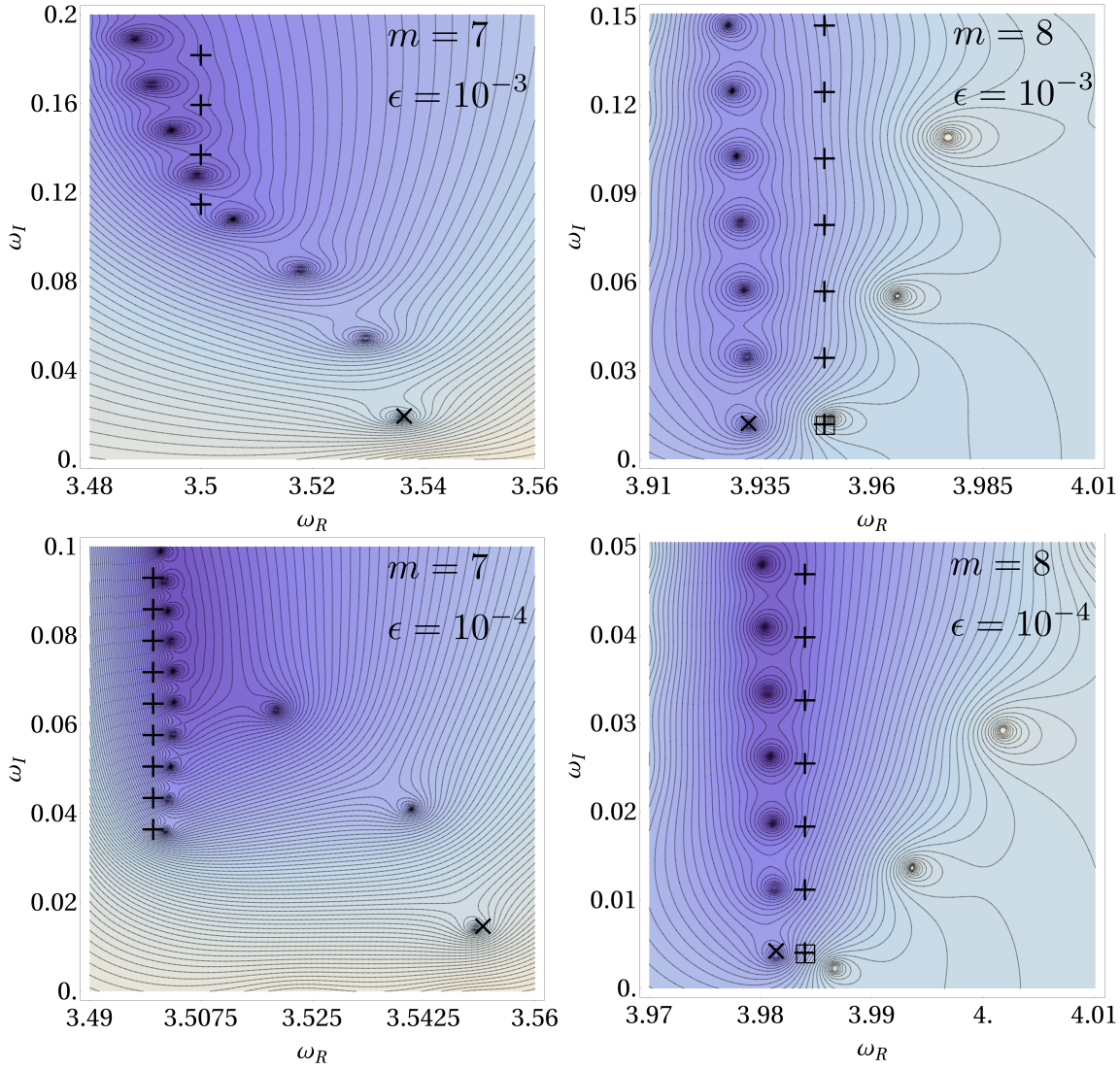

Figure 8.3: (Color online.) QNM frequencies with $l = 10$ for NEK BHs. Contours are constant values of the logarithm of the continued fraction in the complex plane; darker shading indicates values near zero. The + symbols are the ZDM predictions, a × is the lowest-overtone WKB prediction from [15] (i.e. Chapter 7), and the box is centered at the WKB prediction from Eq. (8.5). No branching is observed for modes with $m = 8$. Note that the closed contours with light shading have large values and do not correspond to any QNM. Further discussion of the figure is in the text.

spin at which the imaginary part of the *fundamental* ZDM is equal to that of the *fundamental* DM:

$$\frac{\sqrt{\epsilon_c}}{2\sqrt{2}}(1 + 2|\delta|) = \frac{1}{2}\frac{\sqrt{2V_r''}}{\partial_\omega V_r}\bigg|_{r_0} . \tag{8.12}$$

The right-hand side of Eq. (8.12) can be evaluated using the approximate WKB formula in [15] (i.e. Chapter 7). Since both sides of Eq. (8.12) depend on ϵ, we solve for ϵ_c iteratively; this converges quickly for a variety of initial spins. By computing ϵ_c for $l \leq 15$ and $0 < m < (l + 1/2)\mu_c$, we find

that $L^2\epsilon_c = 10^{-3}(11.6 - 3.12\mu - 18.0\mu^2)$ is a reasonable fitting formula. For the $l = 10$, $m = 7$ case, Eq. (8.12) gives $\epsilon_c \sim 10^{-5}$, which is in agreement with numerical results; for the $l = 2$, $m = 1$ case it gives $\epsilon_c \sim 10^{-3}$.

In Fig. 8.3, however, it is clear that the bifurcation actually starts when the *fundamental* ZDM's imaginary part equals the imaginary part of the *highest-overtone* DM (in Fig. 8.3 it is the third overtone). This happens at a spin $a_s < a_c$. Because we do not have a good estimate of the number of modes in the DM branch (beyond the fact that it should be proportional to L and a function of μ in the eikonal limit [19]) and because WKB techniques are not accurate for these high-overtone DMs, finding an analytic solution for a_s remains an open problem.

8.6 Conclusions

We identified two different regimes in the NEK QNM spectrum. In the double-phase regime, we found that the lowest ZDM becomes less damped than the lowest DM at some critical a_c, for which we provided an analytical estimate. For sufficiently large a, Eq. (8.3) is accurate at the least for those ZDMs with smaller decays than the point where the branches bifurcate. We estimate that the number of ZDMs below the bifurcation is $\propto \sqrt{\epsilon_s/\epsilon}$ [19]. In the future, we would like to investigate the behavior of the ZDM branch in the high-overtone limit [22], where these approximations break down.

Bibliography

[1] L. W. Brenneman *et al.*, Astrophys. J. **736**, 103 (2011).

[2] R. Wald, Ann. Phys., **83**, 548, (1974); S. Hod, Phys. Rev. Lett. **100** 121101 (2008); T. Jacobson and T. P. Sotiriou, Phys. Rev. Lett. **103**, 141101 (2009); E. Barausse, V. Cardoso, and G. Khanna, Phys. Rev. Lett. **105**, 261102 (2010); P. Zimmerman, I. Vega, E. Poisson, and R. Haas (2012), arXiv:1211.3889.

[3] A. Strominger and C. Vafa, Phys. Lett. B **379**, 99 (1996).

[4] J. Bardeen and G. T. Horowitz, Phys. Rev. D **60**, 104030 (1999).

[5] M. Guica, T. Hartman, W. Song, and A. Strominger, Phys. Rev. D **80**, 124008 (2009); O. J. C. Dias, H. S. Reall, and J. E. Santos, JHEP **0908**, 101 (2009); I. Bredberg, C. Keeler, V. Lysov, and A. Strominger, Nucl. Phys. Proc. Suppl. **216**, 194 (2011); G. Compere, Living Rev. Rel. **15**, 11 (2012).

[6] G. Dotti, R. J. Gleiser, I. F. Ranea-Sandoval, and H. Vucetich, Class. Quant. Grav. **25**, 245012 (2008); P. Pani, E. Barausse, E. Berti, and V. Cardoso, Phys. Rev. D **82**, 044009 (2010); G. Dotti, R. J. Gleiser, and I. F. Ranea-Sandoval, Class. Quant. Grav. **29**, 095017 (2012); J. Lucietti and H. S. Reall, Phys. Rev. D **86**, 104030 (2012).

[7] E. Berti, V. Cardoso, and A. O. Starinets, Class. Quant. Grav. **26**, 163001 (2009).

[8] I. Bredberg, T. Hartman, W. Song, and A. Strominger, JHEP **1004**, 019 (2010).

[9] S. A. Teukolsky and W. H. Press, Astrophys. J. **193**, 443 (1974).

[10] S. Detweiler, Astrophys. J. **239**, 292 (1980).

[11] M. Sasaki and T. Nakamura, Gen. Rel. Grav. **22**, 1351 (1990).

[12] N. Andersson and K. Glampedakis, Phys. Rev. Lett. **84**, 4537 (2000).

[13] S. Hod, Phys. Rev. D **78**, 084035 (2008).

[14] V. Cardoso, Phys. Rev. D **70**, 127502 (2004).

[15] H. Yang, D. A. Nichols, F. Zhang, A. Zimmerman, Z. Zhang, and Y. Chen, Phys. Rev. D **86**, 104006 (2012).

[16] S. Hod, Phys. Lett. B **715**, 348 (2012).

[17] E. W. Leaver, Proc. R. Soc. A **402**, 285 (1985); E. W. Leaver, Phys. Rev. D **34**, 384 (1986).

[18] S. Chandrasekhar and V. Ferrari, Proc. Roy. Soc. Lond. A **434**, 449 (1991).

[19] H. Yang, F. Zhang, A. Zimmerman, D. A. Nichols, E. Berti, and Y. Chen, in preparation.

[20] S. Iyer and C. M. Will, Phys. Rev. D **35**, 3621 (1987).

[21] S. Detweiler, Proc. R. Soc. A **352**, 381, (1977).

[22] E. Berti, V. Cardoso, and S. Yoshida, Phys. Rev. D **69**, 124018 (2004); U. Keshet and A. B. Meir (2012), arXiv:1207:2460.